

THE SOVIET-AMERICAN
CONFERENCE ON
COSMOCHEMISTRY OF THE
MOON AND PLANETS

CASE FILE
COPY



NATIONAL AERONAUTICS AND SPACE ADMINISTRATION

THE SOVIET-AMERICAN CONFERENCE ON COSMOCHEMISTRY OF THE MOON AND PLANETS

Edited by

John H. Pomeroy
NASA Headquarters

and

Norman J. Hubbard
NASA Johnson Space Center

A conference held in Moscow, U.S.S.R.,
June 4-8, 1974



Scientific and Technical Information Office

NATIONAL AERONAUTICS AND SPACE ADMINISTRATION

1977
Washington, D.C.

For sale by the Superintendent of Documents,

U.S. Government Printing Office, Washington, D.C. 20402

(2-Part Set; Sold in Sets Only) Stock Number 033-000-00633-1

Library of Congress Catalog Card Number 75-600013

Preface

The joint Soviet-American Conference on the Cosmochemistry of the Moon and Planets was held in Moscow, June 4-8, 1974. It was proposed by the Soviets, primarily as a conference on the chemistry of the Moon, and was agreed to by the United States during the joint meeting on cooperation in space held in August 1971. At that time, we envisioned that it would occur within one to two years. Several factors led to delaying the date of the Conference, the main ones being a problem of scheduling around the annual Houston Lunar Science Conferences and, more important, a desire to wait until the end of the Apollo program so that the scientific contributions might not become outdated within a few months. During the gestation period between 1971 and 1973, it became evident to both the United States and the USSR that data from the successful U.S. Mariner 9 mission to Mars and the Soviet Venera mission to Venus were not only pertinent but essential to the lunar discussions, as were new data and theories on Jupiter, comets, and meteorites. Thus, the content of the Conference was expanded to become "cosmochemical" and to include the planets in the broadest sense. I believe that this format, emphasizing comparative planetology, will become the norm for all similar future conferences.

I judge the Conference to have been a success. Papers were lucidly presented, most visual material was prepared especially for the Conference, the Soviet interpreters and translators were excellent, and significant exchanges of ideas and data did occur on the personal level. A key ingredient in this, evident in the preparatory work leading up to and continuing at the Conference, was a clear recognition by all concerned of the scientific contributions by both the United States and the USSR and a gratifying lack of protocol and paperwork. The tone for this was admirably set by Academician A. P. Vinogradov.

The formal papers of the Conference, contained in this volume and in a companion volume printed in the USSR, should stand for many years as one of the best consolidated treatises on the state of our knowledge of planetology and cosmochemistry. The other benefits of the joint Conference, such as an increased respect for each other's ideas and capabilities, cannot be similarly committed to paper but may, in the long run, be the more valuable.

NOEL W. HINNERS
*Associate Administrator
for Space Science*

Page intentionally left blank

Page intentionally left blank

Foreword

In the course of the last several years the possibility has developed for extensive studies of the material of the Moon, thanks to samples brought back from the Moon's surface by man or with the help of automatic space stations. Samples of soil and rocks have been returned from five maria: Mare Tranquillitatis, Oceanus Procellarum, Mare Imbrium, Mare Serenitatis, and Mare Fecunditatis; and from three terra regions of the Moon's nearside: the Fra Mauro region, the central highlands near the crater Descartes, and the highland region between Mare Fecunditatis and Mare Crisium. Through extensive study of these samples by scientists of many countries, a huge quantity of data has been accumulated about the physical, chemical, petrographic, mineralogical, and geochemical features of lunar rocks. Along with the great general similarity of some surface rocks of the Moon, especially lunar basalts, to basic igneous rocks of the Earth's crust, i.e., tholeiitic basalts, differences also have been found between the character of lunar rocks and that of terrestrial rocks. Many cardinal questions arise on comprehensive examination of all the extensive data that have resulted from study of the material of the Moon and planets.

The present volumes contain papers presented at the Soviet-American Conference on the Cosmochemistry of the Moon and Planets held in Moscow from the 4th to the 8th of June, 1974. The basic goal of the conference was consideration of the origin of the planets of the solar system, based on the physical and chemical data obtained by study of the material of the Moon and planets.

Papers at the conference were presented in the following sessions:

1. Differentiation of the material of the Moon and planets
2. The thermal history of the Moon
3. Lunar gravitation and magnetism
4. Chronology of the Moon, planets, and meteorites
5. The role of exogenic factors in the formation of the lunar surface
6. Cosmochemical hypotheses about the origin and evolution of the Moon and planets
7. New data about the planets Mercury, Venus, Mars, and Jupiter

The results presented in the papers are of exceptional scientific interest since on the one hand they contain new knowledge about the matter of the Moon and planets, while on the other they summarize significant material accumulated during recent years as the result of spacecraft missions to the Moon, Venus, Mars, Mercury, and Jupiter.

During consideration of the problem of accretion of the Moon and other planets, attention has turned to the possibility of an inhomogeneous protoplanetary nebula. Differentiation of the matter of the Moon into concentric layers, and especially the formation of a lunar crust, has directed

much attention to the mechanism of formation, composition, and thickness of the lunar crust. Hypotheses about the formation of the mascons of the circular maria on the Moon were reviewed during the conference.

Significant material about the mineralogical, petrographic, and chemical composition of igneous lunar rocks (basalts, norites, anorthosites) as well as the lunar regolith, permitted the presentation of ideas about their formation to be based on comparison with analogous terrestrial rocks.

Significant interest was aroused by consideration of questions about the composition of rocks, particularly those within the interior of the Moon. Numerous data give no indication of a metallic core in the Moon. Problems of magnetic, gravitational, and thermal fields of the Moon were considered. Papers also dealt with the role of exogenic factors in the transformation of rocks on the lunar surface and in the development of the lunar landscape. Especially memorable were the new images of the surface of Mars, which is significantly more complex than the lunar surface, and the images of the surface of Mercury, whose relief is analogous to that of the lunar surface.

A view was given of "lunar" topography found on Venus by Earth based observations, and a movie was shown which illustrated the dynamics of the cloud layer of Venus. Finally, from the results of an American automatic spacecraft, scientists acquired the first data on the possible composition of the outer layers of Jupiter.

All of this taken together permitted participants of the conference to gain a fuller understanding of, and to propose models for, the origin and evolution of the Moon and planets of the solar system.

The work presented at the conference contains extensive and original information about the cosmochemistry of the Moon and planets.

Academician A. P. Vinogradov
Academy of Sciences of the USSR

Contents

	<i>Page</i>
Preface	iii
Noel W. Hinners	
Foreword	v
Vinogradov	
DIFFERENTIATION OF LUNAR AND PLANETARY MATTER	
Differentiation of the Matter of the Moon	5
A. P. Vinogradov	
A Survey of Lunar Rock Types and Comparison of the Crusts of Earth and Moon	35
John A. Wood	
Geochemical Zoning and Early Differentiation in the Moon	55
S. R. Taylor and P. Jakes	
Evolution of the Moon: the 1974 Model	63
Harrison H. Schmitt	
Petrogenesis of Lunar Rocks: Rb-Sr Constraints and Lack of H ₂ O	81
Arden L. Albee and Alexander J. Gancarz	
Lunar Highland Rock Types: Their Implications for Impact-Induced Fractionation	91
W. C. Phinney, J. L. Warner, and C. H. Simonds	
Lunar Igneous Rocks and the Nature of the Lunar Interior	127
James Fred Hays and David Walker	
A Chemical Model for Lunar Non-Mare Rocks	137
Norman J. Hubbard and J. Michael Rhodes	
Lunar Elemental Analysis Obtained from the Apollo Gamma-Ray and	153
X-Ray Remote Sensing Experiment	
J. I. Trombka, J. R. Arnold, I. Adler, A. E. Metzger, and R. C. Reedy	
Comparison of Lunar Rocks and Meteorites: Implications to Histories of	183
the Moon and Parent Meteorite Bodies	
Martin Prinz, R. V. Fodor, and Klaus Keil	
Radioactivity of the Moon, Planets, and Meteorites	201
Yu. A. Surkov and G. A. Fedoseyev	
The Effect of Temperature and Pressure on the Distribution of Iron Group	219
Elements Between Metal and Olivine Phases in the Process of	
Differentiation of Protoplanetary Material	
A. P. Vinogradov, N. P. Il'yin, and L. N. Kolomeytseva	
The Chemical Composition of the Cores of the Terrestrial Planets and the Moon	231
O. L. Kuskov and N. I. Khitarov	

	<i>Page</i>
To the Problem About the Origin of Lunar Maria and Continents ----- (Mössbauer Investigations)	243
T. V. Malysheva	
The Surface Abundance and Stratigraphy of Lunar Rocks from Data ----- About Their Albedo	253
V. V. Shevchenko	
New Data for the Luna 20 Core and a Survey of Published Chemical Data -----	259
N. J. Hubbard, A. P. Vinogradov, G. I. Ramendik, and M. S. Chupakhin	
Chemical Composition of Crystalline Rock Fragments from Luna 16 ----- and Luna 20 Fines	263
A. Cimbáľníková, M. Palivcová, J. Frána, and A. Maštalka	
Investigation of the Composition of the Luna 16 Lunar Sample -----	277
L. Bakos, M. Chayka, L. Cher, A. Cheke, N. N. Dogadkin, A. Elek, K. Kulchar, A. Nagy, D. L. Nagy, E. Szabo, B. Forzats, and E. Zemplén	
THERMAL HISTORY OF THE MOON	
In-Situ Measurements of Lunar Heat Flow -----	283
Marcus G. Langseth and Stephen J. Keihm	
The Evolution of the Moon and the Terrestrial Planets -----	295
M. Nafi Toksöz and David H. Johnston	
Heat Flow and Thermal History of the Moon -----	329
Ye. A. Lyubimova	
Calculations of the Moon's Thermal History at Different Concentrations of Radio- active Elements, Taking Into Account Differentiation on Melting -----	347
O. I. Ornatskaya, Ya. I. Al'ber, and I. L. Ryazantseva	
Riddles About the Origin and Thermal History of the Moon -----	367
B. Yu. Levin and S. V. Mayeva	
LUNAR MAGNETISM AND GRAVITY	
Results From the Apollo Passive Seismic Experiment -----	389
Gary Latham, Yosio Nakamura, James Dorman, Frederick Duennebie, Maurice Ewing, and David Lammlein	
Lunar Mascons -----	403
V. N. Zharkov and A. P. Trubitsyn	
Some Geologic Observations Concerning Lunar Geophysical Models -----	407
James W. Head	
Magnetic and Dielectric Properties of Lunar Samples -----	417
D. W. Strangway, G. W. Pearce, and G. R. Olhoeft	
Magnetic Field in Le Monnier Bay According to Data of Lunokhod 2 -----	433
Sh. Sh. Dolginov, Ye. G. Yeroshenko, L. N. Zhuzgov, V. A. Sharova, G. A. Vnuchkov, B. A. Okulesky, and A. T. Bazilevsky	
Deep Electromagnetic Sounding of the Moon with Lunokhod 2 Data -----	443
L. L. Van'yan, I. V. Yegorov, and E. B. Faynberg	
Lunar Electrical Conductivity, Permeability, and Temperature from ----- Apollo Magnetometer Experiments	447
P. Dyal, C. W. Parkin, and W. D. Daily	

	<i>Page</i>
On the Mechanism of the Magnetic Dynamo of the Planets -----	493
Sh. Sh. Dolginov	
The Intensity of the Ancient Lunar Field from Magnetic Studies on Lunar Samples -----	499
A. Stephenson, D. W. Collinson, and S. K. Runcorn	
CHRONOLOGY OF THE MOON, PLANETS, AND METEORITES	
Early History of the Moon: Implications of U-Th-Pb and Rb-Sr Systematics -----	507
Mitsunobu Tatsumoto, Paul D. Nunes, and Daniel M. Uhrh	
^{39}Ar - ^{40}Ar Dating of Basalts and Rock Breccias from Apollo 17 and -----	525
the Malvern Achondrite	
T. Kirsten and P. Horn	
The Exposure History of the Apollo 16 Site: An Assessment Based on -----	541
Methane and Hydrolysable Carbon Measurements	
C. T. Pillinger, G. Eglinton, A. P. Goward, A. J. T. Jull, and J. R. Maxwell	
Pre-Mare Cratering and Early Solar System History -----	553
G. W. Wetherill	
THE ROLE OF EXOGENIC FACTORS IN THE FORMATION OF THE LUNAR SURFACE	
The Role of Exogenic Factors in the Formation of the Lunar Surface -----	571
K. P. Florenskiy, A. T. Bazilevskiy, and A. V. Ivanov	
Microcraters on Lunar Samples -----	585
H. Fechtig, W. Gentner, J. B. Hartung, K. Nagel, G. Neukum, E. Schneider, and D. Storzer	
The Micrometeoroid Complex and Evolution of the Lunar Regolith -----	605
F. Hörz, D. A. Morrison, D. E. Gault, V. R. Oberbeck, W. L. Quaide, and J. F. Vedder,	
D. E. Brownlee, and J. B. Hartung	
Lunar Highlands Breccias Generated by Major Impacts -----	637
Odette B. James	
Meteoritic Material on the Moon -----	659
John W. Morgan, R. Ganapathy, Hideo Higuchi, and Edward Anders	
Primary Cosmic Rays on the Lunar Surface -----	691
S. N. Vernov and A. K. Lavrukhina	
Results of Special Mechanical Analyses of Luna 16 Material -----	697
H. Stiller, H. Vollstädt, R. Wäsch, P. Bankwitz, E. Bankwitz, F. C. Wagner, and J. Schön	
The Analysis of Various Size, Visually Selected and Density and Magnetically -----	703
Separated Fractions of Luna 16 and 20 Samples	
The Royal Society Lunar Sample Investigation Team (G. Eglinton, A. P. Goward, A. J. T. Jull,	
C. T. Pillinger, S. O. Agrell, J. E. Agrell, J. V. P. Long, S. H. U. Bowie, P. R. Simpson,	
R. D. Beckinsale, J. J. Durham, G. Turner, P. H. Cadogan, T. C. Gibb, R. Greatrex,	
N. N. Greenwood, D. W. Collinson, S. K. Runcorn, A. Stephenson, S. A. Durrani,	
J. H. Fremlin, F. S. W. Hwang, and H. A. Khan)	
Mössbauer Spectroscopy of Iron in the Luna 20 Regolith -----	729
T. Zemčík and K. Raclavsky	
The Main Peculiarities of the Processes of the Deformation and -----	735
Destruction of Lunar Soil	
A. K. Leonovich, V. V. Gromov, A. D. Dmitriyev, V. N. Penetrigov, P. S. Semenov,	
and V. V. Shvarev	

	<i>Page</i>
The Radiation History of Matter Returned by the Soviet Automatic Stations Luna 16 and Luna 20, According to Track Studies L. L. Kashkarov, L. I. Genayeva, and A. K. Lavrukhina	745
Antipodes on the Moon Yu. N. Lipsky and Zh. F. Rodionova	755
Measurement of the Optical Properties of Lunar Rocks in the Transition Zone, Resulting from Observations Made by Lunokhod-2 Yu. N. Lipskiy and V. V. Shevchenko	763
COSMOCHEMICAL HYPOTHESES OF THE ORIGIN AND EVOLUTION OF THE MOON AND PLANETS	
Clues in the Rare Gas Isotopes to Early Solar System History John H. Reynolds	771
Heterogeneities in the Solar Nebula Robert N. Clayton, Lawrence Grossman, Toshiko K. Mayeda, and Naoki Onuma	781
Chemical Fractionation in the Solar Nebula Lawrence Grossman	787
Time Scale for the Formation of the Earth and Planets and Its Role in Their Geochemical Evolution V. S. Safronov	797
Mechanical Processes Affecting Differentiation of Proto-Lunar Material W. M. Kaula	805
The Origin of the Moon Ye. L. Ruskol	815
Formation and Composition of the Moon Don L. Anderson	823
NEW DATA ON THE PLANETS	
The Interior Structure of Jupiter (Consequences of Pioneer 10 Data) R. Smoluchowski	849
The Magnetic Field of Mars Estimated from the Data of Plasma Measurements by Soviet Artificial Satellites of Mars K. I. Gringauz, V. V. Bezrukikh, T. K. Breus, M. I. Verigin, and A. P. Remizov	859
Television Observations of Mercury by Mariner 10 Bruce C. Murray, Michael J. S. Belton, G. Edward Danielson, Merton E. Davies, Donald E. Gault, Bruce Hapke, Brian O'Leary, Robert G. Strom, Verner Suomi, and Newell Trask	865
Studies of Chemical Abundances in the Outer Solar System Tobias Owen	887
The Use of Ground-Based Telescopes in Determining the Composition of the Surfaces of Solar System Objects Thomas B. McCord and John B. Adams	893
Comets: Data, Problems, and Objectives Fred L. Whipple	923

part 2

section 4

Chronology of the Moon, Planets, and Meteorites

Early History of the Moon: Implications of U-Th-Pb and Rb-Sr Systematics

Mitsunobu Tatsumoto, Paul D. Nunes,
and Daniel M. Unruh
*U. S. Geological Survey
Denver, Colorado*

Anorthosite 60015 contains the lowest initial $^{87}\text{Sr}/^{86}\text{Sr}$ ratio (0.69884 ± 0.00004) yet reported for a lunar sample. The initial ratio is equal to that of the achondrite Angra dos Reis and slightly higher than the lowest measured $^{87}\text{Sr}/^{86}\text{Sr}$ ratio for an inclusion in the C3 carbonaceous chondrite Allende. The Pb-Pb ages of both Angra dos Reis and Allende are 4.62×10^9 yr. Thus, the initial $^{87}\text{Sr}/^{86}\text{Sr}$ ratio found in lunar anorthosite 60015 strongly supports the hypothesis that the age of the Moon is about 4.65 b.y. The $^{238}\text{U}/^{204}\text{Pb}$ value estimated for the source of the excess lead in "orange soil" 74220 is ~ 35 and lower than the values estimated for the sources of KREEP (600–1000), high-K (300–600), and low-K (100–300) basalts. We hypothesize from these and other physical, chemical, and petrographic results that (1) the Moon formed ~ 4.65 b.y. ago; (2) a global-scale gravitational differentiation occurred at the beginning of lunar history; and (3) the differentiation resulted in a radical chemical and mineralogical zoning in which the $^{238}\text{U}/^{204}\text{Pb}$ ratios increased toward the surface, with the exception of the low $^{238}\text{U}/^{204}\text{Pb}$ surficial anorthositic layer which "floated" at the beginning of the differentiation relative to the denser pyroxene-rich material. All Apollo and Luna U-Pb data which scatter about a 3.9–4.5-b.y. concordia chord (and its extension above concordia) and Rb-Sr whole-rock model ages older than 3.9 b.y. may be readily interpreted as reflecting multiple impact events occurring between ~ 4.5 b.y. and ~ 3.9 b.y. ago. We propose that the ~ 4.47 -b.y. age observed for some KREEP material corresponds to the "South Imbrium" impact event. Abundant Rb-Sr internal isochron and $^{40}\text{Ar}/^{39}\text{Ar}$ ages of lunar basalts indicate that a major period of mare basalt flooding occurred from ~ 3.8 b.y. to ~ 3.2 b.y. ago.

The purposes of this paper are to present an extremely primitive $^{87}\text{Sr}/^{86}\text{Sr}$ ratio observed in lunar anorthosite 60015, to compare the ratio to similar data obtained from meteorites, and to summarize how U-Th-Pb and Rb-Sr systematics of lunar samples relate to the early history of the Moon. Although we have tried to cite most of the important papers relating to this subject, no attempt has been made to complete an exhaustive bibliography of all U-Th-Pb and Rb-Sr reports, owing to space and time limitations.

Enrichment of refractory elements and deficiency in volatile elements in the lunar rocks and their source regions down to a few hundred kilometers depth relative to chondritic

and terrestrial abundances have been well documented by many investigations. For example, Vinogradov (refs. 1 and 2), Ganapathy et al. (refs. 3 and 4), Ganapathy and Anders (ref. 5), Gast et al. (ref. 6), and Haskin et al. (ref. 7) clearly demonstrated that volatile chalcophile (Ag, Zn, Cd, In, Tl, and Bi) and siderophile (Au, Ir, Co, and Ni) elements are depleted in lunar rocks, whereas refractory elements (Ca, Zr, Hf, Ta, and rare earth elements) are tenfold to hundredfold enriched relative to chondritic abundances. The Lunar Sample Preliminary Examination Team (LSPET) (refs. 8 and 9) and Tera et al. (ref. 10) have shown that alkali elements are depleted in Apollo 11

rocks, and the K/U ratios of lunar material (~ 2500) are low compared to terrestrial (10^4) and chondritic (8×10^4) values. Chronological studies have also shown that the U/Pb ratios are high and the Rb/Sr ratios low in lunar material (e.g., refs. 11 through 14). These unique features have been interpreted as being due to the preferential accretion of high-temperature condensates in the later stage of the Moon's formation from the solar nebula (refs. 6 and 15). Alternatively, it might be argued that some volatile elements escaped from a dominantly chondritic Moon during accretion. Although it is still debatable whether the Moon originally accreted heterogeneously or homogeneously, geophysical, geochemical, and petrological studies indicate that the Moon is now heterogeneously zoned both chemically and mineralogically.

Initial $^{87}\text{Sr}/^{86}\text{Sr}$ for Meteorites

If a rock of a planetary body is Rb free and remains closed with respect to Rb and Sr migration, the $^{87}\text{Sr}/^{86}\text{Sr}$ ratio is constant from the time of rock formation. The lower the $^{87}\text{Sr}/^{86}\text{Sr}$ ratio in such a rock, the earlier we infer that it formed and that the host planetary body must have separated from the solar nebula. This reasoning assumes that the solar nebula had a uniform Sr isotopic composition and Rb/Sr ratio at the time of its formation. Achondrites are nearly Rb free, and the initial $^{87}\text{Sr}/^{86}\text{Sr}$ ratio can be determined rather accurately. Extensive studies on initial $^{87}\text{Sr}/^{86}\text{Sr}$ values in different planetary bodies have been performed, especially by Wasserburg's group. Papanastassiou and Wasserburg (ref. 16) reported a primitive initial $^{87}\text{Sr}/^{86}\text{Sr}$ value of BABI (Basaltic Achondrite Best Initial) for seven basaltic achondrites. Since then, $\text{BABI} = 0.69897 \pm 0.00003$ (standardized) has been used as a reference value to calculate Rb-Sr model ages of planetary bodies.

All laboratories normalize their Sr data to $^{86}\text{Sr}/^{88}\text{Sr} = 0.11940$ to correct for mass fractionation. Measured $^{87}\text{Sr}/^{86}\text{Sr}$ ratios among

different laboratories, however, reflect a small bias which must be considered if meaningful comparison of very precise $^{87}\text{Sr}/^{86}\text{Sr}$ ratios measured in the different laboratories is to be made. The National Bureau of Standards' SRM-987 $^{87}\text{Sr}/^{86}\text{Sr}$ ratios (the certified value is 0.71014) obtained in Wasserburg's, Nyquist's, and our laboratories are 0.71015, 0.71026, and 0.71018, respectively. In this paper, we standardize all data to the NBS value.

Papanastassiou (ref. 17) reported a lower initial $^{87}\text{Sr}/^{86}\text{Sr}$ ratio for the augite achondrite Angra dos Reis ($\text{ADOR} = 0.69883 \pm 0.00003$) and suggested the achondrite was formed earlier than other achondrites. Recent $^{207}\text{Pb}/^{206}\text{Pb}$ age determinations of three achondrites—Angra dos Reis, Sioux County, and Nuevo Laredo (ref. 18)—support Papanastassiou's relative age interpretation. Using the Canyon Diablo troilite Pb as a common initial Pb, Tatsumoto et al. (ref. 18) calculated a $^{207}\text{Pb}/^{206}\text{Pb}$ age of 4.62×10^9 yr for the angrite Angra dos Reis and ages $\sim 30 \times 10^6$ yr younger than this for the eucrites, Sioux County, and Nuevo Laredo.

A more primitive initial $^{87}\text{Sr}/^{86}\text{Sr}$ ratio for Ca-Al-rich chondrules separated from the Allende carbonaceous chondrite was reported by Gray et al. (ref. 19) ($\text{ALL} = 0.69876 \pm 0.00002$) and Wetherill et al. (ref. 20) (0.69880). Theoretical and petrographic studies suggest that the Ca-Al-rich inclusions in Allende are among the earliest condensates of the solar nebula (refs. 21 through 24). Although Wetherill et al. (ref. 20) observed that all their Allende Rb-Sr data points lay between lines corresponding to ages of 4.5 b.y. and 4.7 b.y., Gray et al. (ref. 19) showed, in their more extensive study, that the Allende inclusions do not form an isochron in a Rb-Sr evolution diagram. Rather, their data scattered between 4.63- and 3.59-b.y. BABI model ages. They concluded that the Rb-Sr isotopic systems in Allende may have been seriously disturbed within the past 3.6 b.y., and they further pointed out that the range of initial $^{87}\text{Sr}/^{86}\text{Sr}$ ratios they found for Allende inclusions

could reflect differences of time and possibly places of condensation from the solar nebula prior to agglomeration.

U-Pb Ages of Meteorites

Recently, Tatsumoto et al. (ref. 18) and Tilton (ref. 25) verified Patterson's (ref. 26) original meteorite age of 4.55 b.y. and reported more precise lead isotopic compositions and Pb-Pb ages of meteorites. Tilton (ref. 25) reported a whole-rock $^{207}\text{Pb}/^{206}\text{Pb}$ age of 4.635 b.y. for two carbonaceous and four ordinary chondrites, while Tatsumoto et al. (ref. 18) reported that the Pb-Pb age of Angra dos Reis is 4.62 b.y. and that two eucrites are 4.59 b.y. old, using the uranium decay constants $\lambda_{238\text{U}} = 0.15369 \times 10^{-9} \text{ yr}^{-1}$; $\lambda_{235\text{U}} = 0.97216 \times 10^{-9} \text{ yr}^{-1}$.

Tatsumoto et al. (ref. 27) reported a Pb-Pb "internal isochron" of the Allende meteorite that will be presented in detail elsewhere. Their analyses of the matrix material, a magnetic separate, and six inclusions (chondrules and aggregates) yielded a range of $^{206}\text{Pb}/^{204}\text{Pb}$ ratios from 9.9 to 56 and defined as isochron with a slope of 0.6188 ± 0.0016 (2σ , ref. 28) in a $^{207}\text{Pb}/^{204}\text{Pb}$ versus $^{206}\text{Pb}/^{204}\text{Pb}$ diagram. This line passes within error through the primordial Pb isotopic values (ref. 18) and corresponds to an age of 4.62 b.y. This age is in good agreement with the Pb-Pb age of Angra dos Reis, although the position of one chondrule below this line may reflect later "metamorphic processes," which Gray et al. (ref. 19) considered to explain the scatter they obtained for a Rb-Sr isochron plot of the various Allende inclusions.

In view of the irregularities displayed by Allende Rb-Sr data, it is perhaps surprising that the Pb isotope data are so linear. Because a Pb-Pb age is not sensitive to very recent U-Pb fractionation and the Allende inclusions do not yield concordant U-Th-Pb ages, it seems likely that the hypothesized time of the Rb-Sr system disturbance is very recent—possibly related to the breakup of a parent body. Angra dos Reis is a well-

differentiated augite-rich achondrite, but Allende is an agglomerate of chemically unequilibrated materials. We interpret the Allende 4.62-b.y. internal Pb-Pb isochron age as probably reflecting the time of agglomeration. The significance of the Pb-Pb age agreement and the initial $^{87}\text{Sr}/^{86}\text{Sr}$ difference between the two meteorites are not clear to us. The Pb-Pb age agreement for these two meteorites may indicate that the time span separating accretion of many planetesimal bodies was rather short. A detailed discussion about the inconsistency among Pb-Pb, Rb-Sr, and K-Ar ages (ref. 29) is beyond the scope of this paper. The above discussion is presented to show that Allende contains the most primitive $^{87}\text{Sr}/^{86}\text{Sr}$ ratio yet reported and that the Allende Pb-Pb internal isochron age is 4.62 b.y.

Initial $^{87}\text{Sr}/^{86}\text{Sr}$ of the Moon

If we find a lunar rock with an initial $^{87}\text{Sr}/^{86}\text{Sr}$ ratio as primitive as the meteorites discussed above, it would be indirect evidence for a similar old age of the Moon. The lunar anorthosites are excellent candidates for the search for primitive $^{87}\text{Sr}/^{86}\text{Sr}$ ratios because (1) they concentrate Sr and exclude Rb during crystallization and (2) at least some of them may have formed during an early stage of lunar differentiation (refs. 30 and 31). Rather primitive initial $^{87}\text{Sr}/^{86}\text{Sr}$ values as low as BABI have been reported for lunar anorthosites 15415 (0.69896 ± 0.00004 , ref. 32) and 60025 (0.69893 ± 0.00003 , ref. 33).

ANORTHOSITE 60015

The lunar rock 60015 is a football-sized, white, coarse-grained anorthosite coated with about a 1-cm-thick rind of dark-brown glass. The glass contains white fine-grained plagioclase clasts. The clasts appear to have been incorporated in the glass from either preexisting anorthosite or anorthositic breccia when the glass formed by meteoroid im-

pacting (as may be seen in refs. 34 and 35).

A coarse-grained interior gray plagioclase sample, a portion of plagioclase about 2 mm from the plagioclase-glass boundary, white plagioclase clasts in the glass, and the dark glass coating itself were all analyzed for Rb, Sr, U, Th, Pb, and K. The analytical results of the U-Th-Pb and the Rb-Sr analyses for these samples of 60015 are shown in tables 1 and 2, respectively. We obtained each $^{87}\text{Sr}/^{86}\text{Sr}$ ratio by averaging 10 sets of 20 ratios measured on an automated mass spectrometer, using programed magnet switching and online digital data acquisition and processing. The rubidium and strontium concentrations were determined by isotope-dilution analysis using ^{87}Rb and ^{84}Sr spikes. Corrections for mass spectrometric fractionation were made by normalization to $^{86}\text{Sr}/^{88}\text{Sr} = 0.11940$. The errors given in table 2 are twice the standard deviation of the mean. Interlaboratory comparison and reproducibility of our data were checked with replicate ^{84}Sr spiked runs of the National Bureau of Standards' standard SRM-987, which gave an average $^{87}\text{Sr}/^{86}\text{Sr}$ ratio of 0.710184 ± 0.000025 ($2\sigma_m$) for 10 separate Sr isotope analyses during this investigation.

The U-Pb data of various portions of anorthosite 60015 yield insight into times of Pb migration relative to U in the glass rind and interior of anorthosite 60015. In the following section, this age information is briefly considered in order to justify the ages used for the in-situ Rb decay corrections in calculating initial $^{87}\text{Sr}/^{86}\text{Sr}$ ratios.

U-Pb AGE OF 60015

As we previously discussed (ref. 36), although the Pb in the interior of anorthosite 60015 may have been slightly contaminated with terrestrial Pb, calculated U-Pb model ages of 3.57 and 3.80 b.y., using two- and three-stage U-Pb evolution models, respectively, agree well with the $^{40}\text{Ar}/^{39}\text{Ar}$ age of 3.55 ± 0.05 b.y. that Schaeffer and Husain (ref. 37) reported for this rock. Indeed, this agreement between the $^{40}\text{Ar}/^{39}\text{Ar}$ age and

the U-Pb model ages suggests that terrestrial Pb contamination in our sample of 60015 was negligible. In any case, these age data, together with the very primitive $^{87}\text{Sr}/^{86}\text{Sr}$ ratio observed in this anorthosite, indicate that Pb was probably introduced into the interior of a preexisting anorthosite about 3.5 to 4.0 b.y. ago due to metamorphism likely related to one or more impact events. Introduction of the Pb into anorthosite 60015 at this time was apparently accompanied by Ar loss from the plagioclase, as indicated by the $^{40}\text{Ar}/^{39}\text{Ar}$ age, and may have been accompanied by gain, or loss, of Rb as well.

U-Th-Pb data for the 60015 rind, plagioclase clasts within this rind, glassy white material taken from the glass-plagioclase boundary, plagioclase ~ 2 mm from the boundary, and gray plagioclase from the interior of the rock (table 1) are plotted in figure 1. Also plotted for reference in figure 1 is the Apollo 16 South Ray crater soil field (ref. 36).

The 60015 plagioclase clast sample and the glassy white boundary material (fig. 1) apparently both underwent an increase of their $^{206}\text{Pb}/^{207}\text{Pb}$ ratios and possibly a net gain

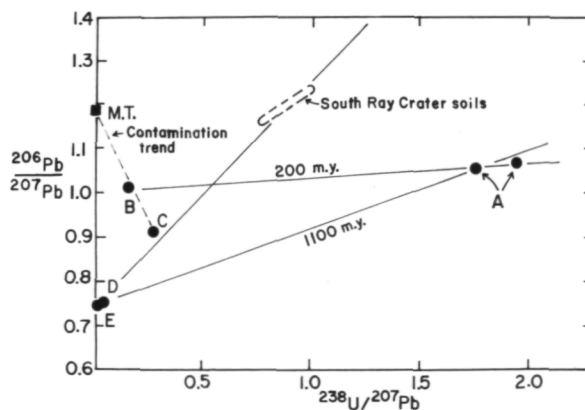


Figure 1.— $^{206}\text{Pb}/^{207}\text{Pb}$ versus $^{238}\text{U}/^{207}\text{Pb}$ plot for anorthosite 60015. Data are corrected only for blank. A = black glass rind; B = plagioclase clasts in the glass rind; C = glassy white-plagioclase boundary; D = plagioclase 2 mm inside the boundary; E = plagioclase interior; M.T. = modern terrestrial lead.

Table 1.—*U-Th-Pb Concentrations and Pb Isotopic Compositions of Anorthosite 60015 Samples*

Description	Comp.	Weight (mg)	Concentrations (ppm)			Observed Ratios ⁽¹⁾			Ratios Corrected Analytical Blank ⁽²⁾						
	Conc.		U	Th	Pb	$\frac{^{206}\text{Pb}}{^{204}\text{Pb}}$	$\frac{^{207}\text{Pb}}{^{204}\text{Pb}}$	$\frac{^{208}\text{Pb}}{^{204}\text{Pb}}$	$\frac{^{232}\text{Th}}{^{238}\text{U}}$	$\frac{^{235}\text{U}}{^{238}\text{U}}$	$\frac{^{206}\text{Pb}}{^{204}\text{Pb}}$	$\frac{^{207}\text{Pb}}{^{204}\text{Pb}}$	$\frac{^{208}\text{Pb}}{^{204}\text{Pb}}$	$\frac{^{207}\text{Pb}}{^{206}\text{Pb}}$	$\frac{^{208}\text{Pb}}{^{206}\text{Pb}}$
Black Glass Rind	P	165.5				219.9	205.5	220.9			251.8	236.0	245.2	0.9373	0.9738
	C1	108.0	0.409	1.539	0.566	231.9	217.0	—	3.89	628.4	345.6	324.1	—	0.9376	—
	C2	92.4	0.398	1.466	0.621	189.2	179.3	—	3.81	364.1	217.9	206.8	—	0.9491	—
Plagioclase Clast in the Glass Rind	P	117.7				29.26	27.17	47.27			33.15	31.34	50.82	0.9454	1.533
	C	87.7	0.0077	0.0248	0.1486	38.43	38.10	—	3.33	6.29	41.14	40.74	—	0.9902	—
Glassy White- Plagioclase Boundary	P	60.0				63.17	67.28	75.61			94.89	104.0	102.7	1.096	1.082
	C	80.0	0.0421	0.1567	0.3881	71.27	77.47	—	3.85	24.36	81.65	89.48	—	1.096	—
Plagioclase 2 mm From the Glass—Plagioclase Boundary	P	126.4				50.66	62.23	63.19			71.20	91.60	79.66	1.287	1.119
	C	115.2	0.0023	0.0060	0.171	73.82	95.66	—	2.70	4.32	107.9	144.5	—	1.339	—
Plagioclase Interior ⁽³⁾	P	375				70.27	92.52	79.03			75.45	100.27	83.35	1.329	1.105
	C	355	0.0009	0.0026	0.198	69.12	91.36	—	3.45	1.00	73.90	98.98	—	1.339	—

NOTES: (1) ²⁰⁶Pb spike contribution has been subtracted from concentration data.

(2) Analytical total Pb blanks ranged from 1.1 ng to 3.8 ng.

(3) From Nunes et al. (ref. 36).

of Pb relative to U when the glass rind formed. The glass rind itself lost much Pb relative to U during formation. It appears from figure 1 that (1) the U-Pb system of the plagioclase 2 mm from the plagioclase-glass boundary was very slightly or not at all affected by this event; (2) the plagioclase interior was negligibly affected; and (3) the plagioclase clast sample included in the glass was the most strongly affected plagioclase sample measured. If the Pb isotopic compositions of the glass rind and the plagioclase sample from within this glass rind completely equilibrated during the glass formation and these samples remained closed to the migration of U and Pb after glass formation, the line connecting these two samples (line BA, fig. 1) which corresponds to an age of ~ 200 m.y. dates the time of the glass rind formation.

The U concentrations of the black glass rind (~ 0.4 ppm, table 1), the South Ray Crater soils (~ 0.6 ppm, ref. 36), and the anorthosite interior (~ 0.0015 ppm U, ref. 36) suggest that the glass rind is a mixture of about ~ 65 percent soil and ~ 35 percent anorthosite.

Because evidence of Pb-isotope equilibration between the plagioclase clasts and the glass is elusive, the 200-m.y. age may have no meaning at all. In any case, a *maximum* age of glass formation of ~ 1.1 b.y. may be obtained from the line connecting the 60015 interior sample with the glass rind sample (line EA, fig. 1), since it is highly unlikely that the initial $^{206}\text{Pb}/^{207}\text{Pb}$ ratio in the glass was any lower than that in the anorthosite. The $^{40}\text{Ar}/^{39}\text{Ar}$ temperature-release pattern for the glass rind was highly irregular and did not yield a reliable age (Schaeffer and Husain, oral communication, 1974) compatible with the very young glass age of < 1.1 b.y. we infer from the U-Pb systematics.

INITIAL $^{87}\text{Sr}/^{86}\text{Sr}$ RATIO OF 60015

Except for the plagioclase clast sample included in the black glass, the observed

$^{87}\text{Sr}/^{86}\text{Sr}$ ratios of 60015 plagioclase (table 2) are similar to BABI. The observed $^{87}\text{Sr}/^{86}\text{Sr}$ ratio of the plagioclase clasts included in the glass rind is 0.69887 ± 0.00003 —significantly below BABI. Because the clasts may have gained Pb at the time of glass rind formation as discussed above, the Rb we measured in this sample may also have been incorporated at that time. If this is the case, the observed $^{87}\text{Sr}/^{86}\text{Sr}$ ratio would closely approximate the initial $^{87}\text{Sr}/^{86}\text{Sr}$ ratio, since a ^{87}Sr correction due to in-situ decay of Rb over the last 1.0 b.y. would lower the ratio by only 0.00002. Of course, some Rb may have been present prior to ~ 1.0 b.y. ago, and the observed $^{87}\text{Sr}/^{86}\text{Sr}$ ratio of the clast sample is therefore an upper limit for the true initial value. Assuming a residence time of 4.0 b.y. for the Rb inside the plagioclase sample collected 2 mm from the glass-plagioclase boundary, we calculate a Rb-corrected $^{87}\text{Sr}/^{86}\text{Sr}$ initial ratio of 0.69886—in good agreement with the observed $^{87}\text{Sr}/^{86}\text{Sr}$ ratio obtained from the plagioclase included in the glass (fig. 2). Similarly correcting the plagioclase interior sample for in-situ decay

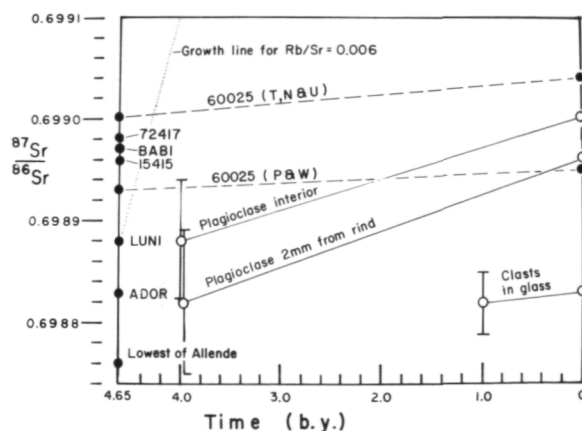


Figure 2.—Rb-Sr evolution diagram. For the initial $^{87}\text{Sr}/^{86}\text{Sr}$ ratio, ages 1.0 b.y. and 4.0 b.y. are used for plagioclase and clasts in glass rind of 60015 (open circles). Anorthosites 15415 and 60025, dunite 72417, BABI, LUNI, ADOR, and ALL are shown by solid dots for comparison. For anorthosite 60025, P & W denotes the data of Papanastasiou and Wasserburg (ref. 33), and T, N & U denote data by Tatsumoto et al. (this paper).

Table 2.—*K, Rb, and Sr Data From Football-Sized Anorthosite Sample 60015 and Anorthosite 60025*
All Data Have Been Corrected for Interlaboratory Bias Relative to NBS-SRM 987 Standard $^{87}\text{Sr}/^{86}\text{Sr} = 0.71014$

Sample	Weight (mg)	Concentration (ppm)			$^{87}\text{Rb}/^{86}\text{Sr}$	$^{87}\text{Sr}/^{86}\text{Sr}$			
						Observed ⁽¹⁾	Corrected for in-situ Rb Decay		
		K	Rb	Sr			$t = 1.0 \text{ b.y.}$	$t = 4.0 \text{ b.y.}$	$t = 4.65 \text{ b.y.}$
60015									
Black Glass Rind	15.8	694	1.910	156.8	0.03520	0.70116 ± 0.00006	0.70067	0.69915	0.69882
Plagioclase, 2 mm From Rind	30.3	68	0.1353	163.0	0.00240	0.69896 ± 0.00007		0.69882	0.69880
Plagioclase Interior	2.6	54	0.1221	166.2	0.00212	0.69900 ± 0.00006		0.69888	0.69886
Plagioclase Clast in Glass	28.3	79	0.0810	182.9	0.00128	0.69883 ± 0.00003	0.69881	0.69876	0.69874
60025									
Anorthosite Whole Rock	20.0	60	0.02017	213.6	0.000276	0.69904 ± 0.00006		0.69902	0.69902

NOTES (1) All errors are $2\sigma_m + \lambda_{^{87}\text{Rb}} = 1.39 \times 10^{-11} \text{ yr}^{-1}$. The estimated errors for concentrations are ± 2 percent for K and ± 1 percent for Rb and Sr.

of Rb over the past 4.0 b.y. yields an initial $^{87}\text{Sr}/^{86}\text{Sr}$ ratio of 0.69892. We obtain the initial $^{87}\text{Sr}/^{86}\text{Sr}$ ratios of 0.69888 ± 0.00007 , 0.69882 ± 0.00006 , and 0.69881 ± 0.00003 (standardized) for the gray plagioclase interior, a portion of plagioclase 2 mm from the glass-plagioclase boundary, and the plagioclase clast sample in the glass, respectively. The averaged initial $^{87}\text{Sr}/^{86}\text{Sr} = 0.69884 \pm 0.00004$ for anorthosite 60015 compares with higher values for lunar anorthosites 60025 (0.69902 ± 0.00006 , this paper; 0.69893 ± 0.00003 , ref. 33), 15415 (0.69896 ± 0.00004 , ref. 32), and BABI (0.69897 ± 0.00003 , ref. 16).

Papanastassiou and Wasserburg (ref. 33) reported the initial $^{87}\text{Sr}/^{86}\text{Sr}$ value for anorthosite 60025 as 0.69893 ± 0.00003 and stated that this was the first clear-cut evidence that the Moon formed with a slightly more primitive $^{87}\text{Sr}/^{86}\text{Sr}$ ratio than BABI. Subsequently, Nyquist et al. (ref. 38) reported a still lower initial $^{87}\text{Sr}/^{86}\text{Sr}$ ratio for anorthositic clasts in breccia 61016. Correcting their observed data for in-situ Rb decay over the last 4.6 b.y., they obtained LUNI (lunar initial) = 0.69888. The initial $^{87}\text{Sr}/^{86}\text{Sr}$ ratios reported here for anorthosite 60015 appear to be the lowest yet reported for any lunar sample, although these initial $^{87}\text{Sr}/^{86}\text{Sr}$ ratios are not outside of error below LUNI (ref. 38). Further efforts to verify the 60015 lowest $^{87}\text{Sr}/^{86}\text{Sr}$ initial ratio are in progress. Birck and Allegre (ref. 39) recently reported orally that the initial $^{87}\text{Sr}/^{86}\text{Sr}$ ratio for the anorthosite 60015 is 0.6988.

The above discussion is presented not only to compare small differences in the initial $^{87}\text{Sr}/^{86}\text{Sr}$ ratios of lunar samples, but also to emphasize that the lowest $^{87}\text{Sr}/^{86}\text{Sr}$ ratio yet found for the Moon is essentially equal to that found for the achondrite Angra dos Reis (ADOR = 0.69883 ± 0.00003 , ref. 17) and apparently slightly higher than the lowest measured $^{87}\text{Sr}/^{86}\text{Sr}$ ratio found for the Allende carbonaceous chondrite (ALL = 0.69876 ± 0.00002 , ref. 19; 0.69880 , ref. 20). The agreement between the lowest $^{87}\text{Sr}/^{86}\text{Sr}$ ratio for the Moon and Angra dos Reis indicates that the Moon formed about the

same time or earlier than did Angra dos Reis, since the lowest *documented* lunar initial $^{87}\text{Sr}/^{86}\text{Sr}$ ratio (this paper) is an upper limit for the absolute lunar initial $^{87}\text{Sr}/^{86}\text{Sr}$ ratio (i.e., the lowest lunar $^{87}\text{Sr}/^{86}\text{Sr}$ ratio may not have been found yet). Because Angra dos Reis has a Pb-Pb age of ~ 4.62 b.y. (ref. 18) it follows that the Moon formed at least ~ 4.62 b.y. ago. This reasoning assumes, of course, that the Moon and Angra dos Reis both condensed from the same solar nebula which was homogeneous with respect to its Sr isotopic composition and Rb/Sr ratio.

Recently, Albee et al. (ref. 40) reported an old Rb-Sr two-point isochron age of 4.60 ± 0.09 b.y. for Apollo 17 dunite breccia 72417 and concluded that the rock represents a cumulate formed during early lunar differentiation. Although the Pb model age on the leach of the rock is 4.48 b.y., indicating Pb addition at later times (ref. 41), the Rb-Sr isochron age strongly supports our hypothesis that the Moon is ~ 4.65 b.y. old.

Summary of U-Th-Pb and Rb-Sr Systematics of Lunar Samples

LUNAR DIFFERENTIATION MODEL

Many researchers have demonstrated from Apollo 11 sample studies that refractory elements—e.g., Zr, Hf, and the rare earths—are enriched in lunar surface material with respect to solar abundances and that, on the other hand, volatile elements—e.g., Bi, Zn, Cd, Tl, Pb, Cl, and Br—are significantly depleted with respect to solar abundances. We use the U/Pb ratio as one way to measure relative refractory enrichment and volatile depletion of rocks. The ratio is commonly expressed in the ratio $^{238}\text{U}/^{204}\text{Pb}$ (μ) as measured today. The Pb isotopic compositions of lunar samples are quite radiogenic compared to compositions of carbonaceous chondrites, ordinary chondrites, and terrestrial samples. The observed μ 's for low-K lunar basalts range from about 300 to

Table 3.—*Observed $^{238}\text{U}/^{204}\text{Pb}$ Ratios and First-Stage Estimated $^{238}\text{U}/^{204}\text{Pb}$ Ratios Assuming a Two-Stage U-Pb Evolution Model With an Age of 4.65 b.y. for the Origin of the Moon*

Rock Type	$^{238}\text{U}/^{204}\text{Pb}$ (observed)	$^{238}\text{U}/^{204}\text{Pb}$ (estimated for source)
Anorthosites	<10	indeterminate
KREEP	1000–3000	600–1000
High-K Basalts	600–1000	~ 300
Low-K Basalts	300–600	~ 100
Excess Pb in Orange Soil	—	35

500 and those for high-K basalts range from about 600 to 1000 (table 3), whereas the μ 's of ordinary chondrites (refs. 18 and 25) and terrestrial basalts (e.g., ref. 42) are about 8 to 30 and those of carbonaceous chondrites are < 1 to 4. Ca-Al-rich inclusions in Allende meteorites (ref. 27) have μ 's ranging from 15 to 40, while μ 's of Mg-rich inclusions range from 7 to 10. Only the μ 's (about 200) of achondrites approach those of lunar mare basalts (ref. 18).

U-Th-Pb systematics of the lunar rocks indicate that typical mare basalts and KREEP rocks were derived from sources in which μ ranged from about 100 to 300 and from 600 to 1000, respectively, assuming an age of 4.65 b.y. for the Moon and a simple two-stage U-Pb evolution history. Of course, the μ values will be different if we use a different lunar origin age and/or different evolution models for the Moon, although relative relations for the source μ 's are not grossly changed. It is not clear to what extent large multiple impacts may have altered μ values in source rocks, thereby making these observations qualitative rather than quantitative.

Most lunar breccias and soils contain excess Pb relative to U. The excess Pb in these materials was apparently released from other rocks during lunar outgassing due to volcanic activity and meteoroid impact events. In particular, anorthosites 15415 (refs. 43 and 44) and 60015 (ref. 36), a "Rusty Rock" breccia 66095 (ref. 45), and orange Glass 74220 (ref. 46) contain considerable excess Pb that is not supported by

in-situ decay of U and Th. Excess Pb in the anorthosites appears to have been produced in $\mu \sim 300$ source environments equivalent to basaltic sources, and that in breccia 66095 appears to have been produced in $\mu \sim 1000$, which is typical of KREEP sources. All these U-Pb data indicate that the Moon was originally extremely depleted in the volatile element Pb relative to cosmic abundances.

A recent U-Th-Pb systematics study of Apollo 17 orange soil 74220, however, indicates that Pb in this sample was derived from a source with a μ of about 35 (refs. 46 and 47). The origin of the glass spherules in soil 74220 is thought to have resulted from either meteorite impact into a lava lake or lava fountaining (refs. 48 through 52). We prefer the lava fountain hypothesis because Pb and other volatile element concentrations are too high to be easily derived from a volatile-rich carbonaceous chondrite via some sort of impact transfer.

On the basis of geophysical and geochemical constraints, some investigators have suggested that the Moon formed from a mixture of high-temperature condensates (like the Ca-Al-rich inclusions in the Allende meteorite) and Cl carbonaceous chondritic material. Anderson (ref. 53) postulated that the Moon is composed almost entirely of pre-iron, high-temperature condensates like the Ca-Al-rich inclusions in the Allende meteorite (ref. 54); Wanke et al. (refs. 55 and 56) suggested that the Moon is made of 60 percent high-temperature condensates and 40 percent chondrites; and Ganapathy and Anders (ref. 5) suggested a mixture of 25

percent high-temperature condensate component and 75 percent chondritic component. The Cl carbonaceous chondrites contain about 8 ppb U, and the Ca-Al-rich chondrules and aggregates in Allende contain about 110 ppb U. If a simple two-component mixing model for the Moon is appropriate, the U concentration data suggest that the Moon is a 50–50 mixture of the high-temperature condensate and chondritic material. However, Clayton et al. (ref. 57) and Grossman et al. (ref. 58) pointed out that the oxygen isotope data for the Allende high-temperature inclusions are very different from anything yet found on the Moon, and that consideration of the Allende Ca-Al-rich inclusions as a significant lunar component is therefore not strictly correct.

In any case, the Moon did accrete from the solar nebula into a body in which volatile elements were depleted and refractory elements enriched relative to cosmic abundances about 4.65 b.y. ago. We find most attractive the hypothesis that the Moon underwent large-scale and possibly total melting by mostly gravitational energy at the beginning of its history (ref. 59). This hypothesized primary accretional global melting would result in global differentiation, with feldspar “floating” (refs. 30 and 60) relative to the more dense succession of pyroxene-rich assemblages accumulating in the mantle (refs. 7, 61, 62, and 63).

As previously discussed (ref. 64), a plagioclase-rich noritic layer was likely formed between an anorthositic surface layer and a pyroxenite mantle as a result of silicate liquid accumulation during the primary differentiation stage. Apparently the lunar crust consists of both anorthositic and noritic layers and is about 60 km thick (ref. 65). The anorthositic surface layer contains only small amounts of K, Rb, Pb, U, and Th. Anorthosite 60015, which has an initial $^{87}\text{Sr}/^{86}\text{Sr}$ ratio as low as that determined for Angra dos Reis, probably formed in this outer anorthositic layer during the hypothesized primary differentiation. Although preliminary data on anorthosite 15415 (refs. 43 and 44) suggested ~ 0.2 ppm Pb might be

typical of lunar anorthosites, later studies (refs. 66 and 67) revealed that at least some anorthosites could be almost free of Pb as well as of U and Th.

The noritic layer contained a large amount of compatible lithophile elements such as K, REE, P, Rb, U, and Th. This layer was presumably the source of the KREEP component in KREEP-rich rocks. We hypothesize that the crust upper mantle layering was established ~ 4.63 b.y. ago, and that the mantle likely continued to differentiate after this time. The 4.60-b.y. age for dunite 72417 (ref. 40) strongly supports this hypothesis. Meteoroid impact events around 4.47 b.y. ago may well have induced extrusion of KREEP-rich basalts (ref. 68). KREEP-rich igneous rock 14310 contains 3.10 ppm U (refs. 69 and 70), and KREEP itself was estimated to contain 4.5 ppm U (ref. 68). If KREEP source material contains only ~ 0.1 ppm U as suggested by Hubbard and Gast (ref. 71), then KREEP is only about a 2-percent partial melt of the source material, assuming that the partition coefficient of U measured for the terrestrial diopside-liquid system (ref. 72) is applicable to lunar rocks. In our model, as we discuss below, we assume that the noritic layer contains 0.4 ppm U or more and that the U in KREEP was increased to ~ 4 ppm U by ~ 10 -percent partial melting.

The lunar pyroxenite mantle—whose μ 's appear to decrease from ~ 300 downward to 100—provided the source material for the mare basalts that were produced ~ 3.2 to 3.9 b.y. ago. The excess Pb in orange soil 74220, whose calculated first stage μ is about 35, was probably produced from a still deeper part of the lunar mantle than the mare basalt source region. These estimated μ changes suggest that the Moon had well differentiated and formed a zonal structure in which μ 's decrease downward.

We prefer an extensive lunar differentiation model such as that proposed by Nakamura et al. (ref. 73) and Taylor and Jakes (ref. 74). If such a model is appropriate and the lunar asthenosphere deeper than 1000 km (or more) consists of pyroxenite (ref.

53) or Fe-FeS (refs. 75 and 76), then the noritic layer must contain 0.4 ppm or more uranium, assuming the present-day average U concentration is 0.06 ppm for the Moon (ref. 77). In this calculation we followed Taylor and Jakes' (ref. 74) geochemical zoning model and assumed that U concentrations in the mantle decrease downward from 70 to 20 ppb. The depth assignment for the lunar basalt sources of the Taylor-Jakes model might be too deep, considering possible U-Pb clock resetting of the sources by planetesimal impacts (ref. 78). If this is the case, the U concentration of the noritic layer is probably higher than 0.4 ppm.

EARLY CHRONOLOGY OF THE MOON

Well-documented Rb-Sr internal isochron and $^{40}\text{Ar}/^{39}\text{Ar}$ ages of lunar mare basalts range from 3.2 b.y. to 3.8 b.y. (refs. 14 and 79 through 85). In this section we consider the Moon's early history prior to the 4.0-b.y. "cataclysm" (ref. 86).

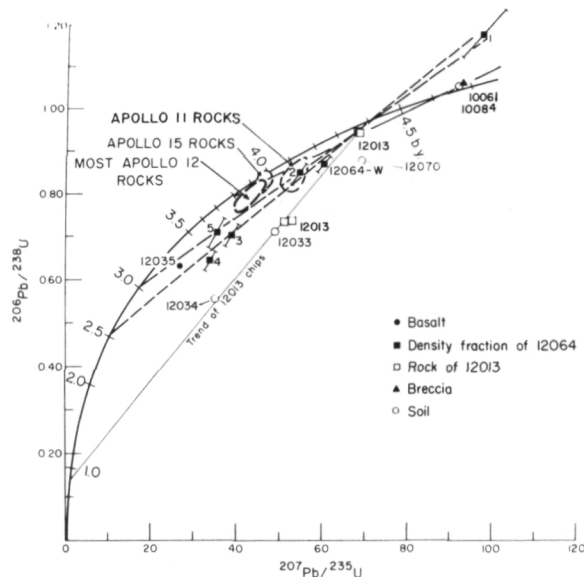


Figure 3.—U-Pb concordia diagram. Data points are for whole-rock analyses of Apollo 11 and 12 rocks and soils, density separates of basalt 12064 (numbers 1 through 5 are from lower density), and portions of rock 12013.

The first Apollo 11 lunar breccia and soil U-Pb analyses (fig. 3) yielded nearly concordant U-Pb ages of ~ 4.65 b.y. These data, together with the slightly discordant U-Pb Apollo 11 mare basalt analyses and ~ 3.8 -b.y. Rb-Sr isochron age (ref. 13) prompted Tatsumoto (ref. 87) to explain the mare basalt data with a simple two-stage U-Pb evolution model that would have 4.60 to 4.66-b.y.-old source material produce mare basalt at ~ 3.8 b.y. ago. Using this model, Tatsumoto (ref. 87) postulated that approximately one-third of the Pb that had accumulated in the basalt source material by in-situ decay of U and Th was transferred to the soil by volatilization during eruption ~ 3.8 b.y. ago. Acid leaching (ref. 12) and size fraction (ref. 88) studies provided evidence for lead mobility on the lunar surface. However, the U-Pb data of the acid leaches and of the acetone float fraction of soil 10081 do not exactly lie on the upper extension of the 3.8- to 4.65-b.y. discordia line, but rather on an extension of the 3.8- to 4.4-b.y. chord (fig. 4). U-Pb analyses of silicic brecciated rock

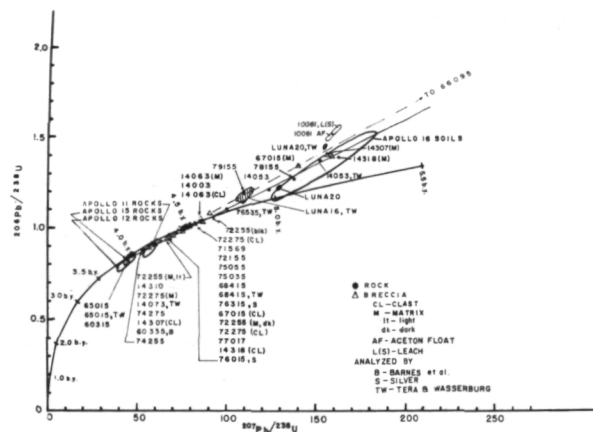


Figure 4.—U-Pb concordia diagram. Data points are for Apollo 14, 15, 16, 17 and Luna 16 and 20 samples. B, S, and TW denote data reported by Barnes et al. (ref. 89), Silver (ref. 47), and Tera and Wasserburg (refs. 66 and 70) respectively. The 4.0- to 4.47-b.y. concordia chord (dashed line) and the 3.8- to 4.65-b.y. concordia chord (solid line) are shown. Acid leach (denoted by L, ref. 12) and acetone float (AF) are also plotted.

12013 (ref. 90) and of mineral separates of basalt 12064 (ref. 88) also yielded upper concordia intercept ages at ~ 4.4 b.y. This event became unambiguously clear when Tera and Wasserburg (ref. 70) obtained U-Pb internal isochrons for KREEP-rich basalts 14310 and 14053 that yielded concordia intercept ages of ~ 4.47 and ~ 3.95 b.y. Rb-Sr whole-rock data of some KREEP-rich basalts and breccias also suggested a Rb-Sr equilibration event occurred approximately 4.45 b.y. ago (refs. 38, 68, and 91). In addition, whole-rock U-Pb data for igneous rock 68415 are concordant at ~ 4.47 b.y. Nunes et al. (ref. 36), and Tera et al. (ref. 86) also obtained an upper concordia intercept age of ~ 4.47 b.y. from a two-point whole-rock-plagioclase isochron for this rock. Chemical and petrographic studies suggest that 14310, 14053, and 68415 (refs. 69, 92, 93, and 94) are probably of regolith (impact melt) origin. We suggest that the upper concordia ages of about 4.47 b.y. for these rocks represent a period of impact melting and regional differentiation rather than a primary global differentiation resulting from lunar accretionary heating. The ~ 4.0 -b.y. "Imbrium event" is then envisioned as another much later impact event. U-Pb data of almost all terra cataclastic anorthosites, breccias, and soil samples from Apollo 14, 15, and 16 and Luna 16 and 20 sites plot on or near an extension of the 4.0- to 4.47-b.y. concordia chord on a U-Pb evolution diagram (ref. 41) (fig. 4). The distinct nonlinear scatter of these data, however, requires at least three stages of U-Pb evolution for lunar highland rocks and suggests that the 4.47-b.y. age may be of regional rather than global scale (ref. 45).

Whole-rock U-Pb analyses of the Apollo 17 mare basalts 74235, 72155, 71569, and 75035 (ref. 78) are within error concordant at 4.57 b.y., 4.54 b.y., 4.53 b.y., and 4.50 b.y., respectively (fig. 4). The 4.57 ± 0.01 b.y. age of mare basalt 74235 is the oldest lunar concordant whole-rock U-Pb age yet determined and may be considered as a minimum age of the Moon. Albee et al.'s (ref. 40) Rb-Sr two-point isochron age of 4.60 ± 0.09 b.y. for

a lunar dunite is compatible with this interpretation.

A suggestion that the Moon is older than 4.85 b.y. was made by Silver (ref. 12). Later, Silver (ref. 47) reported a soil from Apollo 16 with U-Pb concordant ages in excess of 5 b.y. and pointed out that the determination of the age of the Moon by a concordia treatment of soils and breccias is not yet feasible. Although most breccia and soils have apparent $^{207}\text{Pb}/^{206}\text{Pb}$ ages > 4.65 b.y. and plot above concordia which is indicative of Pb gain relative to U, none of the breccia samples plot below the extension of the 4.0- to 4.65-b.y. chord above concordia in a U-Pb evolution diagram. U-Pb data of some soil samples that plot below this chord can be easily explained by "third event(s)" which occurred at a younger time; e.g., ~ 0.8 b.y. for Apollo 12 soils (ref. 88) and ~ 2 b.y. for Apollo 14 (ref. 69) and Luna 20 soils (ref. 64). Soils lost Pb relative to U by the third event(s). These events may be only apparent, due to an integrated bombardment history and associated Pb loss throughout the last ~ 4.0 b.y. (refs. 64 and 95).

As Tatsumoto and Rosholt (ref. 11) originally pointed out, accepting the age of the Moon as ~ 4.65 b.y. from their U-Pb data of Apollo 11 breccia and soil samples involved some speculation, and these samples may have been only coincidentally nearly concordant at ~ 4.65 b.y. Regardless of whether or not this is the case, the very primitive $^{87}\text{Sr}/^{86}\text{Sr}$ ratios reported in this paper (anorthosite 60015) and by Nyquist et al. (ref. 38) (61016 anorthosite clast) strongly support an age of ~ 4.65 b.y. for the origin of the Moon. As discussed above, all U-Pb and Rb-Sr data obtained from lunar samples are compatible with this primary age of ~ 4.65 b.y.

Schaeffer and Husain (ref. 37) interpreted their $^{40}\text{Ar}/^{39}\text{Ar}$ ages obtained from Apollo 16 and 17 samples as being related to the McGetchin et al. (ref. 96) basin excavation stratigraphy model and suggested that their $^{46}\text{Ar}/^{39}\text{Ar}$ ages of 4.20 ± 0.05 , 4.13 to 4.20, and 4.13 ± 0.05 b.y. were related to the Nectaris, Humorum, and Crisium excava-

tions, respectively. Nunes et al. (ref. 78) recently attempted to correlate U-Pb lunar whole-rock data with the McGetchin et al. (ref. 96) basin excavation stratigraphy model. They suggested that the U-Pb and Rb-Sr whole-rock documented ages of ~ 4.0 to ~ 4.5 b.y. correspond to multiple major basin excavation events. The preponderance of KREEP material in the Apollo 12 and 14 samples and high radiation just south of the Imbrian area led Nunes et al. (ref. 78) to suggest KREEP was produced by a "South Imbrian" excavation event that occurred ~ 4.47 b.y. ago (fig. 5). The unofficial term "South Imbrian" refers to the large basin whose center lies just east of Copernicus. Schonfeld and Meyer (ref. 68) have argued, primarily from the distribution of KREEP on the lunar surface, that the Imbrian event must predate the formation of KREEP some 4.4 b.y. ago. If the Nunes et al. (ref. 78) explanation is correct, however, KREEP may have been confined to an area just south of the Imbrian basin, and the Imbrian impact event may not have caused as much KREEP redistribution as Schonfeld and Meyer (ref. 68) thought it should have. Therefore, it appears that the South Imbrian basin (rather than the Imbrian basin) formed immediately prior to KREEP extrusion in this region. This explanation allows us to continue to accept the well-documented 4.0-b.y. event as the time of the Imbrian excavation. The basin-excavation chronology, developed at length by Nunes et al. (ref. 78), is summarized in figure 5, which is a modified version of Wilshire and Jackson's (ref. 98) figure. The original geologic map showing the main outer mountain rings of major lunar basins and the approximate extent of their continuous ejecta blankets was published by Wilhelms and McCauley (ref. 97). The basin excavation ages presented in figure 5 were suggested by Schaeffer and Husain (ref. 37) for Nectaris and younger basins and Nunes et al. (ref. 78) for Nectaris and older basins. The relative age assignments primarily follow those of Stuart-Alexander and Howard (ref. 97).

Numerous Rb-Sr internal isochron ages

and $^{40}\text{Ar}/^{39}\text{Ar}$ ages indicate mare basalts were extruded from ~ 3.8 to ~ 3.2 b.y. ago. Thus, the older whole-rock Rb-Sr and U-Th-Pb ages discussed above must represent still earlier periods of equilibration possibly related to earlier episodes of melting and crystallization resulting from impacting planetesimals (ref. 78).

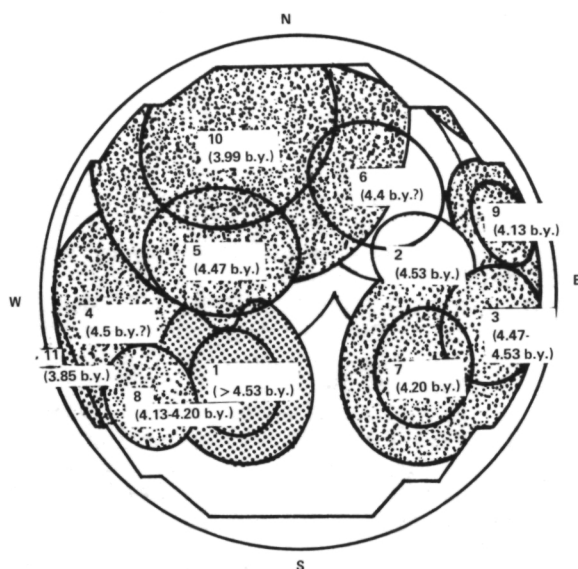


Figure 5.—Map showing main outer mountain rings of major lunar basins (drawn by Wilhelms and McCauley (ref. 97), ejecta blankets, and relative ages. Numbered in order of decreasing relative age: 1. Nubium, 2. Tranquillitatis, 3. Fecunditatis, 4. Procellarum, 5. South Imbrium, 6. Serenitatis, 7. Nectaris, 8. Humorum, 9. Crisium, 10. Imbrium, and 11. Orientalis.

Acknowledgment

The authors wish to thank NASA and the Soviet Academy of Science for providing the opportunity to present this paper; R. J. Knight for laboratory assistance; and B. R. Doe and R. E. Zartman for manuscript review.

References

- VINOGRADOV, A. P., Preliminary Data on Lunar Ground Brought to Earth by Automatic Probe "Luna 16." *Proc. Second Lunar Science Conference, Geochimica et Cosmochimica Acta*, Supplement 2, 1971, pp. 1-16.
- VINOGRADOV, A. P., Preliminary Data on Lunar Soil Collected by the Luna 20 Unmanned Spacecraft. *Geokhimiya*, pp. 763-774. English translation in *Geochimica et Cosmochimica Acta*, Vol. 37, 1973, pp. 721-729.
- GANAPATHY, R., R. R. KEAYS, J. C. LAUL, AND E. ANDERS, Trace Elements in Apollo 11 Lunar Rocks: Implications for Meteorite Influx and Origin of Moon. *Proc. Apollo 11 Lunar Science Conference, Geochimica et Cosmochimica Acta*, Supplement 1, 1970, pp. 1117-1142.
- GANAPATHY, R., J. W. MORGAN, J. KRAHENBUHL, AND E. ANDERS, Ancient Meteoritic Components in Apollo 15 and 16 Samples. *Proc. Fourth Lunar Science Conference, Geochimica et Cosmochimica Acta*, Supplement 4, 1973, pp. 1239-1261.
- GANAPATHY, R., AND E. ANDERS, Bulk Composition of the Moon and Earth, Estimated From Meteorites. *Lunar Science*, Vol. V, Lunar Science Institute, Houston, 1974, pp. 254-256.
- GAST, P. W., N. J. HUBBARD, AND H. WIESMANN, Chemical Composition and Petrogenesis of Basalt From Tranquillity Base. *Proc. Apollo 11 Lunar Science Conference, Geochimica et Cosmochimica Acta*, Supplement 1, 1970, pp. 1143-1163.
- HASKIN, L. A., R. O. ALLEN, P. A. HELMKE, T. P. PASTER, M. R. ANDERSON, R. L. KOROTEV, AND K. A. ZWEIFEL, Rare Earths and Other Trace Elements in Apollo 11 Lunar Samples. *Proc. Apollo 11 Lunar Science Conference, Geochimica et Cosmochimica Acta*, Supplement 4, 1970, pp. 1275-1296.
- LSPET (Lunar Sample Preliminary Examination Team), Preliminary Examination of Lunar Samples from Apollo 11. *Science*, Vol. 165, 1969, pp. 1211-1227.
- LSPET (Lunar Sample Preliminary Examination Team), Preliminary Examination of Lunar Samples From Apollo 12. *Science*, Vol. 167, 1970, pp. 1325-1339.
- TERA, F., O. EUGSTER, D. S. BURNETT, AND G. J. WASSERBURG, Comparative Study of Li, Na, K, Rb, Cs, Ca, Sr and Ba Abundances in Achondrites and in Apollo 11 Lunar Samples. *Proc. Apollo 11 Lunar Science Conference, Geochimica et Cosmochimica Acta*, Supplement 1, 1970, pp. 1637-1657.
- TATSUMOTO, M., AND J. N. ROSHOLT, Age of the Moon: An Isotopic Study of Uranium-Thorium-Lead Systematics of Lunar Samples. *Science*, Vol. 167, 1970, pp. 461-463.
- SILVER, L. T., Uranium-Thorium-Lead Isotopes in Some Tranquillity Base Samples and Their Implications for Lunar History. *Proc. Apollo 11 Lunar Science Conference, Geochimica et Cosmochimica Acta*, Supplement 1, 1970, pp. 1533-1581.
- Lunatic Asylum, Ages, Irradiation History, and Chemical Composition of Lunar Rocks From the Sea of Tranquillity. *Science*, Vol. 167, 1970, pp. 463-466.
- COMPSTON, W., B. W. CHAPPELL, P. A. ARRIENS, AND M. J. VERNON, The Chemistry and Age of Apollo 11 Lunar Material. *Proc. Apollo 11 Lunar Science Conference, Geochimica et Cosmochimica Acta*, Supplement 1, 1970, pp. 1007-1027.
- GAST, P. W., AND R. K. MCCONNELL, JR., Evidence for Initial Chemical Layering of the Moon (abs.). *Lunar Science*, Vol. III, Lunar Science Institute, Houston, 1972, pp. 257-258.
- PAPANASTASSIOU, D. A., AND G. J. WASSERBURG, Initial Strontium Isotopic Abundances and the Resolution of Small Time Differences in the Formation of Planetary Objects. *Earth Planet. Sci. Letters*, Vol. 5, 1969, p. 361.
- PAPANASTASSIOU, D. A., The Determination of Small Time Differences in the Formation of Planetary Objects. Ph.D. Thesis, California Institute of Technology, 1970.
- TATSUMOTO, M., R. J. KNIGHT, AND C. J. ALLEGRE, Time Differences in the Formation of Meteorites as Determined by $^{207}\text{Pb}/^{206}\text{Pb}$. *Science*, Vol. 180, 1973, pp. 1279-1283.
- GRAY, C. M., D. A. PAPANASTASSIOU, AND G. J. WASSERBURG, The Identification of Early Condensates From the Solar Nebula. *Icarus*, Vol. 20, 1973, pp. 213-239.
- WETHERILL, G. W., R. MARK, AND C. LEE-HU, Chondrites: Initial $^{87}\text{Sr}/^{86}\text{Sr}$ Ratios and Early History of the Solar System. *Science*, Vol. 182, 1973, pp. 281-283.
- CLARKE, R. S. JR., E. JAROSEWICH, B. MASON, J. NELEN, M. GOMEZ, AND J. R. HYDE, The Allende, Mexico, Meteorite Shower. *Smithsonian Contrib. Earth Sci.*, Vol. 5, 1970.
- MARVIN, U. B., J. A. WOOD, AND J. S. DICKEY, JR., Ca-Al-Rich Phases in the Allende Meteorite. *Earth Planet. Sci. Letters*, Vol. 7, 1970, pp. 346-350.
- KEIL, K., AND L. H. FUCHS, Hibonite $[\text{Ca}_2(\text{Al,Ti})_2\text{O}_8]$ From the Leoville and Allende Chondritic Meteorites. *Earth Planet. Sci. Letters*, Vol. 12, 1971, pp. 184-190.
- GROSSMAN, L., Condensation in the Primitive Solar Nebula. *Geochimica et Cosmochimica Acta*, Vol. 36, 1972, pp. 597-619.
- TILTON, G. R., Isotopic Lead Ages of Chondritic Meteorites. *Earth Planet. Sci. Letters*, Vol. 19, 1973, pp. 321-329.

26. PATTERSON, C. C., The $^{207}\text{Pb}/^{206}\text{Pb}$ Ages of Some Stone Meteorites. *Geochimica et Cosmochimica Acta*, Vol. 7, 1955, pp. 151-153.
27. TATSUMOTO, M., D. M. UNRUH, AND G. A. DESBOROUGH, The U-Th-Pb Systematics of the Allende Carbonaceous Chondrite (abs.). *Meteoritics*, Vol. 8, 1973, p. 446.
28. YORK, D. K., Least Squares Fitting of a Straight Line With Correlated Errors. *Earth Planet. Sci. Letters*, Vol. 5, 1969, pp. 320-324.
29. FIREMAN, E. L., J. DEFELICE, AND E. NORTON, Ages of the Allende Meteorite. *Geochimica et Cosmochimica Acta*, Vol. 34, 1970, p. 873.
30. WOOD, J. A., J. S. DICKEY, U. B. MARVIN, AND B. N. POWELL, Lunar Anorthosites and a Geophysical Model of the Moon. *Proc. Apollo 11 Lunar Science Conference*, *Geochimica et Cosmochimica Acta*, Supplement 1, 1970, pp. 965-988.
31. SMITH, J. V., A. T. ANDERSON, R. C. NEWTON, E. J. OLSEN, AND P. J. WYLLIE, Petrologic History of the Moon Inferred From Petrography, Mineralogy, and Petrogenesis of Apollo 11 Rocks. *Proc. Apollo 11 Lunar Science Conference*, *Geochimica et Cosmochimica Acta*, Supplement 1, 1970, pp. 897-925.
32. WASSERBURG, G. J., AND D. A. PAPANASTASSIOU, Age of an Apollo 15 Mare Basalt: Lunar Crust and Mantle Evolution. *Earth Planet. Sci. Letters*, Vol. 13, 1971, pp. 97-104.
33. PAPANASTASSIOU, D. A., AND G. J. WASSERBURG, Rb-Sr Systematics of Luna 20 and Apollo 16 Samples. *Earth Planet. Sci. Letters*, Vol. 17, 1972, pp. 52-63.
34. *Lunar Sample Information Catalog, Apollo 16*. Lunar Receiving Lab., MSC, NASA, Houston, 1972.
35. SCLAR, C. B., AND J. F. BAUER, Shock Effects in Lunar Rocks 60015 and 77017. *Lunar Science*, Vol. V, Lunar Science Institute, Houston, 1974, pp. 687-689.
36. NUNES, P. D., M. TATSUMOTO, R. J. KNIGHT, D. M. UNRUH, AND B. R. DOE, U-Th-Pb Systematics of Some Apollo 16 Lunar Samples. *Proc. Fourth Lunar Science Conference*, *Geochimica et Cosmochimica Acta*, Supplement 4, 1973, pp. 1797-1822.
37. SCHAEFFER, O. A., AND L. HUSAIN, Chronology of Lunar Basin Formation and Ages of Lunar Anorthositic Rock. *Lunar Science*, Vol. V, Lunar Science Institute, Houston, 1974, pp. 663-665.
38. NYQUIST, L. E., N. J. HUBBARD, P. W. GAST, H. WIESMANN, B. M. BANSUL, S. E. CHURCH, AND B. M. JAHN, Rb-Sr Systematics for Chemically Defined Apollo 15 and 16 Materials (abs.). *Lunar Science*, Vol. IV, Lunar Science Institute, Houston, 1973, pp. 567-569.
39. BIRCK, J. L., AND C. J. ALLEGRE, Constraints Imposed by ^{87}Rb - ^{87}Sr on Lunar Processes and on the Composition of the Lunar Mantle. *Lunar Science*, Vol. V, Lunar Science Institute, Houston, 1974, pp. 64-65.
40. ALBEE, A. L., A. A. CHODOS, R. F. DYMEK, A. J. GANCARZ, D. S. GOLDMAN, D. A. PAPANASTASSIOU, AND G. J. WASSERBURG, Dunite From the Lunar Highlands: Petrography, Deformational History, Rb-Sr Age. *Lunar Science*, Vol. V, Lunar Science Institute, Houston, 1974, pp. 3-5.
41. TERA, F., D. A. PAPANASTASSIOU, AND G. J. WASSERBURG, The Lunar Time Scale and a Summary of Isotopic Evidence for a Terminal Lunar Cataclysm (abs.). *Lunar Science*, Vol. V, 1974, p. 792.
42. TATSUMOTO, M., Genetic Relations of Oceanic Basalts as Indicated by Lead Isotopes. *Science*, Vol. 153, 1966, pp. 1094-1101.
43. TATSUMOTO, M., C. E. HEDGE, R. J. KNIGHT, D. M. UNRUH, AND B. R. DOE, U-Th-Pb, Rb-Sr and K Measurements on Some Apollo 15 and Apollo 16 Samples. *Apollo 15 Lunar Samples*, Lunar Science Institute, Houston, 1972, pp. 391-395.
44. TERA, F., L. A. RAY, AND G. J. WASSERBURG, Distribution of Pb-U-Th in Lunar Anorthosite 15415 and Inferences About Its Age. *Apollo 15 Lunar Samples*, Lunar Science Institute, Houston, 1972, pp. 396-401.
45. NUNES, P. D., AND M. TATSUMOTO, Excess Lead in "Rusty Rock" 66095 and Implications for an Early Lunar Differentiation. *Science*, Vol. 182, 1973, pp. 916-920.
46. TATSUMOTO, M., P. D. NUNES, R. J. KNIGHT, C. E. HEDGE, AND D. M. UNRUH, U-Th-Pb, Rb-Sr and K Measurements of Two Apollo 17 Samples. *EOS, Trans. Am. Geophys. Union*, Vol. 54, 1973, pp. 614-615.
47. SILVER, L. T., Uranium-Thorium-Lead Isotope Characteristics in Some Regolithic Materials From the Descartes Region (abs.). *Lunar Science*, Vol. IV, Lunar Science Institute, Houston, 1973, pp. 672-674.
48. ROEDDER, E., AND P. W. WEIBLEN, Origin of Orange Glass Spherules in Apollo 17 Sample 74220. *EOS, Trans. Am. Geophys. Union*, Vol. 54, 1973, pp. 612-613.
49. PRINZ, M., E. DOWTY, AND K. KEIL, A Model for the Origin of Orange and Green Glasses and the Filling of the Mare Basin. *EOS, Trans. Am. Geophys. Union*, Vol. 54, 1973, pp. 605-606.
50. MCKAY, D. S., AND G. H. HEIKEN, Petrography and Scanning Electron Microscope Study of Apollo 17 Orange and Black Glass. *EOS, Trans. Am. Geophys. Union*, Vol. 54, 1973, pp. 599-600.
51. CADENHEAD, D. A., Lunar Volcanic Glass and Cinder Formation. *EOS, Trans. Am. Geophys. Union*, Vol. 54, 1973, p. 582.

52. REID, A. M., G. E. LOFGREN, G. H. HEIKEN, R. W. BROWN, AND G. MORELAND, Apollo 17 Orange Glass, Apollo 15 Green Glass and Hawaiian Lava Fountain Glass. *EOS, Trans. Am. Geophys. Union*, Vol. 54, 1973, pp. 606-607.
53. ANDERSON, D. L., The Composition and Origin of the Moon. *Earth Planet. Sci. Letters*, Vol. 18, 1973, pp. 301-316.
54. GROSSMAN, L., Refractory Trace Elements in Ca-Al-rich Inclusions in the Allende Meteorite. *Geochimica et Cosmochimica Acta*, Vol. 37, 1973, pp. 1119-1140.
55. WÄNKE, H. H. BADDENHAUSEN, G. DREIBUS, E. JAGOUTZ, H. KRUSE, H. PALME, B. SPETTEL, AND F. TESCHKE, Multielement Analyses of Apollo 15, 16, and 17 Samples and the Bulk Composition of the Moon. *Proc. Fourth Lunar Science Conference, Geochimica et Cosmochimica Acta*, Supplement 4, 1973, pp. 1461-1481.
56. WÄNKE, H., H. PALME, H. BADDENHAUSEN, G. DREIBUS, E. JAGOUTZ, H. KRUSE, B. SPETTEL, AND F. TESCHKE, Composition of the Moon and Major Lunar Differentiation Process (abs.). *Lunar Science*, Vol. V, Lunar Science Institute, Houston, 1974, pp. 820-822.
57. CLAYTON, R. N., L. GROSSMAN, AND T. K. MAYEDA, A Component of Primitive Nuclear Composition in Carbonaceous Meteorites. *Science*, Vol. 182, 1973, pp. 485-488.
58. GROSSMAN, L., R. N. CLAYTON, AND T. K. MAYEDA, Oxygen Isotopic Compositions of Lunar Soils and Allende Inclusions and the Origin of the Moon. *Lunar Science*, Vol. V, Lunar Science Institute, Houston, 1974, pp. 298-300.
59. MIZUTANI, H., T. MATSUI, AND H. TAKEUCHI, Accretion Process of the Moon. *The Moon*, Vol. 4, 1972, pp. 476-489.
60. WOOD, J. A., Thermal History and Early Magmatism in the Moon. *Icarus*, Vol. 16, 1972, pp. 229-240.
61. RINGWOOD, A. E., AND E. ESSENE, Petrogenesis of Lunar Basalts and the Internal Constitution and Origin of the Moon. *Proc. Apollo 11 Lunar Science Conference, Geochimica et Cosmochimica Acta*, Supplement 1, 1970, pp. 769-799.
62. PHILPOTTS, J. A., C. C. SCHNETZLER, D. F. NAVA, M. L. BOTTINO, P. D. FULLAGAR, H. H. THOMAS, S. SCHUMANN, AND C. W. KOUNS, Apollo 14: Some Geochemical Aspects. *Proc. Third Lunar Science Conference, Geochimica et Cosmochimica Acta*, Supplement 3, 1972, pp. 1293-1305.
63. HASKIN, L. A., C. Y. SHIH, B. M. BANSAL, J. M. RHODES, H. WIESMANN, AND L. E. NYQUIST, Chemical Evidence for the Origin of 76535 as a Cumulate. *Lunar Science*, Vol. V, Lunar Science Institute, Houston, 1974, pp. 313-315.
64. TATSUMOTO, M., U-Th-Pb Measurements of Luna 20 Soil. *Geochimica et Cosmochimica Acta*, Vol. 37, 1973, pp. 1079-1086.
65. TOKSÖZ, M. N., A. M., DAINITY, S. C. SOLOMON, AND K. R. ANDERSON, Velocity Structure and Evolution of the Moon, *Proc. Fourth Lunar Science Conference, Geochimica et Cosmochimica Acta*, Supplement 4, 1973, pp. 2529-2547.
66. TERA, F., AND G. J. WASSERBURG, U-Th-Pb Systematics in Lunar Highland Samples From the Luna 20 and Apollo 16 Missions. *Earth Planet. Sci. Letters*, Vol. 17, 1972, pp. 36-51.
67. NUNES, P. D., R. J. KNIGHT, D. M. UNRUH, AND M. TATSUMOTO, The Primitive Nature of the Lunar Crust and the Problem of Initial Pb Isotopic Compositions of Lunar Rock: A Rb-Sr and U-Th-Pb Study of Apollo 16 Samples. *Lunar Science*, Vol. V, Lunar Science Institute, Houston, 1974, pp. 559-561.
68. SCHONFELD, E., AND C. MEYER, The Abundances of Components of the Lunar Soils by a Least Squares Mixing Model and the Formation Age of KREEP. *Proc. Third Lunar Science Conference, Geochimica et Cosmochimica Acta*, Supplement 2, 1972, pp. 1397-1420.
69. TATSUMOTO, M., C. E. HEDGE, B. R. DOE, AND D. M. UNRUH, U-Th-Pb and Rb-Sr Measurements on Some Apollo 14 Lunar Samples. *Proc. Third Lunar Science Conference, Geochimica et Cosmochimica Acta*, Supplement 3, 1972, pp. 1531-1555.
70. TERA, F., AND G. J. WASSERBURG, U-Th-Pb Systematics in Three Apollo 14 Basalts and the Problem of Initial Pb in Lunar Rocks. *Earth Planet. Sci. Letters*, Vol. 14, 1972, pp. 281-304.
71. HUBBARD, N. J., AND P. W. GAST, Chemical Composition and Origin of Nonmare Lunar Basalts. *Proc. Second Lunar Science Conference, Geochimica et Cosmochimica Acta*, Supplement 2, 1971, pp. 999-1020.
72. SEITZ, M. G., Uranium and Thorium Partitioning in Diopside-Melt and Whitlockite-Melt Systems. *Carnegie Inst. Year Book*, Vol. 72, 1973, pp. 581-586.
73. NAKAMURA, Y., G. LATHAM, D. LAMMLEIN, M. EWING, F. DUENNEBIER, AND J. DORMAN, Deep Lunar Interior Inferred From Seismic Data. *Geophys. Res. Letters*, Vol. 1, 1974, pp. 137-140.
74. TAYLOR, S. R., AND P. JAKES, Geochemical Zoning in the Moon. *Lunar Science*, Vol. V, Lunar Science Institute, Houston, 1974, pp. 786-788.
75. BRETT, R., Sulfur and the Ancient Lunar Magnetic Field. *EOS, Trans. Am. Geophys. Union*, Vol. 53, 1973, p. 723.
76. TOKSÖZ, M. N., A. M. DAINITY, AND S. C. SOLOMON, A Summary of Lunar Structural Con-

- straints (abs.). *Lunar Science*, Vol. V, Lunar Science Institute, Houston, 1974, pp. 801-803.
77. LANGSETH, M. G., JR., S. P. CLARK, JR., J. L. CHUTE, JR., S. J. KEIHM, AND A. E. WECHSLER, The Apollo 15 Lunar Heat-Flow Measurement. *The Moon*, Vol. 4, 1972, pp. 373-382.
 78. NUNES, P. D., M. TATSUMOTO, AND D. M. UNRUH, U-Th-Pb Systematics of Some Apollo 17 Lunar Samples and Implications for a Lunar Basin-Excavation Chronology. *Proc. Fifth Lunar Science Conference, Geochimica et Cosmochimica Acta*, Supplement 5, in press, 1974.
 79. PAPANASTASSIOU, D. A., G. J. WASSERBURG, AND D. S. BURNETT, Rb-Sr Ages of Lunar Rocks From the Sea of Tranquillity. *Earth Planet. Sci. Letters*, Vol. 8, 1970, pp. 1-19.
 80. PAPANASTASSIOU, D. A., AND G. J. WASSERBURG, Lunar Chronology and Evolution From Rb-Sr Studies of Apollo 11 and 12 Samples. *Earth Planet. Sci. Letters*, Vol. 11, 1971, pp. 37-62.
 81. PAPANASTASSIOU, D. A., AND G. J. WASSERBURG, Rb-Sr Ages of Igneous Rocks From the Apollo 14 Mission and the Age of the Fra Mauro Formation. *Earth Planet. Sci. Letters*, Vol. 12, 1971, pp. 36-48.
 82. TURNER, G., Argon-⁴⁰/Argon-³⁹ Dating of Lunar Rock Samples. *Proc. Apollo 11 Lunar Science Conference, Geochimica et Cosmochimica Acta*, Supplement 1, 1970, pp. 1665-1684.
 83. HUNEKE, J. C., E. K. JESSBERGER, F. A. PODOSEK, AND G. J. WASSERBURG, ⁴⁰Ar/³⁹Ar Measurements in Apollo 16 and 17 Samples and the Chronology of Metamorphic and Volcanic Activity in the Taurus-Littrow Region. *Proc. Fourth Lunar Science Conference, Geochimica et Cosmochimica Acta*, Supplement 4, 1973, pp. 1725-1756.
 84. HUSAIN, L., O. A. SCHAEFFER, J. FUNKHOUSER, AND J. SUTTER, The Ages of Lunar Material From Fra Mauro, Hadley Rille, and Spur Crater. *Proc. Third Lunar Science Conference, Geochimica et Cosmochimica Acta*, Supplement 3, 1972, pp. 1557-1567.
 85. STETTLER, A., P. EBERHARDT, J. GEISS, N. GROGLER, AND P. MAURER, Ar³⁹-Ar⁴⁰ Ages and Ar³⁷-Ar³⁸ Exposure Ages of Lunar Rocks. *Proc. Fourth Lunar Science Conference, Geochimica et Cosmochimica Acta*, Supplement 4, 1973, pp. 1865-1888.
 86. TERA, F., D. A. PAPANASTASSIOU, AND G. J. WASSERBURG, A Lunar Cataclysm at ~3.95 AE and the Structure of the Lunar Crust (abs.). *Lunar Science*, Vol. IV, Lunar Science Institute, Houston, 1973, pp. 723-725.
 87. TATSUMOTO, M., Age of the Moon: An Isotopic Study of U-Th-Pb Systematics of Apollo 11 Lunar Samples—II. *Proc. Apollo 11 Lunar Science Conference, Geochimica et Cosmochimica Acta*, Supplement 1, 1970, pp. 1595-1612.
 88. TATSUMOTO, M., R. J. KNIGHT, AND B. R. DOE, U-Th-Pb Systematics of Apollo 12 Lunar Samples. *Proc. Second Lunar Science Conference, Geochimica et Cosmochimica Acta*, Supplement 2, 1971, pp. 1521-1546.
 89. BARNES, I. L., E. L. GARNER, J. W. GRAMLICH, L. A. MACHLAN, J. R. MOODY, L. J. MOORE, T. J. MURPHY, AND W. R. SHIELDS, Isotopic Abundance Ratios and Concentrations of Selected Elements in Some Apollo 15 and Apollo 16 Samples. *Proc. Fourth Lunar Science Conference, Geochimica et Cosmochimica Acta*, Supplement 4, 1973, pp. 1197-1207.
 90. TATSUMOTO, M., U-Th-Pb Age of Apollo 12 Rock 12013. *Earth Planet. Sci. Letters*, Vol. 9, 1970, pp. 193-200.
 91. NYQUIST, L. E., N. J. HUBBARD, AND P. W. GAST, Rb-Sr Systematics for Chemically Defined Apollo 14 Breccias. *Proc. Third Lunar Science Conference, Geochimica et Cosmochimica Acta*, Supplement 3, 1972, pp. 1515-1530.
 92. GREEN, D. H., A. E. RINGWOOD, N. G. WARE, AND W. O. HIBBERSON, Experimental Petrology and Petrogenesis of Apollo 14 Basalts. *Proc. Third Lunar Science Conference, Geochimica et Cosmochimica Acta*, Supplement 3, 1972, pp. 197-206.
 93. JAMES, O. B., *Crystallization History of Lunar Feldspathic Basalt 14310*. U.S. Geol. Survey, Prof. Paper 841, 1973.
 94. HELZ, R. T., AND D. E. APPLEMAN, Mineralogy, Petrology, and Crystallization History of Apollo 16 Rock 68415. *Proc. Fourth Lunar Science Conference, Geochimica et Cosmochimica Acta*, Supplement 4, 1973, pp. 643-659.
 95. CHURCH, S. R., AND G. R. TILTON, Lead Isotope Systematics of some Apollo 17 Soils and Some Separated Components From 76501. *Proc. Fifth Lunar Science Conference, Geochimica et Cosmochimica Acta*, Supplement 5, in press, 1974.
 96. MCGETCHIN, T. R., M. SETTLE, AND J. W. HEAD, Radial Thickness Variation in Impact Crater Ejecta: Implications for Lunar Basin Deposits. *Earth Planet. Sci. Letters*, Vol. 20, 1973, pp. 226-236.
 97. WILHELMS, D. E., AND J. F. MCCAULEY, Geologic Map of the Near Side of the Moon. U. S. Geol. Survey, Misc. Geol. Inv., Map I-703, 1971.
 98. WILSHIRE, H. G., AND E. D. JACKSON, *Petrology and Stratigraphy of the Fra Mauro Formation at the Apollo 14 Site*. U.S. Geol. Survey, Prof. Paper 785, 1972.
 99. STUART-ALEXANDER, D. E., AND K. A. HOWARD, Lunar Maria and Circular Basins—A Review, *Icarus*, Vol. 12, 1970, pp. 440-456.

Page intentionally left blank

Page intentionally left blank

^{39}Ar - ^{40}Ar Dating of Basalts and Rock Breccias From Apollo 17 and the Malvern Achondrite

T. Kirsten and P. Horn
*Max Planck Institut für Kernphysik
Heidelberg, Germany*

The principles and the potential of the ^{39}Ar - ^{40}Ar dating technique are illustrated by means of results obtained for 12 Apollo 17 rocks. Emphasis is given to methodical problems and the geological interpretation of lunar rock ages. Often it is ambiguous to associate a given lunar breccia with a certain formation, or a formation with a basin. In addition, large-scale events on the Moon have not necessarily reset radiometric clocks completely. One rock fragment has a well-defined plateau age of 4.28 b.y., but the ages of two Apollo 17 breccias define an upper limit for the formation age of the Serenitatis basin at 4.05 b.y. Ages derived from five mare basalts indicate cessation of mare volcanism at Taurus-Littrow \sim 3.78 b.y. ago. Ca - ^{37}Ar exposure ages show that Camelot Crater was formed by an impact \sim 95 m.y. ago.

After a short summary of the lunar timetable as it stands at the end of the Apollo program, we report about ^{39}Ar - ^{40}Ar and rare gas studies on the Malvern meteorite. This achondrite resembles lunar highland breccias in texture as well as in rare-gas patterns. It was strongly annealed at some time between 3.4 and 3.8 b.y. ago. The results indicate that very similar processes have occurred on the Moon and on achondritic parent bodies at comparable times, leading to impact breccias with strikingly similar features, including the retention of rare-gas isotopes from various sources.

A major goal in exploring the history of the solar system is to establish an absolute time scale for the evolution of planetary objects such as the Moon or meteorites and their parent bodies. This implies the application of various dating techniques to physically accessible materials. In principle, ages of ancient rocks can be determined by the Rb-Sr, U-Pb, or K-Ar methods. Difficulties arose in applying these methods to lunar samples. The major shortcomings of the three methods turned out to be very low Rb concentrations in many lunar rock types, the extreme volatility of lead under lunar conditions, and diffusion of Ar, respectively.

In the case of Rb-Sr dating, many rock types became accessible for dating due to an extreme refinement of the experimental techniques by the California Institute of Technology group (ref. 1); but this still does not apply to anorthosites (an important lunar rock type) or to very small rock frag-

ments extracted in great variety from lunar soils ("coarse fines").

Fortunately, the pioneering work of G. Turner made it possible to account for Ar-diffusion losses in K-Ar dating by introducing an improved version of the K-Ar method, the so-called ^{39}Ar - ^{40}Ar method (refs. 2 and 3).

At present, Rb-Sr and ^{39}Ar - ^{40}Ar dating are the two principal tools for dating lunar rocks. Each of the two methods has its strengths and weaknesses, but together they complement each other rather favorably.

In this paper some general features and methodical problems of ^{39}Ar - ^{40}Ar dating will be described first. They will be illustrated by means of results obtained in dating rocks from the Apollo 17 site. Then the problems involved in the geological interpretation of measured radiometric ages will be discussed. This leads to discussion of the selenochronological significance of the results

obtained for Apollo 17 samples in particular and to a short glimpse at the timetable of the evolution of the lunar crust in general. Finally, similar studies concerning the Malvern achondrite will be reported, and relations which might exist between the early evolution of the Moon and of meteorite parent bodies will be discussed.

^{39}Ar - ^{40}Ar DATING

Principles

A basic feature of the ^{39}Ar - ^{40}Ar method is the extraction of the radiogenic ^{40}Ar contained in a sample in a stepwise fashion at progressively higher temperatures in order to resolve the ^{40}Ar released from various phases or lattice sites of different activation energies. In addition, one is aiming at a simultaneous determination of the K concentration in exactly the same sites that release their ^{40}Ar at a given temperature. This is achieved by converting a fixed proportion of ^{39}K into 269 γ -lived ^{39}Ar by a fast neutron irradiation via the reaction $^{39}\text{K}(n,p)^{39}\text{Ar}$. Provided that the release of ^{39}Ar produced in a given type of lattice sites follows the release of radiogenic ^{40}Ar from the same sites, one can in principle determine the K-Ar age of each phase by a mass-spectrometric determination of $^{40}\text{Ar}/^{39}\text{Ar}$ isotopic ratios. If the less retentive phases had suffered ^{40}Ar losses during geological times, the apparent ages obtained at lower degassing temperatures would be lower than ages obtained at temperatures sufficiently high to degas those phases that did not undergo natural diffusion losses. If a sample contains at least some highly retentive phases that quantitatively retained their radiogenic ^{40}Ar since the initial cooling of the rock, then the ages obtained above a certain release temperature must approach a constant (maximal) value that defines a "plateau" in a plot of age versus release temperature or $^{40}\text{Ar}/^{39}\text{Ar}$ -ratio versus cumulative fraction of ^{39}Ar released. It is this plateau age not affected by natural ^{40}Ar losses

that might imply geochronological significance.

Practical Conditions

Elaborate descriptions of experimental details may be found in the literature (e.g., refs. 3, 4, and 5). Here we will repeat some facts of more general interest.

The threshold of the $^{39}\text{K}(n,p)^{39}\text{Ar}$ reaction is 0.218 MeV. Assuming a typical reactor spectrum, 10^{19} neutrons/cm² with energies above 0.1 MeV produce $\sim 5 \cdot 10^{-4}$ cm³STP ^{39}Ar per gram of potassium. A total neutron dose largely in excess of $\sim 5 \cdot 10^{19}$ fast neutrons/cm² (> 0.1 MeV) should be avoided since the radiation damage caused by such a high fluence could lead to a complete breakdown of the crystal structure (metamictization). If we consider a lunar rock with an extremely low K content of, say, 10 ppm, we obtain $\sim 5 \cdot 10^{-10}$ cm³STP ^{39}Ar in a 100-mg sample, or $\sim 5 \cdot 10^{-11}$ cm³STP ^{39}Ar in a single temperature step in which 10 percent of the total ^{39}Ar is released. With an advanced rare gas mass spectrometer one can easily handle such Ar-quantities. This consideration illustrates once more the nearly universal applicability of the K-Ar method.

In an actual experiment, ^{36}Ar , ^{37}Ar , and ^{38}Ar are recorded, together with ^{39}Ar and ^{40}Ar , in order to gain additional information about cosmic-ray-produced Ar-isotopes and to infer appropriate corrections for side reactions leading to ^{39}Ar and ^{40}Ar , as well as for a possible ^{40}Ar -contribution entrapped in the sample at the lunar surface.

The principal target element for cosmic-ray-produced ^{38}Ar in lunar samples is calcium. Therefore, 35.1-day-lived ^{37}Ar produced in the reactor by $^{40}\text{Ca}(n,\alpha)^{37}\text{Ar}$ allows one to infer cosmic ray exposure ages from $^{38}\text{Ar}/^{37}\text{Ar}$ ratios in a fashion very similar to the determination of ^{39}Ar - ^{40}Ar ages. In addition, the $^{37}\text{Ar}/^{39}\text{Ar}$ ratios obtained in the stepwise release pattern yield the apparent Ca/K ratios of the mineral phases responsible for the gas release at a given temperature. Since the Ca/K ratio is

indicative of the mineral composition, this information can be very helpful in the interpretation of complex ³⁹Ar/⁴⁰Ar release patterns (ref. 4).

The most serious side reaction is the production of ³⁹Ar from n-reactions with ⁴²Ca and ⁴³Ca.

Typical Ca/K ratios for common lunar rock types range between ~ 100 and ~ 1000. This corresponds to Ca-derived ³⁹Ar contributions of about 5 to 35 percent of the total ³⁹Ar. A correction can be made based on the ³⁷Ar/³⁹Ar ratio produced from Ca. Since this ratio depends on the energy spectrum of the neutrons under the actual irradiation conditions, K-free Ca targets like CaF₂ must be irradiated together with the samples.

Other side reactions of neutrons with various K and Ca isotopes are less severe, but must nevertheless be taken into account (ref. 6). Further complications caused by thermal neutron capture reactions can be prevented by appropriate Cd shielding. Atmospheric Ar adsorbed at the samples is usually released by predegassing at ~ 300°C, but it may occasionally account for high ⁴⁰Ar/³⁶Ar ratios in the very first temperature fraction.

Surface exposed samples rich in implanted ³⁶Ar, ³⁸Ar, and ⁴⁰Ar from the solar wind or the lunar atmosphere should be avoided whenever possible. Small residues of trapped ⁴⁰Ar can be recognized from their ³⁶Ar and ³⁸Ar complements. A regular isochron plot of ⁴⁰Ar/³⁶Ar versus ³⁹Ar/³⁶Ar for the various temperature fractions may help to elucidate the proper ⁴⁰Ar/³⁶Ar ratio of the trapped component (actual values range from ~ 0.5 to ~ 10; see fig. 1).

To convert the measured Ar isotope ratios into ages, a monitor is required for which age, K content, and Ca content are accurately known. Precambrian hornblende standards have proved to be most suitable for this purpose. Flux gradients along the ampoule can be recognized from the ⁵⁸Co activity induced by fast neutrons in various segments of an included Ni wire.

⁴⁰Ar/³⁹Ar ratios are transformed into ages according to

$$t_s = 4.34 \cdot 10^9 \log(1 + R_s \cdot J) \text{ where}$$

$$J = [\exp(t_m/\tau) - 1]/R_m$$

$$\tau = \text{mean life of } ^{40}\text{K}; 1,885 \times 10^9 \text{yr}$$

$$R = ^{40}\text{Ar}_{\text{radiogenic}} / ^{39}\text{Ar}_{\text{corrected}}$$

Subscripts *s* and *m* refer to sample and monitor, respectively. The ³⁸Ar-Ca exposure age is given by

$$T = \left(\frac{^{38}\text{Ar}_c}{^{37}\text{Ar}_s} \right) \frac{\sum ^{37}\text{Ar}_m}{\text{Ca}_m} \cdot \frac{1}{P} \text{ where}$$

$\sum ^{37}\text{Ar}_m$ is the total ³⁷Ar released from the monitor at all temperature fractions, Ca_m is the Ca content of the monitor in g/g sample, and *P* is the ³⁸Ar production rate per gram Ca and unit time.

³⁸Ar_c is cosmogenic ³⁸Ar as deduced from a split of the total ³⁸Ar and ³⁶Ar contents and the isotopic compositions of cosmogenic and trapped Ar (see ref. 5). ³⁷Ar must be corrected for decay between irradiation and measurement.

The total K and Ca contents of a sample are obtained by

$$K_s = K_m (\sum ^{39}\text{Ar}_s / \sum ^{39}\text{Ar}_m) \text{ and}$$

$$\text{Ca}_s = \text{Ca}_m (\sum ^{37}\text{Ar}_s / \sum ^{37}\text{Ar}_m)$$

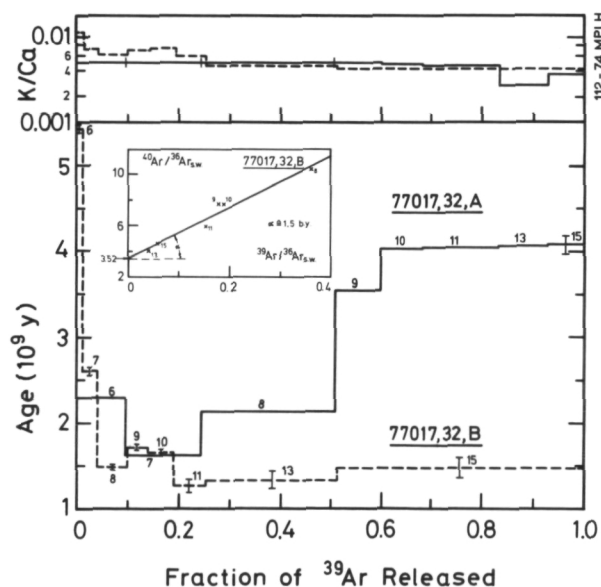


Figure 1.—Ar release patterns of anorthositic breccia 77017,32,A and glassy vein 77017,32,B. Apparent K/Ca ratios are also shown. Small numerals indicate degassing temperature in 100°C. The insert illustrates the determination of the ⁴⁰Ar/³⁶Ar ratio of nonradiogenic Ar included in the glass.

In the further discussion, the Apollo 17 highland rock 77017 will be used as an example. This rock is a white anorthositic breccia (subsample "A") veined by a black vuggy glass (subsample "B"). After separation of the two components, samples of 100 mg and 32.6 mg, respectively, were cleaned in ethanol, wrapped in Al foil, stacked alternately in quartz ampoules, and vacuum sealed together with three samples of a 2.67 ± 0.02 -b.y.-old hornblende monitor, two CaF_2 crystals, and an Ni wire. The Cd-shielded ampoule was irradiated for 78 hours in the core of the BR-2 reactor at Mol, Belgium. The total neutron dose above 0.1-MeV energy was $\sim 1.5 \times 10^{19}/\text{cm}^2$. The flux gradient along the whole length of the ampoule was 3.6 percent. For the sample positions, J values were 0.0628 and 0.0631.

After degassing for 1 hour each at 600, 700, 800, 900, 1000, 1100, 1300, and 1500°C, the extracted Ar was analyzed in a high sensitivity mass spectrometer. The results are summarized in table 1.

Ar Release Patterns, Exemplified by Apollo 17 Samples

Figure 1 shows a plot of the apparent ages at the various temperature fractions, together with the apparent K/Ca ratios of the corresponding release fractions. The age pattern for the anorthositic breccia 77017,32,A exhibits three typical features of general interest:

1. A relatively high apparent age in the very first temperature step. This can be due either to an atmospheric contamination or to Ar that was lost from less retentive sites, but partially preserved through uptake at grain boundaries.
2. A monotonous increase of ages with increasing temperature, reflecting gas loss in the less retentive mineral sites.
3. A rather constant plateau age at higher temperatures, indicating that the rock does in fact contain retentive domains that behaved as isotopically closed

microcells, since the rock was formed at the time indicated by the plateau age— 4.05 ± 0.04 b.y. ago in our example. Note that conventional K-Ar dating would have yielded an age of 3.23 ± 0.07 b.y. only.

Another feature frequently observed in highland rocks but not displayed in our example is a decrease of apparent ages from the plateau value at very high temperatures. Turner et al. (ref. 7) noticed that pyroxenes are responsible for this effect. The physical reason is not clear at present. Subsolidus crystallization of pyroxenes from glass long after rock formation could be responsible (early Ar losses from low-retentive glass, high activation energy of pyroxene today) (ref. 5).

A further frequent deviation of age patterns from the ideal case is a sudden increase of age above the plateau value at very high temperatures close to the liquidus (refs. 8 and 9). There are two possible explanations:

1. Relicts of ancient rock clasts with sufficient retentivity to resist the thermal metamorphism that had reset the radiometric clocks for the other constituents are included within a breccia.
2. ^{39}Ar deficit occurred due to the recoil displacement of ^{39}Ar by a few hundred Å in statu nascendi. Following intense preheating in the earlier degassings, a more than proportional share of ^{39}Ar may have been lost.

More generally, physico-chemical reactions during gas extraction may lead to mixing of phases that were previously earmarked by different $^{39}\text{Ar}/^{40}\text{Ar}$ ratios. Also, perceptible quantities of ^{39}Ar may be directly lost during production in the irradiation from very fine-grained minerals ($\leq 1 \mu\text{m}$ diameter). Apart from these experimental reasons, structured release patterns may be due either to contributions from various mineral phases with different ages and/or different solid-state properties or to different types of imperfections in the same type of mineral, either of primary nature or caused by such things

as shock effects or radiation damage. The latter case is most likely when the K/Ca variation through the whole temperature range is as insignificant as for our example 77017,32,A (fig. 1). If, on the other hand, K-rich interstitials or feldspars exist in a breccia, then the K/Ca ratio may vary by orders of magnitude.

In our opinion, one should be rather reluctant in assigning geological significance to singularities in release patterns like "humps" and "dips" in various temperature ranges. Even if such a deviation is resolved into some closely spaced temperature fractions, one should keep in mind that an ideal crystal with just one type of gas-bearing lattice sites would release its gas over a range of temperatures rather than at one temperature. Obviously, methodical studies are required before too much emphasis is given to the interpretation of details. At present one should be satisfied if it is possible to infer a plateau age. This is by no means always the case. Quite often release patterns show a contin-

uous increase with temperature up to completely unreasonable ages, and no plateau is defined at all. These samples contain either excess ⁴⁰Ar (neither produced in situ nor accompanied by trapped ³⁶Ar), or their retention characteristics are completely disturbed by some unidentified process that must be rather radical but still not sufficient to completely reset the radiometric clock for all constituents of the sample.

The glassy vein 77017,32,B must be the result of a melt injection into the breccia, possibly at the time of the final brecciation. Shock melting in situ can be excluded from the fact that the glass contains large quantities of ³⁶Ar that must be derived from the solar-wind-loaded regolith as source material of the glass. The breccia itself is essentially free of trapped Ar (table 1). Trapped Ar contains variable proportions of ⁴⁰Ar (refs. 10 and 11). For samples like our glass, this proportion must be known in order to distinguish the in-situ-produced radiogenic ⁴⁰Ar. It may be obtained from a plot of

Table 1.—Analytical Results for Highland Breccia 77017,32

77017,32,A K 410 ± 30 ppm; Ca 9.6 ± 0.8%; Exposure age 80 ± 10 m.y. Total Ar age 3.23 ± 0.07 b.y.; Plateau age 4.05 ± 0.04 b.y.						77017,32,B (glassy vein) K 475 ± 30 ppm; Ca 10 ± 0.8%; Exposure age 90 ± 40 m.y.; Total Ar age 1.67 ± 0.3 b.y.; Plateau age 1.5 ± 0.2 b.y.				
Temperature °C	⁴⁰ Ar _R	³⁹ Ar _K	³⁸ Ar _C	³⁷ Ar _{corr.}	³⁶ Ar _T	⁴⁰ Ar _R	³⁹ Ar _K	³⁸ Ar _C	³⁷ Ar _{corr.}	³⁶ Ar _T
600	68.1	1.80	0.65	193	0.20	83.2	0.312	0.08	15	1.33
700	62.8	2.91	1.39	314	0.16	27.9	0.586	0.23	44	1.50
800	166	4.99	2.81	545	0.30	24.4	1.284	0.65	112	3.57
900	153	1.72	1.03	193	0.12	21.7	0.914	0.49	70	5.15
1000	200	1.67	1.06	194	0.14	25.7	1.154	0.57	84	6.14
1100	335	2.78	1.85	338	0.17	20.5	1.350	0.80	120	8.85
1300	229	1.89	2.17	375	0.23	94.7	5.77	4.76	653	142
1500	169	1.38	1.11	194	0.11	204	10.8	8.04	1352	177
Total	1385	19.2	12.1	2345	1.43	500	22.2	15.6	2450	346

NOTES: Explanation of subscripts: R—radiogenic
K—potassium-derived
C—cosmogenic
corr.—corrected for decay
T—trapped

Due to rounding, figures may not add to totals.

$^{40}\text{Ar}/^{36}\text{Ar}_{\text{s.w.}}$ versus $^{39}\text{Ar}/^{36}\text{Ar}_{\text{s.w.}}$ (insert of fig. 1). In spite of large errors introduced by this correction, we can infer a plateau age of 1.5 ± 0.2 b.y. for the glass. Obviously, the glass was injected into the breccia ~ 2.5 b.y. after the crystallization of the anorthositic breccia clasts. The extremely high "age" in the 600°C release of the glass sample could be caused by surficial inclusion of extraneous ^{40}Ar or atmospheric argon.

Apart from samples 77017 discussed above, we have dated 10 more Apollo 17 samples in an analogous manner. For our discussion, the data given in table 2 are sufficient. With reference to the foregoing discussion, a short characterization of the release type of each sample is also included. Further details are given in Kirsten et al. (ref. 12) and Kirsten and Horn (ref. 9).

INTERPRETATION OF PLATEAU AGES

It is very encouraging to note that the agreement between ^{39}Ar - ^{40}Ar plateau ages and Rb-Sr-ages is very good in nearly every case for which comparisons have been made (see ref. 13 and Kirsten and Horn, unpublished). This applies also to samples for which the age plateau covers only an intermediate temperature range. Three conclusions can be drawn from the observed consistency.

1. In general, ^{39}Ar - ^{40}Ar -plateau ages are reliable also in cases for which Rb-Sr ages cannot be obtained (e.g., coarse fines).
2. The "geological" half life of ^{87}Rb is once more confirmed.
3. Rock-forming processes or metamorphism on the Moon reset K-Ar and Rb-Sr clocks at essentially the same time (± 20 m.y.).

The latter point leads to the discussion of the geological interpretation of plateau ages. ^{39}Ar - ^{40}Ar ages are gas-retention ages. The time at which the temperature dropped below a critical level and the rock became

isotopically closed is determined. Implied is the assumption that preexisting ^{40}Ar was expelled at that time and that the K-Ar clock was in fact set to zero.

On the Moon the critical thermal event could be

1. Crystallization of a cooling magma or of volcanic pyroclastics; metamorphism might occur at the contacts
2. Local impact melting or volcanic fire fountaining
3. Displacement of rocks passing different P-T levels (e.g., uplift)
4. Large-scale basin-forming impacts with all grades of shock metamorphism

The first case most likely applies to the mare basalts, but younger lava dikes or sills penetrating older ones may affect their ages. The second case is responsible for ages of particular glass samples or glass splashes and veins such as our sample 77017,32,B.

Most highland rocks are rather complex multistage breccias. They are believed to be ejecta of the large basin-forming events that occurred during the childhood of the Moon. Further brecciation was caused by more local impacts. The question then is whether the ages of highland rocks can tell us the sequence of the major basin-forming events and of the respective lunar formations. Here are two crucial problems:

1. It is by no means clear to what extent the large-scale events have reset the radiometric clocks.
2. It is quite ambiguous to associate a given lunar breccia with a certain formation and/or event.

These two points will now be discussed in some detail.

Some authors have concluded, mainly from the predominance of a certain age for a suite of samples tentatively assigned to the same formation, that the basin-forming event has equilibrated the radioisotopes by (1) extensive thermal metamorphism associated with the event (refs. 14, 15, and 16) and (2) uplift from depths where the temperature prevents retention of Ar (refs. 15 and 17).

Table 2.—Summary of ^{39}Ar - ^{40}Ar Results for Apollo 17 Rocks

Sample Number	Rock Type	Sampling Site and Probable Origin	Exposure Age ⁽⁴⁾ (m.y.)	Total Ar-Age (b.y.)	Plateau Age (b.y.)	Type of Release Pattern ⁽⁶⁾
70215,21	Mare basalt fine grained	Near Lunar Module Camelot Crater ⁽¹⁾	100 ± 12	3.81 ± 0.10	3.84 ± 0.04	a,b,B
79155,24	Mare basalt coarse grained, shocked	Rim of Van Serg Crater, Cochise, Shakespeare, Henry Craters?	575 ± 60	3.73 ± 0.07	3.80 ± 0.04	a,b,c,C
75055,11,2	Mare basalt coarse grained	Camelot Crater	85 ± 10	3.62 ± 0.07	3.82 ± 0.05	a,b,d,C
78503,13,B	Mare basalt medium grained	Base of Sculptured Hills; Camelot Crater ⁽¹⁾	105 ± 15	3.68 ± 0.08	3.83 ± 0.04	a,b,C
74243,4,A	Mare basalt coarse grained	Shorty Crater ⁽²⁾	315 ± 40	3.76 ± 0.08	3.78 ± 0.04	a,b,d,C
74243,4,B	Mare basalt very fine grained	Shorty Crater ⁽²⁾	57 ± 10	4.04 ± 0.10	No plateau	Steady increase to 5.9 b.y. (excess Ar); C
74243,4,C	Poikilitic mare basalt, medium grained	Shorty Crater ⁽²⁾	58 ± 8	3.82 ± 0.08	(3.93) ⁽⁵⁾	b,c,d,C
77017,32,A	Anorthositic breccia, poikilitic clasts	Base of North Massif	80 ± 10	3.23 ± 0.07	4.05 ± 0.04	a,b,c,A; see figure 1
77017,32,B	Black glass vein penetrat- ing A	Base of North Massif	90 ± 40	1.67 ± 0.3	1.5 ± 0.2	See discussion and figure 1, A
76055,4,1	Polymict breccia, noritic matrix	Base of North Massif	120 ± 15	4.05 ± 0.08	4.05 ± 0.07	a,A
70053,8	Anorthositic breccia, monomict	Base of North Massif ⁽³⁾	160 ± 20	4.06 ± 0.08	(4.3 ?)	
78503,13 A	Poikilitic gabbro	Base of Sculptured Hills	290 ± 35	4.26 ± 0.08	4.28 ± 0.04	Steady increase from 3.5 to 4.3 b.y.; A

NOTES: (1) Inferred from exposure age.

(2) Probably preirradiated since exposure age of Shorty Crater is ~ 30 m.y.

(3) Picking pot; eventually broken from 76335.

(4) Based on $(^{39}\text{Ar}/^{39}\text{Ar})_T = 0.187$, $(^{39}\text{Ar}/^{39}\text{Ar})_C = 1.7$; production rate $1.7 \pm 0.17 \times 10^{-8}$ ccSTP $^{39}\text{Ar}/\text{g Ca}$, m.y. Fe and Ti neglected.

(5) Maximum value, only in one temperature fraction.

(6) Key: a—well-defined plateau; b—initial increase (gas loss); c—decrease at high temperatures; d—raised value at 1500°C; e—high value at 600°C; A—K/Ca ratio constant within factor of ~ 3; B—K/Ca ratio decreases monotonously by factor of ~ 20; C—K/Ca ratio decreases monotonously by factor of ~ 200.

However, it becomes increasingly clear that, in fact, a range of ages occurs also for rocks from within *one* formation or even among clasts of the same breccia (refs. 8 and 17). This unavoidably asks for the inheritance of some of the preexisting radiogenic species that were not equilibrated in the basin-forming event. Also, from the variety of metamorphic effects recorded in Apollo 14 breccias (ref. 18) it was concluded that these rocks cannot have been produced and/or metamorphosed by a single event, but that they also retain imprints of previous igneous, metamorphic, and collisional phenomena.

We have concluded that radiometric ages do not necessarily date the events responsible for the deposition of rocks, but that, nevertheless, the ages measured on rocks from a given formation can be used to infer an upper age limit for the formation itself since a sedimentologic formation cannot be older than the youngest rock found within this formation. The youngest rock age may date the respective event, possibly because the rocks were melted or heated at that time, but probably because they were excavated from a depth in which temperatures were high and isotopic systems were open (ref. 17).

All these discussions depend on the proper assignment of rocks to formations and of formations to basins. Such assignments are usually made on the basis of

- (1) proximity of the basin closest to the sampling site; (2) stratigraphic relations (ejecta rays, etc.); and (3) petrographical similarities among various rocks.

An additional approach is a distinction based on meteoritic trace element admixtures related to the different basin-forming projectiles (ref. 19).

As the observational evidence increases, it seems that most authors (including those of this paper) may previously have been too optimistic in accepting proposed relations between rocks and formations, especially since mixing of ejecta from various formations, as well as locally derived components, is more important than had been thought before (see, for example, refs. 20 and 21). Schaeffer and

Husain (ref. 15) propose to use statistical predictions of the abundance of ejecta from different basins at a given site (ref. 22) for the respective assignments, but the used ejecta blanket thicknesses are inferred from a rather simplistic model. Without supporting evidence, it is not justified to ascribe different ages found within one sampling site to rocks from different formations. For example, the chemical classification of Morgan et al. (ref. 19) does not lead to a correlation between formations and the *face* values of radiometric ages. In conclusion, only a firm assignment of samples, together with the use of *minimum* ages of related rock suites, can lead to the establishment of a proper chronological sequence of the major lunar structures as tentatively attempted in the next sections.

DISCUSSION OF APOLLO 17 RESULTS

The Apollo 17 module has landed in the Taurus-Littrow highlands in a topographical low filled by high Ti basalts and bordered by three highland units: North Massif, Sculptured Hills, and South Massif. We have dated seven mare basalts (three larger rocks: 70215, 79155, 75055; four independent small fragments: 78503, 13B, 74243, 4A, B, and C) and four highland rocks (breccias 77017, 76055, small fragments 70053, 8 and 78503, 13A) (table 2).

Mare Basalts

For five out of seven dated mare basalts, we obtain plateau ages within the very narrow range of $(3.78 \pm 0.04) - (3.84 \pm 0.04)$ b.y. (table 2). This age is interpreted as the crystallization age of the upwelling magma and very probably dates the end of valley filling at Taurus-Littrow almost contemporaneously with the end of the filling of Mare Tranquillitatis (Apollo 11). Since the five dated basalts represent at least two different types, subsequent lava flows must have occurred within only 60 m.y. or so.

As can be seen from the total argon ages,

gas losses have been rather moderate. In the 1500°C-fraction, some of the samples display an increase in apparent age. This could be due to inherited ancient crustal material incorporated into the upwelling basaltic magma at this locality, analogous to comparable contaminations in many continental terrestrial basalts. For a more detailed discussion, see Kirsten and Horn (ref. 9).

Highland Rocks

Breccias 77017,32,A and 76055 represent material from the North Massif. They contain rock clasts within a crushed and annealed matrix. Both breccias give well-defined plateau ages of 4.05 b.y., which is within the age range of other Apollo 17 highland samples recently reported by various authors at the Fifth Lunar Science Conference (3.9 to 4.3 b.y.).

Contrary to 76055, breccia 77017,32,A has suffered appreciable gas loss. This and the observed shock effects are probably related to the earlier mentioned glass injection caused by a local impact about 1.5 b.y. ago.

The age of 4.05 b.y. could eventually date the time of metamorphism of these rocks. However, before we continue in the interpretation let us first discuss a topic that was rather controversial until the Fifth Lunar Science Conference. It concerns the observation of ³⁹Ar-⁴⁰Ar ages in excess of 4.1 b.y. in small rock fragments extracted from coarse fines (ref. 23). Skepticism was expressed because of the dominant opinion that basin-forming impacts equilibrate isotopic systems and because no larger rocks of comparable age had been found. A cataclysm had been proposed to account for the observation that highland rocks from the various basins were isotopically equilibrated within a rather narrow time interval of 3.95 ± 0.1 b.y. (refs. 24 and 25). Accordingly, all the major circular lunar basins should have been produced during this violent era by an episodic period of giant impacts. Consequently, older rocks should have had little chance to survive that catastrophic period without isotopic reequili-

bration. In the meantime, ages between 4.1 and 4.3 b.y. have been repeatedly found by various authors in Apollo 16 and 17 coarse fines (refs. 16, 17, 26, and 27) and also in larger rocks or clasts (refs. 8, 16, 27, and 28).

If the current view of the relation between formations and impact basins is adopted, all the accumulated age data would indeed suggest that the major lunar basins were formed within a time span of ~ 200 m.y. centered at ~ 3.95 b.y. ago (see next section). However, such a distribution can also be interpreted in terms of an exponential decrease of crater-forming projectiles (above 200 m in diameter) with time. The rocks with ages in excess of 4.1 b.y. could have been stored in that violent early phase at a depth of a few kilometers, thereby escaping destruction through the high meteorite flux rate at early times. Their ages, as well as those of the old breccia clasts included in some highland breccias, are proof that isotopic equilibration is not an unavoidable consequence of the metamorphism occurring ~ 4 b.y. ago, whatever its cause might have been.

Returning to the data given in table 2, coarse fine fragment 70053,8 is possibly, fragment 78503,13A certainly, another example for very old highland fragments. Anorthositic breccia 70053,8 shows a continuous increase in apparent age. It is doubtful whether the higher temperature fractions can be interpreted in terms of a plateau age near 4.3 b.y. On the other hand, poikilitic gabbro 78503,13A displays a very well-defined plateau age of 4.28 ± 0.04 b.y. The plateau is paralleled by a very constant K/Ca ratio, indicating that essentially only one single mineral phase has contributed to the ³⁹Ar-release. The gas loss of this sample is as low as 2.7 percent.

Altogether, the evidence supports the idea that rocks have crystallized within the lunar crust as early as 4.3 b.y. ago and that some of them have survived ever since (ref. 26).

Before we draw some conclusions from the results of the investigated highland samples with respect to the origin of Taurus-Littrow, let us briefly discuss the measured cosmic ray exposure ages.

Cosmic Ray Exposure Ages

Due to the limited range of the cosmic radiation, exposure ages date the integral time period in which a particular rock was deposited in the upper meter or so of the lunar regolith. Frequent turnover may give rise to a complex exposure history, and only in favorable cases does it become possible to associate certain exposure ages with particular local craters. At a smaller scale, the problem of assignment is quite analogous to the case of gas retention ages, and only from the repeated occurrence of a certain exposure age within the range of a particular local crater can the age of the latter be concluded with some confidence.

The exposure ages of our Apollo 17 rocks range from 57 to 575 m.y. Samples 70215, 75055, and 78503,13B were collected near Camelot Crater and yield within the limits of error a consistent exposure age of 95 ± 15 m.y. (table 2). The exposure ages of the other mare basalts cannot be related to specific cratering events. The exposure age of 575 m.y. for 79155 is among the highest so far measured for larger rocks. For small soil particles only, exposure ages occur up to at least 1.5 b.y. (ref. 5). The exposure ages of 74243, A,B, and C may reflect the typical complex exposure history of small regolith constituents. The similar exposure ages of ~ 58 m.y. for subsamples B and C seems to be coincidental, since these fragments are taken from a mixed lunar soil and are not a priori inter-related. They do not date Shorty Crater (near their sampling site), since the latter is known to be ~ 30 m.y. old (ref. 30). The exposure ages of highland rocks (table 2) have to be interpreted in terms of mass wasting at North Massif. No specific events can yet be recognized.

Chronology of the Lunar Highlands

Provided that the association of the Apollo 17 highland breccias to the Serenitatis event is correct, we may conclude from the age of 77017 and 76055 that this event occurred ≤ 4.05 b.y. ago. Crater counts and strati-

graphical observations indicate that Serenitatis is the oldest of all circular basins (ref. 31). In particular, it is older than the Imbrium basin with an age of ~ 3.9 b.y. (ref. 17). Consequently, the Serenitatis basin was excavated between 3.9 and 4.05 b.y. ago, consistent with the observation that the stratigraphically younger basaltic lava flows at Taurus-Littrow solidified between 3.78 and 3.84 b.y. ago (ref. 12).

The youngest lunar basin dated is Orientale (3.82 to 3.85 b.y.) (ref. 17). Lunar areas inaccessible for sampling can be included in the established time sequence on the basis of crater counts and stratigraphical relations. Accordingly, at least 28 lunar basins must have been formed between 3.82 and 4.05 b.y. ago. The sequence of the most prominent of those basins is Orientale, Imbrium, Nectaris, Crisium, Serenitatis (ref. 31).

LUNAR TIMETABLE

Since a review of the lunar time scale is given elsewhere in this conference (ref. 32), only a brief outline on this subject will be given in our context. It is summarized in figure 2.

At least a part of the lunar material must have condensed within 100 m.y. after chondrite formation ~ 4.6 b.y. ago. This can be concluded from the observation that certain lunar breccias contain the recycled decay products of the now extinct radioisotopes J^{129} and Pu^{244} , which have half lives of 17 and 82 m.y., respectively (ref. 33). However, it remains possible that this decay occurred in solidified protolunar material that only later became incorporated into the Moon, provided that cold accretion occurred. Based on Rb-Sr and U-Pb studies, it has been found that the primary chemical separation of the primitive lunar crust must have occurred between 4.6 and 4.3 b.y. ago (refs. 32 and 34). This requires in the beginning a molten state at least for the outer 100 km or so.

As time went on between 4.3 and 4 b.y., the heat proceeded inward, and a solid lithosphere developed on top of the molten layers. It was impinged or penetrated by asteroid-

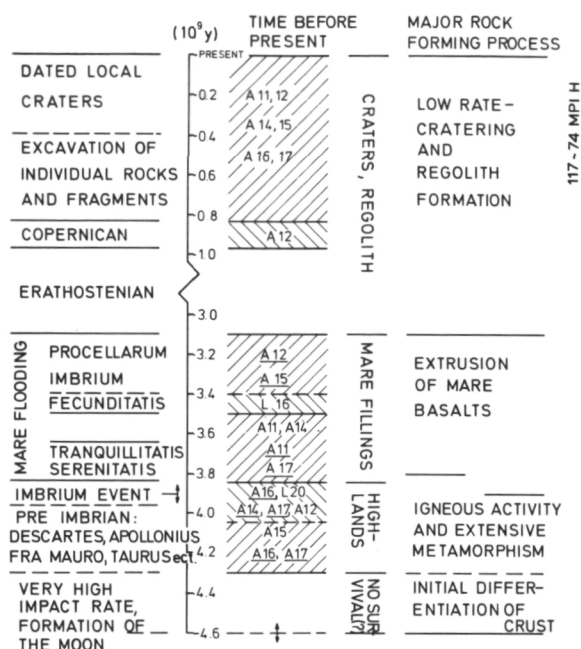


Figure 2.—Lunar Timetable based on radiometric age determinations. A = Apollo mission; L = Luna Mission.

sized bodies that formed basins like Nubium or Fecunditatis. Due to the high impact rate at that time, rocks already solidified had little chance to survive. The oldest surviving rocks with ages between 4.3 and 4.1 b.y. were probably partially protected at some depth. The oldest interrelated rock suites have ages of ~ 4 b.y. and are believed to be associated with the Serenitatis basin. Many basins were formed between 3.85 and 4.05 b.y. ago. Such ages are found for many rocks sampled from ejecta blankets of large basins, the most prominent one being the Imbrium basin that was excavated between 3.85 and 3.9 b.y. ago.¹ The youngest large circular basin is Orientale with an age between 3.82 and 3.85 b.y. Beginning about 3.85 b.y. ago, the face of the Moon was changed by the onset of a new type

¹ This is not the place to discuss the entirely controversial view of Schonfeld and Meyer (ref. 35) who give arguments not easily disproved that Imbrium is in fact 4.3 to 4.4 b.y. old and that dated rocks result from more local events. However, this illustrates the difficulty in the geological assignments.

of igneous activity, the extrusion of mare basalts, which were upwelling from depths of about 150 to 250 km. These basalts are the differentiation product of a Fe- and Mg-rich source magma at greater depths. The fluid basaltic liquids filled the various basins in subsequent floodings, where for each mare the uppermost lava flow is the latest one. The Tranquillitatis basin was flooded between ~ 3.8 and ~ 3.5 b.y. ago, Mare Imbrium between 3.35 and 3.15 b.y. ago, and the Oceanus Procellarum between ~ 3.3 and ~ 3.1 b.y. ago. Thus, the period of mare filling extended from ~ 3.8 to 3.1 b.y.

No lunar igneous rock of younger age has been found. It seems clear that the large-scale features of the Moon are today the same as 3.1 b.y. ago. Since that time, only occasional impacts like that producing the Crater Copernicus have altered the face of the Moon. However, on a smaller scale, exposure ages tell us that most rocks that are now found at the top of the surface of the Moon were excavated by smaller impacts during the last 1 b.y., and that regolith formation and mixing is an ongoing process, although at progressively lower intensity.

A proper time scale provides random conditions that limit the choice of possible models for the evolution of planetary objects that include condensation, accretion, differentiation, heat transfer, and metamorphism. For instance, the occurrence of lava flows as late as 1.5 b.y. after the formation of the Moon is incompatible with an initially cold Moon (ref. 36). Considerations of this type must be seen in the context of the planetary system as a whole. For this reason, meteorite chronology is presently experiencing a renaissance, as will be discussed in the following section.

THE MALVERN ACHONDRITE

We became curious about Malvern because of its striking textural similarity with annealed polymict lunar highland breccias, e.g., those collected at the Fra Mauro site (ref. 37). The meteorite was found in South Africa in 1933. Based on chemical evidence, Malvern has been classified as a howardite,

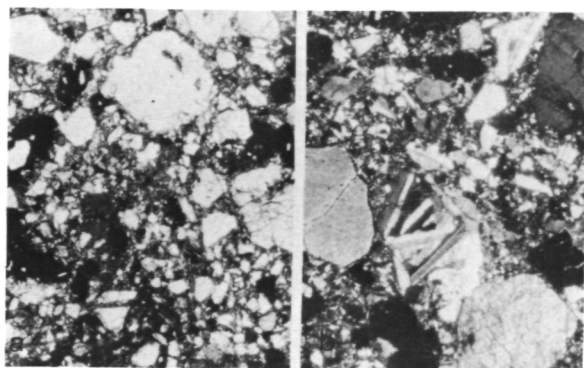


Figure 3.—Sections of the achondrite *Malvern* in plain transmitted light. Left: dark grey and black areas are glass and recrystallized glass, respectively; large fractured angular fragments are orthopyroxenes; plagioclase is clear white. Widths of picture equals 2 mm. The textural resemblance of this breccia is that of moderately annealed Apollo 14 breccias. Right: as above, with an intact rock clast.

but texturally it seems rather unique (Ramdohr, personal communication). It is highly brecciated (fig. 3) and contains various clasts. The dominant clast type (denoted A) is glassy to devitrified with small, but abundant, disseminated opaques and various amounts of trapped angular mineral fragments (fig. 3). Clast C is a coarse-grained aggregate of orthopyroxene, plagioclase, and clinopyroxene. As a whole, the meteorite resembles a moderately annealed Apollo 14 breccia. The glass occurs in the form of spherules and angular fragments up to 1 mm in diameter. The mineral fragments are shocked orthopyroxenes (hypersthene-bronzite), clinopyroxene, small olivine fragments, and larger plagioclases. The plagioclases appear to be recrystallized since they are clear with no signs of shock. We have separated the major constituents and performed ^{39}Ar - ^{40}Ar dating as well as rare gas analyses. The results are compiled in table 3; the age release patterns are shown in figure 4.

The apparent age of the glassy clast A1 shows an initial rise to 3.8 b.y. at 900°C. At higher temperatures it assumes values between 3.6 and 3.8 b.y. The ages of clast C vary in a similar fashion between 3.4 and

37 b.y. (the larger errors for sample C are mainly due to the low K content of 63 ppm). The fluctuations are not understood in detail, but it may be safe to state that *Malvern* was affected by a strong outgassing event between 3.4 and 3.8 b.y. ago. (In an earlier investigation, Podosek and Huneke (ref. 41) found nearly the same age range for the Stannern achondrite.) Most likely the minimum age of 3.6 b.y. for clast A1 corresponds to the age of the glass, whereas small admixtures of older material cause the scatter. This is substantiated by microscopical observation and the behavior of the K/Ca ratios for clasts A1 and C. The drastic decrease of this ratio above 1300°C in clast C suggests that the high ages for the 1300°C and 1400°C fractions are due to Ar release from distinct

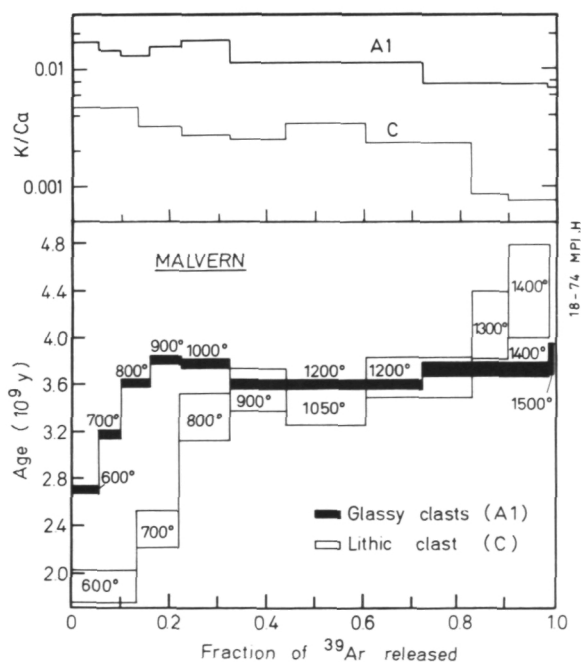


Figure 4.— ^{39}Ar - ^{40}Ar age release pattern for the *Malvern* achondrite. Sample A1 is enriched in glass splashes and spherules, sample C is a pyroxene-rich clast. Apparent K/Ca ratios are also shown. Degassing temperatures are indicated. The age patterns reveal a strong outgassing event between 3.4 and 3.8 b.y. ago, very probably associated with the formation of the glass. Only the most retentive sites of the lithic clast escaped complete outgassing.

residuals of material inherited from the parent.

Rare Gas Analysis

The rare gas contents of glassy clasts and glass-free matrix chips of Malvern are given

in table 3. Malvern is not a "gas-rich" meteorite, but the matrix does contain moderate amounts of heavily fractionated trapped gasses (table 3). This indicates heavy outgassing during intensive metamorphism. Trapped Ne and Ar included in the glassy

Table 3.—Analytical Results of the Malvern Achondrite

	Glass-Free Matrix Chips		Glassy Clasts		Lithic Clast
	B1	B2	A2	A1 ⁽¹⁾	C ⁽¹⁾
³ He ⁽²⁾	7.7 ± 0.4	5.4 ± 0.4	5.2 ± 0.3		
⁴ He	1000 ± 60	1970 ± 100	645 ± 50		
²⁰ Ne	4.60 ± 0.25	6.79 ± 0.3	4.84 ± 0.25		
²¹ Ne	3.34 ± 0.1	3.62 ± 0.15	3.64 ± 0.1		
²² Ne	3.83 ± 0.15	4.19 ± 0.2	4.24 ± 0.15		
³⁶ Ar	15.5 ± 0.5	15.0 ± 0.8	4.4 ± 0.3	5.95 ± 0.7 ⁽⁴⁾	2.55 ± 0.3 ⁽⁴⁾
³⁸ Ar	4.6 ± 0.2	4.6 ± 0.3	2.3 ± 0.1	2.77 ± 0.3 ⁽⁴⁾	1.6 ± 0.2 ⁽⁴⁾
⁴⁰ Ar	1010 ± 30	1930 ± 100	2170 ± 60	2325 ± 120 ⁽⁴⁾	255 ± 30 ⁽⁴⁾
⁸⁴ Kr	~0.014	⁽³⁾	< 0.005		
¹³² Xe	~0.006	⁽³⁾	< 0.005		
K (ppm)				525 ± 40	63 ± 12
Ca (%)				5.05 ± 0.4	3.25 ± 0.2
²⁰ Ne _T ⁽⁵⁾	1.3 ± 0.3	3.2 ± 0.4 ⁽⁶⁾	1.2 ± 0.3		
³⁸ Ar _C ⁽⁷⁾	1.91 ± 0.2	2.02 ± 0.2	1.66 ± 0.2	1.86 ± 0.2	1.26 ± 0.2
³ He _C / ²¹ Ne _C ⁽⁸⁾	2.25 ± 0.3	1.44 ± 0.2	1.4 ± 0.2		
²¹ Ne _C / ³⁸ Ar _C	1.75 ± 0.2	1.79 ± 0.2	2.19 ± 0.20		
⁴ He/ ²⁰ Ne _T ⁽⁹⁾	< 750	< 600	< 500		
²⁰ Ne _T / ³⁰ Ar _T	0.09 ± 0.03	0.23 ± 0.05	0.35 ± 0.1		
³⁰ Ar _T / ⁸⁴ Kr _T	~1000		> 700		
T ₃ (m.y.) ⁽¹⁰⁾	3 ± 0.5	2 ± 0.5	2 ± 0.5		
T ₂₁ (m.y.) ⁽¹⁰⁾	7 ± 1	8 ± 1	8 ± 1		
T ₃₈ (m.y.)	16 ± 3 ⁽¹⁰⁾	17 ± 3 ⁽¹⁰⁾	14 ± 3 ⁽¹⁰⁾	19 ± 4 ^(10,11)	17 ± 4 ^(10,11)
Total Ar-age (10 ⁹ y)				3.62 ± 0.1	3.48 ± 0.3
Plateau age (10 ⁹ y)				3.7 ± 0.15	3.6? (see fig. 4)

NOTES: (1) ³⁹Ar-⁴⁰Ar-analysis.

(2) Unit for rare-gas isotopes is 10⁻⁸ccSTP/g.

(3) Sample weight 10 mg only.

(4) Corrected for reactor-produced isotopes.

(5) Subscripts C and T refer to "cosmogenic" and "trapped," respectively.

A three-isotope plot of all Ne data gave (²⁰Ne/²²Ne)_T = 10.5 ± 1; (²²Ne/²¹Ne) ~ 32; assumption: ²⁰Ne_C = ²¹Ne_C.

(6) ~1 percent of the pyroxenes of this particular sample contain heavily annealed solar flare tracks (Storzer and Pellas, private communication).

(7) Based on (³⁰Ar/³⁸Ar)_C = 0.59; (³⁰Ar/³⁸Ar)_T = 5.35.

(8) Allowance is made for a possible contribution of ³He_T.

(9) ⁴He_{radiogen} not known, possibly 100 percent of total ⁴He.

(10) T denotes cosmic ray exposure age.

Production rates are calculated from the chemical composition (ref. 37) and relations given by Herzog and Anders (ref. 38), Yaniv et al. (ref. 39), and Bogard et al. (ref. 40).

We arrive at (2.7 ± 0.3) × 10⁻⁸cc ³He/g, m.y.; (0.465 ± 0.050) 10⁻⁸cc ²¹Ne/g, m.y.;

(0.12 ± 0.012) × 10⁻⁸cc ³⁸Ar/g meteorite, m.y.

(11) ³⁷Ar-³⁸Ar exposure ages. Production rate derived from relations mentioned above is

(2.4 ± 0.24) × 10⁻⁸cc ³⁸Ar/g Ca, m.y. To account for Fe and Ti, it was multiplied by a factor 1.2.

samples are probably due to the adherent matrix material.

Due to diffusional loss of spallogenic gases, the ^3He and ^{21}Ne exposure ages are much lower than the ^{38}Ar exposure ages (table 3). The $^{38}\text{Ar}/\text{Ca}$ exposure age of clast C is 14 m.y. for fractions released up to 1200°C and rises to ~ 20 m.y. at the same high temperatures at which the ^{39}Ar - ^{40}Ar age rises above 4 b.y. This fact is suggestive of a preirradiation of the inherited parent material in clast C, but it could also be due to an exceptionally high Fe content of the mineral phase responsible for the gas release at very high temperatures.

Implications

There are two indications that Malvern must have contained solar-type rare gases sometime in its early history:

1. The high trapped $^{36}\text{Ar}/^{84}\text{Kr}$ ratio of ~ 1000 makes it unlikely that all the trapped ^{36}Ar is dissolved gas of the planetary type.
2. About 1 percent of the pyroxenes from sample B2 contain heavily annealed solar flare-induced tracks (Storzer and Pellas, private communication).

Where then is the trapped He and Ne complementary to trapped ^{36}Ar ? The relative abundance of Ne is depleted by more than a factor of 200 if compared to solar abundance ratios and it is still an order of magnitude lower than in lunar soil. The only explanation is that Malvern has once experienced extreme thermal stress and was heavily out-gassed and annealed.

It needs little imagination to suppose that it was the same event that was responsible for the formation of the glass and for the resetting of the K-Ar clock in all but the most retentive constituents at some time between 3.4 and 3.8 b.y., as indicated by the ^{39}Ar - ^{40}Ar data.

The occurrence of light trapped gases (ref. 42) and solar flare tracks (ref. 43) in meteorites indicates that the respective mete-

orites were derived from a parent body that was covered by a regolith (ref. 44), a rather common feature on top of planetary bodies (ref. 45).

The Moon as well as meteorite parent bodies were both bombarded with interplanetary debris, and giant impacts like those on the Moon must also have occurred on meteorite parent bodies. As on the Moon, such impacts had the potential to reset radiometric clocks to some extent. The age patterns of Malvern suggest that similar impact events took place on the Moon and meteoritic parent bodies and led to striking similarities in texture and retention characteristics of rare gases from various sources. For example, concentrations and fractionation patterns of trapped gases in lunar breccia 14303 (ref. 5) are nearly identical to those observed in Malvern (table 3). Evidence that collisional reheating of meteorite parent bodies is relatively frequent, not restricted to a certain time period and not restricted to a particular meteorite class, was first inferred from the distribution of total U-He and K-Ar ages (ref. 46). More recently, substantial details have been added to our knowledge about giant collisions in the solar system. Ages substantially below 4.6 b.y. have been found for an iron meteorite and two achondrites by Rb-Sr dating (refs. 47 and 48), four Ca-rich achondrites (ref. 41), and four chondrites (ref. 49). The plateau ages reported by authors of the latter reference are all below 0.6 b.y. However, resistant phases with higher ages coexist quite frequently with the annealed matrix (e.g., Malvern C, and Pasamonte) (ref. 41). Consistent with the near but not total obliteration of early irradiation records, this indicates intensive, but not annihilating, metamorphism.

References

1. PAPANASTASSIOU, D. A., AND G. J. WASSERBURG, Lunar Chronology and Evolution From Rb-Sr Studies of Apollo 11 and 12 Samples. *Earth Planet. Sci. Letters*, Vol. 11, 1971, p. 37.
2. MERRIHUE, C. M., AND G. TURNER, Potassium-argon dating by activation with fast neutrons. *J. Geophys. Res.*, Vol. 71, 1966, p. 2852.

3. TURNER, G., Argon 40-Argon 39 Dating of Lunar Rock Samples. *Proc. Apollo 11 Lunar Science Conference, Geochimica et Cosmochimica Acta*, Supplement 1, Vol. 2, 1970, p. 1665.
4. TURNER, G., J. C. HUNEKE, F. A. PODOSEK, AND G. J. WASSERBURG, ^{40}Ar - ^{39}Ar Ages and Cosmic Ray Exposure Ages of Apollo 14 Samples. *Earth Planet. Sci. Letters*, Vol. 12, 1971, p. 19.
5. KIRSTEN, T., J. DEUBNER, P. HORN, I. KANEOKA, J. KIKO, O. A. SCHAEFFER, AND S. K. THIO, The Rare Gas Record of Apollo 14 and 15 Samples. *Proc. Third Lunar Science Conference, Geochimica et Cosmochimica Acta*, Supplement 3, Vol. 2, 1972, p. 1865.
6. BRERETON, N. R., Corrections for Interfering Isotopes in the ^{40}Ar / ^{39}Ar Dating Method. *Earth Planet. Sci. Letters*, Vol. 8, 1970, p. 427.
7. TURNER, G., J. C. HUNEKE, F. A. PODOSEK, AND G. J. WASSERBURG, ^{40}Ar - ^{39}Ar Systematics in Rocks and Separated Minerals From Apollo 14. *Proc. Third Lunar Science Conference, Geochimica et Cosmochimica Acta*, Supplement 3, Vol. 2, 1972, p. 1589.
8. HUNEKE, J. C., E. K. JESSBERGER, AND G. J. WASSERBURG, The Age of Metamorphism of a Highland Breccia (65015) and a Glimpse at the Age of Its Protolith. *Lunar Science*, Vol. V, Lunar Science Institute, Houston, 1974, p. 375.
9. KIRSTEN, T., AND P. HORN, ^{39}Ar - ^{40}Ar Chronology of the Taurus-Littrow Region III: Ages of Mare Basalts and Highland Breccias and Some Remarks About the Interpretation of Highland Rock Ages. *Proc. Fifth Lunar Science Conference, Geochimica et Cosmochimica Acta*, Supplement 5, Vol. 2, to be published, 1974.
10. HEYMANN, D., AND A. YANIV, ^{40}Ar Anomaly in Lunar Samples From Apollo 11. *Proc. Apollo 11 Lunar Science Conference, Geochimica et Cosmochimica Acta*, Supplement 1, Vol. 2, 1970, p. 1261.
11. KIRSTEN, T., F. STEINBRUNN, AND J. ZÄHRINGER, Location and Variation of Trapped Rare Gases in Apollo 12 Lunar Samples. *Proc. Second Lunar Science Conference, Geochimica et Cosmochimica Acta*, Supplement 2, Vol. 2, 1971, p. 1651.
12. KIRSTEN, T., P. HORN, AND D. HEYMANN, Chronology of the Taurus-Littrow Region I: Ages of Two Major Rock Types From the Apollo 17 Site. *Earth Planet. Sci. Letters*, Vol. 20, 1973, p. 125.
13. STETTLER, A., P. EBERHARDT, J. GEISS, N. GRÖGLER, AND P. MAURER, ^{39}Ar - ^{40}Ar Ages and ^{37}Ar - ^{38}Ar Exposure Ages of Lunar Rocks. *Proc. Fourth Lunar Science Conference, Geochimica et Cosmochimica Acta*, Supplement 4, Vol. 2, 1973, p. 1865.
14. HUNEKE, J. C., E. K. JESSBERGER, F. A. PODOSEK, AND G. J. WASSERBURG, ^{40}Ar / ^{39}Ar Measurements in Apollo 16 and 17 Samples and the Chronology of Metamorphic and Volcanic Activity in the Taurus-Littrow Region. *Proc. Fourth Lunar Science Conference, Geochimica et Cosmochimica Acta*, Supplement 4, Vol. 2, 1973, p. 1725.
15. TURNER, G., P. H. CADOGAN, AND C. J. YONGE, Argon Selenochronology. *Proc. Fourth Lunar Science Conference, Geochimica et Cosmochimica Acta*, Supplement 4, Vol. 2, 1973, p. 1889.
16. SCHAEFFER, O. A., AND L. HUSAIN, Chronology of Lunar Basin Formation and Ages of Lunar Anorthositic Rocks. *Lunar Science*, Vol. V, Lunar Science Institute, Houston, 1974, p. 663; submitted to *Proc. Fifth Lunar Science Conference*, 1974.
17. KIRSTEN, T., P. HORN, AND J. KIKO, ^{39}Ar - ^{40}Ar Dating and Rare Gas Analysis of Apollo 16 Rocks and Soils. *Proc. Fourth Lunar Science Conference, Geochimica et Cosmochimica Acta*, Supplement 4, Vol. 2, 1973, p. 1757.
18. CHAO, E. C. T., J. A. MINKIN, AND J. B. BEST, Apollo 14 Breccias: General Characteristics and Classification. *Proc. Third Lunar Science Conference, Geochimica et Cosmochimica Acta*, Supplement 3, Vol. 1, 1972, p. 645.
19. MORGAN, J. W., R. GANAPATHY, H. HIGUCHI, AND E. ANDERS, Lunar Basins: Characterization of Projectiles From Meteoritic Trace Elements in Highland Samples. *Proc. Soviet-Am. Conference Cosmochem. Moon and Planets*, in press, 1975.
20. OBERBECK, V. R., F. HÖRZ, R. H. MORRISON, W. L. QUAIDE, AND D. E. GAULT, Effects of Formation of Large Craters and Basins on Emplacement of Smooth Plain Materials. *Lunar Science*, Vol. V, Lunar Science Institute, Houston, 1974, p. 568.
21. STÖFFLER, D., M. R. DENCE, M. ABADIAN, AND G. GRAUP, Ejecta Formations and Pre-Impact Stratigraphy of Lunar and Terrestrial Craters: Possible Implications for the Ancient Lunar Crust. *Lunar Science*, Vol. V, Lunar Science Institute, Houston, 1974, p. 746.
22. MCGETCHIN, T. R., M. SETTLE, AND J. W. HEAD, Radial Thickness Variation in Impact Crater Ejecta: Implications for Lunar Basin Deposits. *Earth Planet. Sci. Letters*, Vol. 20, 1973, p. 226.
23. SCHAEFFER, O. A., AND L. HUSAIN, Early Lunar History: Ages of 2-4 mm Soil Fragments From the Lunar Highlands. *Proc. Fourth Lunar Science Conference, Geochimica et Cosmochimica Acta*, Supplement 4, Vol. 2, 1973, p. 1847.
24. TERA, F., D. A. PAPANASTASSIOU, AND G. J. WASSERBURG, A Lunar Cataclysm at ~ 3.95 AE and the Structure of the Lunar Crust. *Lunar Science*, Vol. IV, Lunar Science Institute,

- Houston, 1973, p. 723.
25. TERA, F., D. A. PAPANASTASSIOU, AND G. J. WASSERBURG, The Lunar Time Scale and a Summary of Isotopic Evidence for a Terminal Lunar Cataclysm. *Lunar Science*, Vol. V, Lunar Science Institute, Houston, 1974, p. 792.
 26. KIRSTEN, T., AND P. HORN, ^{40}Ar - ^{39}Ar Chronology of the Taurus-Littrow Region II: A. 4.28 b.y. Old Troctolite and Ages of Basalts and Highland Breccias. *Lunar Science*, Vol. V, Lunar Science Institute, Houston, 1974, p. 419.
 27. STETTLER, A., P. EBERHARDT, J. GEISS, N. GRÖGLER, AND P. MAURER, Sequence of Tera Rock Formation and Basaltic Lava Flows on the Moon. *Lunar Science*, Vol. V, Lunar Science Institute, Houston, 1974, p. 738.
 28. CONSORTIUM INDOMITABLE, AND J. A. WOOD, Investigations of a KREEPy Stratified Boulder From the South Massif. *Lunar Science*, Vol. V, Supplement A, Lunar Science Institute, Houston, 1974, p. 4.
 29. BOGARD, D. D., L. E. NYQUIST, B. M. BANSAL, AND H. WIESMANN, 76535: An Old Lunar Rock? *Lunar Science*, Vol. V, Lunar Science Institute, Houston, 1974, p. 70.
 30. KIRSTEN, T., P. HORN, D. HEYMANN, W. HÜBNER, AND D. STORZER, Apollo 17 Crystalline Rocks and Soils: Rare Gases, Ion Tracks and Ages. *EOS Trans.*, AGU 54, 1973, 595.
 31. HARTMANN, W. K., AND C. A. WOOD, Moon: Origin and Evolution of Multiring Basins. *The Moon*, Vol. 3, 1971, p. 3.
 32. WASSERBURG, G., A Summary of the Lunar Time Scale and Implications for the Chronology of the Solar System. *Proc. Soviet-Am. Conference on Cosmochem. Moon and Planets*, in press, 1975.
 33. BEHRMANN, C., R. DROZD, AND C. HOHENBERG, Extinct Lunar Radioactivities: Xenon From ^{244}Pu and ^{129}I in Apollo 14 Breccias. *Earth Planet. Sci. Letters*, Vol. 17, 1973, p. 446.
 34. SCHONFELD, E., AND C. MEYER, JR., The Abundances of Components of the Lunar Soils by a Least Square Mixing Model and the Formation Age of KREEP. *Proc. Third Lunar Science Conference, Geochimica et Cosmochimica Acta*, Supplement 3, Vol. 2, 1972, p. 1397.
 35. SCHONFELD, E., AND C. MEYER, JR., The Old Imbrium Hypothesis. *Proc. Fourth Lunar Science Conference, Geochimica et Cosmochimica Acta*, Supplement 4, Vol. 1, 1973, p. 125.
 36. TOKSÖZ, M. N., AND S. C. SOLOMON, Thermal History and Evolution of the Moon. *The Moon*, Vol. 7, 1973, p. 251.
 37. JEROME, D. Y., AND M. C. MICHEL-LEVI, Quelques Aspects Remarquables de la Meteorite Achondritique de Malvern (Afrique du Sud). *Bull. Soc. Fr. Mineral. Cristallogr.*, Vol. 94, 1971, p. 156.
 38. HERZOG, G. F., AND E. A. ANDERS, Absolute Scale for Radiation Ages of Stony Meteorites. *Geochimica et Cosmochimica Acta*, Vol. 35, 1971, p. 605.
 39. YANIV, A., G. J. TAYLOR, S. ALLEN, AND D. HEYMANN, Stable Rare Gas Isotopes Produced by Solar Flares in Single Particles of Apollo 11 and 12 Fines. *Proc. Second Lunar Science Conference, Geochimica et Cosmochimica Acta*, Supplement 2, Vol. 2, 1971, p. 1705.
 40. BOGARD, D. D., J. G. FUNKHOUSER, O. A. SCHAEFFER, AND J. ZÄHRINGER, Noble Gas Abundances in Lunar Material. Cosmic Ray Spallation Products and Radiation Ages From the Sea of Tranquility and the Ocean of Storms. *J. Geophys. Res.*, Vol. 76, 1971, p. 2757.
 41. PODOSEK, F. A., AND J. C. HUNEKE, Argon 40-Argon 39 Chronology of Four Calcium Rich Acondrites. *Geochimica et Cosmochimica Acta*, Vol. 37, 1973, p. 667.
 42. ZÄHRINGER, J. Über die Uredelgase in den Achondriten Kapoeta und Staroe Pesjanoe. *Geochimica et Cosmochimica Acta*, Vol. 26, 1962, p. 665.
 43. PELLAS, P., G. POUPEAU, J. C. LORIN, H. REEVES, AND J. AUDOUZE, Primitive Low Energy Particle Irradiation of Meteorite Crystals. *Nature*, Vol. 223, 1969, p. 272.
 44. POUPEAU, G., T. KIRSTEN, F. STEINBRUNN, AND D. STORZER, *The Records of Solar Wind and Solar Flares in Aubrites*. To be published, 1974.
 45. DOLLFUS, A., Regolith in the Solar System. *Lunar Science*, Vol. V, Lunar Science Institute, Houston, 1974, p. 71.
 46. KIRSTEN, T., D. KRANKOWSKY, AND J. ZÄHRINGER, Edelgas- und Kalium Bestimmungen an Einer Größeren Zahl von Steinmeteoriten. *Geochimica et Cosmochimica Acta*, Vol. 27, 1963, p. 13.
 47. BURNETT, D. S., AND G. J. WASSERBURG, Evidence for the Formation of an Iron Meteorite at 3.8×10^6 Years. *Earth Planet. Sci. Letters*, Vol. 2, 1967, p. 137.
 48. PAPANASTASSIOU, D. A., R. S. RAJAN, J. C. HUNEKE, AND G. J. WASSERBURG, Rb-Sr Ages and Lunar Analogs in a Basaltic Achondrite; Implications for Early Solar System Chronologies. *Lunar Science*, Vol. V, Lunar Science Institute, Houston, 1974, p. 583.
 49. BOGARD, D. D., R. J. WRIGHT, AND L. HUSAIN, Dating of Degassing Events in Ordinary Chondrites by the ^{40}Ar - ^{39}Ar Technique. *EOS Trans.* AGU 55, 1974, p. 334 (abs.).

The Exposure History of the Apollo 16 Site: An Assessment Based on Methane and Hydrolysable Carbon

C. T. Pillinger, G. Eglinton, A. P. Gowar, A. J. T. Jull,
and J. R. Maxwell

*Organic Geochemistry Unit, School of Chemistry
University of Bristol
Bristol, United Kingdom*

Nineteen soils from eight stations at the Apollo 16 landing site have been analyzed for methane and hydrolysable carbon. These results, in conjunction with published data from photogeology, bulk chemistry, rare gases, primordial and cosmogenic radionuclides, and agglutinate abundances have been interpreted in terms of differing contributions from three components—North and South Ray Crater ejecta and Cayley Plains material.

Analysis of the gases released from lunar fines and soil breccias by DCl dissolution has revealed that trapped hydrocarbons (particularly CH₄) and hydrolysable carbon (indicated by the evolution of deuterocarbons, predominantly CD₄) are ubiquitous components of these samples (refs. 1 and 2). The location of methane and hydrolysable carbon at particle surfaces (ref. 2), a number of correlation studies (refs. 1, 2, and 3), and the simulation of lunar conditions (ref. 4) suggest that the distribution of both types of carbon is controlled by extralunar processes. More specific location studies (refs. 5 and 6) have identified the particle types containing the highest concentrations of methane and hydrolysable carbon as very fine grains (0.5 to 10 μ m in diameter) and glassy agglutinates and microbreccias, both the latter being themselves aggregates of finer grains. These observations are consistent with the finest grains' being the major reaction site for the initial synthesis of lunar carbon compounds from solar-wind-implanted species. The energy for further reaction to take place is presumably provided by micrometeorite impact, which is also responsible for commi-

nuting, aggregating, and reworking the soil. Recently, it has been shown (refs. 7 and 8) that the formation of the hydrolysable carbon giving rise to CD₄ is also dependent on the availability of Fe^{II} in silicate for reduction to Fe⁰. The major hydrolysable carbon species is in fact carbon in solid solution in iron (ref. 9) and not iron carbide as previously anticipated (refs. 1 and 10). The reduction process is also thought to be exposure-induced and to involve a reducing agent such as implanted solar wind hydrogen (refs. 7, 8, 11, 12, and 13).

All the evidence now available suggests that methane and hydrolysable carbon are formed as a result of exposure of lunar samples at the very surface of the regolith. As a corollary, the abundance of these carbon species should be important indicators of exposure and reworking, provided the effects of bulk chemistry are taken into consideration. Indeed, carbon chemistry has already contributed to the understanding of the history of the lunar regolith as a result of the analysis of the Apollo 12 double core, the Apollo 14 surface samples, and the Apollo 15 and 16 drill stems (ref. 14). In the case of the

double core, methane and hydrolysable carbon measurements have indicated that although layer-by-layer deposition may be the predominant mechanism of regolith formation, small-scale mixing across stratigraphic boundaries can be important (ref. 2). For the Apollo 14 samples, both natural lunar and accidental (astronaut-induced) mixings of soils have been inferred from the amounts of CH_4 and CD_4 released by acid dissolution (refs. 2 and 15).

The purpose of the present paper is to demonstrate that carbon chemistry, in conjunction with other exposure measurements and geochemical data, may assist in recognizing the major events at the Apollo 16 site.

Experimental Studies

All acid dissolution studies to measure CH_4 and CD_4 were performed by use of DCl

(38 percent in D_2O) on bulk soils samples (10–20 mg) in the usual way (refs. 2 and 6). To check that systematic errors were unaltered, a sample of Apollo 11 fines 10086 was analyzed and the CH_4 and CD_4 concentrations released shown to be within ± 10 percent of those from samples previously measured.

All the samples analyzed are soils (table 1). The majority (those having 1 as the final integer of their catalog number) have been sieved at the curatorial facility to remove particles greater than 1 mm in diameter. Samples having a catalog number which ends in 0 are unsieved. For the purposes of comparison in this discussion, sieved and unsieved samples are assumed to be identical. A map showing the essential features of the Apollo 16 landing site, together with the location of the various sampling stations, is shown as figure 1.

Table 1.— CD_4 and CH_4 Released by DCl Dissolution of Apollo 16 Bulk Soils

Latitude	Sample Number	Station	CD_4 ($\mu\text{g/g}$ as C)	CH_4 ($\mu\text{g/g}$ as C)	CD_4/CH_4
North of LM	63321	13	3.1	1.1	2.9
	63340	13	4.2	1.6	2.6
	63500	13	5.7	1.1	5.1
	67701	11	3.4	1.6	2.2
	67941	11	2.4	0.7	3.3
	67960	11	2.2	1.7	1.3
Same Latitude as LM	60501	10	5.4	1.6	3.4
	61141	1	7.2	3.2	2.2
	61161	1	7.4	3.2	2.3
	61501	1	4.6	2.3	2.0
South of LM	64421	4	8.8	3.2	2.8
	64501	4	3.6	2.2	1.6
	66040	6	10.6	3.5	3.0
	66081	6	10.8	4.1	2.7
	68121	8	12.2	4.1	2.9
	68501	8	5.7	1.8	3.1
	69921	9	9.5	2.4	4.0
	69941	9	9.7	2.7	3.7
	69961	9	15.7	5.4	2.9

Note on Errors: Absolute amounts of CD_4 and CH_4 are measured ± 10 percent by gas chromatography.

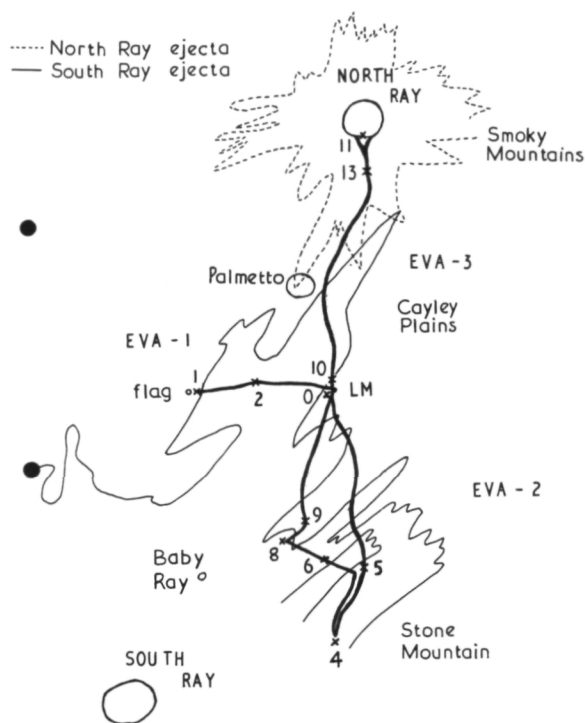


Figure 1.—Map of the Apollo 16 landing site: sampling stations are indicated by number. The extent of the North and South Ray Crater ejecta blankets is outlined, as determined by photogeology (refs. 16 and 17).

Results

The amounts of CH_4 and CD_4 released by DCl dissolution are given in table 1. We have previously reported (refs. 7 and 8) that the concentrations of hydrolysable carbon as indicated by CD_4 in Apollo 16 lunar fines are decreased in comparison with samples from other missions having similar exposure (estimated from the abundance of solar-wind-implanted ^{36}Ar). Thus, we suggested that synthesis of hydrolysable carbon was dependent not only on exposure of the samples but also on the availability of Fe^{II} for reduction to Fe^0 . At present, no definite relationship between CH_4 and Fe^{II} has been observed, although the quantities of CH_4 released from Apollo 16 samples also appear to be reduced compared with amounts in previous missions (ref. 8). Such differences may be due to in-

creased diffusion losses from minerals low in Fe^{II} rather than the lessened extent of a hypothetical synthetic process for CH_4 involving either Fe^{II} or Fe^0 (ref. 18).

In addition to the differences observed between the CH_4 and hydrolysable carbon contents of Apollo 16 soils and those of samples from other sites, considerable differences are apparent between samples collected at various stations of the Apollo 16 site. Samples from stations south of the Lunar Module (LM) (64421, 66081, 68121, 69921, 69941, and 69961), with the exception of 68501 and 64501, release more CD_4 and CH_4 than samples from north of the LM (63321, 63340, 63500, 67701, 67941, and 67960). Soils from approximately the same latitude as the LM (60501, 61141, 61161, and 61501) release intermediate quantities. Although bulk chemistry varies across the site (for example, iron as FeO increases from 4.0 in the north to 6.1 percent in the south (see, among others, refs. 19–22)), the differences involved are insufficient to account for the large variations observed in CH_4 and hydrolysable carbon. The small increase in the amount of Fe^{II} available for reduction to Fe^0 south of the LM could play only a minor role in accounting for the increased quantities of hydrolysable carbon found in samples from this region. The major differences in CH_4 and hydrolysable carbon content must reflect the exposure history of the samples.

Discussion

Gross differences between samples from opposite ends of the Apollo 16 landing site have previously been reported for a number of other parameters. Kirsten et al. (ref. 23) have suggested that the concentrations of trapped solar rare gases in soils increase from north to south. Similarly, samples collected at the rim of North Ray Crater have larger graphic mean grain sizes (ref. 24) and a smaller proportion of agglutinates (ref. 25) compared with those from south of the LM.

Photogeologic sequencing suggests that North Ray Crater was formed at an earlier stage of the Moon's history than South Ray

Crater (ref. 16). The exposure ages for rocks thought to be North and South Ray Crater ejecta have been estimated from track and rare gas measurements as $46\text{--}50 \times 10^6$ years and 2×10^6 years, respectively (refs. 26 and 27). The ^{21}Ne exposure ages for soils suggest an age of $50\text{--}60 \times 10^6$ years (refs. 23 and 28) for North Ray, which is in good agreement with the rock age and photogeologic sequencing. The high ages ($> 200 \times 10^6$ years) measured for almost all soils of the LM (refs. 23 and 28) suggest that these materials were not formed from South Ray Crater ejecta. McKay and Heiken (ref. 25) have suggested that the apparent discrepancy may be explained if soils south of the LM are pre-existing regolith onto which blocks and fragments from South Ray Crater have been scattered. This argument is strongly supported by carbon chemistry data, and a station-by-station examination of the soils returned by the Apollo 16 mission leads us to conclude that no soil solely from South Ray Crater has been sampled. However, both North Ray Crater soil and a mature soil (referred to as Cayley Plains soil) can be recognized. The CH_4 and hydrolysable carbon data for the majority of samples analyzed may be explained in terms of mixtures of Cayley Plains material with either North or South Ray ejecta (table 2). Wherever possible, we have attempted to verify the assignments made by reference to other appropriate data such as bulk chemistry, primordial and cosmogenic radionuclides, rare gases, and the proportion of glassy agglutinates (table 2).

NORTH RAY CRATER SOIL

Soils from Station 11 at the very edge of North Ray Crater must have derived from the ejecta of this crater. They are very immature and consist mainly of freshly ejected material (i.e., low content of glassy agglutinates (ref. 25)). Therefore, the amounts of CH_4 and hydrolysable carbon now observed in samples 67701, 67941, and 67960 are presumably due to the exposure of these soils since

the North Ray Crater event. The regolith at Station 11 appeared to be very thin (ref. 16); during an exposure of $46\text{--}60 \times 10^6$ years, it should have been very well gardened and thus spent a considerable time exposed to the solar wind. However, methane has only reached a maximum of $1.7\mu\text{g/g}$ (67960) and hydrolysable carbon only $3.4\mu\text{g/g}$ (67701), showing that the accumulation of both species is slow. For the purpose of later discussion, sample 67701 is considered typical of North Ray Crater soil.

CAYLEY PLAINS SOIL

Photogeology shows that Station 9 is in an area of low albedo (ref. 16). This location should be characteristic of Cayley Plains material unaffected by the recent addition of immature ejecta from either North or South Ray Craters.

The CH_4 ($2.4\mu\text{g/g}$) and CD_4 ($9.5\mu\text{g/g}$) released from the surface skim (69921) collected at Station 9 suggests a well-exposed mature regolith consistent with the high ^{21}Ne exposure age of 240×10^6 years (ref. 28).

For the purposes of later discussion sample 69921 is considered typical of Cayley Plains soil.

Two other soil samples were collected from Station 9. A sample (69961) from beneath a boulder has even higher quantities of both methane and hydrolysable carbon than does 69921 (table 1). Sample 69941, which was scooped from immediately below 69921, is intermediate both in absolute amounts of CH_4 and hydrolysable carbon and in CD_4/CH_4 ratio. Possibly during collection of 69941, the scoop may have passed through the highly exposed layer represented by 69921, to collect a small amount of the even more highly exposed layer represented by 69961. On this basis, the latter layer would need to extend horizontally beneath Station 9 for at least a meter.

All three soils (69921, 69941, and 69961) have the same major element chemistry (ref. 22) and primordial radionuclide content

Table 2.—*Proposed Origins of Soils at the Apollo 16 Landing Site*

Sample Number	Station	Proposed Origin Based on Carbon Chemistry ⁽¹⁾			Other Data Used for Corroboration ⁽²⁾					
		North Ray Crater	South Ray Crater	Cayley Plains	Bulk ⁽³⁾ Chemistry	Primordial ⁽⁴⁾ Radionuclides	Cosmogenic ⁽⁵⁾ Radionuclides	Rare ⁽⁶⁾ Gases	Proportion ⁽⁷⁾ of Glassy Agglutinates	Photo- ⁽⁸⁾ geology
60501	10		X (1)	X (1)	+	+			+	—
61141	1	X (1)		X (2)	+	+	+			—
61161	1	X (1)		X (2)	+	+	+			—
61501	1	X		X	+	+	+			—
63321	13	X (2)		X (1)	+			+		+
63340	13	X (2)		X (1)	+			+		+
63500	13	X (2)		X (1)	+			+		+
64421	4		(see text)		+			+	+	(not applicable)
64501	4		X		+			—	—	+
66040	6			X	+				+	—
66081	6			X	+				+	—
67701	11	X			+	+	+	+	+	+
67941	11	X							+	+
67960	11	X								+
68121	8			X	+	+				—
68501	8		X (1)	X (1)	+	+	+			+
69921	9			X	+	+		+	+	+
69941	9			X	+	+				+
69961	9			X	+	+				+

NOTES: (1) Composition of mixtures is given in parentheses; blank spaces indicate no contribution.

(2) Symbols: + Denotes agreement; blank spaces indicate data not available.

— Denotes contradiction.

(3) See references 19, 21, 22, and 29.

(4) See references 30 and 31.

(5) See references 32 and 31.

(6) See references 33, 23, and 28.

(7) See reference 25.

(8) See references 16 and 17.

(ref. 30). Thus, the mature layers probably derived from the same source material.

Photogeology indicates that Station 6 lies on a ray from South Ray Crater. Two samples from Station 6 have been analyzed. The first, 66081, had been collected from a patch of white, indurated material lying on top of the regolith; and the second, 66040, was typical local regolith. The amounts of CH_4 and CD_4 released by the two samples (table 1) suggest that they are essentially similar to each other and highly mature, like 69921. It appears, therefore, that neither sample represents South Ray Crater ejecta as suggested by photogeology and that the white patch could have arisen from a small local impact. Bulk chemistry (ref. 22) indicates that both samples have slightly more total iron than presumed Cayley Plains fines (69921), but nevertheless they probably represent part of the same formation.

SOILS CONTAINING NORTH RAY EJECTA AND CAYLEY PLAINS MATERIAL

From photogeology (ref. 16), Station 13 lies on the North Ray Crater ejecta blanket. However, methane and hydrolysable carbon data, supported by bulk chemistry and rare gas analyses, indicate that soils collected from this site are intermediate between North Ray crater ejecta and Cayley Plains soils, and thus soil mixing may have occurred. We have interpreted the bulk chemical data to indicate that samples 63321, 63340, and 63500 may be a 2 to 1 mixture of North Ray Crater fines (represented by 67701) and Cayley Plains material (represented by 69921). Assuming that the turnover rate for 63500 (the exposed regolith at Station 13) was similar to the turnover rate at Station 11, then calculations suggest that the quantities of CH_4 and CD_4 which might be released from 63500 would be $1.6\mu\text{g/g}$ and $5.3\mu\text{g/g}$, respectively. These values are in good agreement with the actual experimental data (CH_4 , $1.1\mu\text{g/g}$; CD_4 , $5.7\mu\text{g/g}$) obtained for 63500. The CH_4 and hydrolysable carbon in sample 63321, which

was from the permanently shaded area under the boulder at Station 13, would presumably not have received any further contribution from exposure if the shielding boulder was emplaced by the North Ray cratering event. Thus, it may be explained as a 2:1 mixture of North Ray soil (containing no CH_4 or hydrolysable carbon) and mature Cayley Plains fines. Again, the calculated values for CH_4 and CD_4 ($0.8\mu\text{g/g}$ and $3.2\mu\text{g/g}$ respectively) are in good agreement with the measured values ($1.1\mu\text{g/g}$ and $3.1\mu\text{g/g}$, respectively). Sample 63340 has also been shielded since the North Ray event. However, the slightly greater quantities of CH_4 and CD_4 released from this sample may be explained if this sample contains a slightly increased proportion of mature Cayley Plains material. The slightly greater amount of mature soil required would be consistent with the known sampling conditions for 63340; i.e., this sample was collected from a slightly greater depth (below 63321) and may have sampled more material from an underlying layer.

Concentrations of ^{36}Ar for the Station 13 soils measured by Kirsten et al. (ref. 23) and Eberhardt et al. (ref. 33), are also consistent with an approximately 2:1 mixture of North Ray Crater ejecta and Cayley Plains material.

Comparison of the CH_4 and hydrolysable carbon concentrations of 63500, the local exposed regolith, and the shaded soil 63321 shows no evidence of migration of lunar volatiles to the latter sample as a "cold trap" (refs. 34, 35, and 36). This is in agreement with the observation that shaded soils do not show the presence of excess lead in comparison with reference samples (ref. 35) and with other CH_4 and hydrolysable carbon measurements of 63320 and 63340 (ref. 37).

SOILS DERIVED FROM SOUTH RAY CRATER EJECTA AND CAYLEY PLAINS MATERIAL

The presence of rocks of low exposure age (about 2×10^6 yrs) (ref. 38) confirms

the interpretation of photogeologic sequencing that Station 8 at the Apollo 16 site lies on a ray of ejecta from South Ray Crater (ref. 16). However, a boulder fillet soil (68121) from this station releases quantities of CH_4 and CD_4 ($4.1\mu\text{g/g}$ and $12.2\mu\text{g/g}$, respectively) indicative of mature fines. The fillet also has a similar major element chemistry (refs. 21 and 22) and primordial radionuclide content (ref. 30) to 69921. Therefore, like other mature soils south of the LM, 68121 may represent Cayley Plains soil. Another soil (68501) collected at Station 8 is far less mature (CH_4 , $1.8\mu\text{g/g}$; CD_4 , $5.7\mu\text{g/g}$) than 68121.

The differences in CH_4 and hydrolysable carbon concentrations between 68121 and 68501 are explicable in terms of one of two mechanisms proposed by Hörz et al. (ref. 39) for the formation of boulder fillets. Formation by micrometeorite erosion of the adjacent boulder requires that the fillet and parent boulder should differ only with respect to exposure history; major and minor element chemistry should be basically similar. Primordial radionuclide measurements show that while the potassium contents of 68121 and the adjacent boulder (68115) are similar, the thorium and uranium contents are very different; thus Rancitelli et al., (ref. 30) have concluded that the fillet could not have resulted from boulder erosion. The alternative mechanism for fillet formation, i.e., lateral displacement of the regolith at the time of boulder deposition (ref. 39), is more consistent with the carbon chemistry data. Thus fillet 68121, located at the north west face of boulder 68115, which is presumably South Ray ejecta, appears to be mature regolith shielded by the boulder from burial by fine material traveling on a ballistic trajectory from South Ray Crater.

The lower maturity of the soil represented by 68501 may be explicable in terms of an addition of fresh South Ray soil ejecta to an area of mature unshielded soil.

The maximum quantities of CH_4 and CD_4 released from a well-gardened North Ray Crater soil (exposure age, 46 to 60×10^6 years) are $1.7\mu\text{g/g}$ and $3.4\mu\text{g/g}$, respectively;

therefore, during an exposure age of 2×10^6 years, fresh South Ray crater soil which was well gardened and exposed to the solar wind, would accumulate very little CH_4 and hydrolysable carbon. Assuming the same rate of production as for North Ray material, then a soil of 2×10^6 years would release not more than $0.07\mu\text{g/g}$ CH_4 and $0.25\mu\text{g/g}$ hydrolysable carbon. Therefore, the observed CH_4 and hydrolysable carbon content of 68501 could be explained if the sample was a mixture of immature South Ray Crater soil and mature Cayley Plains fines in the approximate ratio 1:1 (compare calculated $\text{CH}_4 = 1.3\mu\text{g/g}$ and $\text{CD}_4 = 4.9\mu\text{g/g}$, with actual experimental results $\text{CH}_4 = 1.7\mu\text{g/g}$ and $\text{CD}_4 = 5.7\mu\text{g/g}$).

The hypothesis that 68501 is an admixture of South Ray Crater fines and Cayley Plains soil is supported by the abundance of carbon species released by pyrolysis (ref. 40) and major element chemistry. The bulk chemistry (ref. 19) of 68501 shows differences from 68121 (ref. 21) and 69921 (ref. 22); for example, the FeO and MgO are diminished while CaO and Al_2O_3 are increased. This may suggest that South Ray Crater ejecta is more typical of highland material than is Cayley Plains soil.

The South Ray Crater soil observed at Station 8 may extend as far as Station 10, although photogeology suggests that the LM landed in an area of low albedo (ref. 16). A rock, 60315, with an exposure age of 2×10^6 years (ref. 38), has been identified at this location. Methane and hydrolysable carbon measurements from sample 60501, supported by bulk chemistry (ref. 21) and primordial (ref. 30) and cosmogenic radionuclides (ref. 32) suggest that the composition of the soil at Station 10 approximates that of unshielded Station 8 material, as represented by 68501. Therefore, 60501 may be an approximately 1:1 mixture of South Ray Crater soil and Cayley Plains material. The content of highly reworked glassy agglutinates and mineral grains and metamorphic microbreccias in 60501 (ref. 6) confirms the presence of both recent and mature particles at Station 10.

Station 4 on Stone Mountain appears to be similar to Stations 8 and 10. The site has many angular blocks covering the sampling area, and may be part of the South Ray Crater ejecta blanket (ref. 16). The low quantities of CD_4 from surface fines 64501 suggest the presence of immature South Ray Crater soil, and the low FeO and MgO contents (ref. 41) would support this. However, CH_4 rare gas measurements (ref. 23) and agglutinate data (ref. 25) indicate that 64501 is a mature soil. Another sample (64421) analyzed from the bottom of a trench at Station 4, is mature as indicated by carbon chemistry, rare gases (ref. 23), and agglutinate content (ref. 25). This sample also has concentrations of FeO and MgO (ref. 21) much lower than does Cayley Plains soil. Clearly, Station 4 is an interesting site and requires further study by all techniques.

STATION 1

Photogeology suggests that Station 1 is situated on a ray from South Ray Crater (ref. 16). However, this site is in a region where ejecta from both South and North Ray Craters might be found. Carbon chemistry data, considered together with bulk chemistry and primordial and cosmogenic radionuclide measurements, indicate that the ray at Station 1 is from North Ray Crater.

The CH_4 and CD_4 released from samples 61141, 61161, and 61501 are consistent with samples of intermediate maturity or a mixture of mature and immature fines. Assuming the mature material is Cayley Plains soil, then the immature material could be either South or North Ray Crater soil. South Ray Crater soil is presumed to be extremely immature (see above) and only a very small proportion need be added to Cayley Plains fines (i.e., less than the amount added to Cayley Plains fines to generate 68501 at Station 8) to obtain the quantities of CH_4 and CD_4 released from Station 1 soils. Such a small amount would not be consistent with the bulk chemistry data (ref. 29) for 61141, 61161, and 61501, all of which have lower

FeO contents than 68501 (ref. 21). North Ray Crater soil (67701), as well as being immature, has a low FeO content (ref. 21). Thus, 61141 and 61161 could represent an approximately 2:1 mixture of mature Cayley Plains material and immature North Ray soil (compare calculated CH_4 , $2.2\mu\text{g/g}$; and CD_4 , $7.5\mu\text{g/g}$ with the measured quantities of $3.2\mu\text{g/g}$ and 7.2 to $7.4\mu\text{g/g}$, respectively). All three soil samples from Station 1 have uranium and ^{26}Al contents (refs. 30, 31, and 32) which suggest similarities to soil 67701 rather than 68501.

Conclusions

Several different individual measurements such as rare gas data (refs. 23 and 28), agglutinate abundances (ref. 25), and particle size distribution (ref. 24) have been used previously to discuss the exposure history of the Apollo 16 site. The CH_4 and CD_4 data obtained from the DCl dissolution of lunar soils could also be good indicators of relative surface exposure (at present, insufficient data are available to allow absolute determination) (ref. 2). However, it is more satisfactory to interrelate several parameters. The understanding of regolith dynamics will depend on disentangling the various source materials contributed to the regolith, at a particular site, by taking into consideration all the available information concerning the chemical and physical properties of the soil. In this paper we have used carbon chemistry in conjunction with bulk chemistry, rare gases, primordial and cosmogenic radionuclides, the proportion of glassy agglutinates, and photogeologic sequencing. Other data which would be desirable include mineralogy and petrology, particle size distribution, and total carbon and nitrogen.

At the Apollo 16 site almost all the soils analyzed can be traced to a comparatively minor number of major events. Only a small number of discrete components have been recognized, the remaining soils being attributed to mixtures of these components. Wherever possible, we have attempted to es-

establish the proportions of soils recognized as mixtures.

At Station 9, mixing may have occurred adventitiously during collection of the samples. However, at Stations 1, 8, 10, and 11, a thin surface layer of more recent ejecta would have been apparent to the astronauts (ref. 17). In these cases, immature South or North Ray Crater material may have been stirred into the surface of well-exposed Cayley Plains soil. Only the careful examination of core material from the various stations of the Apollo 16 site will be able to detect whether distinct layers have been deposited or whether mixing to a depth of a few centimeters has occurred.

The two immature materials indicated by the carbon chemistry measurements both appear to be low in Fe^{II} (North Ray (67701) about 4.2 percent as FeO , and South Ray soil estimated as about 5.2 percent FeO from sample 68501) compared with the mature Cayley Plains (5.7 to 6.0 percent FeO). In each case, the immature samples appear to have come from impacts into more truly highland anorthosite type materials. South Ray ejecta may represent Descartes formation, and the North Ray impact may have penetrated the Cayley basin to reveal material from the Smoky Mountains.

Acknowledgment

The authors express their thanks to the Science Research Council for the Research Grants (SGS-128 and SGS-232), and to the British Steel Corporation for a Fellowship (CTP).

References

1. ABELL, P. I., P. H. CADOGAN, G. EGLINTON, J. R. MAXWELL, AND C. T. PILLINGER, Survey of Lunar Carbon Compounds: I. The Presence of Indigenous Gases and Hydrolysable Carbon Compounds in Apollo 11 and Apollo 12 Samples. *Proc. Second Lunar Science Conference, Geochimica et Cosmochimica Acta*, Supplement 2. Vol. 2, 1971, pp. 1843-1863.
2. CADOGAN, P. H., G. EGLINTON, J. N. M. FIRTH, J. R. MAXWELL, B. J. MAYS, AND C. T. PILLINGER, Survey of Lunar Carbon Compounds: II. The Carbon Chemistry of Apollo 11, 12, 14 and 15 Samples. *Proc. Third Lunar Science Conference, Geochimica et Cosmochimica Acta*, Supplement 3, Vol. 2, 1972, pp. 2069-2090.
3. CADOGAN, P. H., G. EGLINTON, J. R. MAXWELL, AND C. T. PILLINGER, Carbon Chemistry of the Lunar Surface. *Nature*, Vol. 231, 1971, pp. 29-31.
4. PILLINGER, C. T., P. H. CADOGAN, G. EGLINTON, J. R. MAXWELL, B. J. MAYS, W. A. GRANT, AND M. J. NOBES, Simulation Study of Lunar Carbon Chemistry. *Nature*, Vol. 235, 1972, pp. 108-109.
5. CADOGAN, P. H., G. EGLINTON, J. R. MAXWELL, AND C. T. PILLINGER, Distribution of Methane and Carbide in Apollo 11 Fines. *Nature Phys. Sci.*, Vol. 241, 1973, pp. 81-82.
6. CADOGAN, P. H., G. EGLINTON, A. P. GOWAR, A. J. T. JULL, J. R. MAXWELL, AND C. T. PILLINGER, Location of Methane and Carbide in Apollo 11 and 16 Lunar Fines. *Proc. Fourth Lunar Science Conference, Geochimica et Cosmochimica Acta*, Supplement 4, Vol. 2, 1973, pp. 1493-1508.
7. PILLINGER, C. T., B. D. BATTS, G. EGLINTON, A. P. GOWAR, A. J. T. JULL, AND J. R. MAXWELL, Formation of Lunar Carbide From Lunar Iron Silicates. *Nature Phys. Sci.*, Vol. 245, 1973, pp. 3-5.
8. PILLINGER, C. T., P. R. DAVIS, G. EGLINTON, A. P. GOWAR, A. J. T. JULL, J. R. MAXWELL, R. M. HOUSLEY, AND E. H. CIRLIN, *Proc. Fifth Lunar Science Conference, Geochimica et Cosmochimica Acta*, in press, 1974.
9. JULL, A. J. T., P. R. DAVIS, G. EGLINTON, L. R. GARDNER, J. R. MAXWELL, C. T. PILLINGER, G. M. BIGGAR, D. HUMPHRIES, AND B. D. BATTS, Simulation of Lunar Processes: II—Redistribution of Carbon in the Lunar Regolith During Meteorite Impact. *Lunar Science*, Vol. VI, pp. 457-459.
10. CHANG, S., J. W. SMITH, I. KAPLAN, J. LAWLESS, K. A. KVENVOLDEN, AND C. PONNAMPERUMA, Carbon Compounds in Lunar Fines From Mare Tranquillitatis: IV. Evidence for Oxides and Carbides. *Proc. Apollo 11 Lunar Science Conference, Geochimica et Cosmochimica Acta*, Supplement 1. Vol. 2, 1970, pp. 1857-1869.
11. CARTER, J. L., AND D. S. MCKAY, Metallic Mounds Produced by Reduction of Material of Simulated Lunar Composition and Implications on the Origins of Metallic Mounds on Lunar Glasses. *Proc. Third Lunar Science Conference, Geochimica et Cosmochimica Acta*, Supplement 3, Vol. 1, 1972, pp. 953-970.
12. GRANT, R. W., R. M. HOUSLEY, AND N. E. PATON, Origin and Characteristics of Excess Fe Metal

- in Lunar Glass Welded Aggregates. *Proc. Fourth Lunar Science Conference, Geochimica et Cosmochimica Acta*, Supplement 4, Vol. 3, 1973, pp. 2737-2749.
13. HOUSLEY, R. M., R. W. GRANT, AND M. ABDEL-GAWAD, Study of Excess Fe Metal in Lunar Fines by Magnetic Separation, Mossbauer Spectroscopy and Microscopic Examination. *Proc. Third Lunar Science Conference, Geochimica et Cosmochimica Acta*, Supplement 3, Vol. 1, 1972, pp. 1065-1076.
 14. WSZOLEK, P. C., AND A. L. BURLINGAME, Carbon Chemistry of the Apollo 15 and 16 Deep Drill Cores. *Proc. Fourth Lunar Science Conference, Geochimica et Cosmochimica Acta*, Supplement 4, Vol. 2, 1973, pp. 1681-1692.
 15. MAYS, B. J., Survey of Apollo 14, 15 and 16 Carbon Chemistry. M.Sc. Thesis, University of Bristol, England, 1973.
 16. AFGIT (Apollo Field Geology Investigation Team), Apollo 16 Exploration of Descartes: A Geologic Summary. *Science*, Vol. 179, 1973, pp. 62-69.
 17. ALGIT (Apollo Lunar Geology Investigation Team), Documentation and Environment of the Apollo 16 Samples: A Preliminary Report. *Astrogeology*, Vol. 51, 1973.
 18. Royal Society Luna Sample Investigation Team, *The Analysis of Various Size, Visually Selected and Density and Magnetically Separated Fractions of Luna 16-20 Samples*, 1974.
 19. BANSAL, B. M., P. W. GAST, N. J. HUBBARD, L. E. NYQUIST, J. M. RHODES, C. Y. SHIH, AND H. WEISMANN, Lunar Rock Types. *Lunar Science*, Vol. IV, 1973, pp. 48-50.
 20. BRUNFELT, A. O., K. S. HEIER, B. NILSSON, E. STEINNES, AND B. SUNDVOLL, Elemental Composition of Apollo 15 and 16 Rocks Fines and Materials. *Lunar Science*, Vol. IV, 1973, pp. 100-102.
 21. COMPSTON, W., M. J. VERNON, B. W. CHAPPELL, AND R. FREEMAN, Rb-Sr Model Ages and Chemical Composition of Nine Apollo 16 Soils. *Lunar Science*, Vol. IV, 1973, pp. 158-158b.
 22. LAUL, J. C., AND R. A. SCHMITT, Chemical Composition of Apollo 15, 16 and 17 Samples. *Proc. Fourth Lunar Science Conference, Geochimica et Cosmochimica Acta*, Supplement 4, Vol. 2, 1973, pp. 1349-1367.
 23. KIRSTEN, T., P. HORN, AND J. KIKO, Ar^{40} - Ar^{39} Dating of Apollo 16 and Apollo 15 Rocks and Rare Gas Analysis of Apollo 16 Soils. *Lunar Science*, Vol. IV, 1973, pp. 438-440.
 24. BUTLER, J. C., G. M. GREENE, AND E. A. KING, Grain Size Frequency Distribution of Apollo 16 Fines Samples and Model Analyses of Grain Size Fractions From Apollo 15 and Apollo 16 Fines. *Lunar Science*, Vol. IV, 1973, pp. 106-108.
 25. MCKAY, D. S., AND G. H. HEIKEN, The South Ray Crater Age Paradox. *Proc. Fourth Lunar Science Conference, Geochimica et Cosmochimica Acta*, Supplement 4, Vol. 1, 1973, pp. 41-47.
 26. BEHRMANN, C., G. CROZAZ, R. DROZD, C. HOHENBERG, C. RALSTON, R. WALKER, AND D. YUHAS, Cosmic-Ray Exposure History of North Ray and South Ray Material. *Proc. Fourth Lunar Science Conference, Geochimica et Cosmochimica Acta*, Supplement 4, Vol. 2, 1973, pp. 1957-1974.
 27. TURNER, G., P. H. CADOGAN, AND C. J. YONGE, Argon Selenochronology. *Proc. Fourth Lunar Science Conference, Geochimica et Cosmochimica Acta*, Supplement 4, Vol. 2, 1973, pp. 1889-1914.
 28. WALTON, J. R., S. LAKATOS, AND D. HEYMANN, Distribution of Inert Gases in Fines From the Cayley-Descartes Region. *Proc. Fourth Lunar Science Conference, Geochimica et Cosmochimica Acta*, Supplement 4, Vol. 2, 1973, pp. 2079-2095.
 29. WÄNKE, H., H. BADDEHAUSER, G. DREIBUS, H. QUIJANO-RICO, H. PALME, B. SPETTEL, AND F. TESCHKE, Multielement Analysis of Apollo 16 Samples and About the Composition of the Whole Moon. *Lunar Science*, Vol. IV, 1973, pp. 761-763.
 30. RANCITELLI, L. A., R. W. PERKINS, W. D. FELIX, AND N. A. WOGMAN, Primordial Radionuclides in Soils and Rocks From the Apollo 16 Site. *Lunar Science*, Vol. IV, 1973, pp. 615-617.
 31. WRIGLEY, R. C., Radionuclides at Descartes. *Lunar Science*, Vol. IV, 1973, pp. 799-800.
 32. RANCITELLI, L. A., R. W. PERKINS, W. D. FELIX, AND N. A. WOGMAN, Lunar Surface and Solar Process Analyses From Cosmogenic Radionuclide Measurements at the Apollo 16 Site. *Lunar Science*, Vol. IV, 1973, pp. 609-611.
 33. EBERHARDT, P., O. EUGSTER, J. GEISS, N. GRÖGLAR, AND M. MORGELI, Noble Gases in Apollo 16 Lunar Fines. *Lunar Science*, Vol. IV, 1973, pp. 209-211.
 34. SILVER, L. T., Lead Volatilization and Volatile Transfer Processes on the Moon. *Lunar Science*, Vol. III, 1972, pp. 701-703.
 35. SILVER, L. T., Uranium-Thorium-Lead Isotopic Characterization in Some Regolith Materials From the Descartes Region. *Lunar Science*, Vol. IV, 1973, pp. 672-674.
 36. REED, G. W., S. JOVANOVIĆ, AND L. FUCHS, Trace Element Relations Between Apollo 14 and 15 and Other Lunar Samples, and the Implications of a Moon-Wide CI-KREEP Coherence and Pt Metal Noncoherence. *Proc. Third Lunar Science Conference, Geochimica et Cosmochimica Acta*, Supplement 2, Vol. 2, 1972, pp. 1989-2001.
 37. WSZOLEK, P. C., R. F. JACKSON, AND A. L. BURLINGAME, Carbon Chemistry of Apollo 15

- and 16 Samples and Solar Wind Simulation Studies. *Lunar Science*, Vol. IV, 1973, pp. 801-803.
38. MORRISON, D. A., D. S. MCKAY, AND H. J. MOORE, Microcraters on Apollo 15 and 16 Rocks. *Lunar Science*, Vol. IV, 1973, pp. 540-542.
39. HÖRZ, F., W. D. CARRIES, J. W. YOUNG, C. M. DUKE, J. S. NAGLE, AND R. FRYXELL, Apollo 16 Special Samples. *Supplementary Report of the Apollo 16 Lunar Sample Information Catalog*, 1972.
40. DESMARAIS, D. J., J. M. HAYES, AND W. G. MEINSCHEIN, The Distribution in Lunar Soil of Carbon Released by Pyrolysis. *Proc. Fourth Lunar Science Conference, Geochimica et Cosmochimica Acta*, Supplement 4, Vol. 2, 1973, pp. 1453-1458.
41. MORRISON, G. H., R. A. NADKARNI, J. JAWORSKI, R. B. BOTTO, J. R. ROTH, AND K. K. TUNEGAN, Elemental Abundances of Apollo 16 Samples. *Lunar Science*, Vol. IV, 1973, pp. 543-545.

Page intentionally left blank

Page intentionally left blank

Pre-Mare Cratering and Early Solar System History

G. W. Wetherill

*Department of Planetary and Space Science
University of California, Los Angeles
Los Angeles, California*

An evaluation of the application of the high extralunar flux in pre-mare times to more general problems of early solar system history is attempted by combining the results of dynamic studies with lunar chronological data.

There is a twofold to fourfold contrast in the integral impact flux between the Apollo 14 and 16 sites and the older mare surfaces. This is judged insufficient to account for the contrasting lithology between these two sites: basalts and soil breccias in the maria, annealed breccias and impact melts in the highlands. Therefore these rocks and their ages (3.9–4.0 b.y.) are thought to predate the surfaces in which they are found. Estimation of the flux needed to produce these lithologies, and difficulties associated with extrapolating this further back in lunar history give support to the "cataclysm" hypothesis of Tera, Papanastassiou, and Wasserburg.

Dynamical studies permit separate evaluation of the possible sources for both the "normal" flux during the first 600 million years of lunar history and the "peak" that apparently occurred 4.0 billion years ago. The most likely sources for the normal flux are comets from the vicinity of Uranus and Neptune. The most promising source for the peak is tidal disruption by Earth or Venus of a Ceres-size asteroid initially in a Mars-crossing orbit. Alternative possibilities are suggested.

Dynamical studies have been carried out in order to determine the extent to which a heliocentric flux could be confined to the Moon (and Earth). A Monte Carlo method, based on that of Arnold (ref. 1), has been used to calculate the relative impact rates of planet-crossing bodies with the Moon and the terrestrial planets. It is found that except for nearly circular initial orbits, the resulting impact density on these bodies is similar. Nearly circular initial orbits at the distance of Mercury greatly favor impact with that planet. In the case of Earth and Venus, they tend to share the material with one another.

It is concluded that the time variation of the flux on these planets is closely related to that on the Moon.

The Extralunar Flux in the Early History of the Moon

In order to understand the evolution of planetary interiors and surfaces, it is necessary to establish a time scale to which the major events in its history may be referred. Prior to obtaining samples of a planet it is possible to establish a relative time scale based on geological principles of superposition, in which contact relationships between units resulting from identifiable events are used to determine which of the events occurred first. Unless erosion processes are too

severe, it is possible to go further and establish a planet-wide time scale based on crater frequencies and crater morphology. A time-related parameter

$$\tau = \int_0^t \phi(t') dt'$$

is thereby determined, where $\phi(t)$ is the flux of impacting bodies at time t in the past. Work in a number of laboratories is establishing the relationship between absolute time, t , and the flux time, τ , for the Moon by determination of $\text{Rb}^{87}\text{-Sr}^{87}$, $\text{K}^{40}\text{-Ar}^{40}$, and $\text{U, Th} \rightarrow \text{Pb}$ ages of suitable lunar rocks. Under fairly general circumstances, as will be explained later,

establishment of this time scale for the Moon represents a major step in establishing a cratering time scale for all of the inner planets, as the extralunar flux forms a link connecting the history of the terrestrial planets.

An early result of the task of relating ϕ to t was the demonstration that ϕ was not a linear function of time. Although the integrated flux indicated by crater frequencies at the Apollo 11 site in Mare Tranquillitatis was $\approx .1$ that of the lunar highlands (ref. 2), the age of the basalts flooding this region was found to be 3.6×10^9 yrs, the greater part of the entire age (4.6×10^9 years) of the Moon (refs. 3 and 4). More detailed information on the relationship between ϕ and t has been provided by subsequent lunar missions (refs. 5, 6, and 7).

Particularly striking is the rapid decline in flux between the time of filling of the oldest mare surfaces, and the younger pre-mare surfaces (Cayley and Fra Mauro). As will be discussed in somewhat greater detail subsequently, there is some uncertainty as to the exact time interval over which this decrease took place. It is clear, however, that the decrease in flux during a few hundred million years about 4×10^9 years ago was greater than the decrease in flux during all of subsequent lunar history. This has been interpreted by Tera et al. (refs. 8 and 9) as indicating a lunar "cataclysm," a peak of extralunar bombardment about 3.9×10^9 years ago.

Both the Fra Mauro (Apollo 14) and Descartes Highlands (Apollo 16) sites are relatively lightly cratered terra surfaces which have received two to four times the impact flux of the older mare surfaces in Mare Tranquillitatis and Mare Serenitatis. At both these sites igneous rocks (including probable impact melts) and shock-metamorphosed breccias have yielded ages of 3.84 to 4.01×10^9 years by the Rb-Sr and K-Ar methods (refs. 10-16), and U-Pb measurements indicate that this was also a time of U-Pb fractionation, presumably associated with volatilization of Pb (refs. 17, 18, and 19). Most, if not all, of these ages are best inter-

preted as impact-related. Post-mare impact-melted rocks and well-annealed breccias are notably absent from the mare sites sampled. Although such rocks are undoubtedly produced by the same flux that has produced melted rocks on the earth (e.g., the Ries basin), the overall effect of this flux for the past 3.6 b.y. has caused a negligible resetting of ages on the mare surfaces. A few post-mare breccias have been investigated from the Apollo 15 site (refs. 15 and 20) and the age of the mare basalts in these rocks has not been noticeably affected by their later brecciation. Therefore it is thought unlikely that increasing this integrated flux by a factor of only two to four would result in the impact metamorphism dated by the Apollo 14 and 16 rocks. Consequently, it is believed that these ages of 3.84 to 4.01×10^9 years *predate* the surfaces on which they have been collected. On the other hand, Rb-Sr ages of 3.77 to 3.82×10^9 years are obtained on Mare Serenitatis basalts at the Apollo 17 site (refs. 9 and 21). These mare ages nearly overlap those found at the terra sites. This small difference in ages makes it difficult to calculate precisely the rate of decrease of the flux of impacting bodies, as the difference between the mare and terra ages is comparable to differences found for the same rock in different laboratories by the same method, and also comparable to the uncertainty introduced by half-life errors in comparing ages measured by different methods. Probably the most consistent way of calculating the change in flux is to use four Rb-Sr ages measured at the California Institute of Technology: Fra Mauro rocks 14073 and 14310 ($3.88 \pm .03$ b.y.), Descartes Highlands rock 68415 ($3.84 \pm .01$ b.y.) and Mare Serenitatis basalt 75055 ($3.77 \pm .06$ b.y.). Use of Rb-Sr ages on the same or related rocks from other laboratories will shift the absolute ages somewhat but will not change the differences appreciably. Fitting the measured integral flux to these ages, as well as to those of the Apollo 11, 12, and 15 mare basalts, and the present measured flux requires a component of flux decaying with a half-life of 40 ± 10 m.y., joined to at least two longer lived components.

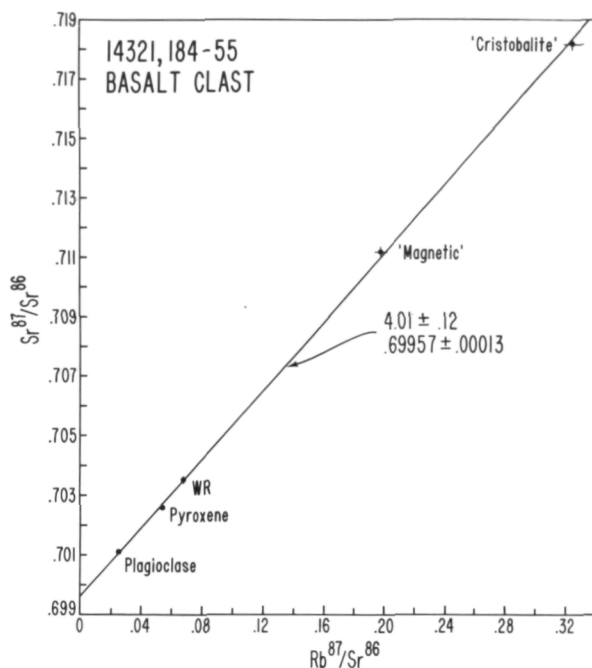


Figure 1.—Mineral isochron for basaltic clast from breccia 14321.

The gap between the youngest terra rocks and the oldest mare basalts becomes even smaller if the mare age of 3.9 b.y. found by Stettler et al. (ref. 22) is included. However, it is possible that these older mare samples somewhat predate the surface on which they are now found.

The half-life of the short-lived component will be lengthened to about 60 m.y. if 14310, 14073, and 68415 are not interpreted as being impact melts, but as minor extrusive or intrusive rocks, postdating the surface on which they are found. The meteoritic component found in these rocks (ref. 23) argues against this interpretation.

The foregoing discussion made no assumptions regarding the relationship of the rocks studied to basin-forming events, e.g., the relationships of the Apollo 14 samples, the Fra Mauro formation, and Imbrium ejecta. Such a discussion is not necessary in order to demonstrate the rapid decay of the extralunar bombardment. However, these results are entirely consistent with the view that the Fra Mauro formation is an Imbrium

ejecta blanket and that the rocks collected near the rim of Cone Crater are derived from the Fra Mauro formation. As discussed above, the age of the Fra Mauro surface is known to be less than 3.88 b.y., if 14310 and 14073 are impact melts, and less than 3.95 to 4.01 b.y., if they are small-scale igneous rocks of internal origin. Compston et al. (ref. 13) have presented reasons for believing that the mineral ages of 3.95 to 4.01×10^9 years found for basaltic clasts in 14321 are metamorphic ages, their resetting resulting from metamorphism in a hot Imbrium ejecta blanket. Although the difference is not far outside of experimental error, this conclusion is at least nominally inconsistent with the view that the age (3.88 b.y.) of 14073 and 14310 is Pre-Imbrium.

We have carried out some Rb-Sr measurements which show it to be unlikely that these ages are metamorphic. We have determined a mineral isochron for a basaltic clast in 14321 (fig. 1) as well as for a microbreccia clast in the same rock (fig. 2). The ages calculated from these isochrons are equal, well within experimental error. However, the initial Sr^{87}/Sr^{86} ratios are entirely different, showing that the basaltic clast and microbreccia clast were not in isotopic equilibrium at that time. This result, however, did not exclude the possibility that the basalt did not equilibrate internally, even though such equilibration did not extend between clasts. In order to check this possibility we have obtained Rb-Sr data at the contact between a basalt clast and adjacent microbreccia clasts, all within 1 mm of one another (fig. 3). If the surface region of the basalt clast had equilibrated with the adjacent microbreccia clasts, all three would lie along an isochron of slope 4.0 b.y. This is not the case. The basaltic material does not deviate at all from the previously determined internal basalt isochron, and there is no suggestion that any of the more radiogenic strontium from the microbreccia has entered into the basalt. Therefore it seems unlikely that re-equilibration of the basalt has been completely internal, if this rock represents a fragment of, or a clast within, the Fra Mauro

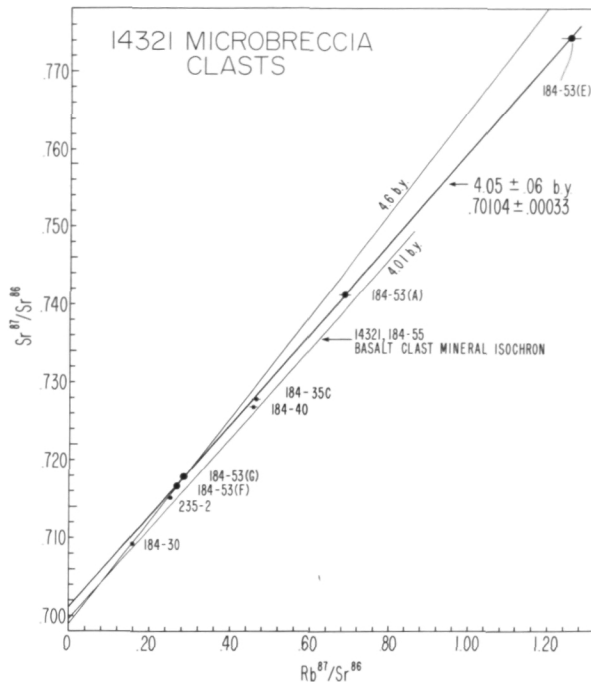


Figure 2.—Mineral isochron for microbreccia clasts from breccia 14321. The line marked $4.05 \pm .06$ b.y. is the isochron drawn through density fractions of clast 184-53. The others are "whole-rock" microbreccia clasts.

formation. However, as discussed by Chao (ref. 24) it is by no means necessary to believe that the Fra Mauro formation at the Apollo 14 site was ever very hot, and is more likely to represent a debris blanket more analogous to the Bunte breccia of the Ries basin. In this case, the age of 4.0 b.y. found for the basalt and microbreccia represents a Pre-Imbrium age, consistent with the previous interpretation that such ages, as well as those slightly younger, predate the cratered surface at this site.

Following this line of thought, the ubiquitous ages (~ 4.0 b.y.) found in the highlands must represent the effect of an integrated flux considerably greater than the fairly moderate twofold to fourfold increase found at the Apollo 14 and 16 sites. In order for these ages to dominate in the manner they do, a much greater integrated flux, e.g., a further tenfold increase, is required in the interval 3.95 to 4.05 b.y. Alternatively, or

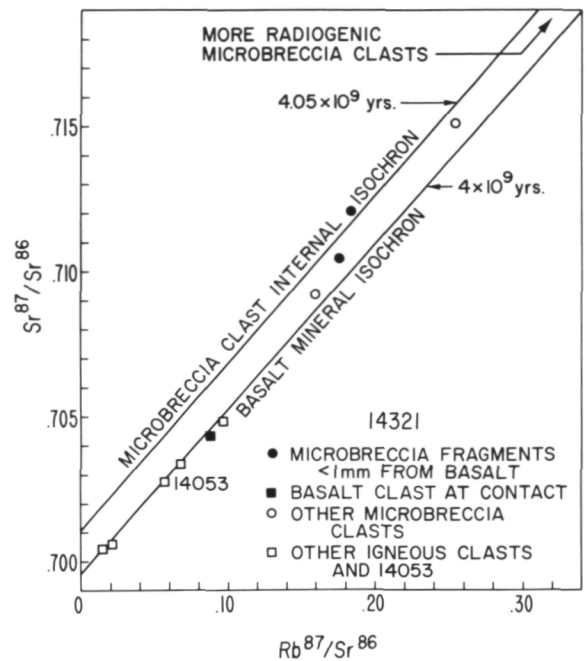


Figure 3.—Rb-Sr evolution diagram showing lack of isotopic equilibrium at the contact between a basalt clast and adjacent microbreccia clasts.

possibly equivalently, this could represent a period of major basin formation. In this case it is necessary to assign at least the Imbrium and Orientale impacts, and possibly that of Crisium and Nectaris as well, to this short interval of time. If this rapid decline in bombardment by basin and/or crater-forming bodies is extrapolated back in time, an integrated flux more than 1000 times that found on the oldest mare surfaces would be expected on a surface of 4.4 b.y. Such a rapid increase would greatly reduce the probability of finding ages of 4.2 to 4.3 b.y. still preserved, as found in several laboratories (refs. 25, 26, and 27). In addition, it would seem difficult to confine the radioactive KREEP material to the Procellarum-Imbrium region, as found by the orbiting γ -spectrometer experiments. Rb-Sr data on KREEP-rich rocks show that the original Rb enrichment of this material took place about 4.4 b.y. ago, and a continued increase in bombardment beyond that found at 4.0 b.y. would be expected to result in more uniform distribution of this material.

In view of the foregoing, the most plausible

interpretation of the data is that given by Tera et al., that the lunar bombardment went through a peak about 4.0 b.y. ago, and the rapid decline in flux following that time was not merely the "tail" of a continually declining flux beginning 4.6 b.y. ago.

Possible Sources of the Early Extralunar Flux

Regardless of whether the actual lunar flux history was the late-peaking "cataclysmic" one outlined above, or the more frequently stated one of continually declining bombardment, some source which decays with a short lifetime, i.e., ~ 40 – 80 m.y., is required to be still present 600 m.y. after the formation of the solar system.

A fundamental but incompletely resolved problem is whether or not the bodies constituting this source were in geocentric or in heliocentric orbit. The time delay of 600 m.y. in the decay of the flux is much too long for randomly oriented crossing geocentric orbits. However, the lifetime does not rule out special geocentric orbits, such as bodies in circular orbits intersected by the Moon as it moves out to greater geocentric distance as a result of tidal friction. There is no special reason to believe that clusters of bodies in such circular orbits were likely to have ever formed. In fact, current theories of the evolution of a geocentric swarm (refs. 28–31) involve formation of "geocentric planetesimals" much closer to the Earth. Also, if objects of $\sim 10^{22}$ g were in Earth orbit at ~ 50 Earth radii for 600 m.y. it seems surprising that no much smaller bodies exist at somewhat greater geocentric distances today. Nevertheless, understanding of the formative stages of the solar system is insufficient to preclude this possibility.

The principal difference between impact by bodies in geocentric or heliocentric orbit will be their impact velocity: ~ 3 km/s for geocentric bodies and $\gtrsim 15$ km/s for heliocentric bodies of sufficient lifetime. The kinetic energy of the impacting geocentric bodies is barely sufficient to melt the impacting body

itself. At the velocities stated above, the kinetic energy per gram will be about 25 times as great for the heliocentric bodies, and much more extensive shock-melting would be anticipated.

The arguments presented in the preceding section implicitly assumed that the energy of the impacting bodies in early lunar history was the same as that in more recent times (at present ~ 30 km/s). If the earlier bodies were less energetic, the increase in flux necessary to explain the widespread shock metamorphism 4 b.y. ago would be much greater. However, in view of the special orbital circumstances already required for the geocentric source, it does not seem too much of an additional burden to require the bodies to be 100 times larger.

An even lower energy source of lunar impacts, Moon-orbiting bodies $\sim 10^{23}$ g in mass, has been proposed by Reid (ref. 32).

It seems difficult to believe that there is no way to distinguish between the highland breccias and craters being produced by very large slow bodies on the one hand, or by smaller bodies with ~ 100 times as much energy per unit mass on the other. However, this seems to be the case at present, and it would represent a major contribution to lunar science if this uncertainty could be eliminated.

With regard to bodies in heliocentric orbits, there are a number of classes of bodies in various kinds of orbits which have undoubtedly played a role in bombarding the Moon. It would be a mistake to seek to explain all lunar impact phenomena in terms of a single source, even though such interpretations may appear more simple.

In discussing the contributions of various sources, it has been conventional to speak of various "components" of the flux which began to decay 4.6×10^9 years ago with various half-lives. This approach is acceptable, provided it is not taken too seriously. Although an exponential decay is a fair approximation for some classes of initial orbits, there are others that provide a flux with a more complex time history. An example of this is offered by Mars-crossing bodies with peri-

helion near Mars. For such bodies, a discrete interval of .5 to 1.0 b.y. is required for any members of an initial ensemble or "swarm" of such bodies to become Earth-crossing. Therefore the rate of Earth and Moon impacts from such a source will remain zero for a long time, increase to a maximum, and then decay with a half-life of $\sim 10^9$ yrs.

The orbital evolution of a number of classes of initial heliocentric orbits has been studied by Monte Carlo iteration of Öpik's (ref. 33) collision theory (refs. 1 and 34-37). These results will be used in the subsequent discussion. Although there are special cases to which this theory is not applicable, particularly where commensurabilities in period occur, the general lifetime and history of most planet-crossing initial orbits are treated sufficiently well by this method. In any case these calculations are to be preferred over those in which Öpik's collision theory is used without iteration. This is particularly true when more than one planet's orbit is crossed.

Except for the problem of the probable "cataclysm" at 4 b.y., to be discussed later, there is no special difficulty in describing plausible sources for the generally declining flux over most of lunar history. During the earliest accretionary phase of the Moon, low-velocity heliocentric (or geocentric) orbits would be required. After the Moon grew to nearly its present size, the bulk of any residual Earth-crossing bodies would be swept up on a time scale of $\sim 10^7$ years. A similar time scale would apply to bodies with aphelion near Jupiter in orbits similar to those providing the source of most of the large meteoroid flux at the Earth today. Bombardment by these bodies probably played a major role in establishing the present size distribution in the asteroid belt, and may have been important in supplying material for the final stages of the Earth and Moon. However, it is doubtful if any record remains of the impact of these transient sources.

On the more relevant time scale of $\sim 10^8$ years, there are several sources that need to be considered. Some members of the short-lived initial Earth-crossing population will

be perturbed into orbits of high inclination, and their lifetime will be lengthened to $\sim 2 \times 10^8$ years. On this same time scale, Mars' perturbations will transfer into Earth-crossing orbit Mars crossers in initial orbits similar to Eros, i.e., those with initial perihelion near Earth. At the present time both of these sources are of such minor importance that it is very difficult to estimate their initial strength. The total flux required to impact the Moon during the first ~ 500 m.y. after the end of terminal accretion may be estimated at $\sim 10^{22}$ to 10^{23} g. Even for bodies with a high probability of terminating their heliocentric history by planetary impact, rather than by ejection from the solar system, the efficiency of the Moon for capturing such bodies is small because of its small cross section relative to Earth and Venus. An adequate source will therefore require an initial mass of $\sim 10^{24}$ to 10^{25} g in the proper orbits. This is similar to or greater than the present mass of the entire asteroid belt. There is no evidence that such a mass of material was not present in these orbits in the early solar system. With regard to the "Eros-type" orbits, a somewhat special distribution of initial orbits is required to avoid a residue of very long-lived ($\sim 2 \times 10^9$ years) Mars crossers greater than the number actually observed at present.

As mentioned before, data from the Prairie Network (ref. 38) shows that most of the present flux of large meteoroids at the Earth is of cometary origin (ref. 39), primarily nonvolatile residues of short-period comets with aphelion near Jupiter. Therefore, it is appropriate to inquire as to the role of this source in the early solar system. At the present time it is believed that comets are perturbed by passing stars into the inner solar system from the Oort cloud of comets at distances of 10^4 to 10^5 AU. It is usually thought that the Oort cloud was initially generated in the region of the major planets and perturbed into its present position by perturbations of the major planets and later by nearby stars. This process of populating the Oort cloud is roughly the inverse of the process by which they are captured into "Jupiter's

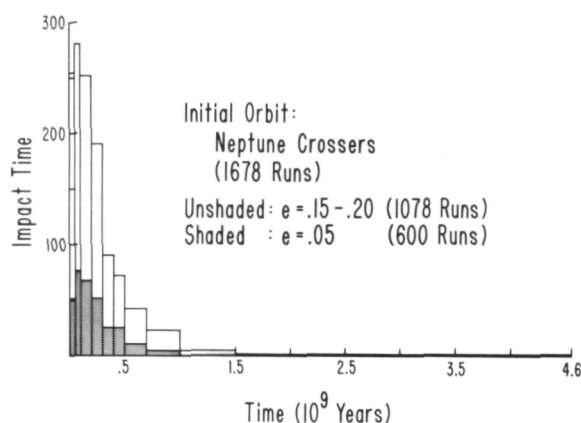


Figure 4.—Histogram showing the time distribution of lunar impacts resulting from comets initially in Neptune-crossing orbits.

family" at the present time. Those cometary bodies which were originally in the vicinity of Jupiter will be lost from the solar system proper on a very short time scale ($\sim 10^6$ years) and will contribute only to the terminal bombardment. However, those comets formed in the vicinity of Neptune and Uranus will evolve more slowly. First, perturbations by Neptune and/or Uranus will cause their perihelion to cross Saturn. In turn, Saturn perturbations will lead to Jupiter-crossing. Once in Jupiter-crossing, the further evolution will be similar to that of a modern short-period comet, and a similar fraction will be brought into Earth-crossing orbits.

The orbital evolution of bodies initially in Neptune-crossing or Uranus-crossing has been calculated by the Monte Carlo technique of Arnold. The initial orbits chosen are

	a	e	i
Neptune-crossing:	36.0 AU	0.2	6°
	28.0 AU	0.15	6°
	30.2 AU	0.05	4°
Uranus-crossing:	23.5 AU	0.2	6°
	18.0 AU	0.2	6°
	19.0 AU	0.05	4.5°

These calculations were made with the original Arnold procedure, rather than that I have used more recently, wherein the ef-

fect of the free oscillations of the secular perturbations was included. At present there are no adequate data on this phenomenon for orbits in the outer solar system.

Histograms showing the time at which the body first becomes Jupiter-crossing are presented in figures 4 through 6. Following Jupiter-crossing, the orbital evolution will follow the course previously calculated for short-period comets. The time scale for this subsequent evolution will be $\sim 10^6$ years,

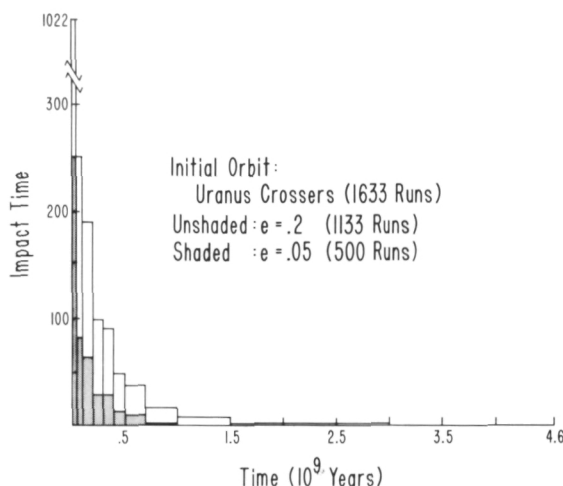


Figure 5.—Histogram showing the time distribution of lunar impacts resulting from comets initially in Uranus-crossing orbits.

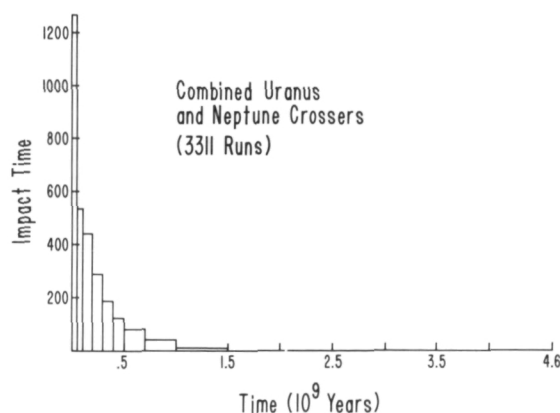


Figure 6.—The time distribution of lunar impacts from the combined effect of Neptune- and Uranus-crossing comets.

usually culminating in ejection by Jupiter into hyperbolic heliocentric orbits. If Earth or Moon impact occurs, it will be within 10^7 years of initial crossing. Therefore, on the time scale of 10^8 to 10^9 years, the time distribution of Jupiter-crossing is equivalent to the time distribution of Earth or Moon impacts.

The shaded portion of the histograms shown in figures 4 and 5 represents those initial orbits with low eccentricity. The general similarity of the low- and moderate-eccentricity results shows that the results are not strongly dependent on details of the initial orbits.

The cumulative impact flux from these sources is shown (on a logarithmic scale) in figure 7. There is considerable similarity between this curve and the lunar impact rate inferred by various authors on the basis of crater investigations (e.g., ref. 7).

The fact that no increase is found at 4 b.y. corresponds to the "cataclysm" of Tera and Wasserburg. The flux of these bodies on the Earth may be estimated to be

$$\frac{\text{present cometary flux}}{\text{primordial cometary flux}} = \frac{\text{lifetime near Neptune}}{\text{lifetime in Oort cloud}} \times \frac{\text{Number in Oort cloud}}{\text{Number in Neptune region}}$$

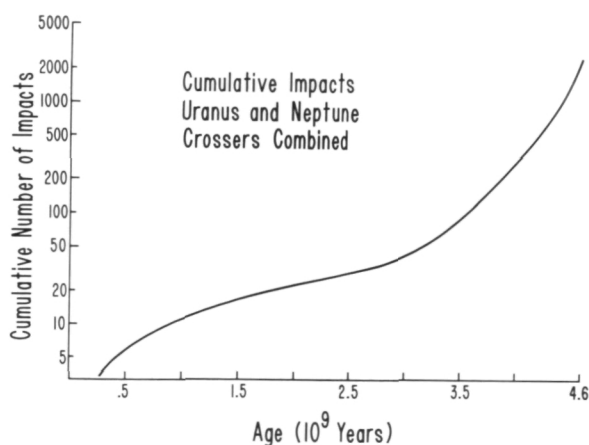


Figure 7.—Cumulative lunar impact flux from Neptune and Uranus sources.

The lifetimes are $\sim 10^8$ and $\sim 10^{10}$ years, respectively, and the ratio of the number of comets in the Oort cloud to the number in the vicinity of Neptune is the efficiency for population of the cloud which may be estimated to be ~ 1 percent. Therefore, it is estimated that the early cometary flux was $\sim 10^4$ times the present flux. This is adequate to provide the integrated early cratering of the lunar terra, and it is quite possible that cometary bodies and their inactive cores have been the primary source of lunar bombardment over almost all of solar system history.

The Lunar Cataclysm

Plausible natural sources have been found for the principal features of the time-dependent lunar meteoroid flux, with the exception of the peak in this flux which appears to have occurred 4 b.y. ago.

Some suggestions can be made as to how this missing peak can be supplied from a heliocentric source in as natural a way as possible.

The interval of 600 m.y. between the origin of the solar system and the appearance of this peak suggests that it be associated with the disruption of a large body belonging to one of the populations previously identified as having a characteristic lifetime of hundreds of millions of years. The rapid decay of the disrupted material must occur from orbits with characteristically short lifetimes of $< 10^8$ years, such as Earth-crossing orbits or those with aphelion near Jupiter.

The mass of material impacting the Moon in this event must be $\sim 10^{22}$ g. As in the case of the integrated "normal" flux, the small cross section of the Moon requires that the total mass disrupted in the inner solar system be much greater, $\sim 10^{24}$ g for bodies with a high (~ 50 percent) probability of impacting a terrestrial planet, and even larger for bodies with a high probability of being deflected into Jupiter-crossing and, from there, into hyperbolic ejection orbits.

Three heliocentric sources of the necessary

lifetime have been identified:

1. High-inclination (e.g., 45°) Earth-crossing orbit
2. Mars-crossing with perihelion well within the orbit of Mars (e.g., Eros)
3. "Comets" in Uranus or Jupiter orbits

The latter two sources have the characteristic that although the lifetime of the source region is maintained in the $\sim 10^8$ -year range by its initial conditions, disruption can occur in low-inclination Earth-crossing orbit, leading to a short residual lifetime for the fragments

The only portion of the solar system definitely known to contain objects anywhere near the proper mass is the asteroid belt. However the required mass of $\sim 10^{24}$ g is about equal to the mass of the largest asteroid, Ceres. There is no special reason why a similar body should or should not have been in a suitable Mars-crossing orbit after the formation of the planets. On a time scale appropriate to the observed interval of 600 m.y. this body will be deflected by Mars into Earth-crossing. Earth perturbations will usually cause it to become Venus-crossing as well, within $\sim 10^6$ years. It is necessary that this body have a high probability of being disrupted while in Earth-crossing orbit rather than of impacting a planet prior to disruption. The reason for this is that in the latter case it would have only a small probability of hitting the Moon. In order to avoid an ad hoc assumption that the one such body surviving until a point in time 4 b.y. ago took the improbable course of hitting the Moon rather than Earth or Venus, it would be necessary to assume there were many such bodies. This would then lead to the problem that the record of their subsequent impact cannot be found on the Earth. In order to produce more than one mare basin, the even more difficult problem of requiring more than one Moon-impacting body would be incurred. A breakup avoids these difficulties by spreading the product of a single impact among the various terrestrial planets and the Moon at a single time.

The most obvious way to cause a disruption

is for the body of 10^{24} g to impact a smaller asteroid (e.g., 10^{20} g) while traversing the asteroid belt. The difficulty with this is that again an improbable event will have been invoked. Calculations of the lifetimes of asteroids (e.g., ref. 40) show that the lifetimes of asteroids of this size are $\sim 10^{11}$ years, and the probability of being destroyed by collision during the $\sim 10^7$ years an asteroid is in Earth-crossing orbit is very small ($\sim 10^{-4}$). The somewhat greater density of bodies in the asteroid belt 4 b.y. ago may increase this probability slightly. However, by this time most of the short-lived bodies would have been removed and the effect would be small.

There exists a much more probable cause of disruption. The Earth- or Venus-impacting probability of an Earth- or Venus-crossing body in an orbit derived from Mars-crossing is about 30 percent. For small bodies, about this fraction will end their course by hitting the Earth or Venus; the remainder will strike Mars or Mercury, make a very close approach to the Sun, or be perturbed by Earth or Venus into Jupiter-crossing and subsequent ejection. However, *prior* to impacting Earth or Venus, there is a high probability that the body will come within ~ 3 planetary radii of one of these planets, i.e., within the Roche limit. This is more probable than actually impacting the planet in the ratio R_R^2/R_p^2 where R_R is the Roche distance and R_p is the planetary radius. Therefore, for bodies of sufficiently low strength relative to the force of tidal disruption, a much more probable event is tidal fragmentation. Most of the remaining fragments will continue in heliocentric orbits. Their slightly different velocities following disruption will result in different subsequent planetary approaches and in divergent orbital evolution. A portion of the fragments will hit the Moon, in accordance with the relative impact probabilities described in the next section.

This is a probable course of events leading to a lunar cataclysm, provided a sufficiently large Mars-crossing body were initially present.

An identical disruption history could be described for an unusually large comet derived from Neptune- or Uranus-crossing. In contrast to the asteroidal situation, no comets of sufficient size are known. The cometary contribution will be dominated by those few bodies which chance to evolve into Earth-crossing orbits with aphelion ≤ 4.2 AU. Such bodies will have about a 5 percent probability of impacting Earth or Venus, and about a .15 percent probability of hitting the Moon. Therefore, a comet with the apparently improbable mass of $\sim 10^{25}$ g is required. This may be compared with the mass of $\sim 10^{18}$ g usually assumed for comets. However, comets have been observed for only a few thousand years, and a comet this large would not necessarily be a conspicuous object if its perihelion were beyond 2 AU. There is at present one body with a mass of $\sim 10^{27}$ g in a Neptune-crossing orbit (Pluto) and the possibility of there being many objects of $\sim 10^{25}$ g early in the history of the solar system cannot be ruled out a priori. The high inclination of Uranus' rotation axis may be a further indication of the former presence of large bodies in this region.

A conceivable way to produce the "cataclysm" without invoking an unusually large comet would be to assume that the formation of Uranus and Neptune were delayed by 600 m.y. Such a delay, owing to their slow rate of accretion, is in itself plausible, as discussed by Levin (ref. 41). In this case the "cataclysm" would correspond to the initial "spike" produced from Uranus-crossers during the first 10^8 years. This alternative is not very attractive. The effect is not large enough. Furthermore, if Uranus were delayed 600 m.y., it is natural to suppose Neptune would be delayed much longer. This would lead to a second "Neptune cataclysm" late in solar system history, which is not observed on either Earth or Moon.

Undoubtedly there are other possibilities, but those I have thought of present more difficulties than those mentioned above. For example, the mechanisms involving asteroid-Jupiter resonances proposed by Williams (ref. 42) and Zimmerman and Wetherill

(ref. 43) almost certainly contribute to the lunar meteoroid flux. However, in order to provide the peak in flux 4 b.y. ago, an asteroid of $\sim 10^{25}$ g would have to be totally disrupted in the asteroid belt. As discussed earlier, this is an unlikely event.

Of those processes considered, the most plausible to produce this peak is probably tidal disruption of a large asteroid perturbed by Mars into an Earth-crossing orbit. The similar process with a cometary source, as well as those involving geocentric bodies, may be considered as possible alternatives.

Cratering on the Terrestrial Planets

Now that a reasonable understanding exists concerning the absolute cratering time scale of the Moon, it is of interest to learn what this can tell us about the cratering time scale of the other terrestrial planets. This possibility is largely confined to the heliocentric component of the cratering flux, again emphasizing the importance of finding some way to separate the effect of these two sources.

An object in Earth-crossing (and Moon-crossing) orbit will make close approaches to the Earth much more often than it will strike the Earth. These close approaches will change the orbital elements of the body. As a result of these changes the body can, for example, become Venus-crossing, after which close approaches and impacts with Venus become possible also. Continuation of this process can lead to the possibility of the body's striking any of the terrestrial planets. The relative probability of striking the various planets will depend upon the initial orbit of the body.

The orbital evolution of various initial orbits has been calculated by use of the development of Arnolds' Monte Carlo method described previously (ref. 44). Some modifications in the calculations were made in order that a statistically significant number of impacts with the smaller bodies, i.e., Moon and Mercury, could be obtained. This was done in two ways:

1. As described by Arnold (ref. 1) (1965), the close approaches are considered as random impacts on a target circle centered on the planet and having an orientation perpendicular to the velocity of the passing body. The radius of the target circle is chosen to be a specified number of planetary radii, K . Impacts on the outer half of this target circle, i.e., approaches at distances greater than $K/2$ planetary radii, are weighted differently from those on the inner half, in order to include the effect of more distant approaches within the sphere of influence of the perturbing planet, but beyond the radius of the target circle. This causes the perturbing effect of a particular planet to be independent of the radius chosen for the target circle associated with that planet, provided it is chosen to be large enough to eliminate large statistical fluctuations. In order to increase the number of interactions with the smaller planets (Moon, Mars, and Mercury) a larger target radius, K , is chosen for these planets. This in itself does not increase the probability of impacting the planet at all, nor does it increase the perturbing effect of the planet. It merely smooths out statistical fluctuations that would otherwise occur if a small planet had to compete on an even basis with large planets in the choice of the next planet to be approached.
2. For intersections on the inner half of the target circle, the only difference between an impact and a close approach is that for an impact a random number is found to have a value between 0 and $4/K^2$, whereas a close approach occurs when the number is between $4/K^2$ and 1.0. For example, for $K = 10$ planetary radii, the area of the inner half of the circle is 25 square planetary radii. The probability of impact is $1/25$, which corresponds to the random number's being between 0 and .04. However, this choice of the range

of the random number designated as "impact" rather than "close approach" is arbitrary. Therefore, close approaches resulting from the number's being between .04 and .08 would have been impacts if impacts had been assigned to random numbers in this interval. In this way close approaches, in the inner half of the target circle, may be "scored" as impacts, and the evolution calculation permitted to continue. In order to do this properly, it is necessary to permit each range of .04 to be counted as an impact only once, and also to continue the orbital evolution when the random number is between 0 and .04. When this procedure of scoring close approaches as impacts is combined with the procedure described in 1., above, of augmenting K for the smaller planets, the apparent relative impact rate on the smaller planets increases, thereby providing a more statistically significant number of impacts. Effectively, the number of runs has been increased by a factor $(K/2)^2$ as each run is now equivalent to $(K/2)^2$ runs with different choices of the random number region designated as impact for each run. At the end, the effect of obtaining more impacts on the smaller planets is corrected for exactly by dividing the number of impacts on each planet by the value of K^2 used for that planet. Without these modifications, the cost of obtaining statistically significant data for lunar impacts would be prohibitive.

The results of these calculations are shown in table 1. All these probabilities are relative to the Moon, which is assigned the value of unity.

The first group (A) of initial orbits correspond to initial orbits which penetrate deeply into the inner solar system. All have aphelia in the asteroid belt. The first two have perihelia within the orbit of Mercury, while the third has perihelion within the orbit of Venus. It is seen that the probabilities per unit area of impacting Mercury,

Table 1.—*Relative Impact Probability per Unit Area*
(Moon = 1.0)

A. At Least Mars-, Earth-, or Venus-Crossing							
Object	Perihelion	Aphelion	Earth Impact Effectiveness (Percent)	Mercury	Venus	Earth	Mars
P/Encke	0.34	4.18	6.0	4.21	2.37	1.23	0.37
Icarus	0.19	1.97	18.5	7.50	1.97	1.08	0.45
1959LM	0.70	3.61	5.2	1.60	2.34	1.34	0.27
B. Aphelion Near 4 AU; Earth- or Mars-Crossing							
	1.01	4.00	24.0	0.30	0.94	2.26	1.15
	1.36	4.67	0.11	0.69	1.26	1.78	0.71
C. Nearly Circular Initial Orbits							
Near:							
Mars	1.27	1.89	27.8	1.08	2.58	2.82	11.9
Earth	0.98	0.99	45.0	1.05	3.02	3.99	0.96
Venus	0.67	0.82	29.6	1.08	2.44	1.36	0.18
Mercury	0.33	0.41	<.01	>1.5 ×10 ⁴	—	—	—

Venus, Earth, or Moon are comparable, whereas that of hitting Mars is somewhat less. The Mercury-crossing bodies have a higher probability per unit area of striking Mercury than the other planets. The statistical uncertainty in these numbers is about 10 percent.

The first entry in Set B corresponds to initial orbits similar to those from which most meteoroids become Earth-crossing at present (ref. 36). Initially the Earth is at its perihelion, and the geocentric velocity is low. This causes the gravitational radius of the Earth to be large, increasing its impact rate relative to the Moon. Further orbital evolution results in frequent Venus impacts and an appreciable rate of Mercury impact. To some extent, Mercury is shielded by Earth and Venus and the rate of Mercury impact is about an order of magnitude lower than that found for the Mercury-crossers in Set A. The rate of impact on the Moon and Mars is comparable, as discussed elsewhere (ref. 39). The second entry in Set B represents an initial orbit beyond the orbit of Earth and with

aphelion near Jupiter. Jupiter perturbations will frequently bring such bodies into Earth-crossing. Again, the impact rate per unit area on all the terrestrial planets is the same order of magnitude.

A more extreme situation is illustrated by the orbits of Set C. Here the initial orbits crossed only one planet. If the planets were in perfectly circular orbits no other planet would be crossed, because of the conservation of relative velocity in subsequent encounters. This is equivalent to the constancy of the Jacobi integral in the restricted 3-body problem. In spite of this tendency for the orbits to remain in the vicinity of one planet, they nevertheless evolve in such a way as to have a comparable probability of impacting all the terrestrial planets, again per unit area. A marked exception is the Mercury-crossing case, which never becomes Venus-crossing. The small mass of Mercury and the large energy change necessary to become Venus-crossing preclude this occurring at a significant rate.

These results do not include the effect of

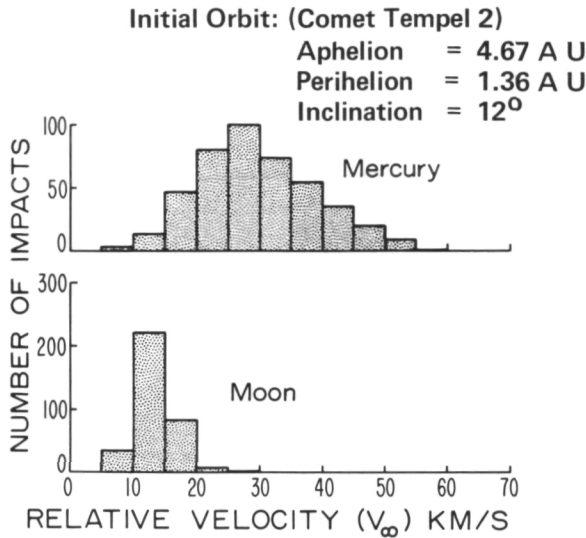


Figure 8.—Calculated impact velocities on Mercury and Moon for a body initially in an orbit similar to that from which meteorites are being derived at present. Although the absolute values of the velocities are somewhat dependent on the initial orbit, the ratio of velocities remains within a factor of ~ 2 for most initial orbits.

the mean energy of the impacts varying from planet to planet. The energy of each impact was also computed. This effect will be particularly important for Mercury, because typical impact velocities on that planet are about twice those on the Moon. Therefore a smaller mass will produce a crater of the same size. The results of a typical calculation of the velocity distribution are shown in figure 8. Depending on the exact size distribution of the impacting bodies, this will increase the integral number of craters greater than a given diameter by a factor of 2 to 3.

It can be concluded that the heliocentric flux producing lunar craters will also produce a similar number of craters per unit area on all the terrestrial planets. If such a flux causes a "cataclysm" at 3.9 b.y. on the Moon, it will cause a "cataclysm" on all the planets. Therefore, a reasonable first approximation might be to assume that, except for a constant factor $\phi(t)$ is the same for all the terrestrial planets. There is still a serious uncertainty in the constant factor. At the present time

the meteoroid flux in the range of 100 g to 10^6 g, as given by McCrosky (ref. 38), is dominated by orbits similar to the earth-grazing orbit A1 and the Venus-crossing orbit B3. Including the velocity effect at Mercury, it is probably most reasonable to use the same proportionality factor for Mercury and the Moon. Mars is a somewhat different case. In addition to the sources prevailing at Earth's orbit, Mars will receive impacts from asteroids on the inner edge of the asteroid belt. In addition, there is significant transport of dust and associated erosion on Mars. Considering these problems, as discussed elsewhere (ref. 39), it is probably best to use a Mars flux/Moon flux factor of 1 to 2 rather than the value of 10 frequently used.

There is still much to be done before an entirely satisfactory time scale exists for the terrestrial planets other than the Earth. It may be expected, however, that present lunar and planetary studies will be a very significant aid in this endeavor.

References

1. ARNOLD, J. R., The Origin of Meteorites as Small Bodies: 2. The Model; 3. General Considerations. *Astrophys. J.*, Vol. 141, 1965, pp. 1536–1547.
2. GAULT, D., Saturation and Equilibrium Conditions for Impact Cratering on the Lunar Surface: Criteria and Implications. *Radio Science*, Vol. 5, 1970, pp. 273–291.
3. PAPANASTASSIOU, D. A., G. J. WASSERBURG, AND D. S. BURNETT, Rb-Sr Ages of Lunar Rocks From the Sea of Tranquillity. *Earth Planet. Sci. Letters*, Vol. 8, 1970, pp. 1–19.
4. TURNER, G., Argon-40/Argon-39 Dating of Lunar Rock Samples. *Proc. Apollo 11 Lunar Science Conference*, Vol. 2, 1970, pp. 1665–1684.
5. SODERBLOM, L. A., AND L. A. LEBOWSKY, Technique for Rapid Determination of Relative Ages of Lunar Areas From Orbital Photography. *J. Geophys. Res.*, Vol. 77, 1972, pp. 279–296.
6. SODERBLOM, L. A., AND J. M. BOYCE, Relative Ages of Some Near-Side and Far-Side Terra Plains Based on Apollo 16 Metric Photography. *Apollo 16 Preliminary Science Report*, NASA SP-315, 1972, pp. 29–3 to 29–6.
7. BOYCE, J. M., AND A. L. DIAL, JR., Relative Ages

- of Some Near-Side Mare Units Based on Apollo 17 Metric Photographs. *Apollo 17 Preliminary Science Report*, NASA SP-330, 1973, pp. 29-26 to 29-28.
8. TERA, F., D. A. PAPANASTASSIOU, AND G. WASSERBURG, A Lunar Cataclysm at ~3.95 AE and the Structure of the Lunar Crust. *Lunar Science*, Vol. IV, 1973, pp. 723-726.
 9. TERA, F., D. A. PAPANASTASSIOU, AND G. J. WASSERBURG, Isotopic Evidence for a Terminal Lunar Cataclysm. *Earth Planet. Sci. Letters*, in press, 1974.
 10. PAPANASTASSIOU, D. A., AND G. J. WASSERBURG, Rb-Sr Ages of Igneous Rocks From the Apollo 14 Mission and the Age of the Fra Mauro Formation. *Earth Planet. Sci. Letters*, Vol. 12, 1971, pp. 36-48.
 11. PAPANASTASSIOU, D. A., AND G. J. WASSERBURG, The Rb-Sr Age of a Crystalline Rock From Apollo 16. *Earth Planet. Sci. Letters*, Vol. 16, 1972, pp. 289-298.
 12. PAPANASTASSIOU, D. A., AND G. J. WASSERBURG, Rb-Sr Systematics of Luna 20 and Apollo 16 Samples. *Earth Planet. Sci. Letters*, Vol. 17, 1972, pp. 52-63.
 13. COMPSTON, W., M. J. VERNON, H. BARRY, R. RUDOWSKI, C. M. GRAY, N. WARE, B. W. CHAPPELL, AND M. KAYE, Apollo 14 Mineral Ages and the Thermal History of the Fra Mauro Formation. *Proc. Third Lunar Science Conference*, 1972, pp. 1487-1501.
 14. MURPHY, V., RAMA, N. M. EVENSEN, BOR-MING, JAHN, AND M. R. COSCIO, JR., Apollo 14 and 15 Samples: Rb-Sr Ages, Trace Elements, and Lunar Evolution. *Proc. Third Lunar Science Conference*, 1972, pp. 1503-1514.
 15. STETTLER, A., P. EBERHARDT, J. GEISS, N. GRÖGLER, AND P. MAURER, Ar^{39} - Ar^{40} Ages and Ar^{37} - Ar^{38} Exposure Ages of Lunar Rocks. *Proc. Fourth Lunar Science Conference*, 1973, pp. 1865-1888.
 16. TURNER, G., P. H. CADOGAN, AND C. J. YONGE, Argon Selenochronology. *Proc. Fourth Lunar Science Conference*, 1973, pp. 1889-1914.
 17. NUNES, P. D., M. TATSUMOTO, R. J. KNIGHT, D. M. UNRUH, AND B. R. DOE, U-Th-Pb Systematics of Some Apollo 16 Lunar Samples. *Proc. Fourth Lunar Science Conference*, 1973, pp. 1797-1822.
 18. TERA, FUAD, AND G. J. WASSERBURG, Uranium-Thorium-Lead Systematics in Three Apollo-14 Basalts and the Problem of Initial Lead in Lunar Rocks. *Earth and Planet. Sci. Letters*, Vol. 14, 1972a, pp. 281-304.
 19. TERA, FUAD, AND G. J. WASSERBURG, Uranium-Thorium-Lead Systematics in Lunar Highland Samples from the Luna-20 and Apollo-16 Missions. *Earth and Planet. Sci. Letters*, Vol. 17, 1972b, pp. 36-51.
 20. MARK, R. K., C. LEE-HU, AND G. W. WETHERILL, Rb-Sr Measurements on Lunar Igneous Rocks and Breccia Clasts. *Lunar Science*, Vol. V, Lunar Science Institute, Houston, 1974, pp. 490-492.
 21. EVENSEN, N. M., V. MURTHY, RAMA, AND M. K. COSCIO, Rb-Sr Ages of Some Mare Basalts and the Isotopic and Trace Element Systematics in Lunar Fines. *Proc. Fourth Lunar Science Conference*, 1973, pp. 1707-1724.
 22. STETTLER, A., P. EBERHARDT, J. GEISS, N. GRÖGLER, AND P. MAURER, Sequence of Terra Rock Formation and Basaltic Lava Flows on the Moon. *Lunar Science*, Vol. V, Lunar Science Institute, Houston, 1974, pp. 738-740.
 23. ANDERS, E., R. GANAPATHY, U. KRÄHENBÜHL, AND J. W. MORGAN, Meteoritic Material on the Moon. *The Moon*, in press, 1973.
 24. CHAO, E. C. T., Geologic Implications of the Apollo 14 Fra Mauro Breccias and Comparison With Ejecta From the Ries Crater, Germany. *J. Res. U.S. Geol. Survey*, Vol. 1, 1973, pp. 1-17.
 25. SCHAEFFER, O. A., AND L. HUSAIN, Early Lunar History: Ages of 2 to 4mm Soil Fragments From the Lunar Highlands. *Proc. Fourth Lunar Science Conference*, 1973, pp. 1847-1863.
 26. KIRSTEN, T., AND P. HORN, ^{39}Ar - ^{40}Ar Chronology of the Taurus-Littrow Region II: A 4.28 b.y. Old Troctolite and Ages of Basalts and Highland Breccias. *Lunar Science*, Vol. V, Lunar Science Institute, Houston, 1974, pp. 419-421.
 27. COMPSTON, W., AND C. M. GRAY, Rb-Sr Age of the Civet Cat Clast 72255,41. *Interdisciplinary Studies of Samples from Boulder 1, Station 2, Apollo 17*, Vol. 1, 1974, pp. 139-143.
 28. KAULA, W. M., AND A. W. HARRIS, Dynamically Plausible Hypotheses of Lunar Origin. *Nature*, Vol. 245, 1973, pp. 367-369.
 29. RUSKOL, E. L., The Origin of the Moon: 1. Formation of a Swarm of Bodies Around the Earth. *Sov. Astron. AJ*, Vol. 4, 1960, pp. 657-688.
 30. RUSKOL, E. L., On the Origin of the Moon: 2. The Growth of the Moon in the Circumterrestrial Swarm of Satellites. *Sov. Astron. AJ*, Vol. 7, 1963, pp. 221-227.
 31. RUSKOL, E. L., The Origin of the Moon: 3. Some Aspects of the Dynamics of the Circumterrestrial Swarm. *Sov. Astron. AJ*, Vol. 15, 1972, pp. 646-654.
 32. REID, MARK J., The Tidal Loss of Satellite-Orbiting Objects and its Implications for the Lunar Surface. *Icarus*, Vol. 20, 1973, pp. 240-248.
 33. ÖPIK, E. J., Collision Probabilities With the Planets and the Distribution of Interplanetary Matter. *Proc. Roy. Irish Acad.*, Vol. 54A, 1951, pp. 165-199.
 34. ANDERS, E., AND J. R. ARNOLD, Age of Craters

- on Mars. *Science*, Vol. 149, 1965, pp. 1494-1496.
35. WETHERILL, G. W., AND J. G. WILLIAMS, Evaluation of the Apollo Asteroids as Sources of Stone Meteorites. *J. Geophys. Res.*, Vol. 73, 1968, pp. 635-648.
36. WETHERILL, G. W., Cometary Versus Asteroidal Origin of Chondritic Meteorites. *Physical Studies of the Minor Planets*, T. Gehrels, ed., NASA SP-267, 1971, pp. 447-460.
37. WETHERILL, G. W., Origin and Age of Chondritic Meteorites (in Russian). *Contributions to Recent Geochemistry and Analytical Chemistry*, A. I. Tugarinov, ed., Nauka, Moscow, 1972, pp. 22-34.
38. McCROSKEY, R. E., *Orbits of Photographic Meteors*. Smithsonian Astrophysical Observatory Special Report 252, 1967.
39. WETHERILL, G. W., Solar System Sources of Meteorites and Large Meteoroids. *Annual Reviews of Earth and Planetary Science*, Vol. 3, in press, 1974.
40. WETHERILL, G. W., Collisions in the Asteroid Belt. *J. Geophys. Res.*, Vol. 72, 1967, pp. 2429-2444.
41. LEVIN, B. J., Revision of Initial Size, Mass, and Angular Momentum of the Solar Nebula and the Problem of its Origin. *Symposium on the Origin of the Solar System*, C.N.R.S., H. Reeves, ed., Paris, 1972, pp. 341-360.
42. WILLIAMS, J. G., Meteorites From the Asteroid Belt? *EOS*, Vol. 54, 1973, p. 233.
43. ZIMMERMAN, P. D., AND G. W. WETHERILL, Asteroidal Source of Meteorites. *Science*, Vol. 182, 1973, pp. 51-53.
44. WETHERILL, G. W., Relationships Between Orbits and Sources of Chondritic Meteorites. *Meteorite Research*, P. M. Millman, ed., Dordrecht, Reidel, 1969, pp. 573-589.

Page intentionally left blank

Page intentionally left blank

section 5

The Role of Exogenic Factors in the Formation of the Lunar Surface

Page intentionally left blank

Page intentionally left blank

The Role of Exogenic Factors in the Formation of the Lunar Surface

K. P. Florenskiy, A. T. Bazilevskiy, and A. V. Ivanov
*Institution for Space Research,
Moscow, U.S.S.R.*

The formation of the surface of planetary bodies is determined by the interaction of endogenic and exogenic forces. Clarification of the mutual role of these forces is one of the most important trends in the geological sciences.

Progress in the study of lunar samples and in geological and morphological observations by man and by automatic equipment now make the solution of this problem for the Moon quite important. However, in spite of the abundance of factual material, the mutual role of these forces in many respects remains unclear. Therefore, it is important to separate from the complex of phenomena that portion in which the nature of the process can be firmly established.

However, the role of any process in geology cannot be studied without consideration of the specific time to which it relates. In studying the geological processes which formed the overall appearance of the Earth, we clearly see the periodicity or unevenness of the actions of various processes in a single region. However, for the Earth overall we are actually studying primarily the history of the Phanerozoic, i.e., the last 600 million years and, even if we include the little-studied upper portion of the Precambrian, we can judge only the last third of Earth's history. For this period of the planetary history of the Earth, we can in general assume a sufficient similarity of the active factors and proceed from the principle of actualism after introducing a few rather controversial corrections.

Stages in the Geological History of the Moon

The surface of the Moon preserves traces of much more ancient processes which encompass, perhaps, up to 90 percent of its planetary history. Under these conditions we can no longer consider the acting forces to be constant, but must distinguish at least three stages, which differ quite sharply as to the nature of the predominant processes (ref. 1).

Stage I, the continental stage, encompasses the period of time from approximately 4.5 to 4.0 billion years ago and can be called the pregeological stage, since there is no direct analogue on Earth. The pregeological stage of formation of the planetary body (ref. 2) from the gas-dust cloud ends with a powerful meteorite bombardment, in which the

force of the impacts increases with growth of the planet. The thermal energy of the impacts is rapidly dissipated into surrounding space, so that the entire planet is not heated (ref. 3). However, each in-falling particle is simultaneously crushed, significantly heated, and subjected to loss of volatile components, which are concentrated at the surface of the planet if the gravitational field of the planet is capable of retaining them. The fraction of heat that remains in local foci of heating remains unclear, but obviously the process of differentiation can occur both from the top downward and from the bottom upward, when forming the primary crust of the planet. Apparently, at this stage of formation of the surface of the planet the concepts "exogenic" and "endogenic" lose their ordinary meaning and require special definition. Near the surface a zone of localized hot foci

is formed through which great masses of matter pass in a process analogous to zone melting, the theory of which was developed by A. P. Vinogradov and his school for magmatic melting (refs. 4, 5, and 6).

It is now important to underline the following characteristic peculiarities of this stage in the history of the Moon:

1. The distribution of the largest impact craters of the Moon is relatively even over its surface and provides no basis for the assumption of the basic asymmetry of the visible and back sides of the Moon, which developed later (fig. 1).
2. During impact accretion, the matter of the Moon underwent significant and repeated conversion with significant losses of volatile elements and compounds.
3. The great majority of craters forming the surface of the lunar continents are of impact origin, complicated with later

tectonic development of weakened jointed zones of circular structures, and in many cases accompanied by quiet effusion of lava, which fills the impact structure.

4. As a result of the powerful impact-explosive processes the predominant type of continental rock is the widely distributed impact breccias.

It is also important to emphasize that, regardless of the stage of formation of the Moon, each impact crater in the dense rock is surrounded by a zone of crushing, which extends one or two radii beyond the limits of the visible crater and continues significantly further out in the form of networks of radial and circular cracks. Such cracks, which may extend hundreds of kilometers in depth around the large craters, form weakened crustal zones, through which the tectonic stresses of the planet are primarily relieved

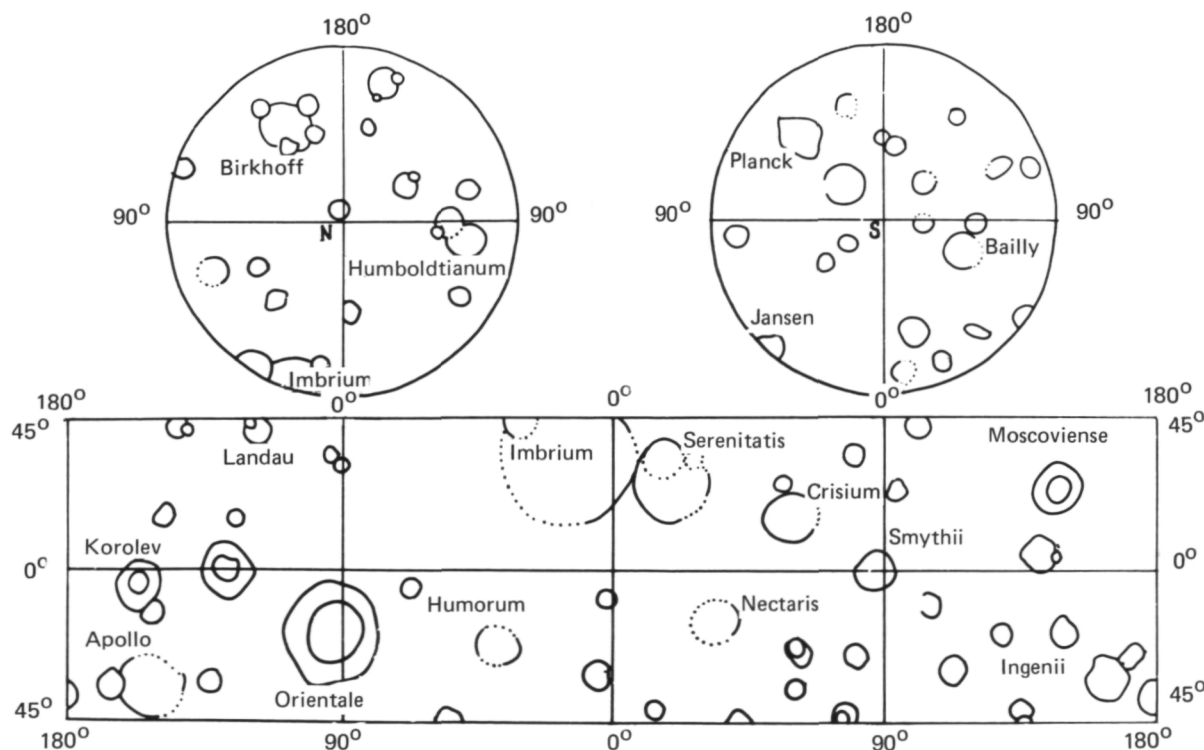


Figure 1.—Distribution of the large circular structures on the surface of the Moon. Considering subsequent lava effusions, the densities of large craters on the visible and back side of the Moon are approximately equal.

to form the characteristic circular structures. As the mass of the Moon grows because of the last impacts at the end of accretion, the zone of fragmented rock is buried, and the system of inherent jointing may manifest itself, in spite of subsequent lithification of the deep zones and development of magmatic processes.

Stage II in the development of the Moon is the maria or volcanic stage which encompasses the period from approximately 3.8 to 3.0 billion years ago and is characterized by extensive fusion of the interior and extensive effusion of superheated, but already degassed, basaltic lava. The asymmetrical distribution of the maria and the incomplete agreement between maria and ancient impact structures on the surface of the Moon basically reflect the internal causes of this process, although there are alternative explanations (ref. 7). This process develops during the sharp reduction of the meteorite flux, and the relative role of purely exogenic factors drops sharply. Apparently, some of the explosive volcanic craters can be related to the general type of this period although they could not be very widespread because volcanic action was the quiet effusion of basaltic lava, which filled the depressions and bottoms of impact craters, primarily on the visible side of the Moon.

Stage III, the postmaria or exogenic stage, lasts approximately 2.5 to 3.0 billion years and is essentially no different from the current stage. It is characterized by the extinction of magmatic activity on the surface, except perhaps for isolated points that are not decisive. Internal activity of the Moon is manifested primarily by the presence of vertical tectonic movements. With this general background of the absence or extremely weak manifestation of planetary magmatism, the leading role is also taken by relatively slight exogenic factors that continually operate over the entire surface of the Moon for billions of years. Their action in purest form is best seen on the surface of the lava flows of the lunar maria, which do not have their structure complicated by ancient crater forms that are repeatedly superimposed upon each other in the continental areas of the Moon.

Since the task of the present report is to analyze the role of exogenic factors, it is natural that many propositions of our report will be developed on the basis of analysis of phenomena that can be studied on the lava plains of the maria.

The relatively slight cratering of the maria surfaces facilitated the development of the concept of the recent nature of the process of lava effusion and overestimation of the possible role of postmagmatic phenomena at the present time and in the recent past. In spite of convincing data on the ancient nature of lunar magmatism that have been obtained by direct study of lunar rocks, these concepts still exist.

The Regolith on the Lunar Surface

The processes of surface formation are reflected in the development of relief and deposits correlated with it. One characteristic representative is the regolith. The lunar regolith is a friable covering layer of clastic material, including rocks and fragments of all sizes, that is displaced from its point of initial deposition (fig. 2). The friable, slightly cohesive nature of the material is an obligatory characteristic of the regolith. It is determined by the thermodynamic conditions of

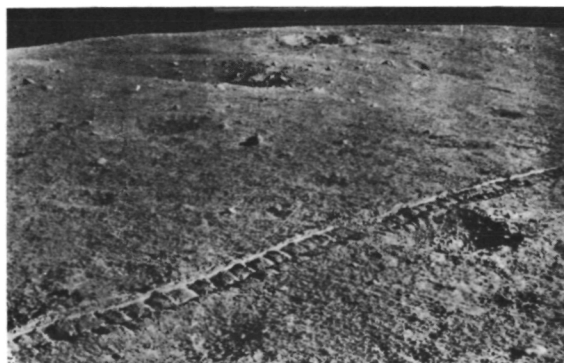


Figure 2.—The regolith surface in the region of operation of Lunokhod 1 in the western portion of Mare Imbrium. The foreground shows the wheel tracks of the Lunokhod. The track width is about 20 cm.

the lunar surface, primarily the presence of free volume.

The regolith blankets the forms of lunar macrorelief and mesorelief. On the plains of the lunar maria the average thickness of the regolith is several meters. In the continental regions, the average thickness of the regolith is generally significantly greater. The thickness of the regolith depends greatly on its position in the relief. In depressions, particularly at the foot of slopes, it probably reaches dozens of meters while on the surfaces of peaks and on slopes it sometimes decreases to some dozens of centimeters. On individual areas of the steep slopes of tectonic depressions (Straight Rille in Le Monnier crater, Hadley Rille) and certain other formations, local outcrops of bedrock are observed.

The greatest influence on the formation of the lunar regolith is the formation and evolution of small craters (with diameters less than several kilometers), which control the form and relief of the lunar landscape. The regolith includes ejecta from these craters and friable material moved by the combination of slope processes. As secondary components, the regolith contains thin ejecta layers from large, distant craters and extralunar (meteorite) material. The single-stage ejecta related to large-scale impacts and combined into rather large, extensive geological bodies such as the Fra Mauro formation, are lithified, i.e., they are not friable and therefore should not be included as part of the regolith. The presence of true volcanic ash in the lunar regolith has not yet been noted, but is improbable because of the facts just mentioned and can represent only a very slight admixture to the products of impact crushing.

The Relief and its Evolution

Small craters are the most typical forms of mesorelief and microrelief of the lunar surface. The peculiarities of their morphology and the nature of their distribution over the surface indicate that the overwhelming majority of the small craters are of impact for-

mation and are related to the bombardment of the lunar surface with meteorite bodies.

The size distribution of craters in various homogeneous areas of the plains of the lunar maria is surprisingly similar. The model of this process is rather simple (refs. 8–11). The logarithmic curve of the dependence of crater density on size consists everywhere of two branches (fig. 3), one of which has a slope near -2 , the other near -3 . The steep lower sector of the curve corresponds to the primary distribution of craters and the averaged distribution law for meteorite masses. The smooth upper sections of the curve characterize the equilibrium surface saturation number of craters, where each new impact is compensated by the corresponding destruction of older craters. As a result, their number remains constant and the process leads only to reworking of the regolith. The point of intersection of the two branches of the curve is called the critical point and corresponds to the critical crater diameter that statistically reflects the age of the surface,

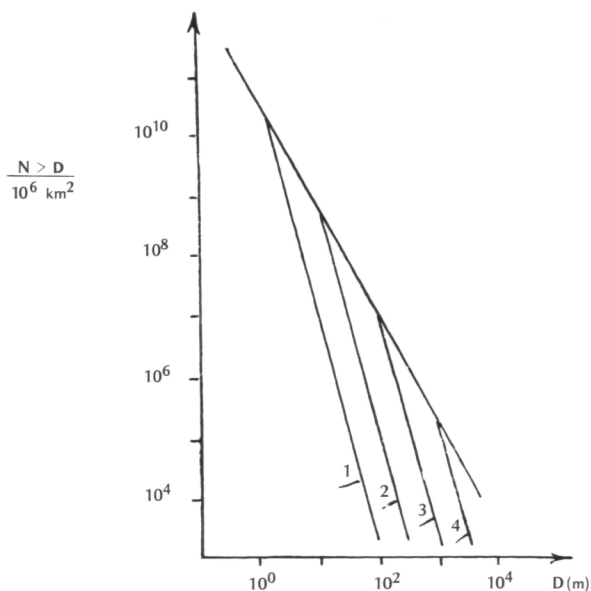


Figure 3.—The crater frequency per unit surface area, as a function of crater diameter. Lines 1, 2, 3, and 4 are the frequency curves in the nonequilibrium portion of the Distribution at various times (isochrons). The flatter, upper limiting line is the curve for the equilibrium distribution.

while the lower branches of the curve move parallel with time and form isochrons. The actual realization of this model is complicated by secondary impact craters formed from local ejecta; by relief; and by the peculiarities of the geological structure of each specific region, as well as by possible unevenness of the meteorite flux, and other factors that require precisising. In the first approximation, however, the model describes well the process of formation and evolution of craters on the lunar surface. The critical diameter of craters fluctuates from 2.7 m in the region of the young deposits from Tycho crater, through 50–200 m for the various maria of Imbrium and Eratosthenian age, and reaches 1000 m in the Fra Mauro formation, where the equilibrium density of small craters changes under the influence of the relief.

Craters form a continuous series of relief

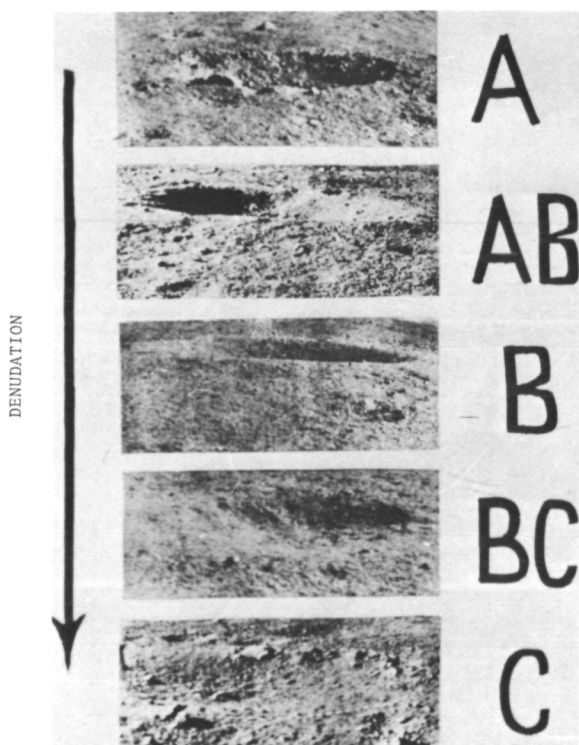


Figure 4.—The morphological classes of small craters. The crater diameter on the photographs is 2 to 3 m. The images are from Lunokhod 1 and 2. The degree of destruction of the primary form increases from Class A to Class C.

forms from fresh, sharply expressed, steep-sloped forms to more ancient, gently sloping formations. It is convenient to divide this series into five morphological classes, reflecting in increasing order the degree of destruction of primary forms: A, AB, B, BC, and C (fig. 4). The criteria for separation might be various morphological characteristics: steepness of slopes, sharpness of ridges, relative depths, etc. (refs. 10 and 12).

Study of the mutual superposition and intersection of craters of different morphological classes, in combination with exposure age data for crater ejecta, has made it possible to estimate, for the postmaria period of lunar history, the mean lifetime of craters with diameters of a few meters to several hundreds of meters on the mare plains (ref. 13) (fig. 5). As seen from figure 5, the evolution of the lunar craters and, consequently, the process of formation of a cover of friable deposits on the lunar surface, have been retarded in comparison with similar processes on Earth. Thus, a crater 10 m in diameter

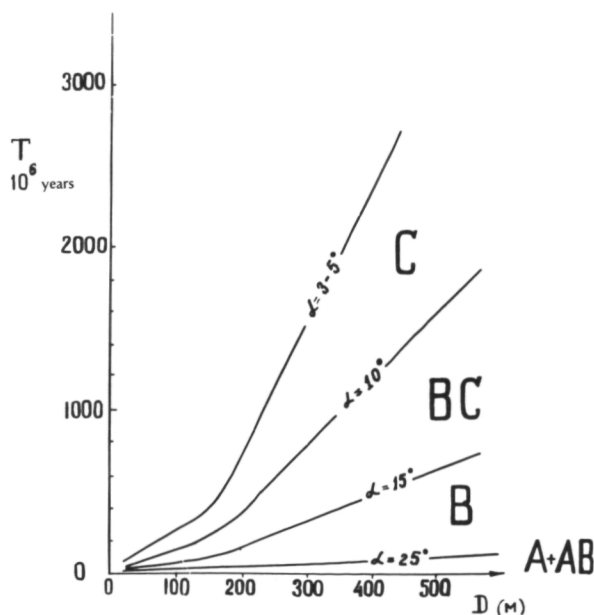


Figure 5.—The potential lifetime of lunar craters. The lines separate fields of various morphological classes and show values of the maximum steepness of the Internal slopes of craters typical of boundaries between classes.

has a statistical lifetime of about 25 million years, while a crater 250–300 m in diameter might even be preserved for about a billion years. The destruction rate of similar relief forms on Earth is approximately three orders of magnitude higher. The exposure time of matter on the lunar surface makes it possible for the important effects produced by the solar wind and cosmic rays to manifest themselves intensively (ref. 14). We will not study these effects in this article.

The processes that destroy lunar craters can be divided into two groups. The relative significance of these groups of jointly acting processes has not been reliably established. The first group includes the processes of impact-explosive crater formation, where the results depend on the scale of the phenomenon, and may either catastrophic or gradual (resulting from the addition of many small-scale phenomena).

The second group consists of processes in-

volving the movement of matter downward along the slopes of craters under the force of gravity. On the steepest slopes in crater classes A and AB, both flowing and slumping processes develop (fig. 6). For class B craters, sliding phenomena are characteristic. In craters in classes A, AB, B, and, probably, BC, massive movement of clastic material down the slopes occurs, i.e., "creep." In craters of morphological class C, the significance of slope processes is apparently not great.

It should be emphasized that slope processes are observed with relatively small angles of inclination of the surface, significantly less than the angle of repose of lunar soil. The agents provoking the movement of the material downward along the slope are apparently moonquakes of both tectonic and impact origin, the ejection of material by micrometeorite impacts, and, possibly, the diurnal temperature fluctuations.

The processes that destroy noncrater lunar

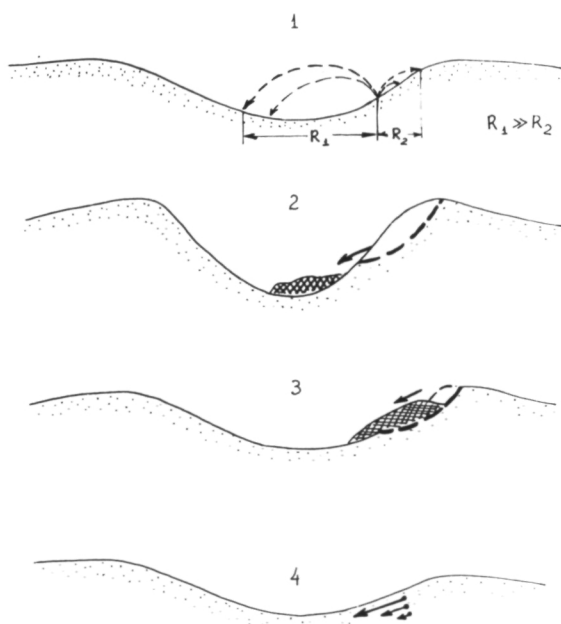


Figure 6.—A diagram of the development of processes of movement of material under the influence of the force of gravity on the internal slopes of craters: 1, directed transfer by small impacts; 2, slumping; 3, flowing; and 4, mass movement such as "creep."

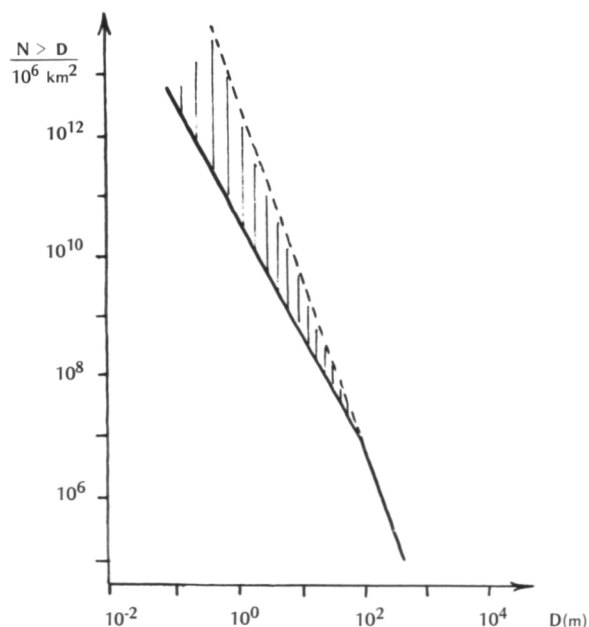


Figure 7.—Density distribution of craters in regions studied by Lunokhod 1 and Luna 16 (solid lines on graphs). The dashed line shows extrapolation of the nonequilibrium distribution to reflect the total number of craters that once existed in this area. The hatched area corresponds to the portion of the crater population which has now disappeared.

relief forms have in principle the same nature and are also determined by the joint effects of meteorite bombardment and slope processes. The predominant type of slope process is controlled by the steepness of the slope.

Processes of Movement of Material

As already noted above, the formation and evolution of forms of lunar relief and the formation of the regolith cover are two aspects of the same process. The characteristic peculiarities of this process are vertical mixing of the regolith material and its horizontal displacement.

The formation of craters and their filling with friable material lead to a constant crushing and mixing of the regolith, which decreases in proportion to depth. We can gain an idea of this if the lower non-equilibrium portion of the curve characterizing the density of impact craters as a function of their size (fig. 7) is extended above the equilibrium portion of the curve. This extrapolation allows us to estimate the total number of craters that have been created in a given area and destroyed by later meteorite impacts. From this, it is easy to determine the intensity of mixing the regolith to any given depth (ref. 15). As seen from fig. 8, for a surface of Imbrian age, the number of generations of craters mixing the regolith down to a depth of a few millimeters reaches 1000; to a depth of 10 cm, near 100; and to a depth of 1 m, near 10.

Naturally, this does not mean that every particle of regolith in a given layer was located in the zone of impact this number of times, because the more powerful impacts are capable of burying regolith particles deeper than the active layer. Nevertheless, these estimates give a general idea of the degree to which impact action is active on the surface layers of the regolith.

In general, the vertical mixing of the regolith is a statistical process, and in some areas undisrupted masses of regolith may exist for extended periods of time. These peculiarities in the formation of the vertical structure of

the regolith should lead to an irregular lens-like stratification in cross section that is coarser in the lower portion of the regolith cover.

The horizontal transport of regolith results from the motion of the material downward along the slopes and from the scattering of matter during explosions. The first process is significant within the limits of each specific form of relief. The range of transport in this case is determined by the length of the slopes, while the intensity of transport is determined by the difference in heights and by the steepness of the slope. Impact ejection can move material on the Moon over arbitrarily great distances, and even expell a portion of the impact products into interplanetary space. This phenomenon raises the problem of the material balance between the Moon and surrounding space.

Ejections of material during impacts are responsible for the formation of the bands of mixing of maria basalt and anorthosite-norite-troctolite rocks at the boundaries between maria and continental areas, with predominant displacement of the material toward the mare. The width of the band of

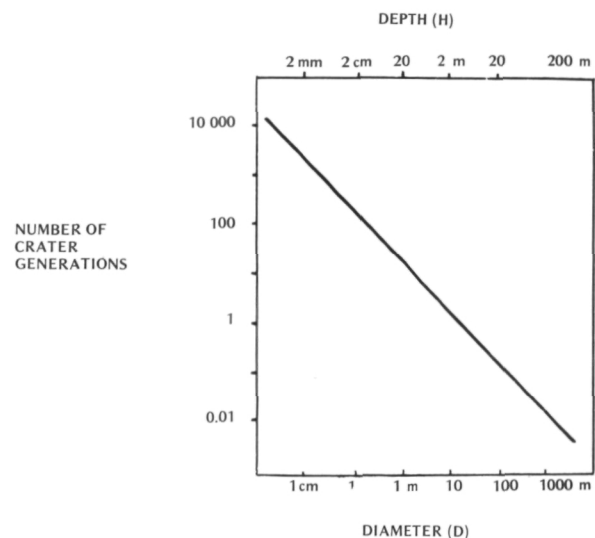


Figure 8.—The number of generations of craters and the calculated depth of reworking of material by craters of various diameters, in regions studied by Lunokhod 1 and Luna 16.

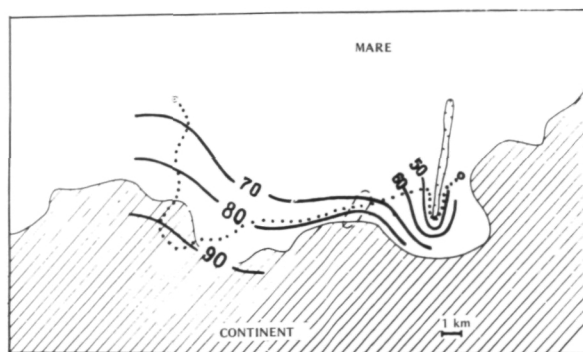


Figure 9.—The fraction of continental material (wt.%) in the surface layer of regolith in the region of investigation of Lunokhod 2 (calculated from the results of chemical analyses by G. Ye. Kocharov and S. V. Viktorov (ref. 16)). The dotted line shows the path of Lunokhod 2. The decrease in admixture of continental material in the neighborhood of Straight Rille in the eastern portion of the path is related to intensive Transport of fine-grained material from the upper regolith layer into the rille.

noticeable mixing may be a few dozen kilometers. This phenomenon can be illustrated in the landing area of Lunokhod 2, where typical maria surface relief is combined with a regolith of low-iron chemical composition (ref. 16) (fig. 9).

This can be seen with equal clarity in the detailed study of the albedo along a line connecting the landing point of Luna 20 with the light continental regolith and the landing point of Luna 16 with the typical dark maria regolith. The study was performed at our request by V. I. Yezersky at the Khar'kov Observatory (fig. 10). We can see from the change in albedo that the zone of significant mixing is about 50 km here, while the downward transfer of material toward the mare, with an altitude difference of about 1 km, is approximately four times greater than the transfer upward in the direction of the continental area.

Formation of the Size Composition of the Regolith

When impact craters are formed on the surface, material which was formerly de-

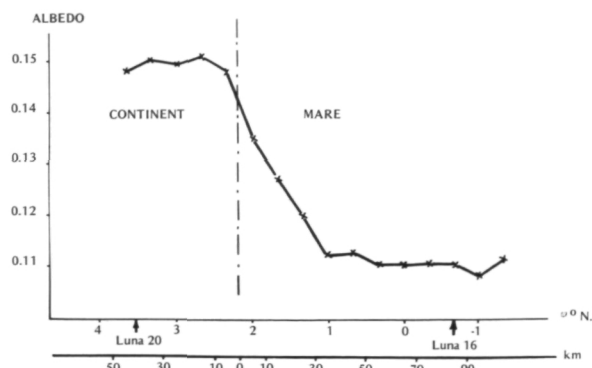


Figure 10.—The photometric section along a line connecting the landing sites of Luna 16 and Luna 20. Produced by V. I. Yezersky at the Khar'kov University Astronomical Observatory.

posited at some depth is ejected. If the crater is large enough and penetrates below the regolith, it will partially crush the underlying rock and deposit large fragments of this material in the ejecta zone in the form of blocks. The ejected material is partially separated by size, with the smaller fractions tending to travel further. This results in the formation of blocky zones on the slopes of fresh craters, and also contributes to the coarsening of the regolith on the slopes of the lunar relief. The burial of stones accounts for the fact that large fragments are sometimes found in the regolith.

Systematic analysis of crater ejecta observations performed by Lunokhod 2 at the edge of Straight Rille and direct study of regolith cores show a significant increase in coarseness of the regolith material with depth, which results from its crushing at the surface (refs. 17, 18, and 19). This phenomenon can be illustrated by Lunokhod data on the granulometry of coarse fragmentary material from the surface layer of the regolith in typical geological conditions (fig. 11).

The situations studied are grouped into an evolutionary series by age. The ejecta from class A craters, 20 to 50 m in diameter, has a probable exposure age of not over a few millions of years. The material in the ejecta zone from class B craters of similar size has been exposed on the surface for 10 to 20 mil-

lion years. Exposure time of the material near class C craters, 20 to 50 m in diameter, and in the space between, is not less than 50 to 100 million years. From the data presented in fig. 11 it also follows that the large fractions are crushed with more intensity than the smaller fractions.

In general, the formation of the granulometric composition of the regolith occurs under the influence of the opposing processes of disintegration and aggregation, primarily caused by meteorite bombardment. The role of aggregation increases in inverse proportion to particle size. In the initial stages of transformation of lunar surface material, disintegration processes dominate, i.e., crushing the primary rocks and their fragments, while as the exposure age of the surface increases and the particle dimensions decrease,

the role of aggregation processing such as sintering, fusion, and remelting increases statistically. The superposition of these two constantly acting processes at a given stage of development leads to an equilibrium state of the granulometric composition of the fine-grained (less than 1 mm) portion of the regolith with a weighted mean particle size of about 60μ (ref. 20). In these cases, it is customary to say that regolith has reached a granulometrically mature state. Judging from the results of investigation of the granulometric composition of samples with various exposure ages, the time required to reach the equilibrium state is approximately 100 million years (ref. 19).

Obviously, slope processes make a significant contribution to the formation of the granulometric composition of the regolith. Comparison of specimens from the upper layer (15 cm) of regolith returned by Luna 16 (mare plain) and Luna 20 (slope of a hill at the edge of the crater Apollonius C) shows that the regolith on the slope has approximately the same median diameter as on the plain, but is distinguished by a significantly lower degree of sorting (fig. 12).

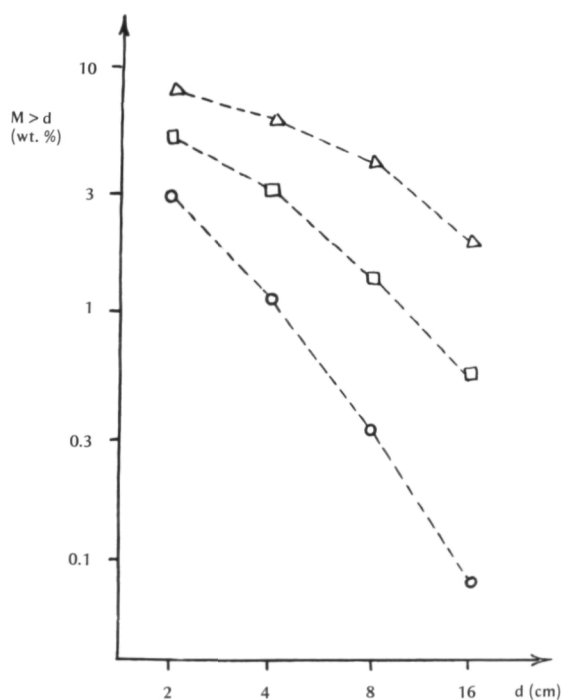


Figure 11.—Dimensional composition of blocky material in ejecta from Class A craters (triangles), ejecta from Class B craters (squares) and ejecta on the surface, within Class C craters and in the space between craters (circles). The craters are 20 to 50 m in diameter. Calculations are based on results of the analysis of Lunokhod 1 panoramas.

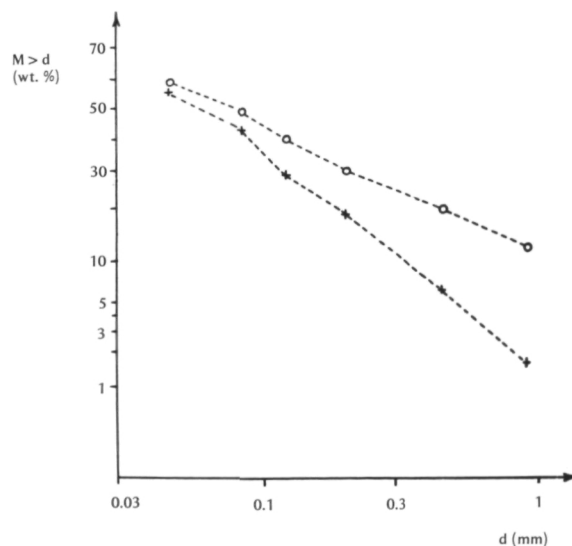


Figure 12.—The size composition of the fine-grain regolith fraction from Luna 16 (crosses) and Luna 20 (circles). Top 15 cm of cores, sieve analysis.

Regolith Lithology

Several types of particles can be distinguished in the composition of the regolith, which reflect the varying nature and degree of exogenic reworking of the initial material.

First of all, these include fragments of primary (in relationship to processes of regolith formation) rocks and the mineral grains which compose them. The presence of these particles reflects the process of crushing—the initial stage of alteration of material on the surface of the Moon. Their content (fig. 13) differs in various regolith samples and decreases significantly with increasing maturity of the regolith, while for a single sample it decreases with decreasing size of fraction. Thus, in a sample of mature mare regolith (Luna 16), for particles more than 0.5 mm in diameter we find about 20 per-

cent fragments of primary rock, while in a sample of regolith whose particles are significantly younger in exposure age, obviously under the influence of slope processes (Luna 20), the fraction of fragments of primary rock increases to 50 percent (refs. 10 and 25).

Rock fragments from the regolith at present are the only direct source of information about the composition of the lunar material. The primary rocks present in the form of fragments relate to two magmatic associations—maria ferrobasalts and the continental series of anorthosite-norite-troctolite rocks. The latter were generally brecciated by the intense early bombardment of the Moon by meteorite bodies.

The chemical composition and mineralogical-petrographic peculiarities of the fragments of these rocks indicate primary magmatogenic formation under conditions of a great deficit of volatile components, which is manifested in the very earliest stages of the geological evolution of the Moon accessible to our study. As noted above, an important factor in the loss of volatiles was probably local heating by collisions during the accretion of the Moon and directly related to the meteorite impacts which formed its surface. The early impoverishment in volatile components, as well as the basic nature of the lunar magma, which had low viscosity, do not allow us to assume any significant development of explosive volcanism in the history of the Moon or any significant admixture of pyroclastic material in the regolith.

Fragments of regolith breccia are typical regolith components. Many peculiarities of these particles—the general lithological composition of the fragments included in the breccia, the smooth form of most of the fragments, the presence of large quantities of glassy fragments, including glass spheres—definitely indicate their formation as a result of compaction and lithification of regolith material. The primary factor in lithification has apparently been the process of diffusion and partial melting at grain interfaces. The occurrence of this process probably requires a significant increase in the contact area,

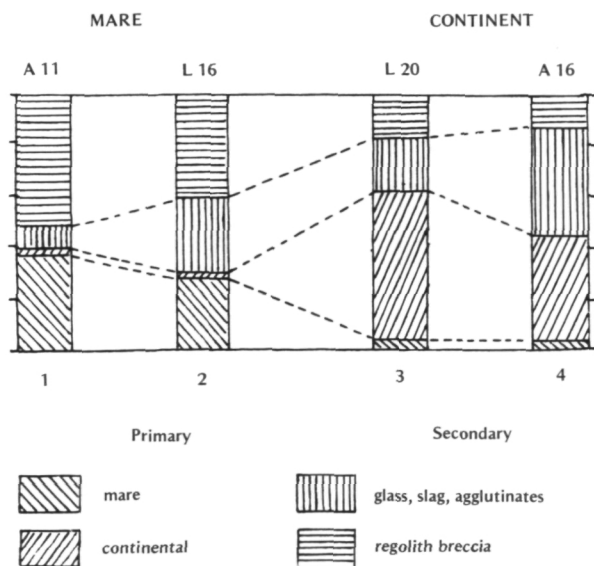


Figure 13.—Lithological composition of regolith fragments: 1, Plain of Mare Tranquillitatus, Apollo 11 collection, fraction size: 1–5 mm (ref. 21); 2, Plain of Mare Fecundatatis, Luna 16 collection, fraction size: 0.25–0.425 mm and larger than 0.45 mm (refs. 22 and 23); 3, Continental Plateau to the north of Mare Fecundatatis, Luna 20 collection, fraction size: 0.25–0.50 mm and larger than 0.45 mm (refs. 22 and 24); 4, Continental Plateau of Descartes, Apollo 16 collection, fraction size: 0.25–0.50 mm (ref. 24).

which is achieved by compaction of the friable mass of the regolith. Two mechanisms of such regolith lithification are possible: (1) rapid compression, with heating due to friction during compaction by impact phenomena; and (2) slow compaction of matter in the lower horizons of the regolith under the pressure of the overlaying masses in the specific conditions of the lunar vacuum. An important peculiarity of the regolith breccia which indicates the multistage nature of its formation, is the presence of multigeneration breccias, i.e., breccia fragments included in younger breccias. This peculiarity is observed on both macroscales and microscales. The content of regolith breccias, like the content of other secondary particles, increases with increasing exposure age and, for fractions larger than 0.5 mm in the Luna 16 and Luna 20 regolith, amounts to about 40 and 20 percent, respectively (fig. 13).

One characteristic type of regolith particle not encountered in terrestrial formations is agglutinates—sintered aggregates of complex irregular shape. Like the breccias, the agglutinates contain all components of the fine regolith fraction, including fragments of crystalline rock and monomineral grains, but are distinguished by a significantly greater glass content and a high degree of surface melting. The composition of the agglutinates indicates that their source is fine-grained regolith material, while the basic textural peculiarities indicate that the most probable process of formation is melting and fusion of the components of the friable surface layer during micrometeorite impact (McKay refs. 20 and 26).

An obligatory component of the regolith is the various particles of secondary glass, whose content, like the agglutinate content, is a function of the exposure age of the sample. Many glass particles have nearly spherical shapes indicating the formation of such particles by cooling of a melt in free flight. The formation of the overwhelming majority of glass particles is a result of spraying and solidification of a melt formed in the central zone of meteorite explosions. Individual glass particles are diaplectic. Thus, the glasses re-

flect the most intensive stage of exogenic reworking of material on the lunar surface.

A special type of particle is fragments of meteorites which have fallen onto the Moon. These particles are rare, because of the extreme conditions of impact of meteorites with the lunar surface, and are represented primarily by iron-nickel chunks.

On the whole, the formation of the lithological characteristics of the regolith occurs under the influence of a complex variety of processes caused by the meteorite bombardment of the lunar surface. They include crushing, lithification, melting, and fusion of various intensities, as well as the process of horizontal transport, sometimes over significant distances, which allows us to study individual specimens and judge the structure of significantly larger regions.

The meteorite bombardment of the lunar surface is also reflected in the formation of many microcraters on the surface of individual regolith particles, which carry information both about the evolution of the regolith and about the parameters of the micrometeorite flux which reaches the surface of the Moon (refs. 27 and 28).

The condensation of material evaporated by impacts has some significance, but judging from the data presently available, this process is limited in morphological effect and is known by the formation, on the particle surfaces, of certain characteristic forms of microrelief (films and ridges of metallic iron) and rare crystalline forms. However, we can assume that further investigations will turn up additional morphological evidence about condensation processes on the lunar surface.

Chemical Composition of the Regolith

The basic features of the chemical composition of the regolith in the various regions of the Moon which have been studied are determined by the composition of the primary rocks of the region. The regolith and the locally underlying rocks differ significantly

in secondary, but very important, details of their chemical compositions (ref. 29). These differences are related to the peculiarities of the processes of formation and evolution of the regolith and are determined by the addition of meteoritic material, the influx of material from other regions of the Moon, and the phenomena of selective evaporation during meteorite impacts.

The influx of meteoritic material is reflected in an increase in the content of a number of characteristic "meteoritic" elements in the regolith (Ir, Au, Ni, Ge, and certain others). In mature regolith from the Mare Imbrium plains the fraction of meteoritic material calculated as chondritic composition has been estimated to be on the order of 2 wt. % (refs. 30, 31, and 32).

The influx of material from other regions of the Moon due to horizontal transport by impacts has already been discussed in the earlier sections of this report. This process, in particular, causes certain increases in the content of Ca and Al in the regolith of the mare plains and an increase in the content of Fe and Ti in the regolith of the continental areas, as well as formation of the aforementioned zones of mixing at the boundaries between maria and continents where hybrid surface chemical compositions are found.

Local heating of material during high-speed impacts is a cause of a whole series of changes in the chemical composition of the regolith. Because of this process, the regolith in general and particularly those components subjected to the most intensive exogenic reworking are significantly impoverished in a number of highly volatile elements, including the alkalis and phosphorus (refs. 33, 34, and 35). However, the differentiation of material by evaporation involves not only the highly volatile elements contained in the primary rocks of the Moon in small quantities, but also the basic petrogenic elements, which have moderate volatility. Some of the glassy particles have lost at least 30 percent of the initial amount of silica which they contained as well as significant quantities of iron (ref. 36).

The loss of petrogenic elements due to se-

lective evaporation has also been confirmed by increases in the heavy isotopes of a number of chemical elements (oxygen, silicon) in the fine fraction of the regolith as a whole, and particularly in its most highly reworked portion—the glasses and agglutinates (ref. 37).

For the regolith overall, as the degree of its exogenic reworking increases, this should lead to a regular change in its petrochemical type.

The peculiarities of the chemical and isotopic composition of the regolith in combination with the data of model experiments (refs. 35 and 38) demonstrate the important role of evaporation processes in the formation of regolith which lead to significant fractionations of the elements and their isotopes. One of the most important geochemical results of this phenomenon is that the ratio of daughter and parent isotopes becomes a function not only of age, but also of degree of exogenic reworking (ref. 39).

It is characteristic that an increase in the heavy isotope of elements in the regolith, in comparison with the primary rocks, is related to evaporation processes during the exogenic reworking of the surface and is observed for all the specimens studied. The universality of the influence of exogenic reworking provides grounds to suppose that this regularity is characteristic of the entire lunar surface.

If this assumption is correct, it may indicate a negative mass balance for the Moon at the current stage of its history.

Thus, analysis of various aspects of the structure, composition, and evolution of characteristic formations of the lunar surface leads to the conclusion that exogenic factors have played an important role in various stages of the geological history of the Moon, and that their role has become decisive over the past 2 to 3 billion years.

References

1. FLORENSKIY, K. P., The Moon is Necessary to Geologists. *The Earth and People*, 1972, pp. 60–64.

2. FLORENSKIY, K. P., The Initial Stage of Differentiation of the Matter of the Earth. *Geokhimiya*, No. 8, 1965, pp. 909-917.
3. SAFRONOV, V. S., *Evolution of the Preplanetary Cloud and the Formation of the Earth and the Planets*, 1969.
4. VINOGRADOV, A. P., *Chemical Evolution of the Earth*, Academy Sciences, Moscow, 1959.
5. VINOGRADOV, A. P., A. A. YAROSHEVSKIY, AND N. P. IL'IN, Physico-Chemical Model of the Separation of Elements in the Process of Differentiation of the Material of the Mantle. *Geokhimiya*, No. 4, 1970.
6. VINOGRADOV, A. P., A. A. YAROSHEVSKIY, AND N. P. IL'IN, A Physico-Chemical Model of Element Separation in the Differentiation of Mantle Material. *Phil. Trans. Roy. Soc. London, Series A*, Vol. 268, 1971, pp. 409-421.
7. WOOD, J. A., Bombardment of a Cause of the Lunar Asymmetry, *The Moon*, Vol. 8, 1973, pp. 73-103.
8. MORRIS, E. C., AND E. M. SHOEMAKER, Craters. *Surveyor Project Final Report, Part II, Science Results*, TR 32-1265, Jet Propulsion Laboratory, Pasadena, 1968, pp. 69-86.
9. SHOEMAKER, E. M., *Origin of Fragmental Debris on the Lunar Surface and the History of Bombardment of the Moon*. Deputation Provincial Barcelona, Instituto de Investigaciones Geologicas, Vol. 25, 1971, pp. 27-56.
10. FLORENSKIY, K. P., A. T. BAZILEVSKIY, A. A. GURSHTEYN, R. B. ZEZIN, A. A. PRONIN, V. P. POLOSUKHIN, Z. V. POPOV, AND I. M. TABORKO, Problem of the Structure of the Surface of the Lunar Maria. *Current Concepts of the Moon*, 1972, pp. 21-45.
11. BAZILEVSKIY, A. T., Distribution Density of Small Lunar Craters—Models and Actual Distribution. *Kosmich. Issled.* Vol. 9, No. 1, 1973, pp. 612-621.
12. FLORENSKIY, K. P., AND I. M. TABORKO, Some Conclusions on the Morphology of Sectors of the Moon Covered by Luna 12. *Fizika Luny i Planet*, 1972.
13. BAZILEVSKIY, A. T., The Age of Small Lunar Craters. *Izv. AN SSSR, Seriya Geologicheskaya*, No. 8, 1974.
14. VERNOV, S. N., AND A. K. LAVRUKHINA, Primary Cosmic Radiation on the Surface of the Moon. *Abstracts of Reports of the Soviet-American Conference on Cosmochemistry of the Moon and Planets*, Moscow, 1974.
15. BAZILEVSKIY, A. T., Estimate of the Thickness and Degree of Transformation of the Lunar Regolith on the Basis of Distribution of Craters. *Kosmich. Issled.*, Vol. 12, No. 5, 1974.
16. KOCHAROV, G. YE., AND S. V. VIKTOROV, Chemical Composition of the Lunar Surface in the Region of Operations of Lunokhod 2. *Dokl. AN SSSR*, Vol. 214, No. 1, 1974, pp. 71-74.
17. FLORENSKIY, K. P., A. T. BAZILEVSKIY, A. A. GURSHTEYN, V. V. ZASETSKIY, A. A. PRONIN, AND V. P. POLOSUKHIN, Geological and Morphological Analysis of the Operating Region of Lunokhod 2. *Dokl. AN SSSR*, Vol. 214, No. 1, 1974, pp. 75-78.
18. STAKHEYEV, YU. I., YE. K. VUL'FSON, A. V. IVANOV, L. S. TARASOV, AND K. P. FLORENSKIY, Granulometric Composition of a Specimen of Lunar Soil From the Sea of Fertility. *Izv. AN SSSR, Seriya Geologicheskaya*, No. 1, 1972, pp. 68-72.
19. CARRIER, W. D., III, Lunar Soil Grain Size Distribution. *The Moon*, Vol. 6, Nos. 3-4, 1973, pp. 250-263.
20. MCKAY, D. S., G. H. HEIKEN, R. M. TAYLOR, U. S. CLANTON, D. A. MORRISON, AND G. H. LADLE, Apollo 14 Soil: Size Distribution and Particle Types. *Proc. Third Lunar Science Conference, Geochimica et Cosmochimica Acta*, Supplement 3, Vol. 2, 1972, pp. 983-994.
21. WOOD, J. A., J. S. DICKEY, U. B. MARVIN, AND B. N. POWELL, Lunar Anorthosites and a Geophysical Model of the Moon. *Proc. Apollo 11 Lunar Science Conference, Geochimica et Cosmochimica Acta*, Supplement 1, Vol. 1, 1970, pp. 965-988.
22. IVANOV, A. V., L. S. TARASOV, O. D. RODE, AND K. P. FLORENSKIY, Comparative Characteristics of Regolith Samples Delivered From the Lunar Mare and Highland Regions by the Automatic Stations Luna 16 and Luna 20. *Proc. Fourth Lunar Science Conference Geochimica et Cosmochimica Acta*, Supplement 4, Vol. 1, 1973, pp. 351-364.
23. REID, G. B., JR., G. J. TAYLOR, U. B. MARVIN, AND J. A. WOOD, Luna 16: Relative Proportions and Petrologic Significance of Particles in the Soil from Mare Fecunditatis. *Earth Planet. Sci. Letters*, Vol. 13, 1972, pp. 286-298.
24. TAYLOR, G. Y., M. J. DRAKE, J. A. WOOD, AND U. B. MARVIN, The Luna 20 Lithic Fragments and the Composition and Origin of the Lunar Highlands. *Geochimica et Cosmochimica Acta*, Vol. 37, 1973, pp. 1087-1106.
25. TARASOV, L. S., K. P. FLORENSKIY, A. V. IVANOV, AND O. D. RODE, Morphological Peculiarities and Types of Regolith Particles Returned by the Luna 20 Spacecraft from a Continental Region of the Moon. *Geokhimiya*, No. 9, 1973, pp. 1275-1286.
26. IVANOV, A. V., YU. I. STAKHEEV, L. S. TARASOV, AND K. P. FLORENSKIY, Nature of the Material Returned by the Automatic Lunar Station Luna 16. *Physics of the Earth and Planetary Interiors*, Vol. 7, No. 4, 1973, pp. 466-476.
27. HORZ, F., D. E. BROWNLEE, D. E. GAULT, J. B. HARTUNG, D. A. MORRISON, F. J. VEDDER, E. SCHNEIDER, V. R. OBERBECK, AND W. L. QUAIDE, Lunar Micrometers: The Micromete-

- oroid Complex and Evolution of the Lunar Regolith. *Abstracts of the Soviet-American Conference on Cosmochemistry of the Moon and Planets*, Moscow, 1974.
28. FECHTIG, H., W. GENTUER, J. B. HARTUNG, K. NAGEL, G. NEUKUM, E. SCHUEIDER, AND D. STORZER, Microcraters on Lunar Samples. *Abstracts of the Soviet-American Conference on Cosmochemistry of the Moon and Planets*, Moscow, 1974.
 29. VINOGRADOV, A. P., Genesis of the Lunar Regolith. *Lunar Soil from the Sea of Fertility*, Collection of Works, 1974, pp. 348-355.
 30. GANAPATHY, R., R. R. KEAYS, J. C. LAUL, AND E. ANDERS, Trace Elements in Apollo 11 Lunar Rocks: Implications for Meteorite Influx and Origin of Moon. *Proc. Apollo 11 Lunar Science Conference, Geochimica et Cosmochimica Acta*, Supplement 1, Vol. 2, 1970, pp. 1117-1142.
 31. LAUL, J. C., J. W. MORGAN, R. GANAPATHY, AND E. ANDERS, Meteorite Material in Lunar Samples: Characterization From Trace Elements. *Proc. Second Lunar Science Conference, Geochimica et Cosmochimica Acta*, Supplement 2, Vol. 2, 1971, pp. 1139-1158.
 32. LAUL, J. C., R. GANAPATHY, J. W. MORGAN, AND E. ANDERS, Meteoritic and Nonmeteoritic Trace Elements in Luna 16 Samples. *Earth Planet. Sci. Letters*, Vol. 13, No. 2, 1972, pp. 450-454.
 33. FREDRIKSSON, K., J. NELSON, AND W. G. MELSON, Petrography and Origin of Lunar Breccias and Glasses. *Proc. Apollo 11 Lunar Science Conference Geochimica et Cosmochimica Acta*, Supplement 1, Vol. 1, 1970, pp. 419-432.
 34. KURAT, G., AND K. KEIL, Effect of Vaporization and Condensation on Apollo 11 Glass Spherules: Implications for Cooling Rates. *Earth Planet. Sci. Letters*, Vol. 14, No. 1, 1972, pp. 7-13.
 35. GIBSON, E. K., JR., N. J. HUBBARD, H. WIESMANN, B. M. BANSAL, AND G. W. MOORE, How to Lose Rb, K, and Change the K/Rb Ratio: An Experimental Study. *Proc. Fourth Lunar Science Conference, Geochimica et Cosmochimica Acta*, Supplement 4, Vol. 2, 1973, pp. 1263-1273.
 36. IVANOV, A. V., K. P. FLORENSKIY, M. A. NAZAROV, AND I. D. SHEVALEYEVSKIY, Some Manifestations of the Processes of Evaporation and Condensation in the Formation of Lunar Regolith Particles. *Dokl. AN SSSR*. In press.
 37. TAYLOR, H. P., JR., AND S. EPSTEIN, O^{18}/O^{16} and Si^{30}/Si^{28} : Studies of Some Apollo 15, 16, and 17 Samples. *Proc. Fourth Lunar Science Conference, Geochimica et Cosmochimica Acta*, Supplement 4, Vol. 2, 1973, pp. 1657-1679.
 38. YAKOVLEV, O. I., A. I. KOSOLAPOV, A. V. KUZNETSOV, AND M. D. NUSINOV, Results of Investigation of Fractional Evaporation of Basalt Melt in a Vacuum. *Dokl. AN SSSR*, Vol. 206, No. 4, 1972, pp. 970-973.
 39. NYQUIST, L. E., N. J. HUBBARD, P. W. GAST, B. M. BANSAL, H. WEISMANN, AND B. JAHN, Rb-Sr Systematics for Chemically Defined Apollo 15 and 16 Materials. *Proc. Fourth Lunar Science Conference, Geochimica et Cosmochimica Acta*, Supplement 4, Vol. 2, 1973, pp. 1823-1846.
 40. FLORENSKIY, K. P., A. V. IVANOV, YU. I. STAKHEYEV, AND L. S. TARASOV, *The Morphology, Types and Distribution of Sizes of Regolith Particles in the Sea of Fertility*. Akademieverlag, Berlin, Space Research XII, 1972, pp. 123-136.
 41. KASHKAROV, L. L., L. I. GENAYEVA, AND A. K. LAVRUKHINA, The Radiation History of the Formation of the Material Returned by Luna 16 and Luna 20 According to Track Study Data. *Abstracts of Reports of the Soviet-American Conference on Cosmochemistry of the Moon and Planets*, Moscow, 1974.

Microcraters on Lunar Samples

H. Fechtig, W. Gentner, J. B. Hartung, K. Nagel,
G. Neukum, and E. Schneider
*Max Planck Institut für Kernphysik
Heidelberg, Germany*

D. Storzer
*Department of Mineralogy
Musée National d'Histoire Naturelle
Paris, France*

The lunar microcrater phenomenology is described. The morphology of the lunar craters is in almost all aspects simulated in laboratory experiments in the diameter range from less than $1\ \mu$ to several millimeters and up to 60 km/s impact velocity. An empirically derived formula is given for the conversion of crater diameters into projectile diameters and masses for given impact velocities and projectile and target densities.

The production size frequency distribution for lunar craters in the crater size range from $\approx 1\ \mu$ to several millimeters in diameter is derived from various microcrater measurements within a factor of up to 5.

Particle track exposure age measurements for a variety of lunar samples have been performed. They allow the conversion of the lunar crater size frequency production distributions into particle fluxes. These fluxes derived from lunar samples are consistent with satellite in-situ measurements. For example, for masses $m \geq (1 \pm 0.4) \times 10^{-12}\text{g}$, the latest HEOS satellite flux of $\phi = (7 \pm 2) \times 10^{-5}\text{ m}^{-2}\text{ s}^{-1}$ agrees with $\phi = (1 - 7) \times 10^{-5}\text{ m}^{-2}\text{ s}^{-1}$ derived from lunar data.

The development of crater populations on lunar rocks under self-destruction by subsequent meteoroid impacts and crater overlap is discussed and theoretically described. Erosion rates on lunar rocks on the order of several millimeters per 10^7 yr are calculated.

Chemical investigations of the glass linings of lunar craters yield clear evidence of admixture of projectile material only in one case, where the remnants of an iron-nickel micrometeorite have been identified.

Microcraters created as a result of hyper-velocity impacts of interplanetary particles are found on most lunar rock surfaces. In this respect the microcraters can be considered as micrometeoroid detectors exposed for geological periods of time.

It is the purpose of this presentation to outline the principal phenomenology of such craters and to give some synthesis of the investigations of a working group at the Max Planck Institut für Kernphysik, Heidelberg, which is concerned with crater statistics, laboratory cratering experiments, solar flare track exposure ages, calculations of inter-

planetary dust fluxes, erosion processes, and chemistry of craters (see also ref. 1).

Crater Phenomenology

Microcraters on silicate target materials consist of a central glass-lined depression (central pit; center of impact) embedded in a so-called spallation zone where target material is spalled off under the influence of a shock wave propagating in the course of the impact process. On glass targets the spallation zone tends to be circular and concentric

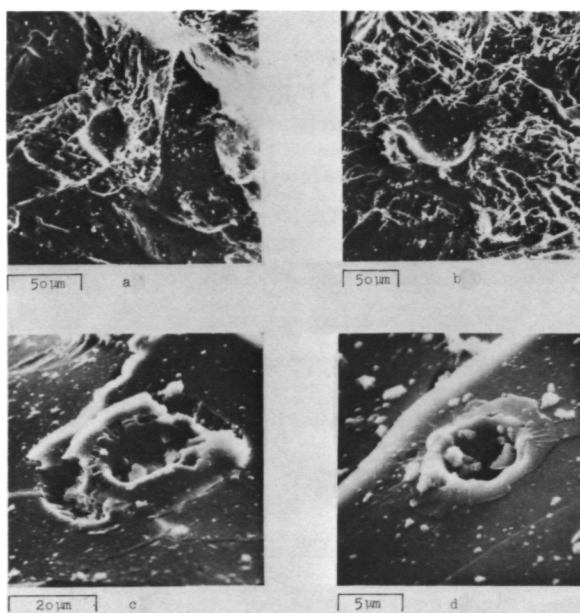


Figure 1.—Scanning electron microscope pictures of microcraters on lunar sample 12063,106. (a) and (b) Craters in crystalline material. (c) and (d) Craters in the glass linings of larger craters.

to the central depression. Spallation zones on crystalline material are mostly irregular in shape and may follow crystal structures or grain boundaries. Occasionally the material affected by the shock process is not completely thrown out of the spallation zone, but parts of it rest there slightly lifted above the undisturbed target surface (refs. 2 and 3). Examples of craters in glassy and crystalline lunar material are shown in figure 1.

In most cases larger craters ($\geq 50\text{-}\mu\text{m}$ central pit diameter) show a circular zone of higher albedo situated between the central pit and the spallation zone. This "halo zone" consists of finely fragmented material underlying the central pit. A crater with a prominent halo zone is displayed in figure 2.

In some cases the central pit is found to sit on some kind of a pedestal raised above the spallation level ("stylus pit"), or it may be not present at all ("pitless craters") (refs. 2, 4, and 5). An example of a stylus pit crater is given in figure 3, together with its laboratory-produced counterpart.

Microcraters on metal targets display only

a central pit, surrounded by a raised lip of "impact-fluidized" material (refs. 6 and 7). A similar behavior is found for very small ($\lesssim 1\text{-}\mu\text{m}$ diameter) craters on silicate material. The spallation zone is not present, and a depression looking very much like craters in metal targets remains. Often these craters are elongated, reflecting the obliquity of impact or irregularity of the impacting particle shape (ref. 8).

The morphology of microcraters on lunar samples can be simulated by laboratory experiments in almost all aspects (ref. 4). Figures 4 and 5 give a selection of lunar- and laboratory-produced craters with corresponding morphologies.

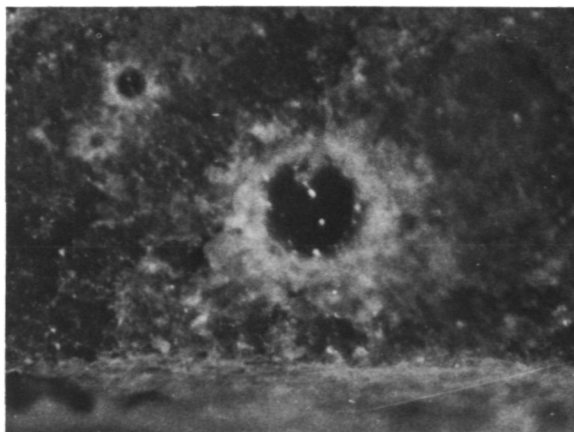


Figure 2.—Crater with prominent halo zone of higher albedo on lunar sample 60015,35 (central pit diameter $300\text{ }\mu\text{m}$).

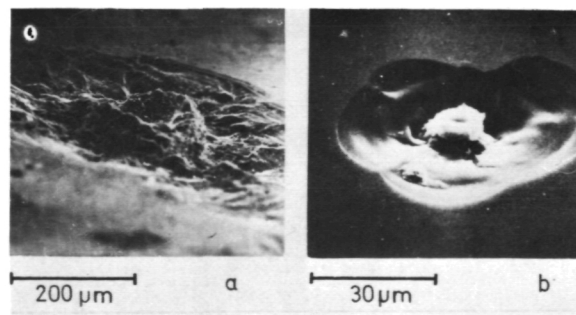


Figure 3.—"Stylus-Pit" craters. (a) Lunar sample 12024,8,1. (b) Laboratory produced crater, $3\text{ km/s} < v < 5\text{ km/s}$, $\text{Al} \rightarrow \text{quartz glass}$.

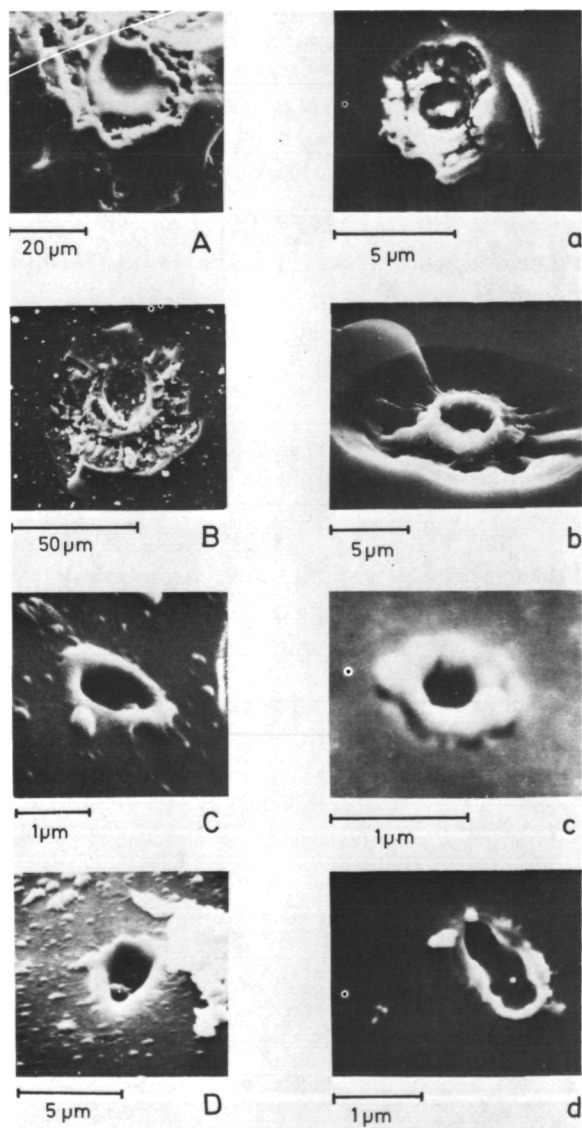


Figure 4.—Types of micron- and submicron-sized craters found on lunar samples, in comparison to craters produced in the laboratory. Lunar sample number: (A) 12063,106a Top (cryst. rock); (B) 14257 (coarse fines); (C) 14257 (coarse fines); and (D) 12063,106a Top (cryst. rock). Impact conditions: (a) Fe → Norite, $v = 7.6$ km/s; (b) Al → Quartz glass, $v = 5$ km/s; (c) Fe → Duran glass, $v = 50$ km/s; (d) Fe → Duran glass, $v = 30$ km/s, impact angle 45° .

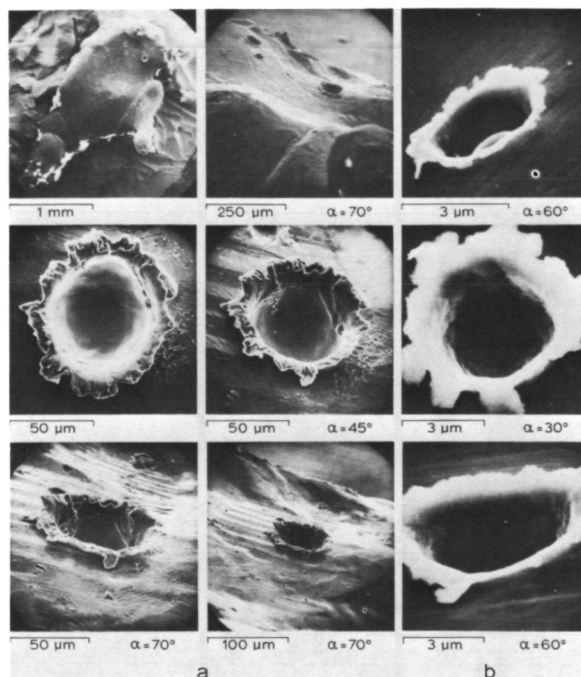


Figure 5.—(a, first two rows) Microcraters on Fe-Ni sample 60502,17 in comparison with (b, third row) laboratory-produced craters on metal targets (SEM-photographs, α = observation angle).

Laboratory Simulation Experiments

Using an electrostatic dust accelerator, projectiles in the mass range between 10^{-10} and 10^{-16} g were accelerated to velocities between 1 and 60 km/s (ref. 4). Using a lithium plasma gun, projectile masses between 10^{-5} and 10^{-8} g were accelerated to velocities between 2.5 and 18 km/s (ref. 9). Light gas gun projectiles of 10^{-2} g were accelerated to velocities between 1 and 4.5 km/s (ref. 10). Projectile materials were aluminum, carbon, iron, glass, and stainless steel, and target materials were glass, norite, stainless steel, aluminium, copper, and gold.

For both the dust accelerator and the light gas gun, it results for normal impacts occurring throughout the velocity range that the ratio of pit diameter to projectile diameter, D_P/d , is proportional to the two-thirds power of the impact velocity. Thus, $D_P/d \sim$

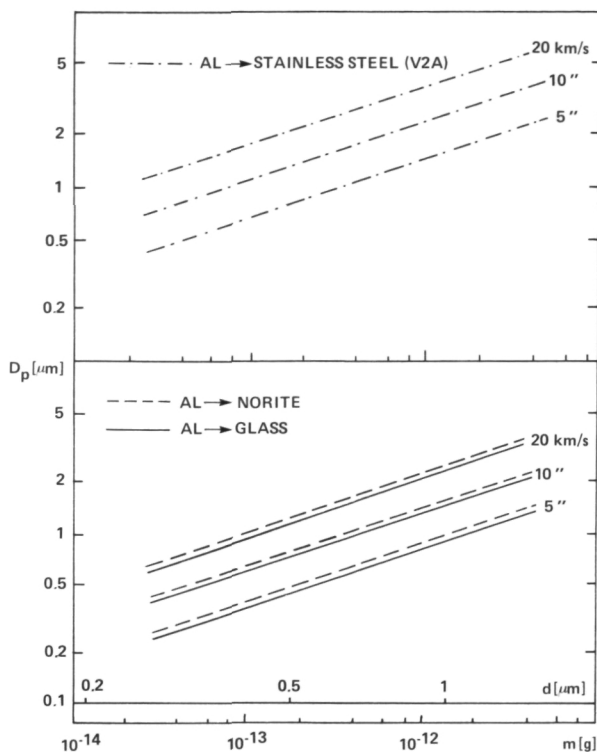


Figure 6.—Dependence of the central pit diameter, D_p , on projectile mass, m , or diameter, d , for different velocities. Data are for micron-sized aluminium projectiles impacting stainless steel, norite, and glass.

$v^{2/3}$. In figure 6, the dependence of D_p on d is given for different impact velocities.

Plasma gun experiments, however, produced mainly pitless craters. The ratio of the spallation zone diameter to projectile diameter, D_s/d , is proportional to the two-thirds power of the impact velocity; thus, $D_s/d \sim v^{2/3}$.

Though over-limited mass ranges, the experimental results can in each case be approximated by the two-thirds power laws, and the ratio D_p/d really slightly increases with increasing mass. From experiments showing pits, D_p/d increases a factor of 2 as projectile mass increases from 10^{-12} g to 10^{-2} g.

The ratio of the spallation zone diameter to projectile diameter, D_s/d , increases by a factor of 2 as projectile mass increases from 10^{-12} to 10^{-5} g. The ratio of the ki-

netic energy of the projectile to the volume of the crater is $E/v = 3.6 \times 10^{11}$ erg/cm³ for a projectile mass of 10^{-12} g, and $E/v = 4 \times 10^{10}$ erg/cm³ for a projectile mass of 10^{-2} g.

Using a formula from Gault (ref. 11) given for micrometer-to-centimeter-sized projectiles, these results can be represented approximately for normal impact over the whole experimental range from micron-sized to millimeter projectiles by slightly changing the constants

$$D_s = 10^{-3.077} \times \rho_t^{-1/2} \times \rho_p^{1/3} \times E^{1/2.65}$$

where ρ_t and ρ_p are target and projectile densities, respectively.

Crater Statistics

Cratered rock surfaces can display three categories of crater size frequency distributions.

As long as every impact crater on a surface exposed to the micrometeoroid bombardment is preserved, it is considered to be in the *production state*. The craters lie far apart and do not superpose one another. Figure 7 shows such a production crater population on a glass-coated lunar rock.

As time goes on, the crater frequency increases and crater superposition occurs; i.e.,

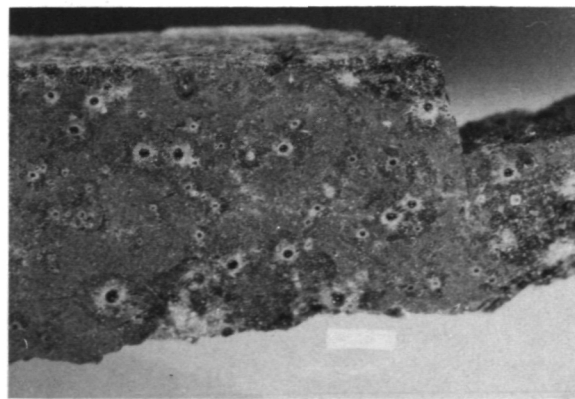


Figure 7.—Production crater population on lunar sample 60015,35. The light bar on top corresponds to 1 mm.

new impacts destroy already existing craters. The surface passes into a *transition state*. This process continues until on the statistical average the crater production rate is equal to the crater destruction rate and, therefore, the crater population remains constant. The surface has reached *crater equilibrium*.

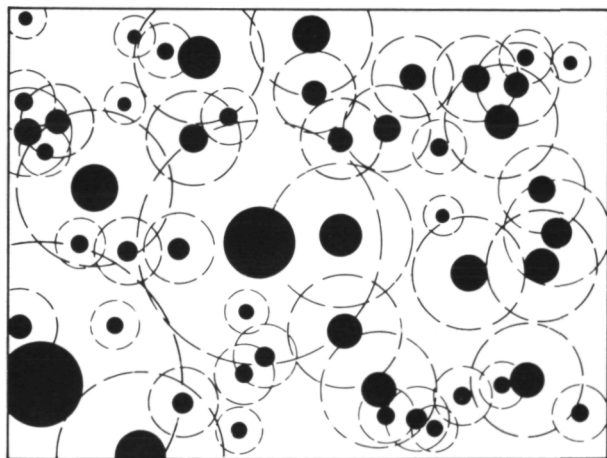
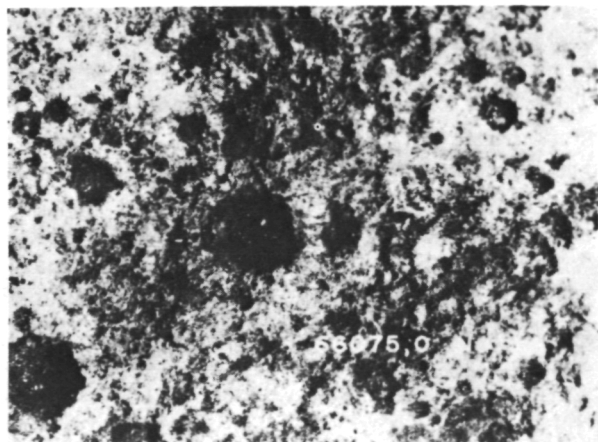


Figure 8.—Closeup photograph of rock 66075,0, considered to represent an equilibrium population. Width of frame approximately 1 cm). For comparison, a sketch depicting actual central pit locations and size (black dots) is added, and the actual, as well as eroded, spall zones (dashed circles) are indicated using the measured D_s/D_r value. Note the close proximity of many events, demonstrating that the effective destruction diameter operating in this surface is D_s . Note also the relative paucity of small events within the (somewhat younger) spall zone of the big crater in the center.

librium. An example of such a surface with a crater population in the equilibrium state is given in figure 8.

Figure 9 shows production size frequency distributions in the optically observable range of crater diameters. To eliminate exposure age differences, the curves are normalized at $D = 100 \mu\text{m}$, where D = central pit

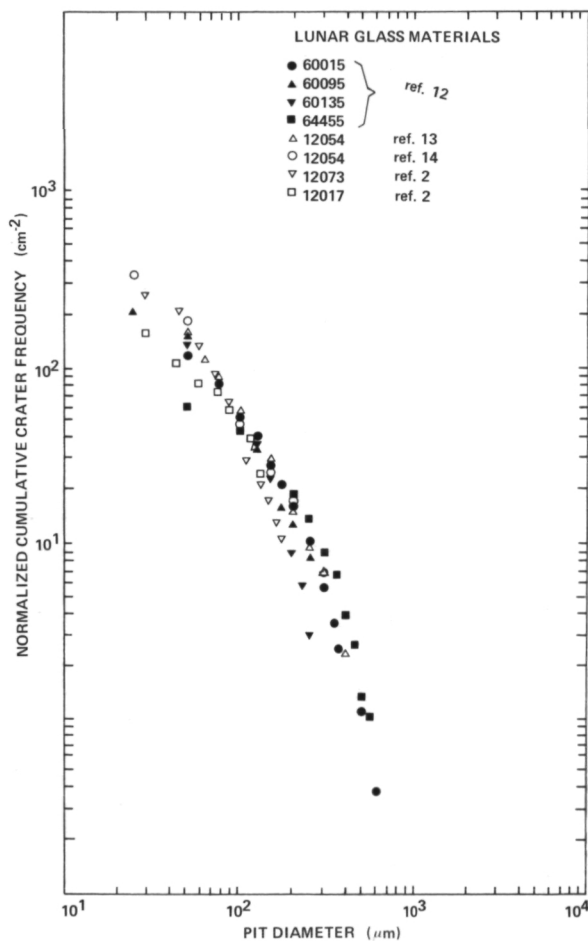


Figure 9.—Cumulative frequencies of microcraters obtained on a variety of glass surfaces representing production populations for microcraters with pit diameters $\geq 25 \mu\text{m}$. The consistent data for 12054 and 60015 are considered to be the most reliable because of the large number of craters counted in both cases. Note the relative steepening of the production slope at about $200\text{-}\mu\text{m}$ pit diameter, resulting in a production slope steeper than -2 . The curves are normalized at a pit diameter of $100 \mu\text{m}$.

diameter. The slopes for $D > 250 \mu\text{m}$ are grouping around -3 and steeper. The differences in slope are attributed to different exposure geometries of the individual lunar samples (ref. 12) and observational and statistical uncertainties. The flattening of the curves for $D < 250 \mu\text{m}$ is real, though somewhat exaggerated by observational losses in some cases and influenced by geometry effects. It means a depletion of craters of this size.

Figure 10 shows cumulative production state crater number densities in the micron and submicron size range, where only scan-

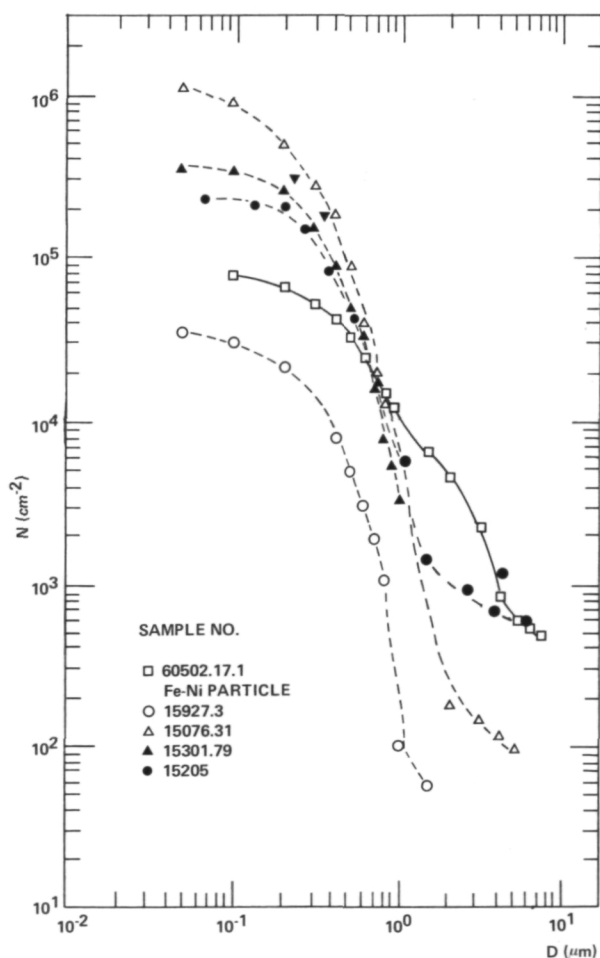


Figure 10.—Cumulative frequencies of micron-sized craters (production populations) as a function of the central pit diameter.

ning electron microscope investigations are feasible. These curves are not normalized and thus reflect differences in exposure age (ref. 6).

Measurements by different authors provide sufficient data to allow one to determine the production size distribution of microcraters on lunar rocks from less than 1μ to almost 1 cm in diameter. To derive the size distribution, we consider the following (1) Size distributions can usually be measured only in certain size ranges that depend on the size of a lunar rock, its exposure age, and the smoothness of its surface. (2) The absolute frequencies of craters in a certain size range vary with the exposure age of a rock. (3) In order to obtain the size distribution over the whole range of crater sizes observed on lunar rocks, normalization of microcrater frequencies derived from different measurements on different rocks is necessary. (4) The normalization range has to be chosen according to the quality of the data and the amount of overlap of the diameter ranges.

Figure 11 gives a compilation of currently available measurements of microcraters on lunar rocks, reduced in the above discussed way (ref. 17). The size distribution is determined within a factor up to 5. The slope is approximately equal to -2 in the micron-to submicron-size range; i.e., the distribution is steepening for $D < 1 \mu\text{m}$ (see also ref. 18). It is close to -1 in the range $1 \mu\text{m} < D < 100 \mu\text{m}$. In the range $D > 300 \mu\text{m}$, the slope has been determined to have the value -3.6 ± 0.3 . Thus, the distribution steepens significantly for the millimeter-sized craters.

Another factor influencing crater statistics is the number of pitless craters that are mostly not accounted for. There is some evidence that the total number of pitless craters observed on cratered surfaces depends on mechanical surface properties, i.e., on the absolute crater frequency which controls the state of erosion. Although the statistics are relatively poor—eight data points for breccias and four data points for crystalline material—there is an indication that the number of pitless craters decreases with increasing areal crater density, an observation

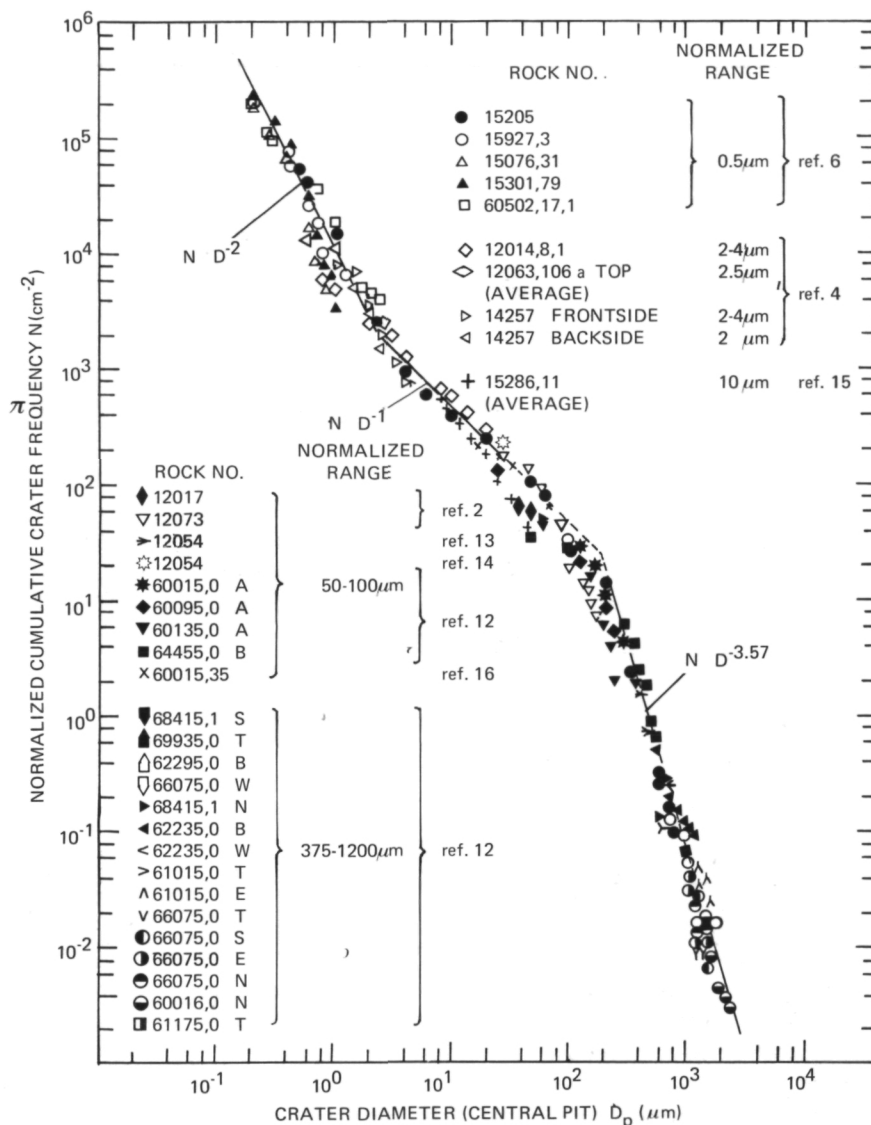


Figure 11.—Compilation of microcrater measurements of different authors. The frequencies are normalized at the ranges indicated (vertical shift of the distributions).

which can be explained in different ways. However, there is no unambiguous explanation yet available, so we prefer not to go into further details (see ref. 5).

Superposition of craters changes the slope of the crater distribution. For any production distribution slope steeper than -2 , it has been shown that the slope expected for the equilibrium crater population is -2 (ref. 19). In figure 12 the development of a crater

distribution with time is schematically shown. The longer the exposure time, t , the larger the craters affected by superposition. Thus, the production size distribution bends over to the equilibrium size distribution with the -2 slope for these sizes. With these assumptions, the tail of the distribution is always in the production state. It reflects the differences in exposure time. An alternative view also exists (ref. 20). Because rocks

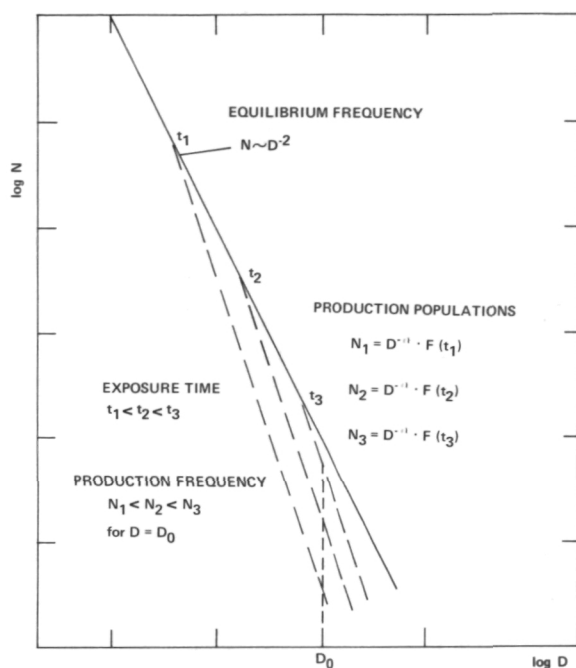


Figure 12.—Schematic display of the development of a crater population. Larger and larger craters are destroyed by superposition as time, t , goes on. The tail of the distribution remains in the production state, whereas small craters are in the equilibrium state.

destroyed early in their exposure lifetime are not collected by the astronauts, we can expect to recover a disproportionately large number of rocks which have survived longer than the expected mean lifetime. Thus, most rocks collected may not have received a representative share of larger craters and have enjoyed a statistical selection effect. Those large craters not accounted for would cause an artificial steepening of the cumulative size distribution curve. Therefore, lunar rock surfaces that have already reached an equilibrium state for small craters do not necessarily yield valid production distributions for larger craters. Shown in figure 13 is a hypothetical log-log cumulative size distribution diagram having a reference equilibrium line with a slope of -2 . Additional lines are shown that indicate how the observed distribution would appear for different numbers of unaccounted large craters due to the selection effect.

Figure 14 shows the behavior of real populations on lunar rocks (ref. 17). The picture is similar to the schematic treatment in figure 12. The difference in the frequencies at the tails of the distributions is greater than 10. The frequencies tend to become equal for smaller sizes where the slope is approximately equal to -2 . The difference between the highest and the lowest frequencies is less than a factor of 3. Ideally, the frequencies should be equal. This spread in the equilibrium frequencies is explained by different destruction conditions because of different ratios of spall sizes to pit sizes on different rocks (ref. 12), irregular spallation, and unobserved pitless craters. Additionally, the low-frequency populations might be still in the transition state.

Quantitatively, the equilibrium frequency N_E is written as $N_E = A \times D^{-2}$, where the

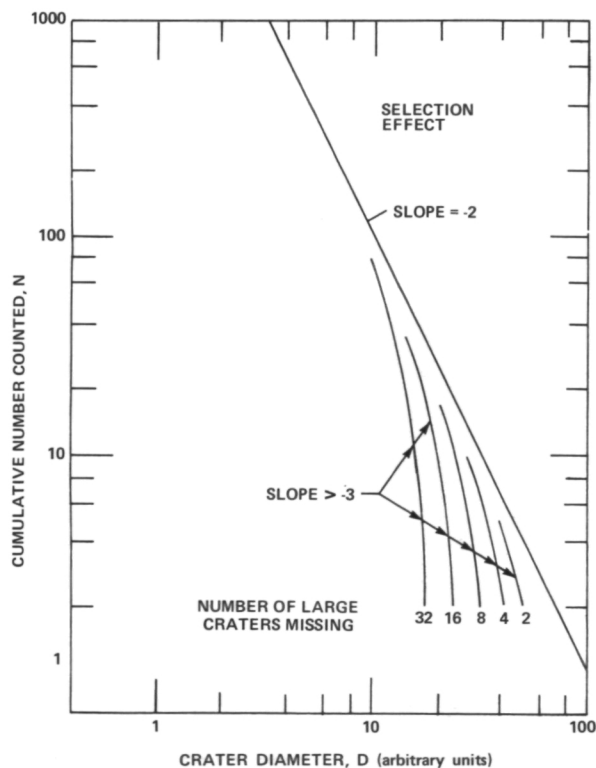


Figure 13.—Diagram illustrating the steepening of an equilibrium size distribution curve due to selection effects.

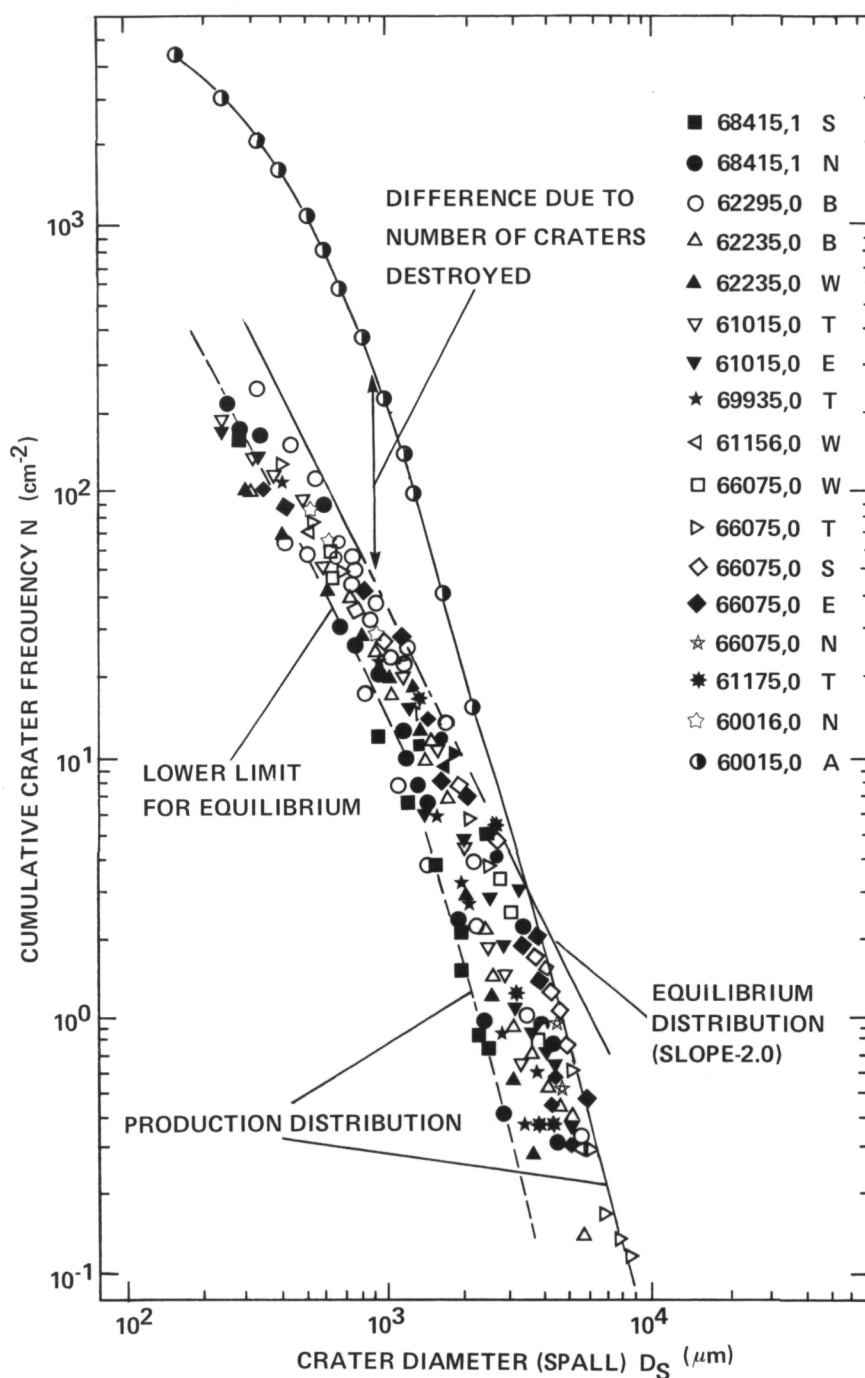


Figure 14.—Compilation of microcrater distributions measured on Apollo 16 rocks (ref. 12). The smaller craters are in the equilibrium state. The frequency variation in this range (a factor ≤ 3) is due to different destruction depending on different D_S/D_P ratios and rock properties. The large craters (steep slope) are in the production state. The number of craters destroyed is indicated by comparison with the extrapolated production distribution derived from the distribution on sample 60015,0.

crater diameter D can be either the spallation diameter D_s or the pit diameter D_p . The areal density coefficient, A , is expressed in the following way:

$$A = \frac{2 \times (\alpha - 2)}{\pi} \left(\frac{D_p}{D_s} \right)^{\alpha-2}$$

where $-\alpha$ is the slope of the production population in the $\log N$ versus $\log D$ plot. The D_p/D_s ratio is generally smaller on crystalline rocks than on breccias. Thus, one has to expect a corresponding variation in absolute equilibrium crater frequencies as is demonstrated in figure 14.

The highest frequencies we found on lunar rocks are limited by the above-discussed processes. Maximum crater number densities found per square centimeter are 100–150 for $D_p \geq 100 \mu\text{m}$; 3000 for $D_p \geq 1 \mu\text{m}$; 10^6 for $D_p \geq 0.1 \mu\text{m}$ (refs. 6 and 12).

As discussed above, the density of craters can be expressed independent of size if the crater distribution follows the law $N = A \times D^{-2}$. This is valid for populations in equilibrium and for the range $D_p < 250 \mu\text{m}$ as a tangential relationship for any lunar microcrater population because the slope flattens for smaller sizes.

Maximum measured areal density coefficients for a number of different rocks with different physical properties are plotted in figure 15, together with the limiting frequency value of Morrison et al. (ref. 21). Gault's (ref. 22) saturation percent values are given for comparison with the areal density coefficient values (ref. 12). We find, especially for the Apollo 16 rocks, a wide range of crater densities. Low maximum values for "glass" surfaces occur because we measured essentially populations in the production state. Other populations with similar values may be considered also in production, provided D_s/D_p is the same, and excessive numbers of pitless craters do not exist.

Regarding the higher areal density values, we have concluded that these populations are in or approaching the equilibrium state. We find no simple relationship between areal density values for populations close to equilibrium and physical properties of the rocks.

In general, however, crystalline rocks seem to have lower maximum densities than breccias.

Exposure Ages

In order to convert crater populations on a given sample into the interplanetary dust flux, the sample's residence time at the lunar surface must be known. Therefore, solar flare exposure ages were determined for samples 15076,31; 15015,24; 15927,3; 15301,79; 15205,51,1; 60502,17; 60015,35; and a glass-lined crater pit found in the Luna 16 core (C 19.118; 20–22 cm). For track observation, both optical and scanning electron microscopy were used. Detailed procedures are described elsewhere (ref. 23).

In all but samples 15076 and 60015 the depth dependence of solar flare tracks was studied in the glass phase. In lunar glasses the solar flare tracks are annealed to a con-

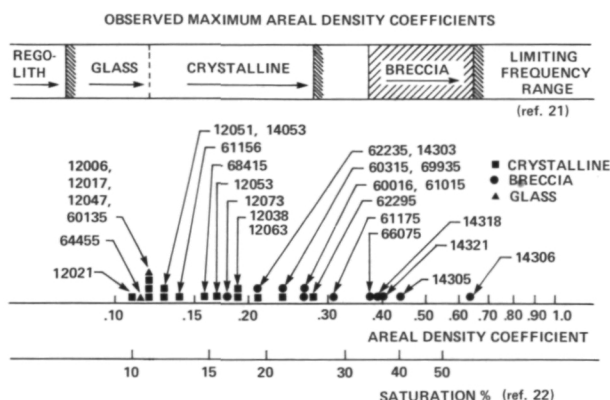


Figure 15.—Comparison of highest areal density coefficients observed to date on various lunar surface materials. Only the highest densities are plotted. Note the systematic difference of the areal density coefficients for various lunar rocks. These differences may be attributed to exposure age, rock properties, or a combination of both. The areal density coefficients for glass do not necessarily mean the highest approachable densities because only production populations have been investigated. For comparison, coefficients for loose regolith are indicated. Also shown are saturation percent values defined by Gault (ref. 22).

siderable extent (refs. 4 and 24). Accordingly, the track sizes are diminished and the track densities reduced (ref. 24). However, this very fact allows accurate track counting in a sample's near-surface, high-track density region and evaluation of the depth dependence of solar flare tracks. Thereafter, the track densities were corrected according to the respective size shrinkage of the track etch pits (ref. 24) and/or normalized to the track densities of pyroxenes that were trapped within the glass phases.

In all samples studied (except sample 60502, probably due to a 100- μ m Ni-Fe cover) the track densities P decrease with depth R from the surface according to $P = \text{const} \times R^{-\alpha}$. The α -values range between 2.5 and 2.8 (ref. 23), agreeing well with the track record of the uneroded Surveyor III glass lens (refs. 25, 26, and 27). We therefore conclude that erosion affected our samples only to a minor degree. Furthermore, the surfaces were irradiated and cratered having a solid angle of exposure of essentially 2π . The solar flare exposure ages are compiled in table 1. For their calculation, track production rates based on the revised Surveyor III track record were used (ref. 23). (In an earlier paper, ref. 6, the track production rates used were different and the ages therefore lower.) The Surveyor III spacecraft was on the Moon during the period of maximum solar activity and for a fraction of the present solar cycle only. On the other hand, the flux data have not to be representative for the long time averaged solar activity. This uncertainty in applying

the Surveyor III record to our lunar samples results in an age uncertainty of about a factor of 2.

Among charged particle track exposure ages of lunar rock surfaces determined by different groups, there exist some apparent systematic discrepancies up to a factor of 3. This might be due to an insufficient calibration and standardization of the particle track method. For example, there exists a difference in the etchable ranges of tracks in the various detectors used (glasses, feldspars, or pyroxenes), differences in the track etching conditions applied (etchant, temperature, and etching time), and differences in the track observation technique (optical, scanning electron, or transmission electron microscopy).

Particle track exposure ages have been determined by different authors for a variety of Apollo 12, 14, 15, and 16 rocks, where mostly millimeter-sized craters have been measured. As seen before, the size distribution in this range follows the law $N \sim D_p^{-3.57}$ on the average, or in terms of spall diameters, $N = Q \times D_s^{-3.57}$. Normalized to crystalline rock, we obtain $N_{\text{norm}} = Q_{\text{norm}} \times D_s^{-3.57}$, where $Q_{\text{norm}} = q^{3.57} \times Q$. The factor q is the ratio of D_s/D_p for crystalline rock and D_s/D_p for the special rock whose crater population is measured: $q = \frac{D_s(\text{cryst.})}{D_s(\text{meas.})}$. It is assumed that for the same impact on different rocks with different composition and texture (e.g., breccias compared to crystalline rocks), the central pit with diameter D_p has the same size, but the ratio of spall diameter to pit

Table 1.—*Exposure Ages Determined by Means of Solar Flare Tracks*

Sample number	15015, Luna 24 ⁽¹⁾ 16 ⁽¹⁾	15927,3	15205, 51,1	15301, 79	15076, 31	60502,17 ⁽²⁾	60015,35
Solar flare exposure age	40 5.7×10^3	4.8×10^3	7.9×10^4	9.6×10^4	2.6×10^5	1.1×10^4	1.5×10^5

NOTES: (1) No microcraters have been found on these samples.

(2) Considering the higher stopping power of iron, we corrected our data to an equivalent shielding of stony material.

diameter, D_s/D_P , is different. The time integral of the cumulative crater production rate $\phi(D)$ gives $N = \phi(D) \times t_A = \text{const} \times t_A \times D_s^{-3.57}$ (time constant influx assumed). Thus it results after normalization (a) for $D_s = 1 \text{ mm}$

$$N_{\text{norm}} = c_1 \times t_A$$

or

(b) $Q_{\text{norm}} = c_2 \times t_A$, independent of D_s .

Particle track exposure ages of dated rocks are plotted against the respective crater frequency measurements in terms of N_{norm} ($D_s = 1 \text{ mm}$) and Q_{norm} in figure 16. The data can be fitted by the expression

$$t_A = 7.3 \times 10^7 \times Q_{\text{norm}}$$

respectively,

$$t_A = 2.10^4 \cdot N_{\text{norm}} \quad (D_s = 1 \text{ mm})$$

which would correspond to a time constant influx between roughly 3×10^5 and 3×10^6 yr ago. These formulae can be used to determine exposure ages by crater statistics that correspond to particle track ages.

A different view is presented by Hartung et al. (ref. 20). The correlation shown in figure 16 may be independent of time because both solar flare tracks and microcraters occur at the surfaces of lunar rocks. Thus, rocks having physical properties permitting a higher erosion rate would have lower track and crater densities at the surface. The correlation observed then reflects different physical properties of rocks rather than different exposure ages.

Meteoroid Fluxes

Using the following formula it is possible to calculate the meteoroid flux ϕ for a production crater population with known exposure time.

$$\phi = \frac{N}{t} \quad (1)$$

where ϕ = meteoroid flux per m^2s

N = cumulative crater number per m^2

t = exposure time

Knowing the impact velocity, the conversion of crater diameters into particle diameters is accomplished with the help of the simulation results. However, the results obtained in this way are for an isotropic spatial distribution. The results of recent space probe and satellite measurements show, however, a rather strong anisotropy in spatial distribution.

The Pioneer 8/9 dust experiment (ref. 35) shows that a sensor orbiting the Sun at 1 AU and spinning in the ecliptical plane is hit by two major dust streams, one from the apex direction (direction of Earth's motion around the Sun) and one from the direction of the Sun. Contrary to the apex particles, the Sun particles are the most frequent ones in terms of event rates. Although it was not possible to measure particle mass and impact velocity separately, there is strong evidence that these particles are extremely small ($< 1 \mu\text{m}$ in diameter), and the impact velocity is higher compared to the apex particles. The impact velocity is considered to be higher than 50 km/s and may even exceed 100 km/s (ref. 35), depending on particle diameter. Zook and Berg (ref. 36) propose that these submicron-sized particles are being produced from normal zodiacal dust particles. These zodiacal dust particles, following the Poynting-Robertson effect (ref. 37), are continuously losing energy and thus spiraling into the Sun. In the neighborhood of the Sun the particles partly melt and/or are fragmented by collisions. As a result of these processes, submicron-sized fragments are accelerated by the radiation pressure and blown out of the solar system on hyperbolic orbits. Hemenway et al. (ref. 38) claim, however, that submicron-sized particles may come off the surface of the Sun and may be blown out of the solar system.

The HEOS 2 dust experiment (refs. 39 and 40) is measuring the dust population in apex, anti-apex, ecliptic north, and ecliptic south directions. It has shown that the apex flux is the most dominant flux. The fluxes in the other directions are approximately 2 orders of magnitude lower compared to the apex flux. The impact velocities of the apex

particles show a broad distribution, from 2 km/s (sensitivity barrier) up to about 25 km/s, and averaging at about 10 km/s. These results are in agreement with results from the Pioneer 8/9 dust experiment (ref. 41), and the velocity distribution is expected as a consequence of the Poynting-Robertson effect.

In conclusion, one can state from the latest in-situ measurements that the Moon is hit by the apex-particle flux for particles $\gtrsim 1 \mu\text{m}$ in diameter at 10 km/s impact velocity and by the Sun-particle flux for particles $\lesssim 1 \mu\text{m}$ in diameter at $> 50 \text{ km/s}$ impact velocity.

Concerning the crater size distributions,

Schneider et al. (ref. 6) have reported a bimodal distribution in crater sizes. Let us assume that the micron-sized and larger craters have been produced by apex particles and the submicron-sized craters by sun particles. It is then possible to convert the crater sizes into the respective particle sizes. For 10 km/s impact velocity, D_P/d is between 1.4 and 2 for crater diameters D_P between $1 \mu\text{m}$ and 1 mm. For 50 km/s impact velocity and crater diameters $< 1 \mu\text{m}$, D/d is 4 for glass targets and 7 for metal targets as shown in figure 6. The conversion into fluxes is then accomplished applying formula (1) to the respective production crater distribu-

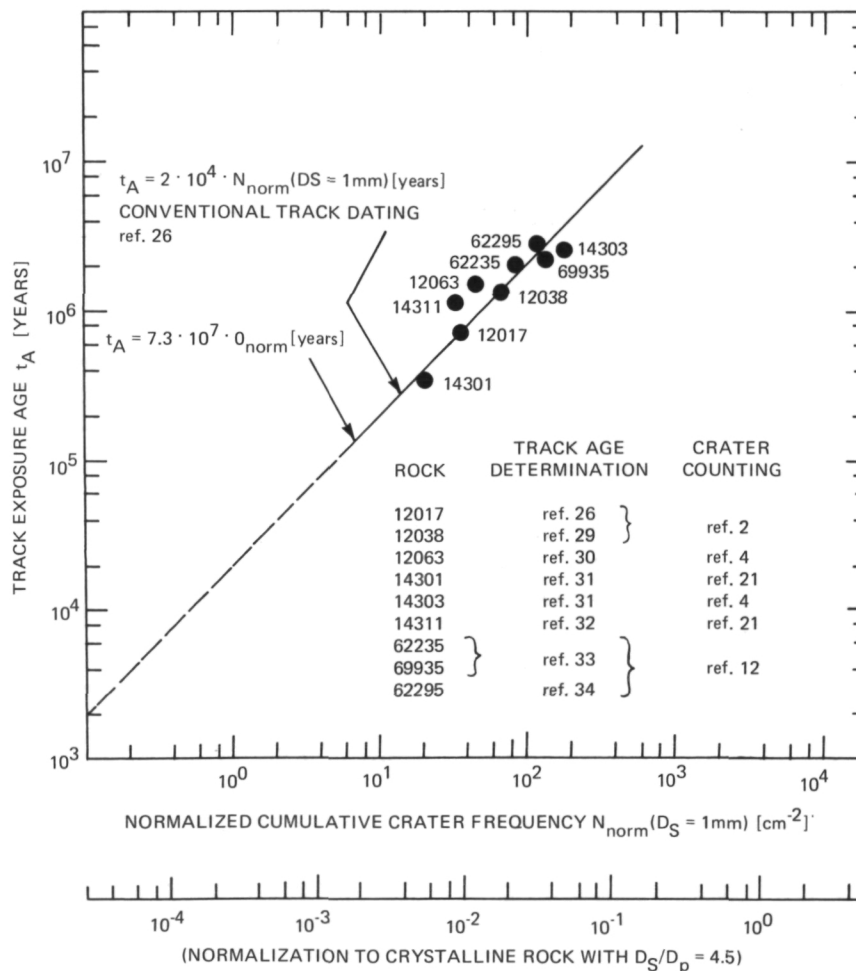


Figure 16.—Relationship between particle track exposure ages of individual lunar rocks and the microcrater production frequencies (tails of the distributions) measured on them.

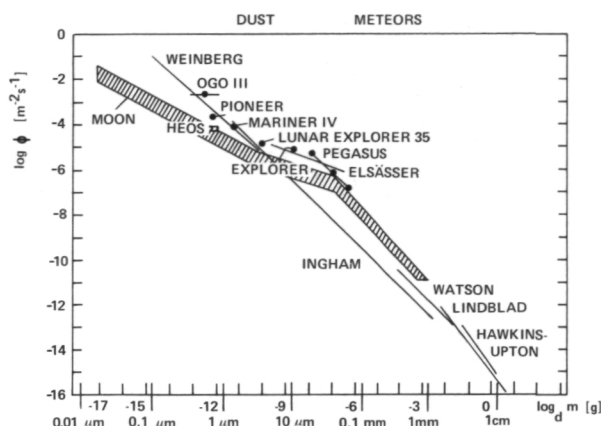


Figure 17.—Comparison of micrometeoroid fluxes derived from lunar microcrater measurements with those obtained in various satellite in-situ experiments.

tion. Since the Moon is a spinning Earth satellite, the surface is hit by the dust streams only part of the time. The results, therefore, have to be multiplied by the factor of π , if unidirectional fluxes are concerned.

The final flux results are given in figure 17. The numbers of dust particles are cumulatively plotted as a function of particle mass. The results obtained from lunar microcrater statistics are labeled "Moon." This is the time-averaged flux on a lunar surface exposed directly to the two major dust streams while the Moon rotates and orbits the Sun with the Earth (ref. 16).

In comparison with other flux results given in the flux diagram, it seems that the Moon flux is lower. However, all measurements with exception of the HEOS value are calculated under the assumption of a 2π -steradian detector exposure geometry and an isotropic flux direction. As discussed above, this assumption has to be revised drastically. For a two-stream particle flux distribution, the HEOS flux comes close to the Moon flux. This suggests that the present meteoroid flux is nearly the same as that averaged over more than 10^5 yr.

Results contrary to this have been obtained based on solar flare track exposure age measurements of individual lunar micro-craters (ref. 42). The age distribution of micro-

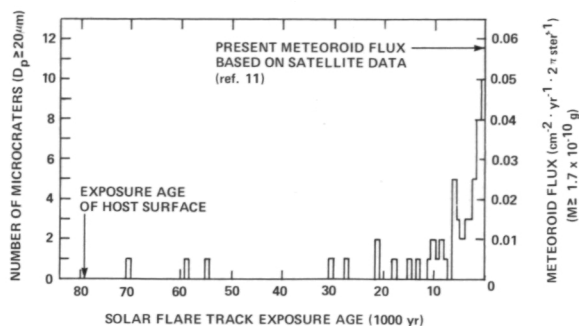


Figure 18.—Solar flare track exposure age measurements of single microcraters ($D_p \geq 20 \mu\text{m}$) on sample 15205,51.

craters found in this way suggests that a higher flux exists now compared with that existing at any time during the last 100 000 yr (fig. 18). Further measurements are needed to explain this discrepancy.

Erosion of Lunar Rocks

Erosion of lunar rocks is dominantly controlled by micro-meteorite impact, which is a random process. Analytical model calculations yield only statistical averages. However, for most applications in lunar rock analysis it is of interest how a rock surface topography develops under continuous meteorite bombardment; deviations from averages and the uniqueness of single-spot exposure histories have to be taken into account. Therefore, a Monte Carlo computer model has been worked out (ref. 43). A given test area was randomly covered with craters of 17 size classes.

The total simulated crater diameter interval extends from $152 \mu\text{m}$ to 2.4 cm in spall diameter. This range contributes dominantly to the abrasion of rocks sampled during the Apollo missions.

The probabilities for the occurrence of different crater sizes were calculated on the basis of production state crater distributions actually observed on lunar sample surfaces.

The test area itself was subdivided into roughly 27 000 area elements (cells), which

were characterized by their center coordinates. The computer kept track of the erosion state, i.e., the depth level of each area element. Some of the main results of this computer model are as follows.

Figure 19 gives the percentages of surface area affected (i.e., number of area elements affected) as a function of total numbers of craters produced. Notice that already after about 8300 craters 50 percent of the total area has been affected, whereas it takes another 70 000 to 80 000 craters to completely cover the remaining 50 percent. With increasing model time the probability for one cell's being affected repeatedly by impacts is increasing, too. The curves in the lower part of the diagram represent these multi-impact percentages of the surface. For ex-

ample, after 100 000 craters have been produced, about 5 percent of the surface will have been impacted not less than 11 times.

Figure 20 illustrates the maximum deviations of certain coherent reference areas from the average erosion depth of the whole surface, again as a function of total crater numbers or model time. Depending on the size of the reference area there may easily occur deviations up to factors of 10 in both directions, which means that small sample chips, usually available for laboratory investigations, cannot be considered as being representative for whole sample surfaces.

If one applies different crater production rates derived from model fluxes of the interplanetary dust (figure 17), the model results can be related with absolute times, and aver-

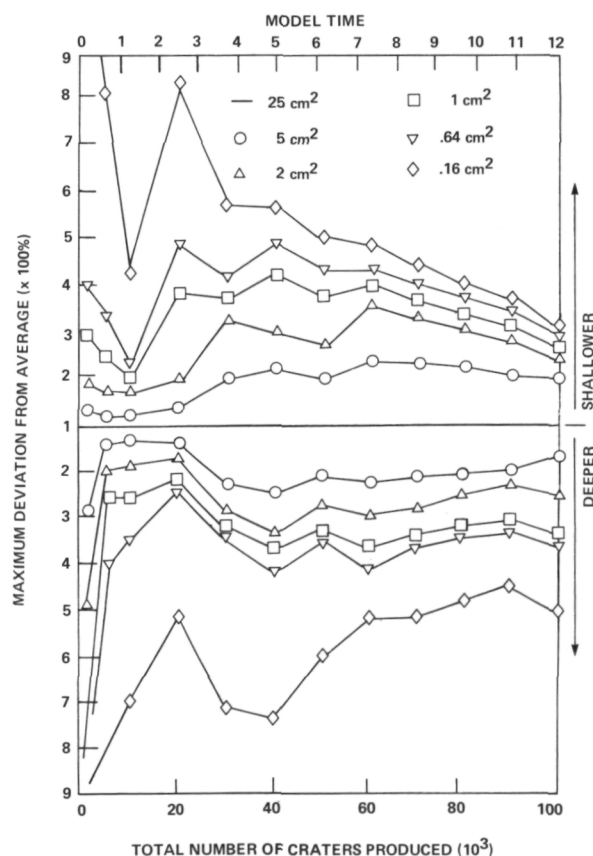


Figure 19.—Percentages of surface area affected X many times ($X = 1, 2, 3, \dots$) as a function of total number of impacts produced.

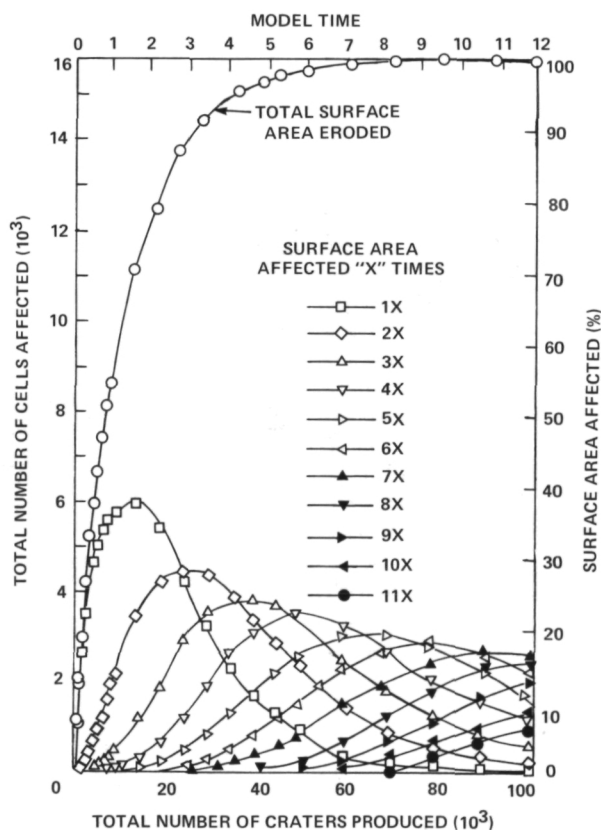


Figure 20.—Maximum deviation from the average erosion depth of the whole test surface plotted against model time for different reference areas.

age erosion rates can be determined. They range roughly between 0.07 mm and 0.7 mm per 10^6 yr.

Erosion rates (single particle abrasion) can be calculated analytically. The mass ejection M_e per impact with mass m at 20 km/s impact velocity can be derived from a formula by Gault (ref. 44), resulting in $M_e = 10^{3.575} \times m^{1.133}$. Following a procedure by Gault et al. (ref. 44), erosion rates of 0.1 to 0.3 mm per 10^6 yr are calculated (ref. 17). This value is dependent on the crater production rate used. In this case, a rate consistent with the data in figure 17 is used.

Chemistry

The glass lining of lunar microcraters has been investigated for admixture of projectile material with an electron microprobe. Detailed analyses of several craters on the glass coating of sample 60015,35 and of one crater on the crystalline sample 12002,100 have been performed.

The coating of 60015 was initially glass a few millimeters thick, but has devitrified to elongate plagioclase crystals with 2- to 50- μ dimensions and pyroxene-composition interstitial material. Point electron microprobe analyses for Fe, Mg, Ca, Al, and Si of glasses lining several 100- μ -sized pits show no indication of material in the pit glasses that is outside the range in composition of the host sample phases. Either the projectile material composition is similar to the host material composition, or little or no projectile material remained in the pit glass in these cases.

Similar measurements that suggest some presence of projectile material or fractional vaporization during the impact process have been performed by Mehl (ref. 45).

A 0.5 mm pit on sample 12002,100 showed numerous mounds associated with its glass coating. The mounds consist of mainly iron and nickel, with an iron-to-nickel ratio of 20:1. This indicates that the mounds are the remnants of an iron-nickel micrometeoroid that formed this crater (ref. 16). Figure 21 shows the distribution of iron and nickel in

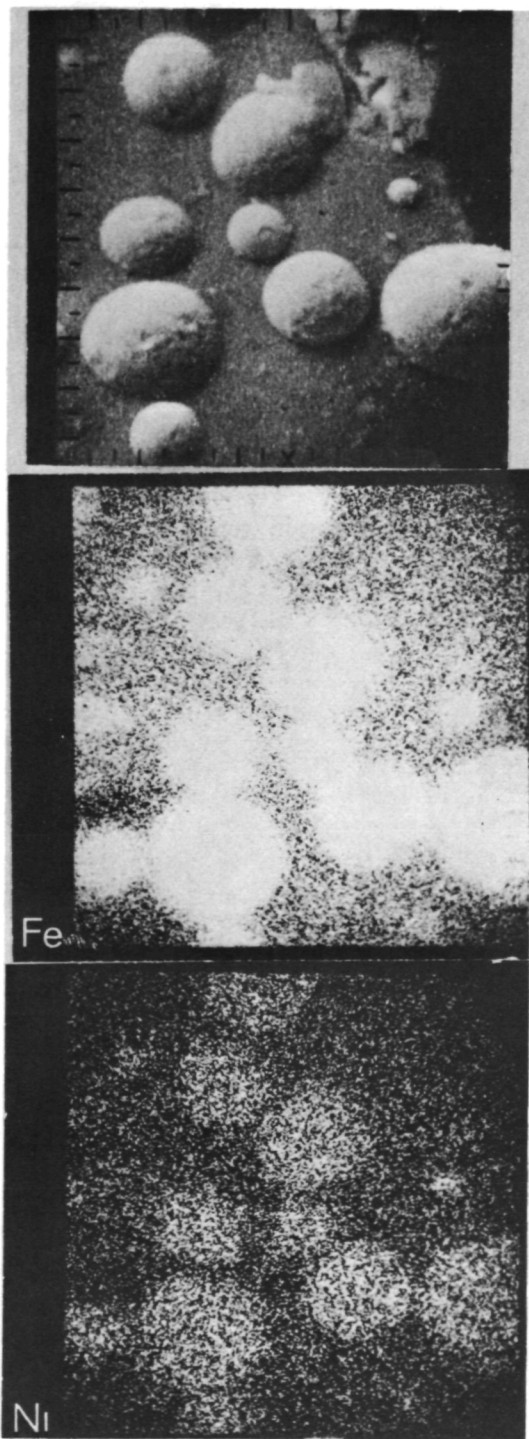


Figure 21.—Nickel-iron mounds in a 500- μ m crater on sample 12002,100. Microprobe secondary electron scanning picture with corresponding Fe-K α and Ni-K α X-ray scanning images (frame width ≈ 30 μ m).

the mounds and the surrounding crater glass lining.

Conclusions

The lunar microcrater phenomenology has been simulated in laboratory experiments in almost all aspects. Additionally, the laboratory experiments allow the conversion of crater diameters into projectile diameters and masses at given impact velocities and projectile and target densities. These experimental results are applied to lunar microcrater populations.

Various measurements of microcrater production size frequency distributions exist in different size ranges. A compilation of these data yields the size frequency distribution for the diameter range between 1 μm and 1 mm, with an uncertainty of up to a factor of 5.

The time development of crater population is qualitatively understood. The crater populations start as production populations, where essentially no craters have overlapped and destroyed each other. As time goes on, crater destruction occurs by subsequent crater superposition. The populations pass through a transition state, where the crater distributions are gradually deviating from the production distributions. Finally, an equilibrium state is reached: on the statistical average, the number of craters in this state does not change. Theoretical descriptions of the equilibrium state satisfactorily agree with the observational data.

Surface exposure ages have been determined from particle track measurements. The flux of interplanetary dust impacting the surface of the Moon is obtained by correlating areal crater densities with surface exposure ages. Such a correlation observed for large craters ($100 < D_p \leq 1000 \mu$) on surfaces approaching equilibrium with respect to cratering may be a basis for a flux determination or, alternatively, an exposure time measurement if the flux (or the crater production rate) is known. Another interpretation of such a correlation is that since

both solar flares and microcraters occur at the exposed lunar surface, they both suffer the same effects of erosion, and the correlation observed reflects only the relative "erodability" of different samples.

The latest in-situ micrometeoroid measurements are important for the interpretation of the lunar crater frequencies: two major dust streams are hitting the Moon from distinct spatial directions—apex and Sun; the correspondent impact velocities are about 10 km/s for the apex dust stream and about 50 km/s for the Sun dust stream.

Taking into account the spin of the Moon relative to the Sun, it is possible to calculate a unidirectional flux valid for the Moon. This flux is fairly consistent with recent in-situ measurements, considered under the same conditions (Pioneer 8/9 and HEOS 2 results). On the contrary, Hartung et al. (ref. 42) have found an increased flux at present from individual microcrater glass linings dated by means of solar flare track measurements. Further measurements are necessary to resolve this discrepancy.

Monte Carlo computer simulation and analytical treatment of the erosion of lunar rocks by micrometeoroid impacts lead to consistent erosion rates of several millimeters per 10^7 yr.

Measurements of the chemical composition of the glass linings of several craters $\geq 100 \mu\text{m}$ in diameter yielded the unambiguous presence of projectile material only in one case, where the remnants of an iron-nickel micrometeorite have been detected.

Acknowledgment

Appreciation is expressed for the financial support provided to D. Storzer by the Deutsche Forschungsgemeinschaft.

References

1. HÖRZ, F., D. E. BROWNLEE, H. FECHTIG, J. B. HARTUNG, D. A. MORRISON, G. NEUKUM, E. SCHNEIDER, AND J. F. VEDDER, Lunar Microcraters, Implications for the Micrometeoroid

- Complex. *Planet. Space Sci.*, in press, 1974.
2. HÖRZ, F., J. B. HARTUNG, AND D. E. GAULT, Micrometeorite Craters and Lunar Rock Surfaces. *J. Geophys. Res.*, Vol. 76, 1971, pp. 5770-5798.
 3. BLOCH, M. R., H. FECHTIG, W. GENTNER, G. NEUKUM, AND E. SCHNEIDER, Meteorite Impact Craters, Crater Simulation, and the Meteoroid Flux in the Early Solar System. *Proc. Second Lunar Science Conference, Geochimica et Cosmochimica Acta*, Supplement 2, Vol. 3, 1971, pp. 2639-2652.
 4. NEUKUM, G., E. SCHNEIDER, A. MEHL, D. STORZER, G. A. WAGNER, H. FECHTIG, AND M. R. BLOCH, Lunar Craters and Exposure Ages Derived From Crater Statistics and Solar Flare Tracks. *Proc. Third Lunar Science Conference, Geochimica et Cosmochimica Acta*, Supplement 3, Vol. 3, 1972, pp. 2793-2810.
 5. SCHNEIDER, E., AND F. HÖRZ, Microcrater Populations on Apollo 17 Rocks. *Icarus*, in press, 1974.
 6. SCHNEIDER, E., D. STORZER, J. B. HARTUNG, H. FECHTIG, AND W. GENTNER, Microcraters on Apollo 15 and 16 Samples and Corresponding Cosmic Dust Fluxes. *Proc. Fourth Lunar Science Conference, Geochimica et Cosmochimica Acta*, Supplement 4, Vol. 3, 1973, pp. 3277-3290.
 7. RUDOLPH, V., Untersuchungen an Kratern von Mikroprojekten im Geschwindigkeitsbereich von 0.5-10 km/s. *Z.f. Naturforschung*, Vol. 24a, 1969, pp. 326-331.
 8. BROWNLEE, D. E., F. HÖRZ, J. F. VEDDER, D. E. GAULT, AND J. B. HARTUNG, Some Physical Properties of Micrometeoroids. *Proc. Fourth Lunar Science Conference, Geochimica et Cosmochimica Acta*, Supplement 4, Vol. 3, 1973, pp. 3197-3212.
 9. NAGEL, K., *Experimente zur Kratersimulation*. Master's Thesis, Universität Heidelberg, 1973.
 10. SCHNEIDER, E., *Mikrokrater auf Mondgestein und deren Laborsimulation*. Ph.D. Thesis, Universität Heidelberg, 1972.
 11. GAULT, D. E., F. HÖRZ, AND J. B. HARTUNG, Effects of microcratering on the lunar surface. *Proc. Third Lunar Science Conference, Geochimica et Cosmochimica Acta*, Supplement 3, Vol. 3, 1972, pp. 2713-2734.
 12. NEUKUM, G., F. HÖRZ, D. A. MORRISON, AND J. B. HARTUNG, Crater Populations on Lunar Rocks. *Proc. Fourth Lunar Science Conference, Supplement 4*, Vol. 3, 1973, pp. 3255-3276.
 13. HARTUNG, J. B., F. HÖRZ, AND D. E. GAULT, Lunar Microcraters and Interplanetary Dust. *Proc. Third Lunar Science Conference, Geochimica et Cosmochimica Acta*, Supplement 3, Vol. 3, 1972, pp. 2735-2753.
 14. NEUKUM, G., *Untersuchungen über Einschlagskrater auf dem Mond*. Ph.D. Thesis, Universität Heidelberg, 1971.
 15. BROWNLEE, D. E., F. HÖRZ, J. B. HARTUNG, AND D. E. GAULT, Micrometeoroid Craters Smaller Than 100 Microns. *The Apollo 15 Lunar Samples*, Lunar Science Institute, Houston, 1972, pp. 407-409.
 16. FECHTIG, H., J. B. HARTUNG, K. NAGEL, G. NEUKUM, AND D. STORZER, Microcrater Studies, Derived Meteoroid Fluxes and Comparison With Satellite-Borne Experiments. *Lunar Science*, Vol. V Abstracts pp. 222-224; *Proc. Fifth Lunar Science Conference, Geochimica et Cosmochimica Acta*, Supplement 5, Vol. 3, in press, 1974.
 17. NEUKUM, G., *The Interaction of Micrometeoroids With Lunar Rocks*. To be published, 1974.
 18. BLANFORD, G., D. MCKAY, AND D. MORRISON, Accretionary Particles and Microcraters. *Lunar Science*, Vol. V Abstracts, Part 1, 1974, pp. 67-69.
 19. NEUKUM, G., AND H. DIETZEL, On the Development of the Crater Population on the Moon With Time Under Meteoroid and Solar Wind Bombardment. *Earth Planet. Sci. Letters*, Vol. 12, 1971, pp. 59-66.
 20. HARTUNG, J. B., F. HÖRZ, F. K. AITKIN, D. E. GAULT, AND D. E. BROWNLEE, The Development of Microcrater Populations on Lunar Rocks. *Proc. Fourth Lunar Science Conference, Geochimica et Cosmochimica Acta*, Supplement 4, Vol. 3, 1973, pp. 3213-3234.
 21. MORRISON, D. A., D. S. MCKAY, H. J. MOORE, AND G. H. HEIKEN, Microcraters on Lunar Rocks. *Proc. Third Lunar Science Conference, Geochimica et Cosmochimica Acta*, Supplement 3, Vol. 3, 1972, pp. 2767-2791.
 22. GAULT, D. E., Saturation and Equilibrium Conditions for Impact Cratering on the Lunar Surface: Criteria and Implications. *Radio Science*, Vol. 5, 1970, pp. 272-291.
 23. STORZER, D., G. POUPEAU, AND W. KRÄTSCHMER, Track Exposure and Formation Ages of Some Lunar Samples. *Proc. Fourth Lunar Science Conference, Geochimica et Cosmochimica Acta*, Supplement 4, Vol. 3, 1973, pp. 2363-2377.
 24. STORZER, D., AND G. A. WAGNER, Correction of Thermally Lowered Fission Track Ages of Tektites. *Earth Planet. Sci. Letters*, Vol. 5, 1969, pp. 463-468.
 25. CROZAZ, G., AND R. M. WALKER, Solar Particle Tracks in Glass From Surveyor 3 Spacecraft. *Science*, Vol. 171, 1971, pp. 1237-1239.
 26. FLEISCHER, R. L., H. R. HART, AND G. M. COMSTOCK, Very Heavy Solar Cosmic Rays: Energy Spectrum and Implications for Lunar Erosion. *Science*, Vol. 171, 1971, pp. 1240-1242.
 27. BARBER, J., R. COWSIK, I. R. HUTCHEON, P. B. PRICE, AND R. S. RAJAN, Solar Flares, the

- Lunar Surface and Gas-Rich Meteorites. *Proc. Second Lunar Science Conference, Geochimica et Cosmochimica Acta*, Supplement 2, Vol. 3, 1971, pp. 2705-2714.
28. FLEISCHER, R. L., H. R. HART, JR., G. M. COMSTOCK, AND A. O. EVWARAYE, The Particle Track Record of the Ocean of Storms. *Proc. Second Lunar Science Conference, Geochimica et Cosmochimica Acta*, Supplement 2, Vol. 3, 1971, pp. 2559-2568.
 29. BHANDARI, N., S. BHAT, D. LAL, G. RAJAGOPALAN, A. S. TAMHANE, AND V. S. VENKATAVARADAN, High Resolution Time Averaged (Millions of Years) Energy Spectrum and Chemical Composition of Iron-Group Cosmic Ray Nuclei at 1 A.U. Based on Fossil Tracks in Apollo Samples. *Proc. Second Lunar Science Conference, Geochimica et Cosmochimica Acta*, Supplement 2, Vol. 3, 1971, pp. 2611-2619.
 30. CROAZ, G., R. WALKER, AND D. WOOLUM, Nuclear Track Studies of Dynamic Surface Processes on the Moon and the Constancy of Solar Activity. *Proc. Second Lunar Science Conference, Geochimica et Cosmochimica Acta*, Supplement 2, Vol. 3, 1971, pp. 2543-2558.
 31. HART, H. R., JR., G. M. COMSTOCK, AND R. L. FLEISCHER, The Particle Track Record of Fra Mauro. *Proc. Third Lunar Science Conference, Geochimica et Cosmochimica Acta*, Supplement 3, Vol. 3, 1972, pp. 2831-2844.
 32. BHANDARI, N., J. N. GOSWAMI, S. K. GUPTA, D. LAL, A. S. TAMHANE, AND V. S. VENKATAVARADAN, Collision Controlled Radiation History of the Lunar Regolith. *Proc. Third Lunar Science Conference, Geochimica et Cosmochimica Acta*, Supplement 3, Vol. 3, 1972, pp. 2811-2819.
 33. YUHAS, D., Personal communication, 1973.
 34. BHANDARI, N., J. GOSWAMI, AND D. LAL, Surface Irradiation and Evolution of the Lunar Regolith. *Proc. Fourth Lunar Science Conference, Geochimica et Cosmochimica Acta*, Supplement 4, Vol. 3, 1973, pp. 2275-2290.
 35. BERG, O. E., AND E. GRÜN, Evidence of Hyperbolic Cosmic Dust Particles. *Space Research*, Vol. XIII, Akademie-Verlag, Berlin, 1973, pp. 1047-1055.
 36. ZOOK, H. A., AND O. E. BERG, A Source for Hyperbolic Cosmic Dust Particles. Presented at COSPAR, Konstanz, 1973; submitted for publication to *Planet. and Space Sci.*, 1974.
 37. WYATT, J. S. P., AND F. C. WHIPPLE, The Poynting-Robertson Effect on Meteor Orbits. *Astrophys. J.*, Vol. 11, 1950, pp. 134-141.
 38. HEMENWAY, C. L., D. S. M. HALLGREN, AND D. C. SCHMALBERGER, Stardust. *Nature*, Vol. 238, 1972, pp. 256-260.
 39. HOFFMANN, H.-J., H. FECHTIG, E. GRÜN, AND J. KISSEL, First Results of the Micrometeoroid Experiment S215 on the HEOS 2 Satellite. Presented at COSPAR, Konstanz, 1973; submitted for publication to *Planet. and Space Sci.*, 1974.
 40. HOFFMANN, H.-J., H. FECHTIG, E. GRÜN, AND J. KISSEL, Temporal Fluctuations and Anisotropy of the Micrometeoroid Flux in the Earth-Moon System Measured by HEOS 2. Presented at COSPAR, Sao Paulo, 1974; submitted for publication to *Planet. and Space Sci.*
 41. BERG, O. E., AND U. GERLOFF, More Than Two Years of Micrometeorite Data From Two Pioneer Satellites. *Space Res.*, Vol. XI, Akademie-Verlag, Berlin, 1971, pp. 225-235.
 42. HARTUNG, J. B., D. STORZER, AND F. HÖRZ, Toward a Lunar Microcrater Clock. *Lunar Science*, Vol. V Abstracts, 1974, pp. 307-309.
 43. SCHNEIDER, E., AND F. HÖRZ, Lunar Rock Erosion. *Lunar Science*, Vol. V Abstracts, Lunar Science Institute, Houston, 1974, pp. 666-668.
 44. GAULT, D. E., Displaced Mass, Depth, Diameter and Effects of Oblique Trajectories for Impact Craters Formed in Dense Crystalline Rocks. *The Moon*, Vol. 6, 1973, pp. 32-44.
 45. MEHL, A., Investigation on the Chemical Modification in an Impact Crater on a Lunar Sample. *Space Research*, Vol. XIV, Akademie-Verlag, Berlin, 1974, pp. 741-743.

Page intentionally left blank

Page intentionally left blank

The Micrometeoroid Complex and Evolution of the Lunar Regolith

F. Horz, D. A. Morrison
*NASA/Johnson Space Center
Houston, Texas*

D. E. Gault, V. R. Oberbeck, W. L. Quaide, J. F. Vedder
*NASA/Ames Research Center
Moffett Field, California*

D. E. Brownlee
*University of Washington
Seattle, Washington*

J. B. Hartung
*Max Planck Institut für Kernphysik
Heidelberg, Germany*

Micrometeoroid Complex: The interaction of the micrometeoroid complex with the lunar surface is evidenced by numerous glass-lined microcraters on virtually every lunar surface exposed to space. Such craters range in size from $< .1\mu\text{m}$ to approximately 2 cm in diameter. With the use of small-scale laboratory cratering experiments for "calibration," the observed crater-sized frequency distributions may be converted into micrometeoroid mass distributions. These "lunar" mass distributions are in essential agreement with satellite data for masses $> 10^{-12}\text{g}$. However, for masses $< 10^{-12}\text{g}$ there is considerable discrepancy. A radiation pressure cutoff does not exist because masses as small as 10^{-15}g can be observed. The absolute flux of micrometeoroids based on lunar rock analyses averaged over the past few 10^6 years is approximately an order of magnitude lower than present-day satellite fluxes; however, there is indication that the flux increased in the past 10^4 years to become compatible with the satellite data. Furthermore, there is detailed evidence that the micrometeoroid complex existed throughout geologic time.

Some physical properties of micrometeoroids may be deduced by comparing lunar crater geometries with those obtained in laboratory experiments. The preponderance of circular outlines of lunar microcraters necessitates equidimensional, if not spherical, micrometeoroids. Irregular shapes such as whiskers, needles, platelets, rods, etc.—postulated in the past—do not contribute substantially to the micrometeoroid population and are rare, if not absent. The depth/diameter ratios of lunar microcraters are compatible with micrometeoroid densities of 2 to 4 g/cm^3 ; densities $< 1\text{ g/cm}^3$ can be excluded. These findings have astronomical significance with respect to comets, i.e., the source area for micrometeoroids.

Regolith-Dynamics: Monte Carlo-based computer calculations, as well as analytical approaches utilizing probabilistic arguments, were applied to gain insight into the principal regolith impact processes and their resulting kinetics. Craters 10 to 1500 m in diameter are largely responsible for the overall growth of the regolith. As a consequence the regolith has to be envisioned as a complex sequence of discrete ejecta blankets. Such blankets constitute first-order discontinuities in the evolving debris layer. The micrometeoroid complex then operates intensely on these fresh ejecta blankets and accomplishes some degree of mixing and homogenization. True mixing, however, can be accomplished only in an uppermost layer of approximately 1-mm thickness, before a new ejecta event covers this

layer and effectively removes it from the zone of active reworking. While, e.g., a layer 1 cm in depth is turned over only one time in approximately 10^7 years, the uppermost 1 mm of that surface has been turned over already 250 times and the uppermost .1 mm more than 2000 times during the same period. Therefore the lunar regolith becomes rapidly quiescent with depth. Though the micrometeoroid bombardment is extensive, a stratigraphic sequence may readily be preserved, as evidenced in returned core tube materials. The erosion of lunar rocks caused by micrometeoroids is calculated at .3 to .6 mm per 10^6 years. The mean surface residence time of a rock of 1 kg in mass is in the order of 3×10^6 years, before it will be catastrophically destroyed by rupturing due to the impact of large micrometeoroids. This catastrophic destruction is far more effective than single particle abrasion in obliterating a lunar rock specimen. Due to the vagaries of the random impact process, caution is necessary to delineate regolith dynamics from lunar sample analyses that are not based on a statistically significant number of observations.

With increasing resolution of lunar surface photographs prior to actual sample return, it became more and more obvious that meteoroid impact had played a substantial role in the evolution of the lunar surface. It was discovered that meteoroid impact had operated on scales from hundreds of km down to a few cm (ref. 1). However, immediately upon cursory inspection of returned rocks it was learned that impact processes also occurred on still smaller scales: the ubiquitous presence of glass-lined lunar microcraters was ample evidence that virtually every lunar surface exposed to space was also subjected to the bombardment of micrometeoroids. In the meantime numerous laboratory investigations revealed that many properties of the lunar regolith are either directly or indirectly dominated by impact processes far beyond the original expectations. A proper understanding of many regolith processes therefore depends critically upon an understanding of the regolith impact history.

A thorough understanding of this history is possible only by combining lunar observational data, laboratory impact experiments, and theoretical calculations. This report attempts to summarize such analyses. We will first discuss observational evidence of lunar microcraters and its implications to the micrometeoroid complex, including some astronomical consequences. We then will present some analytical and computer-based calculations that will aid in the understanding of some principal regolith processes as well as their kinetics. Due to limited space some detailed argumentation cannot be presented,

and the reader must be referred to the original reports. In addition, a multitude of other interesting observations and interpretations had to be deleted. We attempted, however, to present the most important aspects of the impact process as we understand them today.

Lunar Data of the Micrometeoroid Complex

MICROCRATER-MORPHOLOGY

Glass surfaces are by far the most suitable materials to study micrometeoroid impacts, because in comparison with crystalline rocks and breccias, they are usually smooth and observational conditions are optimized (fig. 1). Furthermore, glasses are also the best investigated materials in small-scale laboratory cratering simulations. Thus—unless specified—the detailed morphology data, crater-size frequency distributions, and associated flux considerations are derived from lunar glass surfaces only.

Microcraters on lunar glass surfaces may range in diameter from less than $.1\mu\text{m}$ up to approximately 2 mm; on crystalline rocks craters as large as 20 mm in pit diameter were observed. Crater morphology differs characteristically as a function of absolute crater diameter (refs. 2–5). Craters smaller than $1\mu\text{m}$ are cup-shaped, glass-lined depressions—termed “pit”—with a pronounced rim of molten target material (fig. 2(a)). Craters between $1\mu\text{m}$ and $10\mu\text{m}$ in pit diameter (figs. 2(b) and 2(c)) are transitional between the above morphology and that typical for craters

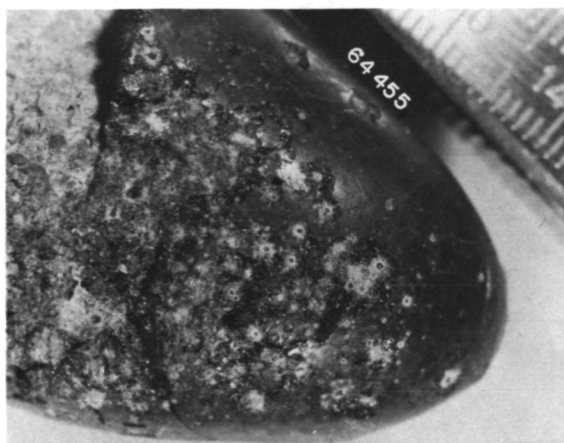


Figure 1.—Large glass-coating on lunar rock 64455 with abundant microcraters. All structures are above $5\ \mu\text{m}$ in diameter and therefore display characteristic spall zones. Close to the fracture zone exposing the underlying anorthositic substrate, the crater densities are very high and in approximate equilibrium. (Sidlength of picture: 3.2 cm.)

larger than $10\ \mu\text{m}$. When above $10\ \mu\text{m}$ in diameter, they not only possess a central glass-lined pit but also a concentric spall zone (fig. 2(d)). The spall zone may or may not be totally spalled off for craters between $10\ \mu\text{m}$ and $50\ \mu\text{m}$, but all craters above $50\ \mu\text{m}$ in diameter have a completely developed spall zone. Morrison et al. (ref. 5) delineated the following relationship: $D_s = 2.37 \times D_p^{1.07}$, where D_s is the spall zone and D_p the pit diameter.

For comparison, identical structures produced in the laboratory are illustrated in figures 2(e) and 2(f). Laboratory crater studies performed by electrostatic particle accelerators (refs. 6–13) indicate that a glass-lined pit is produced only at projectile velocities exceeding 3 km/s. The development and extent of a spall zone characteristic for the larger lunar craters requires velocities in excess of 5 km/s.

PHYSICAL PROPERTIES OF MICROMETEOROIDS

Laboratory simulations by Mandeville and Vedder (ref. 9); Kerridge and Vedder (ref.

14); Vedder and Mandeville (ref. 12); and Mandeville (ref. 13) have demonstrated that the outline of the central pit crater is controlled by projectile shape and angle of incidence and that the crater depth is dependent on projectile density and impact velocity.

Brownlee et al. (ref. 15) measured crater-circularities from Scanning Electro-Microscope (SEM) photographs that were taken with the electron-optical axis normal to the cratered surface. A "circularity index" was defined as the ratio A_m/A_c , where A_m is the area measured along the inferred intersection of the surrounding target surface with the inside of the pit rim, while A_c is the area of the smallest circle which just encloses A_m . Circularity indices measured for 131 micron-sized craters demonstrate the rarity of highly noncircular pits (fig. 3). Many of the noncircular craters in figure 3 are elongated and shallow, indicating that they were produced by oblique impact rather than highly irregular projectiles (refs. 15 and 16). By comparison with laboratory simulations using irregular projectiles (ref. 14), it is concluded that highly nonspherical shapes such as rods or platelets are rare or nonexistent in the micrometeoroid complex. If dust grains were modeled as prolate ellipsoids, then the observed crater circularities suggest an average length to width ration of < 2 .

Depth/diameter ratios were determined for 70 craters (ref. 15) by use of the contamination line profiling technique of Vedder and Lem (ref. 17) and parallax measurements from SEM stereo photos. The crater depth/diameter ratios refer to the maximum pit depth below the original uncratered surface divided by the mean diameter of the inside of the pit rim. Figure 4 illustrates the results of 70 lunar craters in histogram form together with laboratory cratering data of Vedder and Mandeville (ref. 12). Because the laboratory data do not extend beyond 13 km/s impact velocity and because the velocity distribution of small meteoroids is not well known, it is not possible to determine exact particle densities. It is obvious, however, that the data are entirely inconsistent

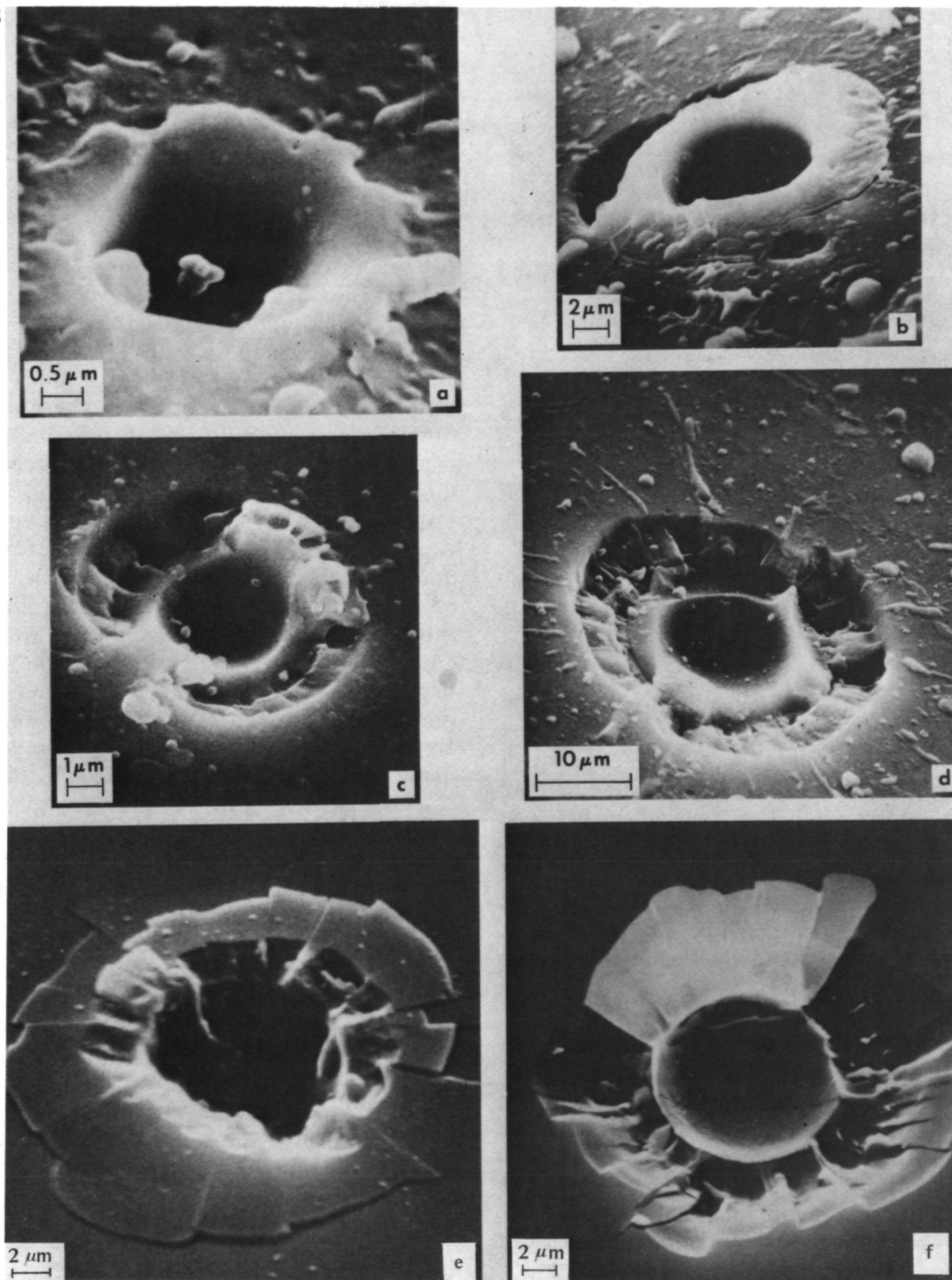


Figure 2.—Typical lunar experimental microcraters on glass surfaces. Note the change of crater morphology with size: (a) very small lunar microcrater that displays neither concentric fractures nor a spall zone (note the raised, glassy rim); (b) lunar crater that displays concentric fracture zone indicative of incipient spallation; (c) lunar crater with partially developed spall zone; (d) lunar crater with completely developed spall zone; (e) experimental crater (Al-projectile into soda lime glass; impact velocity: 9.9 km/s); and (f) experimental crater (polystyrene projectile into soda lime glass; impact velocity: 5.7 km/s. Note shallow crater depth and compare with 2(a)–(e)).

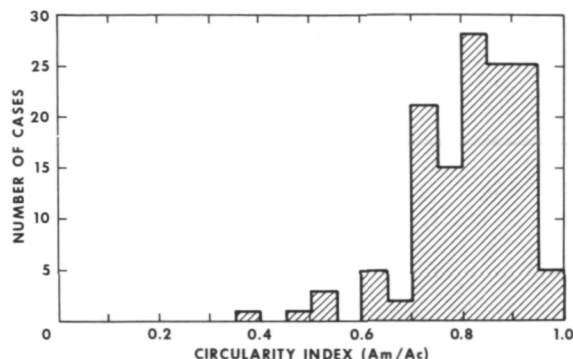


Figure 3.—Histogram of the circularity index of 131 microcraters ranging in size from .2 to 80 μ m in diameter (rock 15286). Though not illustrated, the circularity index is independent of pit crater diameter.

with micrometeoroid densities less than unity. The rarity of deep craters also appears to exclude the possibility that a significant fraction of particles could have densities as high as iron. Figure 4 apparently implies that most micrometeoroids (< 50 μ m in diameter) have densities in the 2 to 4 g/cm³ range, if one assumes an average impact velocity of 20 km/s. Even for velocities between 10 and 30 km/s, the above densities are approximately valid.

Only \approx 10 percent of the total crater population may offer different interpretations. Of those exceptions, the so-called "pitless" craters are by far the most abundant (\approx 80 percent). They do not possess a glass-lined pit (fig. 5(a)) and could be interpreted as low-velocity, "secondary" craters. However, as illustrated in figure 5(b) and as observed numerous times, there is strong evidence that many "pitless" craters did indeed have a glass-lined pit, which was spalled off either during crater formation or thereafter (ref. 18). Thus, many of these structures are also potential candidates for a "primary" origin (ref. 19). Another exceptional crater type, termed "multiple pit crater," is illustrated in figure 5(c); figure 5(d) documents a laboratory equivalent produced by an agglutinate of minute glass spheres (ref. 12). Consequently it is conceivable that "multiple pit

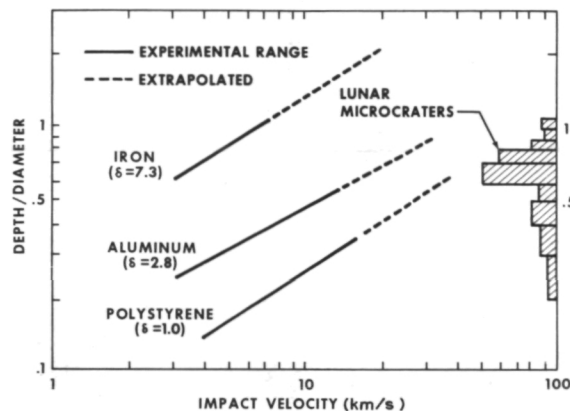


Figure 4.—Experimentally determined depth/diameter ratios using projectiles with densities from 1 to 7 g/cm³ and impact velocities from 3 to 13 km/s. The inserted histogram on lunar depth/diameters is based on 70 craters.

craters" are indeed caused by projectiles of low density and nonhomogeneous mass-distribution, i.e., "aggregate" structure; however, they are rare exceptions and far less frequent than suggested by Verniani (ref. 20), Hughes (ref. 21), and many others.

CRATER POPULATIONS ON LUNAR ROCKS

In analogy to large-scale lunar surfaces (Gault (ref. 22); Shoemaker et al. (ref. 1), and others), two basic types of crater populations need to be distinguished: (a) "production" and (b) "equilibrium" populations. By definition, "production populations" are limited to rock surfaces of low, absolute crater densities, i.e., of short exposure periods. With time, more and more impacts will occur in already cratered areas until finally the surface becomes so densely cratered that each new event will destroy an already existing one. Such a surface has reached "equilibrium." "Transition populations" are intermediate between "production" and "equilibrium" conditions. Most lunar rocks are either in "transition" or "equilibrium" condition; genuine "production populations" are rare.

Because production surfaces exclusively

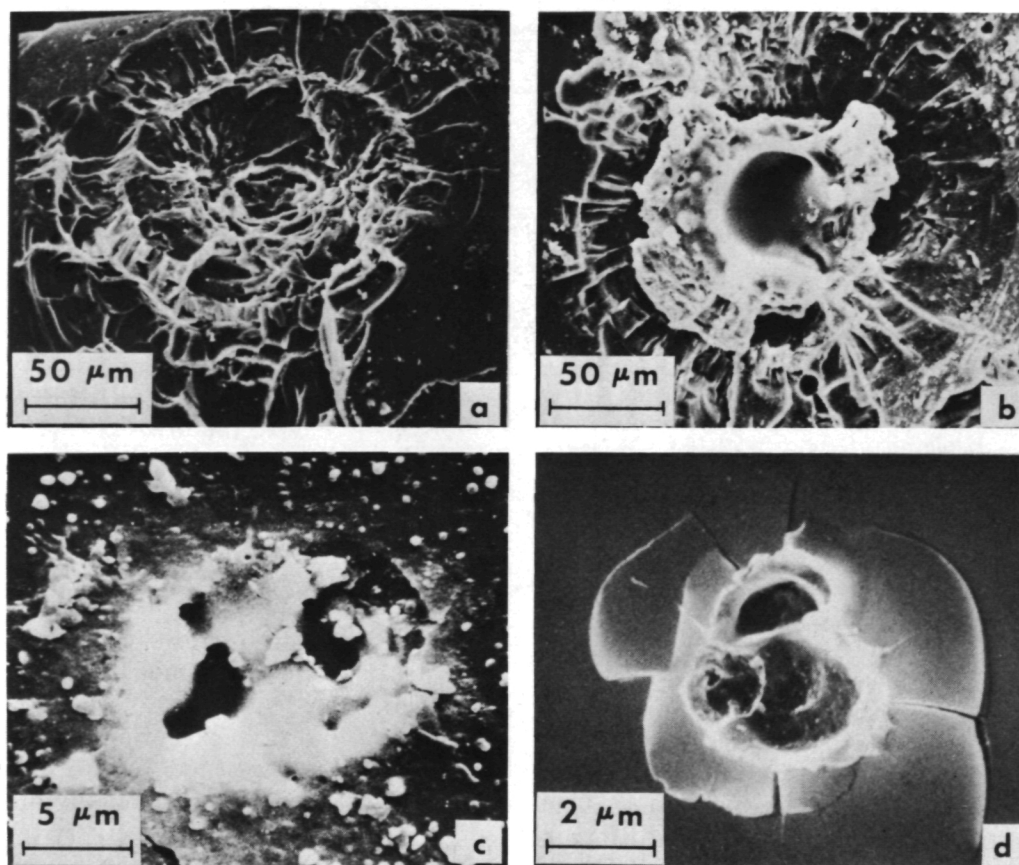


Figure 5.—Unusual craters: (a) "pitless" lunar crater (note the similarities and possible transition to crater 5(b)); (b) similar sized lunar crater with pit (note that spallation action was severe enough to undercut the glass-lined pit, leaving it barely attached to the crater bottom); (c) "multiple pit" crater on lunar glass surface 15286; and (d) "multiple pit" crater produced in the laboratory.

display a complete record of all craters produced, *only they are suitable* to deduce mass-frequencies and the flux of micrometeoroids.

Cumulative crater size distributions for "production populations" on samples 12054 (ref. 4) and 60015 (ref. 23) are shown in figure 6; though other genuine "production populations" were investigated, the two curves illustrated are considered the best available over the size range indicated. The absolute crater densities for the two samples differ by almost a factor of 2, reflecting different times and/or geometry of exposure. The relative crater size frequency, however, is nearly identical.

Figure 7 illustrates "production" data resulting from SEM studies. The relative frequencies were normalized to surface 15205

at a pit diameter of $1\mu\text{m}$. The illustrated data are considered the best available. The differences in the distributions and the presence of an inflection at pit diameters between $1\mu\text{m}$ and $10\mu\text{m}$ are subject to a variety of interpretations. They will be discussed later.

Because the rock surfaces that have reached "transition" and/or "equilibrium" conditions are less suitable for study of the micrometeoroid complex, they will not be treated extensively here (refs. 5, 23, 25, 26, and 27). However—if coupled with solar flare track exposure ages—they may still contribute to the flux determination of micrometeoroids; *minimum* fluxes may be obtained, because a number of the craters produced are destroyed and not observable anymore.

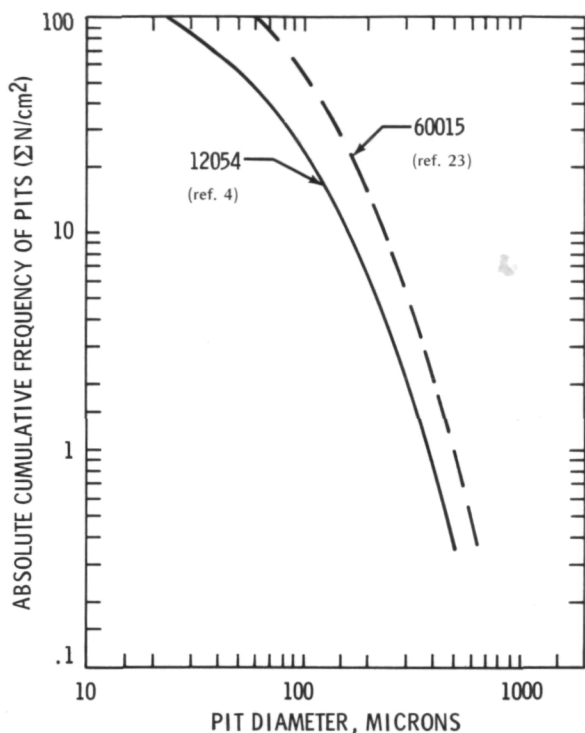


Figure 6.—Typical binocular crater-size frequency distributions for lunar glass surfaces in production state (12054 is based on 960 craters; 60015 is based on 665 craters).

MASS-FREQUENCY OF MICROMETEOROIDS

Crater simulation experiments provide the only basis to obtain information concerning the mass distribution of micrometeoroids by converting crater dimensions into projectile parameters. The physical processes governing impact cratering are complex and presently not understood in great detail, despite considerable laboratory work. Especially, the energy partitioning for small- and large-scale cratering and the effects of target strength, gravitational forces, and varying impact velocities, i.e., appropriate "scaling laws," are still subject to experimental work that ultimately will result in a theoretical understanding. Therefore, extrapolations from laboratory data may allow the use of a

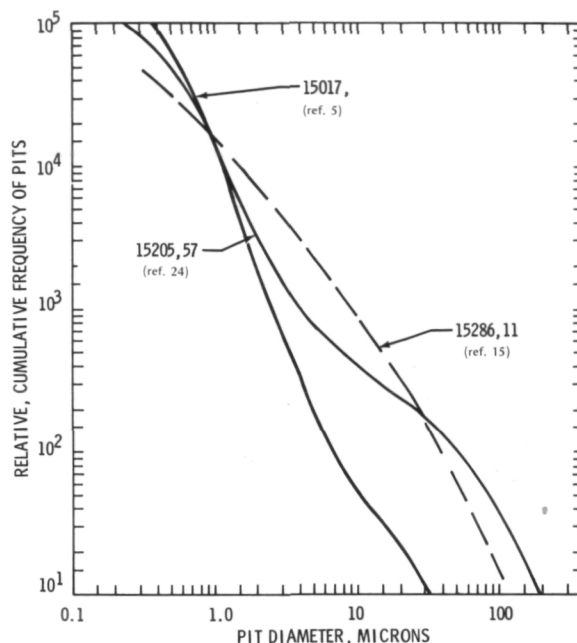


Figure 7.—Typical scanning electron microprobe crater-size frequency distributions for small microcraters on lunar glass surfaces in production state (15205 is based on ≈ 1100 craters, 15286 on ≈ 500 , and 15017 on ≈ 300).

variety of empirical calibration approaches.

Four basic calibration techniques for microcraters are currently in use (fig. 8). Two are based on electrostatic dust accelerator experiments (refs. 6, 9, 24, and 30), and two calibration techniques utilize results from ballistic ranges (refs. 28 and 31), while Nagel (ref. 29) employed a lithium plasma gun (for more detail, see ref. 16).

Relative crater-size frequency distributions ranging from .1 to almost 1000 microns in pit diameter may be constructed from the data presented in figures 6 and 7 by normalizing the absolute crater densities with respect to exposure time, exposure geometry, and surface area. An important assumption underlying such a normalization is that these relative frequencies remained constant with time, because surfaces of different crater

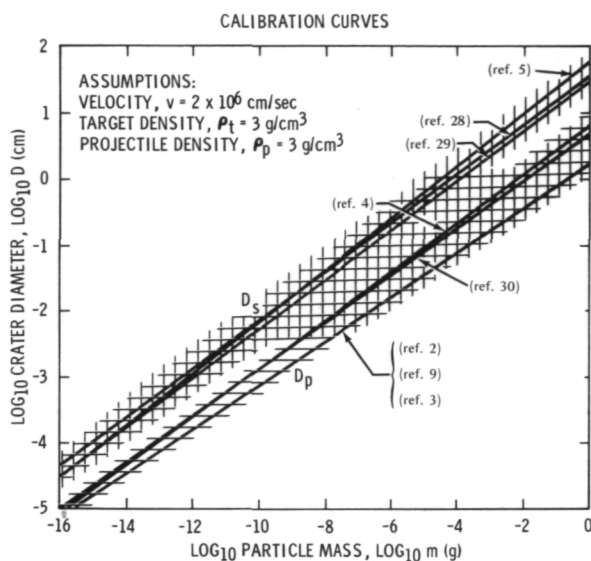


Figure 8.—Various calibration methods presently in use to derive micrometeoroid masses from measured pit diameters (D_p) or spall diameters (D_s). The ratio D_s/D_p is variable from rock to rock with values between 3.8 and 4.5 on lunar glasses. Note that agreement between various techniques is close, if a D_s/D_p of 4.5 is applied.

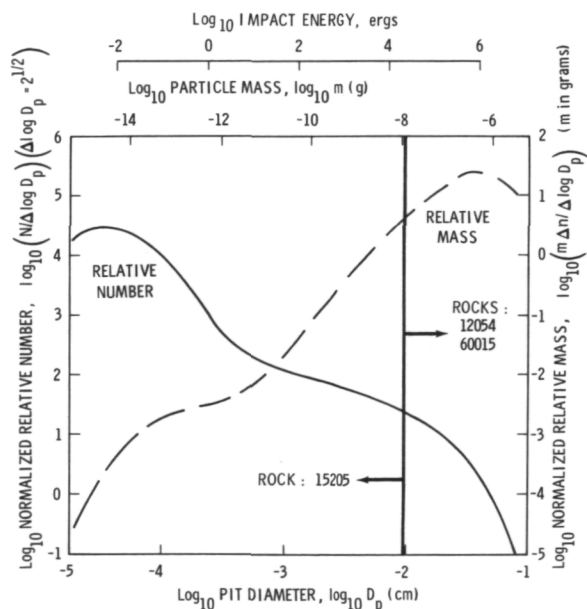


Figure 9.—Differential frequency of pit diameters and their corresponding particle mass and energy distributions. The binocular data (12054, 60015) and SEM data (15205) are joined at a pit diameter of 100 μm as indicated.

densities, i.e., different absolute exposure times, need to be normalized. Figure 9 shows such a normalized, differential crater frequency distribution based on glass-surfaces 12054, 60015, and 15205. The corresponding mass- and energy-scales are based on the calibration by Gault (ref. 28) as shown in figure 8. For masses $> 10^{-10}\text{g}$ (= impact energies above 200 ergs) this distribution is in basic agreement with that obtained by satellite- and ground-based measurements (refs. 32 and 33). Though the irregularity of the distribution at lower masses will be more thoroughly discussed later, it can already be seen that

1. Particles in the 10^{-15} to 10^{-13} g range are most numerous.
2. The bulk of the meteoroid mass or energy impacting the Moon is confined to particles 10^{-8} to 10^{-3} g in mass (see also refs. 4 and 34).

FLUX OF MICROMETEOROIDS

Micrometeoroid fluxes are obtained by correlating absolute crater densities with the

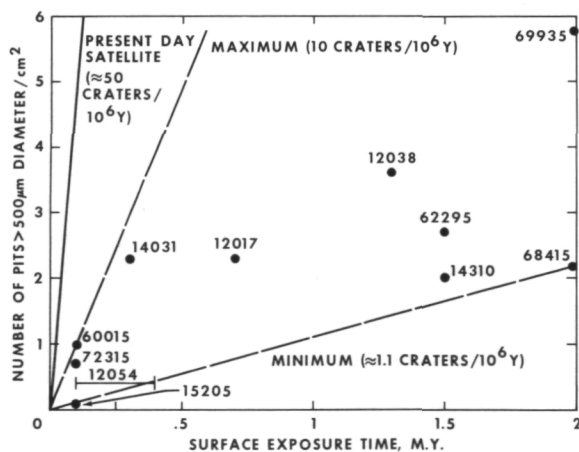


Figure 10.—Correlation of surface residence times of specific rocks mostly determined with solar flare tracks (see table 1) and absolute frequency of pit craters $> 500 \mu\text{m}$ in diameter/ cm^2 . A straight line going through the origin establishes the crater production rate, i.e., the flux of micrometeoroids $> 2 \times 10^{-7}$ g. A best estimate for the average flux over the past 10^6 years is ≈ 5 pits/ cm^2 .

absolute exposure age. A summary of such correlations for binocular crater counts on selected rocks is illustrated in figure 10, with the cumulative crater frequency for pits above $500\mu\text{m}$ in diameter. Most data points shown lie below possible correlation lines and therefore are in or approaching equilibrium with respect to cratering. A correlation line corresponding to a crater production rate of five pits with diameters equal to or greater than 500 microns per cm^2 per million years lies within a factor of 2 of data for 12054, 12017, 12038, and 14301. Upon visual inspection of these samples, only rock 12038 was not clearly in production with respect to cratering. A factor of 2 is the estimated uncertainty in the solar flare track method used for the exposure time measurements.

Another approach to measure the meteoroid flux and possible changes with time has been pursued by Hartung et al. (ref. 35). Separate solar flare track exposure ages were determined for 56 individual pit craters larger than $20\mu\text{m}$ on rock 15205. The results illustrated in figure 11 indicate that the formation ages of these craters are not uni-

formly distributed; significantly more craters are produced during the last 10 000 years. Thus it appears that the present-day micrometeoroid flux is enhanced over that of the past 10^4 to 10^5 years by slightly more than an order of magnitude. The values obtained for the past 3000 years are in good agreement with present-day satellite measurements (refs. 33 and 34).

Discussion of the Micrometeoroid Complex

IMPLICATIONS OF PHYSICAL PROPERTIES

On the basis of laboratory cratering experiments, the morphologies of microcraters are interpreted to indicate that they were formed by equidimensional, nonporous projectiles of densities between 2 and 4 g/cm^3 , which impacted with velocities in excess of 5 km/s . These results are in part contrary to popular hypotheses and they may have

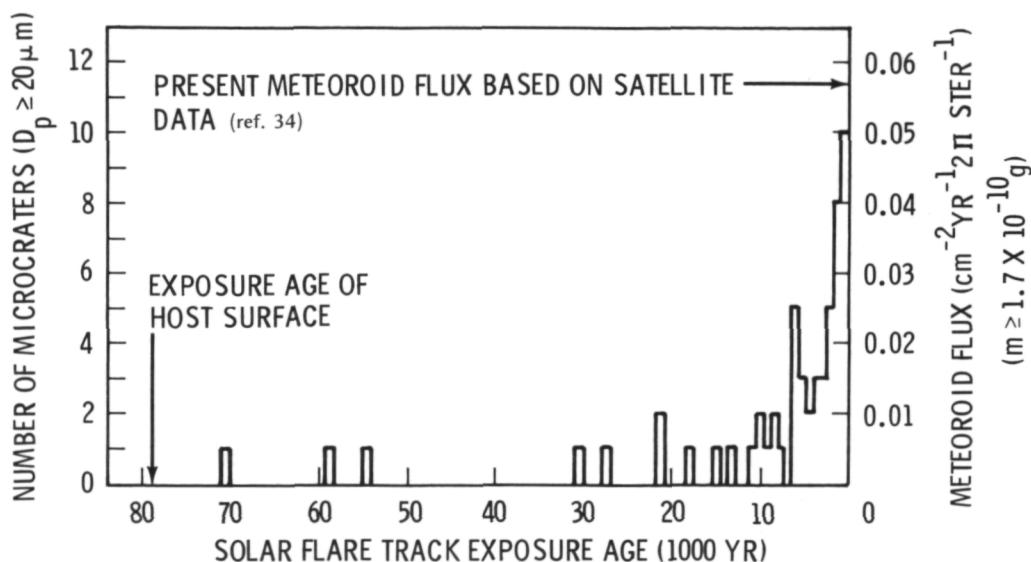


Figure 11.—Preliminary formation ages of 56 individual microcraters ranging in size from 20 to 300 microns in pit diameter on glass surface 15205,51. Note the steep increase in crater production rate between 0 and 10^4 years, corresponding to a twofold increase every 3000 years.

some significant astronomical consequences.

A cometary origin for micrometeoroids is strongly suggested by a variety of independent analyses (e.g., refs. 33 and 36). The particulate matter within comets is believed to represent unfractionated, solar abundances similar to Type 1 carbonaceous (CI) chondrites. Our mass densities are entirely consistent with CI chondrites, the constituents of which range in density from approximately 1.5 g/cm^3 for aggregates of phyllo-silicates to magnetite grains of 5 g/cm^3 in density (ref. 37).

Much lower densities with an average of .5 to $.8 \text{ g/cm}^3$ have been suggested for the somewhat larger meteors, i.e., particles $> 10^{-6} \text{ g}$ (refs. 20 and 21). Though our detailed analysis of crater morphologies is confined to craters below $100 \mu\text{m}$ in diameter, i.e., particles $< 10^{-8} \text{ g}$, even pit craters larger than 1 cm, caused by particles of approximately 10^{-3} g , display qualitatively the same morphologies. Though precise laboratory calibrations are not available for such large structures, we suggest that most particles of 10^{-6} to 10^{-3} g may also have a density of more than unity.

The equidimensional character of micrometeoroids may also have significant astronomical implications, if we accept a cometary source. Traditionally it is suggested that such materials are similar if not identical in chemistry and shape to grains found in carbonaceous chondrites, because they are believed to represent primordial condensates from similar environments in the solar nebula. These grains are thought to be vapor growth products of highly nonspherical shape like platelets, rods, and whiskers (refs. 14, 38, 39, and 40). Such grains were observed in a variety of carbonaceous meteorites, e.g., Allende, which is thought to be a fine example of "early condensates" (ref. 41). Clearly the microcrater circularities are incompatible with such elongated grains. These findings either imply that the postulated grain shapes are incorrect and virtually non-existing in the environment of comet formation or that the micrometeoroid complex is also the result of multiple collisional events

prior (!) to incorporation into cometary matrices. Recent developments in meteorite research provided strong evidence that collisional processes in the early history of the solar system may have played a dominant role.

Regardless of what caused the micrometeoroids' equidimensional if not spherical shape, needles, platelets, rods, whiskers, and other elongated or irregular particles seem not to make up a significant part of cometary silicates, if one accepts at all a cometary source area. The possibility that most of these particles constitute debris of collisional processes during accretion, rather than primary condensates, cannot be excluded.

MASS-FREQUENCY

The frequencies of micrometeoroid masses ranging from 10^{-15} to 10^{-3} g are summarized in figure 12, together with a variety of satellite- and earth-based measurements. Two types of microcrater frequencies are observed: that displayed by samples 15205, 15076, and 15017; and that of sample 15286. Though experimental conditions (most dominantly target-smoothness and total number of craters counted) may be responsible for subtle differences of the first type, the different behavior of 15286 seems beyond statistical error. Rock 15205 is based on 950 craters and sample 15286 on 500 craters. Thus, two questions remain: (1) Why are there two different frequency types? and (2) What causes an apparent bimodal mass distribution?

Sample 15286 is unique, though there are other samples (e.g., 12024,81 and 14257,F (ref. 30)) that may be similar. Their different mass-frequencies may be caused by extreme solid angles of exposure (ref. 23) that effectively influence the energy distribution, because of the increased effects of oblique impact (ref. 28). It is also conceivable that such surfaces were essentially pointing toward lunar North, i.e., out of the ecliptic plane, where they potentially could intercept a different population of cosmic dust than within the ecliptic plane.

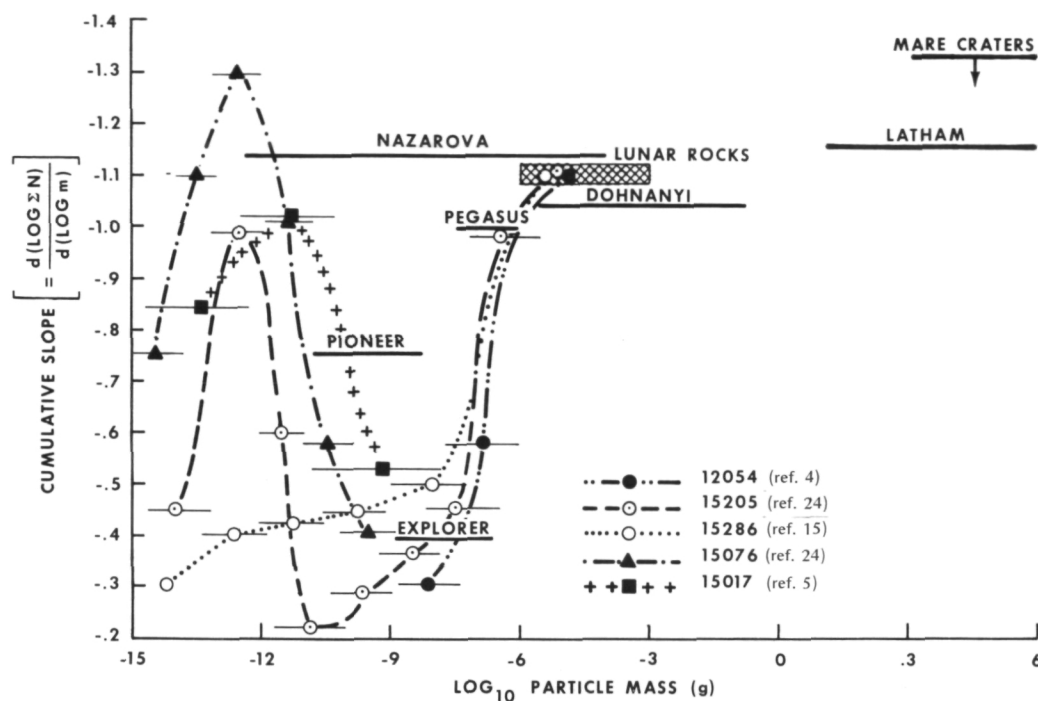


Figure 12.—Comparison of the cumulative mass-frequency slopes of a variety of observational techniques, but, in particular, of five well-documented lunar glass surfaces. Most individual satellite data do not give a differential flux; the position of the satellite data was constructed by extrapolating the slope from the cumulative mass-frequency curve of Dohnanyi (ref. 33, fig. 1). The length of the bars indicates the mass-range over which the corresponding slope is valid.

Curves 15205, 15076, and 15017 are believed to be typical for micrometeoroids impacting the Moon, simply because such distributions are the most frequent ones. Samples 60502,17; 15927,3; 15301,79 (ref. 24); and 15015 (ref. 5) yield similar results. The cause of this apparent bimodal mass distribution is presently unknown. However, it is conceivable that the larger masses represent the cometary particle population that is spiraling toward the Sun. During and upon solar approach, individual particles may suffer fragmentation as well as melting and/or vaporization; both processes would result in numerous particles of very small sizes. Upon close solar approach they may be propelled away from the Sun again by solar radiation and have a second opportunity to encounter the lunar surface (refs. 36 and 42).

Subtle differences in crater populations may yet be caused by a completely different

mechanism. Morrison et al. (ref. 5) and Blanford et al. (ref. 43) report that lunar rock surfaces are significantly modified on the micron scale by the accretion of regolith particles; most dominantly, disk-shaped, glassy splashes and droplets. These accretionary objects are so numerous that they accumulate obviously at a faster rate than the surface is destroyed by microcraters. Given sufficient time they may even build up layers of a few microns in thickness, giving some of the hand specimens a typical, patinated appearance. Thus a "constructive" accretion process is competing with the "destructive" cratering process and the micron-size crater population may be somewhat modified. The unambiguous presence of particles below 10^{-15} g in mass, however, negates the existence of a radiation pressure cutoff. According to Gindilis et al. (ref. 44), the lack of such a cutoff is highly compatible

with particle densities of 2 to 4 g/cm³, i.e., with silicates, for which gravitational forces appear to dominate radiation pressure. This result corroborates our conclusions about particle densities.

Figure 12 also illustrates one fundamental advantage of lunar glass-surfaces as micrometeoroid detectors: at present, the lunar rock detector spans 12 orders of magnitude in mass and thus possesses a "dynamic range" duplicated nowhere. The potential identification of a bimodal size distribution is only due to such a large dynamic range.

Additional work with carefully selected samples is required to clarify what causes the two basic frequency types and the apparent bimodal distributions. The above explanations have to remain tentative until carefully selected and precisely oriented surfaces are investigated in detail.

MICROMETEOROID FLUX

A detailed comparison of micrometeoroid fluxes derived from lunar sample analyses and satellite measurements is presented in figure 13. It is impossible to discuss each detail and thus we offer a few general comments only, quoting Hörz et al. (ref. 16):

The moon is a rotating sampler, and the directional distribution of micrometeoroids is extremely non-uniform as shown by Berg and Grün (1973) (ref. 48) and Hoffmann et al. (1973) (ref. 47). Accordingly, the meteoroid flux differs about 3 orders of magnitude between the direction of the earth's apex and anti-apex. Furthermore, particles $> 10^{-12}$ g are collected almost exclusively during the apex orientation of the Pioneer and HEOS sensors. Hence, in this mass range, also the Moon may collect particles from only the apex direction. As a consequence, a "detector" on the rotating lunar surface can "register" meteoroid impacts effectively only part of the time. Therefore, fluxes derived from lunar crater statistics may have to be increased by as much as a factor of π for comparison with satellite data that

were taken in the apex direction. Also, apex-pointing data generally have been corrected upward to a standard 2π -sterad exposure angle, assuming an isotropic flux. Thus, an actual anisotropy (as reported by the HEOS and Pioneer experiments) leads to an overestimation of the flux. Therefore, the satellite results seem to represent an upper limit for the flux.

The "apex" particles show an average impact velocity of only 8 km/sec (Hoffmann et al., 1973) (ref. 47). The fluxes from lunar rocks, however, are calculated with a standard velocity of 20 km/sec. The necessary corrections will increase the projectile masses and thereby effectively enhance the Moon-based flux for masses $> 10^{-10}$ g by a factor of approximately 5.

The situation for masses $< 10^{-12}$ g is highly complex. Berg and Grün (1973) (ref. 48) have reported that most events of these masses occur with particles that have relative velocities of at least 50 km/sec. The lunar flux curves given for these masses in fig. 12 are, however, based on a 20 km/sec impact velocity; if corrected to 50 km/sec, they will shift towards smaller masses, possibly as much as a factor of 10.

As a consequence, the fluxes derived from lunar crater statistics may agree within the order of magnitude with direct satellite results if the above uncertainties in velocity and directional distribution are considered.

Figure 14 presents some basic constraints derived from a variety of independent lunar studies on the flux of micrometeoroids and larger objects. The only direct measurements are the impact events registered by the Passive Seismic Experiment (ref. 62) and the micrometeoroids encountered by the spacecraft windows (ref. 57). Upper limits on the flux can be derived from more cratering rate (refs. 63, 64, and 65). Accordingly, the flux over the past 3.0×10^9 years has remained fairly constant. The "geochemical" evidence is based on the abundance of siderophile trace elements indicative of type and

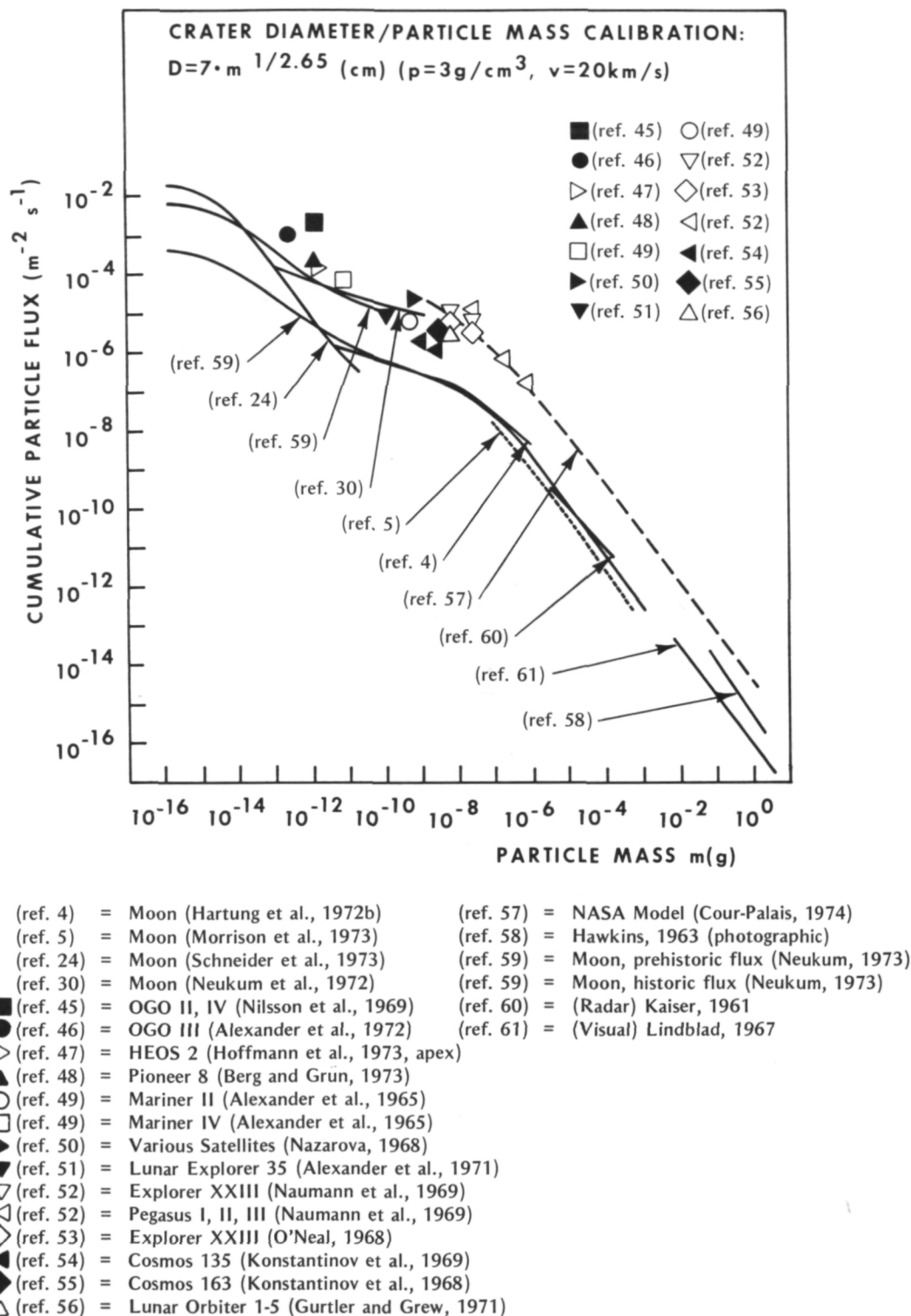


Figure 13.—Comparison of lunar and satellite micrometeoroid flux data.

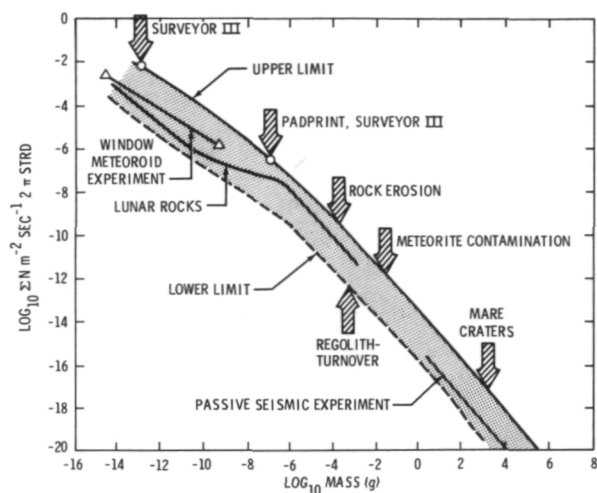


Figure 14.—Constraints on the flux of micrometeoroids and larger objects, according to a variety of independent lunar studies.

amount of meteoritic contamination in the lunar soil (ref. 66). Erosion rates on lunar rocks range from approximately .2 to 2 mm/ 10^6 years (refs. 67, 68, and 69). Taking the highest erosion rate and applying cratering data of Gault (ref. 28) make possible the definition of an upper flux limit. Furthermore, the negative findings on the Surveyor III camera lens (ref. 70) and the perfect preservation of the footpad print of Surveyor III (ref. 71) also define an upper limit. A lower limit results from the study of solar and galactic radiation tracks in lunar soils (refs. 72, 73, and 74). It is found that some cm-thick layers of regolith have resided on the lunar surface essentially undisturbed for ≈ 1 to 2×10^7 years. Because the regolith is believed to be reworked by micrometeoroids only, the flux could not have been significantly lower than indicated; otherwise still older residence times for the soil layers would be obtained. Strictly, only the passive seismometer, the Apollo windows, and the mare craters yield a cumulative mass distribution. All other parameters are a bulk measure of either meteoroid mass or energy; the corresponding "flux" was calculated using the differential mass distribution obtained from lunar microcraters. Accordingly, the corresponding arrows may be shifted any-

where along the line defining the "upper" and "lower" limits.

The data shown in figure 11 (ref. 75) suggest that the present flux is significantly higher than the average flux over the last 10^4 to 10^5 years (ref. 35). Gault et al. (ref. 34) and Morrison et al. (ref. 5) were the first to indicate such a possibility because absolute lunar rock exposure ages, erosion rates, and survival times of rocks appeared to be incompatible with computed values that were based on present-day meteorite fluxes derived from satellites. Neukum (ref. 59) expanded on these interpretations and his "historic" and "prehistoric" fluxes are incorporated in figure 13. Because the annealing behavior for radiation tracks during long-term exposure in the lunar environment is not well known and because all potential errors—both in the age dating as well as crater-counting—enter these considerations, a "historic" and "prehistoric" flux can only be tentatively proposed at present. The data of Hartung et al. (ref. 35) present the strongest evidence to date.

Although the magnitude of the flux may have varied over geological times, the mass-frequency distribution appears to have remained fairly constant. Frequencies measured on surfaces that were constituents of the soil (15927, 15301, 15001, and 60502) most likely do reflect the meteoroid bombardment that is older than that of most rocks. Their size-frequency distributions agree within the accuracy of measurement with "recent" crater populations.

Brownlee and Rajan (ref. 76) and Rajan et al. (ref. 77) discovered microcraters that are identical to lunar craters on the surface of glassy spherules, dislodged from the interior of the Kapoeta meteorite. This meteorite is a loosely consolidated microbreccia and a striking meteoritic analog to lunar soil breccias in many aspects. The formation age of Kapoeta is approximately 4×10^9 years (Rajan, personal communication, 1974). Within the counting accuracy, the size-frequency distribution of the Kapoeta microcraters is identical to lunar ones. Brownlee and Rajan furthermore dated one spherule

via solar flare tracks and derived a micrometeoroid flux that is within an order of magnitude of the present-day flux. Because the track retention over 4×10^9 years in glassy materials is poorly known, however, this exposure age and the resulting micrometeoroid flux has still larger uncertainties than young lunar glass surfaces. Blanford et al. (ref. 43) report numerous microcraters on feldspars separated from the very bottom (soil-sample 15001) of the 240-cm-long Apollo 15 drill core. The observed crater size-frequency distributions are essentially identical to those of rock samples 15205 and 15017 (see fig. 12). Because this soil was deposited at its site of collection more than 400 m.y. ago (ref. 78) the observed crater populations must have formed prior to that time. Micrometeoroid craters are also found in virtually every "soil-breccia" as well as genuine soil samples, though their actual geological time period of exposure is not known at present (ref. 24). Taking typical noble-gas exposure ages of lunar soils as statistically representative average values of the individual components, it may safely be concluded that micrometeoroid bombardment was active throughout geological time. From the presently available microcrater size-frequency distributions it also may be concluded that the mass-frequency distribution of micrometeoroids has not changed significantly if at all.

The studies on surfaces of old exposure ages demonstrate another unique characteristic of the "lunar rock micrometeoroid detector": it is principally possible to delineate the flux and potential variations thereof through geologic history. Such potential variations are of considerable interest to an explanation of the formation of the solar system for a variety of reasons:

1. The presence of a minimum micrometeoroid mass may be determined as a function of geologic time. This mass, in turn, may be used to calculate upper limits on the solar radiation pressure and thus to the luminosity of the Sun. Brownlee and Rajan (ref. 76) have attempted such calculations based on the

minimum crater diameter observed on the Kapoeta materials and they concluded that the solar luminosity at $\approx 4 \times 10^9$ years was not higher than 1.7 times its present value.

2. The main source of micrometeoroids has to be sought in short-period comets. Significant variations in the flux of meteoroids may be related to short-period comet "activities," i.e., to an uneven, possibly sporadic rate of comet encounters that are capable of putting micrometeoroids with bound orbits into the inner solar system. In addition to these relatively short-term fluctuations (millions of years) it is also possible that the rate of comet injection into the inner solar system has undergone a long-term secular change due to a general depletion of the comet inventory.
3. Micrometeoroid detectors onboard Pioneer 8/9 have intercepted a non-negligible fraction of interplanetary particles that have hyperbolic orbits and thus are interpreted to be of interstellar origin (ref. 48). Thus lunar rocks offer a potential opportunity to study interstellar grains.

Most of the above possibilities, however, will require substantial amounts of work and are—at present—considered exciting challenges for future research. They are mentioned above only to stress the uniqueness and exciting potential of cratered lunar rock surfaces.

Lunar Regolith Dynamics

The lunar regolith is a layer of fragmental debris of variable thickness that lies upon fractured bedrock. Photogeologic investigations and detailed analysis of returned lunar materials revealed that repetitive meteoroid bombardment has been responsible for the formation of this layer to such an extent that other geological processes may be excluded. Impact cratering controls the overall growth of regolith; the lateral and vertical redistrib-

bution of material; the downslope mass wasting; the mixing and degree of homogenization of individual layers; the erosion of lunar rocks; the evolution of regolith grain sizes; the formation of impact melts, agglutinates, and breccias; the migration of volatile elements; and the admixture of meteoritic components and other parameters that make up the physical, chemical, and petrographic characteristics of lunar "soils." As a consequence, it appears appropriate to combine observational lunar crater data and experimental impact crater mechanics into computational models to arrive at a theoretical understanding of these processes.

A variety of computational results concerning mass-movement, erosion rate of rocks, etc., are available (refs. 34, 59, 63, 79, and others). However, all these analyses suffer from the fact that they yielded only "average" values because the computations did not account for the vagaries of the random impact process. Models that do, however, account for the randomness of the impact process both in space and time have been developed recently and are described below. The models may be used to gain a qualitative if not quantitative insight into some of the above processes. Some of these models consider craters up to 1500 m in diameter and thus are of drastically different dimensions than the craters treated in the preceding sections. Furthermore, it is also important to note that the models are principally independent of the absolute flux of meteoroids. The time parameter is linearly related to the total number of craters produced. Thus model elapsed times can easily be converted into absolute times by applying the best estimate of the absolute meteoroid and micrometeoroid infall rates.

LARGE-SCALE REGOLITH CRATERING

The gross-accumulation of the regolith debris layer has been the subject of a variety of treatments, e.g., Marcus (ref. 80) and Shoemaker (ref. 63). It has been demonstrated that the overall regolith thickness increases with increasing numbers of craters

that range roughly in diameter from 10 to 1000 m. Oberbeck and Quaide (ref. 81) pointed out that the growing debris layer acts as a buffering medium and thus strongly controls the geometry of different crater sizes. Accordingly, the actual thickness for a given lunar surface area can be related to the total number of craters produced as well as to the relative frequencies of differently shaped craters such as "normal," "flat-bottomed," "concentric," and "central mound" craters.

Oberbeck et al. (ref. 82) have developed a large-scale Monte Carlo-based computer program that simulates the evolution of the regolith and that also predicts the relative frequencies of the above four basic crater morphologies for any given regolith thickness. It is important to note that these calculations were performed with observed lunar cratering parameters, i.e., detailed crater geometries and distributions of associated ejecta blankets. No cratering scaling laws needed to be assumed.

A crater production size-frequency distribution of $N = KD^{-3.4}$ was empirically determined and used throughout these calculations (N = cumulative number of craters larger than diameter D , i.e., > 1 m). Some pertinent results are discussed below; for detailed information the reader is referred to Oberbeck et al. (ref. 82).

Figure 15 illustrates the relationship of the calculated median regolith thickness (R_m) as a function of absolute numbers of craters produced. A relationship of

$$R_m = 6.2 \times 10^{-5} K^{.64} \quad (1)$$

is derived and may be used to predict the median thickness for any surface area where crater size-frequency distributions can be determined and where the cumulative crater production distribution has the form of $N = K \cdot D^{-3.4}$.

However, the regolith thickness is variable over distances measured in hundreds of meters as evidenced by high-resolution photography and field inspection by the astronauts, despite the fact that the overall reference surface must have been exposed to the meteoroid bombardment for the same period of time. Figure 16 compares actually measured

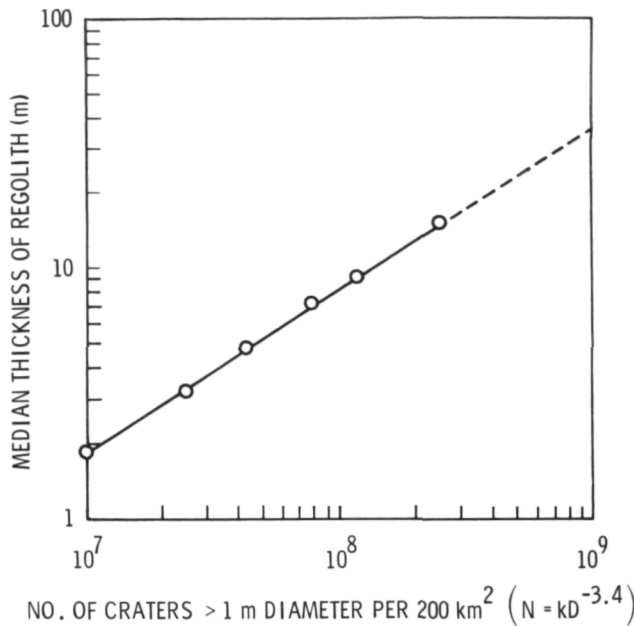


Figure 15.—The overall regolith growth as a function of craters produced, i.e., time (see equation 1).

thickness distributions (ref. 81) with those obtained in the Monte Carlo simulations. The agreement is good and lends additional support to the hypothesis that the regolith at the sites investigated by Quaide and Oberbeck (ref. 81) is primarily caused by impact comminution processes.

However, the above Monte Carlo model on regolith formation yielded additional information: with increasing thickness of regolith, only larger and larger craters are capable of penetrating the existing, buffering debris layer. Thus, with increasing time, it takes larger and larger craters to excavate pristine bedrock. The Monte Carlo simulations therefore continuously monitored, per each crater size class, the total volume excavated from the pristine substrate (V_s) and the already existing regolith layer (V_R) throughout the time required to build up the regolith to a given thickness. Figure 17 illustrates the ratio V_s/V_R for three different regolith depths. The ratio V_s/V_R is a function of crater diameter and is described by

$$V_s/V_R = C \cdot D^n \quad (2)$$

where C is a constant for a given distribution

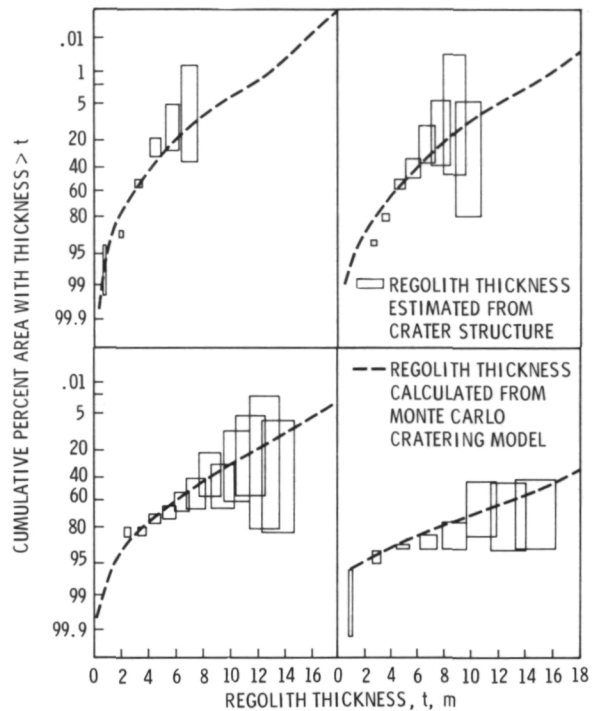


Figure 16.—Empirically determined regolith thickness distribution for four different lunar surfaces measuring $\approx 200 \text{ km}^2$ each. The empirical determination is based on the abundance of various crater geometries reflecting the presence of a competent substrate. Note the good agreement between observations and Monte Carlo cratering simulations.

of craters ($n = 1 - 1.3$); furthermore, C can be related to K in the crater distribution expression $N = KD^{-3.4}$ by

$$C = 1.02 \times 10^6 K^{-1.06} \quad (3)$$

and by substitution

$$V_s/V_R = 1.02 \times 10^6 K^{-1.06} D^n \quad (4)$$

Thus, over the range of values of K characteristic for mare terrains (as an example), the effective size boundary between mixing and new debris-producing craters becomes progressively larger. The average mixing zone therefore becomes deeper. Accordingly, older and thicker regolith deposits should be more thoroughly reworked than more youthful ones.

Figure 18 illustrates the cumulative contributions of various-sized craters that have built up a regolith layer of 4.7 m in median thickness. It is obvious from figures 17 and

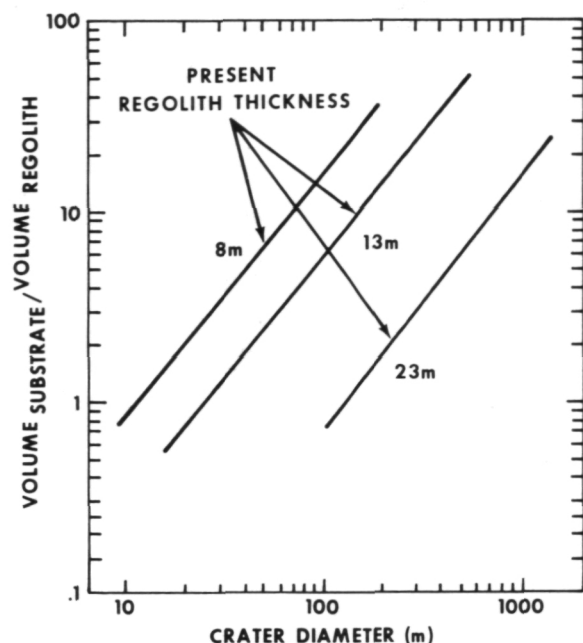


Figure 17.—Relative contributions of pristine bedrock from the "substrate" for various crater sizes and regolith depths. The "volume regolith" is that volume that is reworked debris excavated by prior cratering. Note that predominantly the larger craters excavate bedrock and thus chiefly contribute to the overall regolith growth with increasing regolith thickness, i.e., time.

18 that relatively small craters (e.g., < 10 m in diameter) have contributed significant amounts to the overall regolith, but it is also readily seen that these contributions occurred while the regolith was relatively thin, i.e., in the early stages of regolith formation. At present it is predominantly structures > 100 m in diameter that control the overall regolith growth while the smaller structures are confined to reworking these materials. As a consequence, the regolith thickness increases in general and in particular during its more recent history (i.e., the past $\approx 10^9$ years) due to the effects of relatively large cratering events that are capable of excavating pristine bedrock. This newly added material will always be delivered on top of the existing debris in discrete swaths of ejecta. The regolith therefore has to be envisioned as a complex sequence of numerous,

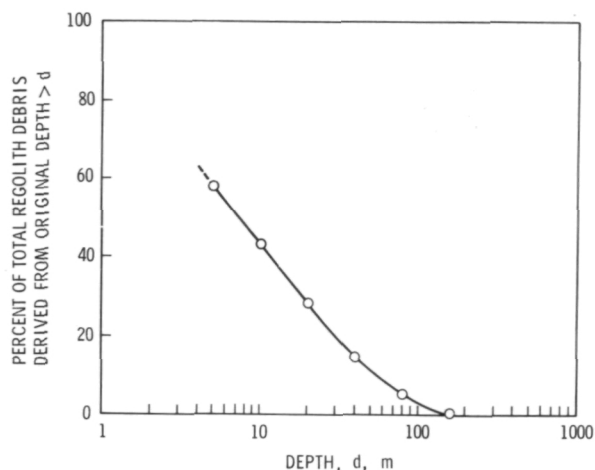


Figure 18.—Contributions (= volume percent) of various source areas at depth "d" to the overall composition of a typical mare regolith having a median thickness of 4.7 m.

overlapping ejecta blankets. These discreet blankets constitute some first-order discontinuities and heterogeneities in the evolving regolith. We will demonstrate in the next chapter that it is principally possible to preserve parts of these blankets despite heavy meteorite bombardment. Though there will be extensive mixing, there will not be complete homogenization of the regolith.

SMALL-SCALE REGOLITH CRATERING

It is obvious from the preserved stratigraphy in returned core tube samples that reworking has not obliterated all stratification in the regolith. It is just as obvious, however, that every stratum that resided at the very lunar surface has been subjected to the meteoroid bombardment and the reworking process which—due to the mass-frequency distribution of interplanetary matter—does operate on a micron-to-meter scale. The extent to which a stratum survives thus must be a function of its original thickness and length of surface residence time before it is blanketed by ejecta of sufficient thickness to effectively remove it from the active zone of reworking. Absolute param-

ters for these variables principally vary with absolute time; i.e., the cumulative number of craters produced. The absolute number of craters that contributed to the history of returned samples must certainly be larger than the numbers presently observable in the respective sampling areas because these are in crater-saturation for craters < 100m in diameter (refs. 22 and 63). Thus the potential surface history of sampled materials can be understood only if a continuous bombardment history is assumed in computational models.

Because meteoritic impact is a random process, any given point on the lunar surface has a unique history as compared with any other given point. On the other hand, the dominant role of meteoroid impact suggests that over extended periods of time any two areas of a given size will have experienced similar histories that differ only in details to a greater or lesser degree. Thus computational analyses that yield "average" values may be useful in understanding the basic processes. However, they should be applied only with extreme caution to actual sample data because of the uniqueness of each individual sampling location. "Averages" are cer-

tainly a valid framework for returned sample interpretations; but they should be applied only if sufficient statistical sample data are available. For any *individual* data point such averages cannot be applied and may lead to grossly erroneous results, because significant deviations from the "average" have to be expected from a random process.

Gault et al. (ref. 83) have shown that the probability P_u of a given point on the lunar surface remaining undisturbed, i.e., lying outside a crater of apparent diameter D in a time interval t is given by

$$P_u = \exp. (-\pi N t D^2 / 4) \quad (5)$$

where N is the flux of the randomly distributed impacting bodies per unit time and area which produce craters of diameter D . The probability P_c of a given point's having been affected, i.e., lying within exactly n craters of size D can be expressed as

$$P_{c(n)} = P_u (\pi N t D^2 / 4)^n / n! \quad (6)$$

Equation 6 is the Poisson probability function. Using the values given by Molina (ref. 84) for a range of $n = 0 - 153$ and $(\pi N t D^2 / 4) = .001 - 100$ and calculating additional terms up to $n = 10^6$, Gault et al. (ref. 83) calculated how many times a given surface area may be impacted. A microme-

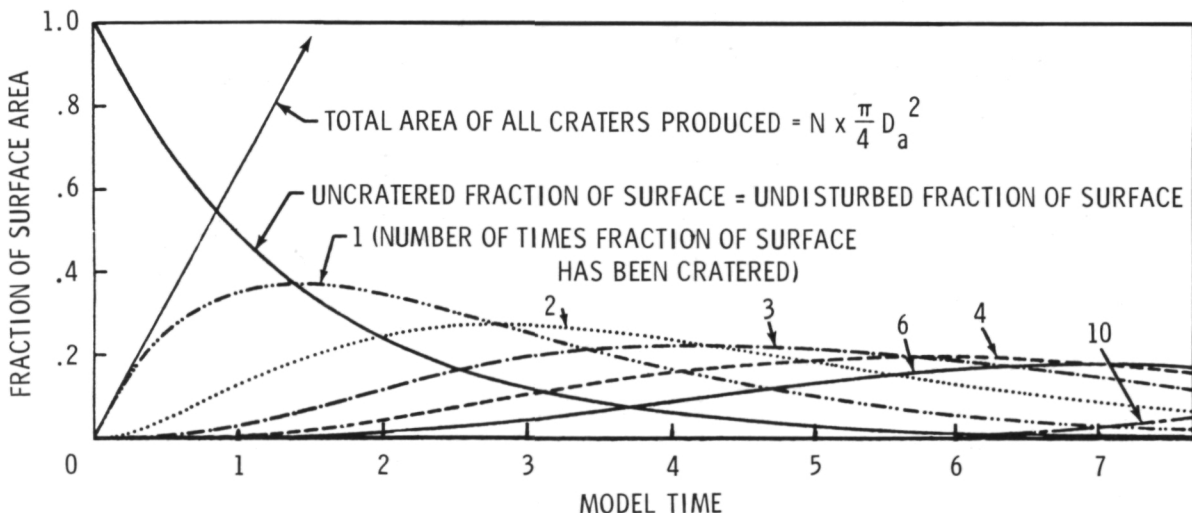


Figure 19.—Analytical model based on Poisson probability function describing the amount of surface area (percent) that will be affected by meteoroid impact, and the number of times impact will have occurred after given model elapsed times.

teoroid mass-distribution of the form $N = 1.45 m^{0.47}$ was used for 10^{-13} to 10^{-7} g meteoroid mass (m) and $N = 9.14 \times 10^{-6} m^{1.213}$ for projectiles 10^{-7} to 10^3 g. Furthermore a standard impact velocity of 20 km/s, together with laboratory cratering data into unconsolidated materials (ref. 28), was applied in these calculations. The principal result is shown in figure 19.

Virtually identical results (fig. 20) were obtained in a Monte Carlo-based computer-simulation by Hörz et al. (ref. 85), that applied the crater size-frequencies of figure 6 and a random number generator to determine impact coordinates and the magnitude of

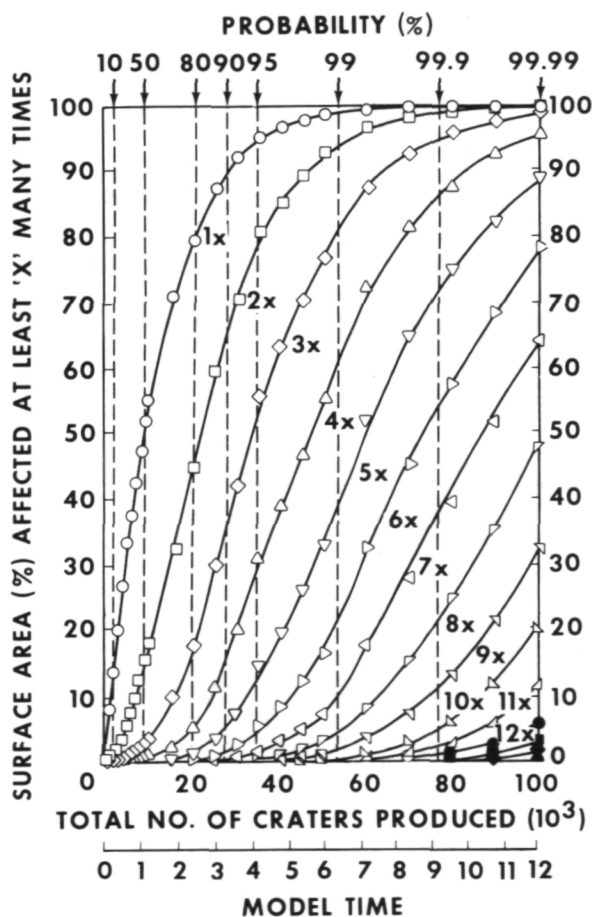


Figure 20.—Almost identical data as in figure 19, resulting from a Monte Carlo computer program. Note the multiple bombardment history of fractional surface areas with increasing time, i.e., 10^5 craters produced.

each cratering event. The curve labeled "1x" in figure 20 indicates how much surface area is affected at least one time. Note that 50 percent of the test surface ($= 44 \text{ cm}^2$) is already cratered after 8300 craters, 152 to $22500 \mu\text{m}$ in spall diameter. It takes more than a factor of 10 additional craters to affect the remaining 50 percent. Though qualitatively not surprising, these absolute numbers were unexpected. Furthermore, figure 20, for example, illustrates that by the time 99 percent of the surface is cratered at least $1 \times$ (99 percent probability), 92 percent of the surface is already cratered twice, 81 percent has suffered at least three impacts, 59 percent is cratered four times, etc. As 99.99 percent of the surface is cratered at least once, 88 percent will already be affected at least five times, etc.

An extension of the data illustrated in figure 20 is presented in figure 21, which is based on 10^6 craters (ref. 85). Per each model-elapsd time, it was determined how often a given fractional surface area was impacted. Note that when the entire area ($= 100$ percent) is cratered at least one time, 50 percent has suffered already 12 impacts and 10 percent surface was cratered at least 17 times. Or, alternatively, if it takes one time to affect 50 percent of a lunar surface, it will take 3.8 times longer to affect 90 percent, a factor of 6.6 longer to cover 99 per-

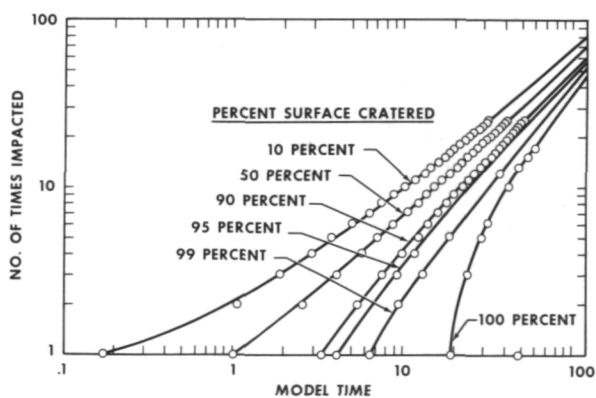


Figure 21.—General probability of multiple bombardment history for various fractional surface areas (total craters produced: 10^6 ; see text).

cent and, finally, 19 times longer to crater 100 percent of the surface. The model times indicated in figures 19 through 21 will be used in identical fashion throughout this report. Unit time is defined as the time required to affect 50 percent of the surface area at least one time.

Figures 19 through 21 illustrate a fundamental characteristic of the impact process. While finite—though admittedly small—surface areas may remain unaffected for long time periods, other areas have already suffered repetitive bombardment. Consequently, within any cratered terrain, small surface areas may be encountered that have dramatically different bombardment histories despite the fact that they were exposed to the same micrometeoroid environment for the same period of time.

We now turn to the mixing of the regolith. The above models are also a measure of how much kinetic energy is deposited randomly in space and time into a unit area of lunar surface. Therefore, one can associate with that energy either a crater diameter (as above) or a corresponding crater depth. Gault et al (ref. 83) applied these concepts using the meteoroid mass distribution and the probability theory given above together with cratering mechanics of Gault (ref. 28). The number of impacts per unit area (e.g.,

fig. 21) were converted into "depth excavated" because each crater diameter may be associated with a given crater depth. Results of such calculations are illustrated in figure 22. The absolute timescale is based on the Gault et al. micrometeoroid flux (ref. 34), assumed to be constant over geological times. Though these absolute rates of regolith turnover are considered realistic for about the past 10^8 to 10^9 years, they are certainly not valid for periods $> 10^9$ years. Gault et al. (ref. 83) therefore also calculated the same data for a time variable flux; these data are shown in figure 23.

The principal result of figures 21 and 23 is of course the high turnover rate of the regolith surface itself, e.g., figure 22: while it takes approximately 10^7 years to completely turn over an 8-mm-deep zone at least once, the uppermost mm of the very same area has been turned over already 25(!) times; or when 99 percent of an 8-mm-deep layer is turned over at least once, 50 percent of the same surface will have already been turned over to a 1.4-cm depth. As a consequence, there exists a very thin surface zone, approximately 1 mm in thickness, in which extreme mixing and homogenization of components occurs. However, the lunar regolith becomes relatively quiescent rather quickly

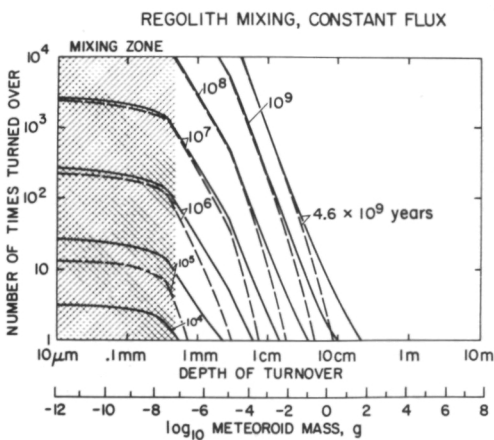


Figure 22.—The detailed turnover history of various regolith depths, as a function of absolute time and a constant flux.

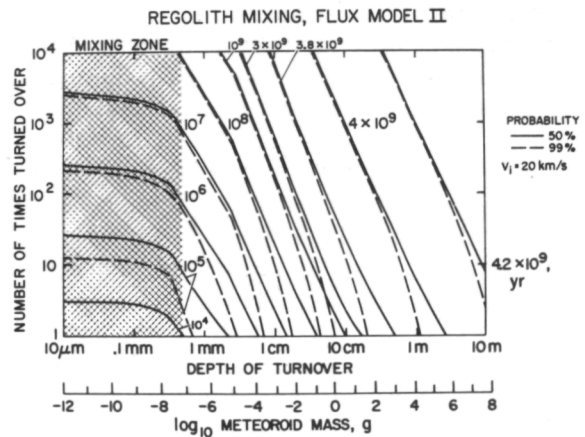


Figure 23.—Same as figure 22, but with use of a meteoroid model flux that increases with geologic time to match the observed crater densities at the Apollo 12 landing site.

with depth; e.g., even with a meteoroid flux that accounts for an increase in bombardment (fig. 23) in early lunar history ($=2$ to 3.8×10^9 years), a 1-m-thick layer is turned over only once with 99 percent confidence. This accounts for the observation of Russ et al. (ref. 78) that a major section of the Apollo 15 deep drill core had been residing completely undisturbed on the lunar surface for the past 500 m.y. We therefore conclude that due to the mass-frequency distribution of interplanetary matter that is vastly dominated by relative small particles in the 10^{-8} to 10^{-4} g mass range, only an upper mm is thoroughly mixed before an adjacent larger impact event covers the area and effectively removes the mixing layer from the active reworking zone. It is thus possible to preserve the observed small-scale stratigraphy in the regolith.

However, though each surface layer undoubtedly has its peculiar surface history, it is not correct to conclude that each layer was *deposited* at the eventual site of recovery by *one* discrete impact event. Gault et al. (ref. 86) and Stöffler et al. (ref. 87) demonstrated that the ejecta blankets of experimental impact craters in layered quartzsand targets have part of the original target-stratigraphy preserved, though in reversed sequence, i.e., overturned. Similar observations are also made around large-scale nuclear and chemical explosion craters as well as terrestrial impact craters (e.g., the 25-km-diameter Reis-structure, Germany (ref. 88)). As a consequence, each regolith crater on the Moon will preserve—though certainly in a somewhat degraded fashion—the original stratigraphic section. Therefore a variety of discrete layers may be excavated and redeposited at the site of recovery by a large single impact regardless of whether they had drastically different exposure histories before this *last* depositional episode.

Furthermore, processes other than direct deposition of impact ejecta blankets may also cause an apparent layering in the recovered regolith cores. For example: small-scale slumping on the walls of regolith craters may be a significant process. It can also be en-

visioned that soft soil breccias ejected by a larger event completely desintegrate upon landing at significant distances from the primary crater. Rocks that survived such a landing at the end of a ballistic trajectory are subject to micrometeoroid erosion and their erosion products may be foreign to the new environment, thus causing a local "heterogeneity" and therefore a "layer" in the regolith stratigraphy. Virtually nothing is known about the lateral dimensions of the regolith "layers" and it is possible that their areal extent is rather limited. Beyond any doubt, however, caution is necessary to postulate that each observed layer was last deposited by one discrete impact event; such interpretations may be grossly in error.

LUNAR ROCK EROSION

Studies of the grain size distribution of individual cratering experiments (refs. 31 and 89) revealed that the ejecta of one given event are significantly more coarse-grained than grain sizes reported from the lunar regolith (e.g., refs. 90 and 91). Thus larger regolith components must be broken up, i.e., "eroded," by small-scale cratering events. The visual inspection of lunar rocks both on lunar surface photographs and in the laboratory reveals that micrometeoroid impact causes erosion and eventual destruction of rock specimens exposed to space. The micrometeoroid complex operates on two different scales and accordingly results in two significantly different effects, i.e., "single particle abrasion" and "catastrophic rupture" (refs. 34, 59, 63, 79, and others).

"Single particle abrasion" is caused by relatively small craters, as compared with the overall size of a specific rock, and it results in an effect similar to sandblasting. It is largely responsible for gradual mass wasting associated with a general rounding of the rocks (fig. 24). In contrast, "catastrophic rupture" is accomplished only by craters of relatively large size with respect to a given rock mass, i.e., only by impacts of sufficient energy to generate penetrative fracture systems (fig. 25).

Hörz et al. (ref. 16) simulated the "single particle abrasion" process via Monte Carlo-based computer models; up to 10^6 craters 152 to 25 000 μm in spall diameter were produced on a 25-cm² surface area. Figure 26 displays some computer-generated profiles after a variety of crater numbers produced. Figure 27 illustrates the average erosion depth as a function of time. Note the influence of a few, though large, events in particular in figure 27, but also in figure 26. Applying a best estimate for the absolute micrometeoroid flux averaged over the past 10^6 years, Hörz et al. (ref. 85) arrive at erosion rates for crystalline lunar rocks of .3 to .6 mm per 10^6 years. The erosion rate for breccias may be higher, because of less compressive target strength (ref. 34).

Figure 28 illustrates an additional result of the above Monte Carlo simulation relating

to the "representative" nature of finite size rock chips available in the laboratory to delineate lunar surface processes. The computer iterated over the entire test surface and searched for the least (=shallowest) and most eroded (=deepest) "unit areas" that were defined as 5, 2, 1, .64, and .16 cm². The "extremes" in erosional state are compared with the average of the entire area in figure 27. The deviation from the average is a direct measure of how typical or atypical small lunar rock chips may be with respect to their parent rock. The deviations observed are considerable and constitute ample evidence that the random nature of the impact process has to be seriously considered in the analysis of discrete, finite-size rock chips. Unless it is demonstrated otherwise, that such a sample is truly "representative" of the parent rock, the results obtained may

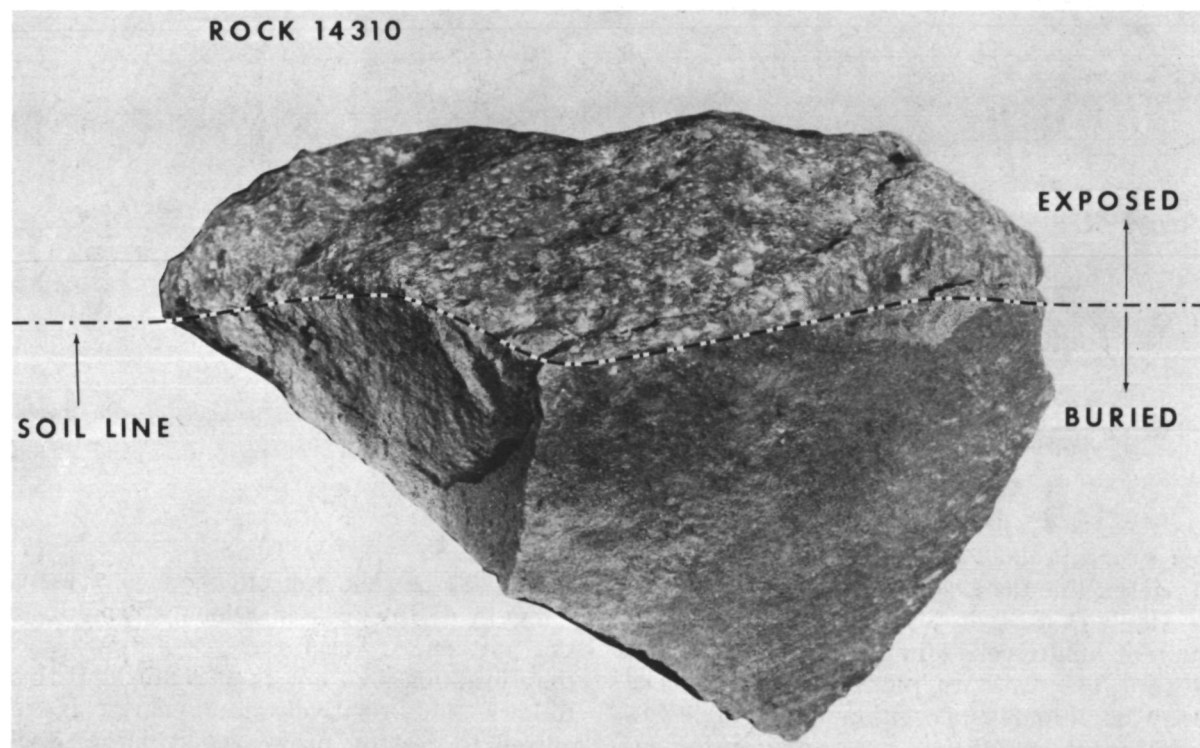


Figure 24.—Typical lunar rock (14310) illustrating the effects of single particle abrasion. As indicated by the soil line, parts of this rock were buried in the lunar regolith. The buried portion is characterized by sharp, angular fracture surfaces. In contrast, the surfaces exposed to the micrometeoroid bombardment are abraded and significantly rounded.

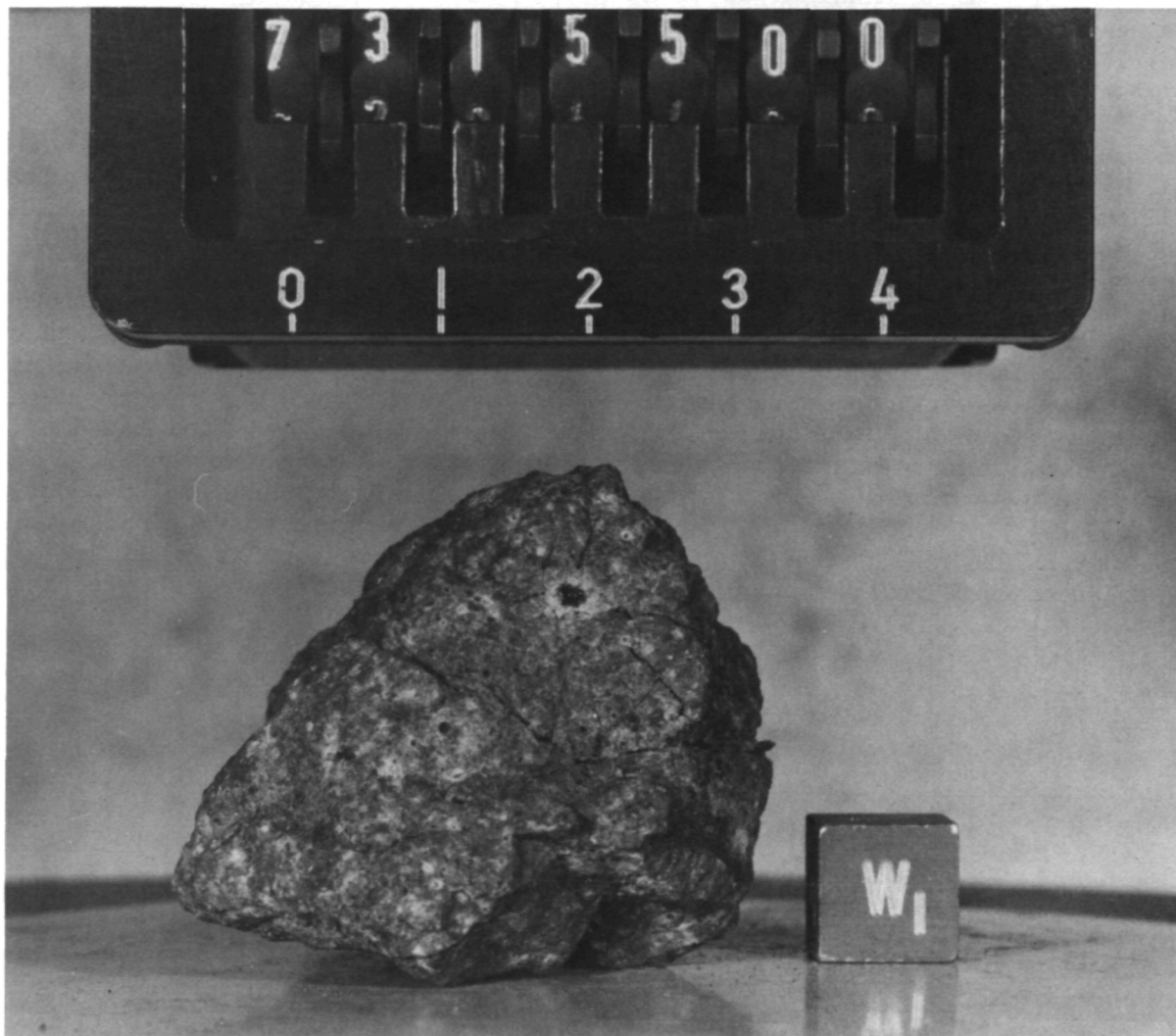


Figure 25.—Lunar rock 73155 that has suffered an exceptionally large impact almost capable of catastrophically rupturing the entire hand specimen.

only be used with caution to delineate “averages,” e.g., solar flare particle track densities to determine the absolute exposure age.

Gault et al. (ref. 34) treated the destruction of lunar rocks due to “catastrophic rupture.” The catastrophic breakup of rocks may be accomplished either by a single impact event of sufficient energy or by the cumulative effects of a number of smaller impacts; the rupture energy (E_R) is cumulative (ref. 92). The energy required to rupture a rock (\cong spherical body) of radius r can be de-

scribed as

$$E_R = 2.5 \times 10^6 S_c r^{-0.225} \quad (7)$$

where S_c is the unconfined compressive strength of the rock in kilobars; and E_R is the unit energy required *per gram*, rather than total mass, of a rock of radius r . It thus follows that relatively less energy is required to destroy progressively larger rock specimens. Figure 29 compares actual measurements of the very largest pit craters observed on lunar rocks and the relations expressed by equation (7). The agreement is

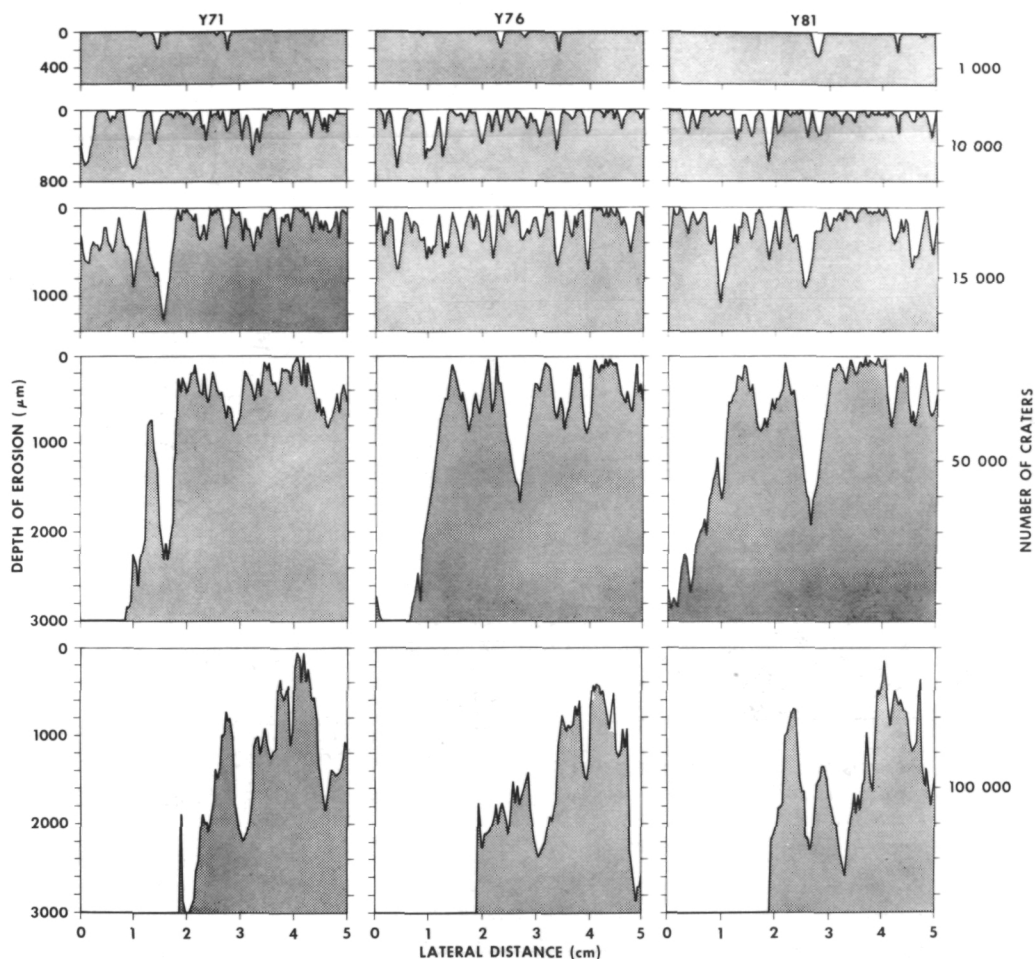


Figure 26.—Computer-generated erosion profiles of a lunar rock. According to each number of total craters produced, profiles taken at three different localities (Y_{71} , Y_{76} , Y_{81}) are illustrated (white—volume eroded; stippled—remaining rock; the vertical exaggeration is 17 times).

good (ref. 26). Figure 29 illustrates the mean survival time before catastrophic rupture occurs for various hypothetical rock material, considering compressive strength and rock mass as the main variables (ref. 34).

When the results of "single particle abrasion" and "catastrophic breakup" are combined, the following conclusions emerge: while, for example, a 1-kg rock will survive catastrophic desintegration for about 3×10^6 years, it has suffered in the meantime "single particle abrasion" that effectively removed a surface layer of only about 1 to 2 mm in thickness. (See figure 30). Thus "catastrophic rupture" must be considered

the vastly superior process in obliterating lunar rocks. "Single particle abrasion" plays a minor role only, but it is still an order of magnitude more effective than sputtering processes caused by high energetic radiation (ref. 79) 1973.

Conclusions

The authors hope their efforts have demonstrated that the study of lunar microcraters has significantly contributed to our present understanding of the micrometeoroid complex:

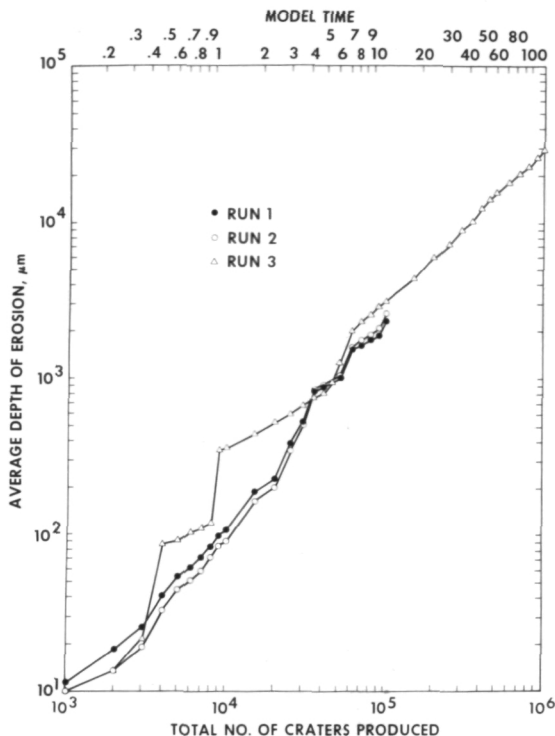


Figure 27.—Average erosion depth resulting from a Monte Carlo computer simulation. The best estimate for erosion is based on 10^6 craters, i.e., run 3. Notice the influence of some few—however, very large—craters.

1. Contrary to popular astronomical hypotheses, the micrometeoroids have densities from 2 to 4 g/cm³. They are also equant if not spherical in shape; forms like needles, whiskers, platelets, rods, etc., may safely be excluded.
2. The mass-frequencies from 10^{-12} to 10^{-3} g are in agreement with previous meteoroid data. However, particle masses as small as 10^{-15} g are responsible for the formation of microcraters $< .1 \mu\text{m}$ in diameter. This result negates the existence of the celebrated “radiation pressure cutoff” at particle masses $< 10^{-12}$ g.
3. The average micrometeoroid flux for the past 10^6 years could be established within a factor of 5. In agreement with satellite measurements, it is likely that the present micrometeoroid activity is

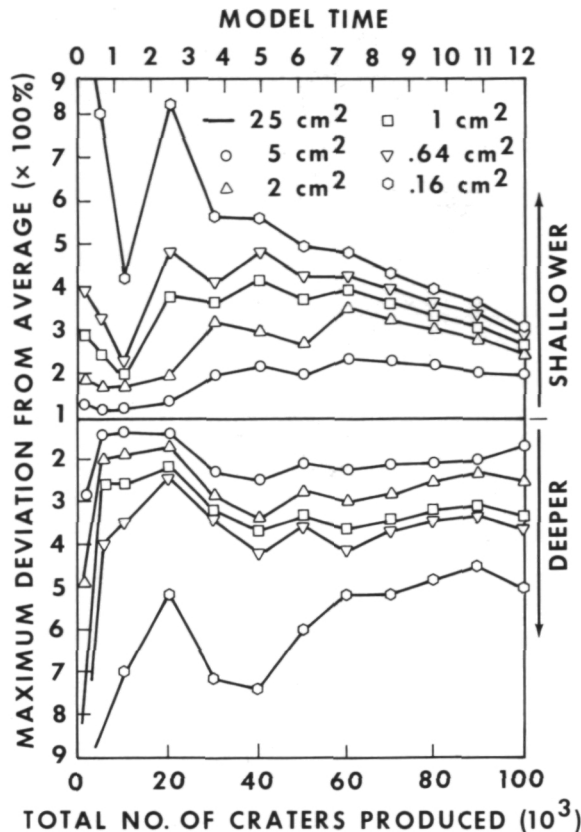


Figure 28.—Extremes in deviation of erosional state of various, absolute surface areas (5, 2, 1, .64, and .16 cm²) compared with the average of a 25 cm² surface.

about an order of magnitude higher than this long-term average.

4. Though absolute flux data do not exist at the moment, there is ample evidence that the micrometeoroid complex existed throughout geological time.
5. The potential of the “lunar micrometeoroid detector” is not fully exhausted at the moment.

The micrometeoroid complex and larger meteoroids are primarily responsible for the evolution and physical-chemical makeup of the lunar regolith; they effectively control the overall regolith growth as well as small-scale stratigraphy. The regolith has to be envisioned as a complex sequence of ejecta blankets that have not necessarily lost their integrity. The mixing, “gardening,” and

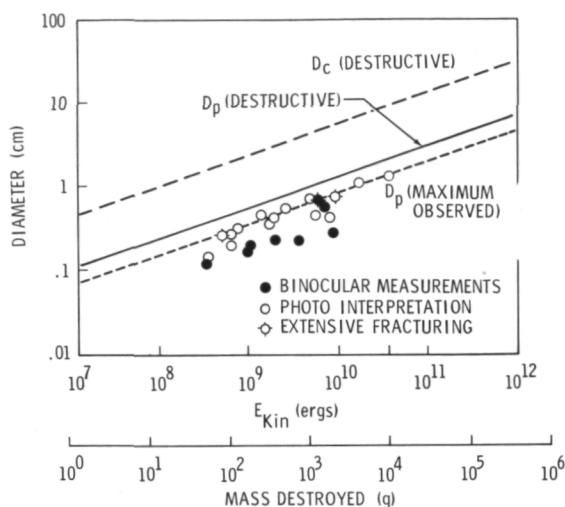


Figure 29.—Spall and pit diameters required for catastrophic rupture of a given rock mass, according to calculations based on experimental and observational results. Diameter, D_p (destructive) is considered an upper limit for pit diameters observable on lunar rocks; D_c is an experimental limit referring to the crater diameter, i.e., spall diameter (D_s). Ratios for D_s/D_p in lunar rocks are typically from 3.8 to 4.6. The agreement of observations on lunar rocks with those on experimental rupture is excellent.

homogenization are largely confined to the uppermost layer of approximately 1-mm thickness. Lunar rocks are effectively destroyed by micrometeoroids, with the “catastrophic rupture” process dominating the “single particle abrasion.” These results will aid not only in the interpretation of lunar materials but also in that of other planetary surfaces as well.

References

1. SHOEMAKER, E. M., R. M. BATSON, H. E. HOLT, E. C. MORRIS, J. J. RENNILSON, AND E. A. WHITAKER, Observations of the Lunar Regolith and the Earth From the Television Camera on Surveyor 7. *J. Geophys. Res.*, Vol. 74, 1969, pp. 6081–6119.
2. BLOCH, M. R., H. FECHTIG, W. GENTNER, G. NEUKUM, AND E. SCHNEIDER, Meteorite Impact Craters, Crater Simulations, and the Meteoroid Flux in the Early Solar System. *Proc. Second Lunar Science Conference, Geo-*

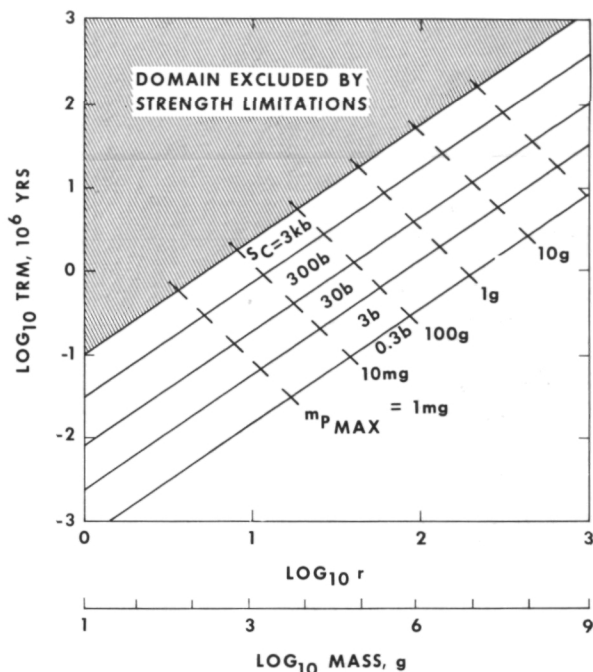


Figure 30.—Calculated mean residence time before destruction by catastrophic rupture for spherical rocks of radius r and compressive strengths (S_c), exposed to the micrometeoroid bombardment. Masses of the largest particles (M_{pmax}) contributing to the rupture process are indicated.

chimica et Cosmochimica Acta, Supplement 2, Vol. 3, 1971, pp. 2639–2652.

3. HARTUNG, J. B., F. HÖRZ, AND D. E. GAULT, Lunar Microcraters and Interplanetary Dust. *Proc. Third Lunar Science Conference, Geochimica et Cosmochimica Acta*, Supplement 3, Vol. 3, 1972, pp. 2735–2753.
4. HARTUNG, J. B., F. HÖRZ, AND D. E. GAULT, Lunar Rocks as Meteoroid Detectors. In *Proc. Internal Astron. Union Colloq. No. 13, The Evolutionary and Physical Problems of Meteoroids*, in press, 1972.
5. MORRISON, D. A., D. S. MCKAY, AND H. J. MOORE, Microcraters on Apollo 15 and 16 Rocks. *Proc. Fourth Lunar Science Conference, Geochimica et Cosmochimica Acta*, Supplement 4, Vol. 3, 1973, pp. 3235–3253.
6. VEDDER, J. F., Microcraters in Glass and Minerals. *Earth Planet. Sci. Letters*, Vol. 11, 1971, pp. 291–296.
7. VEDDER, J. F., Craters Formed in Mineral Dust by Hypervelocity Microparticles. *J. Geophys. Res.*, Vol. 77, 1972, pp. 4304–4309.
8. FECHTIG, H., J. B. HARTUNG, K. NAGEL, AND G. NEUKUM, Microcrater Studies, Derived Me-

- teoroid Fluxes and Comparison With Satellite Borne Experiments. *Lunar Science*, Vol. V, Lunar Science Institute, Houston, 1974, pp. 222-224; also in *Proc. Fifth Lunar Science Conference*.
9. MANDEVILLE, J. C., AND J. F. VEDDER, Microcraters Formed in Glass by Low Density Projectiles. *Earth Planet. Sci. Letters*, Vol. 11, 1971, pp. 297-306.
 10. NEUKUM, G., *Untersuchungen über Einschlagsskrater auf dem Mond*. Doctor's Thesis, University of Heidelberg, 1971.
 11. SCHNEIDER, E., *Mikrokrater auf Mondgestein und deren Laborsimulation*. Ph.D. Thesis, Heidelberg, Germany, unpublished, 1972.
 12. VEDDER, J. F., AND J. C. MANDEVILLE, Microcraters Formed in Glasses by Projectiles of Various Densities. *J. Geophys. Res.*, in press, 1974.
 13. MANDEVILLE, J. C., *Etude de Crateres Formes sur des Surfaces de Verre par L'Impact de Micrometeoroides Artificielles*. Ph.D Thesis, No. 1334, Toulouse, France, unpublished, 1972.
 14. KERRIDGE, J. F., AND J. F. VEDDER, Accretionary Process in the Early Solar System: An Experimental Approach. *Science*, Vol. 177, 1972, pp. 161-162.
 15. BROWNLEE, D. E., F. HÖRZ, J. F. VEDDER, D. E. GAULT, AND J. B. HARTUNG, Some Physical Properties of Micrometeoroids. *Proc. Fourth Lunar Science Conference, Geochimica et Cosmochimica Acta*, Supplement 4, Vol. 3, 1973, pp. 3197-3212.
 16. HÖRZ, F., D. E. BROWNLEE, H. FECHTIG, J. B. HARTUNG, D. A. MORRISON, G. NEUKUM, E. SCHNEIDER, AND J. F. VEDDER, Lunar Microcraters and Their Implications for the Micrometeoroid Complex. *Planet. Space Sci.*, Vol. 23, 1975, pp. 151-172.
 17. VEDDER, J. F., AND H. LEM, Profiling With the Electron Microscope. *Photogrammetric Engr.*, Vol. 38, 1972, pp. 243-244.
 18. CARTER, J. L., AND D. S. MCKAY, Influence of Target Temperature on Crater Morphology and Implications on the Origin of Craters on Lunar Glass Spheres. *Proc. Second Lunar Science Conference, Geochimica et Cosmochimica Acta*, Supplement 2, Vol. 3, 1971, pp. 2653-2670.
 19. HARTUNG, J. B., AND F. HÖRZ, Microcraters on Lunar Rocks. *Proc. 25th Int. Geol. Cong.*, Montreal, Section 15, Planetology, 1972, pp. 48-56.
 20. VERNIANI, F., Structure and Fragmentation of Meteoroids. *Space Sci. Res. Rev.*, Vol. 10, 1969, pp. 230-261.
 21. HUGHES, D. W., Interplanetary Dust and Its Influx to the Earth's Surface. *Space Res.*, Vol. XIV, COSPAR 73, Konstanz, Germany, in press, 1973.
 22. GAULT, D. E., Saturation and Equilibrium Conditions for Impact Cratering on the Lunar Surface: Criteria and Implications. *Radio Sci.*, Vol. 5, 1970, pp. 273-291.
 23. NEUKUM, G., F. HÖRZ, D. A. MORRISON, AND J. B. HARTUNG, Crater Population on Lunar Rocks. *Proc. Fourth Science Conference, Geochimica et Cosmochimica Acta*, Supplement 4, Vol. 3, 1973, pp. 3255-3276.
 24. SCHNEIDER, E., D. STORZER, A. MEHL, J. B. HARTUNG, H. FECHTIG, AND W. GENTER, Microcraters on Apollo 15 and 16 Samples and Corresponding Cosmic Dust Fluxes. *Proc. Fourth Lunar Science Conference, Geochimica et Cosmochimica Acta*, Supplement 4, Vol. 3, 1973, pp. 3277-3290.
 25. HÖRZ, F., J. B. HARTUNG, AND D. E. GAULT, Micrometeorite Craters on Lunar Rock Surfaces. *J. Geophys. Res.*, Vol. 76, 1971, pp. 5770-5798.
 26. HARTUNG, J. B., F. HÖRZ, K. F. AITKEN, D. E. GAULT, AND D. E. BROWNLEE, The Development of Microcrater Populations on Lunar Rocks, *Proc. Fourth Lunar Science Conference, Geochimica et Cosmochimica Acta*, Supplement 4, Vol. 3, 1973, pp. 3213-3234.
 27. SCHNEIDER, E., AND F. HÖRZ, Microcrater Populations on Apollo 17 Rocks. *Icarus*, in press, 1974.
 28. GAULT, D. E., Displaced Mass, Depth, Diameter and Effects of Oblique Trajectories for Impact Craters Formed in Dense Crystalline Rocks. *The Moon*, Vol. 6, 1973, pp. 32-44.
 29. NAGEL, K., *Experiments zur Kratersimulation*. Master's Thesis, University of Heidelberg, Germany, unpublished, 1973.
 30. NEUKUM, G., E. SCHNEIDER, A. MEHL, D. STORZER, G. A. WAGNER, H. FECHTIG, AND M. R. BLOCH, Lunar Craters and Exposure Ages Derived From Crater Statistics and Solar Flare Tracks. *Proc. Third Lunar Science Conference, Geochimica et Cosmochimica Acta*, Supplement 3, Vol. 3, 1972, pp. 2793-2810.
 31. MOORE, H. J., D. E. GAULT, AND E. D. HEITOWIT, *Change of Effective Target Strength With Increasing Size of Hypervelocity Impact Craters*. Seventh Hypervelocity Impact Symposium, Tampa, Florida, Nov. 17-19, Vol. 4, 1965, p. 341.
 32. MILLMANN, P., The Observational Evidence for Mass Distribution in the Meteoritic Complex. *The Moon*, Vol. 8, 1973, p. 228.
 33. DOHNANYI, J. S., Interplanetary Objects in Review: Statistics of Their Masses and Dynamics. *Icarus*, Vol. 17, 1972, pp. 1-48.
 34. GAULT, D. E., F. HÖRZ, AND J. B. HARTUNG, Effects of Microcratering on the Lunar Surface. *Proc. Third Lunar Science Conference, Geochimica et Cosmochimica Acta*, Supplement 3, Vol. 3, 1972, pp. 2713-2734.
 35. HARTUNG, J. B., D. STORZER, AND F. HÖRZ, To-

- ward a Lunar Microcrater Clock. *Lunar Science*, Vol. V, Lunar Science Institute, Houston, 1974, pp. 307-309; also in *Proc. Fifth Lunar Science Conference*.
36. ZOOK, H., AND O. E. BERG, A Source for Hyperbolic Cosmic Dust Particles. *Planet. Space Sci.* in press, 1974.
 37. JEDWAB, J., La Magnetite de le Meteorite D'Orgueil, Vue au Microscope Electronique a Balayage. *Icarus*, Vol. 15, 1971, pp. 319-340.
 38. KERRIDGE, J. F., Low-Temperature Minerals From the Fine-Grained Matrix of Some Carbonaceous Meteorites. *Ann. New York Academy of Sciences*, Vol. 119, 1964, pp. 41-53.
 39. DONN, B., The Origin and Nature of Solid Particles in Space. *Ann. New York Academy of Sciences*, Vol. 119, 1964, pp. 5-16.
 40. ARRHENIUS, G., AND H. ALFVÉN, Asteroidal Theories and Experiments. *Physical Studies of Minor Planets, Proc. 12th Coll. Int. Astr. Union*, Tucson, Ariz., 1971, pp. 213-233.
 41. GROSSMAN, L., Condensation in the Primitive Solar Nebula. *Geochimica et Cosmochimica Acta*, Vol. 36, 1972, pp. 597-619.
 42. HARWIT, M., Origins of the Zodiacal Dust Cloud. *J. Geophys. Res.*, Vol. 68, 1963, pp. 2171-2180.
 43. BLANFORD, G., D. S., MCKAY, AND D. A. MORRISON, Accretionary Particles and Microcraters. *Lunar Science*, Vol. V, Lunar Science Institute, Houston, 1974, pp. 67-68; also in *Proc. Fifth Lunar Science Conference*.
 44. GINDILIS, L. M., N. B. DIVARI, AND L. V. REZNOVA, Solar Radiation Pressure on Particles of Interplanetary Dust. *Soviet Astron., A.J.*, Vol. 13, 1969, pp. 114-119.
 45. NILSSON, C. S., F. W. WRIGHT, AND D. WILSON, Attempts to Measure Micrometeoroid Flux on the OGO II and OGO IV Satellites. *J. Geophys. Res.*, Vol. 74, 1969, pp. 5268-5276.
 46. ALEXANDER, W. N., C. W. ARTHUR, J. L. BOHN, J. H. JOHNSON, AND B. J. FARMER, Lunar Explorer 35: 1970 Dust Particle Data and Shower-Related Picogram Ejecta Orbits. *Space Res.*, Vol. 12, 1972, pp. 349-355.
 47. HOFFMAN, H. J., H. FECHTIG, E. GRÜN, AND J. KISSEL, First Results of the Micrometeoroid Experiment S 215 on the HEOS 2 Satellite. *COSPAR 1973*, Konstanz, Germany, 1973 p. 114; also in press, *Space Res.*, Vol. XIV.
 48. BERG, O., AND E. GRÜN, Evidence of Hyperbolic Cosmic Dust Particles. *Space Res.*, Vol. XIII, Akademie Verlag, Berlin, 1973, pp. 1047-1055.
 49. ALEXANDER, W. M., C. W. MCCracken, AND J. L. BOHN, Zodiacal Dust: Measurements by Mariner IV. *Science*, Vol. 149, 1965, pp. 1240-1241.
 50. NAZAROVA, T. N., Solid Component of Interplanetary Matter From Vehicle Observation. *Space Sci. Reviews*, Vol. 8, 1968, pp. 455-466.
 51. ALEXANDER, W. M., C. W. ARTHUR, AND J. L. BOHN, Lunar Explorer 35 and OGO 3: Dust Particle Measurement in Selenocentric and Cislunar Space From 1967 to 1969. *Space Res.*, Vol. XI, Akademie Verlag, Berlin, 1971, pp. 279-285.
 52. NAUMANN, R. J., D. W. JEX, AND C. L. JOHNSON, Calibration of Pegasus and Explorer XXIII Detector Panels. National Aeronautics and Space Administration, Technical Note TRR-321, 1969.
 53. O'NEAL, R. L., *The Explorer XXIII Micrometeoroid Satellite*, NASA Technical Note TN-D 4784, 1968.
 54. KONSTANTINOV, B. P., M. M. BREDOV, E. R. MAZETS, V. N. PANOV, R. L. APTEKAR, S. V. GOLENETSKII, Y. A. GURYAN, AND V. N. ILLINSKII, Micrometeors in Circumterrestrial Space Observed by "Kosmos 163," *Cosmic Res.*, Vol. 7, 1969, pp. 817-821.
 55. KONSTANTINOV, B. P., M. M. BREDOV, E. R. MAZETS, V. N. PANOV, R. L. APTEKAR, S. V. GOLENETSKII, Y. A. GURYAN, AND V. N. ILLINSKII, Micrometeoroid Investigations on the Satellite "Cosmos 135," *Cosmic Res.*, Vol. 6, 1968, pp. 622-632.
 56. GREW, G. W., AND C. A. GÜRTLER, *The Lunar Orbiter Meteoroid Experiment*. National Aeronautics and Space Administration, Technical Note D-6266, 1971.
 57. COUR-PALAIS, B. G., The Flux of Meteoroids at the Moon in the Mass Range 10^{-8} to 10^{-12} g from the Apollo Window and Surveyor III TV Camera Results. *Lunar Science*, Vol. V, Lunar Science Institute, Houston, 1974, pp. 138-140.
 58. HAWKINS, G. S., Impacts on the Earth and Moon, *Nature*, Vol. 197, No. 4869, 1963.
 59. NEUKUM, G., Micrometeoroid Flux, Microcrater Population Development and Erosion Rates on Lunar Rocks, and Exposure Ages of Apollo 16 Rocks Derived From Crater Statistics (abs.). *Lunar Science*, Vol. IV, Lunar Science Institute, Houston, 1973, pp. 558-560.
 60. KAISER, T. R., The Determination of the Incident Flux of Radio-Meteors II: Sporadic Meteors. *Monthly Notices Roy. Astron. Soc.*, Vol. 123, 1961, pp. 265-271.
 61. LINDBLAD, B. A., Luminosity Functions of Sporadic Meteors and Extrapolation of the Influx Rate to the Micrometeorite Region. *Smithsonian Contr. Astrophys.*, Vol. 11, 1967, pp. 171-180; also in NASA SP-135.
 62. LATHAM, G., J. DORMAN, F. DUENNEBIER, M. EWING, D. LAMMLEIN, AND Y. NAKAMURA, Moonquakes, Meteoroids, and the State of the Lunar Interior. *Proc. Fourth Lunar Science Conference, Geochimica et Cosmochimica Acta*, Supplement 4, Vol. 3, 1973, pp. 2515-2527.
 63. SHOEMAKER, E. M., Origin of Fragmental Debris on the Lunar Surface and the History of Bombardment of the Moon. *Instituto de Investiga-*

- ciones Geologicas de la Diputacion Provincial, Vol. XXV, Universidad de Barcelona, 1971.
64. HARTMANN, W. K., Paleocratering of the Moon, Review of Post-Apollo Data. *Astr. Space Sci.*, Vol. 16, 1972, pp. 183-199.
 65. SODERBLUM, L. A., AND L. A. LEBOWSKY. Technique for Rapid Determination of Relative Ages of Lunar Areas From Orbital Photography. *J. Geophys. Res.*, Vol. 77, 1972, pp. 279-296.
 66. ANDERS, E., R. GANAPATHY, U. KRÄHENBÜHL, AND J. W. MORGAN, Meteoritic Material on the Moon. *The Moon*, Vol. 8, 1973, pp. 1-24.
 67. BARBER, D. J., R. COWSIK, I. D. HUTCHESON, P. B. PRICE, AND P. S. RAJAN, Solar Flares, the Lunar Surface and Gas-Rich Meteorites. *Proc. Second Lunar Science Conference, Geochimica et Cosmochimica Acta*, Supplement 2, Vol. 3, 1971, pp. 2705-2714.
 68. RANCITELLI, L. A., Personal communication, 1973.
 69. CROZAZ, G., R. DROZD, C. M. HOHENBERG, H. P. HOYT, D. RAGAN, R. M. WALKER, AND D. YUHAS, Solar Flare and Galactic Cosmic Ray Studies of Apollo 14 and 15 Samples. *Proc. Third Lunar Science Conference, Geochimica et Cosmochimica Acta*, Supplement 3, Vol. 3, 1972, pp. 2917-2931.
 70. BROWNLEE, D. E., W. BUCHER, AND P. HODGE, Micrometeoroid Flux From Surveyor Glass Surfaces. *Proc. Second Lunar Science Conference*, Vol. 3, 1971, pp. 2781-2789.
 71. JAFFE, L. D., Lunar Surface: Changes in 31 Months and Micrometeoroid Flux. *Science*, Vol. 170, 1970, pp. 1092-1094.
 72. FLEISCHER, R. L., H. R. HART, AND W. R. GIARD, Surface History of Lunar Soils and Soil Columns. *Geochimica et Cosmochimica Acta*, Vol. 38, 1974, pp. 341-484.
 73. BHANDARI, N., J. N. GOSWAMI, S. K. GUPTA, D. LAL, A. S. TAMHANE, AND V. S. VENKATAVARADAN, Collision Controlled Radiation History of the Lunar Regolith. *Proc. Third Lunar Science Conference, Geochimica et Cosmochimica Acta*, Supplement 3, Vol. 3, 1972, pp. 2811-2829.
 74. GOSWAMI, J. N., AND D. LAL, Cosmic Ray Irradiation Pattern at the Apollo 17 Site: Implications to Regolith Dynamics. *Lunar Science*, Vol. V, Lunar Science Institute, Houston, 1974, pp. 284-286.
 75. STORZER, D., AND J. B. HARTUNG, In preparation, 1974.
 76. BROWNLEE, D. E., AND R. S. RAJAN, Micrometeorite Craters Discovered on Chondrule Like Objects From Kapoeta Meteorite. *Science*, Vol. 182, 1974, pp. 1341-1344.
 77. RAJAN, R. S., D. E. BROWNLEE, AND F. HÖRZ, The Ancient Micrometeorite Flux, *Lunar Science*, Vol. V, Lunar Science Institute, Houston, 1974, pp. 616-617.
 78. RUSS, G. P., D. S. BURNETT, AND G. J. WASSERBURG, Lunar Neutron Stratigraphy. *Earth Planet. Sci. Letters*, Vol. 15, 1972, pp. 172-186.
 79. ASHWORTH, D. G., AND J. A. M. McDONELL, Updated Micrometeorite Influx Rates on the Lunar Surface Deduced From New Measurements of the Solar Wind Sputter Rate and Surface Crater Statistics. COSPAR, Konstanz, Germany, May 23 to June 5, 1973; *Space Res.* Vol. 13, pp. 1071-1083.
 80. MARCUS, A. H., A Stochastic Model of the Formation and Survival of Lunar Craters: 2. *Icarus*, Vol. 5, 1966, pp. 165-177.
 81. OBERBECK, V. R., AND W. L. QUAIDE, Genetic Implications of Lunar Regolith Thickness Variations. *Icarus*, Vol. 9, 1968, pp. 446-465.
 82. OBERBECK, V. R., W. L. QUAIDE, M. MAHAN, AND J. PAULSON, Monte Carlo Calculations of Lunar Regolith Thickness Distribution. *Icarus*, Vol. 19, 1973, pp. 87-107.
 83. GAULT, D. E., F. HÖRZ, J. B. HARTUNG, AND D. E. BROWNLEE, Mixing of the Lunar Regolith. *Lunar Science*, Vol. V, Lunar Science Institute, Houston, 1974, pp. 260-262; also in *Proc. Fifth Lunar Science Conference*.
 84. MOLINA, E. C., *Poisson's Exponential Binominal Limit*. Van Norstrand, Princeton, 1942.
 85. HÖRZ, F., E. SCHNEIDER, AND R. E. HILL, Micrometeoroid Abrasion of Lunar Rocks: A Monte Carlo Simulation. *Proc. Fifth Lunar Science Conference*, Vol. 3, 1974, pp. 2397-2412.
 86. GAULT, D. E., W. L., QUAIDE, AND V. R. OBERBECK, Impact Cratering Mechanics and Structures. *Shock Metamorphism of Natural Materials*, B. M. French and N. M. Short, eds., Mono-Book, Baltimore, 1968, pp. 87-99.
 87. STÖFFLER, D., M. R. DENCE, M. ABADIAN, AND G. GRAUP, Ejecta Formations and Preimpact Stratigraphy of Lunar and Terrestrial Craters: Possible Implications for the Ancient Lunar Crust. *Lunar Science*, Vol. V, Lunar Science Institute, Houston, 1974, pp. 746-748.
 88. SCHNEIDER, W., Petrologische Untersuchungen der Bunten Breccie im Nördlinger Ries. *N. Jb. Miner. Abh.*, Vol. 114, 1974, pp. 136-180.
 89. HÖRZ, F., Structural and Mineralogical Evaluation of an Experimentally Produced Impact Crater in Granite. *Contr. Mineral. and Petrol.*, Vol. 21, 1969, pp. 365-377.
 90. KING, E. A., J. C. BUTLER, AND M. F. CARMAN, Chondrules in Apollo 14 Samples and Size Analyses of Apollo 14 and 15 Fines. *Proc. Third Lunar Science Conference, Geochimica*

- et Cosmochimica Acta*, Supplement 3, Vol. 1, 1972, pp. 673-686.
91. MCKAY, D. S., R. M. FRULAND, AND G. HEIKEN, Grain Size Distribution as an Indicator of the Maturity of Lunar Soils. *Lunar Science*, Vol. V, Lunar Science Institute, Houston, 1974, pp. 480-481.
92. GAULT, D. E., AND J. A. WEDEKIND, The Destruction of Tektites by Micrometeoroid Impact. *J. Geophys. Res.*, Vol. 74, 1969, pp. 6780-6794.

Page intentionally left blank

Page intentionally left blank

Lunar Highlands Breccias Generated by Major Impacts¹

Odette B. James
U. S. Geological Survey
Reston, Virginia

The lunar missions have returned a variety of types of breccias. These rocks differ greatly in their mechanisms of formation, source materials, and histories after formation, but all have a common factor involved in their genesis in that all formed by processes related to impact bombardment of the lunar surface. Among all these types of breccias, there is one particular class (if it can be identified) that holds great potential for study of the early history of the lunar crust. This is the class of breccias that formed as a result of the major impacts—the impacts that generated the mare basins and the largest of the lunar craters. Impacts of this magnitude would have penetrated deeply into the lunar crust, and perhaps even through it into the lunar mantle. They would have excavated both materials of the upper parts of the crust and deep-seated rocks; among the latter might have been rocks that had originated in the early stages of crustal evolution and had not been greatly disturbed by impact since they formed. If some breccias can definitely be established as representing little-reworked ejecta from large events, studies of the materials they contain could permit a partial reconstruction of the pre-impact lunar crust at the site of impact. In this paper I discuss the processes that may have been involved in the formation of most of the major types of lunar breccias (table 1), and I identify some of the types of highlands breccias that may have originated in large impacts.

¹Publication authorized by the Director, U.S. Geological Survey.

Terrestrial Impact Breccias

To aid in determining which of the lunar breccias may be related to major impacts, it is of value to compare them with terrestrial impact breccias. The general characteristics of terrestrial impact breccias are briefly described below; the discussion is based mainly on the characteristics of breccias associated with the Ries Crater in Germany (refs. 1 and 13), but data from other structures are also included.

Breccias associated with the Ries Crater are of three main types: (1) brecciated bedrock, (2) Bunte breccia and Gries, and (3) suevite. The brecciated bedrock is material that was deformed during the impact event but remained in place, whereas the Bunte breccia, Gries, and suevite are deposits of different kinds of ejected materials.

Brecciated bedrock lines the floor and walls of the crater cavity. The rocks are sheared and granulated and their minerals locally show weak shock-induced plastic deformation.

Bunte breccia and Gries ejecta deposits form a blanket of wide lateral extent surrounding the crater. These breccias consist of the earliest deposited of the ejected materials. They are composed of crushed but largely unshocked rocks and contain little or no impactite glass or melt rocks. The clasts they contain come from relatively high in the pre-impact stratigraphic sequence.

Suevite ejecta deposits are concentrated on the rim and within the cavity of the crater,

Table 1.—*Types of Lunar Highlands Breccias*

Type	Designations Used by Other Investigators	Site	Examples
Regolith Breccia ^{(1), (12)}	Soil breccia Apollo 14 group F ₁ ⁽²⁾ Apollo 14 metamorphic group 1 ⁽³⁾ Vitric matrix breccias ⁽⁷⁾	All	14042, 14047, 14049, 14313
Cataclastic Anorthosite ^{(4), (5)}	Cataclastic rocks ⁽⁷⁾ Samples are included in Apollo 16 groups C ₁ and B ₁ ⁽⁸⁾ Brecciated anorthositic rocks ⁽¹²⁾	Major type at Apollo 16	60015, 60025, 62237, 67075
Black and White Rocks ⁽⁶⁾ White Fraction Black Fraction	Cataclastic rocks ⁽⁷⁾ Basaltic matrix breccia ⁽⁷⁾ Blue-gray breccia dike ⁽⁹⁾	Important type at Apollo 15, 16, 17	15455, 77075 + 77215
Partially Molten Breccias ⁽⁴⁾ (do not include all samples of this class) White Fraction Black Fraction	Samples are included in Apollo 16 group B ₂ ⁽⁸⁾ Cataclastic rock ⁽⁷⁾ Basaltic matrix breccia ⁽⁷⁾	Minor type at Apollo 16	61015, 64475
Light-Gray Breccias ⁽¹⁰⁾		Minor type at Apollo 17	72215, 72255, 73215, 73255, 72275
Blue-Gray Breccias ⁽¹⁰⁾	Blue-gray matrix-rich breccia ⁽¹⁴⁾ Basaltic matrix breccia ⁽⁷⁾	Major type at Apollo 17	73235, 76315, 77115
Thermally Metamorphosed Breccias	Annealed Fra Mauro breccias ⁽¹⁾ Apollo 14 Group F ₄ ⁽²⁾ Apollo 14 metamorphic groups 4-8 ⁽³⁾ High grade breccias ⁽⁷⁾	Major type at Apollo 14	14270, 14303, 14305, 14306, 14311, 14321, 12013

Glass-poor Feldspathic Breccias	Unannealed Fra Mauro breccias ⁽¹⁾ Apollo 14 group F ₃ ⁽²⁾ Apollo 14 metamorphic group 3 ⁽³⁾ Light matrix breccia ⁽⁷⁾ Apollo 16 group B ₂ ⁽⁸⁾ Polymict breccia ⁽⁹⁾ Feldspathic breccia ⁽¹²⁾	Apollo 14 white rocks on Cone Crater rim, bedrock at Apollo 16 North Ray Crater	14063, 14082, 67015, 67016, 67455
Green-Gray Breccia ⁽¹⁰⁾ or Poikilitic Rock ⁽⁶⁾	Poikilitic matrix breccia ⁽⁷⁾ Samples included in Apollo 16 group C ₂ ⁽⁸⁾	Minor type at Apollo 16, major type at Apollo 17	60315, 65015, 76015, 77135, 62235

NOTES: (1) reference 1; (2) reference 2; (3) reference 3; (4) reference 4; (5) reference 5; (6) reference 6; (7) reference 7, this conference;
(8) reference 8; (9) reference 9; (10) reference 10; (11) reference 11; and (12) reference 12.

and they overlie deposits of the Bunte-breccia type. They consist of the last of the ejected materials. The deposits are poorly sorted and unstratified, but the fragments within them show planar preferred orientations. Abundant clasts of shocked as well as crushed rocks are present. Also present are large proportions of impactite glass, most of which represents impact melt that solidified in flight prior to deposition. Most of the material in the deposit cooled considerably in the time interval between ejection and deposition, and there was little or no consolidation of the breccia by sintering or cementation by hot interstitial glass. Most of the fragments and melt are derived from rocks relatively deep in the pre-impact stratigraphic sequence, although materials from higher levels are also present. Glass content of the breccia and depth of source of the fragments it contains show a rough positive correlation. (Fragment population studies of Ries suevite have been reported by Ackermann (ref. 14) and Chao (ref. 1). Ackermann found that 80 percent by volume of the suevite he studied was fine-grained matrix; of the remaining volume of the rock, from 55 to 90 percent was glass bombs, from 10 to 35 percent was fragments of deep-seated rocks, and less than 5 percent was fragments of shallow origin. Data on fragment abundances given by Chao are as follows: for most suevites he studied he found from 62 to 75 percent glass bombs, from 18 to 30 percent fragments of deep-seated rocks, and from 2 to 8 percent fragments of shallow origin; but one suevite contained 52 percent glass bombs, 15 percent fragments of deep-seated rocks, and 27 percent fragments of rocks from shallow levels.)

Impactite glass was incorporated in the suevite in the form of small fragments, bombs, and coatings on lithic clasts. Much of this glass is vesicular (fig. 1) and there is evidence that the impact melt from which it formed possessed a considerable degree of superheat; Hörz (ref. 15) and El Goresy (ref. 16) estimated original temperatures in excess of 1500° C and 1700° C, respectively, for these melts. The melts incorporated highly

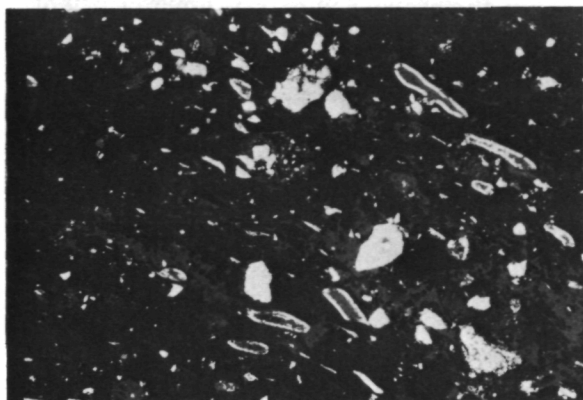


Figure 1.—Photomicrograph of impactite glass bomb from Ries Crater (sample, courtesy of E. C. T. Chao). (Width of field of view is 2.2 mm; crossed polarizers.) The glass (black and gray) contains fragments of unshocked and shocked mineral grains (white) and claylined vesicles (ovoids rimmed in white). Flowage in the impact melt flattened the vesicles and aligned and oriented the included fragments.

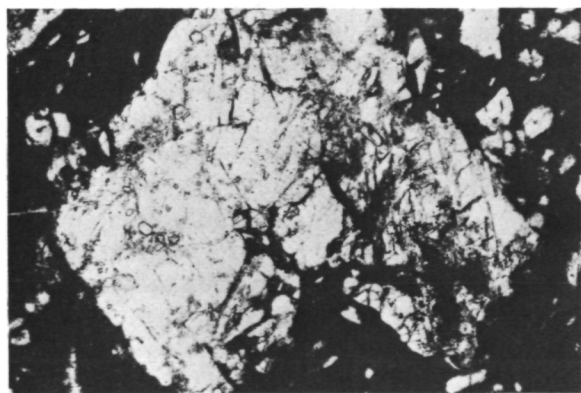


Figure 2.—Photomicrograph of anorthositic lithic clast in impactite glass from Clearwater Lake, Canada (sample, courtesy of M. R. Dence). (Width of field of view is 2.2 mm; plane-polarized light.) The clast shows partial melting along internal grain boundaries (induced by heating after incorporation in the melt). Matrix of the sample is devitrified glass (black) that contains abundant small fragments of unshocked, shock-deformed, and recrystallized mineral grains.

variable proportions of lithic and mineral fragments. Many of these fragments are of broken but undeformed rocks and mineral grains; but significant numbers of grains of the amorphous glass and shock-deformed mineral grains are also present. The fragments show large variations in thermal history that may reflect variations in the post-shock temperatures they attained prior to being incorporated in the melt. Many grains show no evidence of being strongly heated, despite the high temperatures of the surrounding impact melts, and they may have been quite cool when incorporated. In contrast, some of the fragments of the amorphous glass and shocked minerals have recrystallized, and some of the unshocked lithic fragments show partial melting at grain boundaries (fig. 2); such fragments may have been strongly heated during the impact so that the added heating they received after incorporation in the impact melt produced the recrystallization and partial melting.

Lunar Breccias

REGOLITH BRECCIAS

The most widespread type of lunar breccia is regolith breccia (also referred to as soil breccia by many investigators). These rocks are not related to single impacts, but instead represent consolidated lunar surface debris that had been reworked by countless impacts prior to lithification. Such breccias are strongly preponderant at mare sites, but they have been returned from all highlands sites as well. The features diagnostic of this type of rock are illustrated below by an outline of the characteristics of the Apollo 14 regolith breccias, the most extensively studied group of highlands regolith breccias.

The nature of the fragment assemblage and matrix strongly reflects the fact that the particles had a history of extensive impact reworking and mixing at the lunar surface prior to consolidation of the breccia (fig. 3). Clasts tend to be small because they have

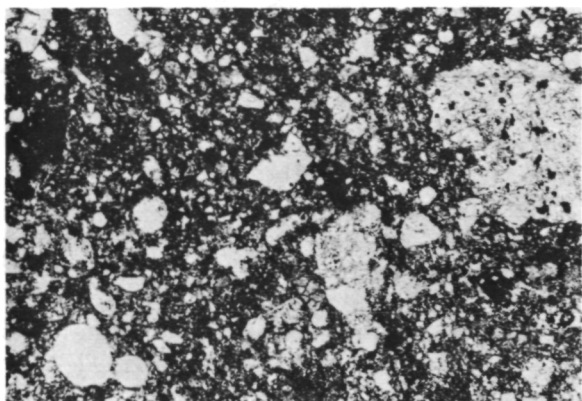


Figure 3.—Photomicrograph of regolith breccia 14313. (Width of field of view is 2.2 mm; plane-polarized light.) Diverse lithic, mineral, and glass clasts are set in a glass-rich matrix. Grain size distribution is roughly seriate. Spheres of fragment-free glass (bottom and center left) and fragments of devitrified glass (lower center) are characteristic of such breccias. Lithic fragments in the field of view are fine-grained hornfelses.

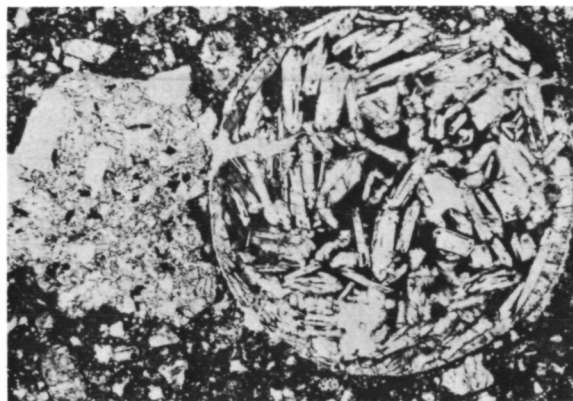


Figure 4.—Photomicrograph of particles in regolith breccia 14313. (Width of field of view is 2.2 mm; plane-polarized light.) The fragment at the left is a fine-grained hornfels. The fragment at the right is a spherule of devitrified glass with chondrule like texture.

been subjected to several episodes of fragmentation (Wilshire and Jackson (ref. 2) found that no more than 10 percent, and usually less than 5 percent, of the clasts are larger than 1 mm across). Size distribution of fragments tends to be seriate. Among the clasts are particles of diverse textures and compositions derived from many different source areas, but most of the clasts come from local bedrock. The breccias are very rich in glass that is free of included fragments; this glass forms much of the matrix material and a very great proportion of the larger clasts (Wilshire and Jackson reported that chips and spheres of fragment-free glass form from 35 to 50 percent of clasts in the 0.1- to 1-mm size range). Several types of clasts are characteristic (figs. 3 and 4), including angular chips and spheres of fragment-free glass; devitrified glasses, some with chondrule-like textures; glasses with flow structures; glass-coated clasts; and fragments that show the effects of multiple impacts.

Bulk composition and physical characteristics reflect the mixing, incorporation of

meteoritic matter, and exposure to solar-wind and extralunar particle bombardment that took place while the breccia constituents formed loose particulate materials in the regolith. The breccias are very similar in bulk composition to fines samples (refs. 17 and 18). They have relatively high contents of iron metal and of the siderophile and volatile trace elements associated with meteorites (ref. 19). They are rich in solar-wind-implanted C and N (refs. 20 and 21) and in trapped solar-wind rare gases (refs. 22 and 23). The O^{18} is enriched relative to O^{16} (ref. 24), and the clasts contain solar-flare and cosmic-ray tracks (refs. 25 and 26).

LIGHT-GRAY BRECCIAS

One suite of lunar breccias may be analogous to terrestrial suevites; if so, these breccias were probably produced in a very large impact event. The rocks of this suite are the Apollo 17 samples that have been termed light-gray breccias (ref. 10). Only six hand samples were returned; four were collected from a single large boulder at the base of South Massif (72215, 72235, 72255, 72275), and two were picked up as loose rock samples

from regolith developed on the light mantle avalanche deposit (73215, 73255). It appears that both the boulder and the avalanche were derived from a layer that caps South Massif, and it has been suggested that this layer represents a deposit of Serenitatis or Imbrian ejecta (H. H. Schmitt and W. R. Muehlberger, oral communication).

The light-gray breccias may be divided into three types. Rocks of the first type (represented by 73255) appear to consist of fragment-laden devitrified glass; they may be analogous to the impactite glass bombs that are found within suevite. Rocks of the second type (represented by 73215, 72255, and 72215) appear to consist of aggregates of fragments bonded by variable amounts of devitrified and recrystallized glass; no analogous materials are found in suevite. Rocks of the third type (represented by 72275 and part of 72235) are poorly consolidated aggregates of mineral and lithic debris, contain clasts of the other two types of light-gray breccia, and may be analogous to bulk suevite.

Light-gray breccia of the first type in hand specimens is a gray aphanite that contains

sparse xenocrysts and xenoliths. Sample 73255, the only large sample of this type, has a vesicular outer rind, a nonvesicular interior, and an ovoid shape that appears to be close to the primary shape of the rock. In thin section (fig. 5), these breccias are composed of abundant small xenocrysts and xenoliths set in a dark groundmass, and grain size distribution appears bimodal rather than seriate. The groundmass consists of minute mineral fragments cemented by material that has a texture suggestive of devitrified glass (fig. 6). It is difficult to distinguish the finest mineral fragments in the groundmass because of possible modification of their outlines by recrystallization; their proportions can only be roughly estimated and may be very great.

Most clasts in light-gray breccias of this type are of angular unshocked mineral grains and show no evidence of strong heating, significant equilibration with groundmass, or partial melting. A small proportion of the clasts, however, do show thermal and deformational effects; some of the lithic clasts show interstitial partial melting that was induced by thermal heating after they were incorporated in the fragment-laden melt

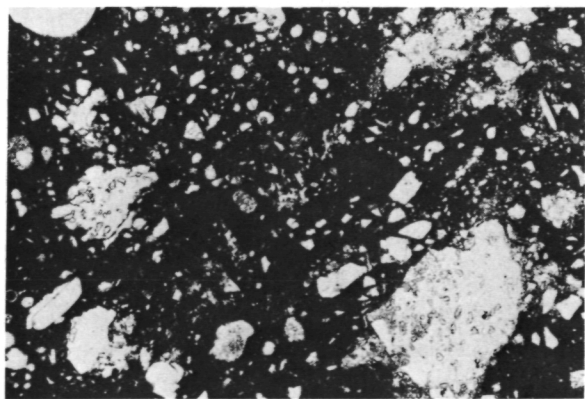


Figure 5.—Photomicrograph of glass-rich light-gray breccia 73255. (Width of field of view is 2.2 mm; plane-polarized light.) Grain size distribution appears roughly bimodal, with clasts clearly distinguishable from the dark, very fine grained groundmass. Most clasts are of mineral fragments, and they show planar preferred orientation (NE. to SW.) produced by flow of the glassy groundmass. The rock is locally vesicular (clear ovoids in upper left part of field).

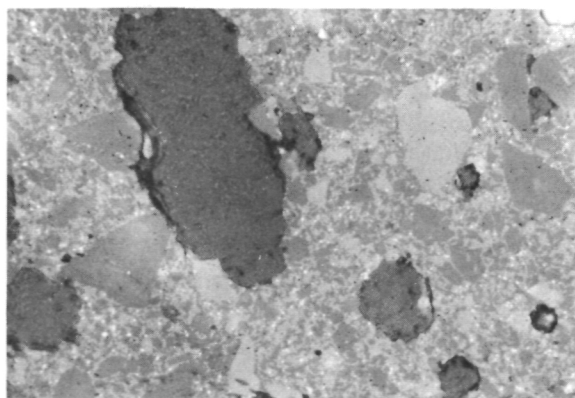


Figure 6.—Photomicrograph of matrix of glass-rich light-gray breccia. (Width of field of view is .22 mm; reflected light.) Dark ovoids with textured appearance are vesicles. Angular and rounded fragments of mafic minerals (high reflectivity) and plagioclase (low reflectivity) are enclosed by material that has minute grain size and a texture suggestive of devitrified glass.

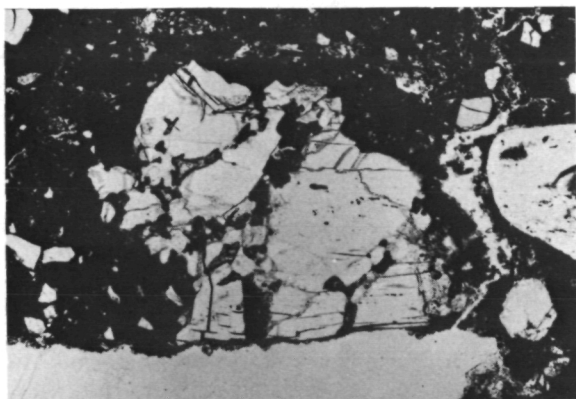


Figure 7.—Photomicrograph of anorthositic lithic clast in glass-rich light-gray breccia. (Width of field of view is 2.2 mm; plane-polarized light.) The clast shows partial melting along internal grain boundaries.

(fig. 7); and some of the monomineralic clasts are of recrystallized shocked plagioclase and devitrified maskelynite (these appear to be more abundant than in other types of detrital lunar breccias, such as regolith breccias). Most of the fragments appear to have been derived from only a few suites of parent rocks. The two major parent suites were (1) coarse-grained plutonic troctolites and troctolitic anorthosites and (2) anorthositic-noritic-troctolitic hornfelses. Clasts of fragment-free glass and clasts that show the effects of multiple impact are rare. This clast assemblage suggests that part of the source terrane was deep and not previously plumbed by impact. (The clast assemblage is described in greater detail in a later section, where an attempt is made to reconstruct the source terrane of the light-gray breccias of types 1 and 2.)

Rocks of the second type of light-gray breccia are similar to the fragment-laden devitrified glasses of the first type, except that they appear to have initially contained more fragments and less glass, and they underwent considerable shearing and recrystallization during or following consolidation. From relations visible in the boulder from which two of these samples were collected, it appears that they were probably deposited

as large "clots" or clasts within a matrix of light-gray breccia of the third type.

Breccias of the third type are friable aggregates of mineral and lithic debris, in which only sparse interstitial glass is present, binding fragments together. However, the dominant kind of clast in these rocks is of fragment-laden devitrified glass equivalent to light-gray breccia of the first type (ref. 27). Significant numbers of these clasts are composite; they have large cores consisting of lithic fragments and rinds of fragment-laden devitrified glass, and in some of these composite clasts the rinds are vesicular.

In the characteristics described above, the fragment-laden devitrified glass that forms the first type of light-gray breccia is remarkably like impactite glass from terrestrial suevite. The shape of the one hand-specimen-sized example, 73255, suggests that this rock may be a lunar analog of the glass bombs from suevite deposits. This type of breccia is very different from regolith breccia, and it probably cannot be interpreted as reheated regolith material. In this type of light-gray breccia the most abundant clasts are of single mineral grains, and fragments of glass are rare, whereas in regolith breccias the most abundant clasts are of glass. The mineral and lithic fragments do not show the diversity of sources that characterizes the regolith breccias; instead, they appear to have been derived from only a few major suites of parent rocks, and deep-seated rocks were abundant in the source terrane. Grain sizes have a bimodal-appearing distribution, in contrast to the seriate-appearing distribution in the regolith breccias. The evidence for variable heating of clasts suggests that not all the clasts had the same thermal history; some may have been hot when incorporated into the glassy groundmass, but others may have been relatively cool. The presence of vesicles establishes that the groundmass was at, or near, melting temperature; so it is necessary that the entire rock would have cooled rapidly to avoid equilibration of clasts with their surroundings.

All these characteristics of this fragment-laden devitrified glass suggest that its genesis

is best interpreted in terms of processes operating during a very large impact event. In this interpretation, the xenocrysts, xenoliths, and fine-grained mineral powder in the groundmass represent debris ejected as a cloud during the impact event. The devitrified glass that binds the fragments together represents impact melt that penetrated this debris cloud while it was still in flight and cemented the particles together. Some fragments in the cloud were hot while others were cool. The entire aggregate solidified and cooled rapidly so that only the hot fragments partly melted, whereas those that were incorporated while cool were unable to react with surrounding material. (An interpretation nearly identical to the one proposed here has also been suggested for similar rocks by members of the consortium studying the light-gray breccia samples from the boulder (ref. 28)). The major difference in textures between these lunar fragment-laden glasses and terrestrial impactite glasses is that the lunar glasses seem to have contained much larger proportions of fragments and much smaller proportions of melt. It may be that this difference is a function of differences in conditions of formation, or it may simply be that the markedly lower viscosities of impact melts of the compositions of lunar

rocks permitted them to incorporate far larger proportions of debris.

In this interpretation, rocks of the second type of light-gray breccia could have formed by the same process as the fragment-laden glasses of the first type, only with the ejected debris penetrated to a lesser extent by impact melt. The friable, glass-poor matrix of rocks of the third type might represent ejected debris that was only sparsely penetrated by impact melt. Thus the glass-rich rocks of the first type would be analogous to impactite glass bombs deposited within suevite; rocks of the second type would have a somewhat similar origin; and rocks of the third type would be analogous to bulk samples of suevite.

OTHER BRECCIAS SIMILAR TO GLASS-RICH (TYPES 1 AND 2) LIGHT-GRAY BRECCIAS

Breccias with textures and fragment populations like the glass-rich light-gray breccias are widespread on the lunar surface. The types that occur as large samples are the black material within "black and white rocks" (described in the following section), and the Apollo 17 blue-gray breccias (ref. 10). Most samples of breccias like these, however, do not occur as large hand specimens; they occur instead as small fragments in fines fractions and as clasts in other breccias. Such rocks form the most abundant type of clast in the greater-than-0.1-mm size range in the Apollo 14 thermally metamorphosed breccias (refs. 1 and 2). They make up the dark material in the highly potassic and siliceous thermally metamorphosed breccia 12013, and they are also important as clasts in glass-poor feldspathic breccias from the Apollo 14 and 16 sites. The abundance and widespread distribution of such rocks suggest that they represent an important facies of lunar impact-generated breccia.

The Apollo 17 blue-gray breccias (fig. 8) are similar to the glass-rich light-gray breccias in that they have a bimodal-appearing grain size distribution (clasts set in an

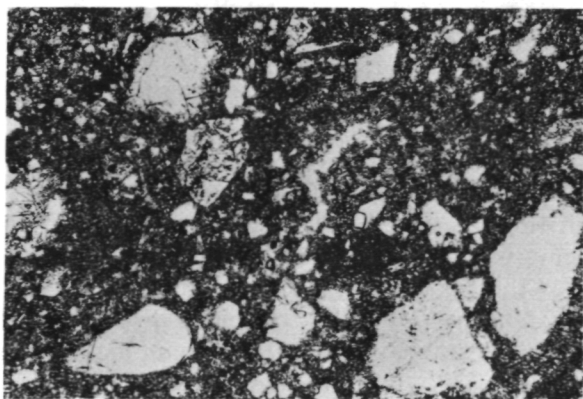


Figure 8.—Photomicrograph of blue-gray breccia 77115. (Width of field of view is 2.2 mm; plane-polarized light.) Fragments are dominantly of mineral grains and are set in a fine-grained dark matrix.

aphanitic groundmass) and they have similar types of fragment suites (derived from fairly restricted source terranes; mineral fragments dominant, glass fragments rare). Also they are locally vesicular. In the blue-gray breccias, however, equilibration between fragments and groundmass was more extensive, and groundmass crystallization was better developed than in the similar light-gray breccias. Blue-gray breccias are themselves quite variable in fragment assemblage and extent of groundmass-clast reactions. One of the samples, 73235, has a fragment assemblage nearly identical with that of light-gray breccia 73215 (type 2). Sample 73235 seems to differ from 73215 primarily in that it was more plastic during its episode of late shear, and its postconsolidation crystallization produced a denser, more coarsely crystalline groundmass. Another sample, 77115, differs considerably from light-gray breccia 73215 both in fragment suite and in groundmass texture. Although the relative proportions of mineral versus lithic clast are roughly similar in 73215 and 77115, the suite of parent rocks from which the fragments were derived appears to have been different. Sample 77115 also shows evidence of very extensive equilibration of clasts with groundmass; for example, some fragments of plagioclase show partial melting textures and overgrowths, and others are zoned; fragments of olivine are zoned; and fragments of subcalcic augite show partial melting textures, resorption of exsolution lamellae, and broad overgrowths of pigeonite.

Possible explanations for the differences between glass-rich light-gray breccias and blue-gray breccias might be that the latter were formed by the same processes as the former, but they had (1) higher initial temperatures, (2) larger initial proportions of melt, (3) longer cooling times, and/or (4) slightly higher confining pressures during cooling. There may have been considerable variation in these parameters even within the suite of blue-gray breccias; in samples like 77115, the initial groundmass melt may have been even hotter or present in even larger proportions, or cooling may have been

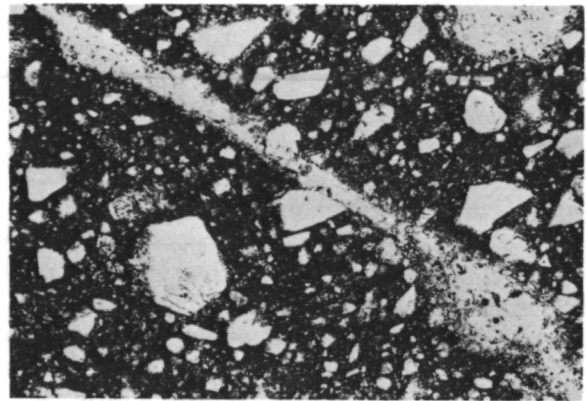


Figure 9.—Photomicrograph of dark material in thermally metamorphosed breccia 12013. (Width of field of view is 2.2 mm; plane-polarized light.) As in light-gray breccia 73255 (see fig. 5), most clasts are of single mineral grains, and fragments and groundmass have the appearance of being two distinct materials. Fragment sizes are similar to those in 73255, and the fragments show rough planar preferred orientation (NE. to SW.). This rock is unusually rich in material of the composition of lunar "granite" and a veinlet of such material cuts the field of view (NW. to SE.).

even slower than in others of the blue-gray breccias like 73235.

In Apollo 14 thermally metamorphosed breccias, the types of clast that are similar to blue-gray and glass-rich light-gray breccias are those that were termed fine-grained hornfelsed noritic microbreccias and annealed fragment-laden glasses by Chao (ref. 1), and were designated as type D₄ by Wilshire and Jackson (ref. 2). The similar material in 12013 (fig. 9) was referred to as the dark lithology (ref. 29), "black end member" (ref. 30), and dark aggregate (ref. 31). Textures of these materials are essentially similar to those of the blue-gray and glass-rich light-gray breccias (though bulk compositions are different). Most fragments they contain are of unshocked, undeformed mineral grains, but significant proportions of devitrified maskelynite and recrystallized shocked plagioclase are present. (In the dark material in 12013, volume percentages of fragments larger than 0.1 mm are as follows (James, unpublished): 36, undeformed plagioclase;

2, shocked plagioclase; 12, pyroxene; and 13, other minerals, for a total of 63 percent mineral fragments; and 5, anorthositic-noritic-troctolitic hornfels; 9, anorthosite; and 20, quartzo-feldspathic rock, for a total of 34 percent lithic fragments.) Reactions of clasts with groundmass are well developed, as in the blue-gray breccias. Locally, the groundmass is vesicular. The major textural difference between these rocks and the glass-rich light-gray and blue-gray breccias is that the groundmass has very fine granoblastic texture rather than subophitic, poikilitic, or devitrified glass texture.

CATACLASTIC ANORTHOSITES AND "BLACK AND WHITE ROCKS"

One suite of lunar breccias is probably analogous to the terrestrial impact breccias that line crater cavities and make up most of the fragments in deposits of the Bunte-breccia type. Large samples of this suite were collected at the Apollo 15, 16, and 17 sites. Among them are the rocks that were termed cataclastic anorthosites by the Apollo 16 LSPET (ref. 4) and "black and white rocks" by the Apollo 15 LSPET (ref. 6); some of the Apollo 16 samples called "partially molten breccias" (ref. 4) are probably also members of this suite.

The cataclastic anorthosites and the white materials of the "black and white rocks" are sheared and granulated samples that were originally medium- to coarse-grained plutonic crystalline rocks (fig. 10). (Here the name "anorthosite" is used as a general term to indicate that most of the samples are anorthosites and troctolitic, noritic, and gabbroic anorthosites; in fact, the suite also includes norites, olivine norites, and troctolites.) Many, perhaps most, of the breccias appear to be monomict or composed of fragments of a few related types of plutonic rocks. Deformation history varies considerably from sample to sample; some were only crushed, some were recrystallized after crushing, and some had several episodes of deformation and recrystallization. Most samples, however, re-

tain some relict areas of medium-grained to coarse-grained textures and mineralogies that indicate they had equilibrated at subsolidus temperatures prior to granulation. (In many samples, compositions and structures of the minerals suggest that, during formation of the coarse-grained texture, the rocks were equilibrated over large volumes at subsolidus temperatures on the order of 600 to 800 degrees Centigrade.)

The nature and degree of deformation shown by these rocks are typical of brecciated bedrock lining crater cavities, or of blocks forming Bunte-breccia-type deposits. Shear and granulation dominate, shock effects are absent or weak, and relict textures are abundantly preserved. The textures, mineral compositions, and mineral structures show that most of these samples cannot have been deformed and recrystallized more than a few times in the period between the impact event that excavated them and the episode of magmatic crystallization or metamorphic equilibration that formed the initial coarse-grained

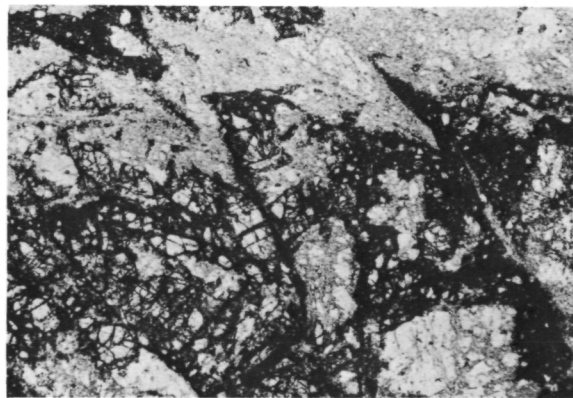


Figure 10.—Photomicrograph of white cataclasite in 15455. (Width of field of view is 2.2 mm; plane-polarized light.) The rock is an intensely sheared and granulated norite in which plagioclase (white, low relief) and orthopyroxene (gray, higher relief) are the dominant minerals. The white and gray areas are composed of minutely granulated aggregates of plagioclase and pyroxene, respectively; the size of these areas reflects the original grain size of the rock. Two intersecting sets of shear planes are prominent in this field of view (E.-W. and NNW.-SSE.).

texture. D. B. Stewart (oral communication) estimates that times on the order of hundreds of millions of years were necessary to achieve the degree of equilibration that was attained during the formation of the initial texture. Because the times involved are so long, the rocks may be relicts preserved from the early stages of crustal evolution. These rocks must have resided during their equilibration period at deep levels within the lunar crust, in order to have been protected from the effects of intense impact bombardment at the highlands' surface. The events required to deform and excavate them must have been very large in order to penetrate to plutonic bedrock that had been little disturbed by previous impacts.

The black materials in the "black and white rocks" appear to represent fragment-laden melts that intruded the white rocks. Evidence leading to this interpretation comes from the characteristics of 15455 (one of the first of the "black and white rocks" to be returned) and 77075 plus 77215 (black dike and white crushed norite in a boulder at the Apollo 17 South Massif). Relationships between the black and white materials seen in the hand specimens and at the outcrop clearly show that the black materials intrude and include the white materials (ref. 32 and 9). In both 77075 and 15455, the black rocks are dense and aphanitic; they consist of abundant xenocrysts and xenoliths set in a very fine grained groundmass that has igneous texture (fig. 11). The xenocrysts and xenoliths are from diverse rock types, and some are clearly not derived from the immediately surrounding white rock. (In 77075, for example, olivine fragments are abundant and clasts of fine-grained hornfels are present, although these materials are rare or absent in the surrounding white norite 77215. Conversely, fragments of the orthopyroxene that typifies the norite are not abundant in the dike.) In both 77075 and the black material in 15455, some of the xenocrysts are of rounded and spherulitic devitrified maskelynite (fig. 11); these grains had a history of more intense shock than the immediately surrounding white rock. In black material in

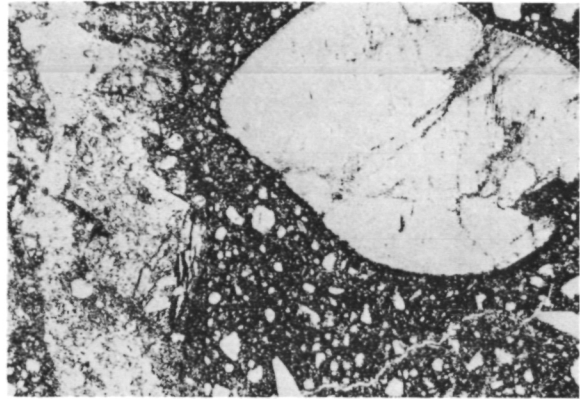


Figure 11.—Photomicrograph of contact of black and white materials in 15455. (Width of field of view is 2.2 mm; plane-polarized light.) The contact is sharp, and the black rock (right) consists of an aggregate of fragments in a dark groundmass that has very fine grained igneous texture. Rounded fragments of spherulitic devitrified maskelynite (top right) are present; such fragments may have originated as ejecta, and their presence suggests an ejection history of some of the material in the black rock.

15455 particles of nickel-iron are present; analyses of siderophile trace elements and Ni show that these are of meteoritic origin and that the associated white rock does not contain any similar material (ref. 33).

The Apollo 16 "partially molten breccias" that may be related to the "black and white rocks" differ from the samples described above in several significant respects. Two examples are 61015 and 64475 (fig. 12). In these breccias the black dike rocks were nearly all melt when emplaced, and contained only sparse fragments. Most of the silicate clasts could have been derived from the white host rocks, but large nickel-iron globules that are probably from an exotic source are also present. These breccias show evidence of a complex injection and deformation sequence (hence the name "partially molten breccias"). Textures and structures visible in the hand specimens and thin sections suggest the following interpretation of the history of these rocks: The black dikes were injected into the white rocks while the latter were undergoing cataclastic deformation.

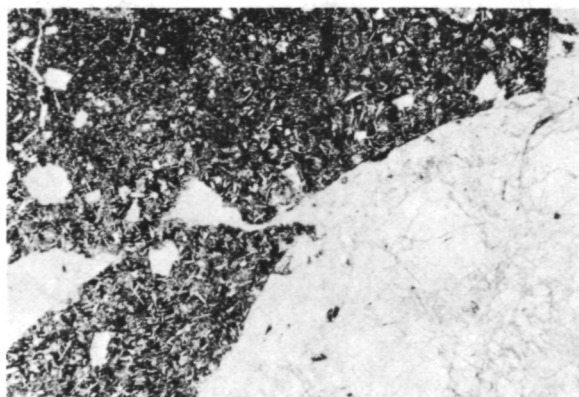


Figure 12.—Photomicrograph of “partially molten breccia” 61015. (Width of field of view is 3.52 mm; plane-polarized light.) The white rock (lower right) is a sheared and granulated anorthosite. The black rock (top and lower left) has fine-grained igneous texture and contains sparse xenocrysts and xenoliths. Contacts between the two materials are smoothly curved shear boundaries.

The dike rocks were quenched and solidified rapidly. The solidified dikes were fragmented by later deformation in the surrounding white rocks, and this deformation separated the fragments of dike rock and injected them with remobilized white rock. Thus, in such samples the black and white materials mutually intrude and include one another.

The black materials in the “black and white rocks” are very similar to the glass-rich light-gray breccias in many respects and most likely formed by similar processes. Thus, they probably represent mixtures of impact melt, material derived from the impacting body, and granulated country rock. They cannot have been derived solely from melting of the surrounding white rocks, for the characteristics of their chemistry and fragment suite require that they contain some material generated within an impact crater cavity. Nor is it likely that they are remobilized regolith breccias; in fragment assemblage and nature of fragment-matrix relationships they resemble the glass-rich light-gray breccias rather than regolith breccias. In most “black and white rocks” these fragment-laden melts probably were injected into the white cataclasites during their de-

formation; in others, they may have been ejected from the craters along with large clasts of cataclasite and may have penetrated fractures in these clasts after ejection. The complex injection and deformation sequence observed in the “partially molten breccias” could have originated in two ways: either the last stages of deformation in the large events that brecciated the cataclasites and generated the black dike materials involved fragmentation of early injected dikes and ejection of the brecciated rocks from the crater cavity; or the deformation of dikes and ejection took place as a result of subsequent impact events.

A similar interpretation of the cataclasites, “black and white rocks,” and related “partially molten breccias,” which differs only in minor details from the one outlined above, has been proposed by Wilshire and Moore (ref. 34).

THERMALLY METAMORPHOSED BRECCIAS

Thermally metamorphosed breccias are one of the lunar breccia types that may possibly represent lithified debris deposits from major impacts. In these rocks, however, the thermal metamorphism has obscured many of the characteristics that might have been diagnostic of origin, and much additional study will be required before any definite conclusion can be reached on their genesis.

The first sample of thermally metamorphosed breccia that was returned was the unique potassic and silica-rich 12013. Minor numbers of thermally metamorphosed breccias were found at the Apollo 15 and 16 sites, but at the Apollo 14 site such breccias were abundant. Here it appears that these rocks are a major constituent of the Fra Mauro Formation, a unit that formed as a deposit of Imbrian ejecta (ref. 35). Either they represent lithified and metamorphosed Imbrian ejecta (refs. 2 and 3), or they are breccias metamorphosed in pre-Imbrian time and transported to the Apollo 14 site to form clasts in the Imbrian deposit (refs. 1 and 36).

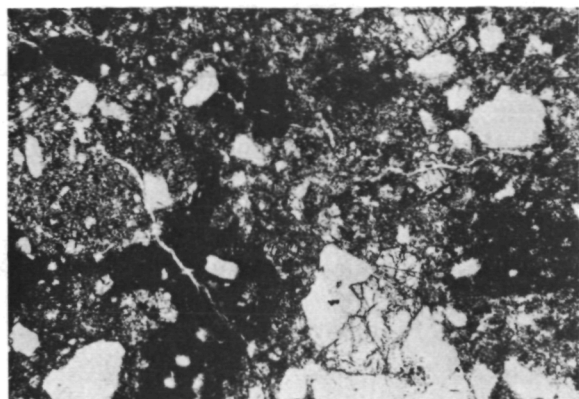


Figure 13.—Photomicrograph of thermally metamorphosed breccia 14312. (Width of field of view is 2.2 mm; plane-polarized light.) Dark patches are clasts of recrystallized fragment-laden glasses similar to glass-rich light-gray breccias. Matrix and clasts are gradational, and grain size distribution appears more seriate than bimodal. Clasts of fragment-free glasses and devitrified fragment-free glasses are sparse.

Fragment assemblages in the Apollo 14 thermally metamorphosed breccias (fig. 13) are unlike those in either the Apollo 14 regolith breccias or the Apollo 17 glass-rich light-gray breccias and blue-gray breccias. Clast sizes tend to be larger than in the regolith breccias, possibly suggesting fewer episodes of fragmentation. (Wilshire and Jackson (ref. 2) found that on the average 25 percent of the clasts in these samples are larger than 1 mm across.) Clasts that were initially fragment-free glass (indicators of a regolith history) are sparse; and clasts of recrystallized fragment-laden glasses (similar to glass-rich light-gray breccias) are abundant. (Wilshire and Jackson reported that these average 28 percent of the clasts in the 0.1- to 1-mm size range, and Chao (ref. 1) found that 55 percent by volume of one thermally metamorphosed breccia he studied consisted of such clasts.) Fragments of single mineral grains are much more abundant than in the regolith breccias. (Wilshire and Jackson reported an average of 56 percent mineral fragments in the 0.1- to 1-mm size fraction in thermally metamorphosed breccias in contrast to a range from 15 to 33 per-

cent in this same size fraction in regolith breccias.) The suite of lithic fragments is not as diverse as in regolith breccias but not as homogeneous as in the Apollo 17 light-gray breccias, and clasts that show the effects of multiple impacts are present in significant numbers.

Many of the compositional and physical indicators that might be used to evaluate whether or not the constituents of these breccias had ever passed through an episode as particles in a regolith have been obscured by thermal metamorphism. During metamorphism at high temperatures or over long periods of time, solar-wind-implanted C and N and trapped solar-wind rare gases are driven off and particle tracks are annealed out; however, one indicator of surface exposure that is not affected by metamorphism is enrichment of O^{18} relative to O^{16} . In the Apollo 14 thermally metamorphosed breccias C and N contents are low and either were always low or were lowered during metamorphism. The rocks, however, may retain a trace of trapped solar-wind rare gases (ref. 37). Particle track contents are also low, but some of the sparse unannealed tracks that are present have been ascribed to irradiation of fragments in a regolith prior to breccia aggregation (ref. 25). The O^{18} does not appear to be significantly enriched relative to O^{16} (ref. 24). In sum, the rare gas and track data indicate some surface exposure, but the particles in these breccias probably have not been as extensively exposed and reworked in the lunar surface debris layer as particles in regolith breccias.

As outlined above, the published studies of the characteristics of the thermally metamorphosed breccias give some indication of the preaggregation histories of the fragments they contain, but these studies are by no means complete enough to be definitive. About all that can be said at present is that the fragments in these rocks probably have undergone more complex histories of multiple impacts than fragments in the glass-rich light-gray breccias, but they have probably had much less extreme reworking than fragments in regolith breccias.

GLASS-POOR FELDSPATHIC BRECCIAS

Glass-poor feldspathic breccias are another of the lunar breccia types that may have originated as debris deposits from large impacts. The characteristics of these rocks and their relations to other types of breccias are not yet well enough known to permit anything more than speculation about this possibility, however.

Samples of glass-poor feldspathic breccias were collected at the Apollo 14, 16, and 17 sites. At the Apollo 14 site they formed white rocks (represented by 14063 and 14082) and irregular layers and patches in boulders of darker rock on the rim of Cone Crater (ref. 38); as the dark rock was not sampled, we do not know of what lithology it is. In any case, however, it is likely that the white rocks and the associated darker rocks were derived from deep within the Fra Mauro Formation. At the Apollo 16 site similiar breccias (for example, 67015, 67016, and 67455) form a layer 100 to 250 m thick underlying the northern part of the sampling area (ref. 39); here there is no clear association with other types of breccia. At the Apollo 17 site, only very minor amounts of such breccias were found; they form schlieren included within light-gray breccias such as 73215.

These breccias consist largely of crushed debris derived from highly feldspathic rocks (fig. 14). The fragment suite is variable, being quite homogeneous in some rocks and much more heterogeneous in others. In all the samples, most fragments are of single mineral grains, with plagioclase greatly dominant. (In the Apollo 14 feldspathic breccias Wilshire and Jackson (ref. 2) found that 45 to 55 percent of the fragments in the 0.1- to 1-mm size range were of plagioclase grains and about 15 percent were of other minerals, for a total of 60 to 70 percent mineral fragments.) Many of these fragments are coarse, and pyroxene clasts show broad exsolution lamellae; these characteristics suggest plutonic source rocks. Fragments of recrystallized shocked plagioclase and devitrified maskelynite are also present. The

most abundant lithic fragments in most samples are of brown devitrified fragment-laden glasses and granulated coarse-grained anorthositic rocks. Highly variable amounts of clasts of other rock types and of brown fragment-free glasses are present.

Generally the rocks are friable and contain very little groundmass glass binding the fragments together; but the amount of such glass varies considerably from sample to sample, and in some cases it is variable within single samples. Compositional and track studies suggest that in many of these rocks the fragments had little or no exposure to the lunar surface environment prior to consolidation of the breccia (refs. 40, 41, and 42), but in other rocks the fragments may have had some history prior to exposure (ref. 43).

The major evidence that some of these breccias may be debris from single large impacts is as follows: (1) The suite of parent rocks from which their fragment assemblage was derived was apparently fairly homogeneous in texture and composition, and contained coarse-grained deep-seated rocks as a major constituent; and (2) the fragments appear to have had very little reworking by multiple impacts. However, it is not clear why

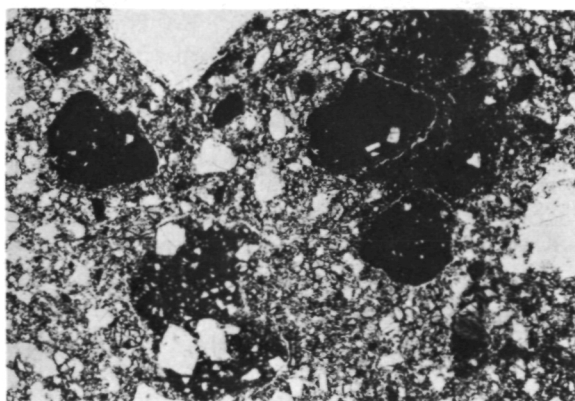


Figure 14.—Photomicrograph of glass-poor feldspathic breccia 14063. (Width of field of view is 2.2 mm; plane-polarized light.) The dark areas are clasts of devitrified fragment-laden glass. The bulk of the rock consists of a poorly consolidated light-colored aggregate of mineral fragments; the light color is due to the strong predominance of feldspar over mafic minerals among fragments.

some of these feldspathic breccias are less homogeneous than others, and how the different variants might be related to one another. It is also unclear how breccias of this type might be related to the other breccias that could represent major-impact debris. In this regard, it is significant that one of the most abundant types of lithic clast in the feldspathic breccias is devitrified or recrystallized fragment-laden glass similar in texture to Apollo 17 glass-rich light-gray breccia. In relationships shown in 73215, where glass-poor feldspathic breccia is included within glass-rich light-gray breccia, it appears that the feldspathic debris may have been formed in the same impact that generated the fragment-laden glass. Thus, in some cases glass-rich light-gray breccia, and glass-poor feldspathic breccia may be two different facies of ejecta of the same impact. On the other hand, it is not yet possible to rule out the alternative that the feldspathic breccias are derived from loose deposits of feldspathic debris that had not experienced extensive reworking prior to consolidation. The relationships seen in 73215 could conceivably have been produced if preexisting loose debris had simply been caught up in the glass-rich light-gray breccia during its formation. It is hoped that these relationships will be clarified by the studies now in progress of feldspathic breccia lithologies in the light-gray breccias.

GREEN-GRAY BRECCIAS, OR POIKILITIC-POIKILOBLASTIC ROCKS

One other type of lunar rock that has been termed breccia is worth noting briefly here. These are the rocks that were designated green-gray breccias (fig. 15) by the Apollo 17 LSPET (ref. 10) and poikilitic rocks by the Apollo 16 LSPET (ref. 4). They appear to represent fragment-laden melts and glasses that crystallized or devitrified at temperatures above or just below the solidus (refs. 44, 45, and 46). Clast proportions are low and clast-groundmass equilibration is extensive in these rocks; thus studies of the

fragments they contain do not have as great a potential for determining the nature of source terrane as do studies of the breccia types described in previous sections. For this reason I will not present here a detailed discussion of these rocks, but I will only indicate what alternatives have been proposed for their origin, and which alternative I prefer. It has been suggested that these rocks represent clast-laden impact melts (Dence, oral communication); clast-laden melts of uncertain origin (ref. 46); clast-laden endogenous melt of deep origin (ref. 47); breccias heated by impact to temperatures just above or below the solidus (refs. 44 and 45); or thermally metamorphosed glassy-matrix breccias (ref. 48). The rocks are texturally gradational with blue-gray breccias and they show simple fragment suites much like those characteristic of the blue-gray breccias. They also contain particles of nickel-iron of meteoritic origin (ref. 33). Because of the similarities to blue-gray breccias, I favor the interpretation that both types of rock had similar ori-

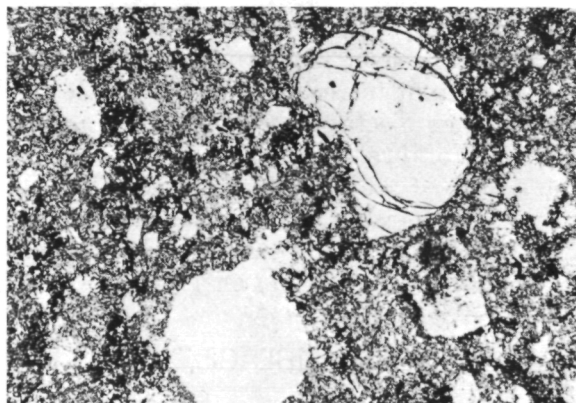


Figure 15.—Photomicrograph of green-gray breccia 77135. (width of field of view is 2.2 mm; plane-polarized light.) Xenocrysts and xenoliths are set in a groundmass that has fine-grained poikilitic texture. Light-colored areas in the groundmass are poikilitic grains of low-calcium pyroxene, and darker colored areas are interstitial to the poikilitic grains and contain concentrations of small ilmenite grains. Much of the plagioclase is euhedral to subhedral (small white laths). The rock is vesicular and a large vesicle is visible at bottom center. The large xenocryst at top right is of olivine.

gins, that is, both represent fragment-laden impact melts, but the green-gray breccias initially contained much higher proportions of melt and much lower proportions of fragments than did the blue-gray breccias. In this interpretation, the clasts were included in this melt and are not relicts from a melting episode that heated the whole rock, although they may have reacted extensively with the melt after incorporation.

Source Terrane of Light-Gray Breccias

Studies are now in progress of the fragment suites in several samples of glass-rich light-gray breccia, for example 73255 and 73215 (consortium led by the author), and 72255 and 72215 (consortium led by J. A. Wood). These studies are only beginning, and among their first objectives will be (1) to determine the amount of reworking of the fragments prior to consolidation of the breccia, and (2) to establish whether or not the analogy to suevites is truly valid. In the discussion below, however, I will assume that it has already been demonstrated that these samples consist of major-impact ejecta, and I will attempt to reconstruct the source terrane of this ejecta, in order to illustrate the potential of breccia studies in determining the nature of the early lunar crust. The data presented consist of a combination of my own observations on 73215 and the observations of Stoesser et al. (ref. 27) on 72255.

FRAGMENT ASSEMBLAGE

The most abundant clasts are of single mineral grains. Fragments of plagioclase are greatly dominant; fragments of olivine and pyroxene are subordinate, and the former is more abundant than the latter. Fragments of recrystallized shocked plagioclase and devitrified maskelynite are common (fig. 16). Sparse fragments of silica minerals, pink to red spinels, opaque minerals, and zircon are also present.

It appears that a significant number of the

mineral clasts may have been derived from plutonic parent rocks. Fragments of single grains as much as 4 mm across have been observed in 73215. All the fragments of pyroxene contain optically prominent exsolution lamellae which are quite coarse in some grains, suggesting deep-seated equilibration.

Clastic lithic material consists primarily of (1) fine-grained anorthositic-noritic-troctolitic hornfelses and granoblastic plagioclase; (2) fine-grained "troctolites" with igneous textures; (3) granulated medium-grained plutonic anorthosites, norites, troctolites, and troctolitic anorthosites; and (4) aggregates of poorly consolidated feldspathic debris (glass-poor feldspathic breccia described above) (fig. 17). Minor numbers of other types of lithic clasts are also present. Stoesser et al. (ref. 27) have reported abundance data on lithic clasts in 72255. They find that, for clasts larger than 0.2 mm, the proportions by percentage are as follows: 49, fine-grained granulitic anorthositic-noritic-troctolitic hornfels; 12, fine-grained granoblastic plagioclase; 15, devitrified maskelynite; 7, granulated anorthosite; 4, fine-grained "troctolite"; 5, devitrified rock glass; 4, felsite and felsic glass ("granitic clasts"); 2, recrystallized pyroxene and olivine; 1, basalt; and 1, plutonic norite. No quantitative data



Figure 16.—Photomicrograph of glass-rich light-gray breccia 73215. (Width of field of view is 2.2 mm; crossed polarizers.) Two large rounded grains of partly recrystallized shock-deformed plagioclase are included within the dark aphanitic matrix.

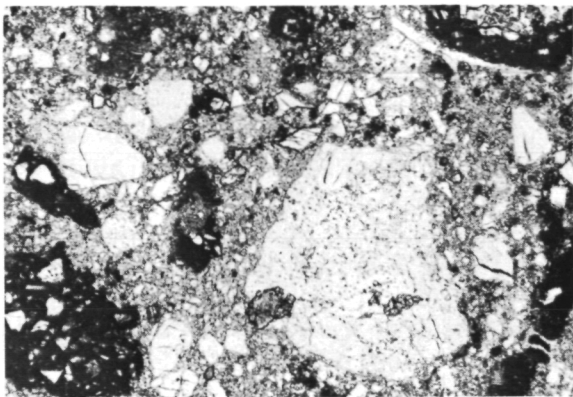


Figure 17.—Photomicrograph of poorly consolidated feldspathic debris included with glass-rich light-gray breccia 73215. (Width of field of view is 2.2 mm; plane-polarized light.) The most abundant clasts are of single mineral grains, dark fragment-laden devitrified glasses, and crushed anorthosites (white clasts to right of center). Only sparse interstitial glass is present binding fragments together. The light color of the matrix is a reflection of the lack of cementing glass and the highly feldspathic bulk composition of the rock. This material is very similar to glass-poor feldspathic breccias described in the text as one of the major lunar breccia types.

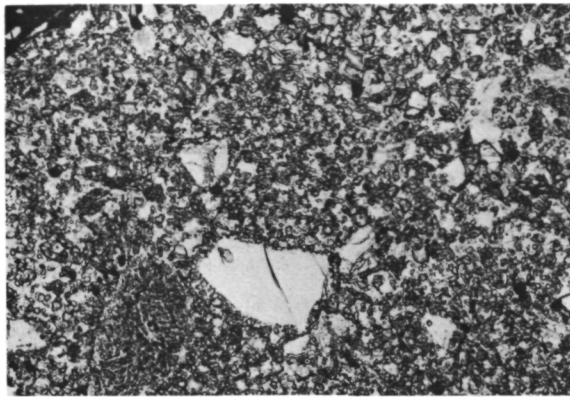


Figure 18.—Photomicrograph of hornfels clast in glass-rich light-gray breccia 73215. (Width of field of view is 2.2 mm; plane-polarized light.) The rock consists of a very fine grained recrystallized granoblastic matrix that contains xenocrysts (such as the angular one of plagioclase below center) and small xenoliths (such as the oval one to the left of the prominent plagioclase xenocryst).

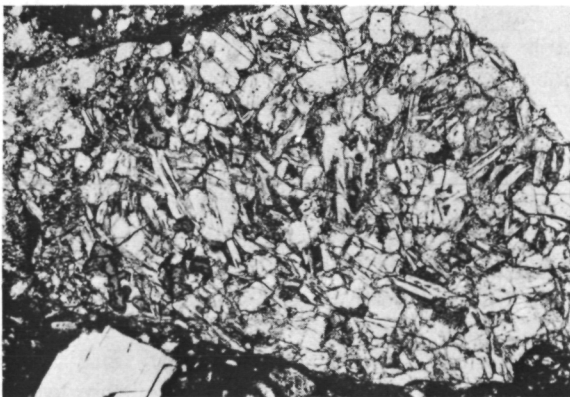


Figure 19.—Photomicrograph of clast of fine-grained basaltic-textured "troctolite" in glass-rich light-gray breccia 73215. (Width of field of view is 2.2 mm; plane-polarized light.) Plagioclase grains are lath-shaped, and olivine grains are roughly equant. A few partly resorbed phenocrysts of aluminous spinel are present (dark-gray skeletal grains near top left and bottom left of clast).

are available for lithic clast abundances in 73215 at present, but rough visual estimates suggest that, in this rock, clast proportions differ from those in 72255 in that fragments of granulated medium-grained troctolite and troctolitic anorthosite are common and fragments of devitrified rock glass are very rare.

The hornfelses occur as small competent clasts, and their textures range from microgranoblastic to micropoikiloblastic. Many are inequigranular, with variable proportions of xenocrysts and small xenoliths set in a very fine grained recrystallized matrix (fig. 18). Some of these rocks are probably of relatively deep-seated origin and formed by recrystallization of sheared zones in coarse-grained parent rocks. Others, those that have heterogeneous textures and contain xenoliths, probably represent recrystallized impact debris deposits and are of shallower origin.

The fine-grained "troctolites" occur as small competent clasts, and they range in texture from devitrified vitrophyres (bearing

spinel and plagioclase phenocrysts), to basaltic-textured rocks (fig. 19), to remelted troctolitic cataclasites (in which large deformed and recrystallized grains of olivine and plagioclase are set in a fine-grained matrix that has igneous texture). The finest grained

members of this suite are probably of very shallow origin and crystallized from rapidly cooled melts. At present it is not known whether these melts were endogenous or generated by impact. Source depth and processes of origin of the remelted cataclasites are also unknown.

In 73215 most of the large lithic clasts are of plutonic troctolites and troctolitic anorthosites. Most of these were granulated prior to incorporation in the breccia, but they show relict grain sizes as large as 4 mm. Others were not deformed, and they preserve original granular textures. The troctolites appear to be like the troctolite sample 76535. It has been proposed by Gooley et al. (ref. 49) and Bogard et al. (ref. 50) that troctolites of this type are from a source more than 10 km below the lunar surface and that they may have formed from 4.3 to 4.4 billion years ago; thus, they may be some of the original rocks of the lunar crust.

The devitrified rock glasses that are common in 72255 and very rare in 73215 are deep red-brown, are xenocryst-poor, and have very fine grained devitrification textures.

Most of the felsitic (or "granitic") clasts consist of either (1) oriented and graphic intergrowths of a silica mineral and potassium feldspar, with or without plagioclase feldspar and glass (fig. 20); or (2) glasses of granitic composition that contain variable amounts of crystals of silica minerals and feldspars. The crystalline felsites tend to be fine grained, and it is unlikely that they were derived from a large body of plutonic granite. They may instead come from small crystallized segregations of late immiscible "granitic" melts formed during igneous differentiation or partial melting processes in the lunar crust (R. W. Wolfe, oral communication).

One of the lithic types present in trace amounts is worth noting here. This is basalt in which pyroxene is dominant over plagioclase. The clasts of these basalts are metamorphosed, but they preserve relict subophitic or vitrophyric textures, indicating that they initially crystallized at shallow depths. Bulk compositions (ref. 27) are intermediate between those of highlands rocks and mare

basalts. Studies of such basalts may shed some light on the relationships between mare and highland rocks and the processes of origin of the lunar crust.

One major contributor to the glass-rich light-gray breccias is an enigma. This is the source material for the glass that binds the fragments together. Bulk composition of this glass (refs. 27 and 51) appears to be that of feldspathic or low-alkali, high-alumina basalt (terminology of Prinz et al., reference 52), containing about 19 percent Al_2O_3 , 10 percent MgO , 10 percent FeO , 0.3 percent K_2O and rare-earth element concentrations about 100 times those in chondrites (with negative Eu anomaly). Plagioclase and low-calcium pyroxene are the dominant normative minerals and are about equal in abundance. No lithic fragments of similar composition have been found within the breccias. Two possible alternatives for the source for the glass are (1) a noritic rock that was completely melted by impact; or (2) a completely melted mechanical mixture of clasts of the anorthositic-noritic-troctolitic suite and clasts of felsite.

SOURCE TERRANE

The fragment suite of glass-rich light-gray breccias such as 73215 and 72255 suggests that the source crust from which they were derived had a layered structure. The deepest material excavated probably came from more than 10 km below the surface; the parent rocks were medium-grained and coarse-grained plutonic troctolites, anorthosites, and norites. They had not previously been excavated by impact, and may represent samples of early lunar crust. Locally, however, these rocks had been sheared and deformed by impacts in overlying rocks, and the sheared zones had later recrystallized. Above the plutonic rocks lay a series of metamorphosed ejecta deposits, perhaps interlayered with igneous-textured rocks that had crystallized from impact-generated and endogenous melts. Among these igneous-textured rocks were fine-grained spinel-bearing "troctolites" and pyroxene-dominant subophitic basalts and



Figure 20.—Photomicrograph of felsite clast in glass-rich light-gray breccia 73215. (Width of field of view is 0.88 mm; crossed polarizers.) The felsite consists of a fine-grained graphic intergrowth of a silica mineral (white) and potassium feldspar (gray). Matrix of the surrounding light-gray breccia is visible in the lower left corner and along the bottom edge of the field of view.

vitrophyres. Material from this upper layer was subjected to varying amounts of impact reworking and some of it may have been deformed or melted, excavated, buried, and subsequently metamorphosed many times.

Summary and Conclusions

The most widespread type of lunar breccia is regolith breccia, representing lithified material from the lunar surface debris layer. Fragment assemblage, nature of the matrix, bulk composition, and physical characteristics of these rocks reflect the fact that the particles they contain had histories of extensive impact reworking and mixing in the regolith prior to being consolidated into a breccia.

Most breccias returned from highlands sites, however, do not show characteristics of extensive reworking at the lunar surface. Some of these may be samples of brecciated bedrock and ejecta deposits related to major impacts. The following is a list of the types of highlands breccias discussed in this paper (other than regolith breccias) with suggestions as to their possible genetic relationships to large impacts.

1. Cataclastic anorthosites.
These probably represent rocks granulated by shock-induced deformation in the walls and floors of large impact crater cavities and in blocks of ejecta thrown out from such crater cavities.
2. "Black and white rocks."
The white material is like cataclastic anorthosites. Black material probably represents fragment-laden melts (mixtures of impact melt, material derived from the impacting body, and crushed bedrock) injected into the white cataclasites during their deformation, or filling fractures in them after deformation ceased.
3. Light-gray breccias.
These rocks are probably analogous to terrestrial suevites. The glass-rich members of this suite (types 1 and 2) probably formed as fragment-laden impact melts and are somewhat analogous to impactite glass bombs in suevites. Other samples (type 3) are mixtures of small glass-rich clasts and debris from crushed and shocked bedrock and may be analogous to bulk suevite.
4. Blue-gray breccias (and the similar fragments that form clasts in thermally metamorphosed and glass-poor feldspathic breccias).
Their origin is probably similar to that of glass-rich light-gray breccias (types 1 and 2) and black materials within "black and white rocks."
5. Thermally metamorphosed breccias.
The possible relationship to major impacts is unclear. Fragments in these breccias appear to have had more complex histories of reworking than fragments in glass-rich light-gray breccias but less complex histories than fragments in regolith breccias.
6. Glass-poor feldspathic breccias.
Again, the possible relationship to major impacts is unclear. Samples of this type may be major impact ejecta deposits, or they may come from deposits of loose feldspathic debris that was

reworked, but not extensively; it is also possible that samples with both these origins may be represented in this suite.

7. Green-gray breccias and poikilitic-poikiloblastic rocks.

These possibly represent fragment-laden impact melts generated in large impacts.

The glass-rich light-gray breccias appear to represent one end member of a gradational series of lunar breccias, and the members of this series are widespread and abundant on the lunar surface. Glass-rich light-gray breccias are gradational in texture, nature of fragment assemblage, and nature of clast-matrix relations with blue-gray breccias and with the black materials in "black and white rocks." Similar rocks are common as clasts in thermally metamorphosed breccias, clasts in glass-poor feldspathic breccias, and fragments in fines fractions. Blue-gray breccias are in turn gradational with green-gray breccias (or poikilitic-poikiloblastic rocks). In this paper I propose a hypothesis for a genetic relationship between all the members of this gradational series, that is, that all represent mixtures of varying proportions of impact melt and finely crushed debris ejected during large impact events. Under this hypothesis, mixing takes place during ejection of melts and debris from the crater cavity; the differences between the various types of breccia are a function of ratio of melt to included particles, initial temperatures of melt and inclusions, and post-aggregation cooling history.

Many of the ideas presented above are speculative, and much more work remains to be done before they can be either confirmed or disproved. Such work is essential, for any breccias that can definitely be established as having been formed in major impacts are potentially of great importance to lunar research. Although the fragment suite of a single sample of major-impact breccia will not be representative of the entire pre-impact source area, studies of such samples can permit partial reconstruction of that source. By such an approach we may eventually be able to decipher some of the history of the Moon's

crust and upper mantle during the first half billion years of lunar history.

Acknowledgment

Many of the ideas in this paper have been developed as a result of frequent and stimulating discussions with E. C. T. Chao over the course of several years. The author also is indebted to H. G. Wilshire and to colleagues on LSAPT for exchange of ideas on some of the topics covered above. This research was supported by NASA Grant T-2357A.

References

1. CHAO, E. C. T., Geologic Implications of the Apollo 14 Fra Mauro Breccias and Comparison With Ejecta From the Ries Crater, Germany. *J. Res. U.S. Geol. Survey*, Vol. 1, 1973, pp. 1-18.
2. WILSHIRE, H. G., AND E. D. JACKSON, *Petrology and Stratigraphy of the Fra Mauro Formation at the Apollo 14 Site*. U.S. Geol. Survey Professional Paper 785, 1972.
3. WARNER, J. L., Metamorphism of Apollo 14 Breccias. *Proc. Third Lunar Science Conference, Geochimica et Cosmochimica Acta*, Supplement 3, Vol. 1, 1972, pp. 623-643.
4. LSPET (Lunar Sample Preliminary Examination Team), The Apollo 16 Lunar Samples: A Petrographic and Chemical Description. *Science*, Vol. 179, 1973, pp. 23-34.
5. WARNER, J. L., C. H. SIMONDS, AND W. C. PHINNEY, Apollo 16 Rocks: Classification and Petrogenetic Model. *Proc. Fourth Lunar Science Conference, Geochimica et Cosmochimica Acta*, Supplement 4, Vol. 1, 1973, pp. 481-504.
6. LSPET (Lunar Sample Preliminary Investigation Team), The Apollo 15 Lunar Samples: A Preliminary Description. *Science*, Vol. 175, 1972, pp. 363-375.
7. PHINNEY, W. C., J. L. WARNER, AND C. H. SIMONDS, Lunar Highland Rock Types: Their Implications for Impact-Induced Fractionation. Paper presented at this conference, 1974.
8. WILSHIRE, H. G., D. E. STUART-ALEXANDER, AND E. D. JACKSON, Apollo 16 Rocks: Petrology and Classification. *J. Geophys. Res.*, Vol. 78, 1973, pp. 2379-2392.
9. AFGIT (Apollo Field Geology Investigation Team), Geologic Exploration of Taurus-Littrow: Apollo 17 Landing Site. *Science*, Vol. 182, 1973, pp. 672-680.

10. LSPET (Lunar Sample Preliminary Examination Team), Apollo 17 Lunar Samples: Chemical and Petrographic Description. *Science*, Vol. 182, 1973, pp. 659-672.
11. SCHMITT, H. H., Apollo 17 Report on the Valley of Taurus-Littrow. *Science*, Vol. 182, 1973, pp. 681-690.
12. CHAO, E. C. T., Preliminary Genetic Classification of Apollo 16 Breccias. *Lunar Science*, Vol. IV, 1973, p. 129.
13. DENNIS, J. G., Ries Structure, Southern Germany, a Review. *J. Geophys. Res.*, Vol. 76, 1971, pp. 5394-5406.
14. ACKERMANN, W., Geologisch-petrographische untersuchungen im Ries. *Geol. Jahrb.*, Vol. 75, 1958, pp. 135-182.
15. HÖRZ, F., Untersuchungen an Riesgläsern. *Beitrage Mineral. Petrogr.*, Vol. 11, 1965, pp. 621-661.
16. EL GORESY, A., Die erzminerale in den Ries- und Bosumtwi-Krater-Gläsern und ihre genetische deutung. *Geochimica et Cosmochimica Acta*, Vol. 28, 1964, pp. 1881-1891.
17. LSPET (Lunar Sample Preliminary Investigation Team), Preliminary Examination of Lunar Samples From Apollo 14. *Science*, Vol. 173, 1971, pp. 681-693.
18. LAUL, J. C., H. WAKITA, D. L. SHOWALTER, W. V. BOYNTON, AND R. A. SCHMITT, Bulk, Rare Earth, and Other Trace Elements in Apollo 14 and 15 and Luna 16 Samples. *Proc. Third Lunar Science Conference, Geochimica et Cosmochimica Acta*, Supplement 3, Vol. 2, 1972, pp. 1181-1200.
19. MORGAN, J. W., J. C. LAUL, U. KRÄHENBÜHL, R. GANAPATHY, AND E. ANDERS, Major Impacts on the Moon: Characterization From Trace Elements in Apollo 12 and 14 Samples. *Proc. Third Lunar Science Conference, Geochimica et Cosmochimica Acta*, Supplement 3, Vol. 2, 1972, pp. 1377-1395.
20. MOORE, C. B., C. F. LEWIS, J. CRIPE, F. M. DELLIS, W. R. KELLY, AND E. K. GIBSON, JR., Total Carbon, Nitrogen, and Sulfur in Apollo 14 Lunar Samples. *Proc. Third Lunar Science Conference, Geochimica et Cosmochimica Acta*, Supplement 3, Vol. 2, 1972, pp. 2051-2058.
21. GOEL, P. S., AND B. K. KOTHARI, Total Nitrogen Contents of Some Apollo 14 Lunar Samples by Neutron Activation Analysis. *Proc. Third Lunar Science Conference, Geochimica et Cosmochimica Acta*, Supplement 3, Vol. 2, 1972, pp. 2041-2050.
22. MEGRUE, G. H., AND F. STEINBRUNN, Classification and Source of Lunar Soils; Clastic Rocks; and Individual Mineral, Rock, and Glass Fragments From Apollo 12 and 14 Samples as Determined by the Concentration Gradients of the Helium, Neon, and Argon Isotopes. *Proc. Third Lunar Science Conference, Geochimica et Cosmochimica Acta*, Supplement 3 Vol. 2, 1972, pp. 1899-1916.
23. ALEXANDER, E. C., JR., AND S. B. KAHL, ^{40}Ar - ^{39}Ar Studies of Lunar Breccias. *Lunar Science*, Vol. V, Part 1, 1974, pp. 9-11.
24. CLAYTON, R. N., J. M. HURD, AND T. K. MAYEDA, Oxygen Isotopic Compositions and Oxygen Concentrations of Apollo 14 and Apollo 15 Rocks and Soils. *Proc. Third Lunar Science Conference, Geochimica et Cosmochimica Acta*, Supplement 3, Vol. 2, 1972, pp. 1455-1463.
25. HUTCHEON, I. D., P. P. PHAKEY, AND P. B. PRICE, Studies Bearing on the History of Lunar Breccias. *Proc. Third Lunar Science Conference, Geochimica et Cosmochimica Acta*, Supplement 3, Vol. 3, 1972, pp. 2845-2865.
26. HART, H. R., JR., G. M. COMSTOCK, AND R. L. FLEISCHER, The Particle Track Record of Fra Mauro. *Proc. Third Lunar Science Conference, Geochimica et Cosmochimica Acta*, Supplement 3, Vol. 3, 1972, pp. 2831-2844.
27. STOESER, D. B., R. W. WOLFE, J. A. WOOD, AND J. F. BOWER, III. Petrology. *Consortium Indomitable, Interdisciplinary Studies of Samples From Boulder 1, Station 2, Apollo 17*, Vol. 1, Smithsonian Astrophysical Observatory, Cambridge, Mass., 1974, pp. 35-109.
28. STOESER, D. B., R. W. WOLFE, U. B. MARVIN, J. A. WOOD, AND J. F. BOWER, Petrographic Studies of a Boulder From the South Massif. *Lunar Science*, Vol. V, Part II, 1974, pp. 743-745.
29. DRAKE, M. J., I. S. MCCALLUM, G. A. MCKAY, AND D. F. WEILL, Mineralogy and Petrology of Apollo 12 Sample No. 12013: A Progress Report. *Earth Planet. Sci. Letters*, Vol. 9, 1970, pp. 103-123.
30. Lunatic Asylum, Mineralogic and Isotopic Investigations on Lunar Rock 12013. *Earth Planet. Sci. Letters*, Vol. 9, 1970, pp. 137-163.
31. JAMES, O. B., *Petrology of Lunar Microbreccia 12013, 6*. U.S. Geol. Survey Interagency Report, Astrogeology 23, 1970.
32. Apollo 15 Lunar Sample Information Catalog, Lunar Receiving Laboratory, NASA, Manned Spacecraft Center, Houston, MSC 03209.
33. GANAPATHY, R., J. W. MORGAN, U. KRÄHENBÜHL, AND E. ANDERS, Ancient Meteoritic Components in Lunar Highland Rocks: Clues From Trace Elements in Apollo 15 and 16 Samples. *Proc. Fourth Lunar Science Conference, Geochimica et Cosmochimica Acta*, Supplement 4, Vol. 2, 1973, pp. 1239-1261.
34. WILSHIRE, H. G., AND H. J. MOORE, Glass-Coated Lunar Rock Fragments. *J. Geol.*, in press, 1974.
35. EGGLETON, R. E., Geologic Map of the Fra Mauro Region of the Moon. In T. W. OFFIELD, and R. E. EGGLETON, *Geologic Maps of the Fra Mauro Region of the Moon*, U.S. Geol. Survey,

- Misc. Geol. Inv., Map I-708, Sheet 2, 1970.
36. DENCE, M. R., AND A. G. PLANT, Analysis of Fra Mauro Samples and the Origin of the Imbrium Basin. *Proc. Third Lunar Science Conference, Geochimica et Cosmochimica Acta*, Supplement 3, Vol. 1, 1972, pp. 379-399.
 37. KIRSTEN, T., J. DEUBNER, P. HORN, I. KANEOKA, J. KIKO, O. A. SCHAEFFER, AND S. K. THIO, The Rare Gas Record of Apollo 14 and 15 Samples. *Proc. Third Lunar Science Conference, Geochimica et Cosmochimica Acta*, Supplement 3, Vol. 2, 1972, pp. 1865-1889.
 38. SWANN, G. A., N. G. BAILEY, R. M. BATSON, R. E. EGGLETON, M. H. HAIT, H. E. HOLT, K. B. LARSON, M. C. McEWEN, E. D. MITCHELL, G. G. SCHABER, J. P. SCHAFER, A. B. SHEPARD, R. L. SUTTON, N. J. TRASK, G. E. ULRICH, H. G. WILSHIRE, AND E. W. WOLFE, *Preliminary Geologic Investigations of the Apollo 14 Landing Site*. U.S. Geol. Survey Interagency Report 29, 1971.
 39. AFGIT (Apollo Field Geology Investigation Team), Apollo 16 Exploration of Descartes: A Geologic Summary. *Science*, Vol. 179, 1973, pp. 62-69.
 40. CLAYTON, R. N., J. M. HURD, AND T. K. MAYEDA, Oxygen Isotopic Compositions of Apollo 15, 16, and 17 Samples, and Their Bearing on Lunar Origin and Petrogenesis. *Proc. Fourth Lunar Science Conference, Geochimica et Cosmochimica Acta*, Supplement 4, Vol. 2, 1973, pp. 1535-1542.
 41. MOORE, C. B., C. F. LEWIS, AND E. K. GIBSON, JR., Total Carbon Contents of Apollo 15 and 16 Lunar Samples. *Proc. Fourth Lunar Science Conference, Geochimica et Cosmochimica Acta*, Supplement 4, Vol. 2, 1973, pp. 1613-1623.
 42. MACDOUGALL, D., R. S. RAJAN, I. D. HUTCHEON, AND P. B. PRICE, Irradiation History and Accretionary Processes in Lunar and Meteoritic Breccias. *Proc. Fourth Lunar Science Conference, Geochimica et Cosmochimica Acta*, Supplement 4, Vol. 3, 1973, pp. 2319-2336.
 43. DRAN, J. C., J. P. DURAND, M. MAURETTE, L. DURRIEU, C. JOURET, AND C. LEGRESSUS, Track Metamorphism in Extraterrestrial Breccias. *Proc. Third Lunar Science Conference, Geochimica et Cosmochimica Acta*, Supplement 3, Vol. 3, 1972, pp. 2883-2903.
 44. SIMONDS, C. H., J. L. WARNER, AND W. C. PHINNEY, Petrology of Apollo 16 Poikilitic Rocks. *Proc. Fourth Lunar Science Conference, Geochimica et Cosmochimica Acta*, Supplement 4, Vol. 1, 1973, pp. 613-632.
 45. BENEC, A. E., J. J. PAPIKE, S. SUENO, AND J. W. DELANO, Pyroxene Poikiloblastic Rocks From the Lunar Highlands. *Proc. Fourth Lunar Science Conference, Geochimica et Cosmochimica Acta*, Supplement 4, Vol. 1, 1973, pp. 597-611.
 46. CHAO, E. C. T., AND J. A. MINKIN, The Petrogenesis of 77135, a Fragment-Laden Pigeonite Feldspathic Basalt—A Major Highland Rock Type. *Lunar Science*, Vol. V, Part I, 1974, pp. 112-114.
 47. CRAWFORD, M. L., Crystallization History of Poikilitic Sample 62235. *Lunar Science*, Vol. V, Part 1, 1974, pp. 142-144.
 48. ALBEE, A. L., A. J. GANCARZ, AND A. A. CHODOS, Metamorphism of Apollo 16 and 17 and Luna 20 Metaclastic Rocks at About 3.95 AE: Samples 61156, 64423, 14-2, 65015, 67483, 15-2, 76055, 22006, and 22007. *Proc. Fourth Lunar Science Conference, Geochimica et Cosmochimica Acta*, Supplement 4, Vol. 1, 1973, pp. 569-595.
 49. GOOLEY, R., R. BRETT, J. WARNER, AND J. R. SMYTH, A Lunar Rock of Deep Crustal Origin: Sample 76535. *Geochimica et Cosmochimica Acta*, in press, 1974.
 50. BOGARD, D. D., L. E. NYQUIST, B. M. BANSAL, AND H. WIESMANN, 76535: An Old Lunar Rock? *Lunar Science*, Vol. V, Part 1, 1974, pp. 70-72.
 51. HASKIN, L. A., D. P. BLANCHARD, R. KOROTEV, J. W. JACOBS, J. A. BRANNON, R. S. CLARK, AND A. G. HERRMANN, V. Major- and Trace-Element Concentrations in Samples From 72275 and 72255. *Consortium Indomitable, Interdisciplinary Studies of Samples From Boulder 1, Station 2, Apollo 17*, Vol. 1, Smithsonian Astrophysical Observatory, Cambridge, Mass., 1974, pp. 121-129.
 52. PRINZ, M., E. DOWTY, K. KEIL, AND T. E. BUNCH, Mineralogy, Petrology and Chemistry of Lithic Fragments from Luna 20 Fines: Origin of the Cumulate ANT Suite and its Relationship to High-Alumina and Mare Basalts. *Geochimica et Cosmochimica Acta*, Vol. 37, 1973, pp. 979-1006.

Meteoritic Material on the Moon¹

John W. Morgan, R. Ganapathy, Hideo Higuchi, and
Edward Anders

*Enrico Fermi Institute and Department of Chemistry
University of Chicago, Chicago, Illinois*

Three types of meteoritic material are found on the Moon: micrometeorites, ancient planetesimal debris from the "early intense bombardment," and debris of recent, crater-forming projectiles. Their amounts and compositions have been determined from trace element studies.

The micrometeorite component is uniformly distributed over the entire lunar surface, but is seen most clearly in mare soils. It has a primitive, C1-chondrite-like composition, and comprises 1 to 1.5 percent of mature soils. Apparently it represents cometary debris. The mean annual influx rate is 2.4×10^{-9} g cm⁻² yr⁻¹. It shows no detectable time variation or dependence on selenographic position.

The ancient component is seen in highland breccias and soils more than 3.9 AE (AE = 10⁹ yr) old. Six varieties have been recognized, differing in their proportions of refractories (Ir, Re), volatiles (Ge, Sb), and Au. All have a fractionated composition, with volatiles depleted relative to siderophiles. The abundance patterns do not match those of the known meteorite classes. These ancient meteoritic components seem to represent the debris of an extinct population of bodies (planetesimals, moonlets) that produced the mare basins during the first 700 Myr of the Moon's history. On the basis of their stratigraphy and geographic distribution, five of the six groups are tentatively assigned to specific mare basins: Imbrium, Serenitatis, Crisium, Nectaris, and Humorum or Nubium.

A few properties of the basin-forming objects are inferred from the trace element data. They were independently formed bodies of roughly chondritic composition, not castoffs of a larger body. They were internally undifferentiated, had radii less than 100 km, contained between ~ 15 percent and ~ 40 percent iron, and struck the Moon at velocities generally less than 8 km/s. None match the Earth or Moon in bulk composition; in fact, several are complementary, being lower in refractories and higher in volatiles than the Earth or Moon. Possibly this implies a genetic link between these bodies, the Earth, and the Moon.

An attempt is made to reconstruct the bombardment history of the Moon from the observation that only $\sim 80 \pm 40$ basin-forming objects, totaling $\sim 2 \times 10^{-8}$ M_D, fell on the Moon after crustal differentiation ~ 4.5 AE ago, and that only one such body, of $\sim 5 \times 10^{-8}$ M_D, was left 3.9 AE ago. The apparent half-life of basin-forming bodies, ~ 100 Myr, is close to the calculated value for Earth-crossing planetesimals. According to this picture, a gap in radiometric ages is expected between the Imbrium (3.9 AE) and Nectaris (4.2 AE) impacts because all seven basins formed in this interval lie on the farside or east limb.

The crater-forming component has remained elusive. Only a possible hint of this component has been seen—in ejecta from Apollo 15 Dune Crater and Apollo 12 KREEP glasses of Copernican origin.

It was evident before the first lunar landing that three types of meteoritic matter would be found on the Moon.

¹This review is based in part on two earlier papers by the authors (refs. 1 and 2).

1. Micrometeorites and small meteorites: in the regolith
2. Debris from post-mare craters: in ray material and other ejecta
3. Debris from the "early, intense bom-

bardment" that produced the highland craters and mare basins (refs. 3 and 4) in ancient breccias and highlands regolith

The amount of meteoritic material had been estimated from crater scaling laws and observed fluxes of interplanetary matter (ref. 5). But the composition of this material could not be directly determined in the absence of a tangible sample.

A new vista opened up with the Apollo 11 mission. It then became possible to study the problem by modern laboratory techniques. Because meteoritic material is largely destroyed on impact with the lunar surface, it seemed more profitable to identify the debris by chemical techniques than by a search for surviving particles. Accordingly, we measured about 18 trace elements that were abundant in meteorites but were expected to be rare in lunar surface rocks (refs. 2 and

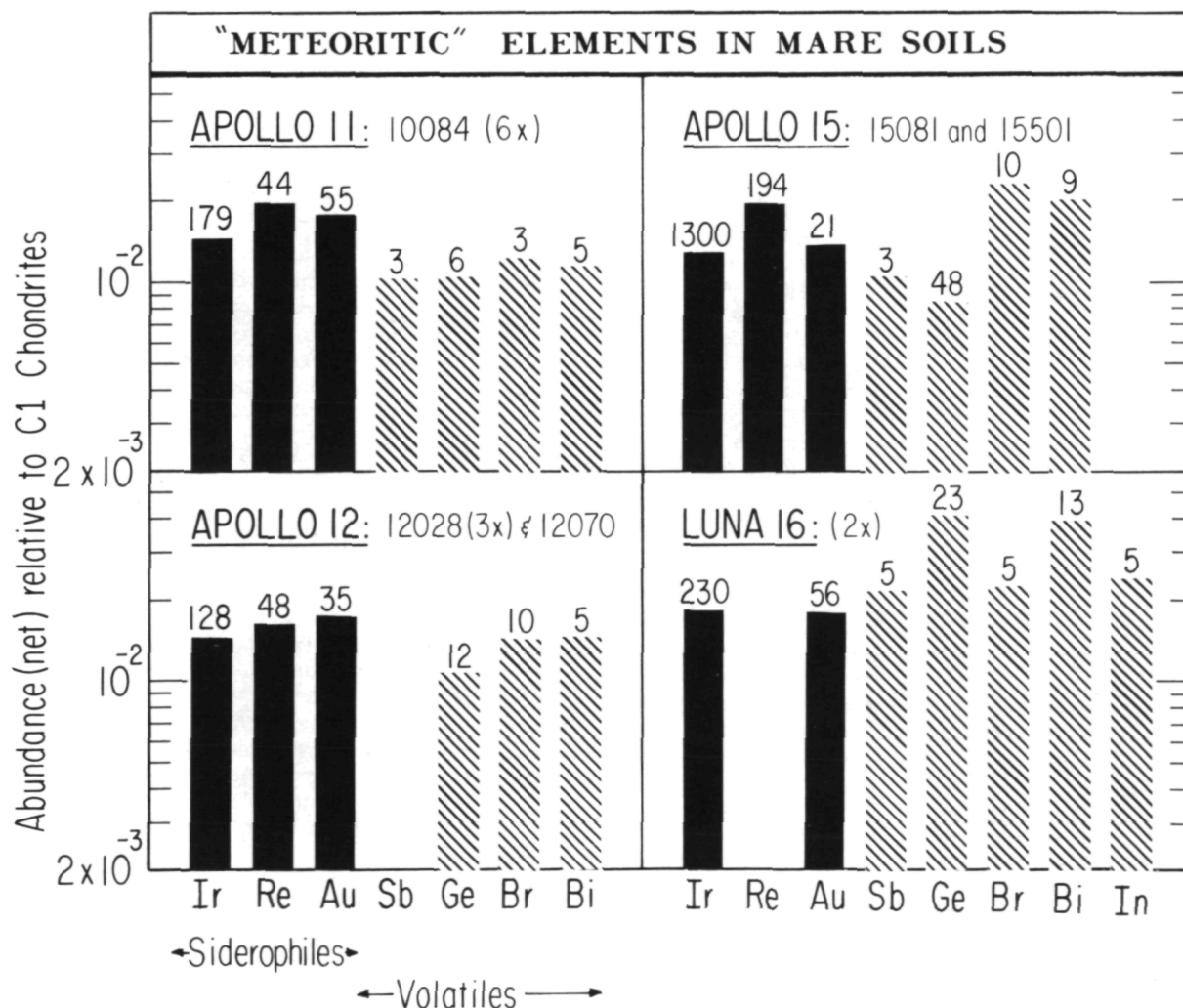


Figure 1.—All mare soils are enriched in "meteoritic" elements, relative to crystalline rocks. Net meteoritic component is obtained by subtracting an indigenous lunar contribution estimated from crystalline rocks. Numbers above histogram indicate ratio of net component to correction (ref. 1). Abundance pattern is flat, with siderophiles and volatiles almost equally abundant. Apparently the meteoritic component has a primitive composition (fig. 2). Data are mainly from this laboratory. (See ref. 11.)

6 through 13). Because many of these elements had abundances of 10^{-9} to 10^{-12} g/g, we used radiochemical neutron activation analysis.

Originally, it appeared that only siderophile elements (Ir, Au, Re, Ni, etc.) would be reliable indicators of meteoritic material. Because they concentrate in metal phase during planetary melting, they are strongly depleted on the surfaces of differentiated planets (e.g., by a factor of $\sim 10^{-4}$ on Earth). Accordingly, they had been used as indicators of meteoritic material in oceanic sediments or polar ice (refs. 14 and 15). However, a number of volatile elements (Ag, Bi, Br, Cd, Ge, Pb, Sb, Se, Te, Zn) turned out to be so strongly depleted on the lunar surface that it became possible to use some of them as subsidiary indicators of meteoritic matter.

The next section of this paper reviews the micrometeorite component, a well explored and essentially closed subject. The section following that, the major portion of the paper, discusses a less finished but more exciting topic: the ancient meteoritic component. The final part reviews the scanty information available on the crater-forming component.

The Micrometeorite Component

All lunar soils are enriched in "meteoritic indicator" elements compared to crystalline rocks from the same site. Not all this enrichment can be attributed to meteoritic material because each soil contains small amounts of exotic rock types not represented among the larger rocks collected at that site. Most important among these are alkali-rich (granitic and noritic) rocks, which account for the fact that soils are almost always richer in alkalis, U, and Th than the local rocks. In order to determine the net meteoritic component, the gross abundances must be corrected for an indigenous lunar contribution. For this correction we have used a mixture of local rocks with a small amount of alkali-rich rock, sufficient to account for the alkali content of the soils.

Data for four mare sites are shown in figure 1. They have been normalized to C1 chondrites to permit compositional characterization of the meteoritic component(s). Siderophile elements are shown by dark shading; volatiles by diagonal shading. Numbers indicate "signal-to-noise" ratio, i.e., ratio of gross abundance to indigenous correction. Only "mature" soils that come from intercrater areas and have high surface exposure age, are shown. Soils of low surface exposure age, from the rims of young craters, generally have lower abundances of meteoritic elements, owing to dilution by freshly excavated bedrock (ref. 11). Soil breccias, not plotted here, are similar to soils (ref. 7).

COMPOSITION

Soils from all four sites show essentially the same picture: siderophiles enriched to 1.5- to 2-percent C1-chondrite equivalent and volatiles enriched to a similar if more variable extent. The volatile enrichment is less well determined, owing to the lower signal-to-noise ratio, but the fact that all four sites consistently show an excess of volatiles suggests that this excess is indeed meteoritic. (Several other volatiles, such as Ag, Cd, Zn, and Te, seem to be largely meteoritic in many soils, but are less reliable indicators for various reasons: higher incidence of contamination, sporadically higher indigenous abundance, mobility in the soil, etc. (refs. 10, 12, 16, and 17).)

The abundance pattern rules out all fractionated meteorite classes (fig. 2, right). Ordinary chondrites, E5,6 chondrites, irons, and stony irons (not shown here) are too deficient in volatiles (especially Bi) relative to siderophiles. Achondrites, in turn, are too low in siderophiles. Thus, attention focuses on primitive meteorites (fig. 2, left), in which volatiles and siderophiles occur in comparable abundance: C1, C2, C3, E3,4, and unequilibrated ordinary chondrites (H3, L3, LL3, not shown here, but basically similar to C3's).

The original Apollo 11 data showed no sys-

tematic depletion of volatiles relative to siderophiles, and thus were most consistent with C1 chondrites (ref. 7). However, now that more data (and better indigenous corrections) are available, a hint of such depletion is discernible. In the three Apollo samples, seven of the 11 volatiles plot below the siderophiles. (Luna 16 soil shows the reverse trend, but this sample seems to be rather extensively contaminated.) This is probably due to an admixture of highland material, with its own fractionated meteoritic component (ref. 1). Still, it appears that the dominant component has C1 composition.

AMOUNT AND INFLUX RATE

The amount of meteoritic material in the soils is therefore most appropriately given as "percent C1 equivalent" (table 1). Evidently all four sites contain essentially similar amounts of meteoritic material. The figures based on siderophiles alone are better determined because the indigenous correction is smaller. On the other hand, they include a sizeable contribution from an ancient meteoritic component (ref. 1). Accordingly, we have given a "best estimate" of the net amount of C1 component. From the latter we

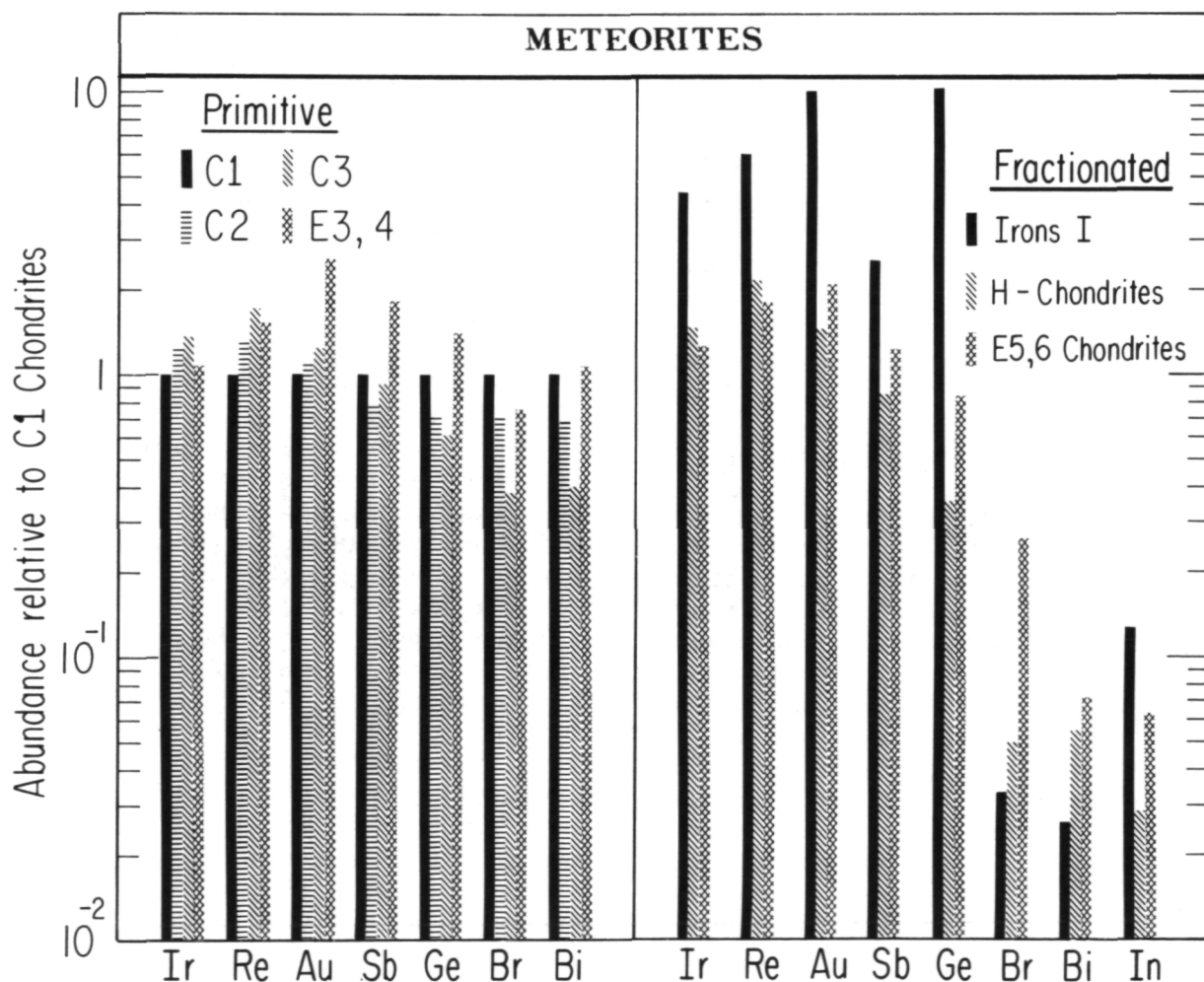


Figure 2.—Primitive meteorites (left) contain siderophiles and volatiles in comparable abundance. Fractionated meteorites (right) are depleted in volatiles (ref. 1). Data taken mainly from Mason (ref. 18).

Table 1.—*Meteorite Components in Mare Soils*
(percent C1 material or equivalent)

	Siderophiles				Volatiles				Mean	Mean	Best	Regolith	Age	Influx Rate
	Ir	Re	Au	Ni	Sb	Ge	Br	Bi	Sid.	Volat.	Estimate	Thickness	(AE)	$10^{-9} \text{ g cm}^{-2} \text{ yr}^{-1}$
											C1-Comp.	(m)		
GROSS	Apollo 11	1.46	2.02	1.81	2.03	1.59	1.23	1.77	1.47	1.83	1.52			
	Apollo 12	1.47	1.68	1.80	2.00	—	1.14	2.60	1.86	1.74	1.87			
	Apollo 15	1.30	1.99	1.45	1.70	1.51	0.88	2.56	2.31	1.61	1.82			
	Luna 16	1.88	<i>10.23</i>	1.85	1.80	2.75	<i>4.39</i>	2.81	<i>4.40</i>	1.84	2.78			
NET	Apollo 11	1.45	1.98	1.77	1.88	(1.03)	1.05	1.23	1.15	1.77	1.12	1.14	4.6	3.65
	Apollo 12	1.46	1.64	1.75	1.80	—	1.08	(1.46)	1.48	1.66	1.34	1.28	4.6	3.26
	Apollo 15	1.30	1.98	1.38	1.55	1.05	0.86	2.32	2.06	1.55	1.57	0.96	4.6	3.32
	Luna 16	1.88	<i>10.19</i>	1.81	1.66	2.19	<i>4.20</i>	2.27	<i>3.94</i>	1.78	2.23	≤ 1.6	4.6?	3.42
CI Chondrites (abundance in ppb)		514	35.2	152	10300	138	31200	4810	110					

NOTES:

Italicized values: contamination suspected.

Parenthesized values: relatively uncertain because indigenous contribution is estimated (or suspected) to be larger than one-third of gross abundance.

Lunar samples: see Morgan et al. (ref. 11) for references.

CI chondrites: from Krähenbühl et al. (ref. 13), except Br (ref. 19).

have calculated the average influx rate at each site, as in ref. 7. The most uncertain factor in this calculation is the mean thickness of the regolith, which has been estimated to be 4.6 m at all four sites (ref. 20). The mean influx rate for the three Apollo sites is $2.4 \times 10^{-9} \text{ g cm}^{-2}\text{yr}^{-1}$.² It agrees rather well with pre-Apollo estimates by Whipple (ref. 21) and Öpik (ref. 5): $1.3 \times 10^{-8} \text{ g cm}^{-2}\text{yr}^{-1}$ (total) and $1.05 \times 10^{-8} \text{ g cm}^{-2}\text{yr}^{-1}$ (micrometeorites only).

At low approach velocities, the meteor impact rate should vary strongly with selenographic position (ref. 22). From the graph given by Wiesel, the following relative fluxes would be expected at the four landing sites: Apollo 11 = 1.3, Apollo 12 = 2.0, Apollo 15 = 1.6, and Luna 16 = 1.0. The data in table 1 do not show any such trend; Luna 16 has, if anything, the highest rather than the lowest flux. The reason for this discrepancy is Wiesel's deliberate choice of a velocity distribution peaking at 4 km/s, far below the actual mean velocity of meteors.

SOURCE

It appears that the C1-like component in lunar soil comes largely from micrometeorites. Two other sources make minor contributions. Solar wind accounts for about 3 to 4 percent of the siderophile elements in the soil (recalculated from ref. 7, with the latest abundance data and solar wind flux). Crater-forming objects provide a somewhat larger fraction, perhaps 5 to 20 percent (refs. 5 and 7). This estimate is rather uncertain because it depends on a host of poorly known quanti-

ties: projectile velocity distribution, crater scaling laws, mixing efficiency of projectile and target material as a function of throw-out distance, etc. The total mass of crater-forming projectiles is more than sufficient to account for the meteoritic material in the soil (fig. 3). However, much of this material seems to remain in the crater or in the ejecta blanket and does not find its way into the soil (see p. 684). Both the ubiquity of the C1 component and its lower abundance in crater-rim soils point to micrometeorites, rather than crater-forming objects as the main source. Indeed, Dohnanyi (refs. 25 and 26) has shown that his best estimate of the micrometeorite flux, based on satellite and photographic meteor data, gives an influx rate very close to the chemically determined value from table 1: 2.0×10^{-9} versus $2.4 \times 10^{-9} \text{ g cm}^{-2}\text{yr}^{-1}$. A lower value (by a factor of 4 to 6) was obtained from lunar microcraters (refs. 26 and 27), but the discrepancy was within the range of uncertainty of the cratering data.

If the C1 component in lunar soil indeed comes from micrometeorites, it may provide some important clues to the composition of comets because there is good reason to believe that comets are the principal source of micrometeorites (21, 26, 28, and 29). Apparently comets have a composition close to that of C1 chondrites, as proposed by Herbig (ref. 30), Anders (ref. 31), Whipple (ref. 32), and others. The present characterization is based entirely on trace elements, but is also supported by spectroscopic studies of Millman (ref. 33), showing that nine Giacobinid meteors have chondritic abundances of Na, Mg, Ca, and Fe. Further evidence comes from lunar microcraters which appear to have been made by volatile-rich projectiles, e.g., hydrated silicates (ref. 34). The only known meteorites consisting mainly of hydrated silicates are C1 chondrites.

Yet, it would be wrong to conclude that C1 chondrites proper come from comets. All C1 chondrites show signs of a preterrestrial exposure to liquid water (ref. 35) and contain solar-wind gases suggestive of irradiation in a regolith (ref. 36). Comets probably

² No reliable value could be calculated for Luna 16, for a variety of reasons. The sample itself was a sieve fraction, finer grained than the Apollo soils ($< 125 \mu\text{m}$ versus $< 1000 \mu\text{m}$) and, hence, presumably enriched in meteoritic material. Contamination seems to have been more severe than in the Apollo soils (ref. 23), and so the volatile abundances, at least, should perhaps be viewed as upper limits. Finally, the regolith thickness at the Luna 16 site is poorly known. Vinogradov (ref. 24) estimates it as 0.5 to 1 m, but suggests that it is similar to that in Oceanus Procellarum which he gives as 1 to 3 m, rather than the 4.6 m cited by Oberbeck and Quaide (ref. 20).

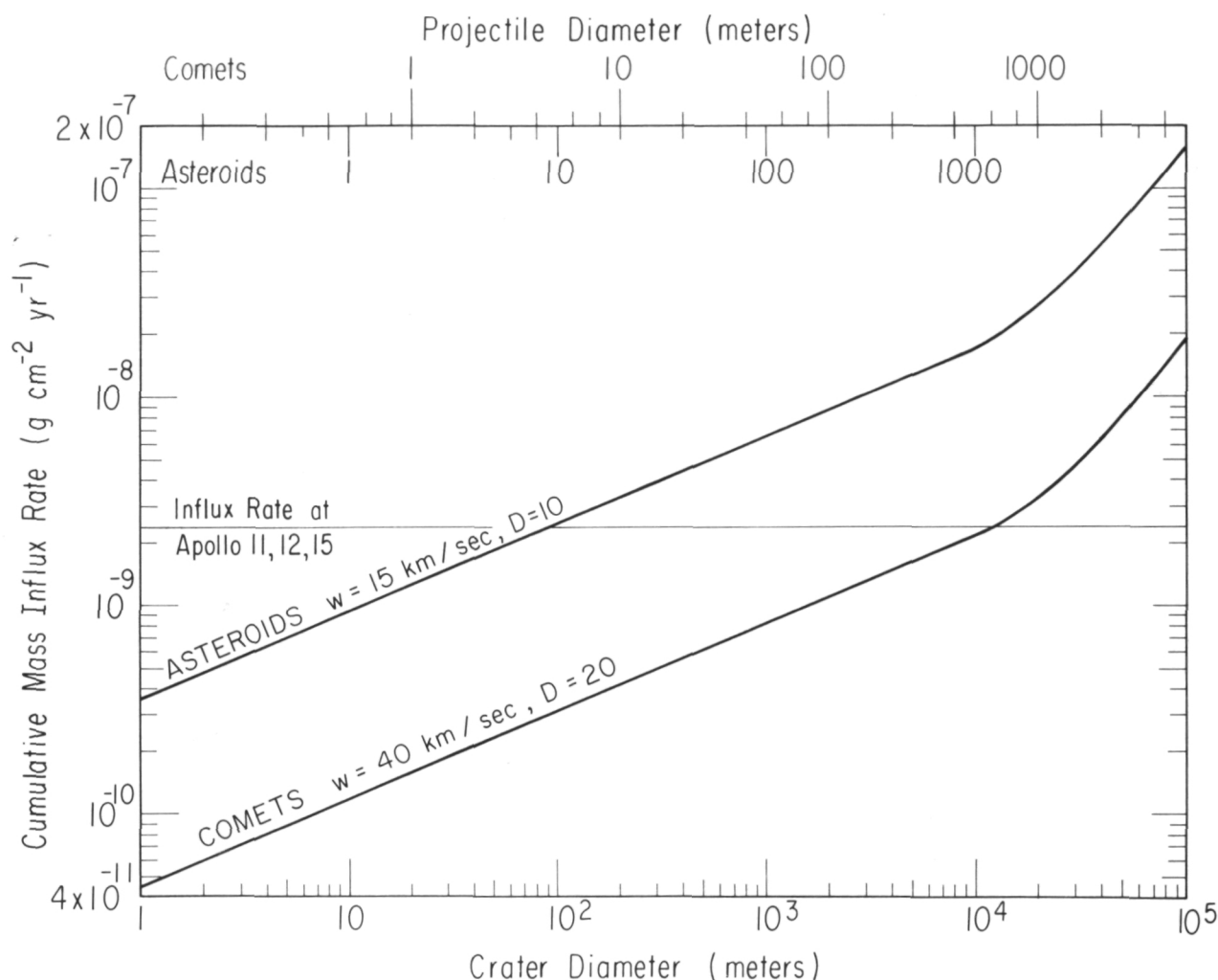


Figure 3.—Mass influx rates predicted from observed crater density in Mare Tranquillitatis for asteroidal and cometary projectiles (w = impact velocity, D = ratio of crater diameter to projectile diameter). Though crater-forming objects contribute more meteoritic material than is actually observed in mare soils (horizontal line), most of this material remains buried in the crater or its ejecta blanket and does not contribute to the fine soil (ref. 1).

are too cold to hold liquid water, too small ($\sim 10 \text{ km}$) to retain a regolith, and too far from the Sun to accumulate a significant amount of solar wind. Thus, larger bodies at closer distances are needed—perhaps asteroids in the outer part of the belt (refs. 37 and 38).

Interestingly, Johnson and Fanale (ref. 39), Chapman and Morrison (ref. 40), and Gaffey and McCord (ref. 41) have found that C1 and C2 chondrites resemble some aster-

oids in albedo and spectral reflectivity. Thus it seems that asteroids are a possible source of C1 chondrites.

The Ancient Meteoritic Component

Highland soils show a markedly different pattern, as first seen by Apollo 14 (ref. 42) and later at four other sites (refs. 1, 43, and 44). Siderophiles are more abundant than

volatiles and often show ratios (Ir/Au, Re/Au) well below the C1 chondrite value.

The excess siderophiles come from highland breccias, the source rocks of the soils. Two lines of evidence suggest that these siderophiles are extraneous, having been added to the breccias during the early intense bombardment.

First, the siderophiles are greatly overabundant in breccias compared to crystalline rocks. This is true of all highland rock types: anorthosites, norites, and granites. Figure 4 shows an alkali-poor and an alkali-rich highland breccia (black circles and black squares). Each is matched with a crystalline rock of similar bulk composition and Rb, Cs, and U content (open symbols). Most of the 16 elements have comparable abundances in the breccia and its crystalline counterpart,

except for the first five, siderophile elements which are enhanced in the breccias by factors of 10^2 to 10^3 . Nickel, not plotted here, behaves similarly.

Second, the lowest abundances of siderophiles in highland rocks, e.g., < 0.05 ppb Au (fig. 5), are consistent with measured metal-silicate distribution coefficients which range from 10^4 to 10^6 (ref. 45). It appears that these abundances represent true indigenous levels. On the other hand, the more common, high abundances around 1 to 10 ppb (fig. 5) exceed equilibrium solubilities in silicates by several orders of magnitude. The extraneous nature of these siderophiles is shown by the fact that they reside largely in discrete metal grains (refs. 9 and 46), which comprises 0.1 to 1 percent of highland breccias and impact melts (refs. 47 and 48). A suspension of

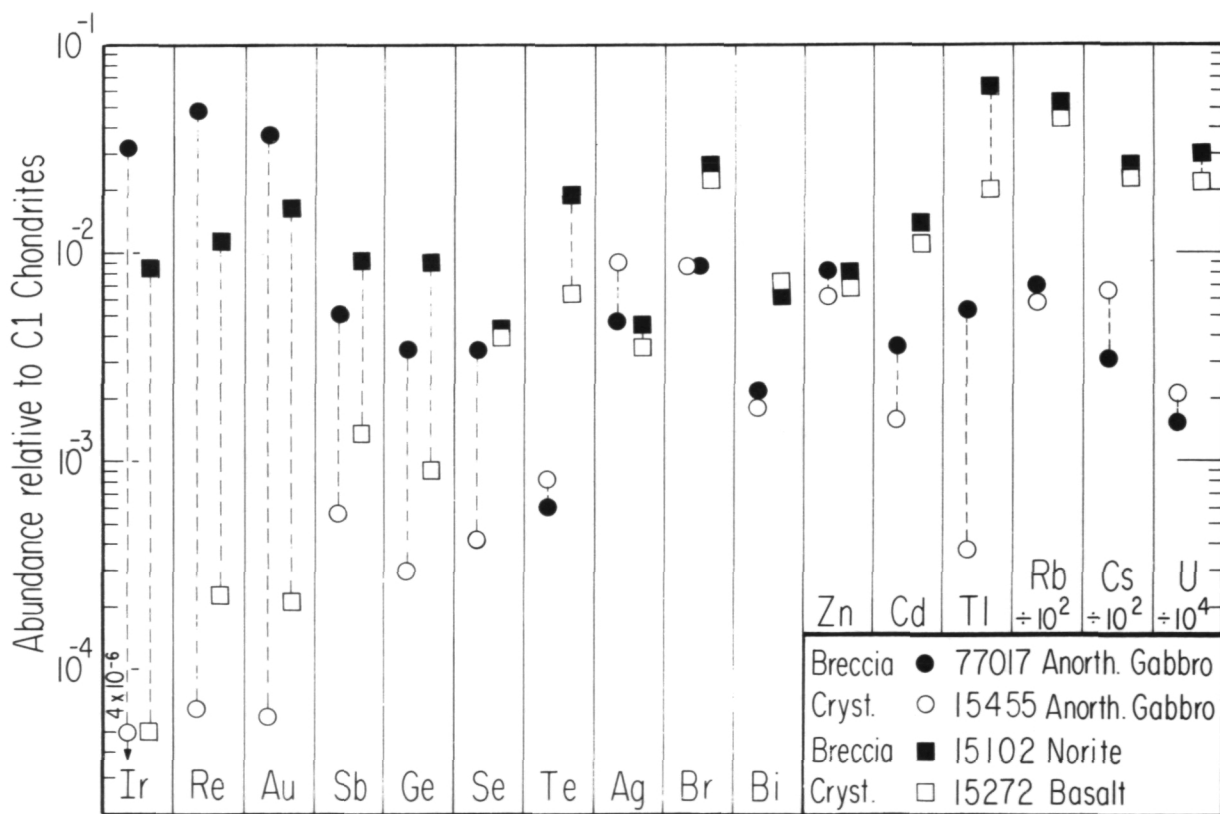


Figure 4.—Highland breccias (solid symbols) are strongly enriched in the first five siderophile elements compared to crystalline rocks of the same Rb, Cs, and U content (open symbols). The enrichment is due to an ancient meteoritic component dating from the era of intense bombardment.

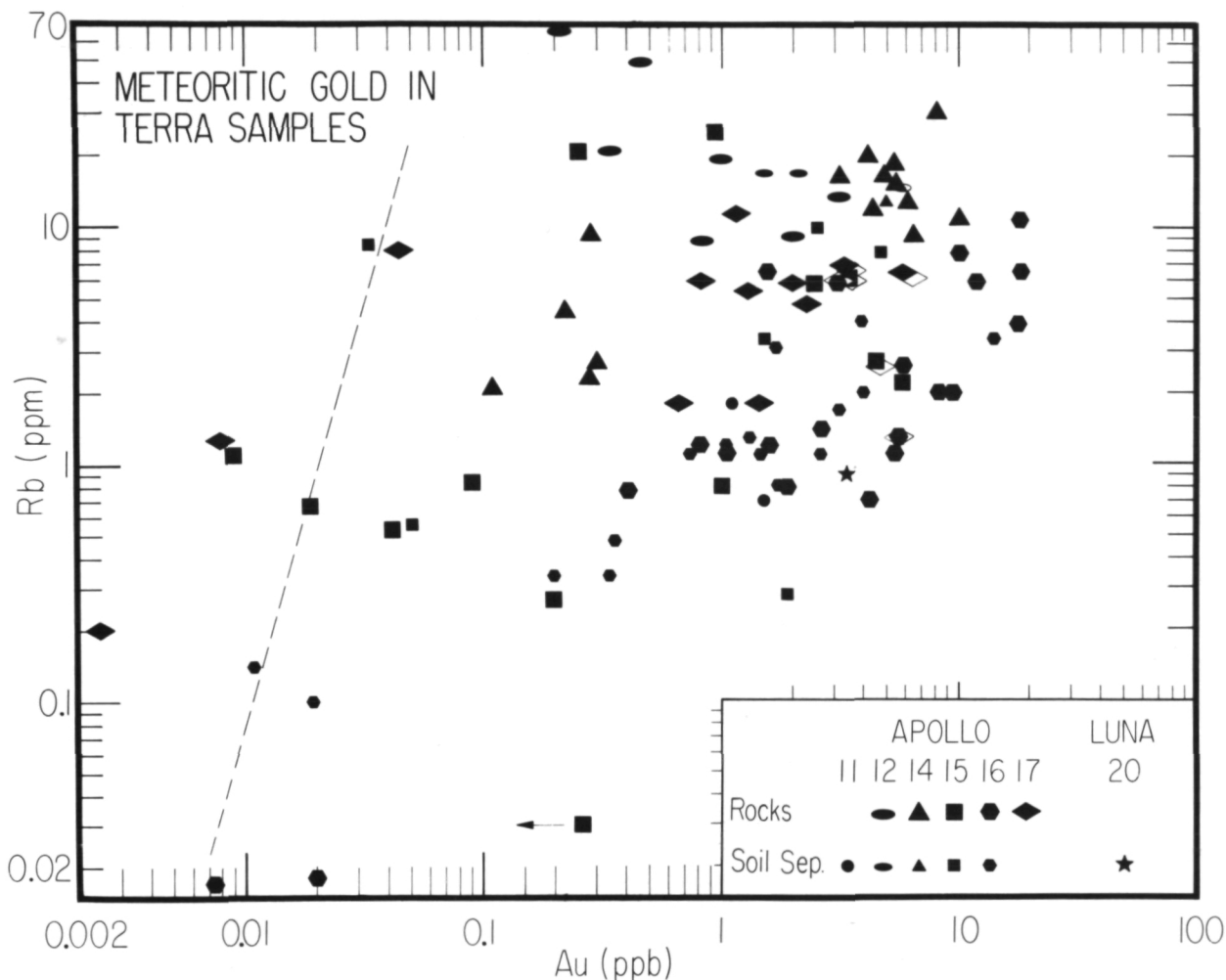


Figure 5.—Most highland samples are enriched in meteoritic gold above indigenous levels (approximated by dashed line). Enrichment is nearly independent of Rb content and rock type. Only anorthosites of < 0.2 ppm Rb tend to be free of meteoritic gold. Perhaps they come from deeper crustal levels not penetrated by meteoritic projectiles.

metal droplets in a silicate melt is dynamically unstable on time scales comparable to the freezing time of basaltic flows (refs. 49 and 50).

For these reasons, it appears that high siderophile abundances in highland rocks are diagnostic of a meteoritic component. Because this component occurs in breccias that have remained closed systems for at least 3.9 AE, it can properly be called an ancient meteoritic component.

CLASSIFICATION

The six diagnostic elements differ greatly in condensation temperature from a solar gas. Re and Ir condense a few hundred degrees above iron, Sb and Ge condense a few hundred degrees below iron, and Ni and Au condense almost concurrently with iron, slightly before and after, respectively, (Grossman, ref. 51 and unpublished data, and ref. 52 Larimer, and unpublished data).

Presumably for this reason these elements show large abundance variations in meteorites, which have been used as the basis for classification (Wasson and Schaudy, ref. 53 and earlier papers, and refs. 54 and 55).

Similar variations in Ir/Au and Ge/Au ratios have been seen in lunar samples, suggesting the presence of more than one kind of meteoritic component (refs. 8 and 11). The trends show up more clearly on ternary plots. Figures 6 and 7 show results for 74 highland samples from five sites. The data are normalized to C1 chondrite abundances (ref. 13) to prevent the plots from being dominated by the element of highest absolute abundance. Corrections have been applied for indigenous contributions (ref. 2). They are typically less than 1 percent for Ir, Au, and Re, and 1 to 30 percent for Ge and Sb. Because the corrections become larger at lower abundances, we used only samples of >0.2 ppb Au. In order to avoid samples

of mixed parentage, we used only rocks and lithic fragments from coarse soils. Agglutinates, magnetic separates, soil breccias, and glasses from coarse soils were excluded.

Approximately six groups seem to be present, as indicated by the dashed lines in figure 6. The elongated shape of the groups reflects the fact that Ge and Sb are less reliable indicator elements than are Ir, Re, and Au. Their indigenous contributions are larger and more variable, and their volatility makes them more prone to metamorphic redistribution. Consequently we used Ir/Au and Re/Au ratios as our prime criteria in defining the groups.

The reality of these groups is supported by the mutual consistency of the two plots (each of which has a volatile element at the apex and a refractory element in the right corner). Most points belonging to a given IrAuGe group fall in a similarly situated, compact cluster on the ReAuSb plot. The principal

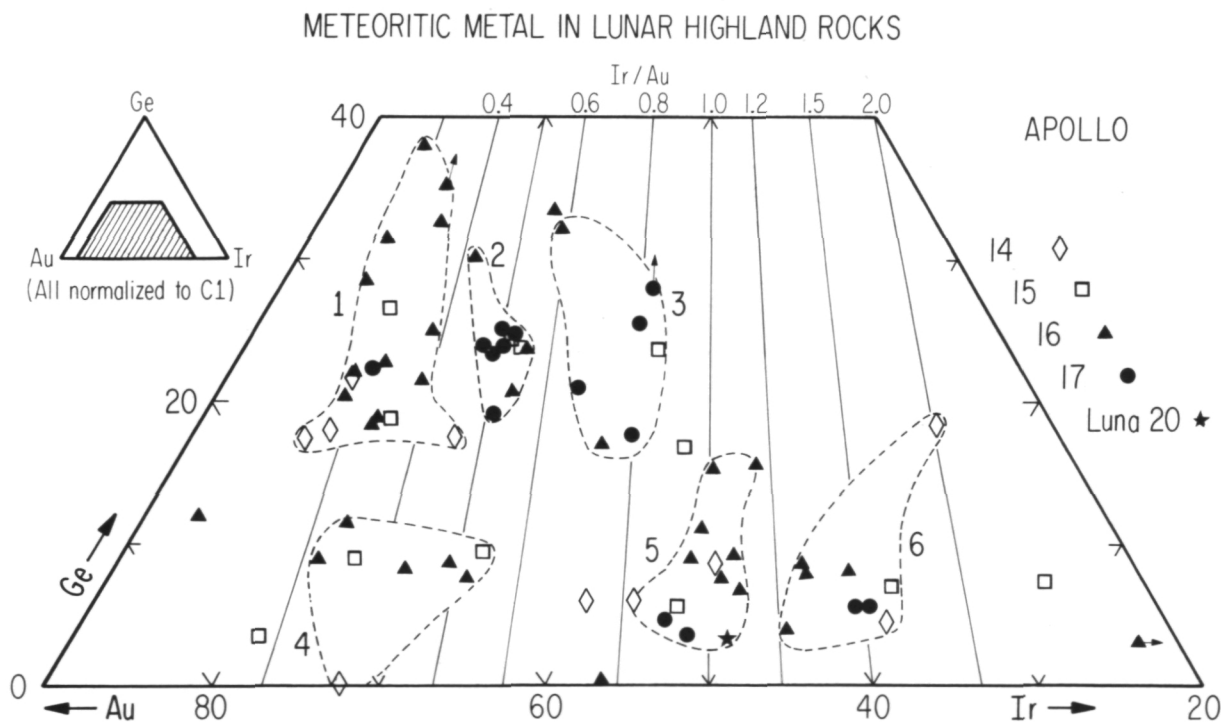


Figure 6.—Six distinct types of ancient meteoritic component differing in their proportions of Ir, Au, and Ge, seem to be present. Both the clustering of the points and their uneven geographic distribution suggest that this material is derived mainly from a few large objects—probably the projectiles that excavated the mare basins.

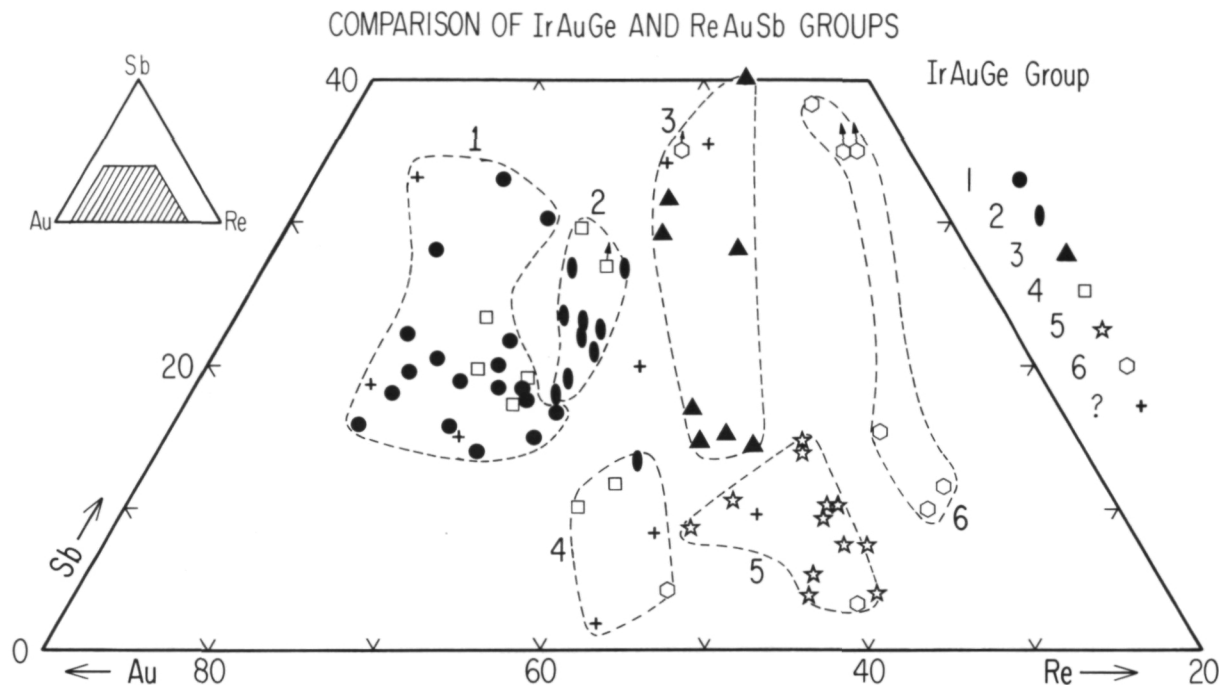


Figure 7.—Six analogous groupings may be recognized on the basis of Re, Au, and Sb content. Most of the points belonging to a given IrAuGe group fall in a similarly situated cluster on an ReAuSb plot. The principal exception is Group 4 which is largely dispersed on this plot.

exceptions are group 4 and a few samples of sporadically high indigenous Sb or Ge.

The definition of these groups involves some subjectivity, and we do not claim that the present six groups are final. In general, we have tried to be conservative, creating as few groups as possible. The separation between some of the groups is not as sharp as one might like, e.g., 1 and 2 or 5 and 6. However, in both cases there were reasons not to combine them. Group 2 contains a compact cluster of Apollo 17 samples which would stand out as a distinctive subgroup in a combined group 1 + 2. Groups 5 and 6 also contained distinctive subsets of samples; moreover, if combined, these two groups would cover a wider range in Ir/Au ratio than any other.

COMPARISON WITH METEORITES

The ancient lunar meteoritic bodies show little resemblance to present-day meteorites

(figs. 8 through 10). Most meteorite groups avoid the lunar fields. Only a few (E4, E6, H-chondrites, and I and IIIA irons) show as much as a marginal overlap. It appears that the ancient meteoritic bodies represent a distinct population, different from present-day meteorites.

One interesting point that emerges from figures 8 and 9 is that the chondrite groups are not much more compact than the lunar meteorite groups. Probably the best indication of the "natural width" of a chondrite group comes from C1 chondrites (figs. 8 and 9) and H, L chondrites (fig. 9), where at least five samples were analyzed for all three elements in the same laboratory (refs. 13, 56, and 57). For most other classes, data were few and from different sources.

BASINS OR CRATERS?

Granted that the ancient meteoritic material dates from the early intense bombard-

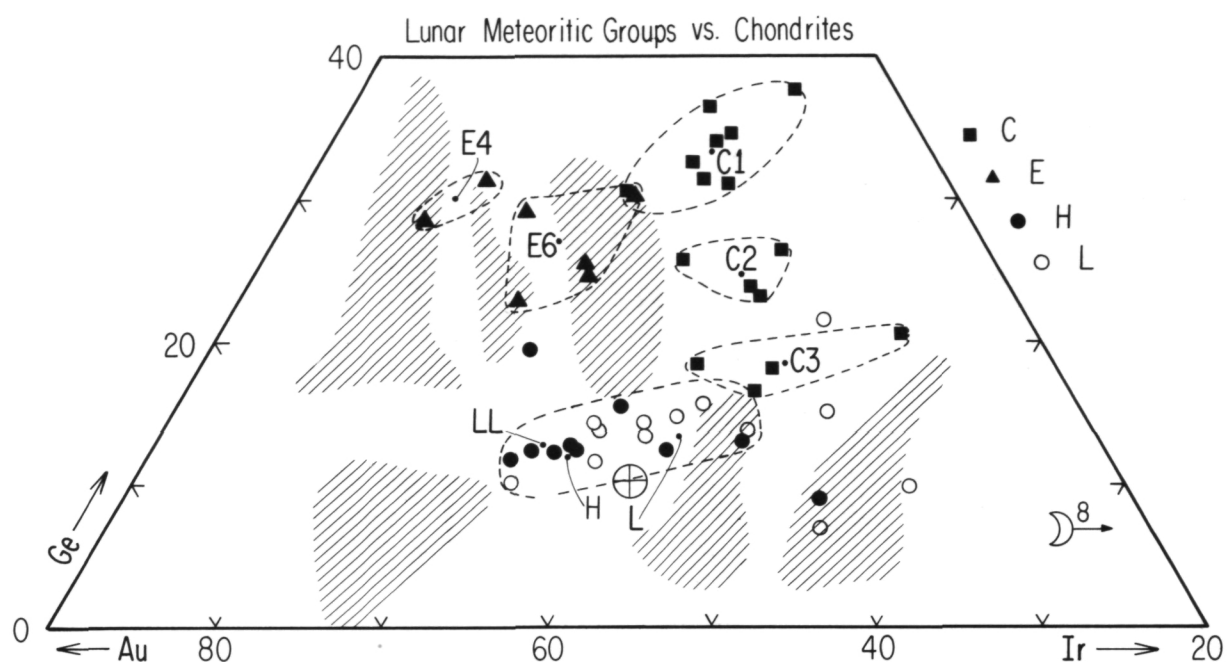


Figure 8.—Ancient lunar meteoritic components show little resemblance to known chondrite classes.

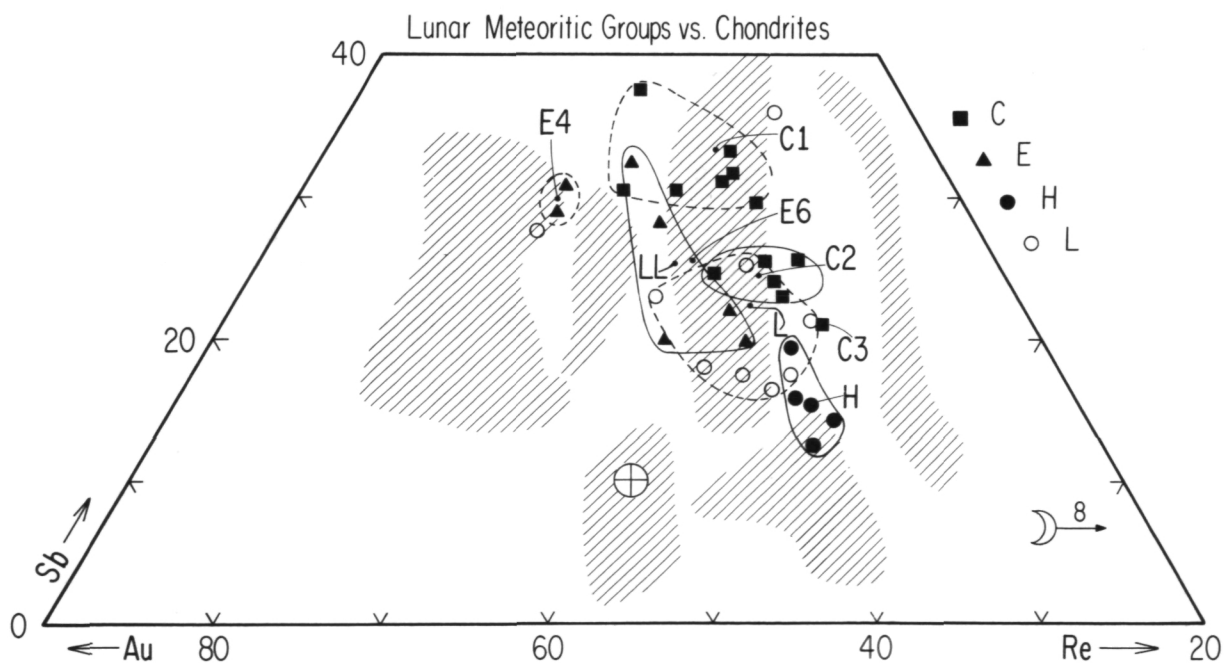


Figure 9.—Ancient lunar meteoritic components show little resemblance to known chondrite classes.

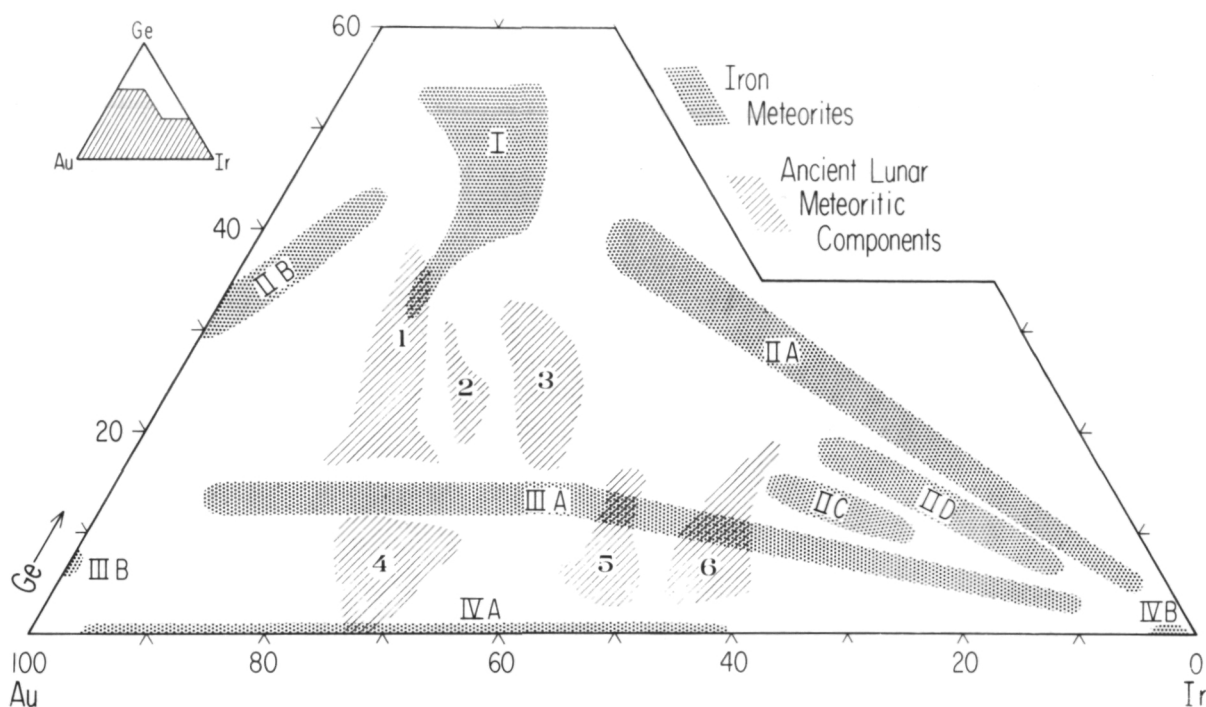


Figure 10.—Ancient lunar meteoritic components do not resemble iron meteorites.

ment, does it come mainly from a few large basins or from a multitude of smaller craters? The clustering into six groups alone does not prove that only six bodies were involved. Six families of crater-forming bodies, each with hundreds of members, would lead to the same result. A more conclusive argument comes from the size distribution of lunar craters and basins.

Contribution of Basins

Various authors have estimated the amount of ejecta in the lunar highlands and their results consistently show that the largest objects will contribute the lion's share. This is a consequence of the small slope of the size distribution function. Öpik (ref. 58), using a single size distribution law (ref. 59), estimated that 56 percent of the highland ejecta will be contributed by craters (actually basins) larger than 412 km in diameter, and an additional 25 percent by craters between 206 and 412 km. Short and Forman

(ref. 60) determined the crater contribution separately by integrating the size distribution function to 400 km and then adding the basins individually. Their results indicate a basin contribution of 30 to 60 percent, depending on the degree of slumping assumed. However, Short and Forman used a relation for the crater depth/diameter ratio which gave preposterously small volumes for the larger basins—comparable to the projectile volume. Thus, the basin contribution is likely to be substantially higher than 30 to 60 percent, probably close to Öpik's 81 percent.

Shallow Ejecta Only?

Even though the basins may account for most of the ejecta, it does not necessarily follow that their projectile debris will dominate at distant sites. Dence and Plant (ref. 61) pointed out that the pre-Imbrian surface was covered with mixed ejecta from many highland craters and argued, by analogy

with Ries Crater "bunte Breccia," that this surface layer contributed the bulk of the ejecta at Fra Mauro and other distant sites. Because of its shallow origin and gentle shock history, it would not contain any Imbrium projectile debris. Deeper, more heavily shocked material analogous to suevite would be found only at closer range, e.g., at the Apollo 15 site. Other authors have also used the Ries analogy to argue for a shallow origin and short range of lunar crater ejecta (ref. 62). However, these arguments neglect the difference in gravity between Earth and Moon. The range R of a fragment ejected with velocity v at an angle β is given by

$$R = (v^2/g) 2 \sin\beta \cos\beta$$

where g is the acceleration due to gravity. Other things being equal, a fragment will thus fly six times farther on the Moon than on the Earth. Indeed, several rocks of deep-seated origin have been found on the lunar surface: a troctolite from a depth of 15 to 40 km (ref. 63) and a number of dunite clasts, presumably from below the 65-km crust (e.g., ref. 64).

Secondary Craters?

Oberbeck et al. (ref. 65) have raised a different objection. They note that any basin ejecta reaching Apollo landing sites would strike at high enough velocities to excavate a secondary crater of several times their own mass. Thus Imbrium or Orientale material reaching the Apollo 16 site would be diluted from four to seven times with local rock. They therefore contend that the ancient meteoritic component is derived mainly from many small local craters, not a few large distant basins.

Oberbeck's mechanism certainly applies to large blocks tens or hundreds of meters in diameter. But observed mass distribution functions and the scarcity of secondary craters (a few percent of the lunar surface) show that such blocks comprise only a minor part of the distant ejecta. Moreover, their very size precludes any admixture of projectile debris. The great bulk of the distant

ejecta seems to have been of from millimeter to decimeter size, judging from both the grain and clast size of lunar breccias and the uniform dispersion of the metal on a millimeter scale.

Now, when the first 10 cm of 100 m of such fine-grained basin ejecta arrive at a given site, they will indeed mix with the local regolith, to a depth on the order of the diameter of the largest fragments, i.e., ~ 10 cm. Successive 10-cm layers will mix not with pristine local regolith, but with material containing progressively larger amounts of basin ejecta. So, before as much as a meter of material has been deposited, the process has turned into orderly sedimentation, without appreciable mixing. The situation is analogous to that in the mare regolith, where lateral deposition greatly predominates over vertical mixing. A spectacular demonstration is the integrity of coarse-grained, Bi- and Cd-rich layers in core 12028 (ref. 10). Greater mixing depths will be attained at the sites of secondary craters, but because these craters account for only a minor part of the ejecta, the resulting polymict breccias will not be very common.

This is confirmed by trace element and electron microprobe data. Thirteen out of fourteen breccias studied at Chicago contain only one kind of meteoritic metal (ref. 2). The Co and Ni contents of metal grains in a given breccia also tend to cluster strongly, at least in cases where the Ni content is low enough for all the metal to be present as kamacite (see, for example, ref. 66).

Finally, we must stress the truism that local impacts can never become dominant over basins if basins contribute the major part of the ejecta. At best, local impacts can mobilize and remobilize older basin ejecta. But if basins contribute 80 to 90 percent of the projectile debris on the Moon, they will dominate the meteoritic component in second-, third-, and n th-generation breccias. The only secular trend of such repeated mixing will be eventual homogenization of the metal. Data on breccias (ref. 2) and figures 6 and 7 show that very little such homogenization has taken place.

Thus it seems safe to conclude that the ancient meteoritic debris comes mainly from a few large events superimposed on a continuum of smaller events. This is consistent with the clustering of the points in figure 6: all but eight of the 74 points fall within the six groups.

Assignment to Basins

EJECTA THICKNESS

We can try to assign the groups to individual basins by comparing their frequency of occurrence at each landing site (fig. 6) with expected contributions of ejecta from each basin, according to McGetchin et al. (ref. 67). We have recalculated their data using the basin coordinates and age sequence of Hartmann and Wood (ref. 68), rather than Stuart-Alexander and Howard (ref. 69), and including the Luna 20 site (table 2).

PREBASIN OVERLAY?

In principle, these trends can be blurred by two-stage transport, i.e., reejection of older ejecta during formation of a basin. To assess the importance of this effect, we have calculated the average overlay thickness at the center of each prebasin surface (ref. 2). It turns out that the old overlay comprises only some 10 to 200 m, or 1 to 5 percent, of the new ejecta, hardly a significant fraction.

Highland craters, on the other hand, contribute ~ 1 km of overlay (ref. 60), and thus may pose a more serious problem. A large crater contribution could manifest itself in two ways, depending on whether or not the crater-forming population was chemically distinct from the basin-forming population. If it was, it would fill the continuum between the groups in figure 6. If it was not, it would merely blur the geographic trends, all groups being equally common at all landing sites. Neither of these is the case: note, for ex-

ample, the scarcity of Apollo 17 samples in groups 1 and 4 and their dominance in groups 2 and 3. We thus conclude that the crater contribution was small compared to the basin contribution. Let us therefore try to assign each group to an individual basin.

TENTATIVE ASSIGNMENTS

Imbrium

Group 1 (fig. 6) has all the attributes expected for an Imbrian origin, according to table 2. It is prominent at all sites except Luna 20 which is the most distant from the Imbrium basin and Apollo 17 which is partly shielded by South Massif from Imbrian ejecta. It seems to comprise the topmost stratigraphic unit everywhere, judging from its prominence in intercrater areas and lower abundance on crater rims (Cone Crater at Apollo 14, North Ray Crater at Apollo 16), where deep-seated material is expected to dominate.

Serenitatis

According to table 2, material from this basin should be dominant at Apollo 17. This clue leads us to group 2, six of whose 10 members come from Apollo 17. Not only is this the largest grouping of Apollo 17 samples, but it also includes all samples of the oldest breccia type at this site, the blue-gray breccias (fig. 11). Two of them come from the Station 6 boulder that originated 1600 m below the crest of North Massif. This suggests a position fairly low in the stratigraphic sequence: Serenitatis or older (table 2).

Crisium

Group 3 is most likely derived from Crisium. It is represented mainly by the gray, foliated boulder from Station 2 of Apollo 17 (fig. 11), which apparently comes from near the top of South Massif (ref. 70) and, hence, must represent one of the younger basins. With Imbrium already assigned, the main

Table 2.—*Ejecta Depth in Meters* ⁽¹⁾

Contributing Basin	Crater Density ⁽²⁾	Apollo 11	Apollo 12	Apollo 14	Apollo 15	Apollo 16	Apollo 17	Luna 16	Luna 20
Oriente	2.4 ± 0.2	1.1	4	4	1.9	1.3	1.1	0.6	0.6
Imbrium	2.5 ± 0.2	59	133	128	560	54	66	19	19
Nectaris	16 ± 2	232	8	10	13	211	35	78	64
Crisium	17 ± 4	42	4	5	13	20	100	482	1134
Humorum	25 ± 2	4	68	47	5	7	3	1.4	1.8
Smythii	27 ± 7	2	0.4	0.5	0.9	1.4	3	18	18
Serenitatis	28	144	20	26	693	57	1089	47	40
Tranquillitatis W.	30	121	0.7	0.9	4	1.8	54	3	3
Tranquillitatis E.		9	0.2	0.3	1.0	1.9	32	5	6
Nubium	30	3	44	63	2	6	1.1	0.6	0.5
Fecunditatis	30	2	0.1	0.2	0.3	1.1	1.8	258	80
Australe		17	6	6	10	15	15	46	39

NOTES: (1) Calculated according to McGetchin et al. (ref. 67).

(2) Relative to average mare = 1. These crater densities refer to ejecta blanket of flooded basins or to floors of unflooded basins and should be proportional to age (ref. 68).

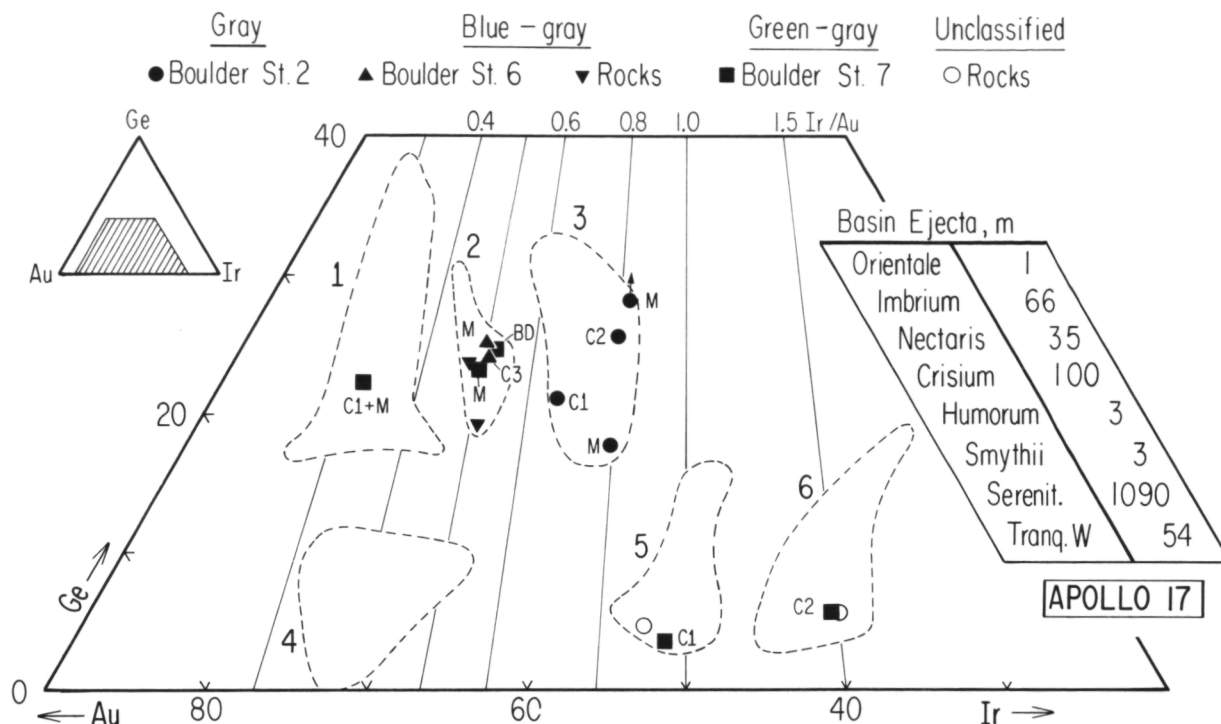


Figure 11.—Distribution of Apollo 17 samples among lunar meteoritic groups. C—clast; M—matrix; BD—black dike.

possibilities are Nectaris or Crisium. If it came from Nectaris, then group 3 should be very common at Apollo 16 (table 2); yet, only two of 37 samples from that site fall in group 3. On the other hand, if it came from Crisium, then group 3 should be more prominent at Apollo 17 than at other sites and, indeed, Apollo 17 accounts for four of the seven samples in this group.

Nectaris

Either group 5 or group 6 may be derived from the Nectaris body. At Apollo 16, both are represented mainly by a distinctive type of alkali-poor, dark-matrix breccia from Stations 11 and 13 near the rim of North Ray Crater (ref. 9). Group 5 also includes three shocked glasses from other stations (fig. 12). The dark-matrix breccias comprise the third stratigraphic unit at that site, being overlain by nearly 300 m of light-matrix breccias and cataclastic anorthosites (refs. 71 and

72). The latter contain no meteoritic component and have therefore been interpreted as deep ejecta from the Nectaris basin (refs. 9 and 73). Thus, groups 5 and 6 must represent basins of Nectarian or older age. We tentatively assign group 5 to the Nectaris body because of its presence at Luna 20 (fig. 12). Both Nectaris and Crisium ejecta should be prominent at that site, but by analogy to the stratigraphy of Apollo 16 all but the bottom portion of the thick Crisium blanket at Luna 20 should consist of deep ejecta, uncontaminated by projectile debris. It must be overlain by a thin blanket of meteorite-bearing Nectaris material. The source crater of Luna 20 soil, Apollonius C (refs. 48 and 74), should have ejected mainly such Nectaris material.

Humorum

Group 6 must be pre-Imbrian in age. It is found mainly in rocks from crater rims

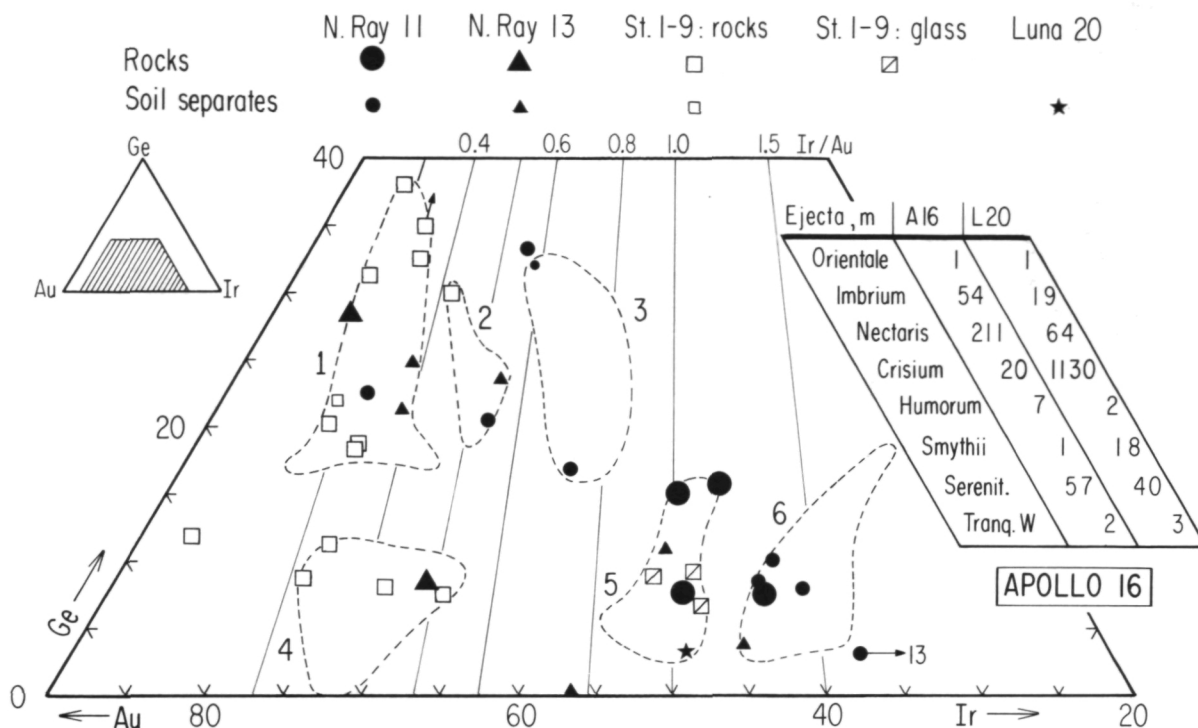


Figure 12.—Distribution of Apollo 16 and Luna 20 samples among lunar meteoritic groups.

which tend to come from lower stratigraphic units: 60017 from Outhouse Rock at North Ray Crater (Apollo 16), and 14063 from one of the White Rocks at Cone Crater (Apollo 14). With Nectaris, Crisium, and Serenitatis already assigned, the principal remaining possibility is the Humorum body. Alternatives are Nubium or the South Imbrium basin at 10°N., 16°W. (ref. 75). Perhaps a further study of Apollo 14 samples will shed some light on this question because material from all three basins should be prominent at that site.

Unassigned

This leaves group 4 unassigned. It is the least well defined of the six groups (note the dispersal of its members in figure 7) and contains a high proportion of impact melts. Perhaps it is not a true group, but merely a chance cluster of samples from groups 1 and 2 that lost some volatiles in impact melting or metamorphism.

Oriente

We also do not have a strong candidate for Oriente material. Early estimates (refs. 72 and 76) suggested that some tens of meters of Oriente material might be present at Apollo 16 and other sites, but the calculations of McGetchin et al. (ref. 67) suggest much smaller thicknesses, 1 to 4 meters (table 2). Moreover, because of the great ejection distances such material probably fragmented on impact and became dispersed throughout the local regolith (ref. 65). Two highly speculative candidates are a subgroup of group 1, distinguished by a high Re/Ir ratio (R group of ref. 8) or some samples of very low Ir/Au ratio (ref. 9).

Summary

Table 3 summarizes our tentative assignments, first for the age sequence of Hartmann and Wood (ref. 68) used above, and

Table 3.—*Tentative Basin Assignments*

Group	Ir/Au	Ge	Mare	
			HW ⁽¹⁾	SH ⁽²⁾
1	0.30–0.40	high	Imbrium	Imbrium
2	0.40–0.55	high	Serenitatis	Serenitatis
3	0.55–0.85	high	Crisium	Nectaris
4	0.30–0.50	low	??	??
5	0.85–1.20	low	Nectaris	Crisium
6	1.50–2.0	low	Humorum or Nubium	Humorum or Nubium

NOTES: (1) HW = Basin age sequence of Hartmann and Wood (ref. 65).

(2) SH = Basin age sequence of Stuart-Alexander and Howard (ref. 66).

then for the sequence of Stuart-Alexander and Howard (ref. 69): Orientale, Imbrium, Crisium, Humorum, Nectaris, Serenitatis, Fecunditatis, and Tranquillitatis W. The latter set, which reverses the assignments of Crisium and Nectaris, is slightly less self-consistent, but not by a decisive margin.

These assignments must be regarded as tentative until they have been thoroughly checked against all available evidence: radiometric ages, petrography, and field geology. In the first round of such tests, only one serious discrepancy has been found (ref. 2). Three clasts from the Apollo 17 Station 7 boulder (fig. 11) fall into groups 1, 5, and 6 assigned to young basins (Imbrium, Nectaris, and Humorum), whereas the matrix falls into group 2 assigned to an older basin (Serenitatis). Under normal circumstances, clasts should be older than matrices, not younger. To resolve this paradox, it may be necessary to assume that the green-gray breccias are Serenitatis material that was remobilized during the Imbrium event, incorporating clasts of Imbrian age or older. Indeed, Schmitt (ref. 70) proposed that the tan-gray³ breccias are younger than the blue-gray breccias, having intruded them in partially molten state. Head (ref. 77) suggested that the Taurus-Littrow area was tectonically reactivated by the Imbrium event.

³ Tan-gray on the lunar surface, green-gray in the laboratory.

Origin of Basin-Forming Objects

Let us try to infer the properties of the basin-forming objects from the clues available.

PRIMARY OR SECONDARY BODIES?

The high siderophile element content of highland breccias (several percent of solar abundance) shows that the basin-forming objects were independently formed primary bodies, not secondary castoffs of a larger body that had undergone a "planetary" segregation of metal and silicate. Such segregation typically depletes siderophiles by factors of 10^{-4} to 10^{-6} . Hence, they cannot represent material spun off the Earth after core formation (refs. 78, 79, and 80), condensates or volatilization residues from a hot Earth (ref. 81), or fragments of a differentiated protomoon disrupted during capture (refs. 82 through 85).

INTERNAL STRUCTURE

The ubiquity of metal in highland breccias suggests that the basin-forming bodies were undifferentiated and chondrite-like, with the metal phase uniformly dispersed throughout. Otherwise, if the metal had segregated into a core, the projectile would have to mix with the target rock to an incredibly uniform de-

gree to produce the distribution in figure 5.

Cooling rates of iron meteorites (ref. 86) support this conclusion. Fricker et al. (ref. 87) have compared the observed cooling rates with thermal models of asteroids and conclude that the IVA irons, with a wide range of cooling rates, came from a 100-km body whose metal phase did not coalesce into a single core, but formed scattered pockets throughout the body. Smaller bodies should be still less completely differentiated. According to published estimates, even the Imbrium body, largest of the basin-forming objects, was smaller than 100 km ($R = 95$ km (ref. 88); $R = 68$ km (ref. 89)).

IMPACT VELOCITY

The consistently high siderophile element content of highland breccias may be a significant clue to the impact velocities of the bodies. According to cratering theory, the ratio of eroded mass, M , to projectile mass, μ , is a function of impact velocity, w . Thus, if the mean value of M/μ is known for a given impact, the velocity can be calculated.

In practice, the true mean value is hard to determine because projectile and target rock do not mix uniformly. At Meteor Crater,

Arizona, rim material and nearby ejecta are very low in meteoritic elements (Morgan et al., unpublished work), while some of the subfloor material is high in Ni (ref. 90). Unless these effects exactly cancel each other, distant ejecta will contain either more or less than their share of projectile material. For large basins, the situation is simpler inasmuch as even rim material (e.g., Apollo 15, 17) typically had flight distances of $\sim 10^2$ km and, thus, must have been strongly shocked and meteorite-bearing. Consequently, all our samples are distant ejecta in the above sense, and so any bias should be the same for all groups. Thus, the M/μ values and the velocities derived therefrom should be reliable at least in a relative sense.

We have estimated M/μ in three ways: from the Au, Ni, and metal content of lunar breccias. To determine M/μ from the mean Au content, Au_B , we need to know the Au content of the projectile, Au_P . This can be estimated via the iron content of the projectile, Fe_P :

$$(M + \mu)/\mu \approx M/\mu = Au_P/Au_B \\ = (Au_P/Fe_P) (Fe_P/Au_B)$$

Because Au and Fe condense together from a solar gas and scarcely fractionate from

Table 4.—Target/Projectile Mass Ratio

M/μ based on ⁽²⁾	M/μ Value ⁽¹⁾					
	Group 1	Group 2	Group 3	Group 4	Group 5	Group 6
Au	10.1 (23)	25.3 (12)	47.6 (8)	36.2 (4)	21.3 (13)	153 (9)
Ni	12.7 (15)	26.0 (10)	41.8 (6)	58.7 (3)	16.4 (10)	96 (6)
Metal ⁽³⁾	15.5 (9)	25.2 (5)	24.0 (3)	19.9 (2)	33.9 (3)	69 (4)
Weighted Mean	12.0	25.6	41.4	40.0	20.9	117

NOTES: (1) Number of samples is given in parentheses. The observed ratios, all based on samples with >0.2 ppb Au, were divided by 0.81 to allow for 19 percent highland samples with lower siderophile element contents.

(2) For a "lunar" iron content of the projectile, i.e., 9 wt %. For a "terrestrial" iron content of 36 percent, the M/μ values will be four times larger.

(3) See Morgan et al. (ref. 2) for references.

each other in chondrites (ref. 91), it is reasonable to assume that Au_p/Fe_p equaled the C1-chondrite ratio, 8.0×10^{-7} . This leaves only Fe_p to be determined. We have assumed two extreme values: "lunar" at 9-percent Fe and "terrestrial" at 36-percent Fe. They bracket all known chondrite classes, which range from 18- to 35-percent Fe.

About 19 percent of the highland breccias in figure 5 contain no meteoritic material, or too little to characterize. In order to make our M/μ values representative of the whole of the ejecta, we have corrected the mean Au contents of each group for a 19-percent contribution of meteorite-poor material.

A second set of M/μ values was calculated in an analogous manner from the Ni contents, using the Ni/Fe ratio of C1 chondrites, 5.67×10^{-2} . The third set was based on the metal contents of the breccias on the assumption that all the iron in the projectiles was in the metallic state. (This may not be such a bad assumption, because the Ni content of the metal is about 6 percent, close to the value of 5.3 percent expected for completely reduced C1-chondrite material.) The three sets of M/μ values, and a weighted average, are given in table 4. Only the values for "lunar" iron content (9 percent) are shown. Those for terrestrial iron content (36 percent) are a factor of 4 higher.

These M/μ values may be converted to impact velocity by a suitable cratering relation. There still is some controversy whether cratering is governed by the momentum or kinetic energy of the projectile, and we have therefore used both kinds of relation.

Momentum: $M/\mu = 5.67 \times 10^{-5} kW$ (refs. 92 and 93)

Energy: $M/\mu = 1.58 \times 10^{-10} W^{2.117}$ (ref. 94) The k in Öpik's equation is a velocity-dependent parameter, varying from 2 to 4.7 in the range 0 to 35 km/s.

The two relations are plotted in figure 13, along with M/μ values for lunar and terrestrial iron contents (solid and open circles).

The velocities are consistently low; indeed, for a lunar iron content, six of the 12 points fall below lunar escape velocity (2.4 km/s) for either cratering relation. To the extent

that these M/μ values are representative, this would seem to suggest that the projectiles had Fe contents higher than 9 percent. But even an iron content as high as 36 percent (open circles) gives quite low velocities: less than 8 km/s in nine of 12 cases. (In this M/μ range, Öpik's relation predicts much higher velocities than Gault's. It is in fact responsible for all three cases above 8 km/s.)

These velocities may not be accurate in an absolute sense because they are based on uncertain cratering relations and the uncertain assumption that M/μ in the ejecta was the same as for the whole impact. However, these uncertainties cancel out when we compare M/μ in ancient breccias and in ejecta from more recent craters. Although we have looked hard for contributions from recent craters, they are at best barely detectable

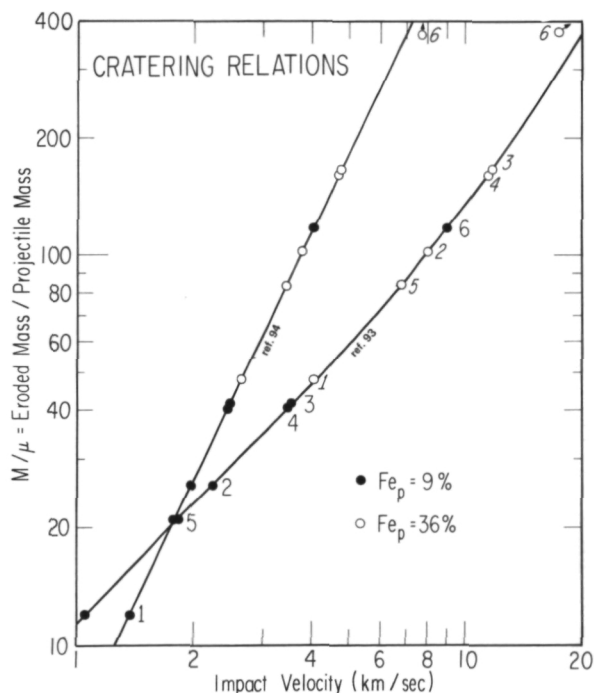


Figure 13.—Nominal impact velocity of basin-forming objects, estimated from cratering relations of Gault and Öpik. The two sets of points represent extreme values of iron content of the projectiles. Except for number 6, these bodies seem to have had impact velocities well below the mean geocentric velocity for present-day meteorites, ~ 15 km/s.

against the background of the ancient component (see p. 684). It seems difficult to escape the conclusion that most of the ancient projectiles had systematically lower velocities than the present crater-forming population (~ 15 km/s for asteroidal material; more for cometary material). Only group 6 comes close to the present-day range.

CHEMICAL COMPOSITION

We can try to characterize the basin-forming bodies more fully, using data on volatile elements. Though we have thus far confined ourselves to the five siderophile elements Ir, Re, Au, Sb, and Ge, eight of the remaining elements measured by us are also in part meteoritic. Figure 14 shows a rather favorable case, with a high content of meteoritic material. The indigenous corrections (black bars) are larger for volatiles than for siderophiles, but remain manageably small for most elements except Br, Zn, and Cd.

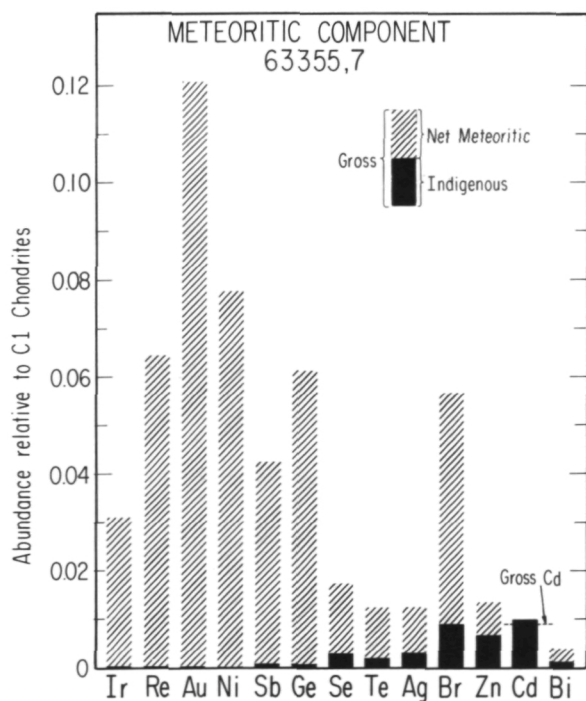


Figure 14.—Even some volatile elements are largely meteoritic in highland samples of high siderophile element abundance.

We have derived the abundance patterns of the six groups in this manner, using three to four samples of high siderophile element content from each group (fig. 15). The patterns were very consistent for the first six elements; less so for the last four, Se to Bi. For those elements, we gave greatest weight to the lowest values.

Several trends are apparent. (1) Groups 1 and 2 have almost identical patterns, except for the higher Au abundance in group 1. (2) In groups 1 to 3, Sb and Ge are equally abundant, while in groups 4 to 6, Ge is less abundant than Sb. Such differences have also been noted between carbonaceous chondrites and ordinary chondrites, where they were attributed to a higher effective temperature of chondrule formation (refs. 13, 95, and 96). (3) In all groups except 6, highly volatile Te and Bi are less abundant than the preceding four, moderately volatile elements. This trend is also observed in ordinary chondrites (refs. 97, 98, and 99), where it has been attributed to accretion in the range of partial condensation of these elements. In terms of this explanation, the flat pattern of group 6 would imply a lower accretion temperature and hence a more distant origin. This is an interesting thought in view of the high M/μ value that implies a high impact velocity (fig. 13) and hence an eccentric orbit. However, as expressed in the high M/μ , the samples of this group have a low content of meteoritic material; hence, the abundance pattern is poorly defined. (4) Group 3, which plots closest to C1 chondrites in figures 8 and 9, is highest in volatiles.

We can extend the comparison to the bulk Earth and Moon (fig. 16), using the compositional model of Ganapathy and Anders (ref. 100). None of the six groups is a perfect match for the Earth or Moon, and perhaps none should be, if these bodies accreted from planetesimals of a range of compositions. The Earth's composition could perhaps be approximated by a combination of groups 3 and 5, or possibly others. The Moon's composition requires a more refractory-rich material than even group 6. Only one sample

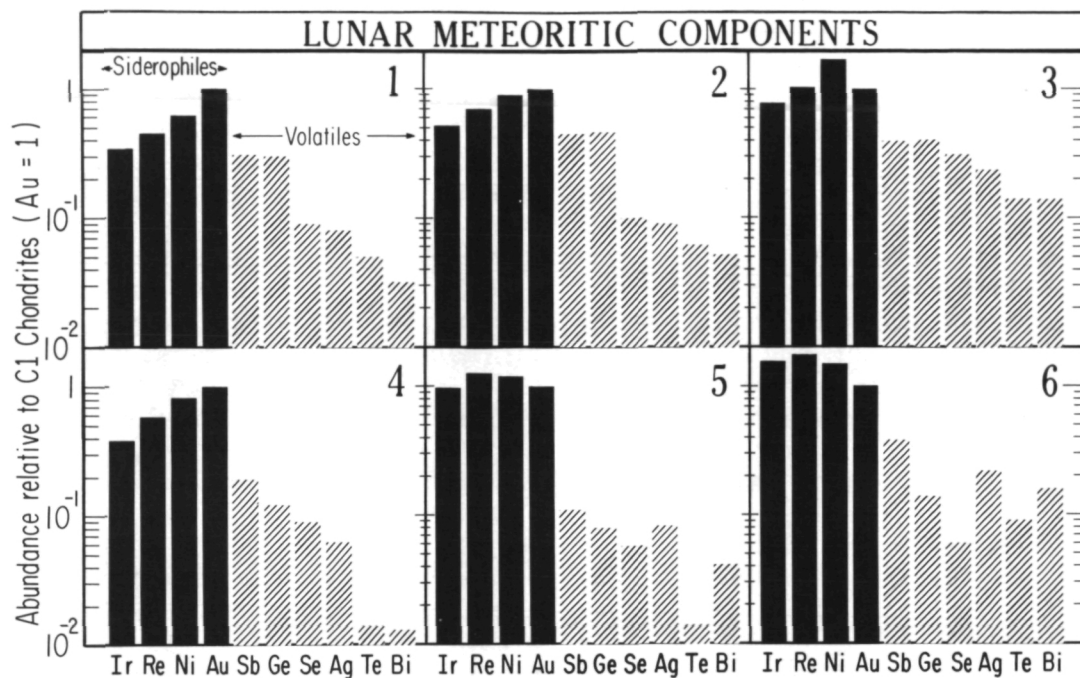


Figure 15.—Abundance patterns of six ancient meteoritic groups, corrected for indigenous contribution.

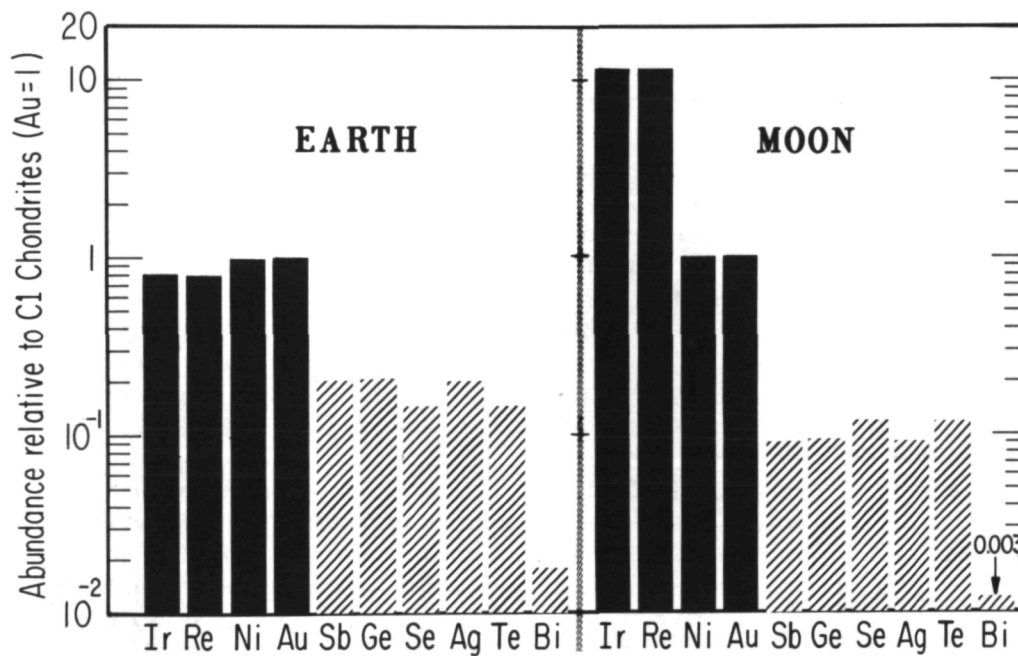


Figure 16.—Abundance patterns of bulk Earth and Moon, according to model of Ganapathy and Anders (ref. 97). Compare with figure 15. Groups 1 and 2 are complementary to Earth and Moon, being poorer in refractories (Ir, Re) and richer in volatiles (Ge, Sb, etc.).

approaching this composition has been found thus far: a breccia fraction from Apollo 16 soil (67602,14-3; off-scale in lower right of fig. 6). However, a mixture of group 5 with an Ir, Re-rich early condensate would give a pretty good match.

Interestingly, groups 1 and 2 are complementary to the Earth and Moon: poorer in refractories (Ir, Re), richer in at least two well-determined volatiles (Sb and Ge). This is consistent with accretion from a cooling nebula (refs. 51, 97, 101, and 102), where refractories concentrate in the large, early-formed bodies, and volatiles in the small, late-formed bodies. This complementarity may signify a genetic link between Earth and Moon on the one hand and basin-forming bodies on the other. In retrospect, it makes sense that the last bodies to fall on the Moon were complementary to it in composition.

Origin of Basin-Forming Objects

CLUES FROM THE BOMBARDMENT HISTORY OF THE MOON

An important clue is the rather young age of the Imbrium basin, 3.9 AE. This is not a statistical fluke, because at least one body (Orientale) fell still later. Apparently the basin-forming objects were stored in orbits of long enough collision lifetime to permit two of them to survive for ≥ 700 m.y.

A second, more ambiguous clue is the clustering of highland rock ages between 3.8 and 4.0 AE (ref. 103, and references cited therein). It is not yet clear whether this clustering implies a genuine cataclysm, i.e., a peak in the bombardment rate (refs. 104 and 105), or merely resetting of a continuum of older ages by the Imbrium impact. In terms of the cataclysm hypothesis, all basins were formed within 100 to 200 Myr of each other; any older ages are due to earlier magmatism or metamorphism unrelated to basin formation. The opposite, "steady bombardment" hypothesis interprets older ages, run-

ning up to ~ 4.5 AE, as the actual impact dates of basins (refs. 106 and 107).

A third clue is the existence of meteorite-free crustal rocks (fig. 5). It limits the amount of meteoritic material that could have fallen on the Moon after crustal differentiation (~ 4.5 AE ago?) (ref. 108), and thus fixes a point on the bombardment curve of the Moon. The crust, comprising $0.1 M_D$, probably contains no more than 2 percent of meteoritic material on the average, or $0.002 M_D$ (Baldwin, ref. 109, arrived at a figure of $0.003 M_D$ from crater counts and an extrapolation of meteorite fluxes. His latest value (private communication, 1974), is $0.002 M_D$.) Another point on the bombardment curve is fixed by the Imbrium impact 3.9 AE ago. Only the Orientale body, of estimated mass $5 \times 10^{-5} M_D$, was yet to fall after that time. These two points are shown in the left-hand portion of figure 17. The right-hand portion shows the same data, but with the number rather than mass of bodies as the ordinate. The number of basin-forming objects 4.5 AE ago is taken as 80^{+80}_{-40} , about twice the number actually known (ref. 68). This is an attempt to allow for additional discoveries (refs. 110 and 111).

It is not certain that the flux in this interval was exponential. However, if we make this assumption (ref. 112), we can estimate the probable formation times of the basins from their relative age. The horizontal bars in figure 17 correspond to the age sequence of Hartmann and Wood (ref. 68), omitting basins of ≤ 300 km in diameter. (The age sequence of Stuart-Alexander and Howard gives fairly similar results, except that Crisium falls at 4.1 AE.)

All of the ages fall between 4.2 and 4.35 AE. The absolute values of these ages should not be taken seriously because they depend critically on the initial number of basin-forming bodies 4.5 AE ago. However, the time gap between 3.9 and 4.2 AE is an interesting and significant feature. It reflects the fact that all seven of the basins formed in the interval between Nectaris and Imbrium lie on the farside or east limb and hence contribute negligible material to the lunar

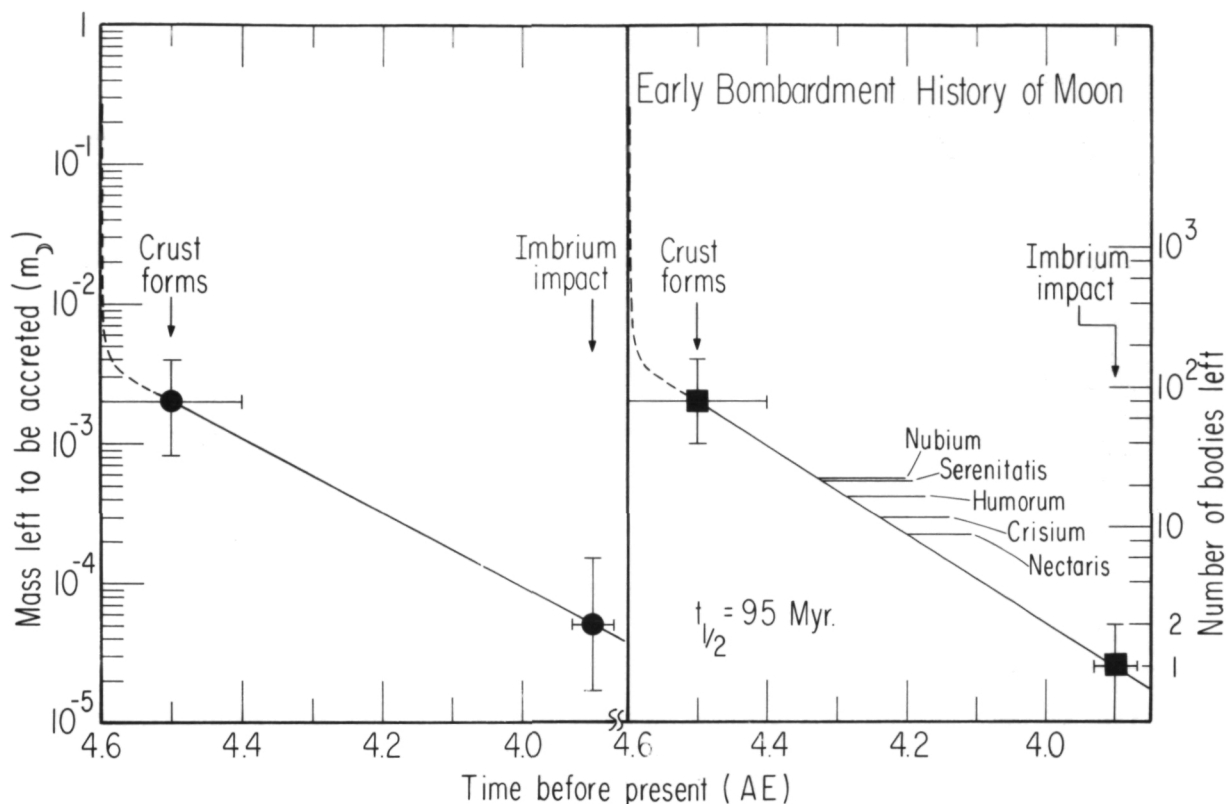


Figure 17.—Two points on the bombardment curve of the Moon are fixed by the mass influx after formation of crust ($\sim 2 \times 10^{-3} M$ or 80_{-40}^{+80} basin-forming objects) and the population surviving after the Imbrium impact 3.9 AE ago (Orientale, $\sim 5 \times 10^{-4} M_{\oplus}$). Horizontal bars at right give expected formation times of major basins. The 300-Myr gap between Nectaris and Imbrium impacts reflects the fact that all seven basins formed in this interval lie on the far side or east limb.

landing sites on the nearside. This fact, rather than a special cataclysm, may be responsible for the scarcity of ages in this interval.

ORIGINS

Four origins may be considered for the basin-forming objects (refs. 68 and 11).

1. Planetesimals in Earth-crossing orbits
2. Planetesimals in Earth-grazing orbits
3. Earth satellites swept up by the Moon during tidal recession or capture
4. Stray asteroids perturbed by Mars or Jupiter into Earth-crossing orbits

Of these four types of bodies, moonlets in Earth orbit (refs. 113, 114, and 115) most readily meet the constraints of survival to

3.9 AE, rapid extinction thereafter, chemical complementarity, and low impact velocity. Planetesimals in Earth-crossing orbits are adequate in most respects, provided their half-life against planetary collision is as long as ~ 100 Myr (fig. 17). The original Monte Carlo calculations by Arnold (ref. 116) and Wetherill (ref. 117) gave a half-life of only ~ 30 Myr (after the initial rapid sweepup of some 90 percent of the bodies). However, the actual lifetime may be longer because secular variations in eccentricity, inclination, and node may put the object out of the Earth's range for part of the time. Unpublished calculations by Mellick and Anders that make some allowance for these effects do in fact give $t_{1/2} \approx 80$ Myr, which is close to the required value.

The other two types of bodies are too long lived to be the main source. However, they may have been a subsidiary source, contributing a few objects of unusual composition or impact velocity (e.g., the group 6 body).

The Crater-Related Component

Of the three meteoritic components mentioned in the introduction, that associated with craters has remained the most elusive. No material definitely attributable to the projectile has been found in soils collected on or near the rims of the following small craters:

Apollo 12: Bench, Surveyor, Head
Apollo 14: Cone, Doublet, Triplet
Apollo 15: Elbow
Apollo 16: North Ray

Only Dune Crater at the Apollo 15 site showed a change in the abundance pattern that could perhaps be attributed to projectile material (ref. 11). However, the data were equally consistent with a mixture of C1 and ancient component.

In principle, the chances of recognizing projectile material were greatest in soils from very young craters (the three Apollo 12 craters and Cone Crater at Apollo 14) which had short surface exposure ages and hence a small C1 component. But these soils all turned out to have a large ancient component which dominated the pattern. To be sure, the expected average amount of projectile material is at most ~ 0.4 -percent C1 equivalent for an impact velocity of 15 km/s (fig. 13). But such amounts should have been detectable in at least the more favorable cases, and so the consistent absence of a crater-related component calls for another explanation. Perhaps the projectiles were chemically inconspicuous (achondrites) or had high velocities. Most likely, however, the crater-rim material contained less than its share of projectile material.

Apart from Dune Crater, the only case where so much as a hint of projectile material has been seen is KREEP glass from

the Apollo 12 site. Most authors believe that this glass represents Copernican ray material (see ref. 118 for references and ref. 119 for a contrary view). The basic pattern in Apollo 12 KREEP looks very much like the group 1 component from Apollo 14 norites, except for a slight, uniform enrichment in Ir, Re, Sb, Se, Zn, Ag, and Bi, relative to Au. Morgan et al. (ref. 118) argue that this enrichment does not represent C1 contamination from recent or post-Imbrian times, but more likely Copernican projectile material. This would imply that the Copernican projectile had a primitive composition (comet?). On the highly tenuous assumption that the amount of projectile material in KREEP glass is representative of the entire Copernican impact, they calculate, from Öpik's cratering equation, an impact velocity of 36 ± 5 km/s.

Clearly, this problem is far from solved. One needs to know how projectile material distributes itself among the ejecta as a function of initial stratigraphy, shock intensity, and throwout distance. With this information (and photogeologic data linking individual soil components to specific craters), it may be possible to make reliable inferences about composition and impact velocities of crater-forming bodies.

Acknowledgment

This work was supported in part by NASA Grant NGL 14-001-167. The authors are indebted to the National Space Science Data Center for illustrative materials used in the verbal presentation of this paper and wish to thank the John Simon Guggenheim Memorial Foundation for providing a fellowship for Edward Anders.

References

1. ANDERS, E., R. GANAPATHY, P. KRÄHENBÜHL, AND J. W. MORGAN, Meteoritic Material on the Moon. *The Moon*, Vol. 8, 1973, pp. 3-24.
2. MORGAN, J. W., R. GANAPATHY, H. HIGUCHI, U. KRÄHENBÜHL, AND E. ANDERS, Lunar Basins: Tentative Characterization of Projectiles,

- From Meteoritic Elements in Apollo 17 Boulders. *Geochimica et Cosmochimica Acta*, Supplement 5, in press, 1974.
3. UREY, H. C., The Duration of Intense Bombardment Processes of the Moon. *Astrophys. J.*, Vol. 132, 1960, pp. 502-503.
 4. HARTMANN, W. K., Early Lunar Cratering. *Icarus*, Vol. 5, 1966, pp. 406-418.
 5. ÖPIK, E. J., The Moon's Surface. *Ann. Rev. Astron. Astrophys.*, Vol. 7, 1969, pp. 473-526.
 6. KEAYS, R. R., R. GANAPATHY, J. C. LAUL, E. ANDERS, G. F. HERZOG, AND P. M. JEFFERY, Trace Elements and Radioactivity in Lunar Rocks: Implications for Meteorite Infall, Solar-Wind Flux, and Formation Conditions of Moon. *Science*, Vol. 167, 1970, pp. 490-493.
 7. GANAPATHY, R., R. R. KEAYS, J. C. LAUL, AND E. ANDERS, Trace Elements in Apollo 11 Lunar Rocks: Implications for Meteorite Influx and Origin of Moon. *Geochimica et Cosmochimica Acta*, Supplement 1, 1970, pp. 1117-1142.
 8. GANAPATHY, R., J. W. MORGAN, U. KRÄHENBÜHL, AND E. ANDERS, Ancient Meteoritic Components in Lunar Highland Rocks: Clues From Trace Elements in Apollo 15 and 16 samples. *Geochimica et Cosmochimica Acta*, Supplement 4, 1973, pp. 1239-1261.
 9. GANAPATHY, R., J. W. MORGAN, H. HIGUCHI, E. ANDERS, AND A. T. ANDERSON, Meteoritic and Volatile Elements in Apollo 16 Rocks in Separated Phases From 14306. *Geochimica et Cosmochimica Acta*, Supplement 5, in press, 1974.
 10. LAUL, J. C., J. W. MORGAN, R. GANAPATHY, AND E. ANDERS, Meteoritic Material in Lunar Samples: Characterization From Trace Elements. *Geochimica et Cosmochimica Acta*, Supplement 2, 1971, pp. 1139-1158.
 11. MORGAN, J. W., U. KRÄHENBÜHL, R. GANAPATHY, AND E. ANDERS, Trace Elements in Apollo 15 Samples: Implications for Meteorite Influx and Volatile Depletion on the Moon. *Geochimica et Cosmochimica Acta*, Supplement 3, 1972, pp. 1361-1376.
 12. MORGAN, J. W., J. C. LAUL, U. KRÄHENBÜHL, R. GANAPATHY, AND E. ANDERS, Major Impacts on the Moon: Characterization From Trace Elements in Apollo 12 and 14 Samples. *Geochimica et Cosmochimica Acta*, Supplement 3, 1972, pp. 1377-1395.
 13. KRÄHENBÜHL, U., J. W. MORGAN, R. GANAPATHY, AND E. ANDERS, Abundance of 17 Trace Elements in Carbonaceous Chondrites. *Geochimica et Cosmochimica Acta*, Vol. 37, 1973, pp. 1353-1370.
 14. BARKER, J. L., JR., AND E. ANDERS, Accretion Rate of Cosmic Matter From Iridium and Osmium Contents of Deep-Sea Sediments. *Geochimica et Cosmochimica Acta*, Vol. 32, 1968, pp. 627-645.
 15. HANAPPE, F., M. VOSTERS, E. PICCIOTTO, AND S. DEUTSCH, Chimie des Neiges Antarctiques et Taux de Deposition de Matiere Extraterrestre: II. *Earth Planet. Sci. Letters*, Vol. 4, 1968, pp. 487-496.
 16. BAEDECKER, P. A., C.-L. CHOU, AND J. T. WASSON, The Extralunar Component in Lunar Soils and Breccias. *Geochimica et Cosmochimica Acta*, Supplement 3, 1972, pp. 1343-1359.
 17. CHOU, C.-L. P. A. BAEDECKER, R. W. BILD, K. L. ROBINSON, AND J. T. WASSON, Volatile Elements in Lunar Soils. *Lunar Science*, Vol. V, Lunar Science Institute, Houston, 1974, pp. 115-117.
 18. MASON, B., ed., *Elemental Abundances in Meteorites*. Gordon and Breach, New York, 1971.
 19. GOLES, G. G., L. P. GREENLAND, D. Y. JEROME, Abundances of Chlorine, Bromine, and Iodine in Meteorites. *Geochimica et Cosmochimica Acta*, Vol. 31, 1967, pp. 1771-1787.
 20. OBERBECK, V. R., AND W. L. QUAIDE, Genetic Implications of Lunar Regolith Thickness Variations. *Icarus*, Vol. 9, 1968, pp. 446-465.
 21. WHIPPLE, F. L., The Meteoritic Environment of the Moon. *Proc. Roy. Soc.*, Vol. 296, 1967, pp. 304-315.
 22. WIESEL, W., The Meteorite Flux at the Lunar Surface. *Icarus*, Vol. 15, 1971, pp. 373-383.
 23. LAUL, J. C., R. GANAPATHY, J. W. MORGAN, AND E. ANDERS, Meteoritic and Non-Meteoritic Trace Elements in Luna 16 Samples. *Earth Planet. Sci. Letters*, Vol. 13, 1972, pp. 450-454.
 24. VINOGRADOV, A. P., Preliminary Data on Lunar Ground Brought to Earth by Automatic Probe "Luna 16." *Geochimica et Cosmochimica Acta*, Supplement 2, 1971, pp. 1-16.
 25. DOHNANYI, J. S., Flux of Micrometeoroids: Lunar Sample Analyses Compared With Flux Model. *Science*, Vol. 173, 1971, p. 558.
 26. DOHNANYI, J. S., Interplanetary Objects in Review: Statistics of Their Masses and Dynamics. *Icarus*, Vol. 17, 1972, pp. 1-48.
 27. HARTUNG, J. B., F. HÖRZ, AND D. E. GAULT, Lunar Microcraters and Interplanetary Dust. *Geochimica et Cosmochimica Acta*, Supplement 3, 1972, pp. 2735-2753.
 28. ÖPIK, E. J., Interplanetary Dust and Terrestrial Accretion of Meteoric Matter. *Irish Astron. J.*, Vol. 4, 1956, pp. 84-135.
 29. WHIPPLE, F. L., On Maintaining the Meteoritic Complex. *The Zodiacal Light and the Interplanetary Medium*, NASA SP-150, 1967, pp. 409-426.
 30. HERBIG, G. H., Comments During Discussion. *Proc. Lunar and Planet. Colloquium*, Vol. 2, 1961, p. 64.
 31. ANDERS, E., On the Origin of Carbonaceous

- Chondrites. *Ann. N.Y. Acad. Sci.* Vol. 108, 1963, pp. 514-533.
32. WHIPPLE, F. L., Origins of Meteoritic Material. *Physics and Dynamics of Meteors*, L. Kresák and P. M. Millman, eds., D. Reidel, Dordrecht, 1968, pp. 481-485.
 33. MILLMAN, P. M., Cometary Meteoroids. *Nobel Symposium 21: From Plasma to Planet*, A. Elvius, ed., Almqvist and Wiksell, Stockholm, 1972, pp. 157-168.
 34. BROWNLEE, D. E., P. W. HODGE, AND F. HÖRZ, Information From Lunar Microcraters Pertaining to Interplanetary Grains. *Meteoritics*, Vol. 8, 1973, p. 18.
 35. DUFRESNE, E. R., AND E. ANDERS, On the Chemical Evolution of the Carbonaceous Chondrites. *Geochimica et Cosmochimica Acta*, Vol. 26, 1962, pp. 1085-1114.
 36. JEFFERY, P. M., AND E. ANDERS, Primordial Noble Gases in Separated Meteoritic Minerals: I. *Geochimica et Cosmochimica Acta*, Vol. 34, 1970, pp. 1175-1198.
 37. ANDERS, E., Interrelations of Meteorites, Asteroids, and Comets. *Physical Studies of Minor Planets*, T. Gehrels, ed., NASA SP-267, 1971, pp. 429-446.
 38. ANDERS, E., Do Stony Meteorites Come From Comets? Submitted to *Icarus*, 1974.
 39. JOHNSON, T. V., AND F. P. FANALE, Optical Properties of Carbonaceous Chondrites and Their Relationship to Asteroids. *J. Geophys. Res.*, Vol. 78, 1973, pp. 8507-8518.
 40. CHAPMAN, C. R., AND D. MORRISON, The Minor Planets: Sizes and Mineralogy. *Sky and Telescope*, February, 1974, pp. 92-95.
 41. GAFFEY, M. J., AND T. B. MCCORD, *The Composition of Asteroid Surfaces*. Paper presented at Am. Astron. Soc., Div. Planet. Sci., Ann. Mtg., Palo Alto, April 1-6, 1974.
 42. GANAPATHY, R., J. C. LAUL, J. W. MORGAN, AND E. ANDERS, Moon: Possible Nature of the Body That Produced the Imbrian Basin, From the Composition of Apollo 14 Samples. *Science*, Vol. 175, 1972, pp. 55-59.
 43. WLOTZKA, F., B. SPETTEL, AND H. WÄNKE, On the Composition of Metal From Apollo 16 Fines and the Meteoritic Component. *Geochimica et Cosmochimica Acta*, Supplement 4, 1973, pp. 1483-1491.
 44. BAEDECKER, P. A., C.-L. CHOU, E. B. GRUDEWICZ, AND J. T. WASSON, Volatile and Siderophilic Trace Elements in Apollo 15 Samples: Geochemical Implications and Characterization of the Long-Lived and Short-Lived Extralunar Materials. *Geochimica et Cosmochimica Acta*, Supplement 4, 1973, pp. 1177-1195.
 45. KIMURA, K., R. S. LEWIS, AND E. ANDERS, Distribution of Gold and Rhenium Between Nickel-Iron and Silicate Melts: Implications for the Abundance of Siderophile Elements on the Earth and Moon. *Geochimica et Cosmochimica Acta*, Vol. 38, 1974, pp. 683-701.
 46. WLOTZKA, F., E. JAGOUTZ, B. SPETTEL, H. BADDENHAUSEN, A. BALACESCU, AND H. WÄNKE, On Lunar Metallic Particles and Their Contribution to the Trace Element Content of Apollo 14 and 15 Soils. *Geochimica et Cosmochimica Acta*, Supplement 3, 1972, pp. 1077-1084.
 47. DICKEY, J. S., JR., Nickel-Iron in Lunar Anorthosites. *Earth Planet. Sci. Letters*, Vol. 8, 1970, pp. 387-392.
 48. VINOGRADOV, A. P., Preliminary Data on Lunar Soil Collected by the Luna 20 Unmanned Spacecraft. *Geokhimiya*, 1972, pp. 763-774; English translation in *Geochimica et Cosmochimica Acta*, Vol. 37, 1973, pp. 721-729.
 49. FISH, R. A., G. G. GOLES, AND E. ANDERS, The Record in the Meteorites: III. On the Development of Meteorites in Asteroidal Bodies. *Astrophys. J.*, Vol. 132, 1960, pp. 243-258.
 50. PROVOST, A., AND Y. BOTTINGA, Rates of Solidification of Apollo 11 Basalt and Hawaiian Tholeiite. *Earth Planet. Sci. Letters*, Vol. 15, 1972, pp. 325-337.
 51. GROSSMAN, L., Condensation in the Primitive Solar Nebula. *Geochimica et Cosmochimica Acta*, Vol. 36, 1972, pp. 597-619.
 52. LARIMER, J. W., Chemical Fractionations in Meteorites: I. Condensation of the Elements. *Geochimica et Cosmochimica Acta*, Vol. 31, 1967, pp. 1215-1238.
 53. WASSON, J. T., AND R. SCHAUDY, The Chemical Classification of Iron Meteorites: V. Groups IIIC and IIID and Other Irons With Germanium Concentrations Between 1 and 25 ppm. *Icarus*, Vol. 14, 1971, pp. 59-70.
 54. BAEDECKER, P. A., Iridium (77). *Handbook of Elemental Abundances in Meteorites*, B. Mason, ed., Gordon and Breach, New York, 1971, pp. 463-472.
 55. SCOTT, E., Chemical Fractionation in Iron Meteorites and Its Interpretation. *Geochimica et Cosmochimica Acta*, Vol. 36, 1972, pp. 1205-1236.
 56. FOUCHÉ, K. F., AND A. A. SMALES, The Distribution of Trace Elements in Chondritic Meteorites: I. Gallium, Germanium and Indium. *Chem. Geol.*, Vol. 2, 1967, pp. 5-33.
 57. FOUCHÉ, K. F., AND A. A. SMALES, The Distribution of Trace Elements in Chondritic Meteorites: II. Antimony, Arsenic, Gold, Palladium, and Rhenium. *Chem. Geol.*, Vol. 2, 1967, pp. 105-134.
 58. ÖPIK, E. J., Cratering and the Moon's Surface. *Advan. Astron. Astrophys.*, Vol. 8, Z. Kopal, ed., Academic Press, New York, 1971, pp. 107-337.
 59. BALDWIN, R. B., Lunar Crater Counts. *Astron.*

- J., Vol. 69, 1964, pp. 377-392.
60. SHORT, N. M., AND M. L. FORMAN, Thickness of Impact Crater Ejecta on the Lunar Surface. *Mod. Geol.*, Vol. 3, 1972, pp. 69-91.
 61. DENCE, M. R., AND A. G. PLANT, Analysis of Fra Mauro Samples and the Origin of the Imbrium Basin. *Geochimica et Cosmochimica Acta*, Supplement 3, 1972, pp. 379-399.
 62. STÖFFLER, D., M. R. DENCE, M. ABADIAN, AND G. GRAUP, Ejecta Formations and Pre-Impact Stratigraphy of Lunar and Terrestrial Craters: Possible Implications for the Ancient Lunar Crust. *Lunar Science*, Vol. V, Lunar Science Institute, Houston, 1974, pp. 746-748.
 63. GOOLEY, R., R. BRETT, L. WARNER, AND J. R. SMYTH, Sample 76535, a Deep Lunar Crustal Rock. *Geochimica et Cosmochimica Acta*, Vol. 38, in press, 1974.
 64. ALBEE, A. L., A. A. CHODOS, R. F. DYMEK, A. J. GANCARZ, D. S. GOLDMAN, D. A. PAPANASTASIOU, AND G. J. WASSERBURG, Dunite From the Lunar Highlands: Petrography, Deformation History, Rb-Sr Age. *Lunar Science*, Vol. V, Lunar Science Institute, Houston, 1974, pp. 3-5.
 65. OBERBECK, V. R., F. HÖRZ, R. H. MORRISON, W. L. QUAIDE, AND D. E. GAULT, Effects of Formation of Large Craters and Basins on Emplacement of Smooth Plains Material. *Lunar Science*, Vol. V, Lunar Science Institute, Houston, 1974, pp. 568-570.
 66. TAYLOR, L. A., H. K. MAO, AND P. M. BELL, "Rust" in the Apollo 16 Rocks. *Geochimica et Cosmochimica Acta*, Supplement 4, 1973, pp. 829-839.
 67. MCGETCHIN, T. R., M. SETTLE, AND J. W. HEAD, Radial Thickness Variation in Impact Crater Ejecta: Implications for Lunar Basin Deposits. *Earth Planet. Sci. Letters*, Vol. 20, 1973, pp. 226-236.
 68. HARTMANN, W. K., AND C. A. WOOD, Moon: Origin and Evolution of Multi-Ring Basins. *The Moon*, Vol. 3, 1971, pp. 3-78.
 69. STUART-ALEXANDER, D. E., AND K. A. HOWARD, Lunar Maria and Circular Basins—A Review. *Icarus*, Vol. 12, 1970, pp. 440-456.
 70. SCHMITT, H. H., Apollo 17 Report on the Valley of Taurus-Littrow. *Science*, Vol. 182, 1973, pp. 681-690.
 71. AFGIT (Apollo Field Geology Investigation Team), Apollo 16 Exploration of Descartes: A Geologic Summary. *Science*, Vol. 179, 1973, pp. 62-68.
 72. HODGES, C. A., W. R. MUEHLBERGER, AND G. E. ULRICH, Geologic Setting of Apollo 16. *Geochimica et Cosmochimica Acta*, Supplement 4, 1973, pp. 1-25.
 73. KRÄHENBÜHL, U., R. GANAPATHY, J. W. MORGAN, AND E. ANDERS, Volatile Elements in Apollo 16 Samples: Implications for Highland Volcanism and Accretion History of the Moon. *Geochimica et Cosmochimica Acta*, Supplement 4, 1973, pp. 1325-1348.
 74. CROZAZ, G., R. WALKER, AND D. ZIMMERMAN, Fossil Track and Thermoluminescence Studies of Luna 20 Material. *Geochimica et Cosmochimica Acta*, Vol. 37, 1973, pp. 825-830.
 75. WILHELMS, D. E., AND J. F. MCCAULEY, Geologic Map of the Near Side of the Moon. *Geologic Atlas of the Moon*, Map I-703. U.S. Geol. Survey, 1971.
 76. CHAO, E. C. T., L. A. SODERBLUM, J. M. BOYCE, D. E. WILHELMS, AND C. A. HODGES, Lunar Light Plains Deposits (Cayley Formation)—A Reinterpretation of Origin. *Lunar Science*, Vol. IV, Lunar Science Institute, Houston, 1973, pp. 127-128.
 77. HEAD, J. W., Morphology and Structure of the Taurus-Littrow Highlands (Apollo 17): Evidence for Their Origin and Evolution. *The Moon*, Vol. 9, 1974, pp. 355-395.
 78. WISE, D. U., An Origin of the Moon by Rotational Fission During Formation of the Earth's Core. *J. Geophys. Res.*, Vol. 68, 1963, pp. 1547-1554.
 79. O'KEEFE, J. A., The Origin of the Moon. *J. Geophys. Res.*, Vol. 75, 1970, pp. 6565-6574.
 80. O'KEEFE, J. A., The Origin of the Moon: Theories Involving Joint Formation With the Earth. *Astrophys. Space Sci.*, Vol. 16, 1972, pp. 201-211.
 81. RINGWOOD, A. E., Origin of the Moon: The Precipitation Hypothesis. *Earth Planet. Sci. Letters*, Vol. 8, 1970, pp. 131-140.
 82. UREY, H. C., AND G. J. F. MACDONALD, Origin and History of the Moon. *Physics and Astronomy of the Moon*, Z. Kopal, ed., Academic Press, New York, 1971, pp. 213-289.
 83. ÖPIK, E. J., Comments on Lunar Origin. *Irish Astron. J.*, Vol. 10, 1972, pp. 190-238.
 84. SMITH, J. V., Origin of Moon by Disintegrative Capture With Chemical Differentiation Followed by Sequential Accretion. *Lunar Science*, Vol. V, Lunar Science Institute, Houston, 1974, pp. 718-720.
 85. WOOD, J. A., AND H. E., MITLER, Origin of the Moon by a Modified Capture Mechanism, or Half a Loaf Is Better Than a Whole One. *Lunar Science*, Vol. V, Lunar Science Institute, Houston, 1974, pp. 851-853.
 86. GOLDSTEIN, J. I., AND J. M. SHORT, The Iron Meteorites, Their Thermal History, and Parent Bodies. *Geochimica et Cosmochimica Acta*, Vol. 31, 1967, pp. 1733-1770.
 87. FRICKER, P. E., J. I. GOLDSTEIN, AND A. L. SUMMERS, Cooling Rates and Thermal Histories of Iron and Stony-Iron Meteorites. *Geochimica et Cosmochimica Acta*, Vol. 34, 1970, pp. 475-491.

88. BALDWIN, R. B., *The Measure of the Moon*, University of Chicago Press, 1963.
89. UREY, H. C., Mascons and the History of the Moon. *Science*, Vol. 162, 1968, pp. 1408-1410.
90. NININGER, H. H., *Arizona's Meteorite Crater: Past, Present, Future*. American Meteorite Museum, Sedona, Arizona, 1956.
91. LARIMER, J. W., AND E. ANDERS, Chemical Fractionations in Meteorites: III. Major Element Fractionations in Chondrites. *Geochimica et Cosmochimica Acta*, Vol. 34, 1970, pp. 367-388.
92. ÖPIK, E. J., Meteorite Impact on Solid Surface. *Irish Astron. J.*, Vol. 5, 1958, pp. 14-33.
93. ÖPIK, E. J., Notes on the Theory of Impact Craters. *Proc. Geophys. Lab.—Lawrence Radiation Lab. Cratering Symp.*, Vol. 2, Paper S, UCRL Report 6438, 1961, pp. 1-28.
94. GAULT, D. E., Displaced Mass, Depth, Diameter, and Effects of Oblique Trajectories for Impact Craters Formed in Dense Crystalline Rocks. *The Moon*, Vol. 6, 1973, pp. 32-44.
95. CASE, D. R., J. C. LAUL, I. Z. PELL, M. A. WECHTER, F. SCHMIDT-BLEEK, AND M. E. LIPSCHUTZ, Abundance Patterns of Thirteen Trace Elements in Primitive Carbonaceous and Unequilibrated Ordinary Chondrites. *Geochimica et Cosmochimica Acta*, Vol. 37, 1973, pp. 19-33.
96. ANDERS, E., Chemical Processes in the Early Solar System, as Inferred From Meteorites. *Acc. Chem. Res.*, Vol. 1, 1968, pp. 289-298.
97. LARIMER, J. W., AND E. ANDERS, Chemical Fractionations in Meteorites: II. Abundance Patterns and Their Interpretation. *Geochimica et Cosmochimica Acta*, Vol. 31, 1967, pp. 1239-1270.
98. LAUL, J. C., R. GANAPATHY, E. ANDERS, AND J. W. MORGAN, Chemical Fractionations in Meteorites: VI. Accretion Temperatures of H-, LL-, and E-Chondrites, From Abundances of Volatile Trace Elements. *Geochimica et Cosmochimica Acta*, Vol. 37, 1973, pp. 329-357.
99. LARIMER, J. W., Chemical Fractionations in Meteorites: VII. Cosmochrometry and Cosmochrometry. *Geochimica et Cosmochimica Acta*, Vol. 37, 1973, pp. 1603-1623.
100. GANAPATHY, R., AND E. ANDERS, Bulk Compositions of the Moon and Earth, Estimated From Meteorites. *Geochimica et Cosmochimica Acta*, Supplement 5, in press, 1974.
101. ANDERS, E., Meteorites and the Early Solar System. *Ann. Rev. Astron. Astrophys.*, Vol. 9, 1971, pp. 1-34.
102. GROSSMAN, L., AND S. P. CLARK, JR., High-Temperature Condensates in Chondrites and the Environment in Which They Formed. *Geochimica et Cosmochimica Acta*, Vol. 37, 1973, pp. 635-649.
103. PODOSEK, F. A., J. C. HUNEKE, A. J. GANCARZ, AND G. J. WASSERBURG, The Age and Petrography of Two Luna 20 Fragments and Inferences for Widespread Lunar Metamorphism. *Geochimica et Cosmochimica Acta*, Vol. 37, 1973, pp. 887-904.
104. TERA, F., D. A. PAPANASTASSIOU, AND G. J. WASSERBURG, A Lunar Cataclysm at ~3.95 AE and the Structure of the Lunar Crust. *Lunar Science*, Vol. IV, Lunar Science Institute, Houston, 1973, pp. 723-725.
105. TERA, F., D. A. PAPANASTASSIOU, AND G. J. WASSERBURG, The Lunar Time Scale and a Summary of Isotopic Evidence for a Terminal Lunar Cataclysm. *Lunar Science*, Vol. V, Lunar Science Institute, Houston, 1974, pp. 792-794.
106. SCHAEFFER, O. A., AND L. HUSAIN, Chronology of Lunar Basin Formation and Ages of Lunar Anorthositic Rocks. *Lunar Science*, Vol. V, Lunar Science Institute, Houston, 1974, pp. 663-665.
107. KIRSTEN, T., AND P. HORN, ³⁹Ar-⁴⁰Ar Chronology of the Taurus-Littrow Region II: A 4.28 b.y. Old Troctolite and Ages of Basalts and Highland Breccias. *Lunar Science*, Vol. V, Lunar Science Institute, Houston, 1974, pp. 419-421.
108. NUNES, P. D., AND M. TATSUMOTO, Excess Lead in "Rusty Rock" 66095 and Implications for an Early Lunar Differentiation. *Science*, Vol. 182, 1973, pp. 916-920.
109. BALDWIN, R. B., On the History of Lunar Impact Cratering: The Absolute Time Scale and the Origin of Planetesimals. *Icarus*, Vol. 14, 1971, pp. 36-52.
110. EL BAZ, FAROUK, All-Khwarizmi: A Newfound Basin on the Lunar Far Side. *Science*, Vol. 180, 1973, pp. 1173-1176.
111. SCOTT, D. H., The Geologic Significance of Some Lunar Gravity Anomalies. *Lunar Science*, Vol. V, Lunar Science Institute, Houston, 1974, pp. 693-694.
112. HARTMANN, W. K., Paleocratering of the Moon: Review of Post-Apollo Data. *Astrophys. Space Sci.*, Vol. 17, 1972, pp. 48-64.
113. RUSKOL, E. L., The Origin of the Moon. *The Moon*, Z. Kopal and Z. Mikhailov, eds., Academic Press, New York, 1962, pp. 149-155.
114. RUSKOL, E. L., On the Origin of the Moon: III, Some Aspects of the Dynamics of the Circumterrestrial Swarm. *Astron. J.*, Vol. 48, 1971, pp. 819-829.
115. RUSKOL, E. L., On the Initial Distance of the Moon Forming in the Circumterrestrial Swarm. *The Moon*, S. K. Runcorn and H. C. Urey, eds., D. Reidel, Dordrecht, 1972, pp. 402-404.
116. ARNOLD, J. R., The Origin of Meteorites as Small Bodies: III. General Considerations. *Astrophys. J.*, Vol. 141, 1965, pp. 1548-1556.

117. WETHERILL, G. W., Dynamical Studies of Asteroidal and Cometary Orbits and Their Relation to the Origin of Meteorites. *Origin and Distribution of the Elements*, L. H. Ahrens, ed., Pergamon Press, Oxford, 1968, pp. 423-443.
118. MORGAN, J. W., R. GANAPATHY, J. C. LAUL, AND E. ANDERS, Lunar Crater Copernicus: Search for Debris of Impacting Body at Apollo 12 Site. *Geochimica et Cosmochimica Acta*, Vol. 37, pp. 141-154.
119. WASSON, J. T., AND P. A. BAEDECKER, Provenance of Apollo 12 KREEP. *Geochimica et Cosmochimica Acta*, Supplement 3, 1972, pp. 1315-1326.

Page intentionally left blank

Page intentionally left blank

Primary Cosmic Rays on the Lunar Surface

S. N. Vernov

*The Scientific Research Institute of Nuclear Physics,
Moscow State University, Moscow, U.S.S.R.*

A. K. Lavrukhina

*V. I. Vernadskiy Institute of Geochemistry
and Analytical Chemistry,
Moscow, U.S.S.R.*

With no atmosphere or magnetic field, the Moon is an ideal object for investigation of the temporal variations of cosmic rays in the region of the Earth's orbit. Results are reported for determination of the galactic cosmic ray flux during various time intervals in the 1965-1972 period, on the basis of data from the instruments of a spacecraft that made a soft landing on the lunar surface, and from the radioactivity of samples returned by the spacecraft. During minimum solar activity (the second half of 1965 and the beginning of 1966) I_0 ($E > 30$ MeV/nucleon) was determined to be $0.43 (\pm 10 \text{ percent})$ particles $\cdot \text{cm}^{-2} \cdot \text{s}^{-1} \cdot \text{ster}^{-1}$; the mean flux in the 1967-1970 period was I_{av} ($E > 100$ MeV/nucleon) = $0.31 (\pm 20 \text{ percent})$ particles $\cdot \text{cm}^{-2} \cdot \text{s}^{-1} \cdot \text{ster}^{-1}$. These values, within the error limits of the determinations, agree with the corresponding values of galactic cosmic ray intensities determined by stratospheric measurements.

The mean flux of galactic cosmic rays over the past million years is equal to I ($E > 100$ MeV/nucleon) = $0.28 (\pm 20 \text{ percent})$ particles $\cdot \text{cm}^{-2} \cdot \text{s}^{-1} \cdot \text{ster}^{-1}$; this value agrees with the mean flux of modulated cosmic rays during the period of the nineteenth solar cycle.

The mean flux of solar protons between 1965 and 1972 was I_p ($E_p > 20$ MeV) = 2.46
 $\left(\begin{matrix} +0.44 \\ -0.74 \end{matrix} \right)$ protons $\cdot \text{cm}^{-2} \cdot \text{s}^{-1} \cdot \text{ster}^{-1}$.

With no atmosphere or magnetic field, the Moon is an ideal object for the study of temporal variations in the modulated galactic cosmic rays of solar cosmic rays at a distance of 1 AU from the Sun. In combination with the data from meteorites with orbits of various sizes which struck the Earth at the same time that samples of lunar soil were taken, studies of the radioactivity of the surface layers of the Moon yield the most precise information on spatial variations in the galactic cosmic rays and allow us to refine the position of the upper boundary of the area of modulation (refs. 1-5). The first estimate of radioactivity on the surface of the Moon was made by an instrument on the Luna 9 space-

craft, which was launched 30 January 1966 (ref. 6). Detailed analysis of the radioactivity of lunar rocks was performed on the specimens taken by the Apollo 11 astronauts on July 17, 1969. These data (ref. 7) allowed the first precise estimate of the mean flux of solar protons over the past million years, indicating that it equaled the average contemporary flux (refs. 8 and 9).

The present article reports some results from studies of the temporal variations of cosmic rays using data on the radioactivity of cosmogenic Na^{22} and Al^{26} in lunar soil samples returned by the Luna 16 and Luna 20 automatic spacecraft, as well as data from the instruments of Luna 9 (ref. 6).

Variations in Galactic Cosmic Rays

The most precise data for the intensity of cosmic rays on the surface of the Moon during various intervals of time can be produced by recording radiation in various energy intervals with instruments on automatic spacecraft soft-landed on the surface. Such an experiment was performed by the Luna 9 spacecraft (ref. 6). The landing was performed on 3 February 1966 at 21:45:30 Moscow time. The spacecraft carried an instrument with an SBM-10 gas discharge counter with the following working dimensions: diameter 6 mm, length 10 mm. The minimum shielding of the counter was $\cong 1$ g/cm² aluminum. The instrument was turned on immediately after the station went into orbit and remained on throughout the life of the station. Data on the intensity of radiation were averaged over 14 time intervals (fig. 1). The first 5 relate to the area traversed during the flight of the spacecraft from the Earth to the Moon. The sixth interval relates to the period of flight near the Moon (beginning at a distance of about 50,000 km from the Moon), the landing, and the first 5 minutes the spacecraft was on the Moon. The last 8 intervals relate to the period of operation of the spacecraft on the lunar surface. After making corrections for geometric shielding of the Moon, the flux of particles of cosmic rays with energies of over

30 MeV/nucleon was determined. Its value in space and on the lunar surface is $I(E > 30 \text{ MeV/nucleon}) = 0.43 \text{ particles} \cdot \text{cm}^{-2} \cdot \text{s}^{-1} \cdot \text{ster}^{-1}$ with an accuracy of 10 percent. This value corresponds to the flux of unmodulated galactic cosmic rays I_0 ($E > 100 \text{ MeV/nucleon}$) = $0.41 \text{ particles} \cdot \text{cm}^{-2} \cdot \text{s}^{-1} \cdot \text{ster}^{-1}$, with an accuracy of ± 20 percent, determined from the Na²² activity in six chondrites which struck the earth during the nineteenth solar cycle (1959–1970) (ref. 1). Similar data (within the error limits) were produced by measurements in the region of the Moon's orbit by the Luna 7 and Luna 8 spacecraft on 4–8 October and 3–6 July 1965, respectively. Thus, the maximum intensity of cosmic rays in the region of the Earth occurred during the second half of 1965 and in January 1966, as measured on the lunar surface, in near Moon orbit, and also by stratospheric measurements (refs. 10 and 11). The intensity of galactic cosmic rays then decreased, in connection with the beginning of the twentieth cycle of solar activity. The delay of the activity maximum of galactic cosmic rays from the minimum of solar activity is about 1.5 years for protons with energies of over 30 MeV. This conclusion is also confirmed by data returned by the Zond 3, Venera 2, and Venera 3 interplanetary spacecraft (ref. 6).

The time which the Luna 7, 8, and 9 spacecraft spent on the surface of the Moon or in orbit near the Moon corresponded to the minimum of solar activity and, therefore, the instruments recorded only galactic cosmic radiation. In all other cases, the measurement corresponds to the integrated intensity of galactic and solar cosmic rays with their widely varying ratios. It is impossible to separate these components.

This possibility is provided by the lunar rocks taken from various depths below the surface, or from lunar regolith cores.

In order to detect the radioactive products of nuclear reactions caused by galactic components of the cosmic rays, we must study samples from a depth of over 10 cm below the lunar surface because theoretical calculations have shown (refs. 8 and 9) that at shallower depths the solar component is quite large.

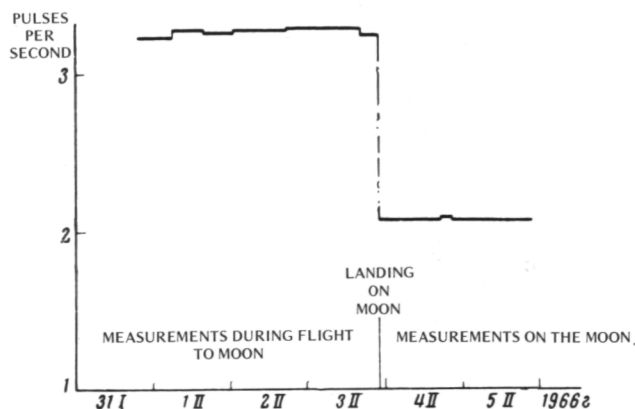


Figure 1.—Mean counting rates of gas discharge counter of the Luna 9 spacecraft (ref. 8).

Because of the small diameter of the drill used to take cores, the weight of the column of lunar soil causing the effect of decreasing radioisotope activity with depth is slight, 10–20 g (a few centimeters). A special apparatus was created to measure the activity of such small samples (ref. 12) and its effectiveness has been tested on meteorite specimens. Nondestructive testing of specimens was performed with a low-background γ scintillation spectrometer in the γ - γ coincidence mode, allowing simultaneous recording of Al^{26} and Na^{22} . The material to be studied, in cylindrical plexiglas cups, was placed between two low-background $\text{NaI}(\text{Tl})$ scintillators 120×100 mm in diameter. The background level was reduced by surrounding the $\text{NaI}(\text{Tl})$ crystals with an anticoincidence ring consisting of a plastic scintillator 500×600 mm in diameter and installing them in a massive shielding chamber with a wall thickness of 400–500 mm (300–400 mm steel + 100–150 mm of a mixture of paraffin with boric acid).

The measurement of activity of cosmogenic isotopes Al^{26} ($T_{1/2} = 7.4 \times 10^5$ years) and Na^{22} ($T_{1/2} = 2.6$ years) was performed in two specimens of regolith returned by the Luna 16 spacecraft; sample 1 weighed 18.87 g and was a mixture of soil from the surface

layer to a depth of 13 cm; sample 2 weighed 10.396 g and was taken from a depth of 15–18 cm. A single 9.792-g specimen of regolith returned by Luna 20 was also tested and was a mixture of soils over the entire depth of the column (refs. 13 and 14). Measurements of the samples were alternated with measurements of the background in 5- to 11-hour cycles. Between cycles a Na^{22} control source in standard geometry was used to test the system, and amplifier drift was adjusted; the displacement of the photopeak at $(511 + 1275)$ KeV did not exceed 1 percent over the duration of a full cycle. Background measurements were made with the use of specimens of powdered dunite in the same quantities and packing as the lunar specimens. The spectrometer was calibrated by the use of moldings similar to the samples in size and weight but with known quantities of $\text{Al}^{26}\text{Cl}_3$ and Na^{22}Cl distributed evenly through the volume (ref. 15). The characteristics of the method and results of measurements are presented in table 1.

In addition to the measured values of Al^{26} and Na^{22} activity in lunar specimens (solid crosses), figure 2 also shows the calculated curves for a depth distribution of these isotopes in the surface layers of cores of lunar soil returned by Luna 16 and Luna 20 down

Table 1.—*Characteristics and Results of Measurements of Radioactivity of Lunar Regolith Returned by Luna 16 and Luna 20 (refs. 15 and 16)*

Specimen	Luna 16		Luna 20	
	Specimen 1	Specimen 2	Specimen 1	
Date of collection of soil from the lunar surface	20 Sept. 1970		22 Feb. 1972	
Weight of sample, g	18.87	10.396	9.792	
Distance from surface, cm	0–13	15–18	Mixed sample	
Measurement time, hours	200	250	500	
Isotope measured	Al^{26}	Na^{22}	Al^{26}	Na^{22}
Calculated photopeak, KeV	511+ 1830	511+ 1275	511+ 1830	511+ 1275
Background in photopeak, $\text{imp}\cdot\text{hr}^{-1}$	0.35	0.84	0.38	0.95
Peak above background, $\text{imp}\cdot\text{hr}^{-1}$	1.17	1.53	0.62	1.08
Effectiveness of recording, percent	1.4	2.3	1.6	2.85
Activity at moment of soil collection, $\text{events}\cdot\text{min}^{-1}\cdot\text{kg}^{-1}$	62 ± 8	42 ± 8	54 ± 9	48 ± 9
			64 ± 5	43 ± 5

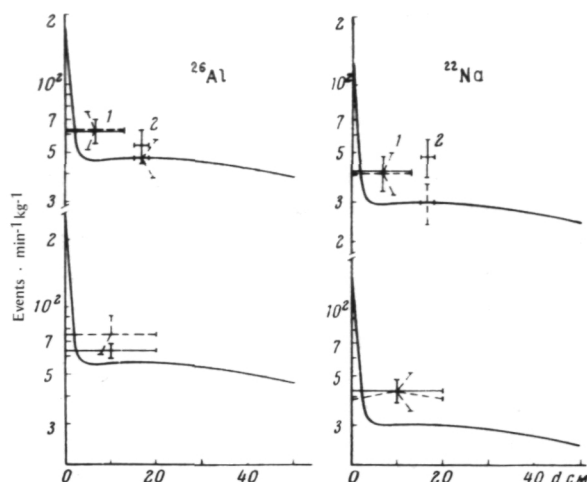


Figure 2.—The depth distribution of Na^{22} and Al^{26} in the regolith cores returned by Luna 16 and Luna 20 (refs. 15, 16, and 17). Experimental values (solid crosses); theoretical values (dotted crosses). The curves produced considerable contribution of galactic and solar components of cosmic rays at various depths. Calculations were performed with data from stratospheric observations for the galactic component (refs. 21 and 22); $I_1 = 0.229$ particles $\cdot \text{cm}^{-2} \cdot \text{s}^{-1} \cdot \text{ster}^{-1}$ (mean value for 1967–1970) and $I_2 = 0.197$ particles $\cdot \text{cm}^{-2} \cdot \text{s}^{-1} \cdot \text{ster}^{-1}$ (mean value for 1968–1972) in agreement with the time of accumulation of Na^{22} in regolith samples returned by Luna 16 and Luna 20, respectively; $I_3 = 0.28$ particles $\cdot \text{cm}^{-2} \cdot \text{s}^{-1} \cdot \text{ster}^{-1}$ (mean value for nineteenth solar cycle) for Al^{26} . Figure shows value of the mean proton flux taken for the solar component $I_p = 2.46$ protons $\cdot \text{cm}^{-2} \cdot \text{s}^{-1} \cdot \text{ster}^{-1}$ (refs. 10 and 11).

to a depth $d = 50$ cm, and the expected theoretical values of mean activity in the specimens analyzed (dotted-line crosses). The calculations were performed by the analytical method of Lavrukhina and Ustinova (ref. 16) and Lavrukhina et al. (ref. 17), whose effectiveness has been confirmed by many analyses of the radioactivity of meteorites (ref. 18), with consideration of differences in the chemical composition of the regolith (refs. 19 and 20). The elements from which cosmogenic Al^{22} and Na^{22} are primarily formed (Mg, Na, Al, Si, and Ca), are present in relatively large quantities in the Luna 20 regolith (for example, aluminum is 33 percent greater) in comparison with the Luna

16 regolith. This leads to differences in the weighted mean cross sections for the formation of these isotopes by various nuclear particles in the regoliths of both types (see fig. 2) and, consequently, two different levels of radioactivity when bombarded by identical fluxes of primary radiation. For example, at a depth of 50 cm the activity of Al^{26} in the Luna 20 regolith should be 1.2 times higher than in the Luna 16 regolith.

The activity of cosmogenic isotopes in the layer of the Luna 16 core between 15 and 18 cm from the surface can serve as an indicator of the intensity of galactic cosmic rays, because the depth effects and the activity induced by the solar component in this layer are negligible (less than 1 percent; see fig. 2). Considering the corrections for possible admixture of surface layers, the measured values of Al^{26} and Na^{22} activity in sample 2 of the Luna 16 core corresponds to the following values of mean intensity of galactic cosmic rays in the orbit of the Earth. The mean flux over the past million years (according to $1.5 T_{1/2}$) for Al^{26} is $I_1(E > 100 \text{ MeV/nucleon}) = 0.28$ particles $\cdot \text{cm}^{-2} \cdot \text{s}^{-1} \cdot \text{ster}^{-1}$, which corresponds to the mean value for the flux of modulated galactic cosmic rays measured in the stratosphere of the Earth between 1958 and 1969 (refs. 10, 21 and 22), and proves the constancy of the mean intensity of galactic cosmic rays at least over the past million years. The mean flux during the period 1967–1970 (according to data for Na^{22}) was $I_2(E > 100 \text{ MeV/nucleon}) = 0.31$ particles $\cdot \text{cm}^{-2} \cdot \text{s}^{-1} \cdot \text{ster}^{-1}$. This last quantity is somewhat greater than the mean intensity of galactic cosmic rays for these years, according to the data from stratosphere measurements. This divergence apparently reflects an increase in the intensity of cosmic rays due to solar protons emitted during solar flares, since the maximum number of flares of the twentieth solar cycle occurred during this time. In this case, the fraction of Na^{22} activity formed in the surface layers of sample 2 should be significantly higher than that for Al^{26} , whose activity reflects the intensity of cosmic rays averaged over many solar cycles.

The Intensity of Solar Cosmic Rays

Low-energy solar cosmic rays cause radioactivity only in the near-surface layers of the lunar regolith, about 4 cm deep. The depth distribution of cosmogenic isotopes in this thin layer is characterized by a sharp drop in activity (by 4 to 5 times) in comparison with the surface activity (see fig. 2).

The mean flux of solar cosmic rays $I_p(E > 20 \text{ MeV}) = 2.46 \left(\frac{+0.44}{-0.74} \right) \text{ protons} \cdot \text{cm}^{-2} \cdot \text{s}^{-1}$.

ster⁻¹, a figure first obtained (refs. 10 and 11) on the basis of data from the analysis of the activity of Na²² in specimen 10017, which was removed from irradiation in July of 1969 by the Apollo 11 crew (ref. 7), and represents the mean flux between July 1965 and July 1969. The agreement of the values of Na²² activity in the samples returned by Luna 16 (sample 1) and Luna 20, calculated on the basis of this flux and the actual measured values (see fig. 2) indicates that the mean intensity of solar cosmic rays, within the limits of these errors, was identical from July 1965 through July 1969, from September 1966 through September 1970, and from February 1968 through February 1972. Consequently, the upper value of the integral intensity of solar protons apparently characterizes the "thickness" of the background of solar protons, whereas the measurement apparatus installed on the spacecraft records bursts of intensity above this background during flares (ref. 16).

Lunar samples provide a unique possibility for the study of long-term cosmic ray variations. Interest in this problem has recently increased in connection with the difficulties that have arisen in the neutron physics of the Sun. Several hypotheses have been suggested to eliminate these difficulties. One of the most common is the idea of the periodic convection of solar matter with a period of several hundreds of millions of years (ref. 23). The last minimum was about 3 million years ago. One result of this should be variations in solar activity and, apparently, the intensity of solar cosmic rays. Detailed investigation of the content of the radioactive isotopes with

long half-life (Al²⁶, Mn⁵³, and K⁴⁰) in specimens taken at various depths from the lunar surface is of great interest in this aspect.

References

1. LAVRUKHINA, A. K., *Vestnik AN SSSR*, No. 9, 1970, p. 72.
2. LAVRUKHINA, A. K., *Geokhimiya*, No. 1, 1973, p. 11.
3. LAVRUKHINA, A. K. AND G. K. USTINOVA, *Izv. AN SSSR, Physics Series*, Vol. 34, 1970, p. 2401.
4. LAVRUKHINA, A. K., G. K. USTINOVA AND A. N. SIMONENKO, *Meteoritics*, No. 31, 1972, p. 24.
5. LAVRUKHINA, A. K., *Acta Phys. Acad. Sci. Hungaricae*, Supplement 1, Vol. 29, 1970, p. 453.
6. VERNOV, S. N., P. V. VAKULOV, YE. V. GORCHAKOV, YU. N. LOGACHEV, G. P. LYUBIMOV, A. G. NIKOLAYEV AND N. V. PERESLEGINA, *Dokl. Akad. nauk. SSSR*, Vol. 169, No. 5, 1966, p. 1044.
7. SHEDLOVSKY, J. P., M. HONDA, R. C. REEDY, J. C. EVANS, D. LAL, R. M. LINDSTROM, A. C. DELANY, J. R. ARNOLD, LOOSLI HEINZ-HUGO, J. S. FRUCHTER AND R. C. FINKEL, *Science*, Vol. 167, 1970, p. 574.
8. LAVRUKHINA, A. K. AND G. K. USTINOVA, *Astron. Vestnik*, Vol. 5, 1971, p. 144.
9. LAVRUKHINA, A. K. AND G. K. USTINOVA, *Nature*, Vol. 232, 1971, p. 462.
10. CHARAKHCH'YAN, A. N. AND T. N. CHARAKHCH'YAN, *Works of the Sixth All-Union Winter School on Space Physics. Apatity*, Part II, 1969, p. 36.
11. ORMES, I. F. AND W. R. WEBBER, *J. Geophys. Res.*, Vol. 73, 1968, p. 4231.
12. GORIN, V. D., *Abstracts of Reports of the Twenty-Second Conference on Nuclear Spectroscopy and Structure of the Atomic Nucleus*, 4.2, Kiev, January, 1972, p. 91.
13. VINOGRADOV, A. P., A. K. LAVRUKHINA, V. D. GORIN AND G. K. USTINOVA, *Dokl. Akad. nauk. SSSR*, Vol. 202, No. 2, 1972, p. 437.
14. LAVRUKHINA, A. K., V. D. GORIN, L. L. KASHKAROV AND G. K. USTINOVA, *Izv. AN SSSR, Physics Series*, Vol. 38, No. 9, 1974, p. 1806.
15. LAVRUKHINA, A. K. AND V. D. GORIN, *Space Research XIII*, Akademie Verlag, Berlin, 1973, p. 991.
16. LAVRUKHINA, A. K. AND G. K. USTINOVA, *Astron. Zhurn.*, Vol. 44, No. 5, 1967, p. 1081.
17. LAVRUKHINA, A. K., G. K. USTINOVA, T. A. IBRAYEV AND R. I. KUZNETSOVA, *Meteorite Research*, 1969, p. 227.
18. LAVRUKHINA, A. K., *Nuclear Reactions and Heavenly Bodies*, 1972.

19. VINOGRADOV, A. P., *Geokhimiya*, No. 11, 1971, p. 2183.
20. VINOGRADOV, A. P., *Geokhimiya*, No. 7, 1972, p. 763.
21. BAZILEVSKAYA, G. A., A. N. KVASHIN, A. K. PANKRATOV, A. K. SVIRZHEVSKAYA, YU. I. STOZHKOVA, A. N. CHARAKHCH'YAN AND T. N. CHARAKHCH'YAN, *Izv. AN SSSR, Physics Series*, Vol. 35, 1971, p. 2483.
22. CHARAKHCH'YAN, A. N., G. A. BAZILEVSKAYA, A. K. SVIRZHEVSKAYA, YU. I. STOZHKOVA AND T. N. CHARAKHCH'YAN, *Izv. AN SSSR, Physics Series*, Vol. 37, 1973, p. 1258.
23. DILKE, F. W. W. AND D. O. GOUGH, *Nature*, Vol. 240, 1972, p. 262.
24. LAVRUKHINA, A. K., *Proc. Twelfth Int. Conference on Cosmic Rays*, August 16-25, 1971, Hobart, Tasmania, Australia, Vol. 5, 1971, p. 1864.

Results of Special Mechanical Analyses of Luna 16 Material¹

H. Stiller, H. Vollstädt, R. Wasch, P. Bankwitz,
E. Bankwitz, and F. C. Wagner
*Akademie der Wissenschaften der DDR,
Zentralinstitut für Physik der Erde,
Potsdam, East Germany*

J. Schön
*Bergakademie Freiberg
Sektion Geowissenschaften
Freiberg (Sa), East Germany*

For the analysis of lunar soil samples in the GDR, under the direction of the GDR Academy of Sciences, a special methodological system for the examination of the regolith has been developed by selected scientific institutions of the Academy of Sciences and some universities. This system consists of the following complex branches:

1. Examination of fractured or split structures for mineral grains or glass grains
2. Consideration of the pressure-dependence of the propagation velocity of elastic waves in lunar rock samples
3. Investigation of the structural behavior of lunar minerals and glasses under normal thermodynamic conditions and at high pressures
4. Electron-optical study of the regolith to clarify mineralogical and crystallographic properties of selected materials
5. Studies into the mineralogy and crystallography of the rock-forming minerals and the petrochemistry of the lunar soil samples
6. Determination of main and trace elements by means of a methodology oriented to very small samples (plus

determination of isotopes, isotopic abundances, and isotopic ratios)

7. Gamma-ray spectroscopic analyses of the radioactivity of the Luna 16 regolith

This methodological system forms the basis of a general scheme consisting mainly of comparative studies of lunar and terrestrial rocks: lunar materials and corresponding analogous terrestrial materials are analyzed in the same way and with the same objective, and the results obtained are brought into the discussion and interpretation of geophysical, physical, chemical, and mineralogical problems of the Earth and the Moon.

For comparative studies of the physico-mechanical behavior of lunar and terrestrial rocks, it is essential that the chemical and mineralogical parameters be known. The studies carried out on the Luna 16 regolith to find these have confirmed the data that were already published internationally. For example, by means of activation analysis under irradiation in the reactor, activation analysis with a 14 MeV U-generator, and mass spectroscopy on samples of 10 or 20 mg, six main and 63 trace elements were quantitatively determined and compared with known data (ref. 1).

¹ Central Earth Physics Institute report No. 409.

Mineralogical and crystallographic studies confirmed that in addition to glass of the most varied composition, mainly olivine, pyroxene, and plagioclase occur (ref. 2). The results of the chemical and mineralogical-crystallographic studies show that the properties and behavior of lithogenetic minerals found on the Moon basically correspond to those of analogous minerals on the Earth (refs. 3 and 4). Nevertheless, the thermodynamic conditions peculiar to the Moon, i.e., absence of free water, vacuum, and mechanical stress through meteorite impacts, etc., ought to have an effect on the rocks forming the upper strata of the Moon. The mechanical-elastic behavior in particular can be affected by these parameters. The extent to which this applies to minerals and glasses can be shown in part by the following studies (ref. 5).

Analysis of Fracture and Cleavage Surfaces of Lunar Mineral and Glass Fragments

The mineral and glass fragments used for these studies are between 0.02 and 0.2 mm in diameter and correspond, "terrestrially" speaking, to the fine sand fraction. The examination of structures for fracture surfaces is justified in that they are a documentation of (1) the course of events in processes of rupture; (2) surface formations differing in age; and (3) the nature of rupture processes (especially their speed) from which, to a certain extent, further information can be obtained as to the causes of rupture.

These experiments are therefore very suitable for the examination of fracture concepts developed on terrestrial material—and in this case on rocks as well—which we have been studying for a long time. Particular features of the fracture surfaces (in rock ruptures the so-called joint structures) give an indication as to the nature of the process of rupture: surface steps radiate from the starting point of the crack, their divergence indicating the direction of propagation. These surface steps can also turn into inde-

pendent secondary fracture surfaces. They are evidence of the propagation of a fracture at different levels.

A conclusion can also be drawn as to the fracture propagation velocity. It is known from fracture physics that the propagation of a fracture usually occurs rapidly (slow fatigue fractures are clearly distinguishable). It can also be deduced from the physical nature of the rupture process that certain surface structures, as well as a rupture process itself, are genetically related to the propagation, refraction, etc., of elastic waves, and that the fracture propagation velocity, being about half the transverse wave velocity, is relatively high. Interruptions in fissuration are marked in particular by initial fields lying in series.

Following is an example to explain the method of work and the object of the investigation. Figure 1 shows a regolith grain (a),

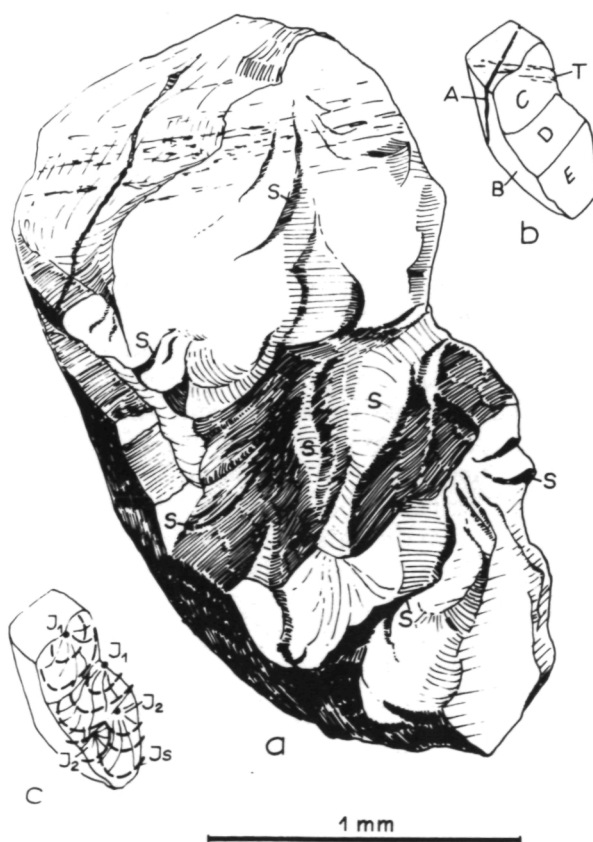


Figure 1.—Analysis of fracture of a regolith-grain.

with two detailed sketches (b + c). Owing to the coarse internal structure, the individual surfaces are unevenly formed, while (b) shows the interrelationship of the ages of the fracture surfaces, (c) shows the centers of cracking and the directions of cracking of the surface portions.

- (1) I_1 and I_2 are initial points that have occurred simultaneously because their structures of rupture interlock at their line of intersection.
- (2) Since C and D on surface B form steep steps, it can be assumed that B is older than C and D. The structures of E develop from D, i.e., E developed after D.
- (3) From two secondary initial points, I_2 , the process of fracture propagation from D to E can be seen (in b). A is a mineralized rupture. One suspects that A and B belong to older surface systems while C, D, and E represent a younger system. Figures 2 and 3 show further examples of fracture surface analysis.

Unlike geologically comparable material, the regolith from Luna 16 is very finely divided. On the surface of the Earth, this occurs only in areas of mylonite. In addition, despite the fineness, the regularity of the larger particles is remarkable. This indicates fracture-producing impacts at fairly large distances. Finally, such a fine disintegration is bound to absorb considerably all continuous elastic waves. The materials under review can reliably be said to have low wave velocities. From the first results obtained up to now the following can be stated: the fracture structures formed on the Moon correspond in all respects to those that have developed on the Earth. The rupture processes must therefore also be the same. It can be assumed that the formation of fractures in crystals, glasses, breccias, etc., took place in a vacuum and in the absence of free water. Both factors clearly have no decisive primary importance for the rupture process itself.

Fracture surface structures are a result

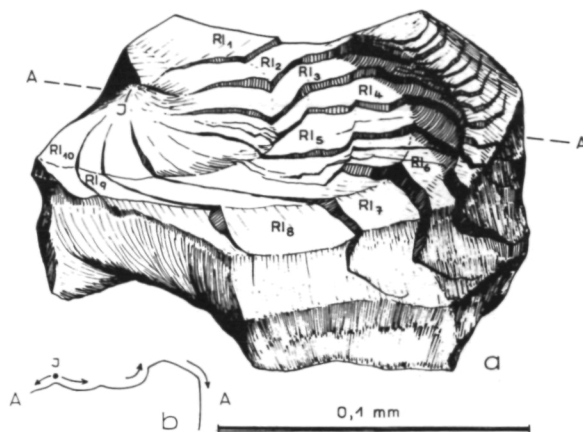


Figure 2.—Example 2 of fracture surface analysis.

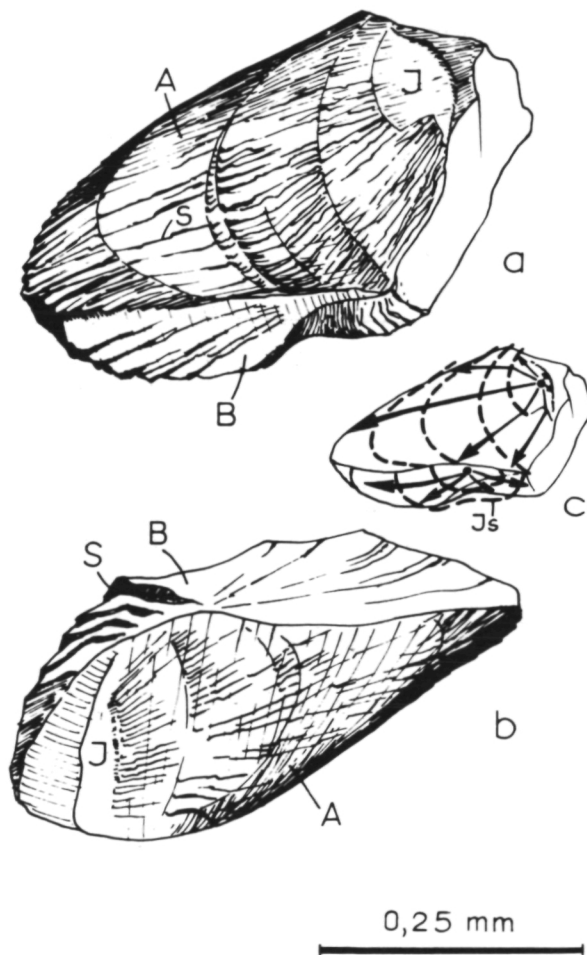


Figure 3.—Example 3 of fracture surface analysis.

of the dissipation of energy in the form of waves. The formation of every microcrack and of every fissure represents a tremor of the very smallest magnitude. In the Luna 16 regolith, the final forms that predominate suggest a highly intense or explosive rupture.

It still remains to be investigated to what extent changes in the internal structure of a material are manifested in different changes in the form of the fracture structures typical for the particular case; to what extent one can infer internal structural features—for rocks as well—from small differences in the formation of the fracture structure; and how these structural features affect the rupture process of individual rock constituents.

Examination of the Pressure-Dependence of the Propagation Velocity of Elastic Waves in Lunar and Terrestrial Rocks

The behavior of the propagation velocity of elastic waves particularly longitudinal waves in this case under increasing pressure found through examination of dense Moon rock samples can be compared with that found for terrestrial rocks. Such comparison shows that (1) lunar rock samples demonstrate a far greater pressure-dependence than terrestrial rock samples of comparable density and chemistry and (2) at low pressures in particular, the velocities of the lunar samples are far below those of the comparable terrestrial samples. Possible causes of the pressure-dependence are changes in the elastic properties of the minerals themselves and changes in pore or fissure volume.

Even with the high density of the material of $\rho = 3.1 \text{ g/cm}^3$, neither of these causes can explain the considerable changes in velocity with increasing pressure. It is more likely that the reason for this dependence is to be found in the occurrence of "imperfectly elastic bonds between the rock constituents." These defects, e.g., in grain or mineral contacts, are not necessarily tied to a "fissure

volume" worth mentioning. The theoretical treatment of this problem leads to the following considerations.

A quantity K_0 can be taken as a coefficient of measure for the cracks in the rocks described. K_0 characterizes the imperfect bond between the rock constituents caused by cracks. K_0 can be expressed by analytical formula corresponding to Stiller et al. (ref. 7). Taking into account this K_0 parameter, a velocity-pressure relation of the following can be obtained:

$$V_P = V_F(1 - K_0 e^{-A\sigma})^{1/2}$$

where V_P = velocity of longitudinal waves of the sample under pressure

V_F = velocity of the flawless compact substance

K_0 = initial value of quantity K , i.e., K at a pressure of $\sigma = 0 \text{ kg/cm}^2$

A = coefficient for the deformability of the sample

Figure 4 shows the dependence

$$\frac{V_P}{V_F} = (1 - K_0 e^{-A\sigma})^{1/2}$$

on a double logarithmic scale. The double logarithmic representation makes it possible to use the curves as "master curves" for the interpretation of experimental results. The measured values are drawn on paper of the same scale as that of the master curve; this is then placed over the master curve, and an attempt is made, by moving the paper and keeping the axes parallel, to bring the measured values into coincidence with the master curve.

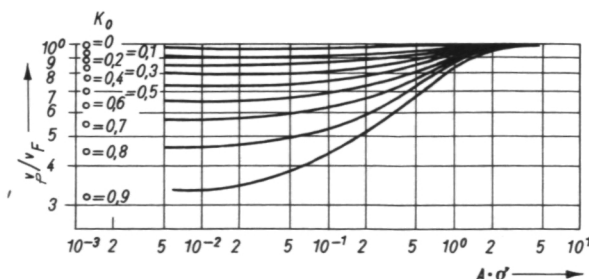


Figure 4.—Function $V_P/V_F = (1 - K_0 e^{-A\sigma})^{1/2}$ in double logarithmic scale.

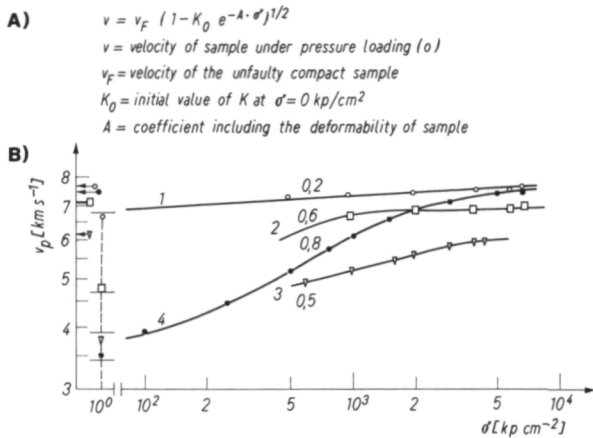


Figure 5.—Experimental results of terrestrial and lunar rocks, evaluated from the relation under A: curve 1 dunite (terrestrial) = 2.31 gcm^{-3} ; 2 chloritic schists (terrestrial) = 2.84 gcm^{-3} ; 3 gneiss (terrestrial) = 2.72 gcm^{-3} ; 4 basalt (lunar) = 3.32 gcm^{-3} .

Figure 5 shows this velocity relation (A) and the results of such an interpretation, obtained from lunar and terrestrial samples (B). In part (B), curves 1, 2, and 3 for terrestrial rocks show K_0 values up to 0.6 (for a gneiss with density $\rho = 2.72 \text{ g/cm}^3$). The results for a lunar sample much denser in comparison (curve 4) show an even higher value for $K_0 = 0.8$, and therefore indicate extreme internal crushing of the rock.

Apart from the curve parameter K_0 , the comparison of the calculated and the measured value at $\sigma = 1 \text{ kg/cm}^2$ and the value for V_F marked by an arrow on the velocity axis are also given. This value V_F is the ordinate value on the experimental curve, corresponding to the ordinate value $V_F/V_F = 1$ on the calculated curves. Of particular interest here is the good agreement in the V_F values between the terrestrial dunite (curve 1) and the lunar "basalt" (curve 4). This underlines the fact that the differences in elastic behavior do not result primarily from the mineralogical composition, but from the nature and degree of the internal bonds. In figure 6, the evaluations of experimental results for lunar rocks are shown. They confirm the assumptions made so far. The

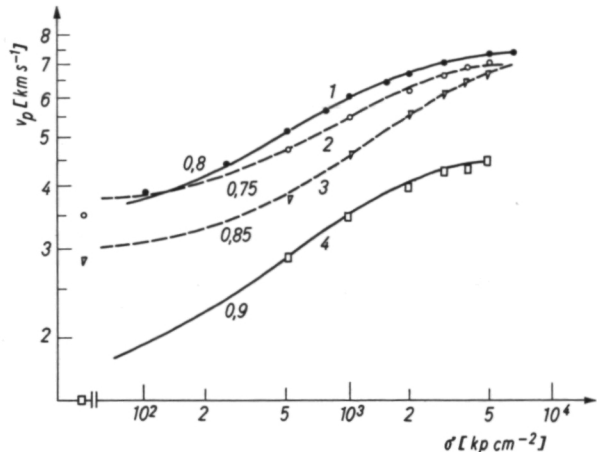


Figure 6.—Experimental results of lunar rocks: curve 1 basalt = 3.32 gcm^{-3} ; curve 2 basalt = 3.18 gcm^{-3} ; curve 3 basalt = $2.88 \dots 3.38 \text{ gcm}^{-3}$; curve 4 breccia = 2.35 gcm^{-3} .

considerable internal disturbance in the bonds between the constituents of the lunar rocks will most probably have been mainly caused by a heavy alternating thermal stress and also a very heavy mechanical stress (meteorite impacts—shock waves). Berzov et al. (ref. 6) brings these last influences together under the heading "impact metamorphosis."

Conclusions

The following conclusions can be drawn from the studies carried out so far:

1. The lithogenetic minerals on the surface of the Moon correspond in most respects to their terrestrial counterparts, as can be deduced from chemical, mineralogical, radiographic, and electronoptical examinations.
2. The mechanical short-term behavior also conforms to this trend.
3. From this it can be deduced that the special thermodynamic conditions on the Moon have no appreciable influence on the physico-mechanical behavior of lunar minerals, although there are some significant differences

- in the distribution of elements.
4. This influence, however, makes itself felt more in the behavior of the lunar rocks, since in contrast to terrestrial conditions lunar rock has been subject to extreme dynamic influence. This is manifest in, among other things, a considerably greater pressure-dependence—above all at low pressures—of the velocity of longitudinal waves. The causes for this can be found in the relatively high degree of crushing in lunar rocks caused by meteorite impacts and other types of mechanical stress; this was substantiated quantitatively.
 5. This mechanical influence has meant that the grain contacts and all other possibilities of connection between the rock constituents (minerals, glass) have not attained the "perfection" which predominates, for example, in most terrestrial rocks.
 6. The results have shown that the physico-mechanical state of lunar rocks can be expressed as a formula on the basis of known dependences.
 7. The velocity-pressure dependences of lunar rocks, corrected with regard to the crushing factor, behave quantitatively and qualitatively like the corresponding terrestrial rocks. Consequently, the velocity-depth dependences in the Moon at sufficient depth must be analogous to the corresponding depth dependences in the Earth, as can also

be seen from the results of lunar seismology (see ref. 8).

8. The analogies of physico-mechanical behavior mentioned above make it possible to use adequate equations of state for the Moon as well.

References

1. BRUNNER, G., Bestimmung Chemischer Elemente Mittels Massenspektroskopie. *Reaktor Und Generatoraktivierung*. In preparation.
2. WÄSCH, R., AND H. VOLLSTÄDT, Mineralogische Kennzeichnung und Klassifizierung des Luna 16 Materials. *Geophys.*, Vol. 82, 1973, pp. 445–453.
3. RÖSLER, H. J., W. KRAMER, AND P. BEUGE, *Ergebnisse Mineralogischer und Petrochemischer Untersuchungen am Luna 16 Material*. In preparation.
4. BAUTSCH, H. J., A. MESSERSCHMIDT, AND J. VETTER, *Mineralogie und Kristallographie Lunarer Kristallite und Gläser*. In preparation.
5. BANKWITZ, P., AND E. BANKWITZ, Bruchflächenanalyse an Luna 16 Material. *Geophysik*, Vol. 82, 1973, pp. 454–464.
6. BERZOV, L. B., A. M. BORSUK, AND V. I. VINOGRADOV, Veščest Luny. *Itogi Nauki*, Ser. geochim., mineral., petrogr., 1971.
7. STILLER, H., H. VOLLSTÄDT, AND F. C. WAGNER, Physical Properties of Rocks and Minerals Under Pressure of 60–100 Kbar; Changes in Wave Velocity in Rocks and Dynamically Stressed Regions. *Paper for the IASPEI Conference about "Earthquake Prediction"*, Tashkent, 1974. In press.
8. MEISSNER, R., Stand der Mondforschung nach Apollo. *Umschau*, Vol. 74, No. 3, 1974, pp. 74–80.

The Analysis of Various Size, Visually Selected and Density and Magnetically Separated Fractions of Luna-16 and -20 Samples

The Royal Society Luna Sample Investigation Team

G. Eglinton, A. P. Gowar, A. J. T. Jull, C. T. Pillinger
School of Chemistry, University of Bristol

S. O. Agrell, J. E. Agrell, J. V. P. Long
Department of Mineralogy and Petrology, University of Cambridge

S. H. U. Bowie, P. R. Simpson, R. D. Beckinsale,
J. J. Durham
Institute of Geological Sciences, London

G. Turner, P. H. Cadogan
Department of Physics, University of Sheffield

T. C. Gibb, R. Greatrex, N. N. Greenwood
Department of Chemistry, University of Leeds

D. W. Collinson, S. K. Runcorn, A Stephenson
Department of Physics, University of Newcastle-upon-Tyne

S. A. Durrani, J. H. Fremlin, F. S. W. Hwang, H. A. Kahn¹
Department of Physics, University of Birmingham

Samples of Luna 16 and 20 have been separated according to size, visual appearance, density, and magnetic susceptibility. Selected aliquots were examined in eight British laboratories. The studies included mineralogy and petrology, selenochronology, magnetic characteristics, Mössbauer spectroscopy, oxygen isotope ratio determinations, cosmic ray track and thermoluminescence investigations, and carbon chemistry measurements.

Luna 16 and 20 are typically mare and highland soils, comparing well with their Apollo counterparts, Apollo 11 and 16, respectively. Both soils are very mature (high free iron, carbide, and methane and cosmogenic ³⁶Ar), while Luna 16, but not Luna 20, is characterized by a high content of glassy materials. An aliquot of anorthosite fragments, hand-picked from Luna 20, had a gas retention age of about 4.3 ± 0.1 Gy.

Two cores of lunar soil have been returned to Earth by the Soviet unmanned landers Luna 16 and 20. The Luna 16 core was collected in September 1970 from the north-

eastern part of the Mare Fecunditatis; Luna 20 landed in a typical highland region of the Moon at latitude $3^{\circ}32'$ W. and longitude $56^{\circ}33'$, near the crater Apollonius C. Both cores have been analyzed by Soviet workers (refs. 1 and 2) and by American and French consortia. (See *Earth Planetary Science Let-*

¹ On leave from Pakistan Institute of Nuclear Science and Technology (PINSTECH), Nilore, Rawalpindi, Pakistan.

ters, Vol. 13, pp. 225-466, and Vol. 17, pp. 3-63; and *Geochimica et Cosmochimica Acta*, Vol. 37, pp. 719-1110, and Vol. 37, pp. 1991-2035, for collected papers.)

Two 0.5g samples (L1627 and L2015, from the 27-cm level of zone B and from the 27- to 32-cm unit of the L16 and L20 cores, respectively) generously provided by the Soviet Academy of Sciences to the Royal Society, have been separated sequentially according to size, visual appearance, density, and magnetic susceptibility.

We report here the collaborative study of a number of selected aliquots by a consortium of eight British laboratories. A number of techniques not previously applied to Luna samples have been used. The investigations performed included mineralogy and petrology, selenochronology, magnetic properties, Mössbauer spectroscopy, thermoluminescence investigation, oxygen isotope ratio determi-

nations, cosmic ray track and micrometeorite crater densities, and carbon chemistry measurements.

Experimental Studies

SAMPLE PROCESSING

All operations were performed in the clean room facility at the Organic Geochemistry Unit, University of Bristol (ref. 3). Sample manipulation was carried out with pre-cleaned equipment. Glass spatulas (cleaned with aqua regia) or aluminium foil squares (toluene/methanol-extracted) were used for sample transfer. Storage vessels were either B14 Quickfit glass tubes (cleaned with aqua regia) or polystyrene vials (as supplied by Dr. M. B. Duke, Curator of Apollo Lunar Samples at the Lyndon B. Johnson Space Center, Houston). The sample processing

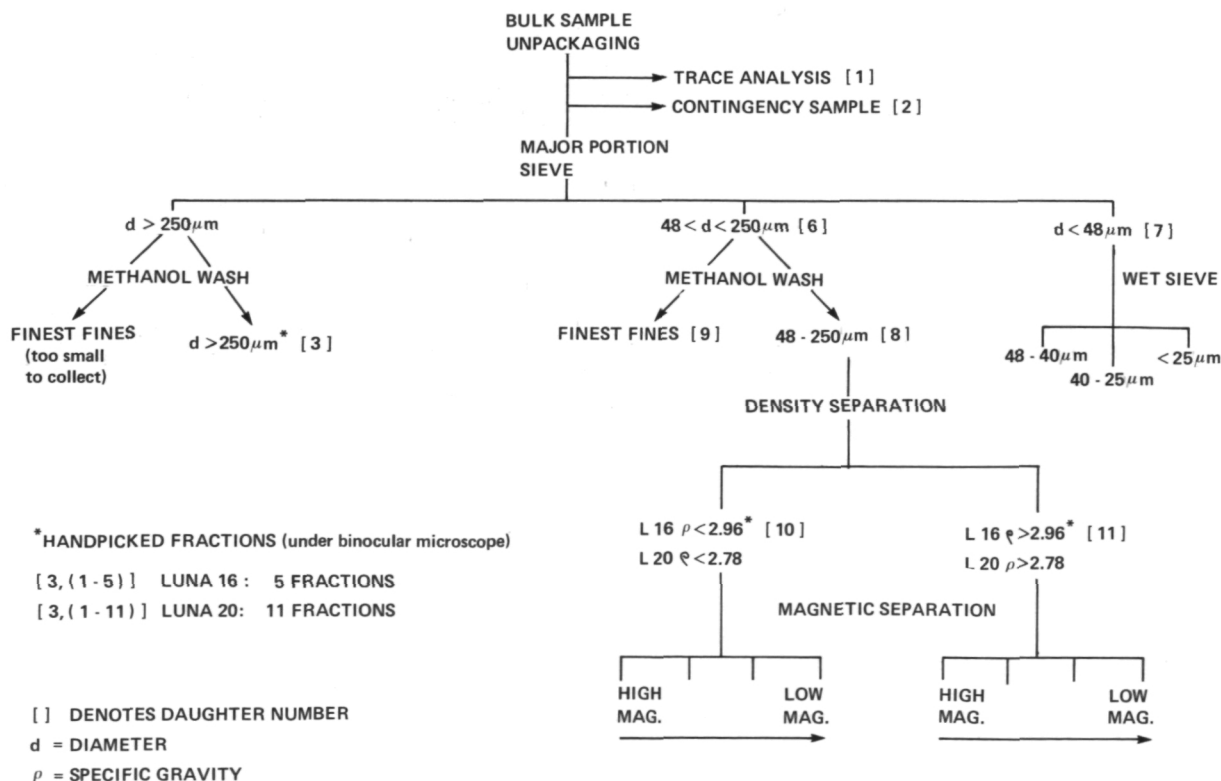


Figure 1.—Separation scheme for processing Luna 16 and 20 fines.

scheme adopted for both samples is outlined in figure 1; the sample distribution is shown in table 1. Material $> 250\mu\text{m}$ was handpicked for further study under the binocular microscope according to the scheme outlined in tables 2 and 3.

ANALYTICAL PROCEDURES

The analytical procedures used in this study have been or will be described in detail elsewhere. Fractions of particles $> 250\mu\text{m}$ and $< 48\mu\text{m}$ were mounted and polished for microscopic and electron probe microanalysis in circular brass mounts of one-inch diameter, drilled to provide individual mounting positions in which each grain was firmly embedded in epoxy resin.

The mineral and rock compositions have been determined with an electron probe and energy-dispersive spectrometer. Spectrum deconvolution, peak integration, and matrix corrections were performed in a small on-line computer. In this procedure, uncertainties in estimation of background result in errors that vary in magnitude from element to element, and in limits of detection which are typically of the order of 0.05 percent except for sodium, where the rapidly increasing absorption of the 0.001" Be window limits sensitivity to ~ 0.3 percent. In most analyses, sodium values were below this limit.

Bulk rock compositions were measured by averaging the results of some 10 determinations carried out with an enlarged probe area. It must be emphasized that this procedure can introduce systematic errors of several percent (relative) in the case of the light elements in mixtures of plagioclase and a ferromagnesian mineral, and caution is necessary in any interpretation depending on differences in measured values of less than 5 percent.

Sample L2015,3,6 was irradiated with high fluence ($J = 0.1295$) of neutrons; the irradiation designated SH31 will be reported separately. Argon was extracted and analyzed (ref. 4) in 12 heating steps, of 30 minutes each step. Natural remanent magnetism

(NRM) measurements were made with a small-scale magnetometer (ref. 5). Mössbauer spectra were recorded at room temperature (294 K) and at liquid nitrogen temperature (77 K), by use of the techniques developed for the Apollo 14 and 15 soils (refs. 6 and 7). Thermoluminescence data were recorded by heating 1-mg samples in an oxygen-free nitrogen atmosphere at $4^\circ/\text{s}$. The thermoluminescence emission spectrum induced by artificial radiations was analysed by the method of Durrani et al. (ref. 8) taking into account the efficiency of the (quartz window) photomultiplier and the transmission characteristics of the filter used. Oxygen isotopes were measured by conversion to carbon dioxide; the procedure is given in detail by Beckinsale et al. (ref. 9). Optical and scanning electron microscopes were used to study surface features, particularly impact craters and charged particle tracks. The deuterocarbon CD_4 (from deuterolysis of hydrolysable carbon phase) and the trapped hydrocarbon CH_4 were released from samples by deuterated acid dissolution (DCl , 38 percent in D_2O , Ciba Ltd.) and quantitated by gas chromatography (refs. 10 and 12).

Results and Discussion

PETROLOGY

Luna 16

The $> 250\mu\text{m}$ grains previously selected under a binocular microscope were mounted, examined under a polarizing reflected light microscope, and reclassified.

Some of the soil breccia and agglutinate fragments broke up on mounting into separate fragments which were then individually classified. One of the "basaltic" fragments classified under the binocular proved, on further examination, to be an agglutinate. With this one exception, all fragments remained within their binocular class. Additional categories related to agglutinate were recognized (e.g., vesicular drops, glassy drops, and

Table 1.—*Sample Distribution* ⁽¹⁾

Sample Type \	Daughter Number	Minerology and Petrology (Agrell and Bowie)	Selenochronology (Turner)	Magnetic (Runcorn)	Mössbauer Spectroscopy (Greenwood)	O Isotope (Beckinsale)	Thermo-Luminescence (Durrani)	Tracks (Durrani)	Carbon Chemistry (Eglinton)
Bulk Unseparated Material	1 or 2	—	—	—	+	—	—	—	+
d > 250 μ m Handpicked	3,1-5 (L16) 3,1-11 (L20)	+	L20*	+	—	—	—	+	L16*
d < 48 μ m	7	+	—	+	—	+	+	+	+
Unseparated 48 < d < 250 μ m	8	+	—	—	—	—	—	+	+
Finest Fines	9	+	—	+	L16*	—	—	+	+
48 < d < 250 μ m Light L16 < 2.96 L20 < 2.78	10	+	—	+	—	—	—	—	+
48 < d < 250 μ m; Heavy L16 > 2.96; L20 > 2.78	11	+	—	+	—	—	—	—	+
48 < d < 250 μ m; Light Magnetic Separates	10g,2	—	—	—	—	—	—	L16*	L16*
48 < d < 250 μ m; Heavy Magnetic Separates	11,2	—	—	—	—	—	—	L16*	L16*

NOTE: (1) Symbols used as follows: d = diameter of sample.
 + = samples of both L16 and L20 examined.
 * = samples of only L16 or L20 examined.
 — = no samples of either L16 or L20 examined.

Table 2.—*Luna 16: Classification Scheme of Handpicked Fragments > 250 μ m*

Section Number	Sample Number	Binocular Sample Classification	Column Number (with number of fragments of each type)							
			(1)	(2)	(3)	(4)	(5)	(6)	(7)	Total
1	L1627,3,B	Residual Fraction	3	11	1	5	3	1	1	25
2	L1627,3,2	Basaltic Fragments	1	0	0	1	0	0	0	2
3	L1627,3,3 ⁽⁸⁾	Soil Breccia	1	2	0	0	1	0	0	4
4	L1627,3,5 ⁽⁸⁾	Agglutinates	0	0	0	5	0	0	0	5
		Totals	5	13	1	11	4	1	1	36

NOTES: (1) Ilmenite Basalt
 (2) Soil Breccia
 (3) Glass-Coated Soil Breccia
 (4) Agglutinate
 (5) Vesicular Drop
 (6) Glassy Drop
 (7) Glassy Fragment
 (8) These fragments broke up on mounting.

glassy fragments). Thirty-six fragments were studied, of which the greater part are soil breccias (13) and agglutinates (11). Ilmenite basalts are represented by five fragments. In the remaining categories there are four vesicular drops and one each of the following: glass-coated soil breccias, glassy drops, and glassy fragments.

The major particle types occurring in Luna 16 are discussed as follows:

Ilmenite Basalt: All five ilmenite basalt grains studied are characterized by a high proportion of ilmenite (about 10 percent) uniformly distributed throughout the basalt, which has well-developed ophitic texture. The largest handpicked fragment contains, in addition, notable phenocrysts of olivine intergrown with a pinkish spinel phase that does not occur elsewhere in the rock fragment. All other fragments studied appear olivine-free; but this may be a reflection of the small sizes of the fragments studied, since the olivine phenocrysts are widely separated in the ophitic groundmass. The order of crystallization for the basalts as a

whole could therefore be summarized as phenocrysts of a spinel and olivine in a groundmass of feldspar, ilmenite, pyroxene, troilite, and iron, crystallizing in that order.

Soil Breccia: Thirteen soil breccia fragments were identified, two of them from the binocular soil breccia class, and the rest from the residual fraction. They comprise weakly aggregated soil clods that break up when touched. More detailed study reveals the presence of unsorted individual mineral grains of the ilmenite basalt suite and clasts comprising one or more basaltic minerals. In addition, angular or rounded grains of nickel-iron were observed. Glass is abundant in the breccia in a multiplicity of forms ranging from perfect spheres to angular fragments, intergranular permeations, and coatings on mineral grains, clasts, and rock fragments. One soil breccia fragment is notable for a glass coating on one side that links this category to that of the agglutinates.

Agglutinate: Nearly half the fragments studied are either agglutinates or a related fragment type such as vesicular drops,

Table 3.—*Luna 20: Classification Scheme of*

Section Number	Sample Number	Binocular Sample Classification				
			(1)	(2)	(3)	(4)
5	L2015,3,B	Residual Fractions	0	1	1	3
6	L2015,3,2	Fine Glassy Agglutinate	0	0	0	0
6	L2015,3,3	Glass-Coated Soil Breccia	0	0	0	0
7	L2015,3,4	Chalky Feldspar Shocked Friable	0	0	0	0
7	L2015,3,5	Vitreous Plagioclase	1	0	0	0
8	L2015,3,6	Microcrystalline Plagioclase Fragments	0	0	0	0
8	L2015,3,7	Coarsely Polycrystalline Plagioclase ⁽¹⁵⁾	0	0	0	0
9	L2015,3,8	Microbreccias Pyroclastic Texture ⁽¹⁵⁾	0	0	0	12
10	L2015,3,8	Microbreccias Pyroclastic Texture	0	0	0	0
Totals			1	1	1	15

- NOTES: (1) Partially Maskelynitized Anorthositic Granulite With Olivine
 (2) Feldspathic Basalt
 (3) Fine-Grained Feldspathic Soil Breccia
 (4) Glass-Bonded Soil Breccia = Shock-Lithified Soil
 (5) Splash Glass Invading Soil Breccia
 (6) Agglutinate
 (7) Very Fine Grained Pale Metaclastic Rock With Small Plagioclase Porphyroclasts

Handpicked Fragments > 250 μ m

(see identifying notes) and Number of Fragments of Each Type

(5)	(6)	(7)	(8)	(9)	(10)	(11)	(12)	(13)	(14)	Total
0	3	5	1	1	1	1	0	0	0	17
0	2	0	0	0	0	0	0	0	0	2
1	2	0	0	0	0	0	0	0	0	3
0	0	0	0	0	0	0	2	0	0	2
0	0	0	0	0	0	0	0	1	0	2
0	0	2	0	0	0	0	0	0	0	2
0	0	0	0	0	0	6	0	0	0	6
0	2	4	2	0	0	0	0	0	1	21
0	0	2	0	0	0	0	0	0	0	2
1	9	13	3	1	1	7	2	1	1	57

- (8) Poikilitic Fragment of Noritic Affinity
 (9) Anorthosite
 (10) Devitrified Maskelynite
 (11) High-Grade Noritic Metaclastic or Fine-Grained Impact Melt
 (12) Shock-Melted Plagioclase
 (13) Vitreous Pale Impact Melt
 (14) Noritic Impact Melt With Subophitic Texture
 (15) These fragments broke up on mounting.

glassy drops, or glassy fragments. The agglutinate is generally vesicular and in many cases has adherent microbreccia along one side of an agglutinate mass, and a smooth, rounded outline on the other. It contains partially digested mineral grains, notably ilmenite-basalt rock fragments and glassy fragments. A fine dissemination of iron and troilite spheres may be present in various sizes down to the resolution limit of the microscope. Vesicular drops, which are an agglutinate type with rounded or sub-rounded outline, lack adherent microbreccia but are otherwise similar to the agglutinate described above. In addition, a glassy drop and a glassy fragment are recorded. The glassy drop has a sub-rounded outline and contains less partially digested mineral fragments and clasts than the normal agglutinate. The polished surface of the drop in reflected light is distinctly mottled, which suggests inhomogeneity in the glass composition on the microscale. The glassy fragment has an angular but smooth outline with a few vesicles and mineral grains and clasts absent. The glass is optically homogeneous in reflected light, and is notable for the presence of many composite spheres of troilite and iron.

Luna 20

After preliminary sieving and handpicking, polished mounts were made from two fractions: 1 mg from the $< 48\mu\text{m}$ fraction (L2015,7), and two fragments from each of the rock types recognized in the handpicked fraction $> 250\mu\text{m}$ (L2015,3). Petrographic examination was undertaken, and the chemical composition of selected minerals and lithic and vitric fragments was determined.

Fraction $< 48\mu\text{m}$: A preliminary examination was made of a sample of the fraction $< 48\mu\text{m}$ (L2015,7,2). Its composition was 65 percent angular mineral fragments (46 percent plagioclase, 18 percent ferromagnesian minerals, 1 percent oxide minerals) and 35 percent glassy fragments. The latter were equally divided between crystal-charged agglutinate and homogeneous glass free from

inclusions. The mineral fragments were dominantly anorthite (An 95–98) with subordinate hypersthene.

Representative analyses are quoted in table 4. One fragment was recorded (analysis 3, table 4) of an aluminous hypersthene whose composition is suggestive of a high-pressure origin.

Representative glass analyses are quoted in table 5 and plotted on figures 2 and 3 along with the Luna 20 glass averages determined by Warner et al. (ref. 13). Of the glass analyses quoted, only three may be considered to have affinities with mare basalts or the melts which correspond to the end stage of their crystallization (analyses 3, 4, and 5, table 5). One silica glass was observed and all the rest are in the composition range of highland rocks. Too few analyses were made to delineate any population groupings within these glasses. But it should be noted that the majority have alumina and lime contents between the averages of the highland basalt and low-potassium Fra Mauro basalts of Warner et al. (ref. 13). It should also be noted that the composition of six of eight lithic fragments analyzed from the $> 250\mu\text{m}$ fines of L2015 also fall in this composition range.

Fraction $> 250\mu\text{m}$: Polished mounts were made of two or three fragments of the several categories recognized in table 3, and from the residual material left over after the initial handpicking. These were reclassified after petrographic examination and electron probe analyses. The types recognized are summarized in table 3.

Mineral Fragments: The majority of the mineral fragments $> 250\mu\text{m}$ were plagioclase; 10 were recognized in the original handpicking, and only one pyroxene was found.

The plagioclase may occur as clear colourless fragments with a vitreous lustre, as maskelynite, as devitrified maskelynite, and possibly as shock-melted material (analysis 5, table 4). Hypersthene (analysis 1, table 4) was represented by a single crystal showing cataclastic features.

The above are the only evidence in sample

L2015 for the existence of rocks with a grain size $> 250\mu\text{m}$ at the Luna 20 site.

Lithic Fragments: All the fragments so far examined are of highland origin and no mare types have been recognized. The principal minerals recognized in these fragments are anorthite, hypersthene, olivine, augite with accessory ilmenite, iron metal, troilite, and spinel. In glassy fragments, or in frag-

ments devitrified on the finest scale, metallic iron occurs as sporadic, rounded droplets usually $< 2\mu\text{m}$ in diameter. In an agglutinate glass in L2015,3,3 one droplet was sufficiently large to analyze, and gave Ni 9.5 percent. In a glass-bonded soil breccia from L2015,3,B, nickel contents of from 5.8 percent to 11.2 percent were recorded in separate metal droplets. No two-phase metals were observed,

Table 4.—*Minerals from L2015*

	(1)	(2)	(3)	(4)	(5)	(6)	(7)	(8)	(9)	(10)
SiO ₂	53.37	52.39	54.72	49.17	43.58	33.46	37.59	54.98	53.93	52.34
TiO ₂	0.60	0.73	0.74	1.52	0.09	0.05	0.08	0.43	0.41	0.29
Al ₂ O ₃	0.70	1.69	5.50	2.06	35.16	0.04	0.11	0.71	0.58	0.73
Cr ₂ O ₃	0.56	0.61	0.76	0.19	0.00	n.d.	n.d.	n.d.	n.d.	n.d.
FeO	15.10	19.61	6.85	29.03	0.00	45.33	37.25	24.61	26.19	16.31
MnO	0.26	0.31	0.18	0.42	0.00	n.d.	n.d.	n.d.	n.d.	n.d.
MgO	25.47	22.31	32.47	10.55	0.00	20.89	25.89	17.24	17.99	15.10
CaO	1.92	2.47	0.48	8.15	19.71	0.10	0.46	1.96	3.71	14.42
Na ₂ O	n.d. ⁽¹¹⁾	n.d.	0.31	n.d.	0.30	n.d.	n.d.	n.d.	n.d.	n.d.
K ₂ O	n.d.	n.d.	n.d.	n.d.	0.04	n.d.	n.d.	n.d.	n.d.	n.d.
Total	97.98	100.12	102.01	101.09	98.88	99.93	101.41	99.93	102.81	99.19
Cations	0 = 6	0 = 6	0 = 6	0 = 6	0 = 8	0 = 4	0 = 4	0 = 6	0 = 6	0 = 6
Si	1.972	1.939	1.866	1.921	2.040	0.983	1.033	2.0009	1.996	1.988
Ti	0.017	0.020	0.019	0.045	0.003	0.001	0.002	0.012	0.012	0.008
Al	0.030	0.074	0.221	0.094	1.940	0.001	0.004	0.031	0.025	0.032
Cr	0.016	0.018	0.020	0.006	—	—	—	—	—	—
Fe	0.466	0.607	0.195	0.948	—	1.113	0.856	0.898	0.809	0.518
Mn	0.008	0.009	0.005	0.014	—	—	—	—	—	—
Mg	1.402	1.230	1.650	0.614	—	0.915	1.060	0.938	0.992	0.855
Ca	0.076	0.098	0.017	0.341	0.989	0.002	0.009	0.077	0.147	0.587
Na	—	—	—	—	0.027	—	—	—	—	—
K	—	—	—	—	0.002	—	—	—	—	—
Fe	24.0	31.3	10.5	49.8	Ca97.1	Fe 54.9	44.7	47.0	41.5	26.4
Mg	72.1	63.6	88.6	32.3	Na 2.7	Mg45.1	55.3	49.0	50.9	43.6
Ca	3.9	5.1	0.9	17.9	K 0.2	Ca —	—	4.0	7.6	30.0

NOTES: (1) Hypersthene crushed fragment from L2015,3,10 associated with minor anorthite.

(2) Hypersthene fragments from $< 48\mu\text{m}$ fraction L2015,7,2.

(3) Aluminous hypersthene $< 48\mu\text{m}$ fraction L2015,7,2.

(4) Ferroaugite $< 48\mu\text{m}$ fraction L2015,7,2.

(5) Plagioclase, annealed shock-melted plagioclase with small irregular gas cavities from L2015,3,4,1.

(6) Olivine includes NiO 0.06 percent.

(7) Olivine includes NiO 0.03 percent.

(8) Hypersthene

(9) Hypersthene

(10) Augite

(11) n.d. = Not detected.

} Melt rock with equigranular texture. Plagioclase ~ 70 percent; Ferromagnesian ~ 30 percent. L2015,3 B,11 Geoscan Analysis P.R.S.

Table 5.—Analyses of Glassy or Microcrystalline Fragments < 48 μ m in Diameter, L2015,7,3

	(1)	(2)	(3)	(4)	(5)	(6)	(7)	(8)	(9)
SiO ₂	43.20	45.70	42.58	48.79	58.91	44.23	44.17	97.82	46.12
TiO ₂	0.21	0.31	5.34	0.32	0.40	0.07	0.40	0.26	0.77
Al ₂ O ₃	24.44	25.54	13.83	22.90	22.07	32.07	25.33	1.19	21.18
Cr ₂ O ₃	0.21	0.09	0.21	0.00	0.07	0.07	0.23	0.00	0.21
FeO	5.94	5.69	17.55	11.05	7.11	1.79	6.09	0.07	9.40
MnO	0.08	0.05	0.21	0.16	0.09	0.00	0.00	0.00	0.09
MgO	8.73	8.74	8.23	0.00	0.66	3.73	6.76	0.00	6.64
CaO	14.31	14.62	10.62	13.49	11.55	17.62	14.52	0.00	15.31
Na ₂ O	0.30	n.d.	n.d.	0.44	n.d.	n.d.	0.59	n.d.	n.d.
K ₂ O	0.03	0.03	0.07	0.28	0.70	0.03	0.20	0.03	0.03
Total	97.45	100.74	98.64	97.43	101.56	99.76	98.29	99.37	99.72
CIPW NORM									
QZ	—	—	—	8.68	24.8	—	—	97.70	0.05
COR	—	—	—	—	0.31	—	—	1.16	—
OR	0.18	—	0.41	1.65	4.12	—	1.18	0.18	—
AB	2.54	—	—	3.72	—	—	4.99	0.01	—
AN	65.25	69.68	37.53	59.68	57.30	87.50	65.88	—	57.78
DI	4.64	2.30	12.60	6.46	—	0.65	5.02	—	15.02
HY	8.67	21.28	37.08	16.63	14.14	9.52	7.85	—	25.08
OL	15.46	6.75	0.57	—	—	1.85	12.28	—	—
CM	0.31	0.13	0.31	—	0.10	0.10	0.34	—	0.31
IL	0.40	0.59	10.14	0.61	0.76	0.13	0.76	0.15	1.46
FS/HY	26.9	25.8	46.7	100.0	85.0	20.31	31.8	—	42.37
Mo1%									

NOTES: (1) Colourless glassy fragments
 (2) Colourless glassy fragments
 (3) Pale brown glassy fragments
 (4) Pale brown glassy fragments
 (5) Pale brown agglutinate
 (6) Colourless microcrystalline fragments
 (7) Colourless microcrystalline fragments
 (8) Fragment of silica glass
 (9) Very pale brown glassy agglutinate

but a skin of troilite was observed in one case.

The majority of the lithic fragments are very fine grained (< 15 μ m) and are probably derived by shock lithification of the finest fractions of an incoherent lunar soil, the clastic origin of the recrystallized or vitrified material being inferred from the presence of small, angular porphyroclasts of plagioclase or—more rarely—olivine, up to 75 μ m in size.

Glass-bonded soil fragments, crowded with minute fragments of plagioclase and subordinate ferromagnesian minerals, occur as the

least modified material. They grade into agglutinates with increase in the amount of glass and the development of an exterior glassy skin. These fragments are often incoherent and composite. One such fragment (table 3, section 9) broke up to reveal an inclusion of pale, recrystallized, feldspathic metaclastic rock with allotriomorphic granular texture and another with fine poikilitic texture and noritic composition.

The majority of the fine-grained, holocrystalline fragments have one of two principal

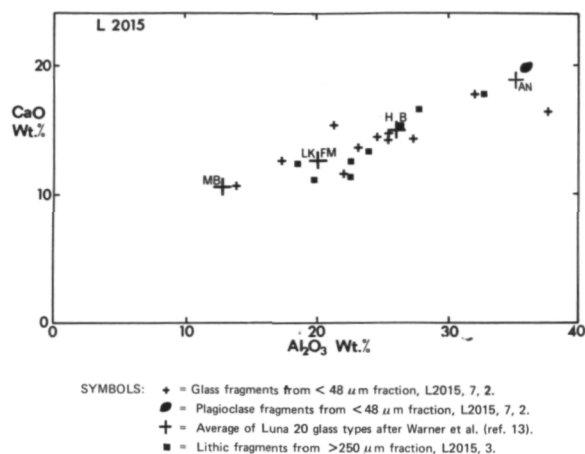


Figure 2.—Plot of weight percent CaO versus weight percent Al₂O₃ for glass and lithic fragments from Luna 2015.

textures, either hypidioblastic granular or poikiloblastic. In the former, when hypersthene is about equal to plagioclase in amount, the hypersthene occurs as rods set in allotriomorphic plates of plagioclase. In more feldspathic fragments the plagioclase forms plate-like crystals and the pyroxene, allotriomorphic interstitial crystals.

Poikiloblastic textures characterize some of the more recrystallized fragments in which plagioclase does not greatly exceed hypersthene in amount. Hypersthene occurs in oikocrysts up to 30 μm in size, including 5 μm crystals of plagioclase. It is possible that these are direct crystallization products of an impact melt rather than the products of annealing of impact-produced glass.

Fragments with a granulitic texture are rare; one such fragment was studied (analysis 8, table 6). It is anorthositic in composition and made up of partially maskelynitized polygonal crystals of plagioclase with sporadic interstitial crystals of olivine (Fo81).

Another fragment (L2015,3,B,11) may be igneous or metamorphic: it has equigranular texture with ~ 80 percent plagioclase, ~ 10 percent pyroxene, and ~ 5 percent olivine. The analyses of the pyroxenes and olivines are quoted in table 4, analyses 6–10.

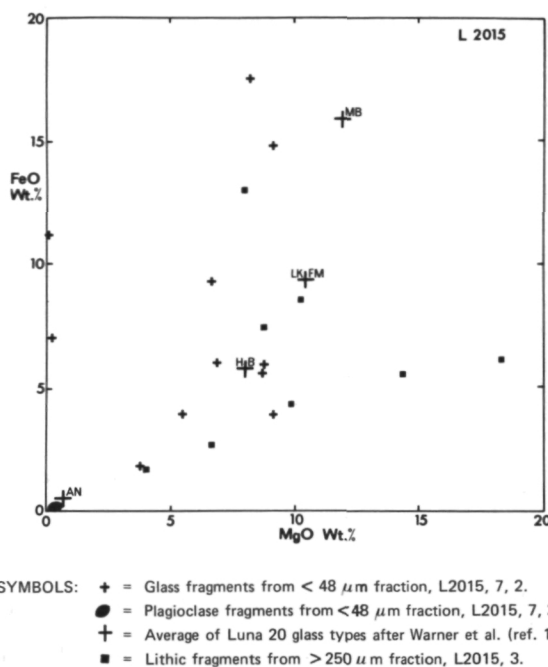


Figure 3.—Plot of weight percent FeO versus weight percent MgO for glass and lithic fragments from Luna 2015.

The fragment shows a unique texture in which sub-rounded crystals of olivine include blebs of 2 μm of metallic iron just within their margins. Their small size precludes quantitative analysis, but they are probably nearly pure iron blebs with less than 0.2 percent nickel. The restriction of the metal drops within the margin of the olivine suggests that they are not just inclusions but are the products of some reducing reaction similar to that observed in the basalt 14053 described by El Goresy et al. (ref. 14). Here the olivine is not nearly pure fayalite but Fo45, Fa55, so that reaction products other than Fe and SiO₂ should be observed. Further work is being undertaken on this fragment.

The chemical composition of the lithic fragments was obtained by defocused beam analysis with the electron probe, and the results are set out in table 6 along with their CIPW NORMS. Reference to figures 2 and 3 and to table 5 shows the general chemical similarity of the lithic clasts to the glass fragments in the < 48 μm fraction. Only one

Table 6.—*Microprobe Analyses of Fine-Grained Lithic Fragments From L2015*

	(1)	(2)	(3)	(4)	(5)	(6)	(7)	(8)
SiO ₂	45.9	46.6	44.5	46.0	43.6	45.3	44.9	44.1
TiO ₂	0.6	0.2	0.2	0.8	0.1	0.1	0.1	n.d.
Al ₂ O ₃	23.8	22.2	22.3	18.4	19.8	28.2	26.1	32.3
Cr ₂ O ₃	0.2	0.2	0.2	0.5	0.4	0.2	0.2	0.1
FeO	7.4	8.5	5.5	13.2	6.1	2.7	4.3	1.7
MnO	0.1	0.1	0.1	0.2	0.1	n.d. ⁽⁹⁾	0.1	n.d.
MgO	8.7	10.5	14.5	8.2	18.6	6.6	9.7	3.9
CaO	13.2	11.3	12.8	12.7	11.3	16.8	14.7	17.9
Na ₂ O	n.d.	0.4	n.d.	n.d.	n.d.	n.d.	n.d.	n.d.
K ₂ O	0.1	n.d.	n.d.	n.d.	n.d.	n.d.	n.d.	n.d.
Total	100.0	100.0	100.0	100.0	100.0	100.0	100.0	100.0
CIPW NORM								
QZ	—	—	—	—	—	—	—	—
COR	—	0.2	—	—	—	—	—	—
OR	0.1	—	—	—	—	—	—	—
AB	—	3.4	—	—	—	—	—	—
AN	64.9	55.6	60.8	49.9	54.8	77.0	71.2	88.2
DI	0.1	—	1.6	10.6	0.6	4.6	1.3	0.3
HY	30.8	30.1	15.8	34.5	11.8	14.8	16.2	7.6
OL	2.5	7.8	20.7	2.2	32.0	2.9	10.7	3.6
CM	0.3	0.3	0.3	0.7	0.5	0.2	0.3	0.2
IL	1.2	0.4	0.4	1.5	0.3	0.3	0.2	—
FS/HY.	30	30	27	46	15	17	19	20
Mo 1 percent								

- NOTES: (1) L2015,3,10,B1: Fine-grained noritic metaclastic with minipoikilitic texture; Na₂O < 0.3 percent.
 (2) L2015,3,11,D: Mean of 1–15 areas. Fine-grained noritic metaclastic with minipoikilitic texture.
 (3) L2015,3,10,B: Shock-melted soil with 25 μ m plagioclase porphyroclasts; Na₂O < 0.30, K₂O < .04 percent.
 (4) L2015,3,10,A: Shock-melted soil or agglutinate, cryptocrystalline; Na₂O < 0.30 percent, K₂O < .04 percent.
 (5) L2015,3,5,2: Pale vitreous impact melt with residual olivine; Na₂O < 0.3 percent, K₂O < 0.03 percent.
 (6) L2015,3,6,1: Fine-grained pale metaclastic; Na₂O < 0.3 percent, K₂O < 0.03 percent.
 (7) L2015,3,7,1: Fine-grained impact melt; Na₂O < 0.3 percent, K₂O < 0.03 percent.
 (8) L2015,3,5,1: Partially maskelynitized anorthositic granulite; Na₂O < 0.3 percent, K₂O < 0.03 percent.
 (9) n.d. = In each use, indicates below limit of detection, all analyses normalized to 100 percent.

of the lithic fragments, a shock-melted soil or agglutinate (analysis 4, table 5) can be considered as possibly containing a mare-derived component. Its higher FeO (13 percent) and significant normative diopside (10.6 percent) distinguish it from all the other fragments which are of unambiguous

highland origin. The latter fragments have the range of compositions found in clastic rocks and glasses of highland regions. Their normative mineralogy is variable, with anorthite from 55 to 90 percent, hypersthene from 7 to 30 percent, olivine from 3 to 30 percent, and diopside from 0 to 5 percent,

and less than 1 percent opaque minerals. The ferromagnesian minerals have a $\text{Fe}/\text{Fe}+\text{Mg}$ ratio < 0.3 .

Insofar as it is possible to determine the modal mineralogy of these fine-grained fragments, there is general agreement with the results obtained from the norm. It is apparent that these fragments were once the finer grained portions of highland soils and that they must have primary igneous parents, even if they are several generations removed. Igneous rocks of the ANT suite of anorthosites, norites, troctolites, and their intermediate variants are ultimately parental to the fine-grained fragments composing the $> 250\mu\text{m}$ fraction of L2015.

SELENOCHRONOLOGY

The analysis of a single 8.7-mg fragment of glassy and friable feldspar (L2015,3,1) has been reported previously (ref. 4). The sample was an extremely unfavorable one for dating, containing only 50 ppm K. An imprecise age of (4.0 ± 0.3) Gy was determined, the uncertainties arising from the small amount of sample gas and the large Ca and trapped ^{40}Ar corrections. This age is comparable to ages from other highland sites and to the ages of two K-rich metaclastic rocks from the Luna 20 site (ref. 15) but is too inaccurate to draw any significant conclusions. The nominal $(^{38}\text{Ar}/^{37}\text{Ar})$ exposure age of L2015,3,1 was accurately determined as 340 m.y. and is typical of the exposure age of fragments from a mature regolith.

More recently, a $^{40}\text{Ar}/^{39}\text{Ar}$ analysis of five fragments of microcrystalline plagioclase L2015,3,6 (total weight 7.7 mg) has been carried out. The potassium content of L2015,3,6 was 180 ppm, a factor of 3 higher than L2015,3,1, and this, coupled with improvements in the analytical technique, permitted the argon composition to be determined with greater precision.

Although the interpretations of the L2015,3,6 results are not limited by analytical precision, there remains the problem of trapped ^{40}Ar . This is apparent in figure 4 where the

results are plotted on a three-isotope correlation diagram of $(^{36}\text{Ar}_t/^{40}\text{Ar})$ against $(^{39}\text{Ar}/^{40}\text{Ar})$. A correction for cosmogenic ^{36}Ar has been applied on the basis of the $(^{36}\text{Ar}/^{38}\text{Ar})$ ratio, assuming a binary mixture of cosmogenic argon, $(^{36}\text{Ar}/^{38}\text{Ar})_c = 0.63$, and trapped argon, $(^{36}\text{Ar}/^{38}\text{Ar})_t = 5.35$. It was assumed that cosmogenic ^{40}Ar would be negligible in samples of anorthositic composition due to the low Fe and Ti content. The effect of the correction is shown by the solid circles, which are the uncorrected ratios. On this diagram pure, trapped argon would plot on the axis $(^{39}\text{Ar}^*/^{40}\text{Ar}) = 0$; pure, potassium-derived argon would plot on the axis $(^{36}\text{Ar}/^{40}\text{Ar}) = 0$. The experimental points represent a mixture of these components. The fact that the points

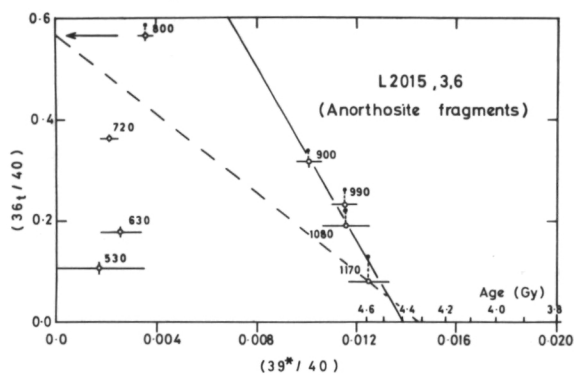


Figure 4.—Three-isotope correlation plot $(^{36}\text{Ar}_t/^{40}\text{Ar})$ against $(^{39}\text{Ar}^*/^{40}\text{Ar})$, for lunar sample L2015,3,6. The extraction temperatures are indicated in $^{\circ}\text{C}$. The solid black circles indicate the $(^{36}\text{Ar}/^{40}\text{Ar})$ ratio before applying the correction for cosmogenic ^{36}Ar . Because the samples are anorthositic, cosmogenic ^{40}Ar is assumed to be negligible. The low-temperature points indicate unambiguously that the $(^{36}\text{Ar}/^{40}\text{Ar})_t$ ratio of trapped gas increases with increasing extraction temperature to 800°C . The four high-temperature extractions represent 80 percent of the radiogenic argon release and, on the assumption that they are a binary mixture of trapped and radiogenic argon of fixed composition, indicate a K-Ar age of (4.4 ± 0.1) Gy (solid mixing line). The somewhat weaker assumption that the trapped $(^{40}\text{Ar}/^{36}\text{Ar})_t$ ratio for the high-temperature points is greater than or equal to that 800°C extraction implies that the apparent age for the final extraction is not less than (4.3 ± 0.1) Gy (dashed line shows limiting case).

are not colinear implies that there is no unique composition for either or both of the end members. Nevertheless, a number of important statements about the chronology of L2015,3,6 may be made, and two interpretations of figure 4 are possible.

The four high-temperature points represent 80 percent of the argon release from the sample and, within the analytical errors, are colinear. If this is a simple binary mixing line it corresponds to a trapped argon composition with $(^{40}\text{Ar}/^{36}\text{Ar})_t = 0.8 \pm 0.2$ and the intercept with the $(^{39}\text{Ar}^*/^{40}\text{Ar})$ axis corresponds to a K-Ar age of (4.4 ± 0.1) Gy. If the interpretation is correct, this would represent one of the oldest K-Ar ages determined on a lunar sample, and significantly older than other dated Luna 20 samples (ref. 15). Whether the high-temperature argon is a binary mixture or not, the composition of the low-temperature argon can *only* be understood in terms of excessive amounts of trapped ^{40}Ar in the initial argon release. The $(^{40}\text{Ar}/^{36}\text{Ar})_t$ ratio of this trapped component decreases *monotonically* from a value of around 10 in the 530°C fraction to < 1.8 in the 800°C fraction.

An alternative interpretation of figure 4 would regard the colinearity of the high-temperature points as fortuitous. In this case, it is necessary to make other assumptions about the trapped argon composition of the high-temperature points. A reasonable assumption would seem to be that the $(^{40}\text{Ar}/^{36}\text{Ar})_t$ ratio decreases monotonically with temperature throughout the experiment, and that for the high-temperature points it is *less than or equal to* that of the 800°C release. This implies $(^{40}\text{Ar}/^{36}\text{Ar})_t \leq 1.8$ or $(^{36}\text{Ar}/^{40}\text{Ar})_t \geq 0.56$ for all temperatures above and including 800°C . The assumption provides a lower limit to the apparent age associated with each heating step. (This value is close to the 2.15 ± 0.22 ratio obtained by Podosek et al. (ref. 15) for a Luna 20 soil fragment.) The reader can see for himself, using figure 4 and a ruler, laid to pass through $(^{36}\text{Ar}/^{40}\text{Ar})_t = 0.56$ and each experimental point in turn, that this assumption corresponds to a monotonically

increasing apparent age for the high-temperature points. It is also clear that while the 900°C – 1080°C points can yield apparent ages less than or equal to 4.1 Gy, the apparent age of the 1170°C point must be greater than (4.3 ± 0.1) Gy. The apparent age of the 1170°C point can only be as low as 4.0 Gy if the $(^{40}\text{Ar}/^{36}\text{Ar})_t$ ratio *rises*, by a factor of 2, to (3.7 ± 0.5) in the final extraction. It is therefore difficult to avoid the conclusion that the argon released in the 1170°C fraction is coming from a very old sample.

In spite of uncertainties in the composition of the trapped argon, L2015,3,6 appears to contain a component which has retained argon from the period prior to 4.3 Gy and possibly since 4.4 Gy. The conclusions, it should be stressed, are based on measurements on a sample which is a mixture of anorthosite fragments with presumably different histories. Nevertheless, the presence of an old component in the Luna 20 soil is suggested. The application of the $^{40}\text{Ar}/^{39}\text{Ar}$ technique to sufficiently large, single fragments of anorthosite may identify this component.

The cosmogenic $(^{38}\text{Ar}/^{37}\text{Ar})$ ratio in L2015,3,6 shows variations which reflect different exposure histories for the fragments. The variations correspond to exposure ages in the range from 400 to 700 m.y., which are typical of fragments from a mature regolith.

MAGNETIC MEASUREMENTS

The natural remanent magnetism (NRM) of two rock fragments has been investigated. L2015,3,1 (11.3 mg) was a whitish, angular chip of glassy feldspar with some black, crystalline inclusions. The NRM of the fragment was $< 3.5 \times 10^{-7}$ G. cm^3 . g^{-1} and there was no detectable growth of viscous remanent magnetism in a weak field. The black inclusions are magnetic to the extent that they show susceptibility effects, with susceptibility in the range from 10^{-2} to 10^{-3} G. cm^3 . g^{-1} . Oe^{-1} . However, this value, together with the fact that no detectable iso-

thermal remanence was acquired in a high field (3500 Oe), suggests that there is a negligible amount of iron in L2015,3,1 and that the black material does not contribute to the NRM.

L2015,3,11 (6.6 mg) was a breccia fragment with sparsely distributed black, opaque material visible in the surface. The magnetic remanence of this fragment is less than the minimum remanence detectable with the magnetometer used (about 40×10^{-6} G. cm³. g⁻¹) (ref. 5). The shape of the isothermal remanence versus field curve was very similar to that obtained from similar Apollo samples, as was the saturation intensity, 0.97×10^{-3} G. cm³. g⁻¹. Thus, magnetically, L2015,3,11 appears to be very much like breccias returned by the Apollo missions.

Several samples of fines were investigated (table 7), including density separates L1627, 10,1; L1627,11,1; L2015,10,1; and L2015, 11,1. Measurement of the room-temperature, low-field susceptibility yielded results which were similar to values found for Apollo fines (ref. 16). However, the susceptibilities of the Luna 16 samples were about a factor of 4

stronger than those of the Luna 20 samples. The density separation is remarkably effective in separating out a strong magnetic component which is present in the lighter fraction; for both Luna 16 and 20 samples, the light fraction was about 2.6 times as strong in susceptibility as the heavy fraction. A Curie point determination on L2015,10,1, sealed in an evacuated quartz tube and using a field of 8 kOe, indicated the presence of metallic iron ($T_c \sim 770^\circ$ C), as in the case of Apollo fines samples. Also similar to the Apollo fines samples, the induced moment decreased to 54 percent of its initial value after heating, presumably due to partial oxidation (ref. 17).

The acquisition of isothermal remanent magnetization (IRM) was measured for density separates. At 4000 oersteds, the samples were within 7 percent of saturation (IRM_s), the extrapolated saturation values being shown in table 7. The Luna 16 samples were stronger in IRM than the Luna 20 samples by a factor of about 4.5; the light fractions were about 2.1 times as strong in IRM as the heavy fractions. Five further fines

Table 7.—Room Temperature Values of Initial Susceptibility (X_i), Extrapolated Saturation IRM (IRM_s) and Induced Magnetization in 10 kOe (J_i)

Sample	Description	X_i (10^{-8} G·cm ³ ·g ⁻¹ ·Oe ⁻¹)	IRM _s (10^{-8} G·cm ³ ·g ⁻¹)	J_i (10 kOe) (G·cm ³ ·g ⁻¹)
L1627,10,1	{ Light ⁽¹⁾ Fraction	3.9	156	1.98
L2015,10,1		1.0	36	0.42
	48 < d < 250 μm)			
L1627,11,1	{ Heavy ⁽²⁾ Fraction	1.4	77	1.44
L2015,11,1		0.4	17	1.24
L1627,3	Handpicked Fraction, d ⁽³⁾ > 250 μm)	1.7	88	1.12
L1627,7	{ d < 48 μm	2.7	97	1.02
L2015,7		0.9	31	0.57
L1627,9	{ Finest Fines (d < 10 μm)	4.0	149	1.89
L2015,9		0.9	31	1.26

NOTES: (1) Light Fractions: L1627, < 2.96 g/cm³; L2015, < 2.78 g/cm³

(2) Heavy Fractions: L1627, > 2.96 g/cm³; L2015, > 2.78 g/cm³

(3) Diameter

samples (see table 7) were also measured. These had IRM curves identical in shape to the density-separated samples and to the Apollo 11 fines (ref. 16), suggesting that the various fractions contained essentially the same iron particle sizes. For seven of the nine samples, the induced magnetization failed to reach saturation in fields of 12 kOe. This behavior indicates the presence of paramagnetism or very small superparamagnetic particles. Samples L2015,7 and L2015,10,1, however, were saturated in fields of about 4 kOe, indicating the absence of this component. Larger superparamagnetic particles are, however, undoubtedly present in L2015,10,1 and the other density-separated samples (other samples were not measured) since their saturated IRM decayed logarithmically at approximately 4.5 percent per decade. Logarithmic decay is caused by relaxation of that part of the magnetic spectrum of the single domain grain distribution on the superparamagnetic stable boundary (i.e., diameter about 130 Å). Apollo 11 fines (susceptibility $X_c = 2.4 \times 10^{-3} \text{ G. cm}^3 \cdot \text{g}^{-1} \cdot \text{Oe}^{-1}$) contained 0.9 percent (± 0.3 percent) of single domain iron grains (ref. 17). Assuming that the single domain iron content, most of which is in the superparamagnetic state with grain size less than about 130 Å is proportional to the susceptibility, then the iron content of various Luna fractions may be estimated (using the Apollo 11 figures) from the susceptibility results in table 7.

MÖSSBAUER SPECTROSCOPY

The iron-bearing minerals in two unseparated 40-mg samples from the original bulk fines (L1627,2 and L2015,2) have been characterized by ^{57}Fe Mössbauer spectroscopy. A 2-mg separate of the very small particles from Luna 16 (finest fines, L1627,9) has also been studied.

The spectra (fig. 5) are very similar to those described by Malysheva (ref. 18) for Luna 16 sample 3-1; however, experience with Apollo 14 and Apollo 15 samples suggests somewhat different assignment of the

central components of the spectra. It has become common practice to attribute the three apparent quadrupole doublets, in order of decreasing quadrupole splitting, to M1 pyroxene/olivine, M2 pyroxene/glass, and ilmenite.

From a close study of the data from both lunar and terrestrial pyroxenes and olivines it has been found that the M1 pyroxene/olivine content is best estimated from the area of the outer pair of peaks at 77 K, and the ilmenite content from the area of the inner pair of peaks at 295 K; the residual area is then attributed to M2 pyroxene/glass.

The greater intensity of the M2 pyroxene/glass component at lower velocity found in previous lunar samples has also been observed in the present study. The asymmetry has

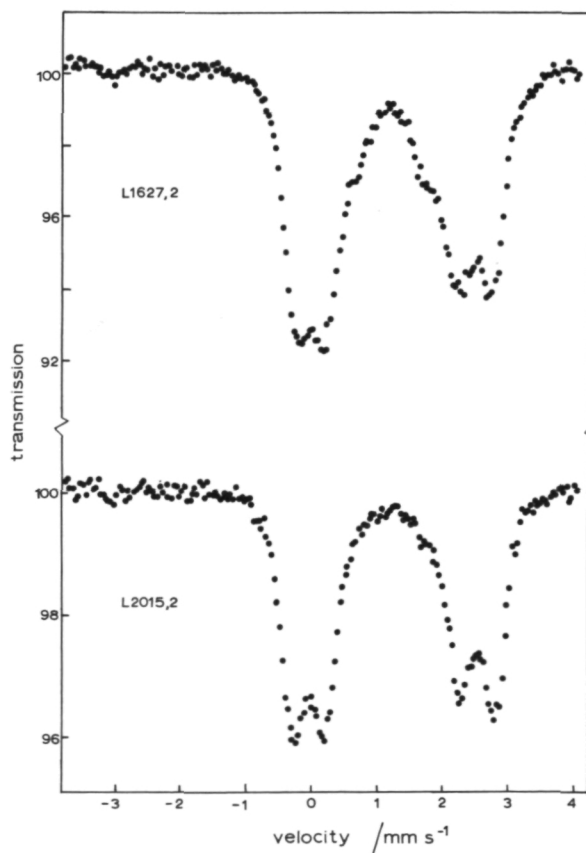


Figure 5.—Mössbauer spectra of Luna 16 and 20 soils recorded at 77 K.

Table 8.—*Distribution of Iron Among Various Phases Expressed as a Percentage of Total Iron*

Sample	M1/Olivine	M2/Glass	Ilmenite	Magnetic Iron	Other Iron
Luna 1627,2	32	53	6.9	~ 5	3.9
Luna 2015,2	41	52	< 0.2	< 2	4.2
Apollo 14 (average of 4)	17	64	8	~ 4	6
Apollo 15 (mare and front)	26	63	2.4	4.1	4
Apollo 15 (rille edge)	36	57	1.3	< 2	3

already been shown to be greatest in samples with a significant enrichment in magnetic iron (ref. 7); thus, the greater part of it must originate from superparamagnetic inclusions of iron or iron-nickel alloy. To test this idea further, the separated sample L1627, 9 has been studied. The spectrum shows lines which are both less well resolved and more asymmetric than those in the spectra of the bulk samples. It is therefore consistent with the presence of a greater proportion of glassy particles and superparamagnetic iron in the separate.

Because of the uncertainty introduced by this component, the analysis shown in table 8, which compares the present results with earlier data on other lunar samples, is based on the area of the high-velocity peaks only. The results for magnetic iron are approximate because of the difficulty of estimating areas of weak lines broadened asymmetrically by the nickel content.

Both Luna samples exhibit relatively high M1 pyroxene/olivine contents in comparison with the Apollo 14 soils, and detailed analysis suggests that this indicates more augite and less pigeonite and orthopyroxene (rather than an excess of olivine). The samples resemble the Apollo 15 rille-edge materials except for the high ilmenite content of Luna 16. The ilmenite content of L2015,2 is so small as to be almost undetectable in the inner wings of the pyroxene absorption, and this is

compatible with the TiO_2 analysis (0.56 percent in Luna 20 as against 3.39 percent in Luna 16 (ref. 13), some of which will be present in non-iron-containing phases). The Luna 16 sample shows a much greater magnetic iron/iron nickel component than the Luna 20 sample, but neither sample gives a significant resonance from species containing troilite or iron (III). The Mössbauer lines for the Luna 20 sample are significantly narrower than those for Luna 16, suggesting a lower glass content or smaller compositional variation in the Luna 20 sample. During the course of this work, other Mössbauer studies on Luna 16 (ref. 19) and Luna 20 samples (refs. 20 and 21) have been reported, and in general the results are in good agreement with the present data. However, the assignment (refs. 20 and 21) of weak peaks in the Luna 20 spectra to ulvospinel (Fe_2TiO_4) is questionable. The resonance lines from iron-titanium spinels are likely to be indistinguishable from those of iron atoms in the M2 pyroxene sites at room temperature (ref. 22). Since ulvospinel is magnetic at low temperature, significant changes should be present in the 77 K spectrum; such changes have not been observed.

THERMOLUMINESCENCE

Two Luna samples < 48 μm in diameter (L1627,7 and L2015,7) have been examined

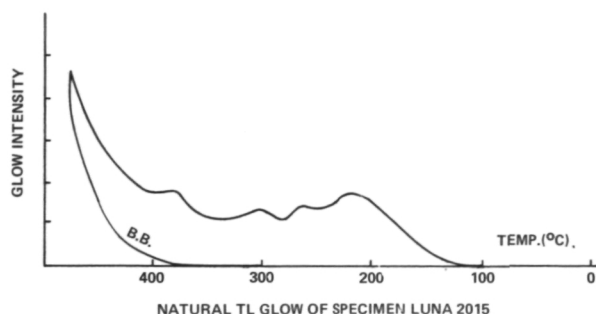


Figure 6.—Natural TL glow of Luna 2015 specimen.

for natural and induced thermoluminescence. The Luna 2015 specimen (yellowish gray in color) was collected at a depth of about 27 cm below ground-level and its natural thermoluminescence (fig. 6) was well preserved by the shielding of the top soil which attenuated the diurnal heat wave on the surface of the Moon.

The thermoluminescence induced in the L2015 sample has a glow spectrum similar to that of the Apollo samples studied. Its response to beta particles (~ 0.5 Ci, Sr-90) is linear up to about 1.2 megarads, where saturation begins. The response to gamma radiation (~ 200 Ci, Co-60) is similar to that induced by beta particles. The natural sample was exposed to five different gamma-ray doses ranging from 410 to 4500 kilorads by positioning aliquots at various distances from the γ source; the induced glows were measured for temperature regions of 0° – 280° C, 280° – 360° C, and 360° – 480° C together with

the total area. The 360° – 480° C glow was used to estimate the effective storage temperature on the Moon, which was found to be 282 K at 27-cm depth. With the use of this result, the effective thermal wavelength for the depth concerned (27 cm) is estimated to be approximately 230 cm, about nine times the value previously assumed (refs. 8 and 23) for the surface samples.

The trapping parameter, energy depth, E , was determined by use of the initial rise technique; and approximate values for the corresponding frequency factor, S , were calculated (table 9). The high value for the frequency factor of the 150° C peak implies that this component is highly unstable at room temperature. The result is consistent with the finding of a fast decay component of all Apollo specimens.

Luna 1627 (darkish in color) showed very little preserved natural thermoluminescence; no glow was observed in the 0° C to 480° C region. The response to beta particles (0.5 Ci, Sr-90) of this specimen is about seven times smaller than that of Luna 2015. The emission spectrum of L1627 (fig. 7) also shows a number of different features compared with the other sample, implying that L1627 and L2015 have different compositions. The differences observed, together with the fact that very little thermoluminescence is exhibited by sample L1627, are consistent with the substantial quantities of glass and glassy material present. Similar results have been obtained for the well-known "orange soil"

Table 9.—Thermoluminescence Trapping Parameters, Energy Depth, E , and Frequency Factor, S , for Various Peaks in the Natural Thermoluminescence Spectrum of L2015

Peak Maximum ($^{\circ}$ C)	Energy Depth, E (ev)	Approximate Frequency Factor, S (sec^{-1})
90	0.91 ± 0.1	10^{12}
150	1.26 ± 0.1	4×10^{15}
210	1.16 ± 0.1	3×10^{11}
305	1.03 ± 0.1	10^8
370	1.17 ± 0.1	2×10^8

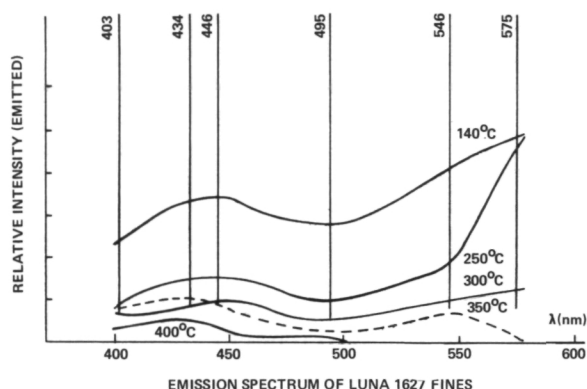


Figure 7.—Emission spectrum of Luna 1627 fines.

from the Apollo 17 mission, which also has a high glass content.

OXYGEN ISOTOPE ABUNDANCES IN FINE-SIZE FRACTIONS

Using "fluorine stripping" experiments, American and French workers have found large enrichments in ^{18}O (and ^{30}Si) on the surfaces of grains in certain samples of lunar soil. However, for Apollo 17 (ref. 24), Luna 16 (ref. 25), and Apollo 15 (ref. 26) there

is not a simple monotonic decrease in ^{18}O content with the fraction of oxygen extracted.

Because the technique of "fluorine stripping" must, to some extent, mask the relationship between the content of ^{18}O and grain size, we have measured the abundance of ^{18}O in the total oxygen extracted from fine-size fractions of Luna 16 and Luna 20 soil. Approximately 10 mg of the $< 48\mu\text{m}$ fraction from the separation scheme were sieved in carbon tetrachloride into fractions of three sizes: $> 40\mu\text{m}$, $25\text{--}40\mu\text{m}$, and $< 25\mu\text{m}$. Samples of fractions of these sizes, weighing between 0.5 mg and 2.0 mg, have been analyzed with conventional BrF_5 extraction techniques and a high-precision mass spectrometer (ref. 9). The results are given in table 10a and b in standard δ notation per mil relative to SMOW (defined from Caltech Rose Quartz at $+8.45\text{‰}$).

The results in table 10a are considered to be analytically accurate to within ± 0.1 to 0.2‰ , and results obtained for the NBS 28 Quartz Standard (ref. 27) during the course of this work are listed in table 10b. However, it should be noted that prior to analysis the samples had not been subject to special handling precautions (they were in contact with

Table 10a.— $^{18}\text{O}/^{16}\text{O}$ Determinations: Luna 16 and Luna 20
Sieved Fractions

Sample	$< 25\mu$	$25\text{--}40\mu$	$40\text{--}48\mu$	Size of Fraction
Luna 16	$+7.05\text{‰}$	$+8.76\text{‰}$	$+5.45\text{‰}$	} $\delta^{18}\text{O}$ relative to SMOW
Luna 20	$+7.44\text{‰}$	$+5.34\text{‰}$	$+7.47\text{‰}$	

Table 10b.— $^{18}\text{O}/^{16}\text{O}$ Determinations: Standards

Sample	$\delta^{18}\text{O}$ (SMOW) (per mil)
NBS 28 Quartz Standard	9.98, 10.00, 9.87, 10.15, 10.21, 9.98, 9.93 Mean 10.02 ± 0.11 (1 σ std. dev.)

the laboratory atmosphere, etc.) and Taylor and Epstein (ref. 28) have also suggested that polythene contamination may have affected their analysis of one aliquot of Luna 20 soil.

Epstein and Taylor (ref. 29) suggested that the observed surface enrichments are due to preferential loss of ^{28}Si and ^{16}O during fractional volatilization (or grain of ^{30}Si and ^{18}O during fractional condensation) resulting from bombardment of the lunar surface by meteorites and/or nuclear particles. Values for $\delta^{18}\text{O}$ between about +5.3% and +6.3% can be regarded as normal for bulk samples of lunar soil. The results presented in table 10a show that grain sizes other than the finest are also enriched in ^{18}O . Such variations in ^{18}O enrichment with grain size are readily understood if the soil at each locality is a mixture of young and mature grains. Mature grains (showing ^{18}O enrichment) in particular grain size fractions may be acquired from impact events at differing distances from the sample localities.

CHARGED PARTICLE TRACKS

Charged particle track analysis has been carried out to study the exposure and mechanical histories of a brown glass speck (~ 0.5 mm across) from the Luna 16 soil (L1627,3,1C).

Because of the roughness of the surface, no craters or features attributable to compositional differences could be recognized from a preliminary examination of the grain. However, the optical microscope showed a high density of bubbles ($\sim 10^5$ bubbles/cm 2) distributed throughout the body of the speck. A more thorough examination of the bubble distribution showed a maximum density in the center of the body and a minimum near the surfaces. Thus, the gas bubbles were probably migrating outward at the time of solidification of the glass.

Annealing experiments were carried out on a part of the speck in order (a) to study the annealing characteristics of the latent damage tracks, and (b) if possible, to utilize

the results from (a) to separate the genuine track density from the background pits. The sample was annealed for 10-minute periods at various temperatures from 200° C to 700° C and then etched in 4.8 percent solution of HF for 5 seconds at $21 \pm 0.5^\circ$ C, prior to track density measurement by scanning electron microscope (SEM). It was found that (a) almost all the genuine tracks were annealed out at $\sim 550^\circ$ C, (above this temperature highly stable pits due to background were left (ref. 30)) and (b) the genuine track density to background pit ratio was 14.

Experiments were also carried out to study the track registration and development properties of the glass, and it was found that the track registration properties of the glass

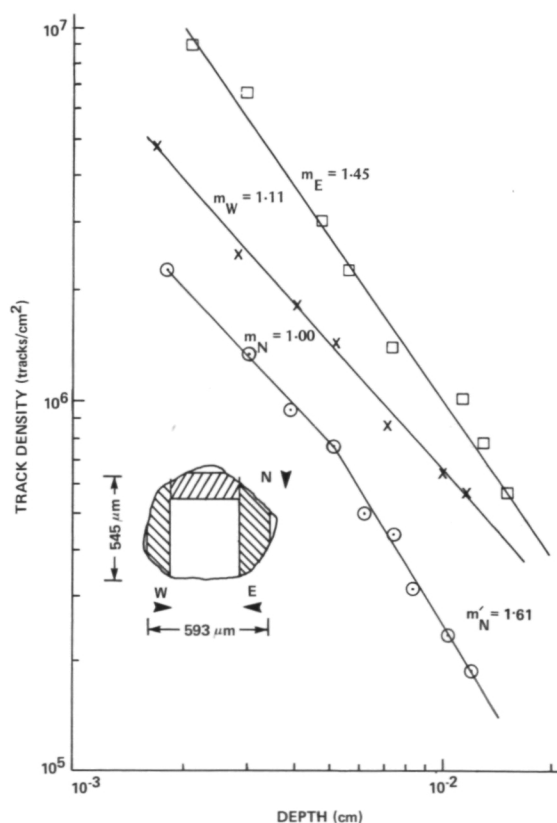


Figure 8.—Variation of track density (tracks/cm 2) with depth on three different faces (E, W, N, as shown in the inset) of a brown glass speck from Luna 16 sample, 1627,3,1C. The tracks were produced mainly by solar flares.

were very similar to tektite and obsidian glasses (ref. 31).

The major portion of the glass speck was mounted in resin on a quartz backing and then polished and etched as previously described. The tracks were observed and counted by using the SEM. The track densities were determined at various depths; the whole process was repeated on three different faces of the glass (fig. 8). The results (fig. 8) show that all three faces examined have track density gradients, and a relation of the type $\rho_D = \rho_0 D^{-m}$ seems to exist (where ρ_0 and ρ_D are the track densities on the surface and at depth " D ," respectively, and " m " is the coefficient showing the nature of the charged particle spectrum). The value of the coefficient " m " is modified by various factors such as the presence or absence of some soil layer on the grain observed, its burial depth, and the extent of erosion due to charged particle and micrometeoritic bombardments. Faces "E" and "W" yield values

for coefficient " m " of 1.45 and 1.11, respectively, while there are two " m " values (1.00 and 1.61) for the face "N." This shows that faces "E" and "W" had simple burial histories, while the burial history of face "N" is somewhat complicated. Thus, the above results suggest that the glass speck remained for most of its life on or near to the lunar surface and that it had at least three orientations. In general, the Luna 16 site seems to be highly irradiated and well churned.

CARBON CHEMISTRY

Dissolution of fractions in DCl (38 percent in D_2O) has been used to measure the trapped CH_4 and the hydrolysable carbon (as indicated by the evolution of CD_4) presents. In general, the results obtained from Luna 16 and 20 (tables 11 and 12) are comparable with those from similar fractions of Apollo 11 and 16, respectively (ref. 11).

Table 11.— CD_4 and CH_4 Released by DCl Dissolution of Selected Fractions of Luna 16 and 20 Fines ⁽¹⁾

Sample Description	Sample Daughter Number	Luna 16			Luna 20		
		CD_4 ($\mu g/g$ as C)	CH_4 ($\mu g/g$ as C)	CD_4/CH_4	CD_4 ($\mu g/g$ as C)	CH_4 ($\mu g/g$ as C)	CD_4/CH_4
Bulk Sample	1	19.3	3.0	6.4	10.9	4.8	2.3
> 250 μm (handpicked agglutinates)	3	12.1	0.86	14.1	n.m. ⁽²⁾	n.m.	n.m.
48–250 μm (washed)	8	19.3	2.7	7.1	4.4	1.7	2.6
< 48 μm	7	18.8	5.7	3.3	8.0	5.3	1.5
Finest Fines (< 10 μm)	9	19.2	6.2	3.1	15.9	8.9	1.8

NOTES: (1) Notation on errors—absolute amounts of CD_4 and CH_4 are measured to ± 10 percent; CD_4/CH_4 ratio ± 2 percent, based on peak height.

(2) In each use, n.m. indicates equivalent fraction from L20 not available in quantities sufficient for analysis.

Table 12.— CD_4 and CH_4 Released by DC1 Dissolution of Density and Magnetically Separated Fractions (48–250 μ m) of Luna 16 and 20 Fines ⁽¹⁾

Sample Parent Number	Sample Daughter Number	Density (g/cm ³)	d (cm) ⁽²⁾	CD_4 (μ g/g as C)	CH_4 (μ g/g as C)	CD_4/CH_4 ⁽³⁾
L1627,10,2	1	< 2.96	0.25–0.35	n.c. ⁽⁴⁾	n.c.	11.9
L1627,10,2	2	< 2.96	0.05–0.25	n.c.	n.c.	9.5
L1627,10,2	3	< 2.96	0.0–0.05	n.c.	n.c.	10.5
L1627,11,2	1	> 2.96	0.2–0.25	n.c.	n.c.	5.2
L2015,10,2	1	< 2.78	n.s. ⁽⁵⁾	7.2	1.6	4.5
L2015,11,2	1	> 2.78	n.s.	1.5	0.85	1.8

- NOTES: (1) Concentration of CD_4 and CH_4 in unseparated washed fines (48–250 μ m) L1627,10 are 19.3 and 2.7 μ g/g, respectively, with $CD_4/CH_4 = 7.1$. Concentration of CD_4 and CH_4 in unseparated washed fines (48–250 μ m) L2015,10 are 4.4 and 1.7 μ g/g, respectively, with $CD_4/CH_4 = 2.6$.
(2) Vertical distance between sample and tip of magnetized soft iron rod, d = 0 means sample touching soft iron.
(3) Errors for CD_4/CH_4 ratio measurement $\pm 2\%$.
(4) In each use, n.c. indicates not calculated, sample size analyzed insufficiently to allow estimation of absolute amounts of CD_4 and CH_4 to greater accuracy than $\pm 50\%$.
(5) In each use, n.s. indicates not separated.

The formation of the hydrolysable carbon giving rise to CD_4 in lunar fines is dependent on both surface exposure and the availability of Fe^{II} in the soil (for reduction to free Fe^0 in particle surfaces and agglutinates (refs. 32 and 33)).

Magnetic susceptibility, X_i , is a measure of free Fe^0 . The direct relationship between Fe^0 and the degree of exposure and Fe^{II} content established for lunar soils is also apparent from the data for X_i and CD_4 for various fractions (> 10 μ m) of Luna 16 and 20 soils (tables 7, 11, and 12). Thus, taking into consideration the lower total Fe^{II} content of Luna 20 (the total iron contents of Luna 16 and 20 are 16.3 percent and 7.0 percent (as FeO), respectively (refs. 1 and 2)) the amounts of CD_4 released from bulk materials (as shown in table 11) indicate that both soils are very mature and have experienced a similar degree of exposure on the lunar surface.

The ratio (CD_4/CH_4) of involatile car-

bon (hydrolysable carbon) to volatile carbon (CH_4) reflects both the Fe^{II} content and the degree of recycling of grains into complex particles. Thus, high CD_4/CH_4 ratios (tables 11 and 12) are observed for agglutinate-rich fractions (handpicked fraction of Luna 16 agglutinates, the low-density/highly magnetic fractions of Luna 16, and low-density fraction of Luna 20). The CD_4/CH_4 ratio of 6.4 measured for the bulk Luna 16 fines is consistent with the higher proportion of glasses and agglutinates present in this soil as compared with Luna 20 ($CD_4/CH_4 = 2.3$).

The analysis of size-separated fractions (table 11) shows that for both Luna soils, the CH_4 concentration increases as particle size decreases, as previously observed for the Apollo 11 fines (ref. 10) and the Apollo 14 soils (ref. 34). Also, for Luna 20, hydrolysable carbon is present in the largest quantities in fine-grained fractions. In contrast, for Luna 16 sieved fractions the carbide con-

centration is virtually independent of grain size, suggesting a considerable volume-related hydrolysable carbon component, again in accord with the much greater abundance of complex particles aggregated from fine, exposed grains (ref. 10). One explanation may be that the rate of particle aggregation at the Luna 16 site was rapid relative to the rate of hydrolysable carbon synthesis in fine grains, as has been suggested in reference 35 for total carbon accumulation in mature samples.

For both Luna 16 and Luna 20, the finer fractions ($< 48\mu\text{m}$) have lower CD_4/CH_4 ratios and higher absolute amounts of CH_4 relative to the fractions which contain larger grains (bulk samples $> 250\mu\text{m}$, 48–250 μm , table 11). These low ratios could suggest that the fine fractions contain few "complex particles," i.e., those which have undergone fractionation of the carbonaceous species during formation.

It has previously been suggested that ultra-fine grains are the primary site for CH_4 and hydrolysable carbon synthesis (refs. 11 and 12). If these particles are relatively simple, then the CD_4/CH_4 ratios must reflect the relative rates of formation of hydrolysable carbon and CH_4 within the constituent silicate matrix and should be low. Hence, the high CH_4 concentrations in low Fe^{II} soil (Luna 20) suggest that the synthesis of the hydrocarbon in fine grains, unlike carbide, does not involve the availability of Fe^{II} within the sample (ref. 36).

Alternatively, if complex particles are present in fractions $< 48\mu\text{m}$, from aggregation of smaller particles or disaggregation of larger complex particles, other interpretations have to be considered. *Either* (a) small complex particles have not suffered the changes in carbon chemistry observed in large complex particles (glassy agglutinates), *or* (b) whatever the nature of the particle, provided it is very small, solar wind exposure effects (formation of CH_4 , etc.) are dominant and generally obliterate the previous history. The last proposition is most appropriate for the ultra-fine grains being the primary site for CH_4 and hydrolysable carbon synthesis.

Conclusions

A concerted analysis of Luna 16 and Luna 20 soils has been carried out. In order to obtain the maximum information from the small samples available, only fractions appropriate to a particular technique have been analyzed by that technique. Some fractions have been subdivided into aliquots and thus data obtained may be considered completely interrelatable.

The conclusions are as follows:

1. Luna 16 is typical of mare material, whereas Luna 20 is typically highland in origin; little or no highland-type glass occurs in Luna 16 and only very rare fragments of mare composition material are present in Luna 20. Both soils are similar to their appropriate Apollo counterparts, Apollo 11 and 16, respectively.
2. Exposure measurements (carbon chemistry and $^{38}\text{Ar}/^{37}\text{Ar}$ measurements) and petrology confirm that both soils are highly mature and well gardened. The higher quantities of free iron (magnetic and Mössbauer measurements) and hydrolysable carbon (carbon chemistry) observed within the mare soil are in agreement with the postulated origin of these species by exposure-induced reduction of indigenous Fe^{II} in lunar silicates rather than from an input of meteorite debris.
3. Petrology, Mössbauer spectroscopy, thermoluminescence studies, and carbon chemistry data all suggest that a greater proportion of glass and glassy materials (such as agglutinates) is present in Luna 16 samples compared with Luna 20, presumably because of the lower temperature required to melt rocks and minerals of mare origin. The relatively higher proportions of CH_4 in fractions of highland material (Luna 20) which contains the least numbers of complex or recycled grains suggest that CH_4 , unlike hydrolysable carbon, is independent of the Fe^{II} content of the silicate.

4. A very high gas retention age (4.3–4.4 Gy) has been recorded for a sample of Luna 20 soil consisting of several handpicked fragments of cataclastic anorthosites, and has identified early crustal material which existed prior to the Imbrium event. A number of ages in the range of 4.0 to 4.3 Gy have been reported for A16 and A17 samples (refs. 37, 38, and 39). This is the only pre-Imbrium sample detected at the Luna 20 site so far. Clearly, more favorable samples should be selected from the bulk of the Luna 20 material, and further studies performed.

Acknowledgment

The authors wish to thank the Soviet Academy of Sciences for providing the samples of Luna 16 and 20 material for study. Appreciation also is expressed to the Royal Society for sponsorship and a grant to enable sample processing to be carried out. The sample analyses were made possible by grants from the Science Research Council and the Natural Environment Research Council. Further acknowledgments with thanks are given to the British Steel Corporation for providing a Fellowship to C.T. Pillinger; and to Mr. B. Scarlett of the University of Technology, Loughborough, for supplying the sieved fractions for oxygen isotope measurements.

References

1. VINOGRADOV, A. P., Preliminary Data on Lunar Ground Brought to Earth by Automatic Probe "Luna-16." *Proc. Second Lunar Science Conference, Geochimica et Cosmochimica Acta*, Supplement 2, Vol. 1, 1971, pp. 1–16.
2. VINOGRADOV, A. P., Preliminary Data on Lunar Soil Collected by the Luna 20 Unmanned Spacecraft. *Geochimica et Cosmochimica Acta*, Vol. 37, 1973, pp. 721–729.
3. ABELL, P. I., G. H. DRAFFAN, G. EGLINTON, J. M. HAYES, J. R. MAXWELL, AND C. T. PILLINGER, Organic Analysis of the Returned Lunar Sample. *Proc. Apollo 11 Lunar Science Conference, Geochimica et Cosmochimica Acta*, Supplement 1, Vol. 2, 1970, pp. 1757–1773.
4. TURNER, G., P. H. CADOGAN, AND C. J. YONGE, Argon Selenochronology. *Proc. Fourth Lunar Science Conference, Geochimica et Cosmochimica Acta*, Supplement 4, Vol. 2, 1973, pp. 1889–1914.
5. COLLINSON, D. W., AND A. DE SA, A New Magnetometer for Small Scale Magnetic Studies. *J. Phys. E.*, Vol. 4, 1971, pp. 337–341.
6. GIBB, T. C., R. GREATREX, N. N. GREENWOOD, AND M. H. BATTEY, Mössbauer Studies of Apollo 14 Lunar Samples. *Proc. Third Lunar Science Conference, Geochimica et Cosmochimica Acta*, Supplement 3, Vol. 3, 1972, pp. 2479–2493.
7. GIBB, T. C., R. GREATREX, AND N. N. GREENWOOD, Mössbauer Studies of Apollo 14 and Apollo 15 Lunar Soils. *J. C. S. Dalton*, in press, 1974.
8. DURRANI, S. A., W. PRACHYABRUED, C. CHRISTODOULIDES, J. H. FREMLIN, J. A. EDGINGTON, R. CHEN, AND I. M. BLAIR, Thermoluminescence of Apollo 12 Samples: Implications for Lunar Temperature and Radiation Histories. *Proc. Third Lunar Science Conference, Geochimica et Cosmochimica Acta*, Supplement 3, Vol. 3, 1972, pp. 2955–2970.
9. BECKINSALE, R. D., N. J. FREEMAN, M. C. JACKSON, R. E. POWELL, AND W. A. P. YOUNG, A 30 cm radius 90° Sector Doubled Collecting Mass Spectrometer With a Capacitor Integrating Detector for High Precision Isotopic Analysis of Carbon Dioxide. *Int. J. Mass Spectrom. and Ion Phys.*, Vol. 12, 1973, pp. 299–308.
10. CADOGAN, P. H., G. EGLINTON, J. N. M. FIRTH, J. R. MAXWELL, B. J. MAYS, AND C. T. PILLINGER, Survey of Lunar Carbon Compounds: II. The Carbon Chemistry of Apollo 11, 12, 14 and 15 Samples. *Proc. Third Lunar Science Conference, Geochimica et Cosmochimica Acta*, Supplement 3, Vol. 2, 1972, pp. 2069–2090.
11. CADOGAN, P. H., G. EGLINTON, J. R. MAXWELL, AND C. T. PILLINGER, Distribution of Methane and Carbide in Apollo 11 Fines. *Nature Phys. Sci.*, Vol. 241, 1973, pp. 81–82.
12. CADOGAN, P. H., G. EGLINTON, A. P. GOWAR, A. J. T. JULL, J. R. MAXWELL, AND C. T. PILLINGER, Location of Methane and Carbide in Apollo 11 and 16 Lunar Fines. *Proc. Fourth Lunar Science Conference, Geochimica et Cosmochimica Acta*, Supplement 4, Vol. 2, 1973, pp. 1493–1508.
13. WARNER, J., A. M. REID, W. I. RIDLEY, AND R. W. BROWN, Major Element Composition of Luna 20 Glass. *Earth Planet. Sci. Letters*, Vol. 17, 1972, pp. 6–12.
14. EL GORESY, A., L. A. TAYLOR, AND P. RAMDOHR, Fra Mauro Crystalline Rocks: Mineralogy, Geochemistry and Subsidiary Reduction of Opaque Minerals. *Proc. Third Lunar Science Conference, Geochimica et Cosmochimica Acta*, Supplement 3, Vol. 1, 1972, pp. 333–349.

15. PODOSEK, F. A., J. C. HUNEKE, A. J. GARCARZ, AND G. J. WASSERBURG, The Age and Petrography of Two Luna 20 Fragments and Inferences for Widespread Lunar Metamorphism. *Geochimica et Cosmochimica Acta*, Vol. 37, 1973, pp. 887-904.
16. STEPHENSON, A., Single Domain Grain Distributions: I. A Method for the Determination of Single Grain Distributions. II. The Distribution of Single Domain Iron Grains in Apollo 11 Lunar Dust. *Phys. Earth Planet. Interiors*, Vol. 4, 1971, pp. 353-369.
17. RUNCORN, S. K., D. W. COLLINSON, W. O'REILLY, M. H. BATTEY, A. STEPHENSON, J. M. JONES, A. J. MANSON, AND P. W. READMAN, Magnetic Properties of Apollo 11 Lunar Samples. *Proc. Apollo 11 Lunar Science Conference, Geochimica et Cosmochimica Acta*, Supplement 1, Vol. 3, 1970, pp. 2369-2387.
18. MALYSHEVA, T. V., Mössbauer Spectroscopy of Lunar Regolith Returned by the Automatic Station Luna 16. *Proc. Third Lunar Science Conference, Geochimica et Cosmochimica Acta*, Supplement 3, Vol. 1, 1972, pp. 105-114.
19. MALYSHEVA, T. V., AND V. V. KURASH, Mössbauer Spectroscopy of Lunar Samples. *Geochem. Internat.*, Vol. 87, 1973.
20. VINOGRADOV, A. P., Preliminary Data on Lunar Regolith Returned by Automatic Probe "Luna-20." *Geochem. Internat.*, 1972, p. 507.
21. MALYSHEVA, T. V., Mössbauer Spectroscopy of a Lunar Regolith Supplied by the Luna 20 Automatic Space Station. *Geokhimiya*, 1973, p. 1079.
22. BANNERJEE, S. K., W. O'REILLY, T. C. GIBB, AND N. N. GREENWOOD, The Behaviour of Ferrous Ions in Iron-Titanium Spinels. *J. Phys. and Chem. Solids*, Vol. 28, 1967, p. 1323.
23. DURRANI, S. A., W. PRACHYABRUED, F. S. W. HWANG, J. A. EDGINGTON, AND I. M. BLAIR, Thermoluminescence of Some Apollo 14 and 16 Fines and Rock Samples. *Proc. Fourth Lunar Science Conference, Geochimica et Cosmochimica Acta*, Supplement 4, Vol. 3, 1973, pp. 2465-2479.
24. EPSTEIN, S., AND H. P. TAYLOR, O^{18}/O^{16} , Si^{30}/Si^{28} , C^{13}/C^{12} , D/H and Hydrogen and Carbon Concentration Data on Apollo 17 Soils. *Eos*, 1973, pp. 585-586.
25. JAVOY, M., J. MARETTE, AND F. PINEAU, $^{18}O/^{16}O$ Ratios in Luna 16 Fines. *Geochimica et Cosmochimica Acta*, Vol. 37, 1973, pp. 2017-2019.
26. JAVOY, M. AND S. FOURCADE, $^{18}O/^{16}O$ Ratios in Lunar Fines and Rocks. *Earth Planet. Sci. Letters*, Vol. 21, 1974, pp. 377-382.
27. FRIEDMAN, I. AND J. D. GLEASON, A New Silicate Intercomparison Standard for ^{18}O Analysis. *Earth Planet. Sci. Letters*, Vol. 18, 1973, p. 124.
28. TAYLOR, H. P., AND S. EPSTEIN, Oxygen and Silicon Isotope Ratios of the Luna 20 Soil. *Geochimica et Cosmochimica Acta*, Vol. 37, 1973, pp. 1107-1109.
29. EPSTEIN, S. AND H. P. TAYLOR, O^{18}/O^{16} , Si^{30}/Si^{28} , C^{13}/C^{12} and D/H Studies of Apollo 14 and 15 Samples. *Proc. Third Lunar Science Conference, Geochimica et Cosmochimica Acta*, Supplement 3, 1972, pp. 1429-1454.
30. KHAN, H. A., On Thermal Annealing of Latent Damaged Trails. *Radiation Effects*, Vol. 18, 1973, pp. 51-54.
31. KHAN, H. A., AND S. A. DURRANI, Efficiency Calibration of Solid State Nuclear Track Detectors. *Nuclear Instruments and Methods*, Vol. 98, 1972, pp. 229-236.
32. PILLINGER, C. T., B. D. BATTS, G. EGLINTON, A. P. GOWAR, A. J. T. JULL, AND J. R. MAXWELL, Formation of Lunar Carbide From Lunar Iron Silicate. *Nature Phys. Sci.*, Vol. 245, 1973, pp. 3-5.
33. PILLINGER, C. T., P. R. DAVIS, G. EGLINTON, A. P. GOWAR, A. J. T. JULL, J. R. MAXWELL, R. HOUSLEY, AND E. H. CIRLIN, The Association Between Carbide and Finely Divided Metallic Iron in Lunar Fines. *Proc. Fifth Lunar Science Conference, Geochimica et Cosmochimica Acta*, Supplement 5, in press, 1974.
34. HOLLAND, P. T., B. R. SIMONEIT, P. C. WSOLEK, AND A. L. BURLINGAME, Compounds of Carbon and Other Volatile Elements in Apollo 14 and 15 Samples. *Proc. Third Lunar Science Conference, Geochimica et Cosmochimica Acta*, Supplement 3, Vol. 2, 1972, pp. 2131-2148.
35. DESMARAI, D. J., J. M. HAYES, AND W. G. MEINSCHIN, Accumulation of Carbon in Lunar Soils. *Nature Phys. Sci.*, Vol. 246, 1973, pp. 65-68.
36. PILLINGER, C. T., P. R. DAVIS, G. EGLINTON, A. P. GOWAR, A. J. T. JULL, AND J. R. MAXWELL, Unpublished results, 1974.
37. SCHAEFFER, O. A., AND L. HUSAIN, Early Lunar History: Ages of 2-4 mm Soil Fragments From the Lunar Highlands. *Proc. Fourth Lunar Science Conference, Geochimica et Cosmochimica Acta*, Supplement 4, Vol. 2, 1973, pp. 1847-1863.
38. KIRSTEN, T., AND P. HORN, ^{39}Ar - ^{40}Ar Chronology of the Taurus-Littrow Region II: A 4.28 b.y. Old Troctolite and Ages of Basalts and Highland Breccias. *Lunar Science*, Vol. V, 1974, pp. 419-421.
39. STETTLER, A., P. EBERHARDT, J. GEISS, GRÖGLER, AND P. MAURER, Sequence of Terra Rock Formation and Basaltic Lava Flows on the Moon. *Lunar Science*, Vol. V, 1974, pp. 738-740.

Page intentionally left blank

Page intentionally left blank

Mössbauer Spectroscopy of Iron in the Luna 20 Regolith

T. Zemčík

*Institute of Physical Metallurgy,
Czechoslovak Academy of Sciences,
Brno, Czechoslovakia*

K. Raclavský

*Mining University of Astrava,
Czechoslovakia*

This paper presents results of the Mössbauer effect measurements on Fe^{57} in the average sample of the Luna 20 regolith, and their comparison with similar measurements of the Luna 16 samples. Room temperature measurements of the nonmagnetic as well as magnetic components of the spectra were performed. By careful least-squares analysis, six quadrupole doublets in the inner parts of spectra were resolved. According to their splittings, they were interpreted as four types of iron in silicates (olivine, two inequivalent pyroxene sites, and a glassy fraction) and two types of nonmagnetic iron-titanium oxides (ilmenite and a spinel). "Velocity-window" measurements, were used to determine the average nickel content of (2.01 ± 0.84) wt. %. These results are discussed in terms of distribution of iron among different phases. In comparison with the Luna 16 sample, the Luna 20 sample contains more olivine and less ilmenite as well as metal with a slightly higher nickel content.

Mössbauer spectroscopy has become a generally accepted method for studying iron—as one of the most significant cosmochemical elements—in a wide variety of mineral materials. In our previous work, we applied this method to investigation of the Luna 16 regolith (ref. 1). We also reported some preliminary results for Luna 20 (ref. 2). Main attention was paid to the nonmagnetic part of the spectra, where as many as five quadrupole split components have been resolved (refs. 2 and 3).

Because of the variability of iron bonding in the phases present, this number of components does not seem to be satisfactory, and leads to discrepancies in the interpretation of our data as well as data of the literature in the field. In this work we attempted (1) to distinguish (under certain constraints) six quadrupole doublets in the spec-

trum of the Luna 20 regolith; (2) to interpret them; and (3) similarly, to reconsider the previous Luna 16 measurements.

By comparing the magnetic splitting of the metallic phase with the standards containing iron and an iron-nickel alloy, we succeeded in estimating the nickel content in the Luna 16 metal (ref. 3). As the Mössbauer effect proves to be a unique tool for gaining such valuable information, a similar measurement was carried out on the Luna 20 metal along with calculation of the complete iron distribution between both the magnetic and nonmagnetic phases.

Experimental Studies

For Mössbauer measurements, the average sample of the Czechoslovak portion of the

Luna 20 regolith has been prepared by encapsulation in a flat acrylic container. Compared with the previously used average Luna 16 sample containing 13.7 percent Fe (0.127 g , $\phi 20 \text{ mm}$, 40 mg/cm^2 , 5.5 mg Fe/cm^2), the appreciably lower content of iron in the Luna 20 material (5.1 percent Fe (ref. 4)) forced us to increase the area density of this sample (0.119 g , $\phi 10 \text{ mm}$, 152 mg/cm^2 , 7.7 mg Fe/cm^2).

All spectra were taken at the double parabolic time mode Mössbauer spectrometer NP-255 (KFKI, Budapest, Hungary) at room temperature with the approximate 5 mC Co^{57} in palladium source in transmission arrangement. Punch tape output served for further data processing at the ZPA-600 computer. Calibration of the velocity scale was performed by measuring the powdered sodium nitroprusside. Isomer shifts are related to the palladium source used.

Three types of measurements were performed:

1. Whole spectra in the approximately $\pm 7 \text{ mm/s}$ range, with division into 512 channels.
2. Precise measurements of the middle part of the spectra (counting statistics up to 10^7 counts/channel), with division into 256 channels. Three runs were performed, the first of which was used for seeking the optimum processing (refs. 2 and 3). The second run, performed as a continuation under identical conditions, was later added to the first.
3. The "velocity-window" measurements of the outermost magnetic lines of the spectra (approximately 6×10^7 counts/channel) into 128 channels. In this case, powdered standards consisting of a mixture of pyroxene, olivine, and iron or iron alloy (Fe-4.8 wt.% Ni) alloy were used.

The measured spectra were processed with the aid of a system of programs for the least-squares analysis. Special attention was paid to the low-velocity components of the spectra. To the spectra sub 2, six asymmetric quadrupole doublets of Lorentzian lines were

fitted with equal line widths. Although this constraint is a substantial one, the procedure is necessary with respect to the limitations of the program system used, and seems to be justified by the resulting improvement in the value of the line width near the calibration width, and by the reproducibility of the line positions in the spectra of the same sample, as well as in those of different samples.

Results and Discussion

NONMAGNETIC FRACTION

A typical nonmagnetic part of the Luna 20 spectrum and its decomposition into six quadrupole doublets (numbered 1 to 6), along with that of Luna 16, is shown in figure 1. As has been shown in reference 2, resolving four quadrupole components in the spectrum is clearly insufficient; decomposition into five doublets is ambiguous, depending on the type of constraints (ref. 3). This situation is shown at the top of figure 2. Only six compo-

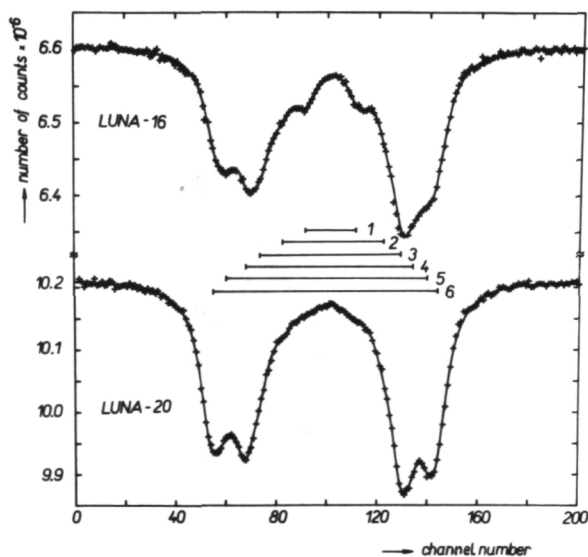


Figure 1.—Mössbauer spectra of the average samples of Luna 20 (bottom) and Luna 16 (top). Velocity scales are identical, both reverse in sign. Smooth lines represent the least-squares fit; numbering of the components corresponds to the tables.

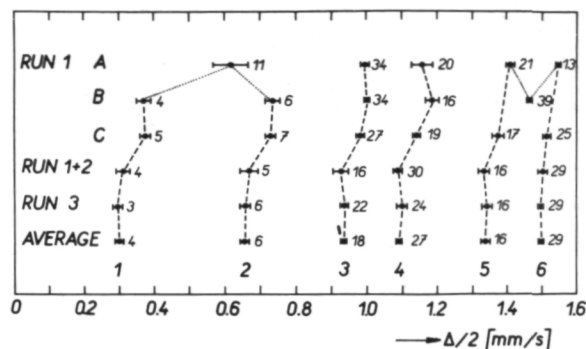


Figure 2.—Comparison of the results of decomposition of the Luna 20 spectra. The figures 1 through 6 below their respective curves indicate individual components; the small figures, their relative areas. A indicates 5 doublets with paired line widths; B, 5 doublets with equal line widths; and C, 6 doublets with equal line widths.

nents fit the spectrum unambiguously and reproducibly for individual runs of measurements (compare in figure 2). Unless otherwise stated, all other cases hereafter refer to the decomposition into six doublets (of equal line widths).

Good reproducibility of these decompositions made it possible to increase the reliability of the results by their averaging for the runs 1, 2, and 3. The main parameters of the components identified in the Luna 20 spectra compared with those of Luna 16 are summarized in table 1. Graphical display of the individual quadrupole splittings and corresponding relative areas for the lunar samples, as well as for some comparative terrestrial materials, is provided in figure 3.

Let us first interpret the components in the nonmagnetic part of the lunar regolith spectra (see figure 3 and table 1). Component 1 refers unambiguously to ilmenite (ref. 5). Lower precision of the corresponding quadrupole splitting value in Luna 20 is the consequence of its low content in the sample. Similarly, the component 6 belongs to olivine. Variations in the quadrupole splittings in comparison with the errors prevent judgment of the relative position in isomorphous series (ref. 6).

The prevailing part of absorption is caused

by components 3, 4, and 5. The outer doublets correspond to two inequivalent Fe^{2+} sites (M1, M2) in pyroxenes, as indicated by comparison with the augite (from the basalt) or pyroxenes in gabbro (Skaergaard massif). These results agree with data of the literature in the field (see, e.g., ref. 7). Unfortunately, the relative areas do not say too much about the site occupancy in pyroxenes because both components 3 and 5 are strongly overlaid by component 4 and cannot hence be completely separated. Nevertheless, the quadrupole splitting of the latter component matches that of the terrestrial volcanic glass.

It has been proposed that the last component, 2, be interpreted as a spinel, near to ulvospinel (ref. 8), although data in the literature give an appreciably higher quadrupole splitting than that of figure 3 (approximately 0.85 mm/s, ref. 9). We therefore carried out a comparative measurement on a synthetic stoichiometric Fe_2TiO_4 (kindly provided by Dr. Z. Šimša, Institute of Solid State Physics, Prague). As is shown in figure 3, besides the main component corresponding to Fe^{2+} in tetrahedral sites, there is a weaker component of Fe^{2+} in octahedral sites. In case they were unresolved, the obtained mean splitting would correspond to that quoted above. It could, therefore, be concluded that our component 2 originates from the tetrahedral iron site in spinel structure, with the octahedral contribution unresolvable within the main absorption region discussed above.

MAGNETIC FRACTION

The quantitative data including hyperfine structure parameters and intensities (relative areas) given in table 1 provide a picture of the differences between the Luna 20 and Luna 16 samples. For the complete discussion of the distribution of iron among individual iron-bearing phases present, one has to take into account also the contribution of the magnetically split component resulting from the metallic iron. Its intensity has been evaluated from the high-velocity spectra (sub 1 in Section 2) and it is summarized in table 2 along

Table 1.—*Parameters of Mössbauer Spectra of the Lunar Regolith*

Sample	Component	Quadrupole Splitting (mm/s)	Isomer Shift (mm/s)	Related Area (percent)	Line Width (mm/s)
Luna 20	1	0.302 ± 0.010	0.910 ± 0.010	3.64 ± 0.20	0.341 ± 0.008
	2	0.656 ± 0.011	0.878 ± 0.025	5.65 ± 0.41	
	3	0.936 ± 0.007	0.925 ± 0.029	18.35 ± 2.84	
	4	1.192 ± 0.007	0.984 ± 0.029	27.26 ± 2.75	
	5	1.340 ± 0.010	0.994 ± 0.029	16.04 ± 1.09	
	6	1.500 ± 0.005	1.001 ± 0.008	29.06 ± 1.09	
Luna 16	1	0.360 ± 0.005	0.918 ± 0.005	10.61 ± 0.54	0.346 ± 0.002
	2	0.715 ± 0.009	0.882 ± 0.009	9.88 ± 0.81	
	3	0.950 ± 0.008	0.915 ± 0.008	25.66 ± 2.22	
	4	1.117 ± 0.029	0.928 ± 0.029	18.65 ± 2.67	
	5	1.312 ± 0.036	0.989 ± 0.036	13.34 ± 2.70	
	6	1.473 ± 0.006	1.003 ± 0.006	21.86 ± 2.19	

with the recalculated intensities of the components from table 1. These intensities express the distribution of iron among individual phases (or structure sites) with the degree of accuracy given by the differences in their Debye temperatures. From table 2, systematic differences of the contents of some phases in the Luna 20 regolith in comparison with Luna 16 can be seen. Setting aside the fractions, the quadrupole doublets of which strongly overlap and thus produce unreliable intensities, we still may state that the Luna 20 sample contains appreciably less ilmenite

and metal, but more olivine than the Luna 16 sample.

We were able to determine the degree of alloying of lunar iron with nickel (providing that only nickel is present), by linear interpolation between differences of the positions of the outermost lines of the magnetic component in the spectra, measured in the "velocity-window" mode (sub .3, Section 2). Linear interpolation also enabled a quantitative estimate of the metallic phase content to be made.

As shown in figure 4, the content of nickel

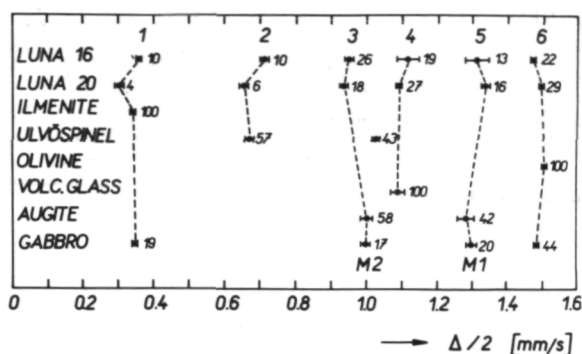


Figure 3.—Quadrupole splittings of individual components in the spectra of the lunar samples and of some terrestrial materials. The figures at the top of the chart indicate the components; the small figures, their relative areas.

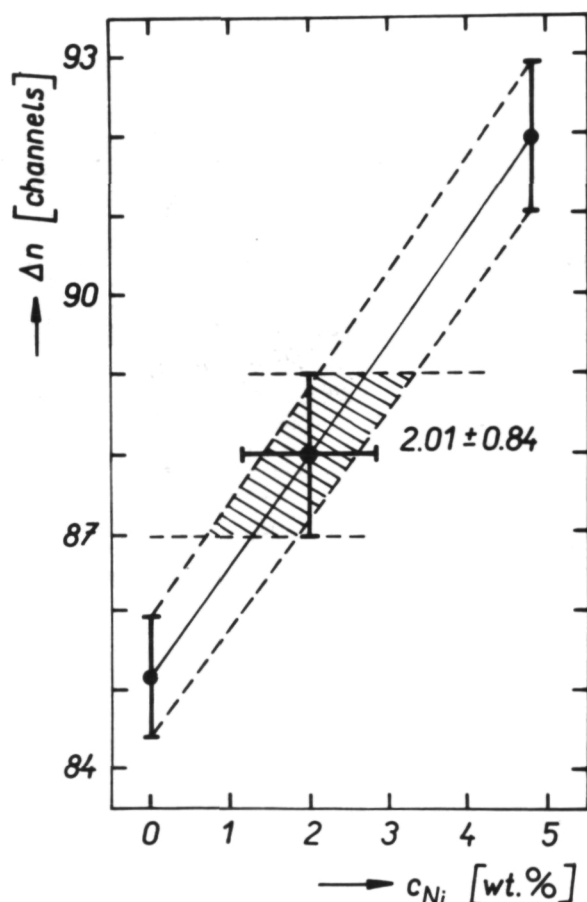


Figure 4.—Determination of Ni content in the Luna 20 metal, by comparison with Fe and Fe-Ni. The term Δn represents difference in the outermost line positions in the velocity window spectrum; c_{Ni} indicates nickel content.

Table 2.—Distribution of Iron in the Lunar Regolith

Phase (component)	Luna 20	Luna 16
Ilmenite (1)	3.51 ± 0.20	10.05 ± 0.49
Olivine (6)	28.10 ± 1.31	20.71 ± 2.06
Pyroxene M1 (5)	15.44 ± 1.05	12.64 ± 2.55
Pyroxene M2 (3)	17.67 ± 2.80	24.32 ± 2.07
Glass (4)	26.28 ± 2.58	17.69 ± 2.52
Ulvöspinel (2)	5.46 ± 0.39	9.36 ± 0.75
Fe-Ni (7)	3.18 ± 0.47	5.23 ± 0.38

amounts to (2.01 ± 0.84) wt.%, i.e., slightly higher than in Luna 16 (1.50 ± 0.96 ref. 3). Taking into account the metallic iron contribution in table 2 and the entire iron content in the sample quoted in Section 2, the concentration of nickel alloyed with iron is approximately 30 ppm in the whole sample. Unfortunately, no activation analysis data for nickel in our portion of the Luna 20 regolith are known. The literature (ref. 10) gives at least 170 ppm Ni, which still means, in comparison with the average, strong enrichment of the metallic phase with nickel.

Conclusions

Although we believe we have presented quite a complete qualitative, and a fair quantitative, analysis of the Mössbauer spectroscopy data for iron in the Luna 20 regolith, we are aware of some weak points in our procedures. The limitation in the line widths is a substantial one, namely, in the case of the glassy fraction in the sample, where an increased line width is to be expected because

of the non-uniformity of iron environments in the amorphous substance. Avoiding this would probably call for a more powerful computing technique and for still better counting statistics. On the other hand, using a modified "semi-stripping" technique with the assumption that some phases were unambiguously defined, one could study the most interesting parts of the spectra in more detail.

In addition to gradually refining the study of nonmagnetic as well as magnetic parts of the spectra, we are aiming at employment of the Mössbauer spectroscopy for measuring smaller, non-average parts of lunar samples. In reference 11 we have presented the iron analysis in a fine (about 10 μg) Luna 16 particle. Similar measurements on the selected Luna 20 particles are in progress.

Acknowledgment

The authors are indebted to Dr. A. Cimbalníková (Geological Institute, Prague) for her outstanding efficiency and invaluable consultation concerning the lunar research in Czechoslovakia. Thanks are also due to the authors' coworkers in the Institute of Physical Metallurgy, Ing. S. Havlíček and Mr. S. Jurnečka, for their efficient laboratory work, to Mrs. J. Klečková for her devoted technical

help, and last but not least, to the staff of the computing center headed by Ing. J. Kucera, for performing the troublesome computations required for this study.

References

1. ZEMČÍK, T., AND K. RAČLAVSKÝ, *Geokhimiya*, No. 7, 1974.
2. ZEMČÍK, T., AND K. RAČLAVSKÝ, *Geokhimiya*, To be published.
3. ZEMČÍK, T., AND K. RAČLAVSKÝ, *Proc. Fifth Int. Conference Mössbauer Spectroscopy*, Bratislava, 1973, To be published.
4. MAŠTALKA, A., *Private Communication of the Activation Analysis Results*. See also this conference.
5. MUIR, A. H., R. M. HOUSLEY, R. W. GRANT, M. ABDEL-GAWAD, AND M. BLANDER, *Science*, Vol. 167, 1970, p. 688.
6. MALYSHEVA, T. V., V. V. KURASH, AND A. N. ERMAKOV, *Geokhimiya*, No. 11, 1969, p. 1405.
7. HAFNER, S. S., AND D. VIRGO, *Proc. Apollo 11 Lunar Science Conference*, Vol. 3, 1970, p. 2183.
8. MALYSHEVA, T. V., *Geokhimiya*, No. 7, 1973, p. 1079.
9. AVRAHAMI, M., AND R. M. GOLDING, *N.Z.J. Sci.*, Vol. 12, 1969, p. 594.
10. VINOGRADOV, A. P., *Geokhimiya*, No. 7, 1972, p. 763.
11. ZEMČÍK, T., K. RAČLAVSKÝ, AND J. LAUERMANOVÁ, *Proc. Fifth Int. Conference Mössbauer Spectroscopy*, Bratislava, 1973. To be published.

The Main Peculiarities of the Processes of the Deformation and Destruction of Lunar Soil

A. K. Leonovich, V. V. Gromov, A. D. Dmitriyev,
V. N. Penetrigov, and P. S. Semenov
*A. I. Ioffe Leningrad Physical-Technical Institute
Academy of Sciences, U.S.S.R.*

V. V. Shvarev
*All-Union Scientific Research Institute
of Optical-Physical Measurements, U.S.S.R.*

The main results of study of the physical and mechanical properties of lunar soil, obtained by laboratory study of samples returned from the Moon by Luna 16 and Luna 20, as well as by operation of the self-propelled Lunokhod 1 and Lunokhod 2 on the surface of the Moon, are analyzed in the report. All studies were carried out by single methods and by means of unified instruments, allowing a confident comparison of the results obtained.

The investigations conducted allowed the following values of the main physical-mechanical properties of lunar soil to be determined: in the natural condition the solid density corresponds to the porosity of 0.8; the modal value of the carrying capacity is 0.4 kg/cm²; adhesion is 0.04 to 0.06 kg/cm²; and the internal angle of friction is 20 to 25°.

The main mechanisms of deformation and destruction of the soil are analyzed in the report, and the relationships between the mechanical properties and physical parameters of the soil are presented.

The return to Earth of samples of lunar soil from different regions of the Moon's surface and the study of properties of the soil in the natural state permit a number of generalizations to be made about the processes of deformation and destruction of the lunar soil. One of the important results of studying the constitution, structure, and physical and mechanical properties of lunar soil has been the discovery of the relative uniformity of the particle size distribution. In addition, information has been gathered concerning the shapes and specific gravity of particles from various sections of the lunar surface. Irregularities in structure of the lunar surface and change in physical-mechanical properties of the lunar soil within broad limits may be explained, to a considerable extent, by different proportions of soil compaction. Despite certain differences in the physical and mechanical

properties of the soil obtained by different investigators, some general regularities that can be considered to be characteristic of lunar soil were revealed.

Nature and Destruction of Lunar Soil Samples

The processes of destruction of lunar soil samples were investigated in a Coulomb apparatus, for two states of the soil: (1) extremely loose and (2) compacted to a density of 1.6 g/cm³.

The Coulomb apparatus is a small box which has transparent walls and a movable partition inside (ref. 1).

The soil in the loose state is deformed by lateral pressure, without formation of visible crags or slip lines (fig. 1a). If the deforma-

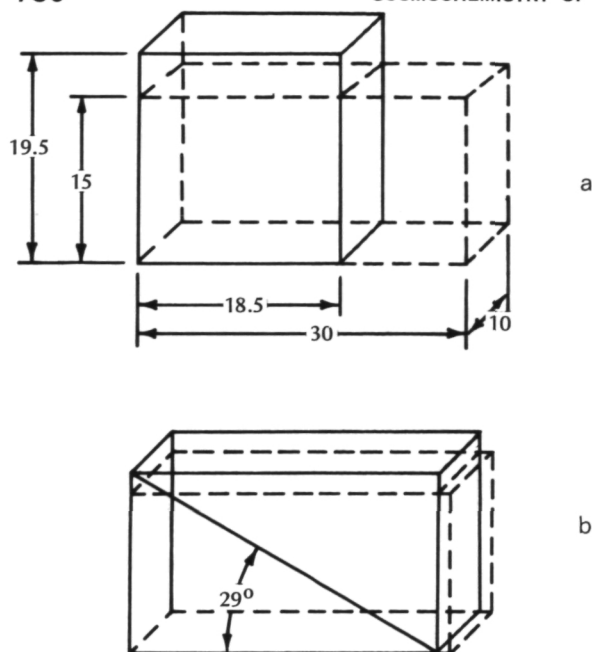


Figure 1.—Diagram of sample deformation: (a) loose state; (b) compacted state.

tion in the Coulomb instrument is considered as a biaxial compression, the coefficient of lateral expansion of the soil, μ , and the coefficient of lateral pressure, ξ , can be calculated.

For Luna 16 and Luna 20 soil samples in the loose state, the following values were obtained: $\mu = 0.44 + 0.45$; $\xi = 0.78 - 0.82$.

On application of lateral pressure to compacted soil, splitting of the sample occurred along a plane inclined to the principal stress by an angle of 22° for the Luna 16 sample and 29° for the Luna 20 sample (fig. 1b). These correspond to internal angles of friction of 46° and 32° (refs. 1 and 2).

Strength Characteristics of Lunar Soil

The main strength indicators of fine-grain, weakly bound soils are the shear strength characteristics (ref. 3).

The shear strength of lunar soil samples was determined in a flat, single-shear instrument, by the supercompaction method.

Graphs of the shearing resistance, plotted in "shear stress"—"normal pressure" coordinates, are shown in figure 2, and the principal portion of them is described well by the Coulomb equation:

$$\tau = c + p \tan \phi \quad (1)$$

where τ is the shear stress (kg/cm^2), c is the corrected adhesion (kg/cm^2), p is the normal shear pressure (kg/cm^2), and ϕ is the internal angle of friction.

The shear strength parameters depend to a great extent on the compaction pressure (fig. 3).

In the incoherent state, the soil has a negligible adhesion and internal angle of friction. In proportion to increasing compaction pressure, an increase in the internal angle of friction and initial adhesion occurs. This can be explained by an increase in the number of contacts between particles and an increase in the quantity of fused particles.

At compaction pressures over $0.4 + 0.5 \text{ kg}/\text{cm}^2$, the number of contacts increases negligibly, and the internal angle of friction and initial adhesion approach a certain steady-state value. Stabilization of the initial adhesion values, on the other hand, is also explained by the fact that, in the process of shear in the absence of normal pressure, decompaction of the soil takes place, and the mutual adhesion between particles decreases. With compaction pressure, decompaction of soil does not take place during shear, and, with pressures greater than a certain value, the soil is still more strongly compacted during shear. This phenomenon may explain the linear nature of the dependence of the normalized adhesion on the compaction pressure. The nature of the occurrence of additional compaction and decompaction of soil in shear tests is shown in figure 4. The following characteristic points can be distinguished in these curves:

1. Intersection with the normal pressure axis during shear, when the sample retains its volume in the shear process
2. Intersection with the vertical axis (magnitude of decompaction of the soil, in the absence of normal shear pressure)

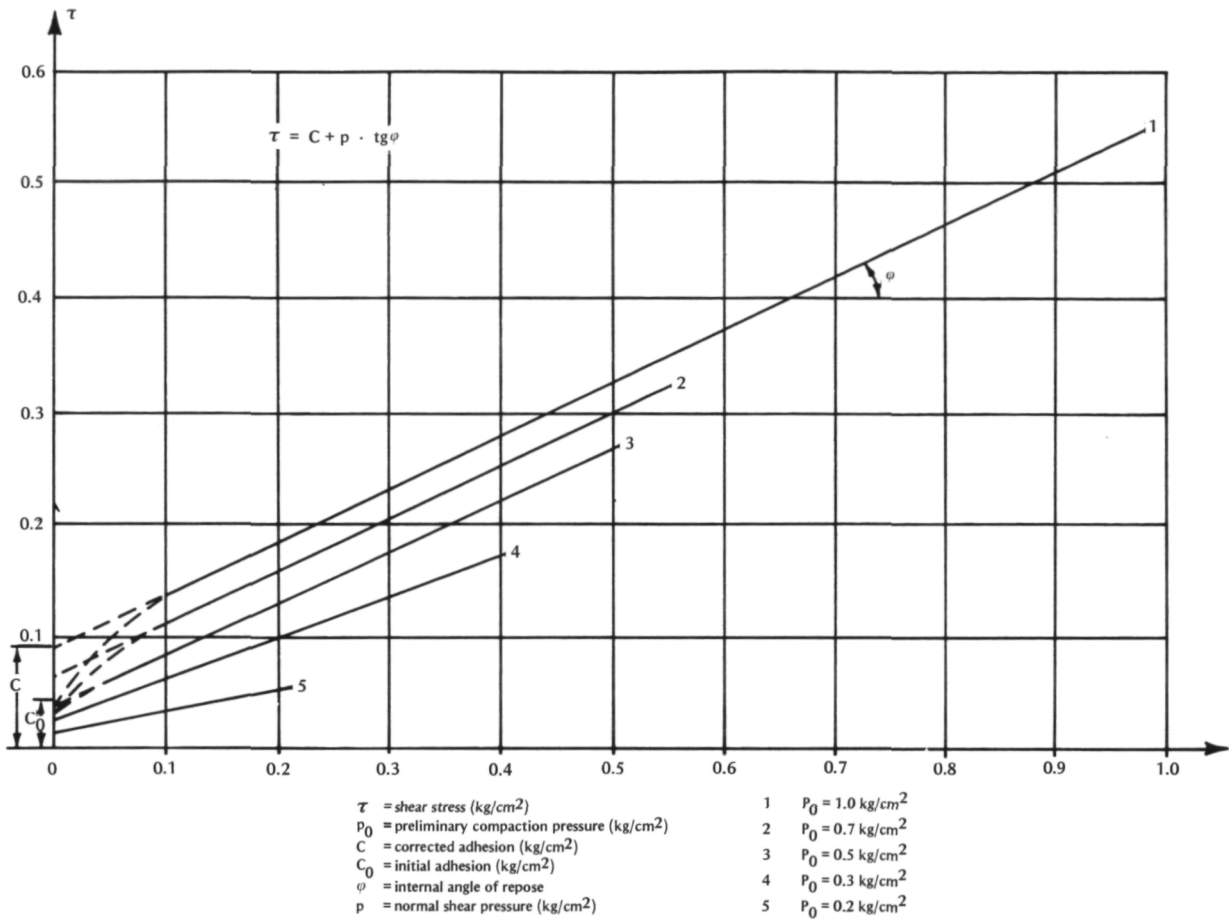


Figure 2.—Shear strength curves. For curve 1, $p_0 = 1.0$; 2, $p_0 = 0.7$; 3, $p_0 = 0.5$; 4, $p_0 = 0.3$; 5, $p_0 = 0.2$.

In the first case, it can be considered that the external normal pressure is equalized by an equivalent internal pressure in the soil, and, therefore, there is no additional change in volume of the soil. The magnitude of this pressure can be considered to be "critical" (p_c) for a given state of the soil.

In the second case, the amount of soil decompaction in the absence of normal pressure indicates the degree of incoherence (decrease in soil porosity). The curve of decompaction versus compacting load is similar to the soil subsidence curve in compression compacting, and in this case the soil has a tendency to go to a state corresponding to an equivalent compaction pressure (p_b).

The quantity p_c can be considered as the

equivalent internal pressure in the soil, which determines the force of adhesion and which is the residual stress from the compacting load. This stress is preserved if the internal normal pressure in the shear process is equal to or exceeds p_c for a given state of the soil. Otherwise, the soil will loosen, and the new state will correspond to a decreased value of p_c . In the absence of normal pressure in the shear process, $p_c = p_b$.

Analysis of the experimental data on shear strength has demonstrated that p_c depends linearly on compaction pressure, and p_b depends little on the degree of compaction of the soil and can serve as a certain characteristic value for determination of shear strength.

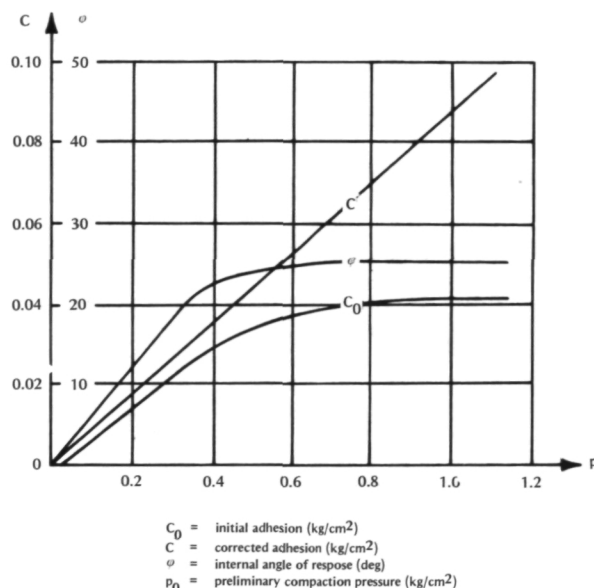


Figure 3.—Shear strength parameters as a function of load.

With the peculiarities revealed in the process of shear of lunar soil samples taken into account, the interconnection between shear stress and normal pressure can be represented in the following form (fig. 5):

$$\tau = C_0 + p \times \tan \phi + C_2 \quad (2)$$

where C_2 is the supplementary value of the adhesion strengths determined by compaction of the soil (cross-hatched part of fig. 5). As is evident from this curve, $C_2 = 0$ at $p = 0$ and reaches its maximum value at pressures above the critical pressure. The following expression satisfies this condition of change in C_2 :

$$C_2 = C - C_0 \times (1 - e^{-Kp}) \quad (3)$$

where K is an exponent ($\text{cm}^2 \times \text{kg}$).

Then, the equation for determination of the shear strength will have the form:

$$\tau = C_0 + P \times \tan \phi + (C - C_0) \times (1 - e^{-Kp}) \quad (4)$$

The quantities C_0 and C can be determined from p_b and p_c :

$$\begin{aligned} C_0 &= p_b \times \tan \phi \\ C &= p_c \times \tan \phi \end{aligned} \quad (5)$$

Taking this equation into account, (2) takes the following form:

$$\tau = \tan \phi \times [p_c - (p_c - p_b) \times e^{-Kp} + p] \quad (6)$$

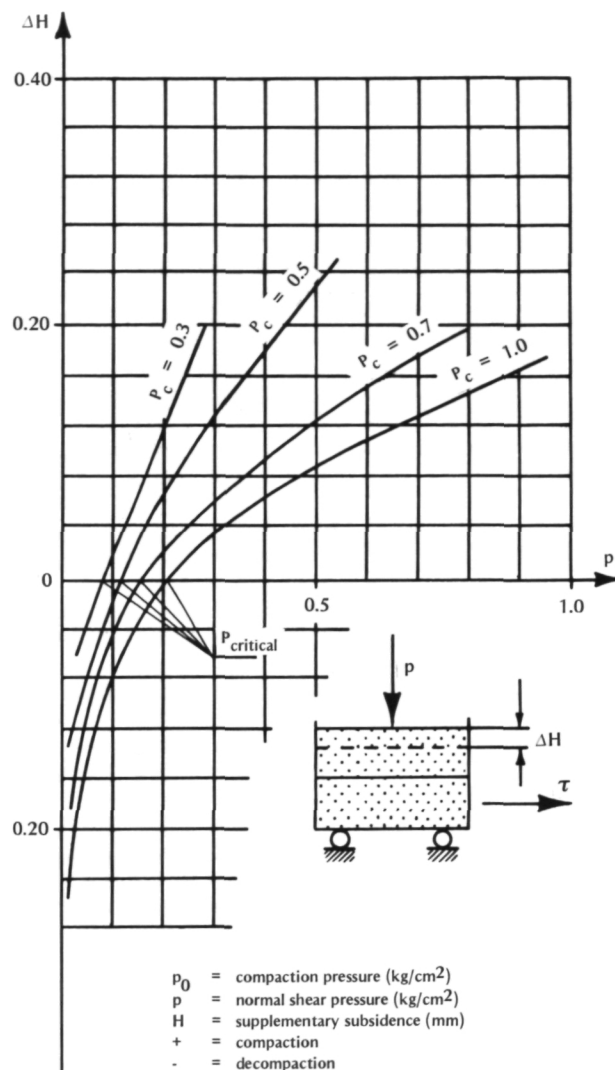


Figure 4.—Change in sample deformation during shear 1— $p_0 = 0.5 \text{ kg/cm}^2$; 2— $p_0 = 0.7 \text{ kg/cm}^2$; 3— $p_0 = 1.0 \text{ kg/cm}^2$.

Exponent K can be determined, on condition that, at $p = p_c$, the magnitude of the supplementary adhesion is sufficiently close to its maximum value. Practically, it can be considered that this condition is satisfied if the cofactor $(1 - e^{-Kp}) = 0.9$. Proceeding from this condition:

$$K = \frac{1}{\log e p_c} = \frac{2.3}{p_c} = \frac{2.3 \times \tan \phi}{C} \quad (7)$$

Then, formula (6) can be written in the following form:

$$\tau = C - (C - C_0) \times \exp \left[-\frac{2.3 p \times \tan \phi}{C} + p \tan \phi \right]$$

or

$$\tau = \tan \phi [p_c - (p_c - p_b) \times \exp \left[-\frac{2.3 p \times \tan \phi}{C} + p \right]] \quad (8)$$

Nonlinearity of the initial part of the shear strength curve leads to a considerable change in the internal angle of friction, determined from the tangent of the slope angle tangent to the shear strength curve.

For any point, the internal angle of friction will be

$$\tan \phi_i = \frac{d\tau}{dp} = \tan \phi \left[(C - C_0) \times \frac{2.3}{C} \times \exp \left[-\frac{2.3 p \times \tan \phi}{C} + 1 \right] \right] \quad (9)$$

The initial internal angle of friction, i.e., at $p = 0$, is

$$\tan \phi_0 = \tan \phi \times \left[\left(1 - \frac{C_0}{C} \right) \right]$$

$$\times 2.3 + 1] = \tan \phi \left[\left(1 - \frac{p_b}{p_c} \right) 2.3 + 1 \right] \quad (10)$$

A comparison of the determination of $\tan \phi_0$ by this formula and in the Coulomb instrument has shown that they coincide well,

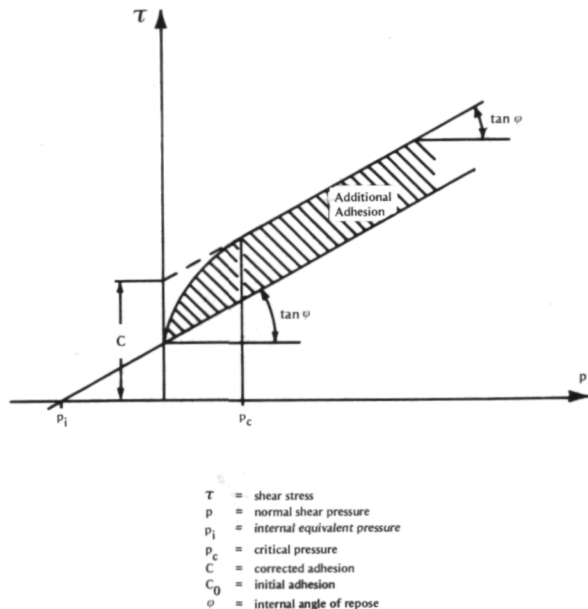


Figure 5.—Curve for determination of adhesion in soil.

which confirms the correctness of the previous conclusions as to the peculiarities of the development of processes of shear of the lunar soil.

Qualitative values of the shear strength parameters for the Luna 16 and Luna 20 samples are quite close to each other.

Similar results were also obtained for finely pulverized basalt, with a particle size composition close to that of the lunar soil.

Peculiarities of Lunar Soil Deformation Processes

The most important deformation characteristics of soil, which have great scientific and applied importance, are

1. Compressibility
2. Process of intrusion of a die into the half-space of the soil.
3. Soil deformation in the shear process.

Compressibility of the lunar soil was studied on the samples returned by Luna 16 and Luna 20. The study was carried out on soil samples 6 cm³ in size. The maximum value of the compaction pressure was 1 kg/cm². The results of the tests are shown in figure 6. Analysis of the behavior of the com-

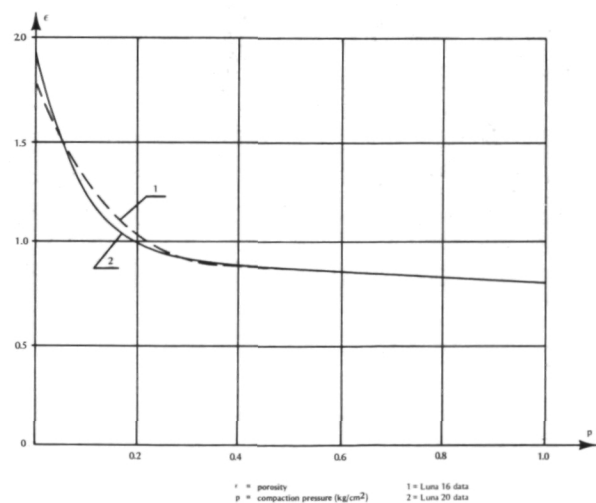


Figure 6.—Lunar soil compressibility curves: (1) from Luna 16 data; (2) from Luna 20 data.

compressibility curve permitted two soil compaction mechanisms to be distinguished.

In the initial stage of compression of the soil, a decrease in porosity takes place, mainly by means of displacement and more dense packing of the aggregates and particles. With further increase in load, destruction of the aggregates and displacement and compaction of the particles themselves begins; in this case, the load is transmitted in the bulk of the soil, through contacts between the particles. In the 0.5 to 1.0 kg/cm² compaction pressure range, the process of compacting the particles and increasing the number of contacts between them is basically completed; subsequent compaction of the soil takes place by means of destruction of the particles at their points of contacts with one another.

The lunar soil compressibility curve is approximated sufficiently well by the following formula:

$$\varepsilon = A \times e^{K_1 \times p} + B \times e^{-K_2 \times p} \quad (11)$$

ε is the density; A , B , K_1 , and K_2 are constants. In this case, $A + B = \varepsilon_0$ is the porosity of the maximally incoherent soil. The compaction coefficient, a , for any point on the compressibility curve described by equation (11), will equal:

$$a = \frac{d\varepsilon}{dp} = K_1 \times A \times e^{K_1 \times p} - K_2 \times B \times e^{-K_2 \times p} \quad (12)$$

In the maximally incoherent state (at $p = 0$), the compaction coefficient equals

$$a_0 = -K_1 \times A - K_2 \times B$$

The modulus of deformation, E , from the decompression curve can be determined by the following formula:

$$E = \frac{1 + \varepsilon_0}{-K \times A \times e^{K_1 \times p} - K_2 \times B \times e^{-K_2 \times p}} \left(1 - \frac{2\xi}{1 + \xi} \right) \quad (13)$$

where ξ is the lateral pressure coefficient.

At small compaction pressures (< 0.5 kg/cm²), formulas (11, 12, 13) can be simplified somewhat, if the second term in the formula is assumed to be constant. Then, for the compressibility curve we will have:

$$\varepsilon = \varepsilon_\infty + (\varepsilon_0 - \varepsilon_\infty) \times e^{-K_1 \times p} \quad (14)$$

where ε_∞ is a certain maximum value of the porosity in compaction.

We then obtain, for the compaction coefficients:

$$a_0 = -K_1 \times (\varepsilon_0 - \varepsilon_\infty) \quad \text{and} \quad a = a_0 \times (1 - p) \quad (15)$$

where $D = \frac{\varepsilon_0 - \varepsilon}{\varepsilon_0 - \varepsilon_\infty}$ is the coefficient of relative density of the soil.

The modulus of deformation will equal:

$$E = \frac{1 + \varepsilon_0}{a_0 \times (1 - D)} \times f(\xi)$$

$$E = \frac{(1 + \varepsilon_0) \times e^{K_1 \times p}}{-K_1 \times (\varepsilon - \varepsilon_\infty)} \times f(\xi)$$

$$E = \frac{1 + \varepsilon_0}{-K_1 \times (\varepsilon - \varepsilon_\infty)} \times f(\xi)$$

where

$$f(\xi) = \left(1 - \frac{2\xi^2}{1 + \xi} \right) \quad (16)$$

It is easy to develop the relationship of the main parameters of compressibility with degree of compaction of the soil, magnitude of the compaction pressure, and the physical state of the soil, from equations (13, 14, 15, 16).

In removing the compression load from a sample of soil in a compression instrument, its porosity is practically unchanged, since the recovery from deformation of the soil is low; on the average, it amounts to tenths of a percent of the residual formation.

With increase in load to the former value, additional subsidence of the soil takes place, the magnitude of which decreases in proportion to increase in compression pressure. A somewhat higher total deformation of the soil sample results than in a continuous increase in load. With repeated application of the load, additional soil subsidence decreases in proportion to the increase in the number of load cycles.

The small value of the recovery and additional subsidences in cyclic loading takes place with its first load and has a residual nature.

The carrying power of the lunar soil samples returned was determined by intrusion of

a die. The limiting size of the samples studied (with respect to the size of the die) allows consideration of the data obtained mainly as a qualitative characteristic of the die intrusion.

With intrusion into soil, which is in the maximally incoherent state, the die leaves a distinct impression, around which the soil surface is not deformed. The general nature of the deformation corresponds essentially to the process of local soil compaction. With increase in soil density, the resistance to intrusion of the die increases noticeably. The nature of the soil deformation also changes, a protrusion zone appears, and radial and concentric cracks appear around the die. Upon intrusion into highly compacted soil (weight by volume $> 1.6 \text{ kg/cm}^3$), the course of the

die subsidence curve changes and corresponds to deformation of the soil at the equilibrium maximum.

Values of the carrying power of the soil as a function of its weight by volume, γ , are presented in figure 7.

The carrying power was determined for the initial part of the intrusion curve, and it corresponds to the pressure on the die, at a subsidence equal to the diameter of the die.

A sharp increase in carrying power is observed, with increase in weight by volume above 1.4 to 1.5 g/cm^3 .

The following characteristic sections can be distinguished in the "carrying power—weight by volume" curve. In regions of low soil compaction ($\gamma < 1.4 \text{ g/cm}^3$), the main role in deformation of the soil is played by compressibility of the soil under the die. In strong compaction ($\gamma > 1.6 \text{ g/cm}^3$), soil deformation takes place by means of general shear. At $\gamma = 1.4\text{--}1.6 \text{ g/cm}^3$, subsidence of the die is determined by compaction of the soil and local shears around the die.

Deformation of the lunar soil in shear tests is indicated in figure 8.

The shear stress reaches a maximum at a certain shear deformation value. A sharp

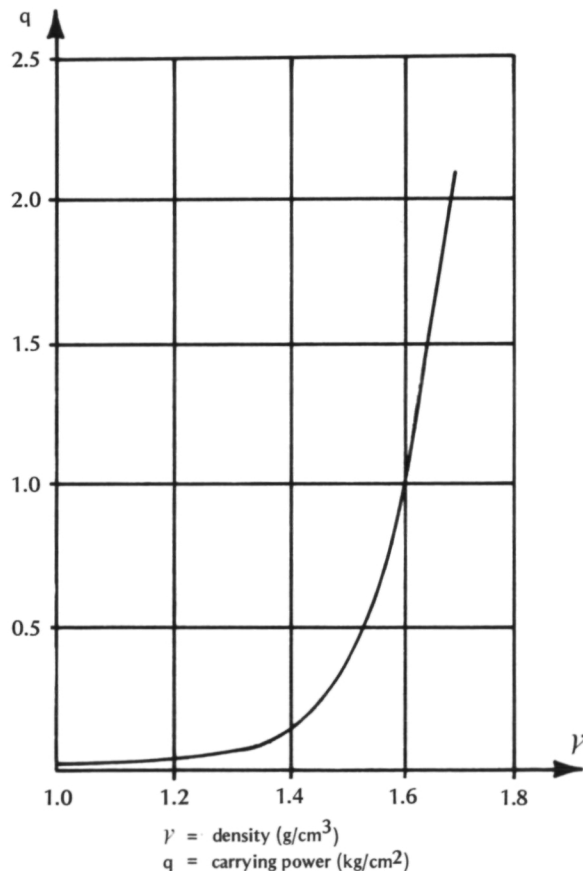


Figure 7.—Carrying power as a function of weight by volume.

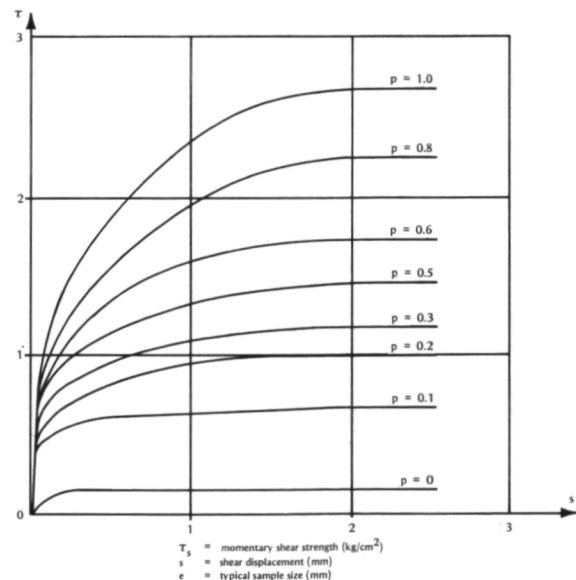


Figure 8.—Deformation of lunar soil in shear tests.

drop in the stress with increase in deformation does not occur, which is evidence of preservation of the relatively constant average value of the forces of adhesion in the soil. A decrease in shear stress is observed, only with a considerable increase in deformation, and is explained mainly by a decrease in cross section of the sample.

The increase in shear stress from displacement of the shear is approximated well by the exponential relationship

$$\tau_s = \varepsilon \times \left(\frac{s}{e}\right)^m \quad (17)$$

where τ_s is the current shear strength (kg/cm²); τ is the maximum shear strength (kg/cm²); s is the shear displacement (cm); e is the typical sample size; and m is an exponent.

Mechanical Properties of Lunar Soil in its Natural State

The mechanical properties of soil on the lunar surface along the paths of Lunokhod 1 and Lunokhod 2 were determined on the basis of regular periodic measurements of the soil properties using a conical-lobe die (ref. 2). About 100 measurements were made in all, over a total path length of 47 km. The die penetrated into the soil up to 100 mm depth.

An averaged differential distribution curve of the carrying power of the soil along the courses is shown in figure 9. Experimental data on distribution of the mechanical properties of the lunar soil are quite well described by a shifter Rayleigh equation:

$$f(q) = 2\lambda \times (q - q_0) \times e^{-\lambda^2(q - q_0)^2} \quad (18)$$

where $f(q)$ is the carrying power probability density; q is the value of the carrying power; q_0 is the minimum value of the carrying power; and λ is the degree of nonuniformity of the soil properties.

The quantity q_0 is determined to a considerable extent by the dimensions of the die and depth of penetration into the soil. With decrease in die dimensions, q_0 also will decrease.

The parameters q_0 and λ in equation (18) can be determined from the value of the

mathematical expectation and dispersion. The average values of these coefficients are $q_0 = 0.08 - 0.1$ kg/cm² and $\lambda = 3.0$ cm²/kg. The modal value of the carrying power was $0.35 - 0.4$ kg/cm².

The distribution of resistance to rotary shear is similar to the distribution of the carrying power. The modal value is $0.045 - 0.055$ kg/cm². A correlative dependence was developed between the carrying power (q) and resistance to rotary shear (t), of the type:

$$t = 0.029 - 0.2q$$

The correlation coefficient is 0.3, which indicates a relatively small functional interconnection of q and t . This can be explained by the fact that the carrying power is determined to a considerable extent by the internal angle of friction, which can change within broad limits for lunar soil, depending on the degree of compaction of the soil and the nature and magnitude of the external load.

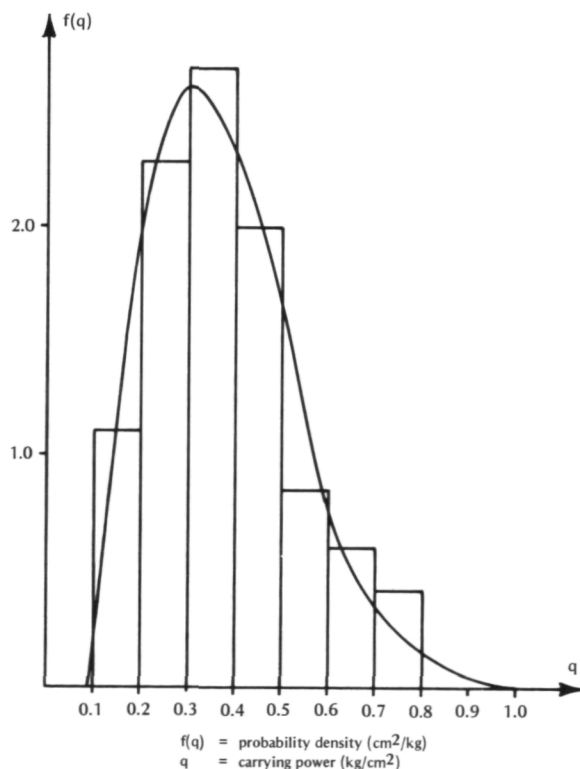


Figure 9.—Distribution of soil carrying power.

Conclusion

Investigation of the processes of deformation and destruction of lunar soil has shown that its mechanical properties can change within broad limits, depending on the physical state of the soil. At the same time, not only the quantitative indicators change, but also the soil deformation mechanisms.

Soil in the maximally incoherent state has very low strength characteristics, and it has high compressibility. From the nature of the behavior of soil upon application of a load in this state, it approximates the properties of a compressed fluid, i.e., it has a small internal angle of friction, negligible adhesion, and a high coefficient of lateral pressure.

With compaction of the soil (a decrease in porosity), an increase in adhesion and internal angle of friction takes place, and the compressibility factor also decreases sharply.

With a porosity of 0.8 to 0.9, stabilization of the internal friction and compressibility parameters occurs. This is in good agreement with the fact that, if the soil compaction process is analyzed in the form of sums of two asymptotic processes, one of which determines the deformation of the soil by means of denser packing of the soil particles under the external pressure, the other characterizes the degree of destruction of the particles in their contact zones.

By the nature of the destruction, lunar soil with a porosity of 0.8 to 0.9 behaves like a solid, having considerable internal friction and appreciable bonding.

The mechanical properties of the lunar soil as it naturally occurs can change within considerable limits. However, the most likely (modal) value of the capacity is 0.35 to 0.4 kg/cm². This is evidence of a considerable degree of compaction of the upper layers of the lunar soil as it occurs naturally. The degree of compaction of the soil was estimated from the correlative dependence between the porosity and carrying power, obtained on finely pulverized basalt, the particle size and

shapes of which were close to the average data on the lunar soil. A carrying power of 0.35 to 0.40 kg/cm² corresponds to a porosity of 0.9. This value is most likely for lunar soil as it occurs naturally.

Study of soil samples returned from various regions of the Moon as well as studies performed by Lunokhod 1 and Lunokhod 2, have shown that, despite significant differences in the geomorphological situation of the sections studied, the lunar soil obeys common regularities in the physical-mechanical characteristics. This allows one to assume the existence of a single mechanism of production and formation of the upper layer of the soil for a considerable part of the surface of the Moon.

Comparison of the data obtained with the results of study of the lunar soil in the Apollo and Surveyor programs has shown that significant differences are observed in a number of characteristics. Nevertheless, in terms of the physical indicators that have a definite effect on the mechanical characteristics, all samples studied are quite close together. The reason for the divergence apparently is a difference in methods of study. Therefore, to obtain comparable data, it is advisable to conduct studies of the soil by agreed upon methods, using standardized apparatus.

References

1. GROMOV, V. V., A. K. LEONOVICH, A. D. DMITRIYEV et al., Mechanical Properties of Lunar Soil Samples Returned by the Luna 16 Automatic Station. *Kosmich. Issled.*, Vol. 9, No. 5, 1971.
2. LEONOVICH, A. K., V. V. GROMOV et al., Study of Physical-Mechanical Properties of a Lunar Soil Sample Returned by the Luna 20 Automatic Station and Along the Path of the Lunokhod 2 Self-Propelled Vehicle. *Report to the XXIV Congress IAF USSR, Baku, October 1973.*
3. ORNATSKAYA, N. V., *Soil Mechanics*, 1962.
4. LEONOVICH, A. K., V. V. GROMOV et al., Study of Mechanical Properties of Lunar Soil by the Lunokhod 1 Self-Propelled Vehicle. *Mobile Laboratory on the Moon: Lunokhod 1*, 1971.

Page intentionally left blank

Page intentionally left blank

The Radiation History of Material Returned by the Soviet Automatic Stations Luna 16 and Luna 20, According to Track Studies

L. L. Kashkarov, L. I. Genayeva, and A. K. Lavrukhhina,
*V. I. Vernadskiy Institute of Geochemistry
and Analytical Chemistry,
Moscow, U.S.S.R.*

Fission tracks formed by the vH (very heavy) nuclei group ($23 \lesssim Z \lesssim 28$) of solar and galactic cosmic rays have been studied in silicate minerals of the lunar regolith returned by the Luna 16 and Luna 20 unmanned spacecraft. It is shown that the material in the Luna 16 core sample, from a typical mare region of the lunar surface, has undergone stronger irradiation by cosmic rays than material returned from a highland region by Luna 20. A low-irradiation component (about 10 percent of the total number of crystals) has been found in the Luna 20 core sample materials, which can possibly be attributed to material added to the main bulk of the regolith in the formation of the crater Apollonius C. From the track density distribution of crystals, as a function of depth in the regolith core sample, it follows that the process of formation of the upper layer of the regolith, both for the lunar mare and for the highland region, includes sequential layering of finely crushed crystalline matter and subsequent mixing of it by micrometeorite bombardment. A portion of the crystals with a very high track density ($\gtrsim 10^9 \text{ cm}^{-2}$) may be a component added to the lunar surface from outer space.

Regolith core samples returned to Earth by Luna 16 and Luna 20 differ mainly in that the former is lunar soil from a mare region (Mare Fecunditatis) of the lunar surface (ref. 1) and the second is typical highland soil taken from the region between Mare Fecunditatis and Mare Crisium (ref. 2). Study and comparison of the history of formation of the material of these two regions on the lunar surface is of special importance for studying the processes that formed the lunar surface.

In the last decade, the use of microdestruction of crystal structures by the heavy nuclei of cosmic rays has become one of the most effective methods of studying the cosmic history of extraterrestrial material (ref. 3). In this case, areas of microdestruction in silicate minerals along the tracks of heavy nuclei with charge $Z \gtrsim 23$, can be detected in the

form of hollow channel-tracks. The tracks can be observed after appropriate chemical etching of the sample surface to be studied has been made by a scanning electron or optical microscope (refs. 4 and 5) as well as by a high-voltage electron microscope (ref. 6).

The present work reports the results of fission track studies in various minerals separated from the entire depth of the lunar regolith cores returned by Luna 16 and Luna 20 in order to compare the radiation histories of the upper layer of the lunar regolith taken from two different regions of the lunar surface. Observation and measurement of the basic characteristics of the tracks were accomplished by means of scanning electron and optical microscopes. The technique allowed a count to be made of track densities ($\rho_{\text{sem}}, \rho_{\text{opt}}$) at 10^4 and 10^3 magnification, re-

spectively, as well as measurements of the length and angular distribution of the tracks of the vH group nuclei of solar and galactic cosmic rays.

Crystals of olivine, feldspar, and pyroxene, 100–200 μm in size, were mounted in tablets of epoxy resin which were used to make polished sections and microsections and to enable subsequent etching. Control of mineralogical identification of the individual samples and the track etching efficiency under various conditions was accomplished by etching artificially induced tracks of ^{252}Cf fission fragments. Among the Luna 16 core samples studied, 50 percent were olivine, 30 percent were feldspar, and 20 percent were pyroxene. The Luna 20 regolith core was represented by olivine (8 percent), feldspar (67 percent), and pyroxene (25 percent). Chemical etching

of the olivine crystals was carried out for periods of 30 to 240 minutes by the method developed by Krishnaswami (ref. 7). Feldspar and pyroxene crystals were etched in a solution of 3g NaOH and 4g H_2O , for a period of 4 to 8 minutes and 20 to 60 minutes, respectively (ref. 8).

Up to the present time we have studied a total of 160 crystals from the Luna 16 regolith core and 294 crystals from the Luna 20 regolith core. It should be noted here that the track densities observed in different minerals may differ because of differences in their sensitivity for recording nuclei with $Z \lesssim 20$, as indicated by Bhandari (ref. 5). It was found that the density of tracks formed in lunar rock at a depth of about 100 μm was approximately the same for feldspar and pyroxene ($\rho_{\text{feld}} = \rho_{\text{px}}$), and that the

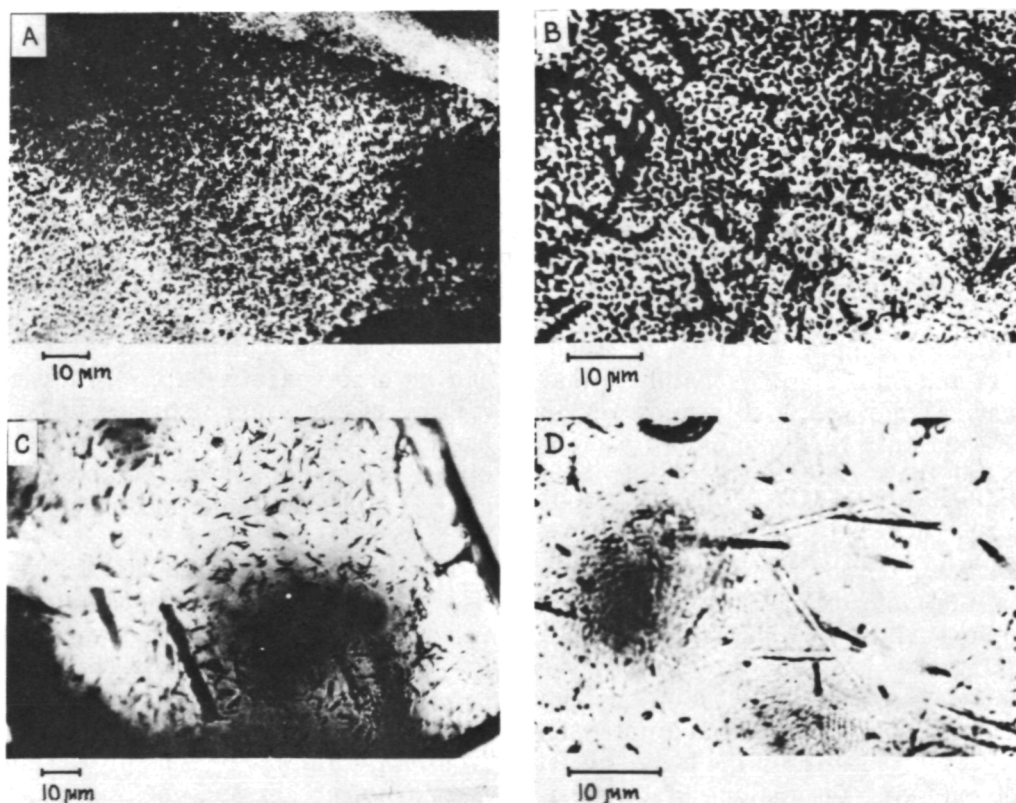


Figure 1.—Microphotographs of tracks observed under various examination conditions on etched surfaces of feldspar crystals from the Luna 20 core: A—scanning electron microscope $\rho \gtrsim 10^8 \text{ cm}^{-2}$; B—optical microscope, with long tracks seen on a background of short tracks $\rho_{\text{opt}} \lesssim 10^7 \text{ cm}^{-2}$; C, D—optical microscope, transmitted light, tracks with density $\rho_{\text{opt}} \lesssim 10^6 \text{ cm}^{-2}$ and $\rho_{\text{opt}} \gtrsim 10^6 \text{ cm}^{-2}$.

track density ratio $\rho_{\text{feld}}/\rho_{\text{ol}} \approx 2$, which characterizes olivine (ρ_{ol}) as the least sensitive track detector among the minerals studied. For our study, in a comparison of the results obtained, we allowed for the mineralogical composition of the regolith core samples—in particular, for the fact that 50 percent of the Luna 16 core samples studied were olivine, while olivine amounted to less than 10 percent in the Luna 20 core sample.

In the fission track studies, the principal attention was given to determining the extent of irradiation for the individual crystals, which was determined from the track densities observed in them. In this case, for estimation of the contribution of the vH group nuclei of solar and galactic cosmic rays to the track density, we used the following criteria:

1. The presence of a track density gradient in the interior of the crystals, related completely to the vH group of solar cosmic rays ($E_{\text{kinetic}} \lesssim 10$ MeV/nucleon), uniquely indicates irradiation of these crystals on the surface of the regolith, without any protective layer of material.

2. Excess values of the observed track densities $\rho_{\text{sem}} \lesssim 10^8 \text{ cm}^{-2}$ also assign the sample of those irradiated by the vH group nuclei solar cosmic rays in the upper ($\sim \text{mm}$) layer of the lunar regolith.

3. Crystals with track density $\rho_{\text{sem}} \lesssim 10^8 \text{ cm}^{-2}$ may contain a considerable portion of tracks, formed by the vH group nuclei of galactic cosmic rays, whose relative contribution increases in proportion to the decrease in observed track densities. On the basis of this dependence of track density on irradiation conditions, it becomes evident that crystals with track density of not over $\sim 10^6 \text{ cm}^{-2}$ contain traces of the effects of little but the heavy nuclei of galactic cosmic rays, and that they can be used to estimate the effective irradiation time in a layer of the regolith at a specific depth. In this case, the contribution of fragments from spontaneous fission of ^{238}U , whose concentration is not over 10^{-8} g/g , is only $\sim 10^4$ tracks per cm^2 .

A comparison of the track densities observed by means of the scanning electron

(ρ_{sem}) and optical (ρ_{opt}) microscopes was made on a large number of crystals in the ρ_{sem} range from $\sim 10^6$ to $\sim 10^9 \text{ cm}^{-2}$. Examples of microphotographs of tracks observed under various conditions are presented in figure 1. Figure 2 is a microphotograph of a section of feldspar crystal (Luna 20), with a clearly expressed track density gradient and the corresponding histograms of change in track density with depth in the sample, as obtained by both optical and scanning electron microscopes (ref. 9). As seen from a comparison of the histograms, a similar distribution of track density with depth in the crystal is given by the data from the optical and scanning electron microscopes. However, under our conditions of etching and examination, $\rho_{\text{sem}} - \rho_{\text{opt}}$ for $\rho_{\text{sem}} \lesssim 10^8 \text{ cm}^{-2}$. With increasing track density, the ratio $\rho_{\text{sem}}/\rho_{\text{opt}}$ changes from two to five times, with increase in track density ρ_{sem} from $1.2 \times 10^8 \text{ cm}^{-2}$ to $5 \times 10^8 \text{ cm}^{-2}$. For large values of ρ_{sem} ($\gtrsim 5 \times 10^8 \text{ cm}^{-2}$), the divergence between ρ_{sem} and ρ_{opt} increases.

Results

TRACK DENSITY GRADIENT IN INDIVIDUAL CRYSTALS

As known (ref. 10), observation of the track densities due to the vH group nuclei of cosmic rays, at various depths in crystals, is determined by the flux, free path length, and energy spectrum of the nuclei forming the tracks. Moreover, under irradiation conditions similar to those of the lunar surface, change in track density with depth in individual crystals also depends on their size, extent of erosion, and depth of occurrence in the regolith layer. In connection with this, the magnitude of the track density gradient, defined by the degree of change in track density with depth in the crystals, depends on many factors that cannot be quantitatively accounted for. However, in the study of crystals with maximum track density gradient values, it appears possible to obtain a quantitative characterization of the energy spectra

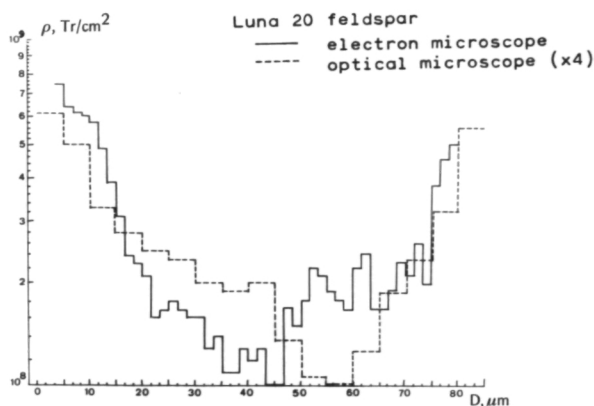
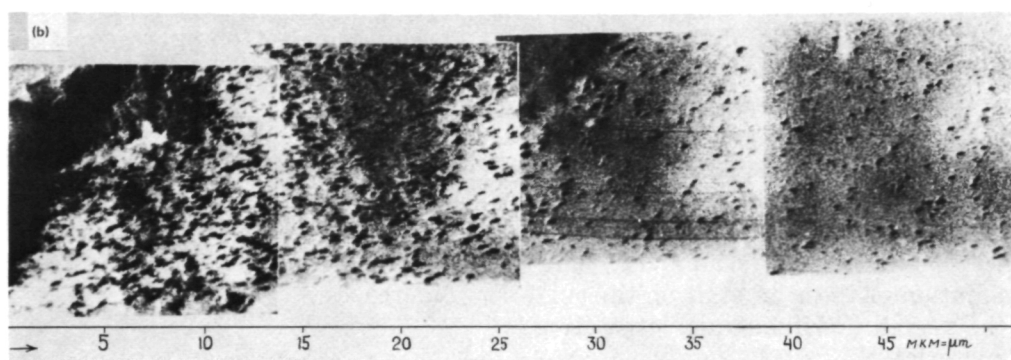


Figure 2.—Track density gradient in feldspar crystal from the Luna 20 core from scanning electron and optical microscope data.



of the heavy nuclei of solar cosmic rays. Moreover, as was pointed out above, we use the fact of the presence or absence of the gradient to estimate the degree of irradiation of the regolith material, a specific part of which was subjected to irradiation on the lunar surface without any protective layer.

Of the total number of crystals from the Luna 16 and Luna 20 regolith core samples studied up to the present time, the fraction of samples with a track density gradient is 30 percent and 5 percent, respectively. The magnitude of the gradient for all samples varies from a twofold to a tenfold change in track density at a depth of $100\mu\text{m}$ (see figs. 2 and 3). The exponent γ , corresponding to the maximum values of the track density gradient, in the formula for the differential energy spectrum of the vH group nuclei, $J = \text{const} \cdot E^{-\gamma}$, is 1.5 to 2 (ref. 11) which is in agreement with other results (refs. 12, 13, and 14).

The results of the measurement of track

density gradient which we obtained showed the following:

1. The relative number of crystals with a track density gradient for the Luna 16 soil is six times that for the Luna 20 core sample, which can be explained by the difference in formation processes for the upper layer of the regolith in the lunar mare and highland regions. In the first case, formation of the upper layer of the regolith, owing to the level terrain, could have taken place by filling and mixing of thinner layers, while in the second case, owing to the presence of highlands, the growth of the regolith layer could have occurred more intensely. Furthermore, the exposure age of the regolith in the mare region of the Moon may be greater on the average than that in the highlands, where formation of the upper layer of the regolith could have occurred at a later time by accumulation of finely crushed material, as a result of meteorite bombardment of nearby bedrock. The

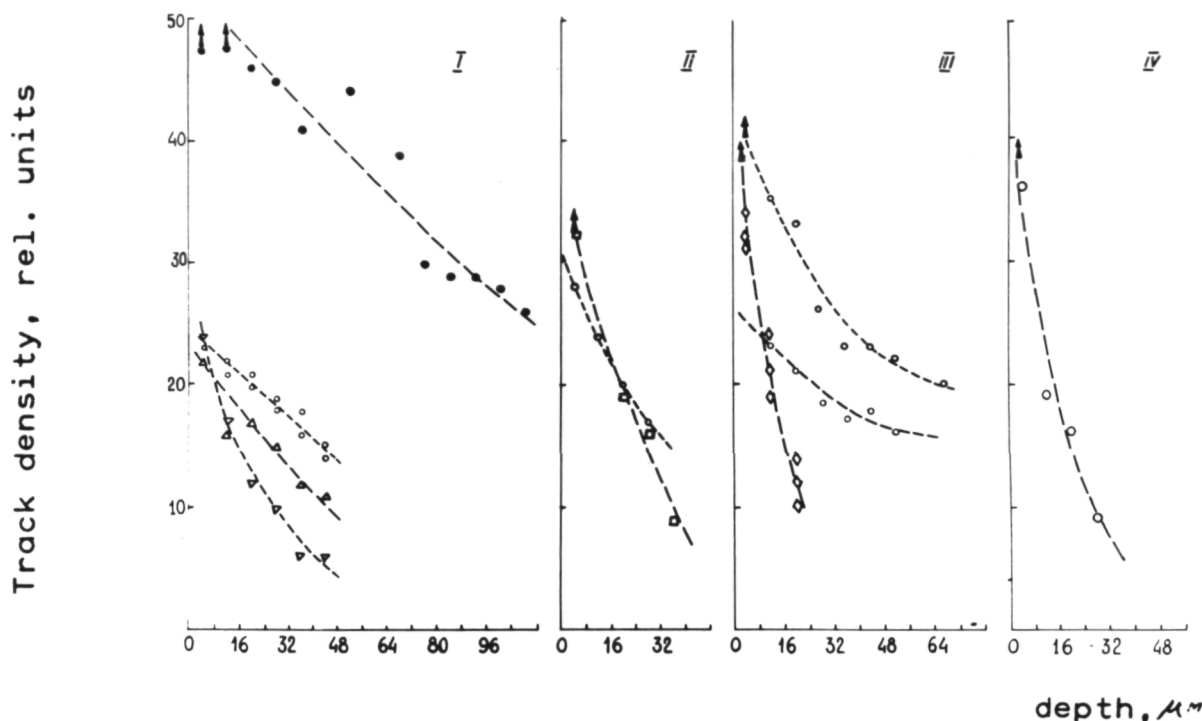


Figure 3.—Examples of track density gradients observed in various crystals from the Luna 16 and Luna 20 cores.

limits of change in track density gradients were the same for both regolith core samples.

2. The size of the gradient in individual crystals does not depend on the absolute track density or the mineralogical composition of the crystals.

Among the crystals having track density gradients, a small number (~ 1 percent) is encountered in which the track densities change from the surface inward from practically all sides. Examples of two such crystals of feldspar from the Luna 20 core sample are presented in figure 4. This track density distribution with depth in the crystals may be the result of uniform irradiation of the crystals from all sides, or of their repeated displacement on the surface of the lunar regolith, or of irradiation of these samples in space. The predominant fraction of the crystals has only a local, one-sided track density gradient, which also can be considered from two points of view: either these crys-

tals were irradiated under 2π -geometry, because of being on the surface of the lunar regolith; or they are fragments of larger (\gtrsim mm) primary objects, irradiated in the free state before falling to the lunar surface and being broken up after this irradiation.

DISTRIBUTION OF CRYSTALS ACCORDING TO THEIR TRACK DENSITY

The results of track density measurements (ρ_{opt}) in crystals separated from various depth zones of the Luna 16 and Luna 20 regolith cores are presented in table 1 and as histograms in figure 5. On the basis of distribution of the crystals studied according to their track densities, three groups can be distinguished with the following ranges of track density: I, $\rho_{\text{opt}} \lesssim 10^6 \text{ cm}^{-2}$; II, $10^6 \lesssim \rho_{\text{opt}} \lesssim 10^7 \text{ cm}^{-2}$; and III, $\rho_{\text{opt}} \gtrsim 10^7 \text{ cm}^{-2}$. Comparison of the data obtained for Luna 16 and

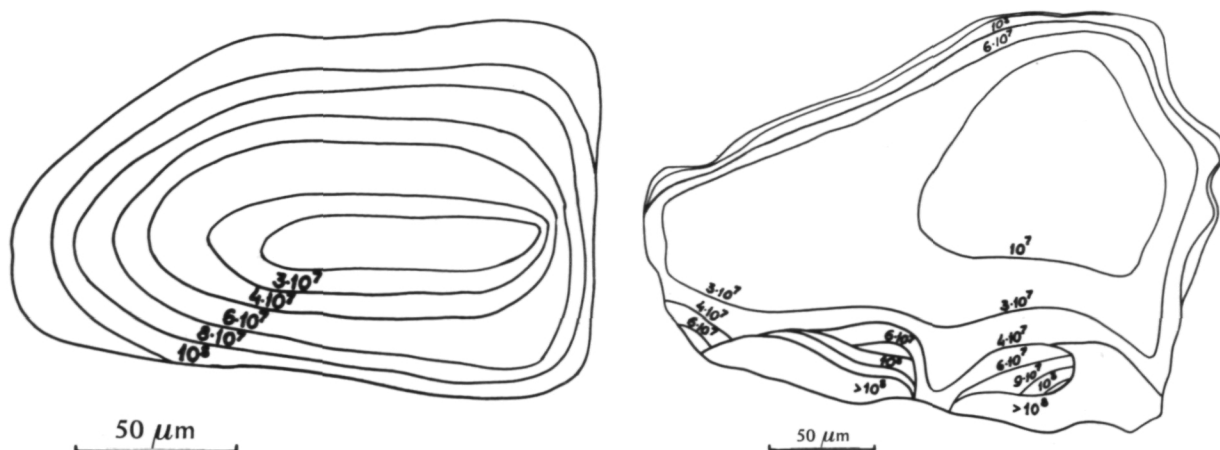


FIGURE 4.—Track density distribution (in cm^{-2}) as a function of depth in crystals that have undergone irradiation from all sides.

Luna 20 regolith core samples reveals the following features:

1. Among the samples from the Luna 16 regolith core, crystals with $\rho_{\text{opt}} \lesssim 10^6 \text{ cm}^{-2}$ are not encountered, while the fraction of such crystals in the Luna 20 regolith core is about 10 percent.

2. In the track density range less than 10^7 cm^{-2} , the number of Luna 16 and Luna 20

crystals on the average is 5 percent and 35 percent, respectively, over the entire depth of the core sample, which also indicates a significant difference in the degree of their irradiation.

3. The relative fraction of strongly irradiated crystals with track density $\rho_{\text{opt}} \gtrsim 10^7 \text{ cm}^{-2}$ is 95 percent and 65 percent for the Luna 16 and Luna 20 regolith cores, respectively.

Table 1.—Observed Distribution of Crystals From Different Zones of the Luna 16 and Luna 20 Regolith Cores by Track Density From *vh* Group Nuclei of Cosmic Rays

Rego- lith Site	Depth Zone in the Core (cm) ^a	Average Number of Crystals Studied	The Fraction (%) of crystals		
			With Track Density $\rho_{\text{opt}} \text{ cm}^{-2}$		
			$< 10^6$	10^6-10^7	$\gtrsim 10^7$
1	2	3	4	5	6
Luna 16	A (0-7)	50	—	4	96
	B (7-15)	38	—	—	100
	C (15-28)	31	—	7	93
	D (28-33)	41	—	10	90
	Average	160	—	5	95
Luna 20	I (0-5)	69	7	20	73
	II (5-10)	53	6	29	65
	III (10-15)	116	15	25	60
	IV (15-20)	56	12	27	61
	Average	294	10	25	65

NOTE: (1) Subdivision of the Luna 16 regolith core is according to Vinogradov (ref. 1). The Luna 20 core was subdivided into zones of equal length (about 20 cm), beginning with upper zone I.

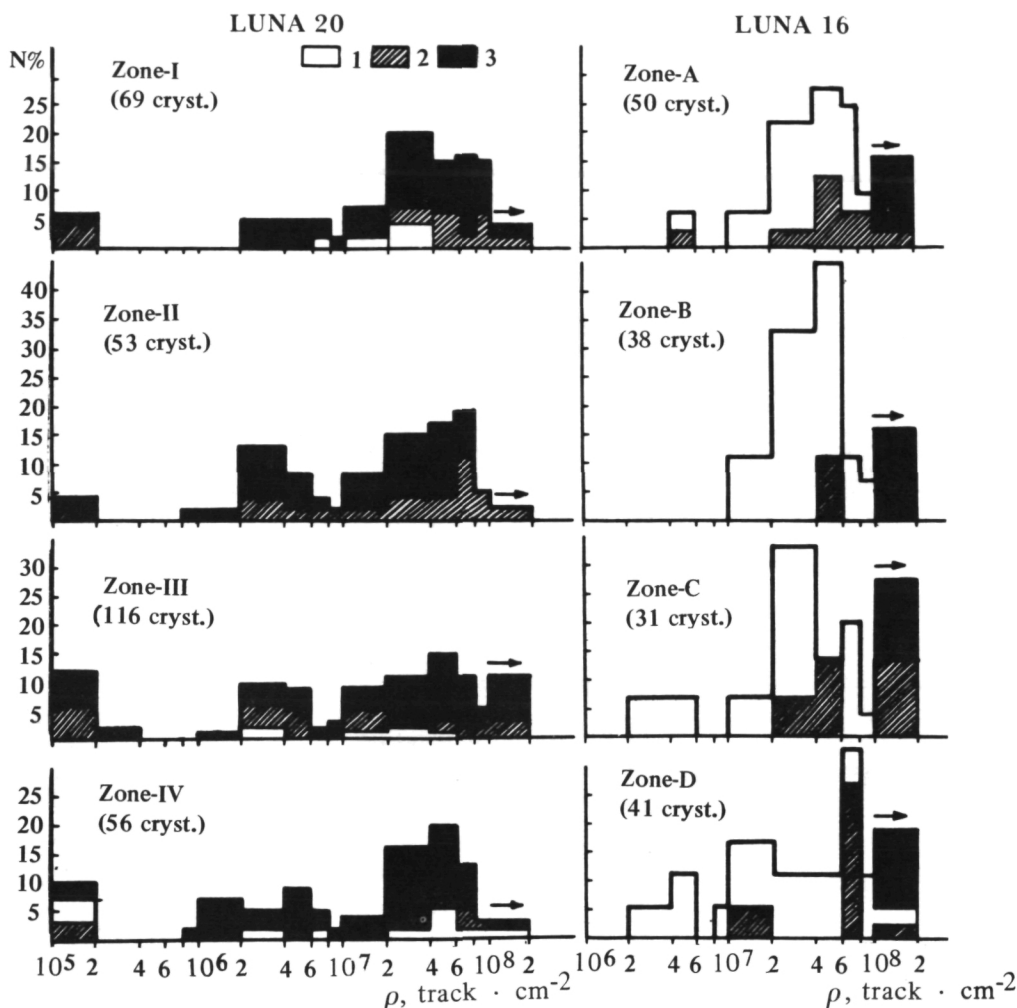


Figure 5.—Track density distribution histograms for feldspar, olivine, and pyroxene crystals, from various zones of the Luna 16 and Luna 20 cores: 1—olivine; 2—pyroxene; and 3—feldspar.

It also can be noted that the relative number of least irradiated samples studied, from both the Luna 16 and Luna 20 station regolith core samples (see table 1), approximately doubles for the deeper zones. At the same time, there is no depth dependence in the distribution of crystals having a high track density.

The question was examined as to whether or not the observed differences in the track density distribution of the crystals might be a consequence of differences in the mineralogical composition of the Luna 16 and Luna 20 regolith cores. First, as was pointed out above,

the track density in feldspar (and pyroxene) is approximately double the track density recorded by olivine under the same irradiation conditions. Correction to the observed track density for the difference in effectiveness (see table 1, column 5), leads only to a decrease in the percentage of slightly irradiated crystals in the Luna 16 core sample. Second, the average particle size distribution of the Luna 16 and Luna 20 core samples is approximately the same (refs. 1 and 2). Therefore, the observed differences in the distribution of crystals according to their track density should not be connected with possible differential

erosion effects on particles of different mineralogical composition.

For a quantitative comparison of the average degree of irradiation of the Luna 16 and Luna 20 lunar regolith material by cosmic rays, as well as for comparison with the results of investigations of other lunar samples, we calculated two parameters by analogy with Arrhenius et al (ref. 4): N_H/N , which characterizes the fraction of crystals irradiated by low-energy nuclei of the vH group of solar cosmic rays during their passage through the upper layer of the regolith, and ρ_q , the track density corresponding to the distribution of all samples studied, of which 25 percent have a track density below ρ_q . The quantity N_H/N , calculated on the basis of our results for crystals from the Luna 16 and Luna 20 cores, gave 0.45 and 0.37, respectively. Crystals with $\rho_{sem} \lesssim 10^8 \text{ cm}^{-2}$ were used in calculation of N_H . It is evident from the data presented that only $\sim 1/3$ of all the crystals studied from the Luna 20 core sample have traces of the action of low-energy solar cosmic rays. Among the Luna 16 samples we studied, about one-half of the crystals have $\rho_{sem} \lesssim 10^8 \text{ cm}^{-2}$. The track densities ρ_q of various zones of the Luna 16 and Luna 20 cores are between 1 to $3 \times 10^7 \text{ cm}^{-2}$ and 0.4 to $2 \times 10^7 \text{ cm}^{-2}$, respectively. Comparison of the results obtained with other results (refs. 4, 15, and 16) indicates that the Luna 20 regolith is among the least irradiated samples of material returned from the lunar surface. One can assume that the regolith at the Luna 20 landing site, compared with the regolith returned by Luna 16, consists mainly (about 65 percent) of material, similar in degree of irradiation to the Luna 16 regolith material, and has a considerable (about 35 percent) fraction of an added component with a lower track density.

EXPOSURE AGE OF THE REGOLITH IN THE SURFACE LAYER

The rate of accumulation of tracks (ρ) from the vH group nuclei of solar and galactic cosmic rays changes as a function of the

depth (X) of the sample in the regolith layer. Nuclei of the vH group of solar cosmic rays are almost completely absorbed in the upper layer $X \lesssim 1 \text{ mm}$; and in agreement with the data of Arrhenius (ref. 4), at a depth of 0.1 mm a track density of over 10^7 cm^{-2} is accumulated in 1 million years. Heavy nuclei of galactic cosmic rays with energies $E_{kin} \gtrsim 100 \text{ MeV/nucleon}$ penetrate to a greater depth and, for $X \approx 10 \text{ cm}$, a track density $\rho \gtrsim 10^4 \text{ cm}^{-2}$ accumulates in the same time (ref. 17). On the basis of this ratio of track density, due to heavy nuclei of solar and galactic rays, it becomes possible to estimate the effective time of track accumulation from galactic cosmic rays by using the minimum observed track density in the crystals. For example, about 10 percent of the crystals separated from zone D of the Luna 16 regolith core have a track density of not over 10^7 cm^{-2} . An estimate of the radiation age of these samples by galactic cosmic rays gives a value of $\approx 450 \times 10^6$ years in this case, which agrees well with the results of Lavrukhina et al. (ref. 18). The lowest track density ($\rho \gtrsim 10^6 \text{ cm}^{-2}$) obtained for samples from the Luna 20 core corresponds to an accumulation time $T_{gal} \gtrsim 20$ million years, if the samples were under a regolith layer more than 10 cm deep. This age can be assumed as the upper limit of the time since the event that added to the Luna 20 regolith about 10 percent of material which had been practically unexposed to cosmic rays.

In the Luna 16 and Luna 20 core samples studied, crystals were encountered that contained a track density exceeding 10^9 to 10^{10} cm^{-2} at a depth of about $100 \mu\text{m}$. On the average, such crystals constituted 5 to 7 percent of both core samples. For accumulation of such a high track density from the vH group nuclei of solar cosmic rays at the present intensity and for crystals located in a surface layer $\sim 1 \text{ mm}$ thick, a time in excess of tens of millions of years is necessary. Observation of high track densities in microcrystals of lunar dust also was reported earlier by Price et al. (ref. 14). This confirms the idea of Gold (ref. 19) that microcrystals of lunar soil with very high track densities can perhaps be at-

tributed to material which was in the free state in space before falling to the surface of the Moon.

Lunar dust particles a few microns in size from the Luna 16 core which were studied earlier (ref. 6) using a high-voltage electron microscope and without preliminary chemical etching, almost all exhibited a track density of over 10^{10} cm^{-2} . These tracks, observed in layers of micron thickness, may be entirely the result of low-energy vH group nuclei of solar cosmic rays. Consequently, the majority of microcrystals in the Luna 16 core must have been subject to such irradiation. However, the low probability of this process also leads to the suggestion that the strongly irradiated material of the lunar regolith is possibly a component that has been added to the lunar surface material from outside.

Conclusions

The following conclusions can be drawn from the data obtained.

1. The track density distributions of crystals from the Luna 16 and Luna 20 cores differ in that a comparatively large amount of less irradiated (with $\rho_{\text{opt}} \lesssim 10^7 \text{ cm}^{-2}$) material is present in the Luna 20 sample, and a considerable excess of highly irradiated material (with $\rho_{\text{opt}} \gtrsim 10^7 \text{ cm}^{-2}$) is present in the Luna 16 sample. This characterizes the regolith material in the Luna 16 landing area (Mare Fecunditatis) as having undergone a stronger degree of cosmic irradiation during its exposure age of ~ 500 million years (ref. 18) than the highland material returned by Luna 20.

2. About 10 percent of the Luna 20 core material is weakly irradiated by heavy nuclei of galactic cosmic rays with $\rho_{\text{opt}} \lesssim 10^6 \text{ cm}^{-2}$. It is possible that this component was brought up from deep layers of the lunar surface during the formation of the crater Apollonius C and added to the main bulk of regolith, as was suggested by Vinogradov (ref. 2). On the basis of the fact that the observed minimum track density is attributed completely to vH group nuclei of galactic cosmic rays, the age

of this event is estimated at less than ~ 20 million years.

3. Regardless of the depth of occurrence of the crystals studied in the Luna 16 and Luna 20 cores, specimens are encountered which bear traces of the action of low-energy vH group nuclei of solar cosmic rays. This indicates that formation of the upper regolith layer, in both the lunar mare and highland regions, includes sequential layering of finely fragmented crystalline material and subsequent mixing of it by micrometeorite bombardment.

4. The crystals with a very high track density (10^9 to 10^{10} cm^{-2}) can be attributed to material possibly brought to the lunar surface from space.

Acknowledgment

The authors express their thanks to A. P. Vinogradov for constant interest and attention to the work, as well as to L. L. Tarasov and A. V. Ivanov for selection of lunar samples.

References

1. VINOGRADOV, A. P., *Geokhimiya*, Vol. 3, 1971, p. 261.
2. VINOGRADOV, A. P., *Geokhimiya*, Vol. 7, 1972, p. 763.
3. FLEISCHER, R. L., P. B. PRICE, AND R. M. WALKER, *Ann. Rev. Nucl. Sci.*, Vol. 15, 1965, p. 1.
4. ARRHENIUS, G., S. LIANG, D. MACDOUGALL, L. WILKENING, N. BHANDARI, S. BHAT, D. LAL, G. RAJAGOPALAN, A. S. TAMBANE, AND V. S. VENKATAVARADAN, *Geochimica et Cosmochimica Acta*, Supplement 2, Vol. 3, 1971, p. 2583.
5. BHANDARI, N., J. N. GOSWAMI, D. LAL, D. MACDOUGALL, AND A. S. TAMBANE, *Proc. Indian Acad. Sci.*, Vol. 77, No. 1, Sec. A, 1972, p. 27.
6. BORG, ZH., D. DVURRO, K. ZHURE, L. L. KASHKAROV, AND M. MORETT, *Lunar Soil from Mare Fecunditatis*, 1974, p. 444.
7. KRISHNASWAMI, S., D. LAL, N. PRABHU, AND A. S. TAMBANE, *Science*, Vol. 174, 1971, p. 287.
8. LAL, D., A. V. MURALI, R. S. RAJAN, A. S. TAMBANE, J. C. LORIN, AND P. PELLAS, *Earth Planet. Sci. Letters*, Vol. 5, 1968, p. 111.

9. KASHKAROV, L. L., A. K. LAVRUKHINA, L. I. GENAYEVA, M. K. ANTOSHIN, AND G. V. SPIVAK, *Rep. on COSPAR*, 1974.
10. FLEISCHER, R. L., P. B. PRICE, R. M. WALKER, AND M. MAURETTE, *J. Geophys. Res.*, Vol. 72, 1967, p. 331.
11. LAVRUKHINA, A. K., V. D. GORIN, L. L. KASHKAROV, AND G. K. USTINOVA, *Izv. Acad. nauk SSSR, ser. fiz.*, Vol. 38, No. 9, 1974, p. 1806.
12. CROZAS, G., U. HAACK, M. HAIR, M. MAURETTE, R. WALKER, AND D. WOOLUM, *Geochimica et Cosmochimica Acta* 34, Supplement 1, Vol. 3, 1970, p. 2051.
13. LAL, D., *Space Sci. Rev.*, Vol. 14, 1972, p. 3.
14. PRICE, P. B., J. H. CHAN, I. D. HUTCHEON, D. MACDOUGALL, R. S. RAJAN, E. K. SHIRK, AND J. D. SULLIVAN, *Geochimica et Cosmochimica Acta*, Supplement 4, Vol. 3, 1973, p. 2347.
15. COMSTOCK, G. M., R. L. FLEISCHER, AND H. R. HART, *Earth Planet. Sci. Letters*, Vol. 13, 1972, p. 407.
16. CROZAS, G., R. WALKER, AND D. ZIMMERMAN, *Geochimica et Cosmochimica Acta* 37, 1973, p. 825.
17. FLEISCHER, R. L., H. R. HART, AND W. R. GIARD, *Geochimica et Cosmochimica Acta*, Vol. 3, 1973, p. 2307.
18. LAVRUKHINA, A. K., AND V. D. GORIN, *Space Research*, Vol. 13, 1973, p. 991.
19. GOLD, T., *The Moon*, Vol. 7 Nos. 3 and 4, 1973, p. 293.
20. KASHKAROV, L. L., M. MORETT, P. MORIS, AND B. VASSAN, *Report to VIII International Conference on Nuclear Photography and Dielectric Track Detectors*, Rumania, 1972.
21. KASHKAROV, L. L., A. K. LAVRUKHINA, AND L. I. GENAYEVA, *Lunar Soil from Mare Fecunditatis*, 1974, p. 241.

Antipodes on the Moon

Yu. N. Lipskiy and Zh. F. Rodionova
*Shternberg State Astronomical Institute,
Moscow, U.S.S.R.*

Cartographic methods are presently used to study not only the Earth, but also the Moon and Mars, and will soon be used for Mercury and other planets. These methods will remain for some time the only possible methods for determination of many quantitative characteristics of surface formations such as coordinates of objects in various systems, linear dimensions of formations, areas of flat surfaces and higher order surfaces, volumes of various objects, and relative indices and characteristics.

In the department of physics of the Moon and planets of the Shternberg State Astronomical Institute (GAISH), cartometric work was done in order to determine the areas of the lunar maria and large craters. The areas of the maria were determined twice in 1968 using a photomap of the visible hemisphere at a scale of 1:5 million (ref. 1) and segments of a lunar globe (ref. 2), and in 1971 using a full map of the Moon (ref. 3). The results of the measurements of areas of the maria are presented in table 1, together with the data of Westfall (ref. 4) and Shoemaker and Hackmann (ref. 5). Table 2 presents the areas of circular maria, measured from the peaks of the surrounding ridges, and their mean diameters calculated from the area.

The lunar surface is characterized by asymmetry in the locations of maria. On the visible hemisphere, lava flows occupy an area of 5937 million km² or 31.2 percent; on the back side, 474 000 km² or 2.5 percent. The northern hemisphere contains 4351 million km² or 22.9 percent; the southern hemisphere 2060 million km² or 10.8 percent. In the west-

ern hemisphere are 3891 million km² or 20.0 percent, and in the eastern hemisphere 2521 million km² or 13.3 percent. Over the entire surface of the moon, maria-type formations occupy 6411 million km² or 16.9 percent of the surface area. Figure 1a presents a diagram of the placement of maria-type formations within 10-degree bands of latitude by quadrants. Some 65 percent of all maria formations are concentrated within latitudes of + 40° to - 10°.

Thalassoids and large craters over 100 km in diameter occupy the same amount of area as all of the maria taken together—16.5 percent. In the northern hemisphere, large craters cover an area of 2371 million km², and in the southern hemisphere 3870 million km². The visible hemisphere contains 1906 million km² of these formations; the back hemisphere contains 4344 million km². Table 3 presents the distribution of large craters by hemispheres. Based on measurements of the areas of large craters, a histogram has been constructed of the dependence of the number of craters on diameter (see fig. 2a). This distribution can be approximated by a curve generated by $y = A e^{-Bx}$. The coefficients $A = +138$, $B = +0.45$ were found by the method of least squares. This curve agrees well with the empirical distribution of craters with diameters of 100 to 300 km according to the criterion of Kolmogorov. Craters over 300 km in diameter predominate on the reverse side, where there are 12 in this range. Figure 2b shows that thalassoids have the same dimensions as do the circular maria and form a special group of formations, which has already been noted (refs. 6 and 7). The 11

Table 1.—*Areas of Maria Formations Measured by Various Authors (in thousands of km²)*

Area	Shoemaker Hackmann 1961	Rodionova 1968	Westfall 1970	Rodionova 1971
Visible Side				
Oceanus Procellarum	—	2102	2147	2102
Mare Imbrium	864	830	835	829
Mare Frigoris	439	347	433	436
Mare Tranquillitatis	402	430	408	421
Mare Fecunditatis	311	311	334	326
Mare Serenitatis	318	305	312	303
Mare Nubium	261	253	240	254
Mare Crisium	165	180	197	176
Mare Humorum	107	113	115	113
Mare Smythii	—	109	77	104
Sinus Roris	—	107	291	—
Mare Nectaris	96	96	99	101
Mare Cognitum	—	73	—	—
Lacus Somniorum	65	66	66	72
Mare Marginis	—	64	82	62
Mare Vaporum	—	51	53	55
Sinus Medii	33	48	49	52
Sinus Aestuum	36	—	43	40
Sinus Iridum	—	—	—	39
Palus Epidemiarum	29	40	29	27
Mare Humboldtianum	99	23	28	22
Mare Undarum	—	13	19	21
Palus Putredinis	—	—	14	12
Mare Spumans	—	14	14	16
Mare Veris	—	20	16	12
Lacus Mortis	41	—	14	12
Mare Anguis	—	8	—	10
Mare Struve	—	—	—	4
Mare Autumni	—	—	4	3
Mare Aestatis	—	4	4	1
Far Side				
Mare Australe	—	147	148	151
Mare Orientale	—	65	60	54
Mare Moscoviense	—	67	49	50
Mare Ingenii	—	—	27	15
Mare Pacificus	—	20	—	13

Table 2.—Areas of Circular Seas Measured From Surrounding Ridges

Area	Area Thousands of km ²	Diameter, km	Note
Mare Imbrium	958	1104	
Mare Orientale	725	961	From Cordillera
	356	642	From Rook Mountains
Mare Nectaris	417	729	From Rupes Altai
	134	413	From Pyrenaeus
Mare Serenitatis	356	641	
Mare Crisium	209	516	
Mare Moscoviense	166	460	
Mare Humorum	153	442	
Mare Smythii	147	433	
Mare Ingenii	93	344	
Sinus Iridium	52	258	
Mare Humboldtianum	51	254	
Lacus Mortis	25	180	

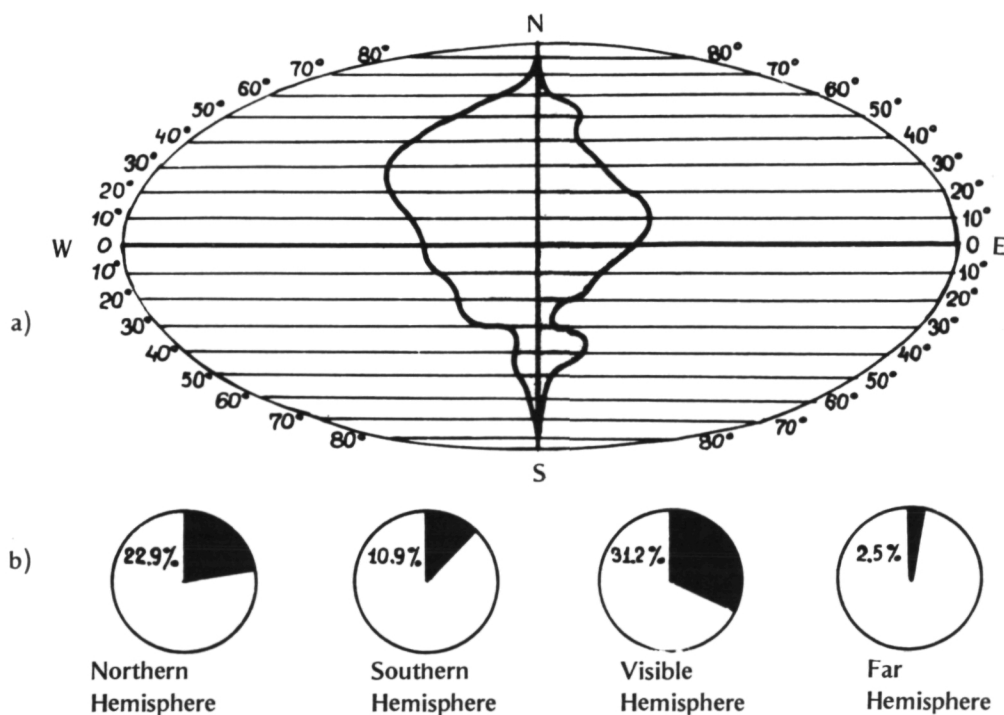
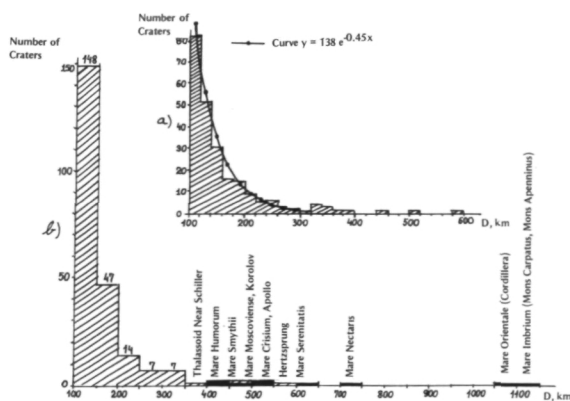


Figure 1.—Distribution of maria areas.

Table 3.—*Distribution of Craters Over 100 km in Diameter by Hemispheres*

Diameter, km	On Visible Hemisphere	Number of Craters		In Southern Hemisphere	Entire Surface
		On Far Hemisphere	In Northern Hemisphere		
100–120	37	46	31	52	83
120–140	26	26	20	32	52
140–160	16	15	12	19	31
160–180	5	11	7	9	16
180–200	5	10	7	8	15
200–220	5	4	4	5	9
220–240	1	4	3	2	5
240–260	2	4	3	3	6
260–280	—	2	—	2	2
280–300	2	—	—	2	2
300–320	—	—	—	—	—
320–340	—	4	1	3	4
340–360	—	3	2	1	3
360–380	1	—	—	1	1
380–400	—	1	1	—	1
400–420	—	—	—	—	—
420–440	—	—	—	—	—
440–460	—	2	1	1	2
460–480	—	—	—	—	—
480–500	—	—	—	—	—
500–520	—	1	—	1	1
520–540	—	—	—	—	—
540–560	—	—	—	—	—
560–580	—	—	—	—	—
580–600	—	1	1	—	1

Figure 2.—*Histogram of the number of craters, according to their diameters.*

formations on the back side over 300 km in diameter correspond to maria formations diametrically opposite on the visible side. Figure 3 shows a diagram of the antipodes, listed in table 4. This diagram shows the contours of the maria on the visible side between the $\pm 60^\circ$ parallels and their antipodes on the opposite side, arbitrarily shown in the areas diametrically opposite. The roman numerals on the map and in the table represent formations on the visible side; the arabic numerals, the far side. Only Birkhoff crater (342 km diameter) fails to fall within this group. It is on a common diameter with a continental area and the area of highest elevation on the visible side.

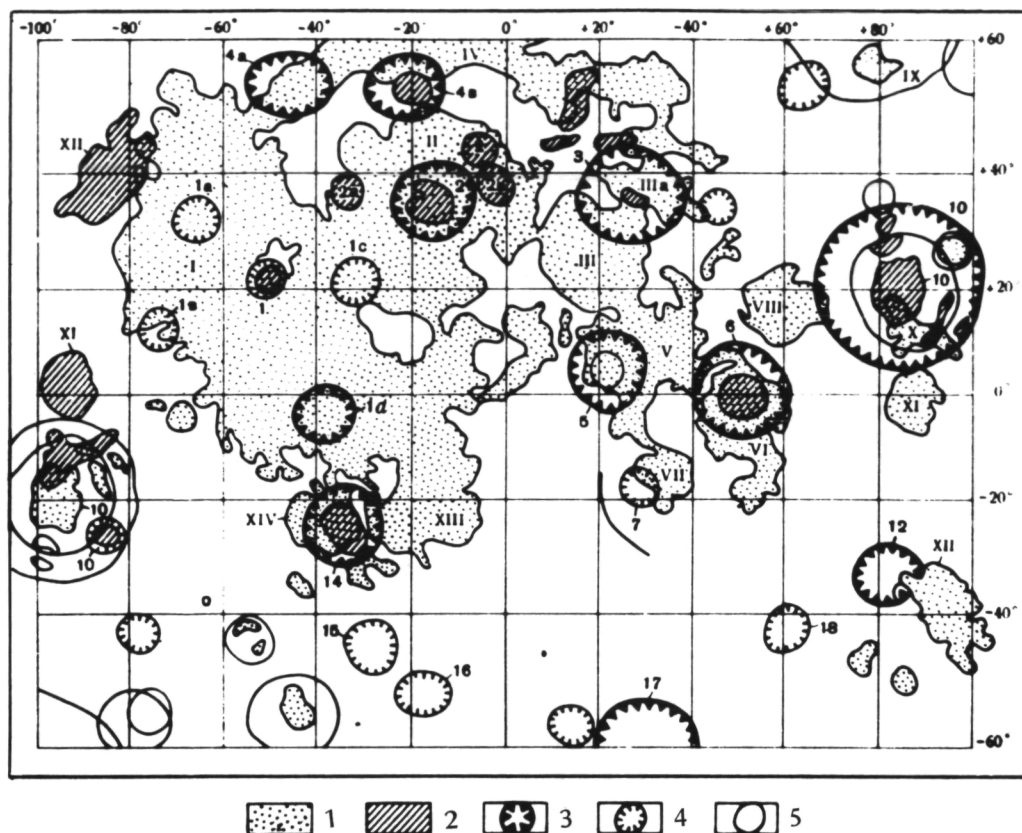


Figure 3.—Map of the antipodes on the Moon. Maria features: 1—on the nearside; 2— on the farside; 3,4—thalassoids and craters on the farside ($D > 300$ km, $200 < D < 300$ km, accordingly; 5—on the nearside.

Of the 11 craters 200 to 300 km in diameter on the far side, eight are antipodes of maria formations on the visible side, and three fall in the same continental areas as does Birkhoff.

Yet another peculiarity has been noted in the distribution of thalassoids and large craters (over 200 km diameter) on the surface of the Moon: most of them are located within the limits of 2 mutually perpendicular circles. The first circle has an inclination to the equator, $i = +37^{\circ}16'$ and intersects the equator at point $\Omega = -81^{\circ}45'$. It passes through the following formations (see fig. 4):

1. Oppenheimer—207 km diameter
2. Apollo—502 km
3. Mare Orientale—961 km
4. Oceanus Procellarum

5. Mare Imbrium—1104 km
6. Mare Serenitatis—641 km
7. Lacus Somniorum
8. Mare Crisium—516 km
9. Mare Marginis
10. Mare Smythii—433 km
11. Pasteur—251 km
12. Fermi—206 km
13. Tsiolkovskiy—189 km
14. Gagarin—269 km
15. Mare Ingenii—344 km
16. Leibnitz—247 km
17. Kármán—198 km
18. Poincaré—339 km

The primary mascons are also located along this circle in Mare Imbrium, Mare Serenitatis, Mare Crisium, and Mare Smythii.

The second circle has an inclination $i =$

Table 4.—*Table of Antipodes on the Moon*

Visible Hemisphere	Far Hemisphere
I Oceanus Procellarium	1 Tsiolkovskiy ⁽¹⁾ —189 km, ⁽²⁾ 1a Milne—250 km, 1b Pasteur—251 km, 1c Gagarin ⁽¹⁾ —269 km, 1d Mendeleev—345 km
II Mare Imbrium	2a Mare Ingenii ⁽¹⁾ —344 km, 2b Leibnitz ⁽¹⁾ —247 km 2c Kármán ⁽¹⁾ —198 km
III Mare Serenitatis	3 Apollo ⁽¹⁾ —502 km
IIIa Lacus Somniorum	
IV Mare Frigoris	4 Planck—332 km, Poincaré ⁽¹⁾ —339 km
V Mare Tranquillitatis	5 Korolev—450 km
VI Mare Fecunditatis	6 Hertzspring ⁽¹⁾ —586 km
VII Mare Nectaris	7 Mach—196 km
VIII Mare Crisium	
X Mare Marginis	10 Mare Orientale ⁽¹⁾
XI Mare Smythii	
XII Mare Australe	12 Lorentz—340 km
XIV Mare Humorum	14 Mare Moscoviense ⁽¹⁾ —460 km
Bailly	Swartzschild—214 km
Unnamed Maria Surface North of Hershel	Schrödinger ⁽¹⁾ —324 km

NOTES: (1) Basins with bottom partially covered by lava.

(2) Diameter of basins in kilometers based on outer edge.

— 52°44' and $\Omega = 124^\circ 50'$ and passes through:

1. Birkhoff—342 km
2. Landau—226 km
3. Lorentz—340 km
4. Gerard Q—217 km
5. Oceanus Procellarum
6. Mare Humorum—442 km
7. Palus Epidemiarum
8. Mare Nubium
9. Deslandres—218 km
10. Mare Australe
11. Humboldt—205 km
12. Mare Moscoviense—460 km
13. Campbell—228 km
14. D'Alembert—227 km.

This circle passes through the mascon in Mare Humorum.

Large formations not included in the two main circles include: Planck—332 km, Schrödinger—342 km. Bailly—295 km, the thalassoid near Schiller on the visible side (coordinates at center 56°S, 46°W)—367 km, Schick-

ard—206 km, Swartzchild—214 km, located on the third circle, passing along meridians —46°, 134° and perpendicular to the contemporary equator, on which are located such large formations as: Korolev—450 km, Hertzprung—586 km, Oceanus Procellarum, Sinus Medii, Mare Tranquillitatis, Mare Fecunditatis, and Al-Khwarizmi discovered by Farouk El-Baz (ref. 8). We should also note the meridional placement (along $\pm 90^\circ$) of such formations as: the Mare Humboldtianum, Mare Marginis, Mare Smythii, Mare Australe, Mare Orientale, and Lorentz.

This distribution of large formations indicates the great importance of continued study of various characteristics along these belts (determination of crustal thickness, tectonic, age, and other peculiarities).

References

1. *Photographic Map of the Visible Hemisphere of the Moon; 1:5 Million Scale*, Nauka Press, 1967.

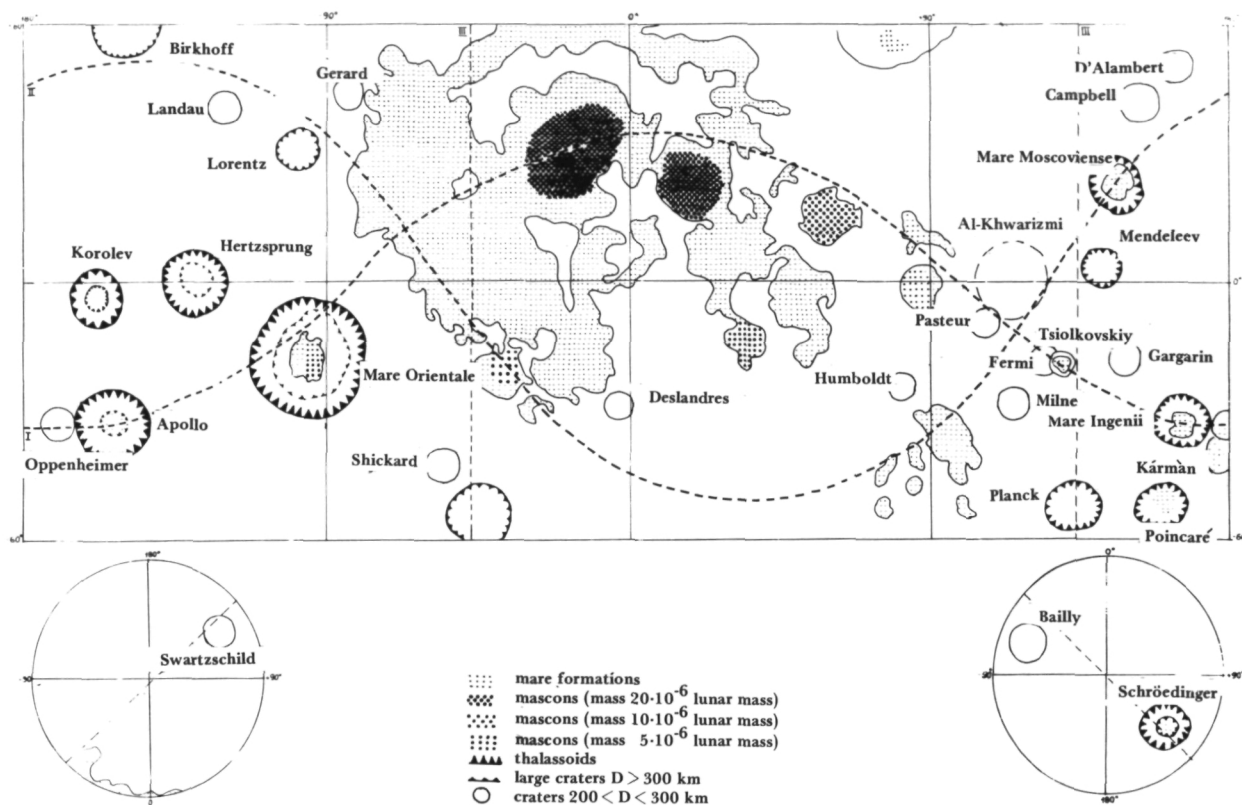


Figure 4.—Diagram of maria, thalassoides, and craters ($D > 200$ km).

2. RODIONOVA, ZH. F., Measurement of the Areas of the Lunar Maria and Thalassoids. *Astron. Tsirk.*, No. 538, 1969.
3. *Full Map of the Moon; 1:5 Million Scale*, Nauka Press, 1969.
4. WESTFALL, J. F., The Areas of the Lunar Lowlands. *Strolling Astronomer*, Nos. 7 and 8, 1970.
5. SHOEMAKER, E. M., AND R. J. HACKMANN, *Advances in the Astronomical Sciences*, Vol. 8, 1961, p. 72.
6. PSKOVSKIY, YU. P., Global Study of the Moon. *Priroda*, No. 4, 1968.
7. *Atlas of the Reverse Side of the Moon, Part II*, Vol. 215, 1967.
8. EL-BAZ, FAROUK, AL-KHWARIZMI: A New-Found Basin on the Lunar Far Side. *Science*, Vol. 180, June 1973, p. 1173.

Page intentionally left blank

Page intentionally left blank

Measurement of the Optical Properties of Lunar Rocks in the Transition Zone, Resulting From Observations Made by Lunokhod 2

Yu. N. Lipskiy and V. V. Shevchenko
*Shternberg State Astronomical Institute,
Moscow, U.S.S.R.*

While traveling in a southerly direction from the landing point, Lunokhod 2 passed through a region of gradually changing albedo when it entered the "dark" highlands. Photometric measurements were carried out directly on the lunar surface with the aid of a calibration device, a plate with fields of different brightness, placed in the field of view of the panoramic telephotometers. The brightnesses of the fields of the calibration plate were measured in preliminary studies, relative to the brightness of a magnesia screen. This permitted determination of the reflectance features of the surficial lunar material relative to the standard most widely used in brightness studies of natural substances. The total brightness of sections a few centimeters across was recorded in direct proximity to the apparatus. The total area investigated in one panorama was about one square meter. Several areas in the mare and highland regions were studied. The albedos of various surface objects were obtained. A comparison of the brightness measurements with data from the RIFMA-M instrument¹ discloses a correlation of the albedo change with change in chemical composition of the surface rock.

The reflectance feature of lunar rocks is one of the characteristics that identify them with mare or highland types. In this respect, direct photometric studies of the lunar surface in the "mare-highland" transition zone assist in tracing the transition from one type of rock to another, and in obtaining information on the processes of material exchange between these two types of lunar landscape.

Technique

To perform photometric measurements on the Lunokhod 2 self-propelled vehicle, plates with fields of different brightnesses were placed in the field of view of the panoramic telephotometers. The total number of brightness fields represents 39 gradations from black to white and permits the brightness of lunar surface objects to be measured by the comparison method, for a broad range of

standard system ensures the possibility of angles of incidence and reflection, with respect to both the plane of the photometric chart and the position of the terrain detail being studied. As a rule, the working range was shifted, depending on the illumination and observation conditions, to the dark or light region of the photometric plate, and encompassed eight gradation fields during measurements. During preliminary studies of the field brightnesses of the photometric plates, the relative brightness of an "absolute white screen" coated with magnesium oxide was determined. This technique permits measurement of the reflectance of lunar material with the standardization most widely used in studies of natural substances. Thus, use of a

¹ RIFMA-M is an automatic X-ray fluorescence spectrometer, using nondispersive detectors and a radioisotopic exciting source. It was used on Lunokhod 2 to measure the chemical composition of several locations on the lunar surface.

more reliably comparing the reflectance of naturally occurring lunar material with similar properties of terrestrial rocks. It should be remembered that the standardization ordinarily used in planetary astrophysics is based on photometric calibration with reference stars.

Presentation and Discussion of the Data

Preliminary data on the reflecting properties of the lunar surface from Lunokhod 2 measurements contain the results of photometric processing of fragments of five panoramas that include images of the photometric plates. These panoramas were obtained during the second lunar day of operation of Lunokhod 2. Two of them are of mare-type regions inside Le Monnier crater about 4.0 km south of the landing site. Three panoramas were obtained in succession, during one session, on the wall of a crater 2 km in diameter, and located in the highland region south of the landing site. Each measurement section was located in direct proximity to the apparatus and occupied an area of about one square meter. The brightnesses of selected objects and areas within these sections were measured relative to the smooth surface. As an example, a diagram of the locations of brightness measurement sections in the highland region is presented in figure 1. The diagram is oriented to the points of the compass; I, II, and III indicate the positions of the camera when taking the panoramas and the directions to the center of the photometric charts; 1, 2, and 3 are areas where the brightness of surface details was measured; 4 is the track left by the wheels of the Lunokhod chassis; and 5 is the track of the ninth wheel, intended for measurement of the distance traveled. The brightness of a number of rocks and lumps of soil, of the soil displaced by the Lunokhod wheels, and of the track left by the ninth wheel were measured in sections 1 and 2. The separate measurements are the total brightness of an area several centimeters across.

The brightness of areas of comparatively smooth surface was distributed uniformly within the sections. Thus, the data in each area provide a small statistical sample that characterizes the brightness distribution. By means of directional light scattering indicatrices for the lunar surface (ref. 1), the measured brightness was recalculated to albedo values. The samples of individual sections were associated in pairs, for the mare and highland regions, respectively. According to these data, the weighted average albedo value for the mare turned out to be $\rho_0 = 5.85$ and, for the highlands, $\bar{\rho}_0 = 6.72$. A comparison with the albedo map for the region of Le Monnier crater, compiled from terrestrial observations in the photometric catalog system (ref. 2), as well as comparison with the albedo map (ref. 3) where the albedo values had been reduced to the catalog system (ref. 2), shows that there is the following linear relation $\rho_0 = 0.790 \frac{k}{\bar{\rho}_0}$. The superscript $\bar{\rho}_0$ designates the albedo value with the magnesia screen standardization (Lunokhod 2 data), and superscript k designates the albedo value in the catalog system (ref. 2), standardized in the reference star system. The relation obtained indicates that the true albedo of the naturally occurring lunar material is somewhat less than the values which are usually given from ground astronomical observations.

During the investigations carried out by the Lunokhod 2 self-propelled vehicle, the chemical composition of lunar rocks was determined by the RIFMA-M instrument. According to these data (ref. 4), the content of aluminum with respect to silicon in the mare region (albedo $\bar{\rho}_0$) is 0.37 and, in the highland region (albedo $\bar{\rho}_0$) equals 0.48. The dimensions of the areas in which the chemical composition and albedo were determined were approximately the same. An overall curve of the dependence of albedo on chemical composition of the rocks is shown in figure 2 according to the Al/Si argument (1 indicates the data of the orbital selenochemical survey and the albedo map (ref. 5)). The albedo values in figure 2 are given in the catalog system (ref. 2). The albedo values for the

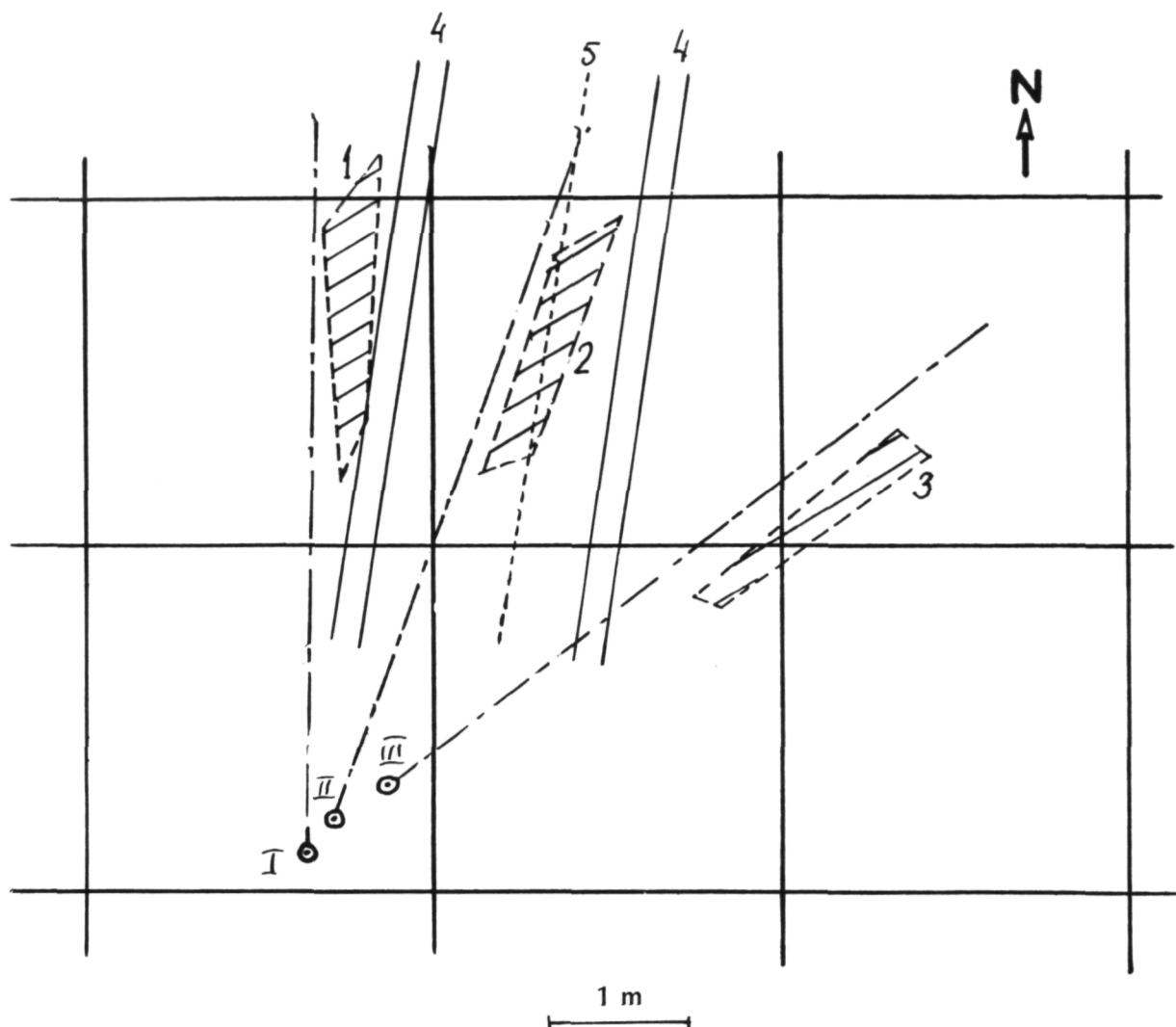


Figure 1.—The locations of brightness measurement sections in the highland region. The arrow indicates north. Roman numerals I, II, and III indicate the positions of the camera when the panoramas were photographed, and the directions to the center of the photometric charts. Arabic numerals 1, 2, and 3 designate areas where the brightness of surface details was measured; 4 indicates the track left by the wheels of the Lunakhod chassis; and 5, the track of the ninth wheel.

mare and highland regions in the area of Le Monnier crater, converted to this system, agree well with the overall relation of albedo to chemical composition of the rock (2 identifies data from the RIFMA-M chemical measurements and the Lunokhod 2 brightness measurements). This circumstance makes it possible to interpret the presence of material with different albedos in the regions being studied in terms of the local distribution of

known types of lunar rocks. According to the data correlated by Shevchenko (ref. 5), the following albedo values correspond to different types of lunar rocks (in the Lunokhod 2 photometric measurement system): the albedo of mare basalts is less than 6.0–6.5; the albedo of noritic rocks is 6.5–9.5; the albedo of anorthositic rocks is over 9.5. Histograms showing the percentage distribution of albedos in “smooth” surface sections for

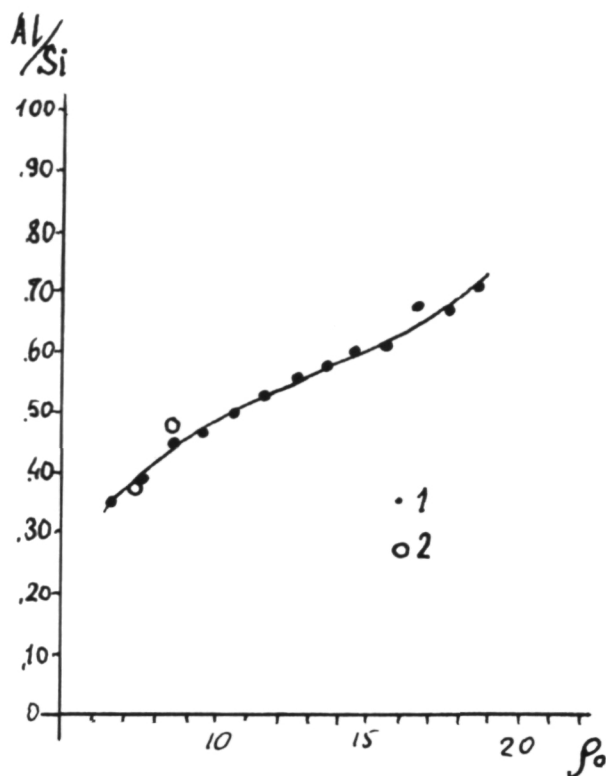


Figure 2.—A general curve of the dependence of albedo on chemical composition of the rocks. 1—data from orbital surveys; 2—data from Lunokhod 2.

mare and highland samples, are presented in figure 3. A covering material with a low albedo predominates in the mare region, i.e., basaltic rocks. However, about one-third of the surface studied is covered with a lighter material, presumably of noritic composition. Both a dark material of basalt composition and a lighter material are encountered in the highland region where there is a clear predominance of rock of noritic composition. As was mentioned above, within the areas studied in the highland region, brightness was measured for individual objects differing in structure. As far as the resolution of the initial images permits, lumps of soil and rocks belong to different groups on the basis of outward appearance. In calculation of the albedo of these objects, change in brightness because of their shapes was taken into account. The albedos of the objects listed are presented in table 1.

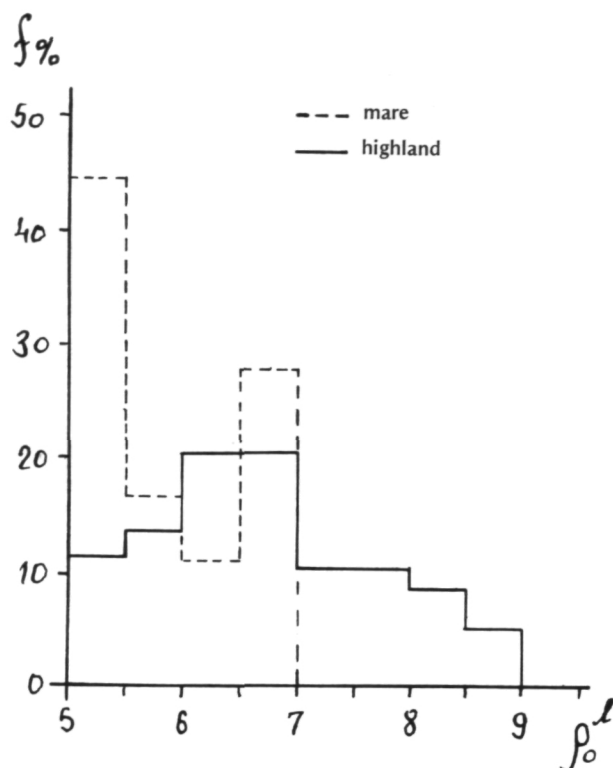


Figure 3.—Histograms showing the percentage distribution of albedos in "smooth" surface sections for mare and highland samples.

Table 1.—Albedos of Specified Objects

Soil in Track of Lunokhod Chassis	Track of Ninth Wheel	Lumps of Soil	"Dark" Rocks	"Light" Rocks
9.5	11.5	8.0	11.0	12.2
	11.3	8.4	11.8	12.7
	10.8	9.0	10.5	13.2
			11.4	
			10.7	

It follows from the data of table 1 that objects distinguished as "lumps of soil" have the same albedo as a number of sections of "smooth" surface. In all likelihood, this circumstance may confirm the identity of their natures and chemical compositions. Soil compacted by the action of the chassis wheels and the ninth wheel of Lunokhod brightens considerably. A similar soil-brightening phe-

nomenon, as a result of its compaction, was repeatedly noted earlier. In this connection, it might be concluded that the "dark" rocks do not differ in composition from the underlying surface. Their higher albedos may be explained by the greater density of the reflecting surface of the layer of material. The fact that the albedos of the "dark" rocks and compacted soil are the same confirms this hypothesis.

The nature of the "light" rocks is different. The high albedo values indicate that they may be crystalline fragments of anorthositic gabbro-type rocks. The nearest region with similar optical characteristics (Roemer crater) is at a distance of about 200 km from the Lunokhod 2 study location. The assumption of material transport does not agree with observational results in this case, since similar light fragments have not been found in the neighboring mare region. It is difficult to assume that the ejection mechanism accompanying formation of Roemer crater acted so selectively. The absence of "light" rocks on the mare surface might be explained by the formation of Roemer crater in the pre-mare epoch. However, structural characteristics of this crater and the high albedo are characteristic of post-mare craters. In figure 3, note the sharply differing distributions of rock types in the mare and highland regions. The distribution approaches the normal for the highlands. The mare region is characterized by a clearly expressed bimodal distribution. In the event of a mutual material transport mechanism, a uniform distribution might be expected.

The described characteristics of the distribution of lunar rocks in the transitional zone lead to the conclusion that a mechanism of vertical mixing of material may turn out to have the greatest effect. The fine fraction and individual fragments that differ from the rock typical of the place being considered may belong to deeper layers, uncovered in the process of crater formation. The depths of individual craters in this region are presented on a preliminary geologic map (ref.

6). Furthermore, crater depths may be obtained from their diameters by using the well-known average ratio between these parameters. It is evident that the depths of layers, differing in albedo from the surrounding terrain, can be estimated from the crater depths. In this case, the results of a lunar surface spectrozonal survey also were drawn on to reveal similar craters. The estimates show that, in the vicinity of the mare region of the study, the thickness of the upper basalt layer may reach a relatively low value of 50–100 m. Such a significant fraction (over 30 percent) of noritic rocks in the surface material apparently is explained by this circumstance. The Apollo 17 seismic study data can be introduced, for an order of magnitude comparison. In the vicinity of the landing point, located 200 km south of Le Monnier crater, the upper layer of the mare basalts proved to be 248 m thick (ref. 7). In the highland region of the Lunokhod 2 study, the noritic rock layer, in all likelihood, reaches a thickness of 200–300 m. A layer of anorthositic gabbro, individual fragments of which were found, can be assumed to lie below this depth. A thicker layer of rocks, with the chemical composition of the surface, explains the differing nature of the distribution histograms for the highland region.

References

1. LIPSKIY, YU. N., AND V. V. SHEVCHENKO, *Kosmicheskkiye Issled.*, Vol. 7, 1969, p. 5.
2. SHORTHILL, R. W., J. M. SAARI, F. E. BAIRD, AND J. R. LECOMPTE, *Photometric Properties of Selected Lunar Features*. NASA CR-1429, 1969.
3. POHN, H. A., AND R. L. WILDEY, *Geological Survey Professional Paper 559-E*, 1970.
4. KOCHAROV, G. YE, AND S. V. VIKTOROV, *Dokl akad nauk SSSR*. In press.
5. SHEVCHENKO, V. V., *Astronomicheskii Zhurn.* In press.
6. *Preliminary Geologic Map of Part of Crater Le Monnier of the Moon*. U.S. Geological Survey, Flagstaff, 1973.
7. KOVACH, R. L., AND J. S. WATKINS, *Science*, Vol. 180, 1973, pp. 4090, 1063.

Page intentionally left blank

Page intentionally left blank

section 6

Cosmochemical Hypotheses of the Origin and Evolution of the Moon and Planets

Page intentionally left blank

Page intentionally left blank

Clues in the Rare Gas Isotopes to Early Solar System History

John H. Reynolds
Department of Physics
University of California
Berkeley, California

Those of us who work with rare gases in meteorites and lunar samples have been stimulated by progress in our subject in the Soviet Union. We remember well the work of Gerling, Pavlova, and Rik (refs. 1 and 2) who in 1951 and 1956 initiated potassium-argon dating of meteorites which has become an area of great importance. It was Gerling and Levskiy (ref. 3) in 1956 who made the striking discovery of the existence of gas-rich meteorites, one of the first manifestations of what we now know to be the solar wind. These two results alone have placed Soviet workers in the forefront of my field. We have also been privileged in my laboratory to work with lunar samples returned by the Luna 16 and Luna 20 landers.

Although this paper deals with work dating back as far as 1959, I feel it is still worthy of review, and I intend to present my latest and less tested thoughts on interpretations.

I first want to review the results we have obtained with the extinct radioactivity iodine-129. I remind you that this is a radioactivity which is produced in the r-process of nucleosynthesis and which decays with a half-life of 17 m.y. Consequently, we can expect this radioactivity to have been present in the early years of the solar system, with its concentration relative to normal ^{127}I changing by a factor of 2 every 17 m.y. In principle, then, it provides a clock sensitive to small time changes even though the events it records took place 4.6 aeons (1 aeon =

10^9 yr) ago. Figure 1 is an old familiar one, but it still makes its point. It is a xenon

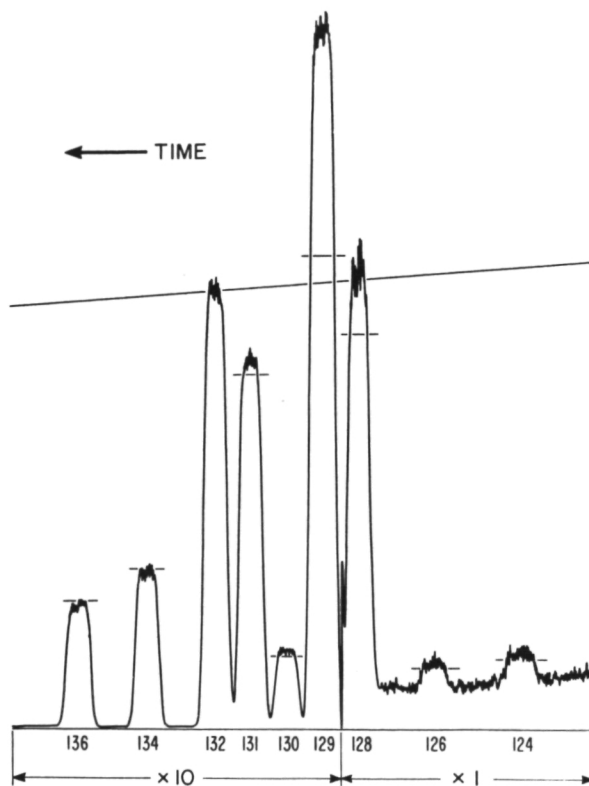


Figure 1.—Mass spectrum for xenon extracted from the Richardton chondrite. The short horizontal lines mark where the peaks would fall if the sample were xenon from the atmosphere. By far the most marked anomaly is an excess at mass 129 due to radioactive decay of extinct ^{129}I .

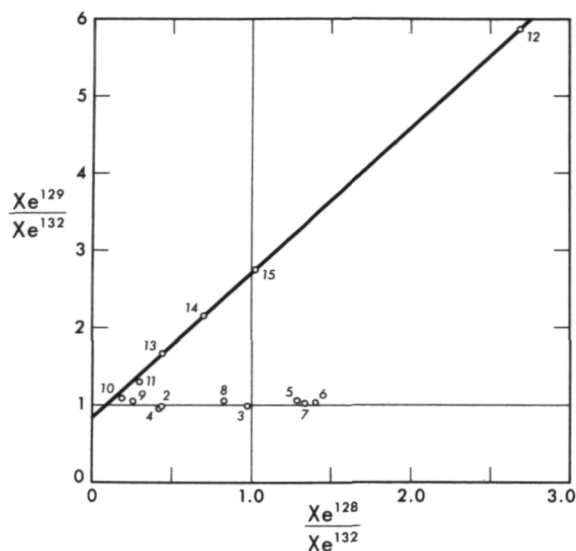


Figure 2.—An isotope correlation plot for xenon from stepwise heating of a neutron-irradiated sample of the Shallowater achondrite. The numerals marking the points are extraction temperatures in hundreds of degrees. Above 1000°C there is a good correlation between the release of excess Xe^{129} from decay of extinct I^{129} and excess Xe^{128} produced from I^{127} during the irradiation. From diagrams of this type, the initial $\text{I}^{129}/\text{I}^{127}$ ratio for the meteorite can be determined precisely (ref. 3).

spectrum taken in 1959 from the Richardton chondrite. The small horizontal lines show where the peak tops would fall if we were examining a sample of xenon from the atmosphere. By far the largest deviation from this atmospheric composition occurs at mass 129 where there is a pronounced "spike" of excess gas. Since 1959, this pattern has proved to be a quite general property of meteorites and has led us to explore what we call the iodine-xenon method of dating. In order to carry this method out with some precision, we irradiate the material with slow neutrons, thereby converting part of the ordinary ^{127}I into ^{128}Xe . We follow this irradiation with a stepwise heating of the meteorite, examining the isotopic composition of the xenon given off at successively higher temperatures. Typically, we enter a high-temperature regime in which the release of excess ^{129}Xe correlates with the release of excess ^{128}Xe produced in the pile.

This correlation is best demonstrated by a plot which is shown in figure 2, where we graph the ratio $^{129}\text{Xe}/^{132}\text{Xe}$ versus $^{128}\text{Xe}/^{132}\text{Xe}$. The meteorite in question is the Shallowater enstatite achondrite (ref. 4). The numerals on the points are the temperatures at which the gas was released in hundreds of degrees Centigrade. We see that above 1000°C there is an almost perfect correlation between the release of excess ^{129}Xe and of excess ^{128}Xe . From the slope of this line plus data about the neutron irradiation it is possible to deduce that the initial ratio of ^{129}I to ^{127}I for this meteorite was 1.1×10^{-4} . By exposing different meteorites to the same neutron irradiation it is possible to measure time differences very directly. Figure 3 shows how we infer a difference in time of formation between the petrologic Type-4 Karoonda carbonaceous chondrite and the Peña Blanca Spring enstatite achondrite. Both these meteorites provide a good correlation line, and we infer a difference in the initial $^{129}\text{I}/^{127}\text{I}$ ratio which corresponds to a time difference of 7.5 m.y. In a study completed in 1970, Podosek (ref. 5) assembled an array

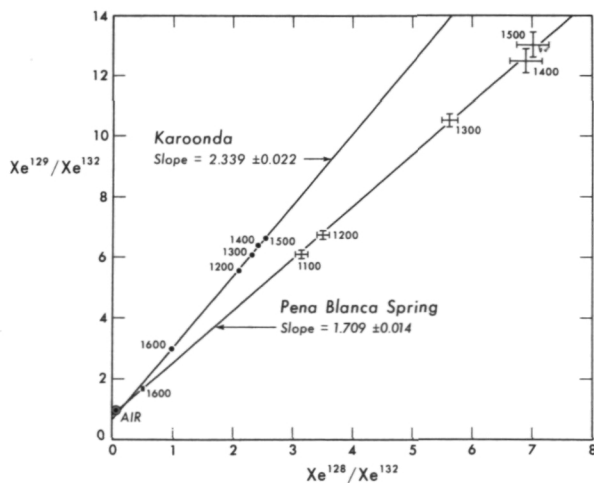


Figure 3.—Correlations (see caption for fig. 2) for two meteorites having different initial $\text{I}^{129}/\text{I}^{127}$ ratios as evidenced by the difference in slope. The difference in time of formation inferred for these two meteorites is 7.5 m.y., with the Karoonda carbonaceous chondrite (petrologic Type 4) antedating the achondrite Peña Blanca Spring (ref. 4).

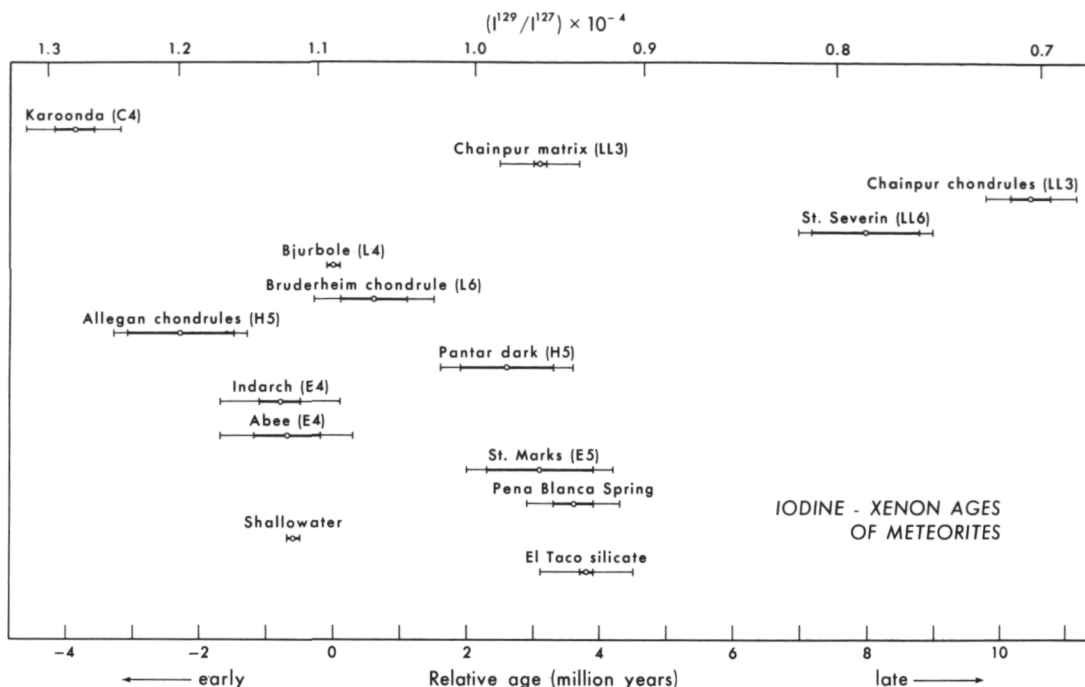


Figure 4.—An array of I-Xe ages assembled by Podosek (ref. 4) in 1970. The formation times for very diverse meteorites, including a silicate inclusion from the iron meteorite El Taco, all lie within a span of 14 m.y.

of these iodine-xenon ages which is shown in figure 4. An important observation to be made from these results is that despite the presence on the diagram of very diverse meteorites—including chondrites, achondrites, and a silicate inclusion from an iron meteorite—the total spread in time inferred by this method is quite short, amounting to only 14 m.y. We have referred to this result (ref. 6) as "sharp isochronism" for the formation of the meteorites. We have thus far not been able to determine very meaningfully the detailed time differences occurring in the figure. Nevertheless, there are some individual results which we find significant. Figure 5 shows a recent result obtained in joint work between my laboratory and that of Professor Anders at the University of Chicago (ref. 7). Professor Anders and his coworkers learned how to isolate magnetite from carbonaceous chondrites, and we have found that

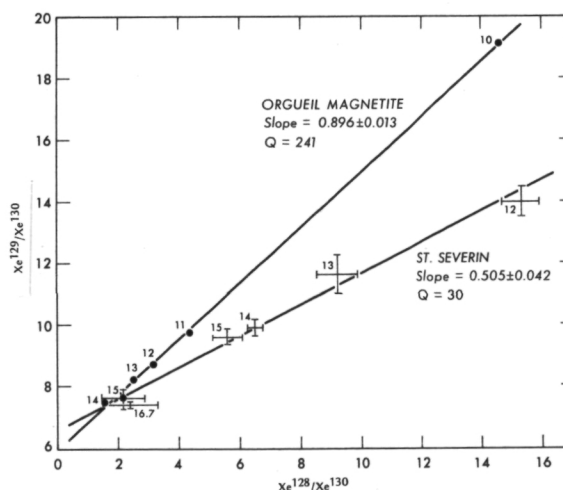


Figure 5.—Another time difference inferred by the I-Xe dating method. A good correlation was obtained for magnetite from the Type-1 carbonaceous chondrite Orgueil. Orgueil is the most ancient object yet dated by this method, but precedes Karoonda (see fig. 3) by only 1.8 m.y. (ref. 6).

this mineral is favorable for iodine-xenon dating. You will note that we obtained an excellent correlation for magnetite from the carbonaceous chondrite Orgueil. When placed in the scheme of relative ages that we saw in figure 4, Orgueil magnetite appears to be the earliest or most primitive object dated so far, but separated in time from the Karoonda stone by only 1.8 m.y. There are two important inferences to be made from this result. First, the carbonaceous chondrites are basically contemporaneous with the rest of the meteorites. Secondly, if there is an evolutionary relationship between the petrologic Type-4 chondrites like Karoonda and the more primitive Type-1 carbonaceous chondrites like Orgueil, this evolution took place with rapidity—that is within about 2 m.y. Another detailed result of iodine-xenon dating that appears significant to us is shown in figure 6, where we exhibit the attempt to establish one of these iodine-xenon correlations for the meteorite Manych, a sample of which we received for this purpose through the generosity of Professor Krinov. Manych is an exceptionally unequilibrated meteorite; it is basically an assemblage of fresh chondrules. It is interesting to us that we were not able to ob-

tain an iodine-xenon correlation for this stone (ref. 8), suggesting that the individual chondrites which made it up had different times of origin so that there was not a single event that we could date. The very well defined correlation for the Abee enstatite chondrite is also shown in figure 6 by way of contrast. In Abee we have an almost perfect correlation; in Manych, none at all. Before leaving the topic of iodine-xenon dating, I want to comment that the correlation, when it occurs, seems to be extremely durable. Hohenberg and I (ref. 9) investigated this question in 1969. We took a sample of the Abee stone and heated it to 1200°C in vacuum for 1 hour *before* carrying out the neutron irradiation. We knew from experience that this preheating would drive out about 90 percent of the xenon. We anticipated, therefore, that the iodine-xenon correlation would be largely destroyed. To our surprise, when we examined the preheated sample, even though as anticipated the xenon had been very largely expelled, the residual xenon which came off at temperatures of 1200°C and above exhibited exactly the same correlation as the sample which had received no preheating whatsoever. That result is shown in figure 7. Professor Wasserburg likes to use the word "magic" to describe this durable correlation. Upon reflection, I think we have to say that this durability is not magic at all, but simply a consequence of the fact that wherever the iodine is located in these objects, that part of it that is not disturbed until very high temperatures behaves exactly the way xenon does when similarly located. In other words, the retentively sited iodine appears to be caged in the very durable minerals in such a way that it makes no difference, as to its release, whether it has changed into xenon or not. This supposition is important for interpreting the results of our work because it says that the iodine-xenon date of a meteorite is very little disturbed by heating. This may account for the fact that these dates comprise a compact group: the iodine-xenon clock is very difficult to reset. We could feel more confident of these assertions if we understood

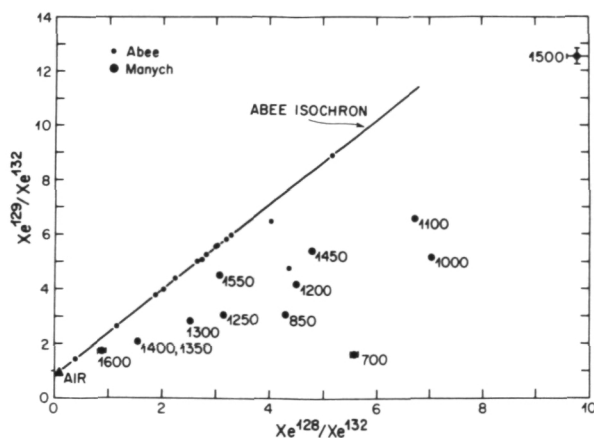


Figure 6.—An interesting case where an I-Xe correlation was not observed. The chondrite Manych is essentially an assemblage of fresh chondrules. The I-Xe data suggest that these chondrules were not all formed at the same time. The excellent correlation for Abee is shown for contrast. (ref. 7).

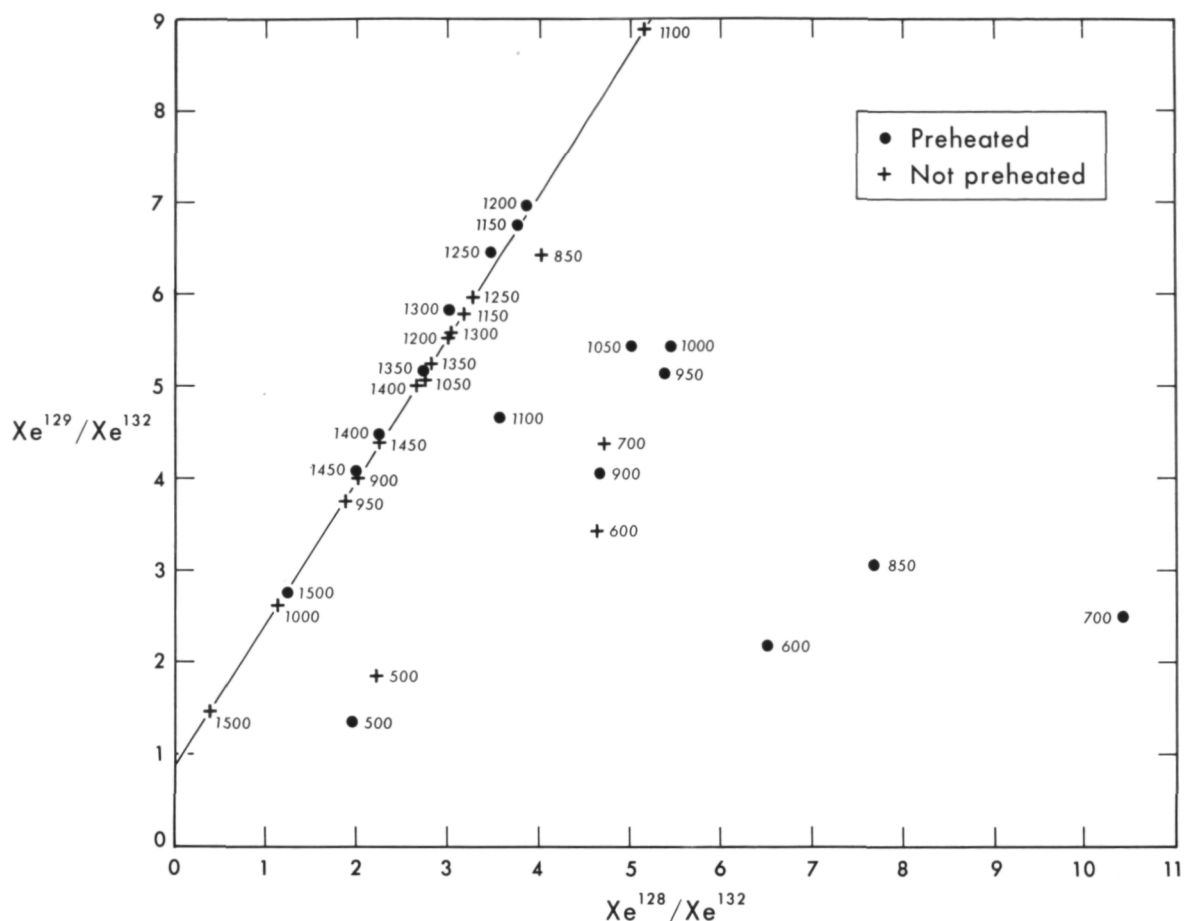


Figure 7.—Evidence of the durability of the I-Xe correlation in the enstatite chondrite Abee. A preheating of the stone to 1200° C before the neutron irradiation removed 90 percent of the xenon, but did not alter the quality or magnitude of the correlation with iodine for that xenon still remaining in the stone. In the Abee stone the I-Xe clock seems to be almost impossible to reset by simple heating. (ref. 8).

better the location of the retentively sited iodine in these objects. Unfortunately we still know very little about its location. Possibly the ion microprobe which is beginning to come into use in research will prove useful in this connection.

Another important chapter in the study of extinct radioactivities concerns the radio-nuclide ^{244}Pu . As early as 1960, Kuroda (ref. 10) recognized that if we were correct about our interpretations of the excess xenon-129 found in meteorites we should also expect to find fissionogenic xenon in these objects from the decay of ^{244}Pu , which disintegrates in part by spontaneous fission. Ku-

roda could make this observation with great certainty because ^{244}Pu would undoubtedly be produced in the r-process and would necessarily outlive ^{129}I because of its 82-m.y. half-life. It was Rowe and Kuroda (ref. 11) who then first obtained experimental indications of the validity of Kuroda's assertion. Studying xenon in achondrites, they detected a prominent excess fissionogenic component which had a characteristic isotopic pattern. We now know beyond any doubt that this pattern comes from ^{244}Pu . In 1969, a group of us at Berkeley (ref. 12) succeeded in examining the fission xenon from a sample of ^{244}Pu produced artificially. The results of

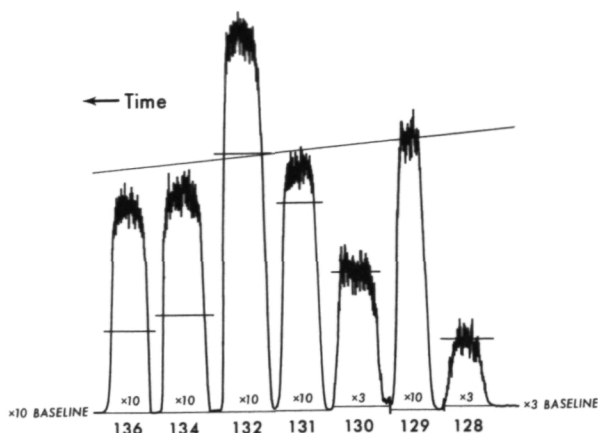


Figure 8.—Isotopic composition of xenon from spontaneous fission of an artificially prepared sample of ^{244}Pu . The short horizontal lines indicate the contributions from air contamination. The small peak from air at mass 128 results from three million atoms. (ref. 11).

that analysis are shown in figure 8. Again the horizontal lines show where the peaks would fall if only atmospheric xenon were present. The excesses, which is to say the heights of the peaks above these horizontal lines, represent the spectrum of the fissiogenic sample. One notes that it consists of a small amount of ^{131}Xe accompanied by almost equal amounts of ^{132}Xe , ^{134}Xe , and ^{136}Xe . In passing I would like to mention that the smallest peak in this spectrum, the peak at mass 128, corresponds to only three million atoms, which is an indication of how sensitive these techniques can sometimes be. Figure 9 shows how well this isotopic pattern fits the pattern we had previously known from the achondrites. The dark circles are the values from the artificially prepared sample of ^{244}Pu . The open circles and squares are from the achondrites Pasamonte and Kapoeta, respectively. As you can see, the match is virtually perfect and differs considerably from the pattern of fissiogenic xenon from another nuclide at mass 244, ^{244}Cu . It is more difficult to utilize ^{244}Pu in a dating scheme because we lack a reference isotope of Pu which can play the role of ^{127}I . The best we can do at present is to suppose that the Pu when it was extant was

associated in meteorites with uranium. We can then carry out a dating experiment that is somewhat analogous to our procedure for the iodine-xenon method. By irradiating the meteorite with neutrons we produce additional fissiogenic xenon at the uranium locations. If these locations had also been the locations for plutonium, the effect of the irradiation is to revise the isotopic compositions of the fissiogenic xenon released from the uranium sites. A successful experiment of this type is shown in figure 10 where Podosek (ref. 13) plotted the ratio $^{130}\text{Xe}/^{132}\text{Xe}$ versus the ratio $^{134}\text{Xe}/^{132}\text{Xe}$ for temperature fractions of xenon from an irradiated sample of the St. Severin meteorite. After correction for spallation effects, which shifted the points from positions designated by the small circles to the positions designated by the crosses (these corrections are quite substantial), the points do lie on a line that is intermediate between one given by fissiogenic xenon from ^{244}Pu and one given by fissiogenic xenon generated entirely by pile neutrons acting on uranium. The detailed position of this line enabled Podosek to

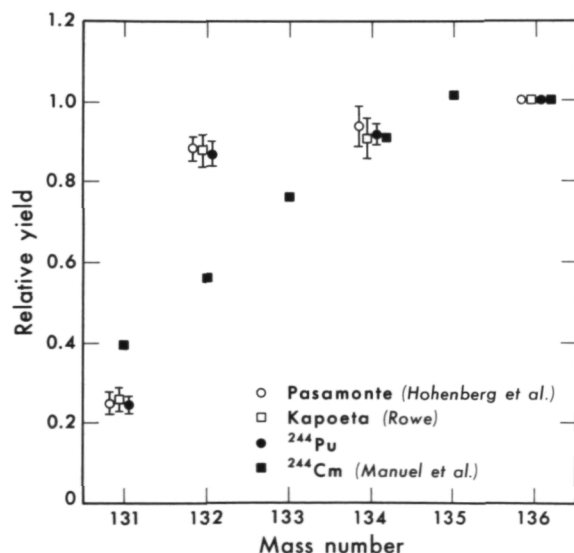


Figure 9.—Agreement between the isotopic pattern for xenon from spontaneous fission of ^{244}Pu (see fig. 8) and fissiogenic xenon found in achondrites. By this comparison, existence of ^{244}Pu as a bona fide extinct radioactivity was confirmed (ref. 11).

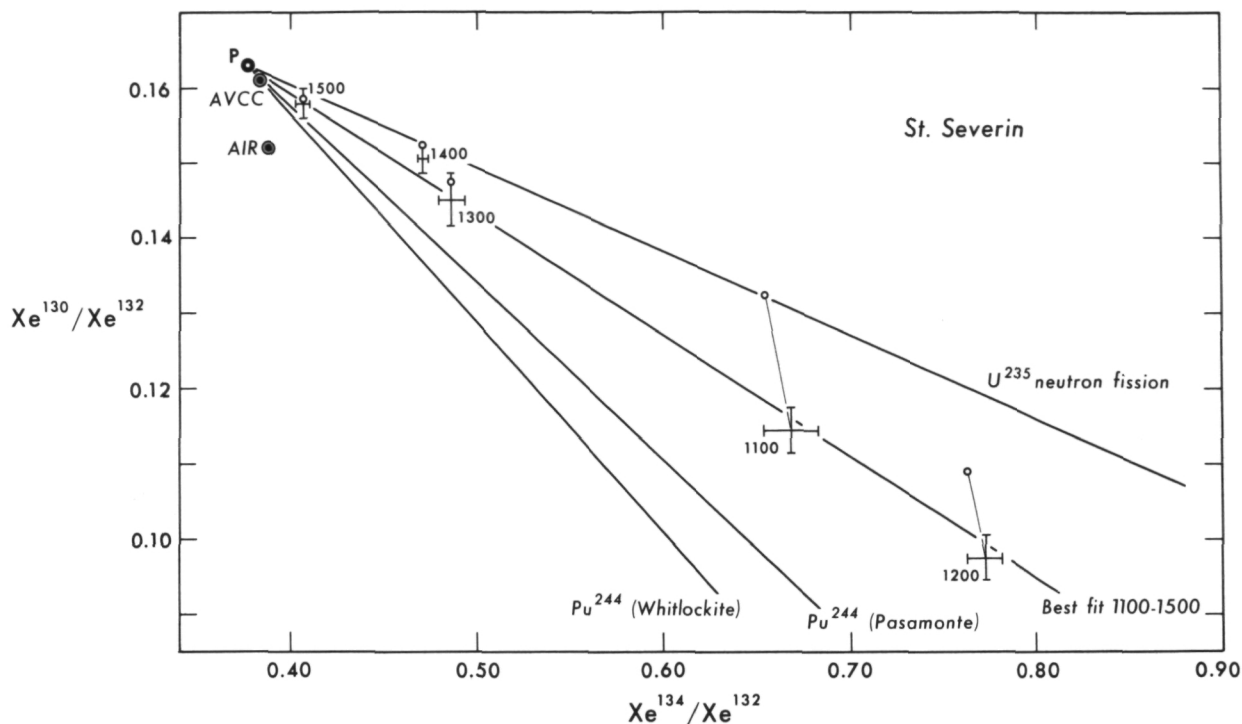


Figure 10.—Evidence for an association between uranium and Pu^{244} in the chondrite St. Severin. The correlation plot is for xenon extracted in stepwise heating from a neutron-irradiated sample. The points have been corrected as indicated for spallation xenon resulting from galactic cosmic rays. The correlated high temperature points define a line intermediate between the lines obtained by mixing trapped xenon with (1) xenon from Pu^{244} fission and (2) xenon from neutron-induced fission of U^{235} . The position of the intermediate line fixes the initial $\text{Pu}^{244}/\text{U}^{235}$ ratio in the sample at 0.013 (ref. 12).

calculate an initial ratio $^{244}\text{Pu}/^{238}\text{U}$ of 0.013 for a bulk sample of St. Severin. Tentatively, we view that number as our best determination up until now of the ratio for the solar system at the time the meteorites commenced to retain xenon. So far it has not been possible to obtain quantitative results of this type for as many meteorites as would be needed for dating. The few cases where success has been obtained do support the idea of general contemporaneity of meteorites. There is no known contradiction between the iodine-xenon and the plutonium-xenon dating schemes.

One of the important applications of these results has been to the subject of cosmo-chronology. If one were provided with a sufficiently large array of radioactive nuclides, both extinct and extant, produced in r-process nucleosynthesis, one could in prin-

ciple deduce in detail the chronological history of that mode of nucleosynthesis. Figure 11 shows how such a chronology might be displayed. If we say that the galaxy was born at $t = 0$ and that the nucleosynthesis which contributed to our solar system went on up until the time, T , we could represent the production rate as a function of time by the function $p(t)$. In the model I have illustrated in the figure there is shown a large amount of early nucleosynthesis, followed by a modest amount of continuous nucleosynthesis, and terminated by a late spike. I should emphasize that this model is only illustrative and many others are possible, although they must be, as we shall see, bound by the constraints imposed from abundance measurements for the array of radioactivities. Following the end of nucleosynthesis there is a dormant period, Δ , during which

COSMOCHRONOLOGY

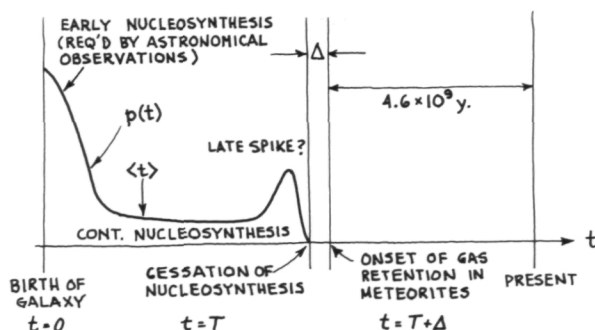


Figure 11.—An illustrative model for r-process nucleosynthesis.

radioactivities decayed but were no longer replenished, and which terminated with the formation of our contemporaneous array of meteorites. Following that event by 4.6 aeons is the present. Turning to figure 12, one sees the equations for the abundance of radionuclides at the time of formation of the meteorites, $t = T + \Delta$. The equation in the top line simply says that the amount left at $T + \Delta$ will be the sum of the amounts produced at various times, t , after taking into account the extent to which radioactive decay will have diminished those amounts. We use $p(t)$ as before to designate the general rate of nucleosynthesis and P_i to represent the production factor for the particular radionuclide in question. Rearranging that equation in the second line, one sees that the ratio of the abundance N_i to P_i , multiplied by a simple exponential factor, is equal to a quantity which is a single value of the function that is essentially the Laplace transform of the production rate $p(t)$. This tells us that a large number of radionuclides, well distributed as to mean life, would provide us with the Laplace transform of the production function. But from the Laplace transform we could deduce the production function as its inverse. In reality, the number of nuclides available for this purpose is quite limited—the radioactive isotopes of uranium, thorium, rhenium, and the extinct nuclides ^{129}I and ^{244}Pu that we have discussed earlier in this report. Thus we can only deduce

a few features of the production function. The principal results obtained on a relatively firm basis are shown at the bottom of figure 12. As Schramm and Wasserburg (ref. 14) were first to point out, one of the important results is a value for the average time for nucleosynthesis, which is to say the center of gravity of the production function. We know from the uranium and thorium isotopes that the average age for r-process material is at least 8 aeons ago. In addition, the results for iodine and plutonium taken together give quite a firm value of Δ , 150 m.y. And, finally, our best value (discussed above) for the initial abundance in the solar system of ^{244}Pu relative to uranium suggests that there was *not* a late spike in the production function. There has recently been proposed by Reeves (ref. 15) an interesting speculation as to what might have led to the 150-m.y. interval of dormancy. Reeves points out that this period is about the time between successive passages of our pre-solar cloud of dust and gas through the dense spiral arms of our galaxy where fresh radioactivities would preferentially be added. He suggests that the last nucleosynthesis coincided with the passage of our cloud through the next to last spiral arm. The measurements of Δ , according to this model, are then measurements of the time we spent cruising between the spiral arm which last put radioactivities into our cloud and the following spiral arm wherein the condensation of our Sun was triggered.

$$N_i(T+\Delta) = P_i \int_0^T p(t) e^{-\lambda_i(T+\Delta-t)} dt$$

$$\frac{N_i(T+\Delta)}{P_i} e^{+\lambda_i(T+\Delta)} = \int_0^T p(t) e^{-\lambda_i t} dt \equiv f(\lambda_i)$$

IF THERE WERE MANY SPECIES WITH DIFFERENT λ_i 's
 $p(t)$ COULD BE OBTAINED AS ESSENTIALLY THE INVERSE LAPLACE
 TRANSFORM OF THE FUNCTION $f(\lambda)$.

FIRM RESULTS: $\langle t \rangle \sim 9$ b.y. AGO (U, Th CONSIDERATIONS)
 $\Delta \sim 150$ m.y. (BASED ON ^{129}I)
 LATE SPIKE? - PROBABLY NOT (BASED ON Pu^{244})

Figure 12.—Equations for the abundances in newly formed meteorites of radioactive nuclear species produced in the r-process. Some inferences about solar system cosmochemistry are also stated.

I have two final topics I want to touch upon. First, I want to mention that the products of extinct radioactive decay have somewhat surprisingly been detected in both terrestrial and lunar samples. I am not referring here to the examples of in-situ decay of ^{244}Pu which have been detected both by nuclear tracks and by xenon measurements in lunar rocks. These results were fully to be expected simply because of the great antiquity of the lunar rocks in question. What I am referring to here is the observation of amounts of ^{129}Xe and fissionogenic xenon from ^{244}Pu in certain Apollo 14 breccias where the abundance of these gases is much higher than can be accounted for by in-situ production. This result was discovered by Drozd et al. (ref. 16) in St. Louis, and has been confirmed in our laboratory at Berkeley. Somehow accumulations of xenon that originated in decay of extinct radionuclides were stored in the Moon before being implanted in certain special Apollo 14 breccias,

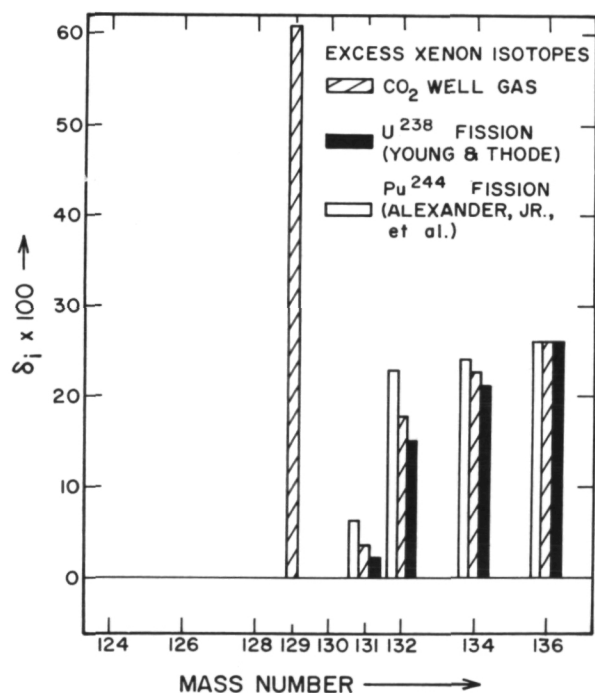


Figure 13.—Isotopic composition of xenon from a CO_2 gas well in New Mexico. The excess Xe^{129} is unambiguous. The fissionogenic xenon may be in part from Pu^{244} (ref. 17).

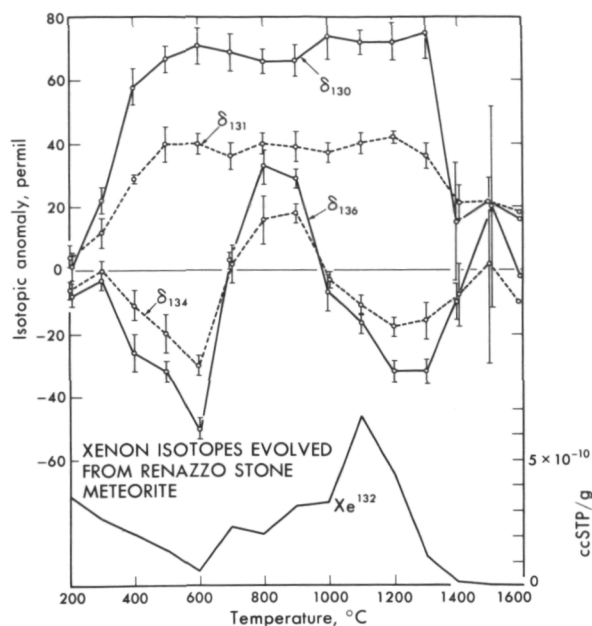


Figure 14.—Evidence for an anomalous fission-like component in the Renazzo carbonaceous chondrite. The component is released in a mid-temperature range (ref. 18).

the implantation presumably having been accomplished by shock. An analogous result for the Earth was the observation of anomalous xenon in certain CO_2 gas wells in the state of New Mexico. First observed at Berkeley in 1963 (ref. 17), this result was beautifully confirmed in 1971 by Boulos and Manuel (ref. 18) at the University of Missouri at Rolla. Their result is shown in figure 13. The excess abundance of ^{129}Xe is completely unambiguous in their work. In addition, they see a fissionogenic component which may be in part from ^{244}Pu . More measurements are needed before we can be sure about the plutonium fossil. Again the place of storage for these xenon samples is unknown.

Finally, let me refer to the anomalous fissionogenic xenon we have seen in the carbonaceous chondrites Renazzo and Murray. In the middle range of temperatures in a stepwise heating extraction, a pronounced fission-like component was seen in both these meteorites. We see in figure 14 that for Renazzo (ref. 19) the effect takes the

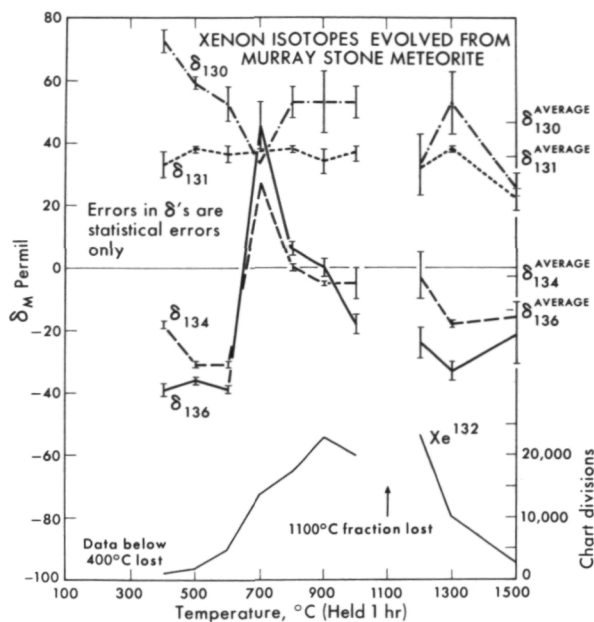


Figure 15.—Occurrence of the anomalous fission-like component of xenon in the Murray carbonaceous chondrite. Again the component is released in a mid-temperature range.

form of simultaneous increases in the relative abundances of ^{134}Xe and ^{136}Xe . A similar result is seen for Murray in figure 15. We have known for many years now that the isotopic pattern for this fission-like component differs in these carbonaceous stones from other fissiogenic patterns. The origin of this component is still unknown. For a time it was attractive to attribute it to fission of a super-heavy element. Such an element could be both fissiogenic and volatile and therefore might be selectively concentrated in the carbonaceous chondrites as suggested by Heymann and Anders (ref. 20) and on other grounds by Dakowski (ref. 21). Theorists who study the likelihood that such a super-heavy nuclide could be produced in the r-process seem lately to be very doubtful (ref. 22). It may be that the anomalous xenon component in the carbonaceous chondrites is somehow related to the anomalous oxygen that Clayton and his coworkers (ref. 23) have recently detected in nonhydrous minerals in carbonaceous chondrites. They have convinced us that the anomalous oxy-

gen is of a nuclear and not a chemical origin; it may represent material from interstellar grains which were not mixed isotopically with the rest of the solar system. If this indeed was the case, these grains may have contributed anomalous xenon as well. Clearly these unanswered questions are much in our minds in the ongoing research.

References

1. GERLING, E., AND T. PAVLOVA, *Dokl. Akad. Nauk. S.S.S.R.*, Vol. 77, 1951, p. 85.
2. GERLING, E., AND K. RIK, *Dokl. Akad. Nauk.*, Vol. 101, 1956, p. 433.
3. GERLING, E., AND L. LEVSKIJ, *Dokl. Akad. Nauk.*, Vol. 101, 1956, p. 750.
4. HOHENBERG, C., *Earth Planet. Sci. Letters*, Vol. 3, 1967, p. 357.
5. PODOSEK, F., *Geochimica et Cosmochimica Acta*, Vol. 34, 1970, p. 341.
6. HOHENBERG, C., ET AL., *Science*, Vol. 156, 1967, p. 202.
7. HERZOG, G., ET AL., *Science*, Vol. 180, 1973, p. 489.
8. PODOSEK, F., AND C. HOHENBERG, *Earth Planet. Sci. Letters*, Vol. 8, 1970, p. 443.
9. HOHENBERG, C., AND J. REYNOLDS, *J. Geophys. Res.*, Vol. 74, 1969, p. 6679.
10. KURODA, P., *Nature*, Vol. 187, 1960, p. 36.
11. ROWE, M., AND P. KURODA, *J. Geophys. Res.*, Vol. 70, 1965, p. 709.
12. ALEXANDER, C., ET AL., *Science*, Vol. 172, 1971, p. 837.
13. PODOSEK, F., *Earth Planet. Sci. Letters*, Vol. 8, 1970, p. 183.
14. SCHRAMM, D., AND G. WASSERBURG, *Ap. J.*, Vol. 162, 1970, p. 57.
15. REEVES, H., *On the Origin of the Solar System*. Centre National de la Recherche Scientifique, Paris, 1972, p. 376.
16. DROZD, R., ET AL., *Earth Planet. Sci. Letters*, Vol. 15, 1972, p. 338.
17. BUTLER, W., ET AL., *J. Geophys. Res.*, Vol. 68, 1963, p. 3283.
18. BOULOS, M., AND O. MANUEL, *Science*, Vol. 174, 1971, p. 1334.
19. REYNOLDS, J., AND G. TURNER, *J. Geophys. Res.*, Vol. 69, 1964, p. 3263.
20. ANDERS, E., AND D. HEYMAN, *Science*, Vol. 164, 1969, p. 821.
21. DAKOWSKI, M., *Earth Planet. Sci. Letters*, Vol. 6, 1969, p. 152.
22. HOWARD, W., AND J. NIX, *Nature*, Vol. 247, 1974, p. 17.
23. CLAYTON, R., ET AL., *Science*, Vol. 182, 1973, p. 485.

Heterogeneities in the Solar Nebula

Robert N. Clayton

*Enrico Fermi Institute and
Departments of Chemistry and Geophysical Sciences
University of Chicago
Chicago, Illinois*

Lawrence Grossman

*Department of Geophysical Sciences
University of Chicago
Chicago, Illinois*

Toshiko K. Mayeda

*Enrico Fermi Institute
University of Chicago
Chicago, Illinois*

Naoki Onuma

*Department of Chemistry
Tokyo Gakugei: University
Tokyo, Japan*

Oxygen isotopic compositions of the high-temperature phases in carbonaceous chondrites define a mixing line with an ^{16}O -rich component and show little superimposed chemical isotope fractionation. Within a single inclusion in Allende, variations of $\delta^{18}\text{O}$ and $\delta^{17}\text{O}$ of 39‰ are found. The ordinary chondrites are slightly displaced from the terrestrial fractionation trend, implying that at least 0.2 percent of the oxygen in terrestrial rocks was derived from the ^{16}O -rich component.

It was recently shown that the anhydrous phases of the carbonaceous chondrites of classes C2 and C3 display a remarkable pattern of oxygen isotope abundances: an almost constant ratio of $^{18}\text{O}/^{17}\text{O}$ and highly variable ^{16}O (ref. 1). The variations of $^{18}\text{O}/^{16}\text{O}$ and $^{17}\text{O}/^{16}\text{O}$ are much greater than can be accounted for by chemical fractionation processes and do not conform to a 2:1 ratio as would be expected for any mass-dependent process. It was concluded that the variations in the C2 and C3 meteorites are ultimately nuclear in origin and represent the mixing of two kinds of oxygen with different nucleosynthetic histories and, hence,

different isotopic compositions. One component of the mixture is here referred to as "ordinary oxygen" and has isotopic abundances near the values of the mean Earth, Moon, and ordinary chondrites; the other component is highly depleted in the heavy isotopes and may be nearly pure ^{16}O . Several lines of evidence suggest that the ^{16}O -rich component existed as solid grains of interstellar dust prior to condensation of solids containing ordinary oxygen from the solar nebular gas.

The purpose of this paper is to present new data on meteorites obtained from refined analytical techniques that yield an order of

magnitude better precision in $^{17}\text{O}/^{16}\text{O}$ determinations than those previously used. It is now possible to examine the small isotopic differences among the Earth, Moon, and ordinary chondrites and to distinguish between the effects of admixture of ^{18}O -rich components into these bodies and the effects of chemical isotope effects during condensation and accretion (ref. 2). It will be shown that even a surficial sample of a differentiated

planet (e.g., Mars) can be used to determine the content of ^{18}O -rich component in the planet—a parameter that may be important in understanding planetary accretion.

Analytical Procedures

In the equilibrated ordinary chondrites and in the achondrites, isotopic equilibration has occurred in metamorphic and igneous

Table 1.—*Oxygen Isotopic Compositions of Terrestrial and Meteoritic Samples*

	Sample Number	Description	$\delta^{18}\text{O}$	$\delta^{17}\text{O}$
Terrestrial	NBS-1a	Yellowstone snow	-24.4	-13.0
	L-water	Distilled water	- 9.3	- 5.1
	M-3	Magnetite	3.0	1.7
	O-120	Quartz	9.5	4.8
	O-120	Quartz	9.6	4.9
	O-120	Quartz (fractionated)	13.2	6.4
	S-863	Quartz	17.6	9.1
Carbonaceous Chondrites Allende	Al-Mx	Matrix	1.3	- 3.1
	Al-Wr	Whole rock	1.6	- 2.6
	Al- 3	Dark inclusion	3.3	- 1.3
	Al-17	White inclusion	-11.2	-14.1
	Al-15	White inclusion	-16.0	-18.2
	Al-15-1	Melilite	- 0.1	- 4.0
	Al-15-2	Melilite and spinel	- 6.7	-10.2
	Al-15-4	Pyroxene	-34.8	-35.7
	Al-15-5	Pyroxene and spinel	-39.0	-40.6
Murray	My-2	Olivine	- 6.9	- 9.7
Ornans	O- 4	Olivine	- 6.5	- 9.5
	O-10	Olivine	- 2.1	- 5.2
	O-12	Olivine	- 2.7	- 6.5
	O-13	Olivine	- 2.8	- 6.4
	O-14	Olivine	- 2.1	- 5.9
	O-15	Olivine	- 0.9	- 5.1
Vigarano	V-6	Olivine	- 4.4	- 7.9
Ordinary Chondrites Pantar	P-Wr	Whole rock	4.1	2.7
	P-A	Partial fluorination	7.3	4.6
	P-B	Partial fluorination	6.5	4.3
	P-II-A	Partial fluorination	5.4	3.8
	P-II-B	Partial fluorination	5.6	3.9
	P-II-C	Partial fluorination	7.8	4.9
Modoc	M-Wr	Whole rock	5.9	4.2

processes, respectively, so that the internal isotopic variations that remain are just the chemical isotopic fractionations between minerals that reflect the maximum temperature of heating (ref. 3). Sampling of such meteorites presents no special problems.

In the unequilibrated chondrites, and especially in the carbonaceous chondrites, large isotopic variations are present, at least down to a submillimeter size range, and information is lost in analyzing larger samples. Hence, our emphasis has been on individual chondrules, crystals, or small clusters of crystals, particularly as exemplified by the refractory aggregates in the C3 meteorite, Allende.

Samples, typically 3 to 10 mg in size, were treated by the bromine pentafluoride technique (ref. 4), and the oxygen thus liberated was analyzed, as O_2 , using a 15-cm, 60°-sector, double-collecting mass spectrometer. Both $^{18}O/^{16}O$ and $^{17}O/^{16}O$ ratios were determined. The results are reported in the δ -notation, relative to SMOW standard (ref. 5). Since SMOW is a fictitious standard defined to have an $^{18}O/^{16}O$ ratio (R^{18}) fixed relative to a real substance, NBS-1 water, by the equation (ref. 5)

$$R_{SMOW}^{18} = 1.008 R_{NBS-1}^{18}$$

we have adopted a similar definition for

R_{SMOW}^{17} , as follows:

$$R_{SMOW}^{17} = (1.008)^{1/2} R_{NBS-1}^{17}$$

Analytical uncertainties are estimated as $\pm 0.1\%$ for both δ^{18} and δ^{17} .

Results

Oxygen isotopic compositions of some terrestrial and meteoritic samples are given in table 1. Data from terrestrial samples and the Allende meteorite are shown graphically in figure 1. It is seen that all of the terrestrial samples lie along a line through the origin with a slope of $+1/2$. This is to be expected

for any samples derived from an initially homogeneous reservoir, in which all subsequent isotopic fractionations are mass-dependent and conform approximately to the relationship

$$\alpha_{AB}^{17} = (\alpha_{AB}^{18})^{1/2} \quad (1)$$

where α_{AB} is defined as a fractionation factor between two phases, A and B:

$$\alpha_{AB}^{17} = (R_A^{17}/R_B^{17}) \quad \text{and} \quad (2)$$

$$R_A^{17} = (O^{17}/O^{16})_A \quad (3)$$

Equation (1) does not hold rigorously for isotopic fractionation processes, but is a good approximation. For example, if isotopic fractionation is brought about by diffusion, with diffusion rates inversely proportional to the squareroot of the masses of the diffusing molecules, equation (1) is in error by only about 1 percent, if the diffusing species are oxygen atoms, and is an increasingly better approximation for oxygen-containing molecules of higher molecular weight. For isotopic fractionation in a chemical equilibrium process, equation (1) implies a linear relation-

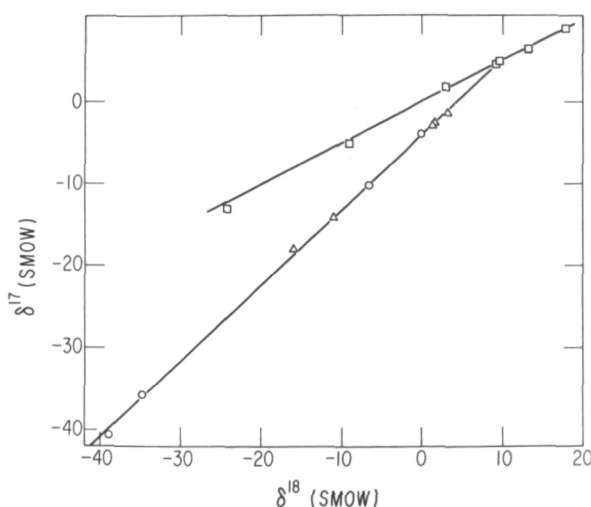


Figure 1.—Oxygen isotopic compositions of various terrestrial materials (squares) and of samples of the Allende meteorite (circles and triangles). The samples represented by circles are density separates from a single inclusion.

ship between free energy and mass difference, which is a good approximation for small relative mass differences.

In the paper of Clayton et al. (ref. 1), data points for the C2 and C3 meteorites were scattered about the mixing line, with deviations from the line on the order of 1%. It was not clear how much of the scatter was due to analytical uncertainty in the $^{17}\text{O}/^{16}\text{O}$ measurements and how much was attributable to chemical isotope fractionations superimposed on the mixing process. It is evident from the new data plotted in figure 1 that the scatter was principally analytical and that chemical shifts from the mixing line are small, probably $<0.5\%$ for all of the Allende samples plotted. Onuma et al. (ref. 2) have discussed the magnitudes of the oxygen isotope effects expected for solids condensing from the solar nebula, in which the principal reservoir of oxygen should be carbon monoxide at the high temperatures involved. The small variability of the chemical isotope shifts implies a narrow range of condensation temperatures and is compatible with the range from 1625 to 1450 K given by Grossman (ref. 6) for the interval between condensation of melilite and condensation of forsterite.

Figure 2 shows data for other C2 and C3 meteorites, with the lines from figure 1 given

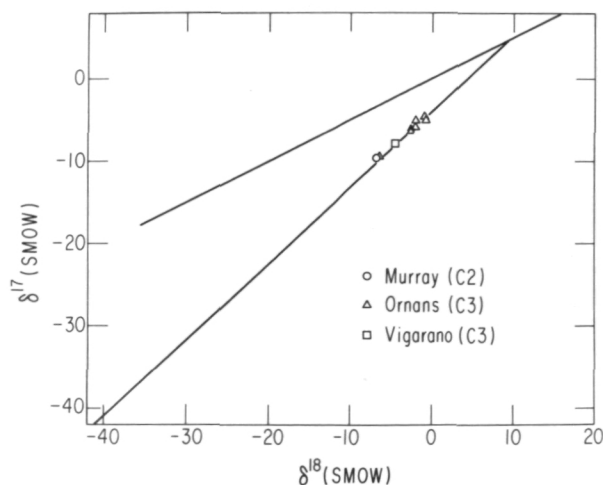


Figure 2.—Oxygen isotopic compositions of separated fractions of Murray, Ornans, and Vigarano. The lines are taken from figure 1.

for reference. It is seen that the points fall on the line defined by the Allende samples. The smaller spread in the data may reflect the sampling technique, which tended to homogenize the samples. It should be noted, however, that the samples from Ornans are all iron-bearing olivines, and it may be surprising that the introduction of lower temperature ferrous iron did not result in a chemical displacement of the data points from the line.

It is of interest to determine whether the various minerals within a single chondrule or inclusion have crystallized together. A large (1 cm-diameter), coarse-grained, round inclusion from Allende was crushed, and mineral concentrates were prepared by heavy-liquid separation. Four fractions, labeled A1-15-1, A1-15-2, A1-15-4, and to A1-15-5 in table 1, showed a range of 39% in δ^{18} and δ^{17} , falling along the mixing line rather than a fractionation line, as would be expected if the minerals had crystallized from a melt.

The densest fraction, composed primarily of titanian clinopyroxene and included spinel, is the most ^{16}O -rich of any sample yet analyzed: the ^{16}O -rich component makes up at least 5 percent of its oxygen. Even at this high concentration, the physical nature of the ^{16}O -rich component is not revealed by microscopic examination.

Clayton et al. (ref. 1) showed that samples from the Moon and the ordinary chondrites fall on or near the terrestrial fractionation line, implying that these bodies have the same fraction of the ^{16}O -rich component and might, in fact, be composed entirely of ordinary oxygen. With the increased precision now available, it can be seen in figure 3 that analyses of two ordinary chondrites, Pantar (H5) and Modoc (L6) define a fractionation trend parallel to, but displaced from, the terrestrial line. The range of data points from Pantar results from a set of partial fluorination reactions such as were first carried out on lunar soils (ref. 7). The variation of about 4% in $\delta^{18}\text{O}$ is greater than would be expected for fractionation among the major minerals in a meteorite of petrographic

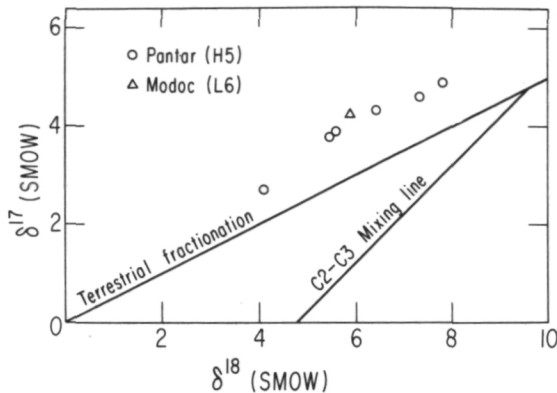


Figure 3.—Oxygen isotopic compositions of ordinary chondrites, Pantar and Modoc. The data from Pantar results from successive partial fluorinations; the Modoc result is a whole-rock analysis.

grade 5 (ref. 3). This probably results from prior exposure of the constituents of this gas-rich meteorite to bombardment while in the regolith of the parent body.

If the apparent displacement of the ordinary chondrite data from the terrestrial fractionation line is supported by subsequent analyses, the implications for accretion of the Earth are significant. Since the ordinary chondrites are displaced in the ^{16}O -depleted direction, the amount of ^{16}O -rich component in the Earth cannot be zero. The magnitude of the displacement sets a lower limit on the content of this component at 0.2 percent of the oxygen of all terrestrial rocks.

The three-isotope plot for oxygen should be useful in future studies of samples returned from other planets. If the two-component model of solar system oxygen is valid, it is possible to determine the relative

proportions of the components in a planet on the basis of a single analysis of a sample of the planet. This is possible even if the planet has undergone extensive differentiation so that the surface sample is not chemically representative of the body as a whole. It would simply be necessary to plot the data point and construct a fractionation line with slope of one-half to find its intersection with the mixing line. The intersection then determines the content of ^{16}O -rich component relative to the Earth and the various meteorite classes.

References

1. CLAYTON, R. N., L. GROSSMAN, AND T. K. MAYEDA, A Component of Primitive Nuclear Composition in Carbonaceous Meteorites. *Science*, Vol. 182, 1973, pp. 485-488.
2. ONUMA, N., R. N. CLAYTON, AND T. K. MAYEDA, Oxygen Isotope Cosmometer. *Geochimica et Cosmochimica Acta*, Vol. 36, 1972, pp. 169-188.
3. ONUMA, N., R. N. CLAYTON, AND T. K. MAYEDA, Oxygen Isotope Temperatures of "Equilibrated" Ordinary Chondrites. *Geochimica et Cosmochimica Acta*, Vol. 36, 1972, pp. 157-168.
4. CLAYTON, R. N., AND T. K. MAYEDA, The Use of Bromine Pentafluoride in the Extraction of Oxygen From Oxides and Silicates for Isotopic Analysis. *Geochimica et Cosmochimica Acta*, Vol. 27, 1963, pp. 43-52.
5. CRAIG, H., Standard for Reporting Concentrations of Deuterium and Oxygen-18 in Natural Waters. *Science*, Vol. 133, 1961, pp. 1833-1834.
6. GROSSMAN, L., Condensation in the Primitive Solar Nebula. *Geochimica et Cosmochimica Acta*, Vol. 36, 1972, pp. 597-619.
7. EPSTEIN, S., AND H. P. TAYLOR, JR., $\text{O}^{18}/\text{O}^{16}$, $\text{Si}^{30}/\text{Si}^{28}$, D/H, and $\text{C}^{13}/\text{C}^{12}$ Ratios in Lunar Samples. *Geochimica et Cosmochimica Acta*, Supplement 2, Vol. 2, 1971, pp. 1421-1441.

Page intentionally left blank

Page intentionally left blank

Chemical Fractionation in the Solar Nebula

Lawrence Grossman

*Department of the Geophysical Sciences
University of Chicago
Chicago, Illinois*

The sequence of condensation of minerals from a cooling gas of solar composition has been calculated from thermodynamic data over the pressure range 10^{-3} to 10^{-5} atm, assuming that complete chemical equilibrium is maintained. The results suggest that the Ca-Al-rich inclusions in Allende and other carbonaceous chondrites are aggregates of the highest temperature condensates. Complete condensation of these elements is followed, 100° later, by the onset of the crystallization of nickel-iron, forsterite and enstatite. Transport of Ca-Al-rich refractory condensates from one part of the nebula to another before the condensation of these lower-temperature phases may have been responsible for the refractory element fractionations between the different classes of chondrites and possibly for the inferred refractory element enrichment of the Moon.

The temperature gap between the condensation temperatures of nickel-iron and forsterite increases with increasing total pressure. Because pressure and temperature probably increased with decreasing heliocentric distance in the solar nebula, Mercury may have accreted from a condensate assemblage having a higher metal/silicate ratio than Venus or Earth which may, in turn, have formed from less oxidized material than Mars. Heterogeneous accumulation models in which the Earth accretes in a stratified fashion with refractory condensates in the interior and volatile materials in the surface layers have some geochemical advantages over homogeneous accretion models.

The availability of accurate thermodynamic data, high-quality data on the abundances of the elements in the solar system, and estimates of the initial physical conditions in the solar nebula allows the accurate calculation of the sequence of condensation of minerals during the cooling of the gas cloud. The purpose of this paper is to present the results of these calculations and to review their applicability to some important problems in meteoritics and planetology. For a more detailed review, the reader is referred to Grossman and Larimer (ref. 1).

Method of Calculation

Recent models for the evolution of the solar nebula (ref. 2) suggest that tempera-

tures as high as 2000 K and total pressures between 10^{-3} and 10^{-5} atm prevailed in the inner part of the nebula. At equilibrium under these conditions all the major elements would have been completely in the vapor state. The relative abundances of the elements in the solar system have recently been reviewed by Cameron (ref. 3). It is probable that the abundances of most of the major elements are now known to within a factor of 2 and that trace element abundances are known to within a factor of 10. Because the pressure and composition of the solar nebular vapor are known, the distribution of the elements between gaseous molecules and crystalline phases can be computed as a function of temperature, using equilibrium thermodynamic models.

The general outline of the method used to calculate the sequence of condensation of elements and compounds from a cooling gas of solar composition is given below. The details of the calculations may be found in Grossman (ref. 4).

The system is assumed to contain only the 20 most abundant elements in the solar system, excluding the noble gases. For each element, a mass-balance equation containing terms for the concentrations of all gaseous species containing that element is written. If a chemical reaction is written in which each polyatomic gaseous molecule is formed from its monatomic gaseous constituent elements, its concentration term in the mass-balance equations can be replaced by the product of the equilibrium constant for the reaction and powers of concentrations of the monatomic gaseous component elements. The equation set, containing terms for 300 gaseous species, thus reduces to a system of 20 simultaneous, nonlinear equations in 20 variables—the concentrations of the 20 monatomic gaseous elements. This equation set can be solved easily by a method of successive approximations using a high-speed computer.

The reaction for the decomposition of a crystalline phase into its monatomic gaseous component elements can be used to obtain its condensation temperature. For each of over 100 solid phases of interest, the temperature variation of the equilibrium constant for this reaction is compared to the concentrations of the relevant gaseous species as calculated at different temperatures from the mass-balance equations.

At a given pressure, the equation set was solved first at the highest temperatures and then at successively lower temperatures, in intervals of 25 or 50°. At each temperature, the solutions were checked against the equilibrium constants for every crystalline phase in order to test for the condensation of solids. When such a phase was found to appear, its exact condensation temperature was calculated, an additional variable was added to the equation set below that temperature to account for its presence, and a new equation was added, imposing the condition that the

new crystalline phase be in complete chemical equilibrium with the vapor. The calculations were continued to lower and lower temperatures where more solid phases were seen to condense and react with the vapor to form new phases. The result of the calculations is a model that describes the progressive condensation of the cooling solar nebula at complete chemical equilibrium. Calculated condensation temperatures would be in error by $\pm 20^\circ$ due to estimated uncertainties in free energies of formation. The year-to-year fluctuations in elemental abundances lead to temperature uncertainties on the order of 10 to 20°.

Results

EARLY CONDENSATES

Figure 1 shows the calculated distribution of Al between crystalline phases and vapor at 10^{-3} atm total pressure. Corundum is the first condensate containing a significant fraction of any of the major elements. It condenses at 1742 K and consumes more than 95 percent of the Al before it begins to react with the vapor to form melilite at 1608 K.

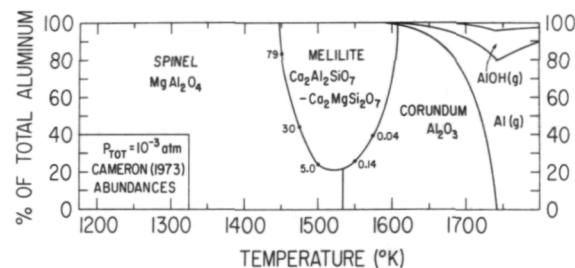


Figure 1.—The calculated distribution of Al between crystalline phases and vapor in the solar nebula. Corundum condenses at 1742 K and begins to react with the vapor of 1608 K to form gehlenite-rich melilite. Excess corundum reacts to form spinel at 1533 K. Between 1500 and 1450 K, melilite reacts with the vapor to produce more spinel and increase its akermanite content (mole % indicated by numbers on the melilite curve). Melilite reacts completely with the vapor at 1442 K to form diopside and more spinel. Al is virtually completely condensed at 1600 K.

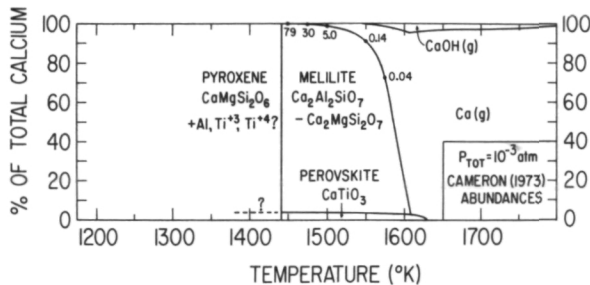


Figure 2.—The calculated distribution of Ca between crystalline phases and vapor in the solar nebula. Perovskite condenses at 1632 K and melilite at 1608 K. Melilite reacts completely with the vapor to form spinel and diopside at 1422 K. Numbers on the melilite curve give the mole % akermanite in solid solution in the melilite. Ti is totally condensed at 1600 K and Ca is 90-percent condensed at 1550 K.

The amount of melilite increases with decreasing temperature, forming at the expense of corundum. The remaining corundum reacts with gaseous Mg at 1533 K to form spinel. Melilite is a solid solution of gehlenite, $\text{Ca}_2\text{Al}_2\text{SiO}_7$, and akermanite, $\text{Ca}_2\text{MgSi}_2\text{O}_7$. The first melilite to form is virtually pure gehlenite. At 1500 K it still contains only 5 mole percent akermanite, but by 1450 K this concentration must reach 79 mole percent, according to ideal solid solution theory. Consequently, the melilite expels Al to form more coexisting spinel below 1500 K. The numbers on the melilite curve in figure 1 indicate the mole percent of akermanite in solid solution. At 1442 K, the melilite reacts completely with the vapor to form diopside and more spinel.

The distribution of Ca between vapor and solids at 10^{-3} atm is shown in figure 2. Perovskite is the first Ca-bearing phase to condense, appearing at 1632 K. Because the Ti/Ca atomic ratio is only 0.03, however, even when all the Ti is consumed by perovskite at 1600 K, only 3 percent of the Ca is condensed. The major sink for Ca at high temperature is melilite. More than 90 percent of the total Ca is condensed at 1550 K. At 1442 K, the total reaction of melilite to spinel and pyroxene is evident. The calculations refer to a pyroxene of diopside composition,

$\text{CaMgSi}_2\text{O}_6$, although there is some evidence from meteorites that this pyroxene might be rich in Al, Ti^{4+} , and Ti^{3+} . Thermodynamic data are lacking, however, for pyroxenes of these compositions.

The early condensates are thus dominated by minerals rich in Al and Ti, which are totally condensed at 1600 K, and Ca, which is 90-percent condensed at 1550 K.

CONDENSATION OF THE MOST ABUNDANT NONVOLATILE ELEMENTS

In distinct contrast to Ca, Al, and Ti, the most abundant metallic elements, Fe, Mg, and Si, are virtually uncondensed above 1550 K, and significant fractions of them begin to condense only below 1460 K (Fe) and 1430 K (Mg, Si). Figure 3 illustrates the distribution of Mg between crystalline phases and vapor at 10^{-3} atm. The condensation curve for metallic nickel-iron is also shown. The bulk of the Mg begins to condense at 1430 K as forsterite, which later reacts with the vapor to form enstatite at 1355 K. Iron begins to condense at 1460 K and is 46-percent condensed when forsterite appears. Figure 4 shows that significant condensation of Si also does not begin until forsterite formation.

This difference in the condensation behav-

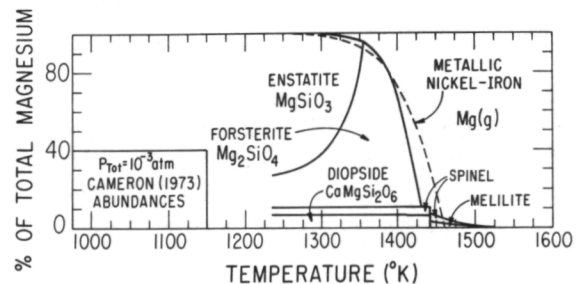


Figure 3.—The calculated distribution of Mg between crystalline phases and vapor in the solar nebula. Less than 10 percent of the total Mg is condensed above 1450 K. Forsterite appears at 1430 K and begins to react with the vapor at 1355 K to form enstatite. The condensation curve for iron as an iron-nickel alloy is shown for reference. Fe and Mg are more than 90-percent condensed at 1350 K.

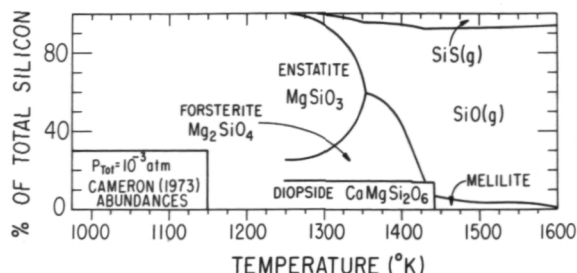


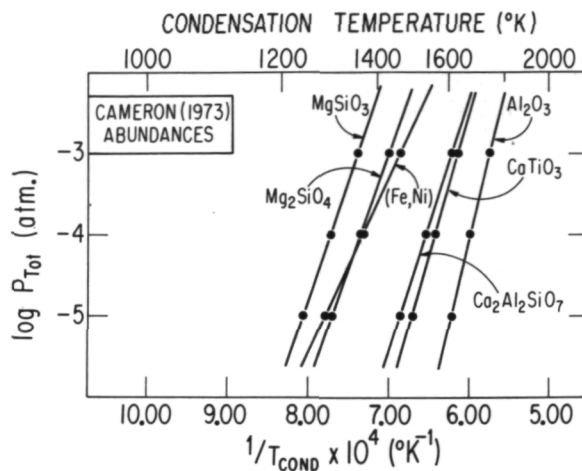
Figure 5.—The pressure variation of the condensation temperatures of some important minerals. All condensation temperatures increase with pressure. The condensation sequence is the same for all the lithophile elements from 10^{-3} to 10^{-5} atm. Nickel-iron condenses at higher temperatures than forsterite for total pressure greater than $\sim 5.5 \times 10^{-5}$ atm. The reverse is true at lower pressures.

ior of Ca, Al, and Ti on one hand and Fe, Mg, and Si on the other may have led to chemical fractionations in the solar nebula. If physical conditions existed during the condensation of the nebula which allowed the efficient separation of dust from gas and the concentration of dust relative to the gas in some regions, then some bodies in the inner solar system may have accreted from materials enriched or depleted in Ca, Al, and Ti, relative to Mg, Fe, and Si, compared to the solar system abundances.

The first metal alloy to condense from a gas of solar composition at 10^{-3} atm should contain 15.1 mole percent Ni, 0.76 percent Co, 0.35 percent Cr, and 83.8 percent Fe. If the metal continues to equilibrate with the vapor as the temperature falls, its composition should be 6.0 percent Ni, 0.28 percent Co, 1.00 percent Cr, and 92.7 percent Fe at 1375 K.

The variation with pressure of the condensation temperatures of some of the phases discussed above is shown in figure 5. The sequence of condensation and reaction is the same from 10^{-3} to 10^{-5} atm for all the litho-

Figure 4.—The calculated distribution of Si between crystalline phases and vapor in the solar nebula. Less than 10 percent of the total Si is condensed above 1450 K. Si is more than 90-percent condensed at 1300 K.



phile elements, with the entire sequence moving downward in temperature by about 70° for each factor of 10 decrease in total pressure. Metallic nickel-iron, however, has a lower condensation temperature than forsterite below $\sim 5.5 \times 10^{-5}$ atm and condenses above forsterite at higher pressure. The temperature gap between the condensation points of metal and forsterite increases with increasing pressure, suggesting that metal/silicate fractionation during condensation increased in importance toward the center of the nebula where the pressure was highest.

SOME LOW-TEMPERATURE CONDENSATION REACTIONS

As Larimer (ref. 5) pointed out, Na and K are relatively low-temperature condensates, appearing below 1250 K at 10^{-3} atm, perhaps in the form of alkali feldspar. The high-temperature magnesium silicates remain FeO-free until the temperature falls below 800 K, when the nebula becomes more oxidizing by

Table 1.—*Chemical Compositions of Allende White Inclusions Compared to Calculated Condensate Compositions at $P_{\text{tot}} = 10^{-3}$ atm.*

Condensate 1475 K		Coarse-Grained Inclusion ⁽¹⁾	Condensate 1450 K	Fine-Grained Inclusion ⁽²⁾	Condensate 1440 K
CaO	32.31	26.76	27.23	21.6	18.86
Al ₂ O ₃	34.81	31.61	29.22	26.6	20.21
TiO ₂	1.77	0.99	1.49	1.3	1.02
MgO	9.39	10.82	16.98	13.1	21.03
SiO ₂	21.71	29.79	25.09	33.7	38.87
Total	99.99	99.97 ⁽³⁾	100.01	96.3 ⁽⁴⁾	99.99

NOTES: (1) Type a chondrule NMNH 3529 (ref. 8).

(2) Single aggregate NMNH 3510 (ref. 8).

(3) Also contains 0.37 percent FeO and 0.11 percent Na₂O.

(4) Also contains 0.1 percent Cr₂O₃, 2.3 percent FeO, and 1.1 percent Na₂O.

the reaction of CO with H₂ to produce CH₄ and H₂O. Sulphur condenses when gaseous H₂S reacts with excess metallic nickel-iron to form troilite at 700 K. Magnetite becomes stable at 405 K, and the hydration of ferromagnesian silicates takes place at approximately 350 K.

Interpretation

CHONDRITES

Refractory Aggregates in the Carbonaceous Chondrites

Irregularly shaped, white aggregates are found in the C2 and C3 carbonaceous chondrites. They are enriched in Ca, Al, and Ti and depleted in Mg, Fe, and Si relative to the solar system abundances. This suggests that they may be related to the highest temperature condensates from the solar nebula (refs. 1, 4, 6, and 7). In table 1, the bulk chemical compositions of two of these inclusions from the Allende meteorite are compared to calculated equilibrium condensate compositions, excluding metallic Fe, in the temperature range 1475 to 1440 K at 10^{-3} atm total pressure. The quantitative similarities reinforce the suggestion that the inclusions may be

samples of the early condensates. The small quantities of alkali metals and FeO may have entered the inclusions as a result of metamorphic reactions inside the parent body, long after condensation was over.

The common mineral assemblage in the Ca-rich inclusions consists of perovskite, spinel, and melilite, which usually contains about 25 mole percent akermanite (refs. 8 through 11). These are precisely the same phases which are predicted to be in equilibrium with the solar nebular gas in the temperature range 1500 to 1450 K at 10^{-3} atm. Sometimes these aggregates are surrounded by narrow rims of diopside which may signify the onset of the reaction of melilite with the vapor to form diopside and spinel at 1442 K. Other types of Ca-rich inclusions are found which contain coarse crystals of pyroxene rich in Al₂O₃, TiO₂, and Ti₂O₃. This mineral might be a condensate or, alternatively, it may be a crystallization product of a liquid formed when a condensate aggregate was later melted.

Although they have very low partial pressures in a gas of solar composition, some trace elements form such stable, refractory compounds that they can condense in the same temperature range as melilite, spinel, and perovskite (ref. 12). Table 2 shows the approximate condensation temperatures of a

Table 2.—*Condensation Temperatures of Refractory Trace Elements Compared to Those of the Major High-Temperature Minerals*

Crystalline Phase	Condensation Temperature (°K)		Enrichment Factor ⁽¹⁾ in Allende Inclusions
	10 ⁻³ atm	10 ⁻⁴ atm	
Os	1925	1840	15
W	1885	1798	13
ZrO ₂	1840	1789	10
Re	1839	1759	21
Corundum (Al ₂ O ₃)	1742	1671	
HfO ₂	1719	1652	10
Y ₂ O ₃	1719	1646	21
Sc ₂ O ₃	1715	1644	22.9 ⁽²⁾
Mo	1684	1603	10
Perovskite (CaTiO ₃)	1632	1557	
RE ₂ ⁽³⁾ O ₃ (in solution)	1632	1557	22.5 ^(3,4)
Ir	1629	1555	24.1 ⁽²⁾
Ru	1614	1541	12
Gehlenite (Ca ₂ Al ₂ SiO ₇)	1608	1528	
V ₂ O ₅	1534	1458	
Spinel (MgAl ₂ O ₄)	1533	1451	
Ta ₂ O ₅	1499	1452	18
ThO ₂	1496	1429	
Diopside (CaMgSi ₂ O ₆)	1442	1375	

NOTES: (1) Enrichment factor = concentration in Allende inclusion/concentration in Type I carbonaceous chondrites.

(2) RE = rare earth element. The rare earths can condense in solid solution in perovskite.

(3) Data from Grossman (ref. 12) who analyzed 16 inclusions. All other enrichment factors are based on one Allende inclusion, analyzed by Wänke et al. (ref. 13).

(4) Average of La, Sm, Eu, Yb

number of these elements compared to the Ca-Al-rich minerals. In the final column of this table are the results of trace element analyses of some Allende inclusions. These show that almost all of these elements are enriched in the inclusions by factors of 10 to 25 relative to CI chondrites. Thus, in spite of the vast differences in geochemical behavior between elements as dissimilar in chemical properties from one another as the rare earths and the platinum metals, for example, these elements are all concentrated into the same mineral aggregates. The only feature common to all of these elements is that they condense from a gas of solar composition over the same temperature range as the

major phases in the inclusions. They may have nucleated upon the major minerals or may have gone into solution in some of them during condensation. Alternatively, the trace elements may have become associated with the Ca-Al-rich phases by serving as the condensation nuclei for them. The trace element characteristics of the Allende inclusions are a very powerful argument in support of a condensation origin.

Gray et al. (ref. 14) reported the lowest Sr⁸⁷/Sr⁸⁶ ratio (0.69877) ever measured in meteorites from a Rb-poor, Ca-rich inclusion in Allende. Such inclusions are thus the most primitive objects yet sampled in the solar system.

High-Temperature Metal and Forsterite Condensates in Carbonaceous Chondrites

Fuchs et al. (ref. 15) and Grossman and Olsen (ref. 16) described single euhedral crystals and loose aggregates of crystals of nearly pure forsterite from Murchison and other C2 chondrites. Their textures suggest that they may be direct condensates from the solar nebula. In that case, their compositions would indicate equilibration with the nebular gas at temperatures in excess of 900 K. Inside the crystals are tiny grains of metal with compositions in the range 3.8 to 8.9 mole percent Ni, 0.16 to 0.70 percent Co, 0.17 to 1.07 percent Cr, and up to 5.7 percent P. The Ni, Co, and Cr concentrations suggest that most of these grains could have equilibrated with a gas of solar composition in the temperature range 1430 to 1350 K at 10^{-3} atm. The phosphorous may have entered the grains when schreibersite formed as a result of the reaction of gaseous P_2 with the metal at 1420 K. The absence of grains with higher Ni contents than are observed may indicate that early, high-Ni metal was able to equilibrate before being isolated from the vapor by the growth of forsterite around it. This implies a time lag between the condensation of metal and that of forsterite, such as would be the case at pressures greater than $\sim 5.5 \times 10^{-5}$ atm.

Fractionation of Refractory Condensates

Larimer and Anders (ref. 6) showed that the ordinary and enstatite chondrites are depleted in the refractory lithophile elements by mean factors of 0.69 and 0.50, respectively, relative to the C1 chondrites. These include Ca, Al, Ti, Hf, Zr, Sc, Th, Y, and rare earths, many of the elements listed in table 2. In addition, the Vigarano Type C3 chondrites appear to be enriched in Ca, Al, and Ti by about 28 percent relative to C1 chondrites (ref. 17). Apparently these elements were transported together, as a group, from one part of the nebula to another prior to the

accretion of the different classes of chondrites. The observed fractionations could have been produced by the addition or removal of only 1 to 2 percent of the total condensable matter in the form of high-temperature condensate aggregates, such as the Allende inclusions, to or from a gas of solar composition.

PLANETS

There is now considerable evidence in the chondritic meteorites that chemical fractionations accompanied the condensation of the solar nebula. This suggests that it may be more reasonable to picture planetary-sized objects as being composed of different proportions of the condensate components found within chondrites than to think of them as having accreted from different mixtures of the various meteorite types.

The Moon

Numerous analytical studies have shown that the lunar surface rocks are enriched in the refractory lithophile elements by factors of 5 to 100 and strongly depleted in the volatile transition metals and alkali metals relative to the solar system abundances (refs. 13, 18, and 19). These data have prompted a number of investigators to propose that this applies to the Moon as a whole and that the Moon accreted from a higher-than-chondritic proportion of the high-temperature condensates. The Allende inclusions represent approximately 4.5 wt% of the total condensable mater. Ganapathy and Anders (ref. 20) suggested that the Moon contains 24 percent early condensate; Wänke et al. (ref. 21) proposed 60 percent, and Anderson (ref. 22), in an extreme version of these models, suggested that the Moon is virtually 100 percent high-temperature condensate.

Condensation calculations suggest, however, and the Allende inclusions confirm, that the early condensate is rich in refractory siderophile metals such as Ir, Re, Os, and Ru (ref. 12). On the other hand, the lunar

rocks are depleted in these elements relative to chondrites by factors of 10^2 to 10^4 . If these models of lunar composition are correct, the entire Moon should be enriched to a similar degree in these elements as it appears to be in the case of the refractory lithophiles. Their absence from the surface rocks would seem to imply that they have been concentrated into the lunar interior by a very efficient process such as partitioning into an Fe or Fe-S melt which sank under the influence of gravity.

Every meteoritic condensate aggregate whose oxygen isotopic composition has been measured is found to contain a 1- to 3-percent enrichment in O^{16} compared to "normal" solar system oxygen. Clayton et al. (ref. 23) attributed this effect to the survival of pre-existing interstellar grains during the early high-temperature stage of the nebula and their incorporation into the forming condensate crystals. Grossman et al. (ref. 24) reported that the lunar samples show no evidence of this anomaly. Furthermore, there is no known meteoritic material which can be mixed with the Allende inclusions to yield the inferred oxygen isotopic composition of the Moon. The major cosmochemical argument against a refractory condensate-rich Moon appears to be that the required early condensates having normal isotopic composition exist only in theory and have not been observed in meteorites.

The Terrestrial Planets

From the densities of the terrestrial planets, Urey (ref. 25) estimated that the Fe/Si ratio of Mercury is three times that of the Earth and five times that of Mars. This progressive decrease in planetary metal/silicate ratio with increasing heliocentric distance can be understood, at least qualitatively, in terms of condensation models. Hoyle and Wickramasinghe (ref. 26) and Cameron and Pine (ref. 2) presented physical models of the solar nebula in which the pressure and temperature in the median plane are highest in the center and decrease with increasing

heliocentric distance. In addition, we have seen that the temperature gap between the condensation temperatures of metal and forsterite increases with pressure. Mercury probably accreted from materials which condensed at a higher pressure than Venus or Earth. Therefore, it might be expected to possess a higher metal/silicate ratio if the nebular gases were dissipated at a time when metal was totally condensed and forsterite only partially condensed. At the same time, both metal and silicates may have been totally condensed in the region of the nebula where Venus and Earth formed because the pressure and temperature were considerably lower there. Mars may have formed largely from volatile-rich condensates containing a high ratio of oxidized iron to metallic iron. Grossman (ref. 4) and Lewis (ref. 27) have both pointed out the similarity between the pressure-temperature gradients required in this model and those actually predicted in hydrodynamic treatments.

The Earth: Homogeneous Versus Heterogeneous Accretion

Ringwood (ref. 28) proposed that the Earth was built homogeneously from material having the composition of C1 chondrites, and that the core formed when accretional heating reduced oxidized iron to the metallic state and melted it, allowing it to sink to the center of the Earth. Ringwood noted some features of terrestrial geochemistry which could not be explained adequately by this model. Among these are the highly oxidized nature and the high siderophile element content of the Earth's crust and upper mantle. Had the upper part of the Earth ever been in chemical contact with a sinking metallic melt, it should be very reduced and stripped of its siderophile elements.

In order to overcome these difficulties, Turekian and Clark (ref. 29) and Clark et al. (ref. 30) proposed that the Earth accreted heterogeneously; that is, that the Earth began accreting from material of one composition and finished with material of another

composition. Specifically, the Earth is pictured as having accreted in a stratified fashion from materials in the order of their condensation from the nebula. Thus, part of the metal core may have formed before lower-temperature magnesium silicates began to condense. A volatile-rich oxidized crust may have been the final layer to accumulate (ref. 31). Any siderophile elements present in this crust would remain in the upper part of the Earth since, in this model, the metal in the core was never in contact with the surface layers. This heterogeneous accumulation model makes use of the high-temperature reducing atmosphere of the solar nebula in order to produce the metallic core and avoids the difficulty of having to lose an enormous primitive atmosphere of CO which is a formidable obstacle to the in-situ reduction process envisioned by Ringwood.

References

- GROSSMAN, L., AND J. W. LARIMER, Early Chemical History of the Solar System. *Rev. Geophys. Space Phys.*, Vol. 12, 1974, pp. 71-101.
- CAMERON, A. G. W., AND M. R. PINE, Numerical Models of the Primitive Solar Nebula. *Icarus*, Vol. 18, 1973, pp. 377-406.
- CAMERON, A. G. W., Abundances of the Elements in the Solar System. *Space Sci. Rev.*, Vol. 15, 1973, pp. 121-146.
- GROSSMAN, L., Condensation in the Primitive Solar Nebula. *Geochimica et Cosmochimica Acta*, Vol. 36, 1972, pp. 597-619.
- LARIMER, J. W., Chemical Fractionations in Meteorites: I. Condensation of the Elements. *Geochimica et Cosmochimica Acta*, Vol. 31, 1967, pp. 1215-1238.
- LARIMER, J. W., AND E. ANDERS, Chemical Fractionations in Meteorites: III. Major Element Fractionations in Chondrites. *Geochimica et Cosmochimica Acta*, Vol. 34, 1970, pp. 367-387.
- MARVIN, U. B., J. A. WOOD, AND J. S. DICKEY, JR., Ca-Al-Rich Phases in the Allende Meteorite. *Earth Planet. Sci. Letters*, Vol. 7, 1970, pp. 346-350.
- CLARKE, R. S., JR., E. JAROSEWICH, B. MASON, J. NELEN, M. GÓMEZ, AND J. R. HYDE, The Allende, Mexico, Meteorite Shower. *Smithsonian Contrib. Earth Sci.*, Vol. 5, 1970.
- KURAT, G., Zur Genese der Ca-Al-reichen Einschlüsse im Chondriten von Lancé. *Earth Planet. Sci. Letters*, Vol. 9, 1970, pp. 225-231.
- FUCHS, L. H., Occurrence of Cordierite and Aluminous Orthoestatite in the Allende Meteorite. *Am. Mineral.*, Vol. 54, 1969, pp. 1645-1653.
- FUCHS, L. H., Occurrence of Wollastonite, Rhönite, and Andradite in the Allende Meteorite. *Am. Mineral.*, Vol. 56, 1971, pp. 2053-2067.
- GROSSMAN, L., Refractory Trace Elements in Ca-Al-Rich Inclusions in the Allende Meteorite. *Geochimica et Cosmochimica Acta*, Vol. 37, 1973, pp. 1119-1140.
- WÄNKE, H., H. BADDENHAUSEN, G. DREIBUS, M. QUIJANO-RICO, H. PALME, B. SPETTEL, AND F. TESCHKE, Multielement Analysis of Apollo 16 Samples and About the Composition of the Whole Moon. *Lunar Science*, Vol. IV, J. W. Chamberlain and C. Watkins, eds., Lunar Science Institute, Houston, 1973, pp. 761-763.
- GRAY, C. M., D. A. PAPANASTASSIOU, AND G. J. WASSERBURG, The Identification of Early Condensates From the Solar Nebula. *Icarus*, Vol. 20, 1973, pp. 213-239.
- FUCHS, L. H., E. OLSEN, AND K. J. JENSEN, Mineralogy, Mineralchemistry and Composition of the Murchison (C2) Meteorite. *Smithsonian Contrib. Earth Sci.* Vol. 10, 1973.
- GROSSMAN, L., AND E. OLSEN, Origin of the High-Temperature Fraction of C2 Chondrites. *Geochimica et Cosmochimica Acta*, Vol. 38, 1974, pp. 173-187.
- VAN SCHMUS, W. R., AND J. M. HAYES, Chemical and Petrographic Correlations Among Carbonaceous Chondrites. *Geochimica et Cosmochimica Acta*, Vol. 38, 1974, pp. 47-64.
- GANAPATHY, R., R. R. KEAYS, J. C. LAUL, AND E. ANDERS, Trace Elements in Apollo 11 Lunar Rocks: Implications for Meteorite Influx and Origin of Moon. *Geochimica et Cosmochimica Acta*, Supplement 1, Vol. 34, 1970, pp. 1117-1142.
- TAYLOR, S. R., R. RUDOWSKI, P. MUIR, A. GRAHAM, AND M. KAYE, Trace Element Chemistry of Lunar Samples From the Ocean of Storms. *Geochimica et Cosmochimica Acta*, Supplement 2, Vol. 35, 1971, pp. 1083-1099.
- GANAPATHY, R., AND E. ANDERS, Bulk Compositions of the Moon and Earth, Estimated From Meteorites. *Lunar Science*, Vol. V, Lunar Science Institute, Houston, 1974, pp. 254-256.
- WÄNKE, H., H. PALME, H. BADDENHAUSEN, G. DREIBUS, E. JAGOUTZ, H. KRUSE, B. SPETTEL, AND F. TESCHKE, Composition of the Moon and Major Lunar Differentiation Processes. *Lunar Science*, Vol. V, Lunar Science Institute, Houston, 1974, pp. 820-822.
- ANDERSON, D. L., The Composition and Origin of the Moon. *Earth Planet. Sci. Letters*, Vol. 18, 1973, pp. 301-316.
- CLAYTON, R. N., L. GROSSMAN, AND T. K. MA-

- YEDA, A Component of Primitive Nuclear Composition in Carbonaceous Meteorites. *Science*, Vol. 182, 1973, pp. 485-488.
24. GROSSMAN, L., R. N. CLAYTON, AND T. K. MAYEDA, Oxygen Isotopic Compositions of Lunar Soils and Allende Inclusions and the Origin of the Moon. *Lunar Science*, Vol. V, Lunar Science Institute, Houston, 1974, pp. 298-300.
25. UREY, H. C., The Abundance of the Elements With Special Reference to the Problems of the Iron Abundance. *Quart. J. Roy. Astron. Soc. London*, Vol. 8, 1967, pp. 23-47.
26. HOYLE, F., AND N. C. WICKRAMASINGHE, Condensation of the Planets. *Nature*, Vol. 217, 1968, pp. 415-418.
27. LEWIS, J. S., Metal/Silicate Fractionation in the Solar System. *Earth Planet. Sci. Letters*, Vol. 15, 1972, pp. 286-290.
28. RINGWOOD, A. E., Chemical Evolution of the Terrestrial Planets. *Geochimica et Cosmochimica Acta*, Vol. 30, 1966, pp. 41-104.
29. TUREKIAN, K. K., AND S. P. CLARK, JR., Inhomogeneous Accumulation of the Earth From the Primitive Solar Nebula. *Earth Planet. Sci. Letters*, Vol. 6, 1969, pp. 346-348.
30. CLARK, S. P., JR., K. K. TUREKIAN, AND L. GROSSMAN, Model for the Early History of the Earth. *The Nature of the Solid Earth*, E. C. Robertson, ed., McGraw-Hill Book Co., 1972, pp. 3-18.
31. LARIMER, J. W., AND E. ANDERS, Chemical Fractionations in Meteorites: II. Abundance Patterns and Their Interpretation. *Geochimica et Cosmochimica Acta*, Vol. 31, 1967, pp. 1239-1270.

Time Scale for the Formation of the Earth and Planets and Its Role in Their Geochemical Evolution

V. S. Safronov
*O. Yu. Schmidt Institute of Earth Physics,
Moscow, U.S.S.R.*

The duration of the process of formation of the Earth and planets is discussed. A short time scale for formation of the Earth (10^4 – 10^5 years) has been proposed, not from a consideration of the rate of its growth, but from geochemical and geophysical considerations. On the basis of the dynamics of a swarm of protoplanetary bodies and the process of accretion of the planets, the author has found an accumulation time for 98 percent of the mass of the Earth of 6×10^4 – 10^5 years and a characteristic time for sweeping out of the protoplanetary cluster (reducing its mass by half) of 10^7 years. It is shown that the shorter accretion time found by Öpik, Cameron, Hallam, and Marcus is related to arbitrary assumptions about the parameters of the model for the swarm (e.g., the relative velocities of the bodies, the cluster density).

The initial mass of the solar nebula is discussed. Models of a massive nebula (two solar masses and more) encounter serious difficulties: an effective mechanism of transfer of the momentum from the central part of the nebula outward, capable of leading to formation of the Sun and removal of half the mass of the nebula from the solar system has not been found. As a consequence of the instability of these models, their evolution can end with the formation, not of a planetary system, but of a binary star. The possibility is demonstrated of obtaining acceptable growth rates for Uranus and Neptune by prolonging the thickening of preplanetary dust in the region of large masses.

The important role of large bodies in the process of formation of the planets is noted. The impacts of such bodies, moving in heliocentric orbits, could have imparted considerable additional energy to the forming Moon, which, together with the energy given off by the joining of a small number of large protomoons, could have led to a high initial temperature of the Moon.

1. In recent years, interest in the time scale of planetary formation has increased considerably, because a close connection has been found between the length of the formation period and initial state of the planets, and, consequently, their subsequent evolution, especially geochemical. A short scale leads to a higher initial temperature of the planet and, in principle, even permits fractionation of the elements in the accretion process.

As a result of two opposing approaches to the problem, two sharply differing scales of the accretion process are now used:

A. In 1945, O. Yu. Schmidt (ref. 1) derived a formula for the growth rate of the planets. The mass of a planet increases in proportion to the geometric cross section of the planet, in proportion to the surface density σ of the solid material remaining in the planet's zone of accretion, and in inverse proportion to the period of revolution P of the planet around the Sun. In 1954, we refined this formula. It was found that the gravity of a planet significantly accelerated its growth. As a consequence of gravitational focusing, the effective collision cross section was larger than the geometric cross section

of the planet πr^2 , by $1 + V_e^2/V^2$ times, where V_e is the parabolic velocity at the surface of the planet and V is the mean relative velocity of a body in the zone of the planet. Thus,

$$\frac{dm}{dt} = 4\pi r^2 (1 + V_e^2/V^2) \frac{\sigma}{P}. \quad (1)$$

Solid material could not be ejected from the region of the terrestrial group of planets by planetary perturbations, and the initial mass of the region was equal to the current mass of these planets. Therefore, the only unknown quantity in the formula is the velocity of the bodies. The relative velocities of the bodies increased, as a consequence of their gravitational interaction upon approaching a rotating system, and it decreased in inelastic collisions. A comparison of these opposing effects (ref. 2) resulted in finding that the relative velocities of gravitating bodies are proportional to the parabolic velocities at the surface on the largest body in this zone (nucleus of the planet): $V^2 = V_e^2/2\theta = Gm/\theta r$. In the absence of a gas slowing the motion of the bodies and with a distribution of the bodies like the distribution of the mass of the asteroids, this proportionality factor is found to be close to $1/3$, which gives a velocity of the body in the zone of the Earth, in the concluding stage of its growth, of about 4 km/s ($\theta \approx 3 - 5$). These data permit the growth rate of the planets to be estimated. The radius of the proto-earth increased at practically a constant rate at 20 to 30 cm per year, to half its current value. Then, as the supply of material in the growth zone was exhausted, growth began to slow down. A characteristic time for sweeping out the material of the swarm, i.e., reducing its mass by half, with these values of θ , is 8 to 12 million years, and the time for accumulation of 98 percent of the mass of the Earth is 60 to 100 million years. In a review of the results of the Cambridge Cosmochemical Symposium, Mitler (ref. 3) notes that this scale is in conformance with the observed differences in ages of different types of meteorites, in particular, with the conclusion that the majority of the achondrites are 50 million years older than the chondrites—a figure obtained from a Rb/Sr estimate and con-

firmed by the Pb/Pb method. Our estimates permit an indeterminacy of half an order of magnitude; therefore, a value of 10^7 years can apparently be considered as the lower limit for the time of growth of the Earth.

B. A few years ago, the hypothesis of a considerably faster accretion of the planets became widespread. It did not arise initially from a consideration of the accretion process. Ringwood (ref. 4) approached it from geochemical considerations based on the idea of a hot initial state of the Earth. Hanks and Anderson (ref. 5) saw, in the idea of rapid accretion, the possibility of accelerating formation of the core of the Earth, and Turekian and Clark (ref. 6) and then Anderson and Hanks (ref. 7) saw the possibility of deriving a hypothesis of nonuniform accretion of the Earth. The last authors named above assumed the accumulation time of the Earth to be 50 thousand years. Such a rapid accretion would lead to a hot, almost molten initial state of the Earth. However, no estimates of accretion times which would reinforce this point of view were made by the authors. Such estimates began to appear somewhat later. They should be dwelt on in greater detail.

The problem was analyzed in greatest detail by Öpik (ref. 8). The characteristic time he found for sweeping out the Earth's swarm is an e -fold decrease in its mass, $\tau_e = 50\,000$ years, which corresponds to the time for reducing the mass of the swarm by half, $\tau_2 = 35\,000$ years, i.e., 2.5 orders of magnitude less than the value of 10^7 years we found. Öpik himself called this the *minimum* time. He did not determine the relative velocities of the bodies, and took the lowest value permissible from his point of view, $3/4$ km/s, for the numerical estimate. In this case, he had to adopt a highly artificial model, to concentrate all the solid material of the zone in a thin, narrow ring around the orbit of the Earth, 0.2 AU wide, that encompasses only one-third of the supply zone of the Earth. If he had considered a more likely model, in which the bodies were distributed over the entire zone of the Earth and had sufficient velocity to be able to fall to Earth, the time for sweeping out the swarm and,

correspondingly, the time of the growth of the Earth would have increased by almost two orders of magnitude. At slower velocities of the bodies, they could only move from the outer parts of the zone to the vicinity of the Earth by diffusion. However, diffusion is a still slower process, and takes over 10^8 years.

Accretion of the preplanetary bodies also is considered in the recently published work of Hallam and Marcus (ref. 9). In it, an accretion time of the Earth $\tau_+ = 200\,000$ years. However, it was obtained with an unrealistically high density of solid material in the zone of the Earth $\rho = 2 \times 10^{-9}$ g/cm³, taken ad hoc for a model similar to that of Cameron. Our model leads to $\rho = 4 \times 10^{-12}$ g/cm³. With such a density, the growth time of the Earth would coincide with our value of 10^8 years.

The shortest time for accretion of the Earth (less than 10^4 years) has been obtained by Cameron (refs. 10 and 11). This is only partially connected with the high mass of the solar nebula adopted in the model of Cameron. The principal cause of very rapid growth of the planets in Cameron's model is that he proposes their accretion in an unrestrictedly flattening layer of particles, with a thickness much less than the diameter of the planet. However, first, this extremely high degree of flattening of the layer is physically impossible, because of gravitational perturbations by the massive protoplanets (ref. 12). Second, the model is internally contradictory: strong flattening means low relative velocities of the bodies and small eccentricities of their orbits. Under such conditions, a planet might gather material located only in a very narrow zone along its orbit, i.e., only a small fraction of the material located in its zone. Expansion of the supply zone takes place only in proportion to increase in the velocities of the body and, correspondingly, should take more and more time.

Thus, in all cases, arguments in favor of a short scale of growth of the planets may disclose arbitrary assumptions, whose elimination also leads to lengthening the scale.

Mizutani et al. (ref. 13) discussed the

rate of accretion of the Moon in an isolated protolunar cloud. The authors calculate the density of the cloud and the velocities of the particles, at which rapid accretion of the Moon takes place (in less than 10^3 years) and the outer part of the Moon turns out to be molten. They consider this melting to be a necessary requirement from geochemical and geophysical data. However, the physical model of the initial cloud analyzed by the authors is very indefinite, and its suitability is not substantiated. Such estimates would make sense only if the protolunar cloud itself could have formed very quickly, significantly more rapidly than the Moon then formed from it. However, assuming that the Moon was formed in a circum-Earth swarm of particles encompassing the Earth during the entire time of its growth, we must conclude that the replenishment time of the cluster and the accretion time of the Moon was 10^7 to 10^8 years.

2. Our concepts of the nature of the physical, chemical, and mechanical processes in the solar nebula and the protoplanetary cloud essentially depend on the initial model of the nebula. In particular, the P-T conditions of condensation of the solid particles that determine the chemical composition of the planets, as well as the rate of accumulation of the planets, depend heavily on the mass of the nebula. In recent years the massive solar nebula model of Cameron (refs. 10 and 11), double the mass of the Sun, has become widespread. In this model, the amount of solid material in the zone of the Earth turns out to be approximately 20 times the mass of the Earth. This would give a 20-fold acceleration in growth of the Earth. However, there are very important problems in the description of this model, which do not permit it to be considered to be internally consistent. The most serious of them are the following:

A. The problem of evolution of the extended rotating gas-dust nebula into a star (Sun), with simultaneous removal of half the mass of the nebula beyond the solar system, has not been solved. Estimates have shown that all of the previously proposed mechanisms for transfer or momentum from

the central region of the nebula outward are extremely ineffective and are not capable of leading to formation of the Sun. There is no basis for expecting that the new, still little-studied method of "meridional circulation," proposed by Cameron only in qualitative form, will prove to be more effective (ref. 14). On the contrary, there are serious doubts, both as to the possibility of effective transfer of momentum from the inside to the outside by means of this mechanism, and as to the possibility of the very existence of a large-scale circulation in highly flattened systems. Moreover, the possibility is not excluded that evolution of a nebula, with such a large momentum as that in the model of Cameron, can culminate in formation, not of a planetary system, but of a binary star.

B. The problem of how to remove more than 90 percent of the solid material from the region of the terrestrial group of planets has not been solved. Existing data testify against the possibility of this removal. Radial displacement of bodies due to their being slowed down by the gas ends quite early, because of the rapid growth of the mass of the bodies. Interaction of the bodies among themselves cannot give them significant velocities and leads to ejection of a considerable fraction of all the bodies from the zone of the terrestrial group of planets (as occurred in the region of the giant planets).

Recently, Levin (ref. 15) proposed a new model of a massive solar nebula. The author sees the principal difficulty of the problem as slow growth of the outer planets. With an initial amount of solid material in the zone of Uranus and Neptune equal to the modern mass of these planets, the time of their growth, according to formula (1), turns out to be on the order of 10^{11} years (ref. 16). The assumption of a large initial mass of the outer sections of the nebula, as well as that the main loss of gas took place by means of thermal dissipation, accompanying a significant approach to the Sun of the residue (jet effect), led Levin to the conclusion of very large initial (post-collapse) dimensions of the nebula (200–300 AU). He assumes the total mass of the nebula, including the proto-

sun, to be 3–4 solar masses, i.e., 1.5–2 times larger than in the model of Cameron. In order to eliminate difficulty B. of the model of Cameron, he takes a considerably smaller density of nebula material (and, correspondingly, total mass) in the region of the terrestrial group of planets, than in the model of Cameron (a slower increase in density toward the center of the nebula).

This model of a massive solar nebula meets with the same serious difficulty A., seen in the model of Cameron; no effective mechanism is known for transfer of momentum from the inside to the outside, which would lead to formation of the Sun. In addition, having a greater extent and lower concentration toward the center, this model of the nebula is still less stable, with respect to decay into a binary system, than the model of Cameron.

We also cannot agree with the opinion of Levin, that such a model of a massive nebula is necessary for solution of the problem of growth of Uranus and Neptune. The process of accumulation of the giant planets was very complicated, and it requires more comprehensive and thorough analysis.

Theoretically, there are three possibilities of reducing the growth time of the outer planets: (1) increase in initial mass of solid material in this region; (2) decrease in relative velocities of the bodies at the stage preceding their ejection from the solar system; and (3) lengthening of the concentration stage in regions of large masses.

It is known that the giant planets ejected a considerable amount of solids from the solar system in the process of growing. The initial mass of solid material in the region of the outer planets could have been much greater than their present mass. However, it is important to determine precisely how much solid material was ejected. According to our estimates, the amount of solid material ejected by a planet is an order of magnitude more than the material absorbed by it. This corresponds to a comparatively small mass of the protoplanetary cloud (0.1–0.15 M.) and to formation of the planets at almost the same distances from the sun as

they now are. However, this does not completely insure the growth of Uranus and Neptune in 4.6×10^9 years.

The possibility of accelerating the process of accretion, by means of lower relative velocities of the bodies, i.e., through an increase in parameter θ in (1), is not clear now, although it is not excluded. The velocities could have been less, for example, because of the great inelasticity of collisions of the bodies and particles of ice (a more intensive disintegration) than in collisions of silicate bodies in the region of the terrestrial group of planets.

There is still another feature of formation of the outer planets, to which insufficient attention was given earlier. According to modern conceptions (refs. 2 and 17), the initial evolution of the preplanetary cloud, with a high degree of probability, should have consisted of a flattening of a dust layer, the generation of gravitational instabilities in it, and formation of numerous dust concentrations. Conditions for gravitational instability were most favorable in the region of the giant planets. In the zones of Uranus and Neptune, the critical value of the velocities of particles of the dust layer ($v < v_{cr}$ is necessary for instability) was quite large. In table 1 are presented the values, assumed in our model, of the initial surface density of solid material (P_0) in the zones of various planets, v_{cr} values, initial masses of dust concentrations m_0 in fractions of the mass of the planet m_p , their initial densities ρ_0 , masses

m_b , at which condensation should stop in solid bodies with $\rho \sim 1-3$ g/cm³, and the time for decrease of the mass of the cluster by half τ_2 in the concluding stage ($m \rightarrow m_p$).

The concentration stage was short in the region of the terrestrial group of planets, and it did not play a significant role in the accretion process. According to our estimate the concentrations as a result of their compression on combining, converted to normal bodies ($\rho \sim 1$ g/cm³) after an increase in their initial masses by approximately 2 orders of magnitude (from 10^{-11} to 10^{-9} earth mass). The situation turns out to be completely different in the region of outer planets. The initial masses of the concentrations are inversely proportional to the sixth power of the distance from the Sun, and were only 5 orders of magnitude less than the mass of Neptune in the zone of Neptune. On the other hand, the initial densities of the concentrations (on the order of the Roche density) in the zone of Neptune were 3×10^4 less than in the zone of Earth, and therefore, to convert them into a body required an increase in their initial mass, not by two orders of magnitude as in the zone of the Earth, but by four orders of magnitude. Consequently, the preplanetary material concentration of Neptune could remain quite a long time, until its mass reached approximately a tenth of mass of Neptune (this idea was expressed by Vityazev). Having greater dimensions than a normal body, it swept up the surrounding material considerably more quickly. We have estimated the growth time of Neptune under these conditions, on the assumption of moderate relative velocities of the bodies ($\theta = 5$). The initial mass of solid material in the zone of Neptune was assumed to be ten times the mass of Neptune. The density of the protoplanetary body was assumed to be monotonically increasing (according to the power law), with increase in its mass up to $\rho = 1$, with a mass of one tenth the mass of Neptune. The time for growth of Neptune to 98 percent of its modern mass turned out to be not over 2 billion years. This is an acceptable result and demonstrates that the possibilities still have not

Table 1.—Values of Initial Surface Density of Solid Material

Zone of Planet	σ_0 (g/cm ²)	v_{cr} (cm/s)	m_0/m_p	ρ_0 (g/cm ³)	n_0/m_p	τ_2 (years)
Mercury	1.5	0.4	10^{-15}	5×10^{-5}	10^{-13}	6×10^6
Venus						
Earth	10	11	10^{-11}	3×10^{-6}	10^{-9}	10^7
Mars						
Jupiter	20	270	4×10^{-9}	2×10^{-8}	10^{-5}	10^6
Saturn						
Uranus	4	380	2×10^{-8}	4×10^{-10}	10^{-2}	2×10^8
Neptune	3	560	10^{-5}	10^{-10}	10^{-1}	3×10^8

been exhausted of solving the problem of growth of the outer planets, without going to a model of a massive nebula. The difficulties of the latter appear to us to be considerably more serious, which forces us to prefer physical, chemical, and mechanical investigations using a model of the solar nebula with a mass of $\sim 1.1 M_{\odot}$ and, correspondingly, a preplanetary cloud, with a mass of $\sim 0.1 M_{\odot}$.

3. The explanation of the large role of large bodies in the process of planetary formation has led to significant corrections in the conceptions of the initial state of the planets. Theoretical research conducted at the Institute of the Physics of the Earth, USSR Academy of Sciences (refs. 2 and 17), has shown that the distribution of mass of the preplanetary bodies, established in the accretion process, can be approximated by an inverse power law $n(m) = cm^{-q}$, at $q \sim 11/6$, i.e., by a law similar to the law describing the distribution of the mass of the asteroids, meteorites incident on the Earth, and bodies forming lunar craters. Bodies hundreds of kilometers in diameter made up a considerable fraction of the mass of all bodies forming the planets. The dimensions of the largest bodies falling onto the planets were estimated from the inclinations of the axis of rotation of the planets, which was created by the infall of large bodies. The impact energy of these bodies was released at considerable depths, and an appreciable part of it did not radiate into space. The layers of the upper mantle, at depths of about 500 km, underwent the greatest impact heating ($\approx 1500^{\circ}\text{C}$).

The largest bodies created large-scale thermal irregularities in the upper mantle. Their extensive regions of impact, with diameters up to 1000 km, became hundreds of degrees hotter than the surroundings at the very start. The basic processes of the early evolution of the Earth are connected with the development of these irregularities (ref. 18). Partial melting took place in these irregularities in the first billion years, and two competing and oppositely directed processes, convection and differentiation, were started.

These processes should have led to formation of the core of the Earth and the crust of the Earth. However, they are extremely complicated, and they still have been studied little.

There is a basis for considering that large bodies played an important part in the formation of the Moon as well. The source of the early heating of the Moon is quite an important question at the present time. Efforts to explain this heating by formation of the Moon at a distance closer to the Sun or by its extremely rapid accumulation are clearly unjustified. Formation of the Moon from a small number of large protomoons (ref. 19) gives a more suitable source, but for melting of the outer layer of the Moon, one of these bodies alone is inadequate because of the comparative low relative velocities of the protomoons. Bodies close to the Earth had considerably higher velocities when they were in heliocentric orbits at distances of 15–20 Earth radii; the velocities of bodies of the Earth zone reached 6 km/s. The energy of their impacts was 6–7 times greater than the gravitational energy on the surface of the Moon. The impact regions underwent severe heating and, possibly, melting. Wetherill (ref. 20) relates the "lunar cataclysm" ending about 4 billion years ago, with the impact onto the Moon of bodies from the region of the asteroids and even of the giant planets. The impact energies of such bodies were still greater.

Thus, the impacts of large bodies moving in heliocentric orbits were a significant additional preplanetary source for heating the forming Moon. This source deserves careful quantitative analysis.

References

1. SCHMIDT, O. YU., *Dokl Akad nauk SSSR*, Vol. 46, No. 9, 1945, p. 392.
2. SAFRONOV, V. S., *Evolution of the Protoplanetary Cloud and Formation of the Earth and Planets*, 1969.
3. MITLER, H. E., The Cambridge Cosmochemistry Symposium. *Icarus*, Vol. 20, 1973, p. 54.
4. RINGWOOD, A. E., Chemical Evolution of the Terrestrial Planets. *Geochemica et Cosmochemica Acta*, Vol. 30, No. 1., 1966.

5. HANKS, T. S., AND D. L. ANDERSON, The Early Thermal History of the Earth. *Phys. Earth Planet. Interiors*, Vol. 2, 1969, p. 19.
6. TUREKIAN, K. K., AND S. P. CLARK, Inhomogeneous Accumulation of the Earth From Primitive Solar Nebula. *Earth Planet. Sci. Letters*, Vol. 6, No. 5, 1969.
7. ANDERSON, D. L., AND T. S. HANKS, Formation of the Earth Core. *Nature*, Vol. 237, No. 5355, 1972, p. 387.
8. ÖPIK, E. J., Cratering and the Moon's Surface. *Advances in Astron. and Astrophys.* Vol. 8, 1971, p. 107.
9. HALLAM, M., AND A. H. MARCUS, *Icarus*, Vol. 21, No. 1, 1974, p. 66.
10. CAMERON, A. G. W., *Icarus*, Vol. 18, No. 3, 1973, p. 377.
11. CAMERON, A. G. W., *Icarus*, Vol. 18, No. 3, 1973, p. 407.
12. SAFRONOV, V. S., *Symposium on the Origin of the Solar System, Nice, 1972*. CNRS, Paris, 1972, p. 89.
13. MIZUTANI, H., T. MATSUI, AND H. TAKEUCHI, *The Moon*, Vol. 5, 1972, p. 476.
14. SAFRONOV, V. S., *Symposium on the Origin of the Solar System, Nice, 1972*. CNRS, Paris, 1972, p. 361.
15. LEVIN, B. J., *Symposium on the Origin of the Solar System, Nice, 1972*. CNRS, Paris, 1972, p. 341.
16. SAFRONOV, V. S., *Astron. Zhurn.* Vol. 31, 1954, p. 499.
17. ZVYAGINA, YE. V., G. V. PECHERNIKOVA, AND V. S. SAFRONOV, *Astron. Zhurn.*, Vol. 50, No. 6, 1973, p. 1261.
18. SAFRONOV, V. S., *Izv. Akad nauk SSSR, Fizika Zemli*, Vol. 7, 1972, p. 35.
19. RUSKOL, YE. L., *This Collection*, 1975. In press.
20. WETHERILL, J., *This Collection*, 1975. In press.

Page intentionally left blank

Page intentionally left blank

Mechanical Processes Affecting Differentiation of Protolunar Material¹

W. M. Kaula

*University of California, Los Angeles
Los Angeles, California*

Mechanisms prior to lunar formation are sought to account for the loss of volatiles, the depletion of iron, and the enrichment of plagioclase. Some of the same mechanisms are necessary to account for achondritic, stony-iron, and iron meteorites. Collisions seem marginally capable of providing the heat to accomplish the differentiation into iron, magnesian silicates, and plagioclase. Once this differentiation is accomplished, the subsequent mechanical history should have been sufficient to sort material according to composition in the protolunar circumterrestrial cloud. Effects operating include the correlation of body size with mechanical strength; the lesser ability of the cloud to trap the larger, denser infalling bodies; the more rapid drawing into the Earth of the larger moonlets; and the higher energy orbits for dominantly plagioclase smaller pieces broken off by collision.

Lunar Structure

An adequate theory of lunar origin must account for three major chemical differences from cosmic or chondritic abundances: (1) the loss of volatiles, (2) the loss of iron, and (3) the gain of plagioclase. As shown by all analyses of lunar samples, the Moon is a very dry place. The oxygen fugacity is extremely low, the only carbon is solar wind implanted, only traces of primordial lead have been found, etc. The mean density of 3.34 g cm^{-3} does not allow more than 14-percent iron, considerably less than the 30 to 35 percent characteristic of the Earth and meteorites. The global lunar magnetic permeability of 1.012 (ref. 1), coupled with seismic velocities indicative of an olivine composition (ref. 2), indicate an iron content as low as 6 percent. The thick crust indicated by gravimetry and altimetry (ref. 3) plus the need for mare basalt source regions to be enriched in lithophiles (refs. 4 and 5) require that at least the outer half of the Moon be enriched about threefold in plagioclase relative to chondrites. Assuming

that the $30 \text{ ergs/cm}^2/\text{s}$ heat flow measured at the Apollo 15 and 17 sites (ref. 6) is representative of the entire globe and thence of the uranium content, and assuming refractory silicate abundance to be proportionate to uranium abundance (ref. 7), the plagioclase enrichment is more than fourfold.

Constraints on origin also come from the present temperature and density structure of the Moon. The crust of 50 or 60 km of anorthositic gabbro (ref. 3) requires that the outer parts be heated enough early in lunar history to accomplish the necessary differentiation. The lithosphere 1000 km thick (ref. 8) requires that this zone have less than a chondritic abundance of radioactive heat sources and, hence, that it be at least partly cleared out of large ion lithophiles. The central asthenosphere of 700 km suggests that this innermost 10 percent of the Moon's bulk formed too cold to participate in the early differentiation and, hence, retained its heat sources, enabling it to warm up to its present state.

¹ Publication No. 1342 of the Institute of Geophysics and Planetary Physics.

Before constructing an hypothesis of lunar origin to account for these data, it is appropriate to review some dynamical considerations and differentiation processes.

Dynamical Considerations

If we accept the uniformitarian principle that the Sun and planets formed from a gas and dust cloud similar to those observed to be associated with new stars now, then the planets formed from a nebula of some sort (refs. 9 and 10). In such a context, a dynamically plausible origin of the Moon is one which is a by-product of the Earth's formation (refs. 11 through 14), i.e., the Moon forms from a cloud of matter around the Earth. The process is initiated by collisions between planetesimals close enough to the Earth for energy loss sufficient for capture, but at the same time retaining momentum sufficient to go into geocentric orbit rather than infall. The resulting moonlets then act as an efficient trap for further protolunar material.

If the assumption is made that with mass incrementation to the cloud the angular momentum incrementation is random, then a major portion of the cloud was drawn into the Earth. For a cloud of bodies each with mass m_i , semimajor axis a_i , and angular momentum H_i , of total mass small compared to the planet embryo, where M is the planet

$$\frac{1}{2a_i} \frac{da_i}{dt} \approx - \frac{1}{m_i} \frac{dm_i}{dt} - \frac{1}{2M} \frac{dM}{dt} + \frac{1}{H_i} \frac{dH_i}{dt} \quad (1)$$

embryo mass (ref. 15). Another process which would have drawn satellites toward the Earth if planetesimal velocities were isotropic with respect to the Earth was "drag" on the satellites by the planetesimals. A satellite's orbiting about a planet gives it a systematic motion with respect to the planetesimals, resulting in (ref. 16) where δ is

$$\frac{da_i}{dt} = - \frac{88}{15} \pi \delta [GMR\theta]^{1/2} [r_i^2/m_i] \quad (2)$$

the space density of planetesimals in the nebula beyond the influence of the planet em-

bryo; G is the gravitational constant; R is the radius of the planet embryo; r_i is the satellite radius; and θ is the factor for relative velocities v_{rel} in the planet's zone:

$$v_{rel}^2 = GM/R\theta \quad (3)$$

The factor θ varies from 3 to 10, depending on the amount of gas present (ref. 10). More detailed calculations show that the protolunar swarm must get started when the Earth itself is a rather minor fraction of its final mass—less than 10 percent—if a final Moon as large as the actual is to be attained at the end of the process (refs. 14, 15, and 16). Furthermore, a consequence of equations (1) and (2) was that the Moon formed largely of material that fell into the Earth-Moon system later than the bulk of the Earth's material.

It seems dubious that planetesimal velocities were purely isotropic or that angular momentum incrementation was entirely random, however. The latter is hard to reconcile with the progradeness of nearly all satellite orbits and planetary rotations. Whether small biases affect satellite orbit evolutions needs to be solved in conjunction with the planetary rotation problem, perhaps following the path suggested by Giulini (ref. 17).

A process which moved satellites outward was tidal friction:

$$\frac{da_i}{dt} = 3km_i \left[\frac{G}{M} \right]^{1/2} \frac{R^5}{a_i^{11/2}} \cdot \frac{1}{Q} \quad (4)$$

where k is the planet's Love number and $1/Q$ is the dissipation factor (ref. 18). The sign of equation (4) depends on the body's being outside the geosynchronous distance; the magnitude of $1/Q$ depends on the difference between rotational and orbital rates, $\omega - n$, as well as the thermal state of the Earth.

The final important effect on the growth of moonlets about the Earth and their orbital evolution was collision, with the resulting accretion and fragmentation. Through collisions, a system isolated from outside influence evolves toward the minimum energy state conserving angular momentum—a set of coplanar circular orbits. But if the surface

density of matter is sufficient, moonlets and, thence, the Moon form by gravitational instability; i.e., relative velocities become gentle enough by collision that any density perturbation grows by gravitational attraction. The time scale for formation of 10-km-sized moonlets is a few years; for the entire Moon, less than 1000 yr (ref. 19). However, the Earth-Moon system was not isolated, but was continually disturbed by infalls from the heliocentric system. Hence, the formation of the Moon was delayed considerably by continual infalls causing breakup of moonlets and repetition of the settling down process until the infall was too small to inhibit the final formation of the Moon, which then occurred rather rapidly. This rapid formation led to significant heating of the outer parts of the Moon, resulting in differentiation of the crust. The heating was of a magnitude suggested by the accretion formula (ref. 20):

$$\rho \frac{Gu(r)}{r} \cdot \frac{dr}{dt} = \delta (T^4 - T_{\text{equil}}^4) \quad (5)$$

However, the actual accretion was not the neat accumulation of small bodies suggested by this formula, but more a rather irregular process entailing a wide mass range of infalling bodies, the largest a significant fraction of the Moon's mass. These infalls supplied energy for the convection associated with the asymmetric crustal differentiation.

Collisions also acted to fragment bodies, of course. The typical planetesimal was rather porous, since its component parts could have come together only by bumping at rather low velocities. Subsequent collisions at higher velocities normally involved bodies differing considerably in size. Hence, the effect of collisions was mainly to chip off pieces from the outer parts of the larger bodies and to fragment only the smaller bodies.

An effect of the porosity was to convert a higher portion of the kinetic energy into heat through melting induced by collapse of voids in the rocks, similar to what is happening on a smaller scale currently on the lunar surface (ref. 21). The portion of bodies involved in collision that was melted was always quite minor. More material received

mild heating, leading to metamorphosis as observed in ordinary chondrites. Much more was not significantly heated at all, but fractured and broken off, the greater part of the energy of impact going into the kinetic energy of pieces flying off.

Most of the foregoing applies to smaller planetesimals of not more than a few tens of kilometers in size. In larger bodies more than 100 km in size and, thus, having some gravitational field, repeated impacts by smaller bodies resulted in some heating and in some compaction of the deeper parts from the recurrent vibrations set up.

The collision regime applying to the protolunar swarm was appreciably more violent than that for the planetesimals in heliocentric orbits, due to the enhancement of infall velocities by the Earth's attraction. For bodies in heliocentric orbit, an important energy input to collisions was the development of Jupiter. When Jupiter became more than about one-tenth its present mass, it threw considerable matter at rather high velocities into the inner solar system, knocking out more matter than it added but, through collisions, producing appreciable energy for heating.

A final dynamical effect that may have been important in sorting protolunar material is tidal disruption of large planetesimals passing the Earth within their Roche limit. As emphasized by Wetherill (ref. 22) and Wood and Mitler (ref. 23), such close approaches are considerably more probable than collisions. However, most planetesimals were too small to be significantly affected by tidal disruption.

Differentiation Processes

Processes leading to compositional differentiation can be classified as condensational, planetary, and mechanical, i.e., condensing from the gas phase, melting within a parent body or colliding and blowing off, respectively.

As emphasized by several authors, e.g., Grossman and Larimer (ref. 24), but par-

ticularly Anderson (ref. 25) with reference to the Moon, the first condensates are calcium-, aluminum-, and titanium-rich minerals, followed by iron, magnesian silicates, etc. However, it is difficult to imagine the small portion of Ca-Al-Ti minerals drifting to the central plane of a hot gaseous nebula to form sizable planetesimals undisturbed by convection currents, etc. It is also hard to imagine how ionization could be maintained to allow plasma effects to be significant separation mechanisms (ref. 26) in such circumstances. The evidence from the Pueblo de Allende meteorite is that the condensation sequence led to moderate enrichment of some particle compositions, but not to segregation of sizable bodies.

Most drastic differentiations among irons and silicates—terrestrial and lunar rocks, achondritic, stony-iron, and iron meteorites—apparently happened as the consequence of melting in a parent body. In the case of terrestrial and lunar rocks, the general circumstances are fairly evident. In the case of meteorites, we have some evidence of the size of parent bodies in the nickel-iron concentration gradients of the Widmanstätten patterns (refs. 27 and 28). However, the heat source is still a major problem. Aluminum-26 appears to be ruled out by the absence of Magnesium-26 (ref. 29). Electromagnetic induction by the T-Tauri hurricane (ref. 30) still seems somewhat contrived, dependent on solar spin decay and mass outflow, both extrapolated from observations of larger stars (refs. 31 and 32). A remaining possibility is collision, whose effect was enhanced by porosity. So far as the problem of the Moon is concerned, we can take as given by the nickel/iron gradient observations of Wood (ref. 27) and Goldstein and Short (ref. 28), that differentiation by melting occurs in some planetesimals of not more than a few tens of kilometers radius. In addition, we all find it convenient to take, as given by the spectroscopic observations of T-Tauri stars by Kuhi (ref. 32), that an outstreaming of matter occurs after a new star forms, even though an understanding of *why* it occurs is remote.

Whipple (ref. 33) suggested that the dif-

fering mechanical strengths of iron and silicates would lead to larger earlier forming bodies having more iron than smaller late-forming bodies. Orowan (ref. 34) and Ruskol (ref. 35) have further pursued this possibility. Offhand, it seems like a rather long regime of repeated coalescence, collision, fragmentation, and re-coalescence would have been necessary to make mechanical strength an effective sorting mechanism. However, this inefficiency applies mainly to getting differentiation started. Once there had been perceptible differentiations due to condensational or planetary processes, these mechanical effects would enhance segregation of iron from silicates, at least (but not magnesian silicates from plagioclase, etc.). In regard to the composition of the protolunar swarm, manifestly small low-density silicate bodies were more easily captured than large high-density iron bodies. Furthermore, mechanical sorting in the circumterrestrial swarm would be a much more rapid and effective process than in the heliocentric nebula and would be enhanced by any dynamical effects dependent on moonlet size.

Lunar Formation

We wish to construct a scenario of lunar formation taking into account the foregoing considerations. This scenario is based mainly on the models of Ruskol (refs. 12, 13, and 14). The principal addition is to explore the planetary differentiation processes and related collision effects resulting in plagioclase enrichment, which may also have effects on the iron and volatile depletions in addition to the factors considered by Ruskol (ref. 35). We also should consider the implications of a much more massive nebula, such as hypothesized by Cameron (ref. 9) and Levin (ref. 36).

Condensation of solids in a nebula led fairly rapidly to the formation of planetesimals by gravitational instability. Applying the formulae of Goldreich and Ward (ref. 37) to the vicinity of the Earth's orbit leads to 5-km radii for the initial bodies in a sparse

nebula of 10 g/cm² solids (ref. 10) and to 500-km radii for the initial bodies in a massive nebula of 1000 g/cm² solids (ref. 9). Mutual perturbations between planetesimals led to the development of relative velocities on the order of $[Gm/r\theta]^{1/2}$, in accord with equation (3). Assuming the higher values of θ dependent on the presence of gas, the initial relative velocities were on the order of 100 cm/s in the sparse nebula and 2×10^4 cm/s in the massive nebula. Using Safronov's (ref. 10) formulae, the resulting formation times for the Earth are 10^8 yr in the sparse nebula and 2×10^4 yr in the massive nebula. (Cameron's figure of 10^3 yr depends on the suppression of all planetesimals but one by an unexplained mechanism.) These growth times are not directly comparable; growth in the sparse nebula terminates because of exhaustion of the solid matter in the zone, while growth in the massive nebula terminates because the remaining material is removed by external causes, presumably a super solar wind.

Our concern is means for heating of planetesimals which are protolunar material in the nebula. The lifetime formulae assume that the terrestrial zone is isolated. In the massive nebula case, there is ample matter for collisions to cause considerable heating: indeed, it is a necessary part of that hypothesis that material be sufficiently pulverized by collision to be blown away. In the sparse nebula case, relative velocities sufficient for collisional heating, say, 1 km/s, occurred when the Earth was only about 2 percent its final mass, if we assume a θ of 4 (appropriate for no gas) in equation (3). The amount of mass per unit time collided with by a larger planetesimal of radius s at this stage is $v_{\text{rel}}\pi s^2\delta$. The space density δ itself is inversely proportionate to the height of the nebula, $R v_{\text{rel}}/v_{\text{orb}} \sim R/30$, where R is the radius of the Earth's orbit, whence

$$\dot{m} = \pi s^2 s v_{\text{orb}} / R \quad (6)$$

Using 10 g/cm² for s and 720 km for s (i.e., a body with 1 km/s escape velocity), we get 3.3×10^{10} g/s for \dot{m} . If this mass influx rate were distributed in small bodies, the heating

would be negligible. The heating must be in impacts by bodies of comparable size or not much smaller, and the amount of heat retained is on the order of the change in potential energies upon combination (ref. 19):

$$E = \frac{3}{5} G \left[\frac{(\mu_1 + \mu_2)^2}{s} - \frac{\mu_1^2}{s_1} - \frac{\mu_2^2}{s_2} \right] \quad (7)$$

For a combination of $s_1 = 720$ km and $s_2 = 360$ km, the energy thus gained is 1.8×10^{33} ergs, or only 3.3×10^8 ergs/g. However, the energy dissipation is highly concentrated near the interface of the collision, most of it in less than 10 percent of the mass. In addition, some of the kinetic energy of approach is trapped if the bodies are porous. If repeated impacts occurred, it is plausible that the outer 100 km or so of planetesimals were heated sufficiently to differentiate plagioclase and iron and to outgas volatiles.

An additional source of energy was bodies thrown into the inner solar system by Jupiter. Such bodies had relative velocities of approach of about 10 km/s; hence, their effect on mass growth was disrupting rather than contributing. However, they would have contributed significantly to heating. They also would have been important in breaking off compositionally different parts of planetesimals from one another and in sorting them by size: the irons tending to be larger because of mechanical strength and the silicates smaller. Due to the longer time scale of Jupiter's formation, these effects probably were not important until the late stages of Earth and Moon formation. A possibility worth exploring is that the protolunar cloud was then enriched by plagioclase-rich material perturbed by Jupiter.

Hence, from dynamical reasoning as well as the evidence of the nonchondritic meteorites, the protolunar material would have arrived in the Earth's vicinity somewhat sorted in composition. Any geocentric belt of matter would have effected further sorting, since it was more capable of catching small silicate chunks than large iron chunks. There would also at this stage have been some discrimination between magnesian silicates and plagioclase; a greater portion of the lat-

ter would be in small pieces chipped from the surfaces of planetesimals and, hence, more easily caught.

For the material in orbit about the Earth, the collision regime was qualitatively similar to that of the planetesimals in orbit about the Sun, but two orders-of-magnitude (at least) faster, due to the much shorter cycle time. Higher energy infalls from outside the system had a disrupting and heating effect analogous to the Jupiter intrusions into the inner solar system. Additional effects were the gravitational tightening of the planet-satellite system, planetesimal drag, and tidal friction, expressed by equations (1), (2), and (4). Equation (1) suggests that if dm/dt were proportionate to the cross section area, or $m^{2/3}$, then smaller bodies would be drawn into the Earth more quickly, since da/dt would then be proportionate to $m^{-1/3}$. However, the high velocities of infall make it quite unlikely that the growth rate would be proportionate to $m^{2/3}$. Rather, taking into account the effect on collision of moonlet size relative to infalling body size, the correlation of the stronger material iron with size of body and gravitational binding energy, dm_i/dt , would be likely to have an exponential dependence m_i^n of $n > 1$. In other words, the smaller bodies would have tended more toward elastic collisions and the larger bodies toward inelastic collisions. Hence, equation (1) acted more to remove the larger bodies from the circumterrestrial swarm. However, equation (2) acted more to remove the smaller bodies.

Layered differentiation of moonlets would also have occurred, with the plagioclase rising to the outer parts and the iron sinking to the deeper parts. Upon collision, small pieces would have been chipped off the outer parts of these moonlets. These chipped pieces would have had higher energy per unit mass, relative to the Earth, than the average and, thus, would have taken up orbits on the whole farther out than their parent moonlet. As a result, a larger-than-average portion of them would survive being drawn back into the Earth and therefore would have been finally incorporated in the Moon. These pieces would

have had a higher-than-average plagioclase content and lower-than-average iron content.

Additional effects of significance for moonlets coming close to the Earth may be tidal disruption and atmospheric drag. Tidal disruption of a single large planetesimal coming close to the Earth from a low approach velocity has been proposed by Wood and Mitler (ref. 23) as a means of obtaining all the protolunar material. However, the low approach velocity implies that this large planetesimal was formed in the Earth's zone; it is extremely improbable that such a big body, 100 times as massive as allowed by Safronov's $(2\theta)^3$ rule (ref. 10), could have found sufficient low-velocity material to collect itself. So far as our hypothesis goes, the effect merely constrains moonlets to be less than about 200 km in size so long as they are inside the Roche limit. Once they have moved beyond the limit, they can combine into larger bodies, as in Öpik's models (ref. 38).

Atmospheric drag acts, of course, to draw down the smaller silicate bodies preferentially, contrary to the eventuality required by lunar composition. A massive atmosphere, as hypothesized by Ringwood (refs. 39, 40, and 41), might exert such an influence, even if it did not gain enough energy to leave the Earth. Although core formation undoubtedly was of major importance in determining the Earth's convective regime for the first 10^9 yr or more, there is no way any significant fraction of this energy could have been concentrated sufficiently to blast volatiles off the Earth. (Even if it could have been, the maximum mass raised to escape would be only 0.06 Earth mass.) The core formation energy was released throughout the body; it was brought to the surface by convection in an almost liquid mantle where it was exchanged with a vigorously convecting atmosphere that radiated it away. However, although this convection was vigorous by planetary standards, the energy density of the process was small compared to stars, and the rate of mass outflux negligible. The Earth could not have developed an expanding corona.

Hence, the planetesimal collision processes discussed earlier must have also operated to

remove volatiles from proto-Earth material. Possibly the Earth's present volatiles were carried by the initial infalling planetesimals, while the later infalling planetesimals were already rather dried out. This raises the problem of why an atmosphere did not form by outgassing of the early infalls and remain while subsequent infalls occurred: why is the Earth so depleted in xenon relative to chondrites, let alone the Sun? Perhaps the devolatilizing of the inner solar system took place when no bodies more than 1000 km or so in radius existed; the initial conglomeration of such planetesimals to make the Earth's center was at too low velocity to cause much outgassing (say about 20 such bodies, constituting 10 percent of the Earth's mass), while the outer bulk of the Earth was made of planetesimals that were all second or later generation, already well outgassed by earlier collisions.

The alternative hypothesis that the Earth and the Moon acquired their volatiles as a veneer from late infalling matter (refs. 7, 42, and 43) requires that the compounds of active volatiles, HCNO, must have been protected from whatever blew away the inert gases. Also, since the Moon has a much higher proportion of late matter than the Earth, the lunar material must have suffered its volatile loss relative to the Earth by processes associated with its geocentric orbit. This loss requires not only heating and breakup, but also sweeping out of the satellite zone so that recondensation onto the protolunar matter does not occur.

To return to the lunar formation problem, any early Earth atmosphere, no matter how hot and seething, would not have had a scale height more than say 100 km, corresponding to silica at 2000 K. Hence, its ability to reach to satellite material at the geosynchronous distance for the 5-hour day, $2.3 R_e$, would have been slight.

Conclusions

To summarize, the circumterrestrial ring of matter about the early Earth was already

appreciably devolatilized, enriched in silicates relative to iron, and probably enriched in plagioclase relative to magnesian silicates by processes occurring in planetesimals in heliocentric orbit and by some selectivity in capturing such planetesimals and their fragments. While the material was in orbit about the Earth, the outer parts of the cloud which constituted the protolunar material suffered loss of iron due to the more rapidly growing bodies' being drawn into the Earth and experienced gain in plagioclase due to the outermost fragments of moonlets subject to collision being put in higher energy orbits. Also during this time appreciable further loss of volatiles occurred. The material that finally got together to form the Moon during a lull of infalls from outside the Earth-Moon system did so rather rapidly so that the outer parts of the Moon were heated sufficiently to bring much of the excess plagioclase up to form the thick crust.

The hypothesis presented here may seem to depend too much on multistage collision processes difficult to model mathematically. However, given the fundamental hypothesis that the planets and satellites were made from a dust and gas solar nebula, it seems unavoidable that the processes described herein occurred; the problem is the quantitative importance of the processes relative to one another.

Acknowledgment

Discussions with A. W. Harris have been helpful. This research is supported by NASA grant NGL 05-007-002.

References

1. DYAL, P., C. W. PARKIN, AND W. D. DAILY, Lunar Electrical Conductivity, Permeability, and Temperature Measurements From Apollo Magnetometer Experiments. *Proc. Soviet-Am. Conference Cosmochem. Moon and Planets*, in press, 1975.
2. LATHAM, G., Y. NAKAMURA, D. LAMMLEIN, J. DORMAN, AND F. DUENNEBIER, Moonquakes, Meteoroids, and the Structure and State of

- the Lunar Interior. *Proc. Soviet-Am. Conference Cosmochem. Moon and Planets*, in press, 1975.
3. KAULA, W. M., G. SCHUBERT, R. E. LINGENFELTER, W. L. SJOGREN, AND W. R. WOLLENHAUPT, Apollo Laser Altimetry and Inferences as to Lunar Structure. *Proc. Fifth Lunar Science Conference*, in press, 1974.
 4. GAST, P. W., The Chemical Composition and Structure of the Moon. *The Moon*, Vol. 5, 1972, pp. 121-148.
 5. RINGWOOD, A. E., AND D. H. GREEN, Maria Basalts and Composition of Lunar Interior (abs). *Lunar Science*, Vol. V, Lunar Science Institute, Houston, 1974, pp. 636-638.
 6. LANGSETH, M. G., AND S. J. KEIHM, In-Situ Measurements of Lunar Heat Flow. *Proc. Soviet-Am. Conference Cosmochem. Moon and Planets*, in press, 1975.
 7. GANAPATHY, R., AND E. ANDERS, Bulk Compositions of the Moon and Earth, Estimated From Meteorites. *Proc. Fifth Lunar Science Conference*, in press, 1974.
 8. LAMMLEIN, D. R., G. V. LATHAM, J. DORMAN, Y. NAKAMURA, AND M. EWING, Lunar Seismicity, Structure, and Tectonics. *Rev. Geophys. and Space Phys.*, Vol. 12, 1974, pp. 1-21.
 9. CAMERON, A. G. W., Accumulation Processes in the Primitive Solar Nebula. *Icarus*, Vol. 18, 1973, pp. 407-450.
 10. SAFRONOV, V. S., *Evolution of the Protoplanetary Cloud and Formation of the Earth and the Planets*. Israel Program for Scientific Translations, Jerusalem, 1972.
 11. KAULA, W. M., AND A. W. HARRIS, Dynamically Plausible Hypotheses of Lunar Origin. *Nature*, Vol. 245, 1973, pp. 367-369.
 12. RUSKOL, E. L., The Origin of the Moon: 1. Formation of a Swarm of Bodies Around the Earth. *Sov. Astron. AJ*, Vol. 4, 1960, pp. 657-668.
 13. RUSKOL, E. L., On the Origin of the Moon: 2. The Growth of the Moon in the Circumterrestrial Swarm of Satellites. *Sov. Astron. AJ*, Vol. 7, pp. 221-227.
 14. RUSKOL, E. L., The Origin of the Moon: 3. Some Aspects of the Dynamics of the Circumterrestrial Swarm. *Sov. Astron. AJ*, Vol. 15, 1972, pp. 646-654.
 15. KAULA, W. M., Dynamical Aspects of Lunar Origin. *Rev. Geophys. and Space Phys.*, Vol. 9, 1971, pp. 217-238.
 16. HARRIS, A. W., AND W. M. KAULA, A Co-Accretional Model of Satellite Formation. *Proc. IAU Coll. No. 28, Planetary Satellites*, in press, 1974.
 17. GIULI, R. T., On the Rotation of the Earth Produced by Gravitational Accretion of Particles. *Icarus*, Vol. 8, 1968, pp. 301-323.
 18. KAULA, W. M., *An Introduction to Planetary Physics: The Terrestrial Planets*. John Wiley & Sons, Inc., 1968.
 19. RUSKOL, E. L., On the Model of the Accumulation of the Moon Compatible With the Data on the Composition and the Age of Lunar Rocks. *The Moon*, Vol. 6, 1973, pp. 190-201.
 20. HANKS, T. C., AND D. L. ANDERSON, The Early Thermal History of the Earth. *Phys. Earth Planet. Interiors*, Vol. 2, 1969, pp. 19-29.
 21. AHRENS, T. J., AND J. D. O'KEEFE, Shock Melting and Vaporization of Lunar Rocks and Minerals. *The Moon*, Vol. 4, 1972, pp. 214-249.
 22. WETHERILL, G., *These Proceedings*, 1975.
 23. WOOD, J. A., AND H. E. MITLER, Origin of the Moon by a Modified Capture Mechanism, or Half a Loaf Is Better Than a Whole One (abs). *Lunar Science*, Vol. V, Lunar Science Institute, Houston, 1974, pp. 851-853.
 24. GROSSMAN, L., AND J. W. LARIMER, Early Chemical History of the Solar System. *Rev. Geophys. and Space Phys.*, Vol. 12, 1974, pp. 71-101.
 25. ANDERSON, D. L., The Formation of the Moon (abs). *Lunar Science*, Vol. IV, Lunar Science Institute, Houston, 1973, pp. 40-42.
 26. ARRHENIUS, G., AND H. ALFVEN, Fractionation and Condensation in Space. *Earth Planet. Sci. Letters*, Vol. 10, 1971, pp. 253-267.
 27. WOOD, J. A., The Cooling Rates and Parent Planets of Several Iron Meteorites. *Icarus*, Vol. 3, 1964, pp. 429-459.
 28. GOLDSTEIN, J. I., AND J. M. SHORT, The Iron Meteorites, Their Thermal History and Parent Bodies. *Geochimica et Cosmochimica Acta*, Vol. 31, 1967, pp. 1733-1770.
 29. SCHRAM, D. N., F. TERA, AND G. J. WASSERBURG, The Isotopic Abundance of ^{26}Mg and Limits of ^{26}Al in the Early Solar System. *Earth Planet. Sci. Letters*, Vol. 10, 1970, pp. 44-59.
 30. SONETT, C. P., D. S. COLBURN, K. SCHWARTZ, AND K. KEIL, The Melting of Asteroidal Parent Bodies by Unipolar Dynamo Induction From a Primordial T Tauri Sun. *Astrophys. and Space Sci.*, Vol. 7, 1970, pp. 446-488.
 31. KRAFT, R. P., Evidence for Changes in the Angular Velocity of the Surface Regions of the Sun and Stars. *Solar Wind*, NASA SP-308, 1972, pp. 276-282.
 32. KUHI, J. V., Mass Loss From T Tauri Stars. *Astrophys. J.*, Vol. 140, 1964, pp. 1409-1433.
 33. WHIPPLE, F. L., The History of the Solar System. *Proc. Nat. Acad. Sci.*, Vol. 52, 1964, pp. 565-594.
 34. OROWAN, E., Density of the Moon and Nucleation of Planets. *Nature*, Vol. 222, 1969, p. 867.
 35. RUSKOL, E. L., On the Possible Differences in the Bulk Chemical Composition of the Earth and the Moon Forming in the Circumterrestrial Swarm. *The Moon, I.A.U. Symp. No. 47*, Reidel, 1972, pp. 426-428.

36. LEVIN, B., Revision of Initial Size, Mass, and Angular Momentum of the Solar Nebula and the Problem of Its Origin. *Symposium on the Origin of the Solar System*, H. Reeves, ed., Cent. Nat. Res. Sci., Paris, 1972, pp. 341-360.
37. GOLDBREICH, P., AND W. R. WARD, The Formation of Planetesimals. *Astrophys. J.*, Vol. 183, 1973, pp. 1051-1061.
38. ÖPIK, E. J., Comments on Lunar Origin. *Irish Astron. J.*, Vol. 10, 1972, pp. 190-238.
39. RINGWOOD, A. E., Some Aspects of the Thermal Evolution of the Earth. *Geochimica et Cosmochimica Acta*, Vol. 20, 1960, pp. 241-244.
40. RINGWOOD, A. E., Chemical Evolution of the Terrestrial Planets. *Geochimica et Cosmochimica Acta*, Vol. 30, 1966, pp. 41-104.
41. RINGWOOD, A. E., Origin of the Moon: The Precipitation Hypothesis. *Earth Planet. Sci. Letters*, Vol. 8, 1970, pp. 131-140.
42. ANDERS, E., Chemical Processes in the Early Solar System, as Inferred From Meteorites. *Acc. Chem. Res.*, Vol. 1, 1968, pp. 289-298.
43. TUREKIAN, K. K., AND S. P. CLARK, JR., Inhomogeneous Accumulation of the Earth From the Primitive Solar Nebula. *Earth Planet. Sci. Letters*, Vol. 6, 1969, pp. 346-348.

Page intentionally left blank

Page intentionally left blank

The Origin of the Moon

Ye. L. Ruskol

*O. Yu. Schmidt Institute of Earth Physics
Academy of Sciences,
Moscow, U.S.S.R.*

This paper discusses fractionation of the chemical compositions of the Moon and the Earth and the thermal history of the Moon for formation of the Moon from an Earth-orbiting swarm of bodies, during the accumulation of the Earth.

This report will consider only a model for formation of the Moon in orbit around the Earth. This model is closely connected with the theory of formation of the Earth and the planets that has been developed in the O. Yu. Schmidt Institute of Earth Physics, Academy of Sciences, Moscow (refs. 1 and 2). We will not dwell on a review of different hypotheses of lunar formation because they are given in published works (refs. 3, 4, and 5).

It is interesting to discuss those questions which traditionally are considered most difficult for this model: (1) differences in chemical composition of the Moon and the Earth and (2) the initial and boundary conditions of the thermal history of the Moon that conform to its current state.

Our physical-mechanical scheme of development for the Moon is built on the concept that during the active stage of growth of the Earth a satellite swarm of small bodies and particles formed around it. In order to become satellites of the Earth, these particles and bodies revolved in heliocentric orbits in the zone of the preplanetary cloud which the growing nucleus of the Earth was gradually sweeping out. As a consequence of inelastic collisions near the Earth, a certain fraction of the particles change to geocentric orbits. The satellite swarm of the Earth is very small. Its maximum radius is 100 times smaller than the distance from the Earth to the Sun, and that part of the swarm where

an increased density over that of the "background" is achieved is tens of times smaller in size, such that the capture of particles in Earth orbit is most likely for near-Earth collisions. In this scheme, the Moon represents the final product of "assembly" of the particles and bodies of the satellite swarm.

If only the mutual collisions of particles in heliocentric orbits are taken into consideration, the mass of the satellite swarm proves to be several orders of magnitude less than the mass of the Moon. If the collision of free particles with those already captured is considered, an exponential growth of the mass of the swarm can be obtained and will overtake the mass growth of the Earth. However, if the density in some part of the cluster exceeds the "background" density by a factor of two or three orders of magnitude, the growth of an Earth satellite is activated in the swarm and quickly (in 10^2 to 10^3 yr) sweeps up newly entering particles, preventing too rapid growth of the swarm. With the process balanced in this manner, the maximum filling of the swarm is applied to the mass of the protoearth and is equal to two-fifths to one-half its modern mass (fig. 1). In order to obtain the required mass and geocentric moment of the swarm, it is not important how much time growth of the Earth takes because formation of the swarm is an accompanying process. However, chemical fractionation between the material of the

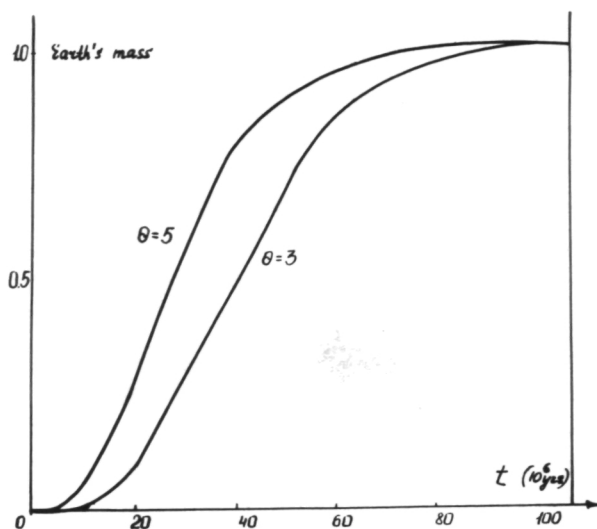


Figure 1.—Rate of accretion of the Earth, according to Safronov (ref. 2).

Earth and the material of the satellite swarm is not indifferent to the duration of the entire process. We assume a long time scale for growth of the Earth (10^8 yr), which is currently the most solidly based from the dynamical point of view (ref. 2).

Differences in Chemical Composition of the Earth and Moon During Formation of the Moon From the Earth Satellite Swarm

PARTIAL LOSS OF VOLATILE AND SEMI-VOLATILE ELEMENTS AND ASSOCIATED ENRICHMENT OF THE SWARM WITH REFRACTORY SILICATES

Because the circumterrestrial swarm is secondary and formed later than the Earth, the material of the Moon should have been in a dispersed state longer: at first in the preplanetary cloud and then in circumterrestrial orbits. This lag in accumulation is at least 5×10^7 to 10^8 yr. During this time, the small bodies and particles experience numerous collisions at velocities determined by perturbations due to the protoearth: in the

protoplanetary cloud the velocities are 3 to 4 km/s on the average and 5 to 7 km/s during capture into the swarm. A characteristic time for dissipation of light gases from the region of the terrestrial group of planets by the solar wind is 10^8 yr. As Kuiper showed (ref. 6), the solar wind is capable of ionizing and blowing the atoms of any element right out of the solar system if the space is free for radiation. It can be shown that the protoplanetary cloud was quite transparent in the radial direction from the Sun ($\tau \approx 1$) out to the distance of the Earth from the Sun, if the radial distribution of the protoplanetary bodies followed the law $dN(a) \sim a^{-n} da$, where $n \leq 3.5$, with the mass of the material equal to the mass of the terrestrial planets and with $a_{max} \approx 10^8$ cm. Much material evaporates in collisions of solid particles with velocities of several km/s; this shows up particularly in the low-melting and volatile components (H_2O , Pb, Bi, Tl, etc.). We (ref. 7) considered an example of selective removal of volatiles in a single collision, where the collision led to capture into the swarm. The colliding particles lose the evaporating components, a certain fraction recondenses into particles within the cluster, and the remaining ones are expelled from the swarm by the solar wind. Particles adsorbed by the growing Earth fall into it with high velocities (10 km/s) and also undergo evaporation. However, the strong gravitational field of the Earth prevents the evaporated material from escaping, and the inner, denser, and more opaque part of the swarm protects them from the action of the solar wind. Thus, two features should be considered as facilitating the Earth's acquiring relatively more volatiles and the Moon's acquiring relatively more refractory material: (1) earlier accumulation of the Earth from material that passed through a shorter sequence of collisions and (2) the presence of Earth gravity when the Earth and the satellite cluster simultaneously acquired material. It should be added that the work of Prof. E. Anders and colleagues (ref. 8), based on analyses of the first basalt samples returned from Mare Serenitatis in 1969 and

in which the fact was established of depletion of volatiles from lunar samples and their enrichment in refractory elements, was an occasion for our discussion in 1971 of selective removal of volatiles from the particles of the circumterrestrial swarm. Subsequent investigations by the same authors and other groups showed how universal the regularity they discovered is for the Moon.

SELECTIVE REMOVAL OF THE SMALLEST PARTICLES BY CAPTURE IN THE SWARM AND ASSOCIATED ENRICHMENT OF THE LUNAR MATERIAL IN SILICATES

Let us proceed to the question of fractionation of iron and silicates. Studies of the size distribution of preplanetary bodies using coagulation theory, with allowance for fragmentation, have shown that this distribution asymptotically approaches the power law $dN(a) \sim a^{-n_1} da$, when $n_1 < 3.5$ (for a mass distribution, this corresponds to the exponent $11/6$) (refs. 2, 9, and 10). A simplifying assumption unavoidably has to be made in these studies, i.e., that the entire set of bodies and particles has uniform physical-mechanical properties, as well as composition. The predominant factor in the collisional interactions of the particles is mass, hence the important role of the largest bodies in the process of planetary growth. During the accretion of the terrestrial planets, the exponential-type distribution mentioned above becomes established among the protoplanetary bodies, where the size range is 12 to 13 orders of magnitude. At $n_1 \sim 3.5$ (and generally, at $3 < n_1 < 4$), there is an interesting feature that is illustrated in figure 2. A large part of the mass of the bodies is concentrated in the largest bodies, and a large part of the total surface is concentrated in the largest bodies, and a large part of the total surface is concentrated in the smaller fraction. This means that in process where the main role is played by the frequency of interactions, the small particles have the greatest activity. We have shown that in capture in the swarm the size distri-

bution of the particles changes in the direction of enrichment with the smaller fraction (ref. 11). Thus, if the exponent for protoplanetary bodies was 3.5 after capture in the swarm (without considering the accumulating satellites) there would be a distribution with the exponent $n_2 \approx 4.0$. Thus, there is a shift in the direction of smaller bodies. In this case, the mass is not concentrated in the largest bodies, but is uniformly distributed over the entire range of particle sizes.

Could this feature of the formation of the swarm lead to its enrichment in silicates or somehow to the depletion of iron? At the present time more data have appeared in favor of this possibility than there were in 1971 when we proposed this process based only on the qualitative considerations of Orowan (ref. 12). Recent experiments on collision of metallic particles have demonstrated that in a large velocity range, from 0.5 km/s to 10 km/s metallic particles weld themselves together, while at velocities less than 0.5 cm/s they undergo semielastic repulsion (ref. 13). Experiments with silicate particles confirmed the idea of Orowan that behavior of silicate particles is completely opposite to the behavior of metallic ones; i.e., in the impact velocity range from 1.5 km/s to 9.5 km/s destruction of the particles predominates over their agglomeration (ref.

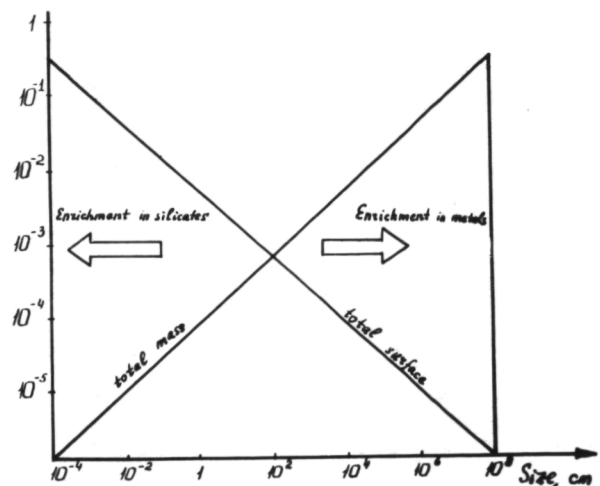


Figure 2.—Characteristic features of the size distribution of bodies of the type $dN(r) \sim r^{-3.5} dr$.

14). Only at velocities of less than 0.4 km/s is agglomeration possible (on condition that there is some adhesive agent on the surface of the silicate particles, e.g., frozen volatiles or an electrostatic charge). Investigations of the changes in materials "treated" by impacts with velocities of several km/s have shown that brittle material—silicates, hydrides—are broken up into very fine particles of micron and submicron sizes which cannot be obtained by other mechanical disintegration methods (ref. 15). But metals display only plastic deformation. The results of these experiments could be applied comparatively simply to protoplanetary particles if they were strictly divided into silicate and iron particles. However, a certain portion of the iron in the protoplanetary cloud could be oxidized and included in the particles in the form of FeO or Fe₃O₄. The oxides are rather more brittle than plastic materials. There are no similar experimental data for them in impacts with cosmic velocities. There is great interest in comparison of the results of impact treatment of iron oxides and silicon oxides as likely structural elements of the protoplanetary material in the region of the terrestrial group of planets. There are indications that at low velocities, on the order of 1 m/s, pulverization of silica (SiO₂) produces two times more total surface than pulverization of magnetite Fe₃O₄ (ref. 16). If the same behavior is displayed at cosmic velocities as a result of mutual collisions, a unique dependence of particle composition and size should develop. On the average, it could be represented in the form of a gradual increase in content of iron and metals in the most massive bodies and a gradual increase in silicate content in the smallest fraction (fig. 2). In this case, there seems to be a basis for enrichment of the circumterrestrial swarm in silicate materials by means of the predominant capture of the smaller fraction.

There are currently few experimental data supporting such a conclusion; however, the tendency is completely clear.

Differentiation in composition between the planets and the satellites occurs in the entire

solar system but, since the "structural material" is different everywhere, the nature of the fractionation differs for different systems.

Accretion of the Moon and Its Initial Temperature

The obviousness of early heating of the Moon has led many authors to the assumption of its rapid collapse during which a considerable portion of its gravitational energy is retained in the interior. If there was a mechanism which would permit accumulation of the satellite swarm during the entire growth of the Earth (10⁸ yr) and then accrete all the material of the swarm into a single mass in a short time (< 10³ yr), the initial temperature of the Moon would have been close to the melting temperature somewhere in the region of the upper mantle (ref. 17). However, this process seems artificial. Assumption of a "short" time scale for growth of the Earth (10⁵ yr) cannot help here because the time scale is also too long to retain the energy of accretion.

Let us examine the possibility of accreting the Moon by an acceptable method within the long time scale for growth of the Earth, 10⁸ yr. By an acceptable method, we mean satisfaction of the following conditions:

1. Accretion of the Moon must be completed at a distance undoubtedly less than 30 R_{\oplus} and, probably close to 20 R_{\oplus} , based on the limits given by the tidal evolution of the lunar orbit (ref. 18) and consideration of the geocentric moment of the swarm (ref. 19) (R_{\oplus} is the radius of the Earth).

2. The initial temperature of the Moon must be higher than some limit $T_0(r)$, in order to ensure heating of the layers responsible for fusion of the continental crust in the "Wasserburg gap" time range (4.6 to 4.0×10^9 yr) (ref. 20), i.e., most likely, within the first 0.3 to 0.4×10^9 yr. Later heating of the deeper layers is responsible for the fusion of the mare basalts. Calculations of Mayeva show that $T_0(r)$ should

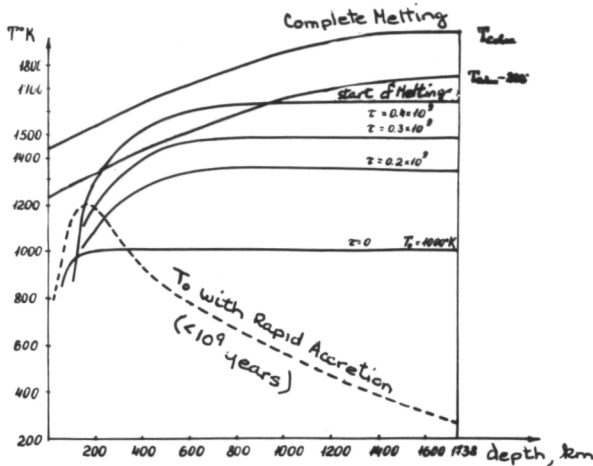


Figure 3.—Diagram of early thermal history of the Moon. The solid curve was calculated by Maysua for $U = 7.7 \times 10^{-6} \%$; $Th/U = 4$; $K/U = 2600$.

have the form shown in figure 3, i.e., reach 1000 K or higher in the upper mantle of the Moon and not increase with depth. In particular, the temperature curve for rapid accretion decreases in temperature toward the center (dashed line). The calculation was carried out for a spherical-symmetrical model having a solid outer layer, 700 to 800 km deep at the present time, and a heat flux equal to that observed. However, the initial conditions of the Moon can scarcely be considered to be spherically symmetrical. The present difference in thickness of the continental crust on the visible and the back sides of the Moon and the great irregularities in structure and composition of the Moon indicate the necessity for asymmetry in the construction, composition, and initial temperature distribution. Therefore, still another condition should be imposed.

3. The rather large structural asymmetry of the Moon may be due to the impacts of very large bodies. We note immediately that the probability of collision of the Moon with a large body moving in a heliocentric orbit is very low. Still less likely (ref. 21) is the collision near Earth of two moon-like masses moving in heliocentric orbits.

With these conditions, we will select one of three versions of accretion of the Moon.

- Formation of an Earth-Moon system from a binary nucleus with initial masses much less than the present ones, mainly by means of absorption of particles from heliocentric orbits
- Gradual growth of the Moon from a small nucleus, in a swarm where the mass of the Earth was about one-half n_{\oplus}
- Accretion of the Moon for several large satellites, which grew in the circumterrestrial swarm

Each of these versions can be analyzed in detail, but we note here that the first and second methods lead to a low (about 300 K) initial temperature of the Moon and do not cause any large irregularities in its structure. We shall consider the third version further.

We (ref. 22) analyzed the possibility of forming several large Earth satellites each with its own supply zone. Within 20 to 25 R_{\oplus} , a system of two to three large satellites could have formed with masses $\frac{1}{2}$ to $\frac{1}{3} \mu_{\oplus}$. With tidal friction such a system could have existed only as long as required for close approaches which result in considerable interactive perturbations of the satellites. The rate of tidal removal at such an early epoch is very indefinite. For agreement with the age of the Earth-Moon system, 4.5×10^9 yr, a whole set of functions of the type $\delta_{\oplus} = \delta_0 + \alpha t^n$ can be used, where δ_{\oplus} is the effective lag angle for the entire Earth, t is the time, δ_0 and α are constants, and $n = 1, 2, 3$, etc. (fig. 4). The time for tidal removal of large protomoons from the system to 10 R_{\oplus} is 10^5 to 10^7 yr and 20 R_{\oplus} requires up to $10^7 - 5 \times 10^8$ yr, which is 10 to 100 times the removal time of such satellites to $\delta_{\oplus} = \delta_{\oplus}$ present $\cong 4^\circ$.

We carried out some numerical experiments for the purpose of determining the evolution of a system of several massive satellites where the satellite orbits were brought together by friction, almost to commensurable 1:1 periods (ref. 23). For simplicity, plane two-satellite systems were studied, with initial circular orbits relative to the Earth. All three bodies were consid-

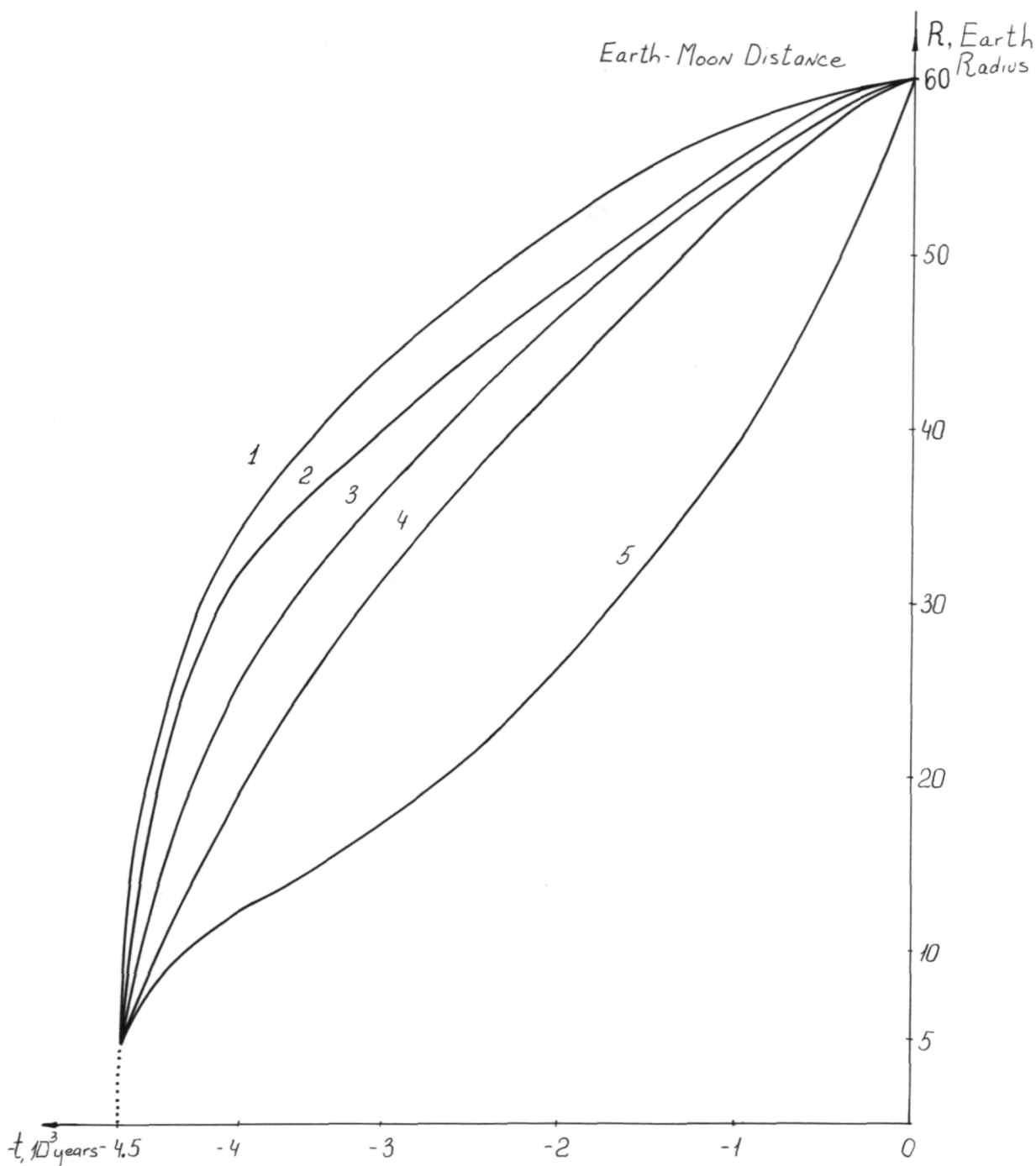


Figure 4.—Rate of tidal removal of Moon from Earth for various forms of the function $\delta_0(p)$:

- | | |
|------------------------------------------------------|-----------------------------------------------|
| 1. $\delta \oplus = \delta_0^I + \alpha_1 t$; | $\delta \oplus \text{ present} = 1^{\circ}.7$ |
| 2. $\delta \oplus = \delta_0^{II} + \alpha_2 t^2$; | $\delta \oplus \text{ present} = 2^{\circ}.2$ |
| 3. $\delta \oplus = \delta_0^{III} + \alpha_3 t^3$; | $\delta \oplus \text{ present} = 4^{\circ}$ |
| 4. $\delta \oplus = \delta_0^{IV} + \alpha_4 t^4$; | $\delta \oplus \text{ present} = 4^{\circ}$ |
| 5. $\delta \oplus = \delta_0^V e^{\alpha_5 t}$ | $\delta \oplus \text{ present} = 10^{\circ}$ |

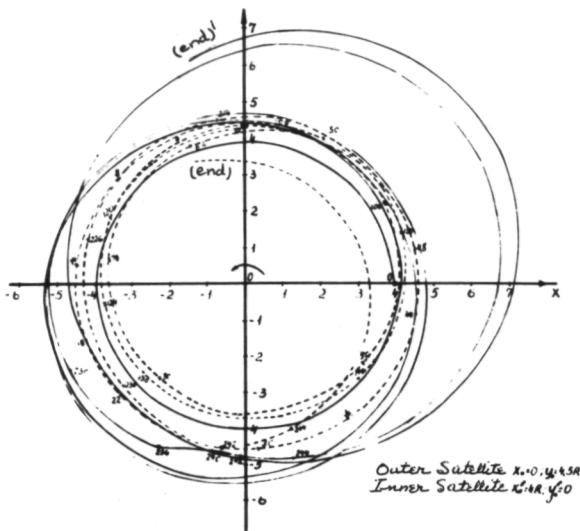


Figure 5.—Example of the evolution of orbits for two massive satellites, with initial circular orbits at distances of $4 R_{\oplus}$ and $4.5 R_{\oplus}$ from Earth.

ered to be physical points. One of the examples of orbital evolution is of two satellites with masses of $\frac{1}{2} \mu_{\oplus}$ is shown in figure 5. We see strong perturbations of the eccentricities of the orbits, frequent crossing of the orbits, and one case of close passage at a distance of a little less than the sum of the two radii of the satellites, which can be considered to be a collision of the bodies. The rate of relative approach of the satellites is close to parabolic (about 2 km/s); therefore, a collision in systems of this type must always be "frontal," as if the satellites strike one another from an infinitely great distance. The time of evolution of the two-satellite system to a probable collision within $10 R_{\oplus}$ is numbered in days and, within $20 R_{\oplus}$, in years. Allowance for three-dimensionality should lengthen the lifetime of the system 10 to 100 yr.

We have not yet carried out such experiments, but, except in the three-dimensional case, the perturbing quantity, except for eccentricity, should be the inclination of the orbit. For such a system, one must consider the precession of the orbits due to the action of the equatorial flattening of the Earth and precession of the axis of the Earth, i.e., a

point approximation for the mass of the Earth must be rejected. The problem with two satellites was considered by Goldreich and becomes a much more complicated problem for the Earth-Moon system (ref. 18). One might think that all the limitations indicated by Goldreich for the initial distance of the Moon would be preserved for a system of two protomoons; in particular, in the extreme case one of the two protomoons may form within $10 R_{\oplus}$ and initially have an "equatorial" orbit. Related to this, we also considered orbits at 4, 6, and $8 R_{\oplus}$.

A fusion of two satellites into one body is a very rapid process, lasting about 1 hour. The energy given off is sufficient to heat the entire mass to an average temperature several hundred degrees above its equilibrium temperature or to produce a temperature distribution in the interior like that caused by rapid accretion, as mentioned above (see fig. 3). In this manner, formation of the Moon from large bodies, comparable to each other in mass, gives the most acceptable initial temperature from the point of view of subsequent evolution of the Moon. Moreover, the possibility is now open for the creation of large inhomogeneities in structure and composition, as a consequence of the inhomogeneous differentiation of the interior of the Moon.

References

1. SCHMIDT, O. YU., *Four Lectures on Theories of the Origin of the Earth*, USSR Acad. of Sci. Press, Moscow, 1957.
2. SAFRONOV, V. S., *Evolution of the Protoplanetary Cloud and Formation of the Earth and Planets*, Nauka Press, Moscow, 1969.
3. KAULA, W. M., Dynamical Aspects of Lunar Origin. *Revs. Geophys. Sp. Phys.* Vol. 9, 1971, pp. 217-238.
4. KAULA, W. M. AND A. W. HARRIS, Dynamically Plausible Hypotheses of Lunar Origin, *Nature*, Vol. 245, 1973, pp. 367-369.
5. RUSKOL, YE. L., Cosmogony of the Moon. *Fizika Luny i Planet*, 1972, pp. 160-167.
6. KUIPER, G. P., Comets and the Dissipation of the Solar Nebula. *La Physique des Comets*, 1953, pp. 361-385.
7. RUSKOL, YE. L., Possible Differences in Chemi-

- cal Composition of the Earth and Moon in Formation of the Moon in a Circumterrestrial Cluster. *Fizika Luny i Planet*, Vol. 48, No. 6, 1971.
8. GANAPATHY, R., R. R. KEAYS, F. C. LAUL AND E. ANDERS, Trace Elements in Apollo 11 Lunar Rocks. Implications for Meteorite Influx and Origin of the Moon. *Proc. Apollo 11 Lunar Science Conference, Geochimica y Cosmochimica Acta*, Vol. 2, 1970, pp. 1117-1142.
 9. ZVYAGINA, YE. V., G. V. PECHERNIKOVA AND V. S. SAFRONOV, Qualitative Solution of the Coagulation Equation, with Disintegration of Bodies Taken into Account. *Astron. Zhurn*, Vol. 50, 1973, pp. 1261-1273.
 10. DOHNANYI, J. F., Fragmentation and Distribution of Asteroids. *Physical Studies of Minor Planets*, 1971, pp. 263-295.
 11. RUSKOL, YE. L., Origin of the Moon III. Dynamics of the Circumterrestrial Cluster. *Fizika Luny i Planet*, Vol. 48, No. 4, 1971, pp. 819-829.
 12. OROWAN, E., Density of the Moon and Nucleation of Planets. *Nature*, Vol. 222, 1969.
 13. DIETZEL, H., G. NEUKUM AND P. RANSER, Micrometeoroid Simulation Studies on Metal Targets. *J. Geophys. Res.*, Vol. 77, No. 8, 1972, p. 1375.
 14. KERRIDGE, J. F. AND J. F. VEDDER, Accretionary Processes in the Early Solar System: An Experimental Approach. *Science*, Vol. 177, 1972, pp. 161-163.
 15. DREMIN, A. N. AND O. N. BREUSOV, Physical-Chemical Processes in Shock Compression. *Vestn Akad nauk SSSR*, Vol. 9, 1971, pp. 55-59.
 16. YUSHKIN, N. P., *Mechanical Properties of Minerals*, 1971.
 17. TOKSÖZ, M. N. AND D. H. JOHNSTON, The Evolution of the Moon. *Icarus*, Vol. 21, No. 4, 1974, pp. 389-414.
 18. GOLDREICH, P., History of the Lunar Orbit. *Revs. of Geophys.*, Vol. 4, No. 4, 1966, pp. 411-439.
 19. RUSKOL, YE. L., Role of the Satellite Cluster in the Origin of Rotation of the Earth. *Astron Vestn*, Vol. 6, No. 2, 1972, pp. 91-95.
 20. TERA, F., D. A. PAPANASTASSIOU AND G. J. WASERBURG, A Lunar Cataclysm at 3.95 AE and the Structure of the Lunar Crust. *Proc. the Fourth Lunar Science Conference*, 1974.
 21. RUSKOL, YE. L., Origin of the Moon II. Growth of the Moon in a Circumterrestrial Satellite Cluster. *Astron. Zhurn.*, Vol. 40, 1963, pp. 288-296.
 22. RUSKOL, YE. L., Model of Accretion of the Moon, Compatible with Data on Composition and Age of Lunar Rocks. *The Moon*, Vol. 6, 1973, pp. 176-189.
 23. RUSKOL, YE. L., YE. V. NIKOLAYEVA AND A. S. SYZDYKOV, Dynamic History of a Plane, Two-Satellite System. *Fizika Luny i Planet*, 1974. In press.

Formation and Composition of the Moon ¹

Don L. Anderson

*Seismological Laboratory, California Institute of Technology
Pasadena, California*

Many of the properties of the Moon, including the "enrichment" in Ca, Al, Ti, U, Th, Ba, Sr, and the REE and the "depletion" in Fe, Rb, K, Na, and other volatiles can be understood if the Moon represents a high-temperature condensate from the solar nebula. Thermodynamic calculations show that Ca-, Al-, and Ti-rich compounds condense first in a cooling nebula. The initial high-temperature mineralogy is gehlenite, spinel, perovskite, Ca-Al-rich pyroxenes, and anorthite. Inclusions in Type III carbonaceous chondrites such as the Allende meteorite are composed primarily of these minerals and, in addition, are highly enriched in refractories such as REE relative to carbonaceous chondrites. These inclusions can yield basalt and anorthosite in the proportions required to eliminate the europium anomaly, leaving a residual spinel-melilite interior. A deep interior high in Ca-Al does **not** imply an unacceptable mean density or moment of inertia for the Moon. The inferred high-U content of the lunar interior, both from the Allende analogy and the high heat flow, indicates a high-temperature interior. The model is consistent with extensive early melting, with shallow melting at 3 AE, and with presently high deep internal temperatures. It is predicted that the outer 250 km is rich in plagioclase and FeO. The low iron content of the interior in this model raises the interior temperatures estimated from electrical conductivity by some 800° C.

The low iron content of the Moon, compared with terrestrial, solar, or meteoritic abundances, has led to many discussions of metal-silicate fractionation mechanisms in the solar nebula, and has been used as an argument for both a fission and a capture origin for the Moon. The Surveyor and Apollo missions have shown that the composition of the Moon is anomalous on other counts. It is depleted in volatiles, as well as iron, and is enriched in refractories. This is true not only for the surface rocks but for their source regions as well, and therefore applies to a considerable fraction of the lunar interior. Therefore, it is clear that more than just metal-silicate fractionation is required in order to create a Moon from solar or "cosmic" abundances. Although many and diverse proposals have been put forth to explain the bulk

and surface chemical properties of the Moon, most of them assume that material of chondritic composition was important sometime in the Moon's ancestry.

For example, Ringwood (ref. 1) proposed that the Moon formed primarily from material that vaporized in a massive primitive terrestrial atmosphere. In the terminal stages of accretion of the Earth, Fe would be selectively retained by the Earth but SiO and Mg, along with conventional volatiles, would enter the atmosphere. Magnesium silicate and silica precipitated before the other volatiles, and collected into planetesimals. These planetesimals would have been selectively depleted in uranium and thorium because of their lower volatility. It was proposed that the Moon accreted cold from a mixture of iron-poor magnesium silicates and planetesimals of primitive origin (Type 1 carbonaceous chondrites). He predicted that iron-free enstatite and quartz would be the most

¹Contribution No. 2482, Division of Geological and Planetary Sciences, California Institute of Technology, Pasadena, California.

abundant minerals on the Moon. Ca and Al, because of their low volatility would be selectively retained, with Fe, by the Earth. The low radioactive content would lead to a permanently cold interior, which would therefore retain the volatile compounds. The hypothesis was modified when it was found that the Moon is a refractory-rich planet (ref. 2). It was proposed that the less volatile material accreted into chunks and the more volatile material remained as "smoke" which was blown away by a conjectured T-Tauri phase of the Sun. In a later paper Ringwood and Green (ref. 3) proposed that the interior was carbonaceous and the exterior refractory. We put forth the alternate hypothesis that the bulk of the Moon is composed of those elements and compounds that condensed prior to the condensation of iron. Iron, MgSiO_3 , Mg_2SiO_4 , and the volatiles were incorporated into the interior in only minor amounts and, probably, only during the terminal stages of accretion. The outer part, ~ 250 km, of the Moon, in our model, is almost identical to that proposed by Gast (ref. 4) on geochemical grounds. However, the deep interior is CaO - and Al_2O_3 -rich and is dominantly diopside, merwinite, and spinel. This assemblage has acceptable densities and is stable to higher pressures than is the Ringwood-Essene low Ca-Al model lunar pyroxenite.

Boundary Conditions

Important constraints have been placed on the origin of the Moon and the evolution of its crust and mantle from detailed geochemical and geophysical studies:

1. The chemistry of the lunar igneous rocks suggests that they are derived from a feldspathic, refractory element-rich, pyroxene-rich interior (ref. 4).
2. The liquids which preceded most lunar rocks were produced by processes that involved extensive separation of igneous liquids and crystalline solids (ref. 4).
3. That part of the Moon involved in the

formation of the surface rocks was deficient in volatile elements including Rb, Na, and K compared with carbonaceous chondrites.

4. A major fractionation occurred at ~ 4.6 AE, which resulted in the creation of a crust high in K, Rb, U, Th, and REE (ref. 5). The interior initially supplied Fe-poor and Al-rich materials. Later volcanism, 3.0–4.0 billion years ago, supplied materials very rich in Fe.
5. The so-called LIL (large ion lithophile) elements such as K, Rb, Cs, Ba, U, Th, REE, and Sr are enriched in the source region of lunar igneous rocks by a factor of 5–20 times chondritic abundances (ref. 4).
6. The composition and temperature of the deep interior must be consistent with the observed mean density and moment of inertia.
7. The outer ~ 200 km of the Moon has had some strength for about 3.7×10^9 years, if the persistence of mascons is to be explained. The stronger constraint of a cold deep interior has been removed by Anderson and Hanks (ref. 6).

These constraints can be satisfied with the refractory model discussed in this paper.

Composition of the Moon

The enrichment of the Moon in refractories and deficiency in volatiles is now well documented (ref. 7). These characteristics are not limited to the surface materials but apply also to their source region, which may involve the outer several hundred kilometers or 30 percent of the Moon (ref. 4). The enrichment of refractories is so great, compared with carbonaceous chondritic abundances, that it has been proposed that a refractory-rich outer layer, plentiful in Al and trace element-rich materials, was accreted late in the formation of the Moon (refs. 3, 4, and 5). The great thickness (~ 60 km) of the lunar "crust" as measured from the lunar seismic experiment (ref. 8) also suggests that a large part of the Moon was involved in the differen-

tiation or fractionation process. The degree of partial melting required to produce the Apollo basalts is probably in the range of 3 to 30 percent (refs. 4 and 9). If the crust is mostly basalt and anorthosite, very extensive differentiation of most if not all of the Moon is required. The high heat flow (ref. 10) suggests that the high concentration of U is not just a near-surface phenomenon but must extend to a depth at least as great as the thermal diffusion length, ~ 100 – 300 km. Therefore the enrichment of Ca, Al, and U—and probably the other refractories such as Ba, Sr, and REE—occurs for a substantial fraction of the Moon and may be a property of the Moon as a whole. That is to say, the whole Moon may be refractory and represent a high-temperature condensate from the solar nebula.

Gast (ref. 4) and Ringwood (ref. 2) have proposed inhomogeneous accretion models in which the interiors of the Earth and the Moon were initially more volatile-rich than the exteriors. This is the reverse of the accretion-during-condensation sequence proposed by Clark et al. (ref. 11) and developed by Anderson (refs. 12 and 13) and Anderson and Hanks (ref. 14). There is abundant evidence that the surface rocks of the Moon and their inferred source regions are enriched in refractories and depleted in volatiles; but it does not follow that a volatile-rich interior exists, and there is no evidence to support its existence, either initially or at present. Gast and McConnell (ref. 15) following Wetherill (ref. 16) and Ringwood and Essene (ref. 9) believe that the whole Moon cannot be rich in Ca and Al because of the presumed inversion to eclogite at modest pressures. They therefore proposed, as have others, that the primitive Moon had a more ferromagnesian interior composition which accreted from material that separated from the solar nebula at low temperatures, and that the interior may approach chondritic composition. We will show that this inference is invalid and that the whole Moon may, in fact, have the characteristics determined by Gast (ref. 4) to be appropriate for the outer shell.

Element-by-element comparison of lunar basalts with carbonaceous chondrites has been made by many workers (see for example, the summaries by Mason and Melson (ref. 17) and Ganapathy et al. (ref. 18)). The basalts are clearly enriched in refractories and depleted in volatiles compared with chondrites. If we quantify the terms "refractory" and "volatile" in terms of condensation temperature from a gas of solar composition, the cutoff seems to occur in the vicinity of iron and K-feldspar or ~ 1470 K (for $P_T = 10^{-3}$ atm). The bulk of the Moon is clearly deficient in iron relative to solar or chondritic abundances and, considering that K is probably concentrated toward the surface, the bulk Moon is likely also to be depleted in potassium; the ratio K/U (a volatile/refractory pair) is lower than terrestrial or chondritic values.

Figure 1 summarizes the well-known basalt-chondrite relations and shows, in addition, that the lunar anorthosites are also enriched in the refractories and depleted in the volatiles. In this figure the circles and the

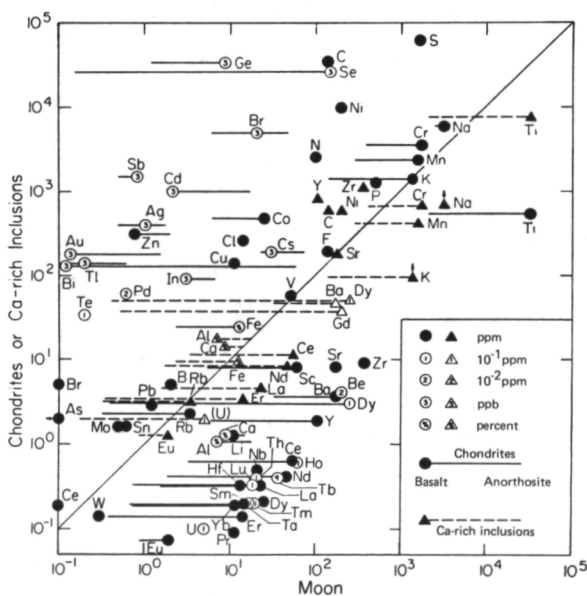


Figure 1.—Composition of lunar basalt (ref. 17) and anorthosite (refs. 35, 59, and 60) versus carbonaceous chondrites (circles and solid lines) and versus Allende Ca-Al-rich inclusions (triangles and dashed lines) (ref. 26).

solid lines refer to lunar versus carbonaceous chondrites. Note that only a few of the data bars—representing the range exhibited by lunar anorthosites and basalts—straddle the 45° line. The triangular data points and the dashed lines are the same lunar data plotted against Ca-Al-rich inclusions of the Allende meteorite. We will discuss these inclusions in detail in the section titled "The Allende Meteorite." There is a very good agreement between the lunar surface rocks and the Allende inclusions for both the major and the trace element refractories.

Properties of the Early Condensate

The condensation sequence of elements and compounds from a cooling cloud of solar composition has been calculated by Larimer (ref. 19), Lord (ref. 20), and Grossman (ref. 21). The early condensates (table 1) are Al, Ca, and Ti compounds such as gehlenite ($\text{Ca}_2\text{Al}_2\text{SiO}_7$), spinel (MgAl_2O_4), and perovskite (CaTiO_3). These compounds all condense before iron. The relative absence of iron in the Moon suggests that it may have accreted from these compounds. Under non-equilibrium or lower pressure conditions such compounds as diopside ($\text{CaMgSi}_2\text{O}_6$), forsterite (Mg_2SiO_4), and anorthite ($\text{CaAl}_2\text{Si}_2\text{O}_8$) also condense before iron. The early condensates will therefore be enriched in Ca, Al, and Ti relative to Mg, Si, and Fe which are the main constituents of the Earth's mantle and chondritic meteorites. They will also probably be enriched in the REE and other refractories which substitute readily for Ca, and may be enriched in Th and U which are relatively refractory. K_2O , S, Na_2O , S, H_2O , and other volatiles will be deficient in the early condensate.

The amount and composition of the material that condenses from the solar nebula at high temperature can be estimated in several ways. The average composition of the solar nebula can be estimated from solar and chondritic abundances. Column (1) of table 2 gives solar abundances recalculated to

Table 1.—*Stability Fields of Equilibrium Condensates at 10^{-3} Atmospheres Total Pressure (ref. 21)*

Phase		Condensation Temperature (K)
Trace Refractories ⁽¹⁾		1931–1768
Corundum	Al_2O_3	1758
	HfO_2	1744
	Mo	1698
Perovskite	CaTiO_3	1647
	Ru	1634
Melilite		
Gehlenite	$\text{Ca}_2\text{Al}_2\text{SiO}_7$	1625
Akermanite	$\text{Ca}_2\text{MgSi}_2\text{O}_7$	
	ThO_2	1517
Spinel	MgAl_2O_4	1513
Merwinite	$\text{Ca}_3\text{MgSi}_2\text{O}_8$	1475
Metallic Iron	(Fe, Ni)	1473 ⁽²⁾
Diopside	$\text{CaMgSi}_2\text{O}_6$	1450
Forsterite	Mg_2SiO_4	1444
	Ti_2O_3	1393
Anorthite	$\text{CaAl}_2\text{Si}_2\text{O}_8$	1362
Enstatite	MgSiO_3	1349
Eskolaite	Cr_2O_3	1294
Rutile	TiO_2	1125

NOTES: (1) Os, Sc_2O_3 , Te, Ta, ZrO_2 , W, Nb, Y_2O_3 .

(2) The relative location of Fe-Ni in the condensation sequence depends critically on pressures in the nebula and on departures from equilibrium, i.e., the nebula may be supersaturated in iron vapor before condensation ensues. Iron condenses after forsterite and (presumably) diopside, at pressures less than 10^{-4} atmospheres.

weight percent oxides. This will presumably be the composition of a fully oxidized planet accreted from the solar nebula. Column (2) gives the amount of SiO_2 , TiO_2 , Al_2O_3 , MgO , and CaO that are involved in the early condensates, CaTiO_3 , $\text{Ca}_2\text{Al}_2\text{SiO}_7$, and MgAl_2O_4 . Column (3) gives the composition of a Ca-Al-rich inclusion in the Allende meteorite, which is taken here as another approximation to the composition of the early condensate. The amount of Fe in the Sun is still uncertain, so we have also calculated the fraction of the early condensate for an iron-free Sun to obtain an upper bound on the amount of the high-temperature condensate.

Table 2.—*Estimates of the Composition of the Early Condensate*

	(1)	(2)	(3)	(4)	(5)	(6)
SiO ₂	37.4	0.6	1.4	33.3	1.1	3.1
TiO ₂	0.1	0.1	.05	—	—	—
Al ₂ O ₃	1.3	1.3	1.1	2.4	2.4	2.4
FeO	43.0	—	0.1	35.5	—	0.2
	(0) ⁽⁷⁾					
MgO	15.6	0.3	0.6	23.5	0.6	1.3
CaO	0.9	0.9	0.9	2.3	1.7	2.0
Total	98.3 %	3.2 %	4.2 %	97.0	5.8 %	9.0 %
		(5.6 %) ⁽⁷⁾	(7.4 %) ⁽⁷⁾			
Enrichment Factor		31x	24x		17x	11x
		(18x) ⁽⁷⁾	(14x) ⁽⁷⁾			

NOTES: (1) Solar abundances recalculated to weight percent of the major oxides.
 (2) Solar "refractory" composition (Ca, Al, and Ti compounds); all Ti in CaTiO₃, remaining CaO in Ca₂Al₂SiO₇, remaining Al₂O₃ in MgAl₂O₄.
 (3) Allende Ca-Al-rich inclusions scaled to solar CaO (ref. 24).
 (4) Carbonaceous chondrites (ref. 17).
 (5) Early condensate assemblage scaled to chondritic Al₂O₃.
 (6) Allende inclusions scaled to chondritic Al₂O₃.
 (7) Ignoring FeO.

These condensates account for 3.2 to 7.4 percent of the total condensable material. This is roughly the fraction of the total condensable material (exclusive of H, C, and S) that will condense from a solar nebula prior to the condensation of iron. Trace element refractories will therefore be enriched in this early condensate by a factor of 14 to 31. An alternate method is to assume that carbonaceous chondrites represent the composition of the starting material. In this case, columns (4), (5), and (6), the early condensate fraction is 5.8 to 9.0 percent and the enrichment factor of the trace element refractories is 11 to 17 times chondritic. In this regard it is of interest that the refractory trace elements are enriched in the Allende inclusions by a factor of 11 over the whole meteorite and that these inclusions constitute ~ 8 percent of the meteorite, a C3 chondrite.

Figure 2 gives the chondritic-normalized lunar abundances as a function of condensation temperature of the element or the first condensing compound containing this element. The condensation temperatures of the REE, Ba, and Sr are uncertain but their

average enrichment, shown by the dashed line, is about the same as the other refractories, suggesting that they condense over a similar temperature range. Grossman (ref. 21) calculates that U, La, Sm, and Eu will

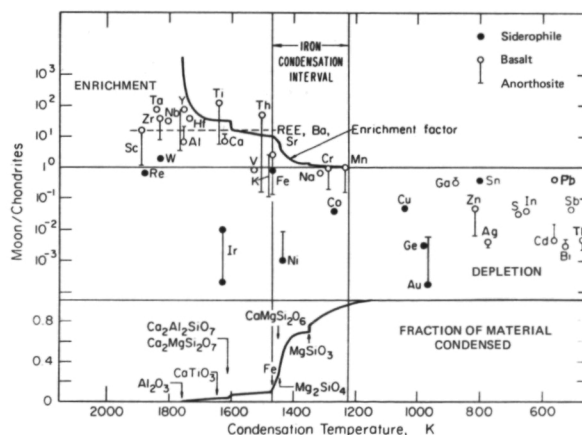


Figure 2.—*Chondritic normalized lunar abundances versus condensation temperature. The fraction of the total material that has condensed is represented by the lower curve, as a function of temperature. The upper curve is the enrichment factor of trace element refractories in the early condensate.*

condense below 1473 K at 10^{-3} atm. The U/Th ratio therefore may be lower in the early condensates than in chondrites. It is likely, however, that solid solution effects will allow the condensation of some refractory trace elements at a higher temperature than is the case for pure phases. Perovskite, for instance, could provide lattice sites for the removal of the rare earths and other trace elements (ref. 21) at temperatures of 1647 K. Grossman (ref. 21) feels that the rare earths will probably condense over the same temperature interval as corundum, perovskite, melilite, and spinel. In the lower part of the figure is shown a plot of the fraction of the available material that has condensed as a function of temperature calculated from the results of Grossman (ref. 21). The initiation of condensation of various compounds is indicated by arrows. Note the rapid increase in the fraction of material which has condensed as the temperature drops below the condensation temperature of iron and the magnesium silicates. Conditions in the solar nebula can be expected to change drastically as temperatures drop to this level. When iron starts to condense, the opacity of the nebula increases substantially and the cooling rate will decrease. One might therefore expect a discontinuity in the evolution of the solar system at the condensation temperature of iron. If a planet is depleted in iron it is probably also depleted in post-iron condensates such as olivine and pyroxene, as well as the more conventional volatiles.

The enrichment factor in figure 2 is simply the reciprocal of the condensed fraction. It indicates the expected enrichment of the trace refractories in the condensed phases relative to chondritic abundances. Note that the refractories are enriched in the Moon to above the level expected in the pre-iron condensates. As the temperature decreases past the condensation temperature of iron, the enrichment factor rapidly approaches unity, i.e., chondritic abundances. Everything that condenses after iron is apparently depleted in the Moon.

Ir is the main anomaly in figure 2. It is commonly concentrated in residual high-

temperature crystals such as chromite and spinel and in sulphide melts (refs. 22 and 23). Ir is a siderophile element and may also reside in a metallic phase at depth in the Moon.

Table 2 gives the condensation sequence in a cooling nebula of solar composition at a total pressure of 10^{-3} atmospheres (ref. 21). We will show in the next section that the Ca-Al-rich inclusions of the Allende meteorite have mineralogies that suggest that they are high-temperature condensates. This is supported by their trace element content.

The Allende Meteorite

Theoretically, the early condensates from a cooling solar nebula include perovskite, spinel, gehlenite, diopside, anorthite, and other Ca, Al, and Ti compounds. This assemblage will be enriched in such refractory trace elements as REE, Sr, and Ba and, possibly, in Th and U; and will be depleted in such volatiles as K, Rb, S, and H₂O. Type II and Type III carbonaceous chondrites contain Ca-Al-rich inclusions which involve these minerals and which are enriched in Ba, Sr, and the REE to about the extent predicted in the previous section.

The spectacular meteorite shower near Pueblito de Allende, Mexico, in February 1969 has provided a wealth of data bearing on the nature of the early condensate. Over 2000 kg of this Type III carbonaceous chondritic material has been collected to date. In common with other Type II and Type III carbonaceous chondrites, the Allende contains numerous large white aggregates and some chondrules of most unusual chemistry and mineralogy. The bulk chemistry of these inclusions is high in Ca, Al, and Ti, and low in Fe, Mg, and volatiles. We shall refer to these as Ca-Al-rich inclusions. The dominant minerals that have been identified in these inclusions include gehlenite ($\text{Ca}_2\text{Al}_2\text{SiO}_7$), spinel (MgAl_2O_4), fassaite, an aluminous titanium-rich pyroxene ($\text{Ca}(\text{Mg},\text{Al},\text{Ti})(\text{Al},\text{Si})_2\text{O}_6$), and anorthite ($\text{CaAl}_2\text{Si}_2\text{O}_8$). Other minerals include perovskite (CaTiO_3), diopside ($\text{CaMgSi}_2\text{O}_6$), ferroaugite ($\text{Ca}(\text{Fe},$

Mg,Al) (Al,Si)₂O₆), grossular (Ca₃Al₂Si₃O₁₂), and corundum (Al₂O₃). They contain no metallic iron or olivine. These aggregates have been studied in detail by Clarke et al. (ref. 24), Marvin et al. (ref. 25), Gast (ref. 26), and Grossman (ref. 21). The texture and the presence of reaction rims indicate that the inclusions were inserted into the matrix at high temperature. Marvin et al. (ref. 25) and Clarke et al. (ref. 24) have noted the similarity between the composition and mineralogy of the aggregates and the early condensates in a cooling nebula. It is extremely unlikely that the peculiarities of these inclusions could be a result of igneous differentiation processes acting on material of solar or chondritic composition. On the basis of their bulk chemistry, mineralogy, texture, and oxygen isotope ratios, the Ca-Al-rich inclusions apparently represent the highest temperature condensates from a gas of solar composition and are therefore the most primitive solids in the solar system. Grossman (ref. 21) has supported this view with detailed thermodynamic calculations. If this interpretation is correct, the Ca-Al-rich inclusions are extremely significant in understanding the origin and composition of the Moon (refs. 6, 12, 13, and 14). We will show that many properties of the Moon, including its overall physical properties and gross layering, and the properties of the source region of lunar igneous rocks can be explained if the bulk composition of the Moon is similar to that of the Ca-Al-rich inclusions. Although the Allende meteorite has provided the greatest amount of material for study, similar inclusions have been observed in numerous C2 and C3 chondrites, for example Kaba (ref. 28), Sharps (ref. 29), Bali (ref. 29), Vigarano (ref. 30), Lance (ref. 31), Felix (ref. 32), Murchison (ref. 33), Leoville (ref. 34), Grosneja, Orans, and Warrentun (ref. 25).

Trace Elements

The concentrations of the trace element refractories have been determined for the

Ca-Al inclusions by Gast et al. (ref. 26) and Grossman (ref. 21) and for the whole meteorite by Mason and Graham (ref. 24) and Wakita and Schmitt (ref. 35). The average enrichment of these elements in the inclusions, which make up ~ 8 percent of the meteorite, is about a factor of 11, implying that these refractory elements are almost entirely contained in the inclusions, and, by implication, in the earliest condensates. Europium is concentrated in the inclusions by ~ 30 percent more than the average of the other elements. The U content of the whole meteorite is 0.019 ppm. If it is concentrated primarily in the inclusions they will contain ~ 0.2 ppm. A single measurement (ref. 21) gives 0.03 for the uranium content of one of the inclusions, which suggests that U is not as refractory as the REE, Sr, and Ba, or is not as easily incorporated into the lattices of the crystal phases found in the inclusions. For comparison the average U content of the Moon has been estimated by Hanks and Anderson (ref. 36) to be ~ 0.1 ppm based on thermal history and heat flow considerations.

Table 3 gives concentrations of Ba, La, REE, Sr, Rb, K, and U for the Ca-Al-rich inclusions of the Allende meteorite, the whole meteorite, carbonaceous chondrites, Apollo 11 basalts, and a lunar anorthosite. The abundances in the inclusions are approximately 16 times the chondritic abundances, column (3). In this respect the Ca-Al inclusions are a much more satisfactory source for the lunar igneous material than are carbonaceous chondrites. Column (1) shows abundances in an Allende Ca-Al-rich inclusion (ref. 26); column (2) gives whole meteorite abundances (ref. 24). The anorthosite and basalt have large and opposite europium anomalies. The anomaly can be suppressed by mixing basalt with about 5 times as much anorthosite, columns (6) and (7). The mixture is normalized to carbonaceous chondrites in column (7) and to the Allende inclusions in column (8). The lunar basalts are enriched in refractories by more than an order of magnitude relative to carbonaceous chondrites and a factor of 5 relative to the Allende inclusions. If the composition of the

Table 3.—*Trace Elements in Allende Meteorite, Carbonaceous Chondrites, and the Moon*

	Meteorites			Moon				Moon/Meteorite	
	(1)	(2)	(3)	(4)	(5)	(6)	(7)	(8)	(9)
Refractories									
Ba	47.3	5	3.6	200	6.28	48.9	33.4	13.6	1.03
La	4.63	0.44	(.28)	18	0.12	4.5	2.62	14.5	0.87
Ce	11.5	1.25	.787	54	0.35	12.2	7.86	15.5	1.06
Nd	8.40	0.91	.652	46	0.18	10.3	6.59	15.8	1.23
Sm	2.82	0.29	.208	15	0.05	3.4	2.14	16.2	1.21
Eu	1.30	0.11	.071	2	0.81	1.1	.96	14.8	0.81
Gd	3.87	0.43	.256	20	0.05	4.4	2.84	17.2	1.14
Dy	4.90	0.42	.303	25	0.04	5.5	3.53	18.2	1.12
Er	3.44	0.31	.182	14	0.02	3.1	1.97	17.0	0.90
Yb	3.96	0.32	.188	13	0.04	2.9	1.85	15.4	0.73
Sm/Eu	2.17	2.64	2.93	7.89	0.06	3.24			
U	(0.2)	.019	0.01	0.5	0.015	0.12	.083	12.	0.60–4.00
	0.03								
Sr	180	13	11	170	178	176	177	16.0	0.98
Volatiles									
Rb	3.5	1.3	3.0	3.4	0.15	.87	0.61	0.29	0.24
K	96–415	250	1000	1400	120	402	299	0.40	4.17–0.97
K/U	500–10,000	1.3×10^4	10^5	2800	9500	3350			
K/Ba	2 – 9	50	278	7	19	8			
K/Rb	30–120	192	330	412	800	462			
Rb/Sr	.019	0.10	3.67	0.02	.0008	.0049			

NOTES: (1) Allende Ca-rich inclusions (ref. 26); U = (0.2) estimated from $10 \times$ whole meteorite and $16 \times$ Cl chondrites; U = 0.03 from Grossman (ref. 21).

(2) Allende—whole meteorite (ref. 24).

(3) Carbonaceous chondrites.

(4) Apollo 11 basalt-mean (ref. 17).

(5) Lunar anorthosite—15415, 11 (ref. 47).

(6) 0.22 basalt + 0.78 anorthosite.

(7) 0.14 basalt + 0.86 anorthosite.

(8) Column 6 normalized to carbonaceous chondrites.

(9) Column 6 normalized to Allende Ca-rich inclusions.

outer shell of the Moon can be accounted for entirely by a mixture of basalt plus anorthosite, the absolute abundances can be made comparable to Allende inclusions, as shown in column (9). This mixture, however, still has a small europium anomaly relative to either carbonaceous chondrites or the Ca-Al inclusions.

Table 4 gives the chondritic normalized trace element refractory abundances for the Allende inclusion and several combinations of the lunar surface material. Grossman (ref. 21) corrected La, Sm, Eu, Sc, Yb, and Ir for matrix contamination and concluded

that the Ca-Al-rich inclusions were enriched in these elements by a factor of 20 to 25, relative to Type I carbonaceous chondrites. Using different data we obtain, column (1), an enrichment factor of 16. Column (2) is the mixture of basalt and anorthosite required to achieve Allende abundance levels. Column (3) gives the mixture of anorthosite and basalt required to satisfy the Allende Sm/Eu and Eu/Gd ratio. Column (4) is the mixture required to achieve the carbonaceous chondritic ratios. In all cases appreciable Sr, Ba, and the REE must be retained in the interior if the Moon has the abundances of

Table 4.—*Enrichment of Refractories: Allende Inclusions/Carbonaceous Chondrites and Lunar Surface/Carbonaceous Chondrites*

	(1)	(2)	(3)	(4)
Ba	13.1	13.6	9.3	12.1
La	16.5	14.5	9.4	12.6
Ce	14.6	15.5	10.0	13.4
Nd	12.9	15.8	10.1	13.6
Sm	13.6	16.3	10.3	13.9
Eu	18.3	14.8	13.5	14.3
Gd	15.1	17.2	11.1	15.0
Dy	16.2	18.2	11.7	15.8
Er	18.9	17.0	10.8	14.7
Yb	21.1	15.4	9.8	13.3
Sr	16.4	16.0	16.1	16.0
Average	16.1	15.8	11.1	14.1

NOTES: (1) Allende Ca-Al-rich inclusions.
 (2) .22 basalt + .78 anorthosite.
 (3) .14 basalt + .86 anorthosite (to eliminate Eu anomaly relative to Allende inclusion).
 (4) .19 basalt + .81 anorthosite (to eliminate Eu anomaly relative to carbonaceous chondrite).

the Ca-Al-rich inclusions. Since the residual crystals in our model amount to ~ 65 percent of the mass of the moon (see section titled "Possible Fractionation of an Allende-like Moon") the average REE concentration in the interior is 17 to 19 times chondritic levels. The Eu anomaly, relative to the Ca-Al inclusions, can be eliminated by mixing 0.86 anorthosite and 0.14 basalt, column (9). The exact proportions depend on the choice of materials, but Wakita and Schmitt (ref. 37) obtained almost identical values. The lunar interior, for our model (spinel, melilite, and perovskite), however, is quite different from those assumed by the above authors. These high-temperature crystals are able to retain the large ions much more efficiently than olivines and pyroxenes and these ions will not be as effectively concentrated in the melt. Tables 3 and 4 give strong support to the hypothesis that the lunar differentiates involve a primitive, refractory source region

and justify Gast's conclusions (ref. 4) regarding the nature of the source region.

The refractory trace elements support the hypothesis that the Allende inclusions represent the early condensates of the cooling solar nebulae. If the refractory trace elements such as Ba, Sr, and the REE condense early they will be concentrated in the early condensate relative to their concentration in the Sun or relative to material such as carbonaceous chondrites, which are presumably representative of the bulk composition of the nebulae. In Table 1 we estimated that the early condensates would be enriched by a factor of 11 to 31 in refractory trace elements, relative to solar or chondritic abundances. Grossman (ref. 21) estimated an enrichment factor of 20 to 25. The average enrichment of Ba, Sr, and the REE in the Allende inclusions over carbonaceous chondrites is 16, in the range of that predicted.

This study attaches profound significance to the Type III carbonaceous chondrites. To date this class includes 12 falls and 3 finds totaling in excess of 2400 kilograms. For comparison, the Type I carbonaceous chondrites, upon which several cosmologies have been constructed, have 4 members and a total recovered weight of 16 kilograms. While it is clear that the Type I carbonaceous chondrites are primitive objects and are relatively unmodified, they have few of the characteristics required for the Moon.

Major Elements

Table 5 gives the major oxide composition of lunar surface material and Ca-Al-rich inclusion and, for comparison, a theoretical estimate of the composition of the early condensate. Columns (3) and (4) are two estimates of the mean composition of the lunar crust based on trace element concentrations. Column (3) is the basalt-anorthosite mixture which is required to give Allende inclusion trace element refractory levels. Column (4) is the mixture which gives the Allende inclusion Sm/Eu ratio. There is little difference as far as the major elements are

Table 5.—*Composition of Lunar and Allende Materials*

	(1)	(2)	(3)	(4)	(5)	(6)	(7)	(8)
SiO ₂	40.4	45.7	44.5	45.0	41.4	33.7	30.8	29.5
Al ₂ O ₃	9.4	30.6	25.9	27.6	25.5	26.6	27.6	30.0
FeO	19.3	4.5	7.7	6.6	7.5	2.3	0	—
MgO	7.2	4.8	5.3	5.1	3.3	13.1	17.8	19.7
CaO	11.1	15.8	14.7	15.1	21.3	21.6	22.2	20.7
TiO ₂	10.9	0.2	2.5	1.7	0.8	1.3	1.6	—
Na ₂ O	0.5	0.3	—	—	—	1.1	—	—
K ₂ O	0.2	—	—	—	—	0.1	—	—
Cr ₂ O ₃	0.3	0.1	—	—	—	0.1	—	—
MnO	0.3	0.1	—	—	—	0.0	—	—

- NOTES: (1) Apollo 11 basalt-mean.
 (2) Lunar anorthosite.
 (3) 0.22 basalt + 0.78 anorthosite (based on trace elements).
 (4) 0.14 basalt + 0.86 anorthosite (based on trace elements).
 (5) Low melting fraction of Allende inclusions; pyroxene + anorthite (40%).
 (6) Allende Ca-Al-rich inclusion.
 (7) Allende inclusion with low melting fraction removed, i.e., implied composition of the lunar interior if the Moon is composed of the high-temperature condensates.
 (8) Composition of early condensate ($T > 1450$ K, $P_T = 10^{-3}$ atm) (ref. 21).

concerned. In the CaO-MgO-Al₂O₃-SiO₂ system with this composition, pyroxene melts at 1235° C, anorthite at 1250° C, and gehlenite at about 1400° C. Spinel remains as a solid until 1550° C. The first melt will therefore be rich in pyroxene and, as melting proceeds, will become more anorthositic. Column (5) gives the composition of the early ($T < 1250^\circ$ C) melt and also the late condensate and can be compared with columns (3) and (4). The amount of this material in the inclusion corresponds to a thickness of ~ 270 km on the Moon.

Column (6) gives the composition of the inclusion as determined by Clarke et al. (ref. 24). The FeO, K₂O, and Na₂O contents of the Ca-Al-rich inclusions are highly variable and may represent contamination from the matrix (ref. 21). The pure inclusions contain less than 1.4 percent Fe (ref. 21). Column (7) gives the composition of the high-temperature crystals in the Allende inclusion, a possible composition of the deep interior (> 270 km). It would perhaps be surprising if the single Allende aggregate that has been analyzed were completely repre-

sentative of the early condensate. An alternate approach is to consider the mineralogy of the early condensate predicted from thermodynamic calculations. Column (8) gives the composition of the condensate prior to the condensation of iron, olivine, and enstatite. The major difference between the theoretical composition and the Allende aggregate composition is the MgO content. This is probably because the Allende inclusion was armored from complete reaction with MgO (g), therefore keeping the akermanite content of the melilite below equilibrium levels.

It appears that the Allende inclusion is capable, in principle, of satisfying the major element and trace element requirements placed on the interior by the lunar igneous rocks. We will show that it is also capable of explaining the geophysical data.

A Ca-Al-Rich Deep Interior

Ringwood and Essene (ref. 9) have ruled out a Ca-Al-rich interior for the Moon on the basis of the mean density and moment

of inertia. They suggest that the coefficient of moment of inertia implies that important phase transitions to much denser states do not occur within the outer 700 km or so of the Moon. They conclude that the Al_2O_3 and CaO contents of the Moon are less than 6 and 5 percent, respectively. This has been adopted as a boundary condition by Gast (ref. 4) and others, leading to the suggestion that the Moon has a Ca-Al-rich outer shell. While it is true that garnet, the principal high-density phase, is stable at relatively low pressures in high-Al assemblages, it is not the dominant phase until plagioclase or spinel disappear, which occurs at much higher pressures. This is illustrated in figure 3, which shows the stability fields of three high-Ca-Al materials. The compositions of these assemblages are given in table 6. Also shown is a temperature depth curve from Hanks and Anderson (ref. 36). For this temperature profile, pyroxene and/or plagioclase

are the dominant stable phases until ~ 35 kilobars, which corresponds to depths of ~ 800 km. The densities of the assemblages down to this depth are of the order of 3.3 to 3.4 g/cm^3 , similar to those in the Ringwood-Essene model lunar pyroxenite, a hypothetical Ca-Al-poor assemblage. The high-pressure phases have theoretical densities of the order of 3.5 g/cm^3 but this theoretical density is only reached gradually as the pyroxenes react with the garnet. Ito and Kennedy (ref. 38), Green (ref. 39), and Boettcher (ref. 40) have all emphasized the two-stage nature of the density increase.

It should be noted that, for the temperature profile shown, the intermediate density assemblage is also stable above some 100 km, which is interesting in that high seismic velocities are found in the lunar "upper mantle" (ref. 8). If the outer several hundred km of the Moon represent a uniform composition, the 70-km discontinuity would represent a kinetic boundary (the temperature at this depth is almost certainly less than 300°C). A substantial decrease in both compressional velocity and density is predicted below some 100 km.

The precipitous drop in electrical conductivity found by Sonett et al. (ref. 41) starting at 250 km has been attributed (ref. 6) to a decrease in the FeO content below this level. This can be interpreted in two ways, both of which are consistent with the present hypothesis. First, iron starts to condense and react with previously condensed silicates after the bulk of the Ca-Al-rich silicates have already condensed. The iron-rich layer may therefore be a relic of an initial inhomogeneous accretion (ref. 6). More reasonable, however, is the view that the outer layers of the Moon are differentiates of the bulk of the Moon. In a solidifying magma, iron is strongly concentrated in the residual melt. For example, in the Skaergaard intrusion of east Greenland the FeO content of the last solidifying layers is almost three times the inferred FeO content of the original liquid (ref. 42). If the lunar basalts and anorthosites are the result of fractional crystallization, as proposed by

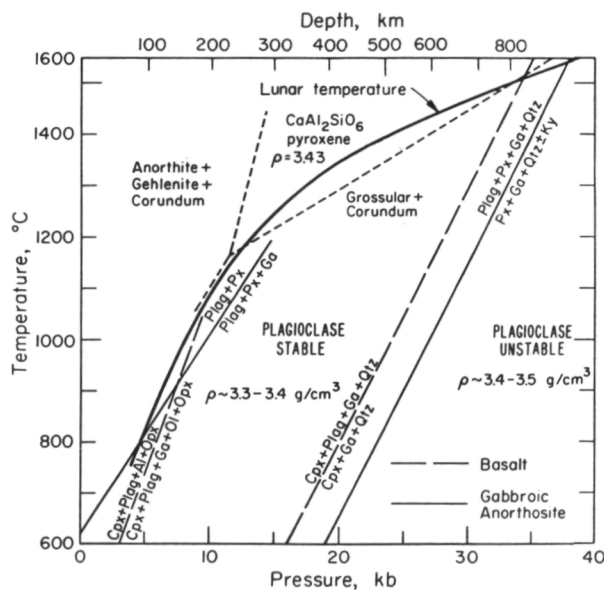


Figure 3.—Equilibrium fields in Ca-Al-rich assemblages. Basalt is from Ito and Kennedy (ref. 38); gabbroic anorthosite, from T. Green (ref. 39); and anorthite + gehlenite + corundum from Hays (ref. 54). The transformation akermanite \rightarrow merwinite + spinel ($\rho = 3.29 \text{ g/cm}^3$) occurs close to the anorthite + gehlenite + corundum \rightarrow pyroxene boundary and its downward projection (ref. 45)

Table 6.—*Composition and Transformation Pressures of Assemblages High in Ca and Al*

	(1)	(2)	(3)	(4)	(5)	(6)
SiO ₂	49.9	59.9	53.5	27.5	47.6	53.1
Al ₂ O ₃	16.8	17.3	22.5	46.8	20.7	5.0
FeO	11.4	6.3	4.7	—	8.2	13.5
MnO	0.2	—	0.1	—	0.1	0.4
MgO	7.6	3.4	2.1	—	7.6	22.5
CaO	9.3	7.1	9.9	25.7	12.5	4.0
Na ₂ O	2.5	3.7	3.7	—	0.7	0.1
TiO ₂	1.3	0.7	1.0	—	1.2	1.0
Pressure Range (kb) ⁽⁷⁾						
Higher	11.	15.	15.	(14) ⁽⁶⁾	9.	10.
Lower	28.	28.	31.	(27) ⁽⁶⁾	21.	25.

NOTES: (1) Olivine tholeiite, NM5 (ref. 27).

(2) Diorite (ref. 39).

(3) Gabbroic anorthosite (ref. 39).

(4) Anorthite + Gehlenite + Corundum (ref. 54).

(5) Plagioclase-rich lunar basalt 14310 (ref. 3).

(6) Model lunar pyroxenite (ref. 9).

(7) Pressure range for intermediate density ($\rho \sim 3.3\text{--}3.4$ g/cm³) phases. In general, the lower pressure is the first appearance of garnet and the higher pressure is for the disappearance of plagioclase, both at 1200°C (1100°C for column (5)).

In the Moon, 27 kb corresponds to approximately 600 km in depth.

(8) In column (4) the pressures correspond to

$\text{CaAl}_2\text{Si}_2\text{O}_8 + \text{Ca}_2\text{Al}_2\text{SiO}_7 + \text{Al}_2\text{O}_3 \rightarrow \text{anorthite} + \text{gehlenite} + \text{corundum} + 3\text{CaAl}_2\text{SiO}_6$ ($\rho = 3.43$ g/cm³)
 pyroxene
 and $3\text{CaAl}_2\text{SiO}_6 \rightarrow \text{grossular} + \text{corundum}$
 both at 1400°C.

Wood et al. (ref. 43), Smith et al. (ref. 44), and others, the outer 250 km (35 wt. % of the Moon) would represent the residual melt. With the bulk composition of the Moon proposed in this paper, the near-liquidus phases would be melilite or merwinite and spinel, all of which are denser than the residual liquid. Spinel and melilite crystallize between 1400 and 1550° C at $P \sim 0$ (ref. 46). Once the melilite and spinel are removed, the remaining liquid is 34.6 percent of the mass of the original melt, in agreement with the above calculation.

The density of the low-pressure assemblage of the residual crystals in the interior is about 3.2 g/cm³ (spinel plus melilite). Akermanite, a major component of melilite, breaks down (at moderate pressure) to merwinite plus diopside (ref. 45).

At lunar temperatures this would occur at ~ 200 km. The spinel + merwinite + diopside assemblage has a density of 3.4 g/cm³.

Possible Fractionation of an Allende-like Moon

The composition of the Allende inclusion, as reported by Clarke et al. (ref. 24) has been recast into a mineral assemblage with the following results (in weight percent): feldspar 28.4, melilite 39.7, spinel 25.7, perovskite 2.3, and diopside 3.9. The near-liquidus phases in a similar assemblage studied by Prince (ref. 46) are spinel and melilite. The crystalline sequence is spinel at about 1550° C followed by melilite at 1400° C, anorthite at 1250° C, and pyroxene

Table 7.—*Model Compositions of Lunar Interior*

	(1)	(2)	(3)	(4)	(5)	(6)
SiO ₂	48.8	47.7	47.1	52.9	26.7	61.0
TiO ₂	3.8	2.7	3.2	0.9	—	0.6
Al ₂ O ₃	25.3	27.8	27.3	17.6	28.3	7.4
MgO	2.1	5.7	6.8	15.4	19.7	24.3
CaO	16.6	15.8	15.6	13.2	25.2	6.5

- NOTES: (1) Allende inclusion with near-liquidus phases removed (spinel and melilite). This is the inferred parent liquid for the lunar basalts and anorthosites (this paper).
 (2) Average crustal composition derived by mixing basalt and anorthosite in the proportions 22 percent basalt, 78 percent anorthosite.
 (3) Hypothetical parent liquid for Apollo 11 igneous rocks derived from fractional crystallization model (Case 1 of Gast et al., ref. 26, renormalized).
 (4) Hypothetical parent liquid for partial fusion model (ref. 61), renormalized.
 (5) Deep interior (near-liquidus crystals); Allende inclusions minus column (1) (this paper).
 (6) Deep interior, partial melt model (refs. 47 and 61); assumptions: (a) CaO and Al₂O₃ contents must be low, and (b) lunar basalts are derived from great depth in a single-stage process.

at 1235° C. Fractional crystallization would give a spinel-melilite or spinel-merwinite-diopside interior and a feldspathic pyroxenitic surface layer. The refractory interior would constitute approximately 65 percent of the mass of the Moon. The residual liquid would be enriched in Fe and any trace elements that are incompatible with the spinel and melilite lattices, and would compose the outer 250 km of the Moon. The basalts and anorthosites could be derived from this layer by further crystal fractionation involving plagioclase floatation or by partial melting after solidification. The high U and Th contents of the surface layer are adequate to remelt the lower portions within several hundred million years after solidification (ref. 36).

The composition of the outer layers of the Moon, obtained by removing the near-liquidus crystals, is given in column (1) of table 7. For comparison, column (2) gives a previous "average" crustal composition of the Moon. The similarity is remarkable. Column (3) gives the hypothetical parent liquid calculated by Hubbard et al. (ref. 47) on the basis of trace element distributions and a fractional crystallization model. The MgO

in column (3) is arbitrary because of lack of information regarding the extent to which olivine is involved in the source region. On the other hand, the MgO content of the early condensates is also uncertain; it increases with falling temperature because of the increasing akermanite content of the melilite, and rises rapidly once olivine and enstatite start condensing. The Moon may have accreted from material that condensed over a slightly broader temperature range than the Allende inclusion. Column (4) is a hypothetical parent liquid derived from a partial melt model. The agreement with this model is not as good as the fractional crystallization model but the inferred Al₂O₃ and CaO content is still considerably greater than models such as Ringwood and Essene (ref. 9). Column (5) is the inferred deep interior (> 250 km) composition (spinel + melilite). For comparison, column (6) gives Gast's deep interior composition (ref. 4) which is based on the (invalid) Ringwood (ref. 2) constraint on total CaO and Al₂O₃. The density of the spinel-melilite assemblage is 3.2 g/cm³, about the same as the mean density of the Allende inclusions but ~ 10 percent greater than the density of the residual melt.

At high pressure, akermanite breaks down to merwinite plus diopside with a density of 3.29 g/cm^3 ; a similar reaction presumably occurs for gehlenite. The assemblage spinel + merwinite + diopside is probably stable through most of the bulk of the Moon. This assemblage has a density of 3.40 g/cm^3 .

The density variation in the Moon is likely to be complex. The Apollo seismic experiment showed that large velocity jumps occurred at 25 and 65 km (ref. 8). The very low velocities in the upper 25 km suggest that this region is porous or fractured and the density may be as low as 2 g/cm^3 . The lower crust, from 25 to 65 km, has velocities consistent with gabbroic anorthosite, and densities may range from 2.7 to 3.0 g/cm^3 in this region. The velocities from 65 to 120 km (ref. 8) are high and may indicate the transformation to a garnet-bearing assemblage with densities from 3.3 to 3.7 g/cm^3 (ref. 48). A garnet-bearing assemblage in the lunar upper mantle is consistent with the phase diagrams presented in Ringwood and Essene (ref. 9) and figure 3. At slightly greater depth the garnet will become unstable because of the rapid rise in lunar temperatures (see figure 3) and lower densities, comparable to those in the lower crust, may prevail until $\sim 300 \text{ km}$, at which depth we again cross the garnet-in curve for Ca-Al-rich assemblages. However, we have inferred a compositional change near $\sim 250 \text{ km}$ to a spinel-merwinite-diopside assemblage with $\rho \sim 3.4 \text{ g/cm}^3$. There is abundant flexibility to satisfy the mean density and the moment of inertia.

Formation and Differentiation of the Moon

The derivation of the lunar surface rocks could proceed from our assumed composition for the Moon in several ways. The following is one possible scenario:

1. The Moon accreted from the material that condensed from a cooling solar nebula prior to the condensation of significant amounts of iron. The un-

condensed materials in the vicinity of the accreting Moon, including most of the iron and the volatiles, were removed by an intense solar wind or were swept up by the more massive and more favorably disposed Earth. From cooling rate and other considerations, the accumulation of the Moon occurred very rapidly.

2. The whole Moon was enriched in Ca, Al, Ti, U, Th, and the REE by approximately the ratio of the fraction of the material that condenses before iron relative to chondritic or solar non-volatile abundances. It was depleted in Fe, Na, Rb, K, and the more volatile elements.
3. The initial mineralogy of the Moon was primarily melilite (solid solution of akermanite and gehlenite), aluminous clinopyroxene, diopside, spinel, anorthite, and perovskite.
4. The rapid accretion, the high initial temperatures which are a consequence of the accretion-during-condensation hypothesis, and the high U and Th abundances (10 to 16 times chondritic) led to early and extensive (and perhaps complete) melting.
5. The near-liquidus phases, spinel and merwinite, settled to the interior. These crystals constitute approximately 65 percent of the mass of the Moon, which corresponds to the volume below some 250 km. The REE, Ba, and Sr are not necessarily strongly fractionated at this stage between crystals and melts. The melt, in fact, may be slightly depleted.
6. The residual liquid was approximately 80 percent anorthosite and yielded anorthosite, upon further cooling, which presumably formed the protocrust and the highlands. Then the residual liquid yielded pyroxenes from which the basalts were derived either directly or by partial melting after solidification. An alternate scheme could involve the complete crystallization of the outer shell followed by remelting and separation of the basalt liquid. The high U and

Th content of the outer shell permits this possibility (ref. 36).

7. The small initial FeO content of the Moon was strongly concentrated in the residual melts and therefore concentrated in the outer 250 km of the Moon.
8. The basalts and anorthosites could be derived either by partial melting or by fractional crystallization, or both, of the outer 250 km of the Moon. The composition of this shell is similar to that inferred by Gast (ref. 4).

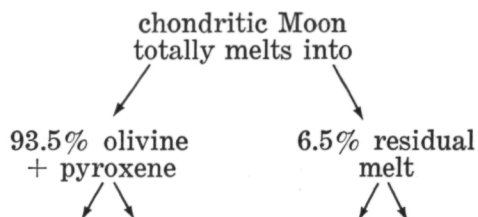
Gast (ref. 4) has ruled out fractional crystallization on the basis that parent liquids with more than 80 percent anorthite were implausible. Anorthite contents of the order of 80 percent are a feature of our model and a similar model of Wakita and Schmitt (ref. 37) for the outer layers of the Moon. These estimates are based on the mixing required to remove the europium anomaly. If KREEP basalts are an important component of the lunar crust, even higher anorthosite contents are required. A further difficulty pointed out by Gast with the fractional crystallization model is that the abundance of such elements as Br, Sr, and REE in the source region must be 15 to 20 times that of the average chondrite. These high abundances are also an intrinsic feature of our model. Independently, Smith et al. (ref. 44) concluded that the Apollo 11 basalts represent a residual fraction after crystallization of more than 80 percent of a parent magma.

The lunar igneous rocks could be either the result of a single-stage extensive fractional crystallization or partial melting process, or could result from a multiple-stage process involving both. The variation in the properties of the lunar basalts suggests that secondary processes may have operated. Some of the basalts may have crystallized from the residual melt after the higher temperature crystals were removed by sinking and floatation, and others may have formed by partial melting at depth after crystallization of the liquid residuum.

In order to facilitate comparison with previous models, we will briefly discuss the model of Wakita and Schmitt (ref. 37). It

has many elements in common with the proposals of Smith et al. (ref. 44) and Wood et al. (ref. 43). They assumed, as have most previous investigators, that the total Moon accreted from material similar to that of ordinary chondritic meteorites. Although their models are quite different, Gast (ref. 4) and Ringwood and Green (ref. 3) also propose that the bulk of the Moon's interior is chondritic. Wakita and Schmitt (ref. 37) considered [on the basis of a personal communication from Anders] the use of "chondrules from carbonaceous meteorites that are significantly depleted in alkalis and are deficient in metal" but did not pursue this suggestion because of the lack of sufficient data on the abundances of REE and other elements in chondrules.

They proposed that the Moon was completely molten early in its history and that, after formation of a small Fe core, fractional crystallization of the high-temperature minerals (in a chondritic assemblage) olivine and orthopyroxene, took place. The light residual magma floated to the surface from which anorthosites and basalts separated, the light anorthosite floating on the denser basalt. During this fractional crystallization process the REE concentration in the residual magma increased with the crystallization of olivine and pyroxene minerals, since these can accommodate very little of the large REE ions. About 93 percent of the mixed olivine plus hypersthene minerals crystallized from the initial melt, leaving ~ 7 percent residual melt with a thickness of ~ 35 km. From this residual melt 84 percent separated as anorthosites and 16 percent remained as basalts. Although not stated by Wakita and Schmitt, a feature of the model is progressive enrichment of the melt in FeO and, probably, TiO₂. The flow chart below illustrates their proposed process.



75%	25%	84%	16%
hypersthene	olivine	anorthosites	basalt
(0.70 mass fraction)	(0.23)	(0.055)	(0.0104)

A basically similar scheme can be proposed if the original composition of the Moon is Ca-Al-rich throughout. The high-temperature minerals in this case, however, are gehlenite-akermanite solid solutions (at low pressure), spinel, and perovskite; and the thickness of the residual is ~ 230 km, of which ~ 30 km is potentially basaltic. The fractionation of iron into the residual melt provides a high-conductivity outer shell. The lattices of the high-temperature minerals, in this model *can* accommodate the large REE and other ions although information is unavailable on the distribution coefficients. The fact that the REE ions substitute readily for Ca^{++} suggests that they may be retained by gehlenite and perovskite. If the initial concentration of the REE in the Allende inclusion is appropriate for the bulk Moon, and if the anorthosite-basalt mix discussed previously is appropriate for the outer shell of the Moon (table 4), it follows that the melt, the parent liquid of the lunar basalts and anorthosites, is slightly depleted in REE, relative to the bulk Moon, rather than enriched, as is the case when olivine and orthopyroxenes are the high-temperature phases.

Smith et al. (ref. 44) propose that the Moon was formed from iron and volatile-depleted chondritic material, after which it was completely melted. The entire interior was subjected to crystallization differentiation, and the basalts are regarded as the residuum. This hypothesis is the antithesis of the one presented by Ringwood and Esene (ref. 9). Ringwood (ref. 49) has vigorously objected to this model, primarily on thermal grounds. Although the interior of the Moon in the Smith et al. model is formed of concentric layers of Fe-Ni, olivine, and pyroxene, rather than melilite and spinel, it has some attractive features—mainly the concentration of Fe and Ti in the residual liquid and upward floatation of

plagioclase (see also Wood et al., ref. 43)—which are in common with the present model. Ringwood's objections would also be directed to our model. His first concern is with the mechanism that caused complete melting of the Moon. In our model complete melting is not necessary but we see no particular difficulty in this regard. The high initial temperature of the material that accretes on the Moon (\sim condensation temperatures), the rapid accretion time proposed by Öpik (ref. 50) and Mizutani (ref. 51), and high U and Th contents (~ 16 times chondritic) all lead to extremely high initial temperatures. Ringwood (ref. 49) considers the evidence for igneous activity 10^9 years after solidification of the Moon has commenced, to be a fatal difficulty with the Smith et al. hypothesis. However, the thermal history calculations of Hanks and Anderson (ref. 36) show that the Moon, even with strong upward concentration of the heat-producing elements (adjusted so that the present-day heat flow is satisfied), will be above the solidus of lunar basalts, at 3.7 AE in the depth interval of 50 to 400 km. The later lunar basalts were probably formed somewhere in this interval and extruded where the lithosphere was thin enough or weak enough that they could make their way to the surface. While it is true that the thermal time constant of the solid outer shell is short, the thermal history models show that the temperature between about 70 and 400 km *increases* during the first 1.5 b.y. of the Moon's life because of the high radioactivity content in the upper layers. The other objections of Ringwood (ref. 49) are directed toward the chondritic nature of the Smith et al. model and are not relevant here.

Depth of Origin

The considerations in this paper and in two previous papers (refs. 6 and 12) reopen the questions of partial melting and fractional crystallization, as discussed in the previous section, and the depth of origin of the lunar basalts.

Ringwood (ref. 49) marshals a series of arguments in support of his belief that the

Apollo 11 basalts, at least, were derived from a depth greater than 200 km:

1. The cooling of the Moon is too rapid to permit melting to occur at shallower depths 1×10^9 years after the birth of the Moon. Hanks and Anderson (ref. 36), however, showed that melts could exist below 50 km at the appropriate time for generating the younger basalts.
2. The persistence of mascons for ~ 3.7 b.y. implies an underlying lithosphere of substantial long-term strength; preservation of mascons would not be explicable, if partial melting occurred in the lithosphere. Anderson and Hanks (ref. 6) showed that substantially higher stresses can be maintained by the lunar lithosphere than are now indicated and that considerable stress relaxation could have occurred in the early history of the Moon. A thin outer shell can support both the nonhydrostatic shape of the Moon and the mascons.
3. Extensive fractionation of a considerable portion of the Moon is required in order to obtain the high levels of the trace element refractories; near surface melting processes are inadequate. This argument is based on presumed chondritic abundance patterns and not on the more plausible 16x chondritic lunar abundances.

The other arguments are also based on presumed chondritic abundances or on melting experiments which allow the basalts to be derived from depths as shallow as 100 km.

The present model is consistent with basalt origin below 200 km, but the small amount of melt and the great thickness and strength of the lithosphere in the Ringwood (ref. 49) model seem incompatible. In one of the alternates discussed in the section "Formation and Differentiation of the Moon," the later lunar basalts formed by complete melting of the region between 200 and 230 km. In the other extreme case, they formed by ~ 20 percent melting of the outer 230 km.

Inhomogeneous Accretion of the Moon

As mentioned previously, it has been suggested several times that the Moon accreted inhomogeneously. However, the motivation has been to enrich the outer layer, in particular, the source regions of the lunar igneous rocks in Ca, Al, U, Th, Ba, REE, and $\text{MgO}/(\text{FeO} + \text{MgO})$. It has been considered unlikely that the whole Moon could exhibit these properties. However, we have shown that the early condensates in general, and the Allende inclusions in particular, provide the necessary characteristics of the source region and do not violate the inferred properties of the deeper interior. No primitive layering is required by the geochemical and geophysical data, but chemical zonation as implied by the inhomogeneous accretion hypothesis (ref. 11) is a distinct possibility.

The chemical zoning that has been proposed has the interior enriched in FeO, MgO, SiO_2 , and the volatiles relative to the exterior, which is enriched in CaO, Al_2O_3 , U, Th, and the REE. This is contrary to expectations based on inhomogeneous accretion directly within a condensing solar nebula. In this case, the CaO and Al_2O_3 would increase with depth, and SiO_2 , MgO, and FeO would decrease with depth. The initial distribution of the refractory trace elements, such as Ba, U, Th, and the REE depends on the phases in which they concentrate upon condensation. If they occur primarily in the gehlenite, perovskite, and spinel they can be expected to be concentrated initially in the center of the Moon. If they are concentrated in the pyroxenes they can be expected to be brought in with the upper layers. If the Moon partially or totally melts upon or after accretion they will be redistributed according to distribution coefficients between the melt and the liquidus phases—gehlenite and spinel. A detailed study of the trace element refractory distribution among phases in the Allende inclusion would help resolve this question.

The present-day gross chemical layering in the Moon would be about the same whether

it resulted from inhomogeneous accretion or homogeneous accretion followed by fractional crystallization or partial melting. In the inhomogeneous accretion model the phases in the deep interior would be merwinite, diopside, spinel, and (possibly) perovskite and corundum, the early condensing phases or reaction products. If the Moon were ever totally molten the interior would also be melilite, or merwinite; these are the near-liquidus phases and are denser than the residual melt. In the partial melt model the low melting point and low-density phases are pyroxenes and anorthite, which would rise to the surface to form the source region for the lunar basalts and anorthosites.

A critical test of the alternates involves the distribution of FeO. In the inhomogeneous accretion model the FeO would be concentrated near the surface because of the late condensation of iron. In the fractional crystallization model the residual melt, and hence the surface layers, would also be strongly enriched in FeO. In the homogeneous accretion, partial melt model the melt would be only slightly enriched in FeO. The main evidence bearing on this point, although controversial, is the conductivity profile of Sonett et al. (ref. 41). They found a drop of three orders of magnitude in electrical conductivity between depths of 250 and 350 km, although other interpretations are possible. This has been interpreted (ref. 6) in terms of a dramatic decrease in the FeO content at this depth. The mass fraction of the Moon below 250 km is 0.6, which is also the amount of gehlenite and spinel (the early condensates and also the near-liquidus phases) in the Al-lende inclusions. Thus the inhomogeneous accretion and fractional crystallization models satisfactorily account for the gross layering as interpreted by Sonett et al. (ref. 41) and Anderson and Hanks (ref. 6). The outer 250 km in either of these models would be the source region from which the lunar igneous rocks are subsequently derived by partial melting or fractional crystallization. This source region must be enriched in U, Sr, and the REE, relative to chondrites. If these are concentrated in the early con-

densates, the deep interior must have been involved in the early and extensive differentiation and this would favor fractional crystallization on the grand scale envisaged by Wood et al. (ref. 43). If these trace refractories are concentrated in the later condensates, the interior need not be involved in a major way in the subsequent evolution of the Moon. In lieu of measurements on the Al-lende inclusions our only recourse is to theoretical thermodynamic calculations. According to Grossman (ref. 21), ThO_2 condenses between the condensation temperature of spinel and gehlenite. Thorium is enriched in the Moon to about the same degree as the higher temperature condensates such as Hf, Y, N, Ta, and Sc. U and the REE also have similar enrichment factors. This suggests that the trace refractories are in the early condensates and that the whole Moon has been involved in the early differentiation event. The present chemical zonation of the Moon, therefore, is not necessarily primitive; the Moon could initially have been a homogeneous mixture of the primarily pre-iron condensates. However, since the Ca-Al-rich inclusions in C2 and C3 chondrites commonly exhibit a zonation, it is of interest to discuss a possible primitive zonation in the Moon.

There are two possible variants of the direct heterogeneous accretion hypothesis. If accretion is rapid and completely efficient in the sense that it keeps up with the condensation, the Moon will grow as a chemically zoned body with successive condensates shielding the early condensates from further reaction with the gas. One would obtain a Moon composed of a corundum nucleus overlain by perovskite, melilite, and diopside shells. More likely some of the early condensate will be available for later reaction with the gas either before accretion or at the lunar surface. In this case the Moon will be composed of diffuse shells grading from a primarily corundum, perovskite, melilite interior to a spinel-rich shell overlain by diopside. The diopside and the spinel can react to form anorthite. The Moon is unlikely to be perfectly prompt or efficient in accreting material that has condensed in its vicinity and

it may therefore be initially a relatively homogeneous mixture of, primarily, perovskite, melilite, spinel, and diopside, with—if temperatures fell low enough—some olivine. The amount of olivine is constrained to be small since its condensation interval overlaps iron and only a small fraction of the available (solar) iron has been incorporated into the Moon. For example, in a cooling gas of solar composition at 10^{-3} atm total pressure, 46 percent of the iron has condensed before forsterite appears (ref. 21). More olivine may be incorporated into the interior if the condensation of iron is delayed by the nonequilibrium considerations of Blander and Katz (ref. 52). As discussed previously, the melilite will break down to pyroxene plus merwinite at high pressure.

Other Considerations

Since the Moon is clearly depleted in iron, it is hard to see why it should not also be depleted in compounds more volatile than iron, as the surface rocks clearly are. There is no evidence that the interior approaches chondritic composition.

If the moon is composed primarily of high-temperature condensates, the interior, as well as the surface rocks, will be enriched in Ca, Al, Ti, U, Th, and the REE relative to carbonaceous chondrites, the Earth, or solar abundances. Similarly, it should be depleted in Fe, K, Na, Rb, S, and H_2O . A Ca-Al-rich interior has been dismissed by Wetherill (ref. 16), Ringwood and Essene (ref. 9), and O'Hara et al. (ref. 53) because it was believed that the high-pressure phases of Ca-Al-rich compounds would lead to densities which would violate the lunar mean density and moment of inertia. Although this is true for some assemblages, such as the Apollo 11 basalts, it is not a general characteristic of all Ca-Al-rich assemblages. Similarly, a high concentration of U in the interior has been ruled out because this would lead to temperatures which have been considered to be too high. The low iron content of the early condensate, and inferred for the lunar in-

terior, leads to a low intrinsic electrical conductivity. The interior temperature must be some 800°C greater than inferred previously from the lunar electrical conductivity experiment and measurements on iron-rich rocks (ref. 6). These measurements have provided some of the main arguments for a cold Moon. The other main argument for a cold Moon is based on its nonequilibrium shape and the persistence of mascons. However, when scaled properly for gravity, the Moon is much closer to hydrostatic equilibrium than is the Earth or Mars, and the stresses being supported by the lunar lithosphere are modest by terrestrial and laboratory standards (ref. 6). The geophysical data do not require a cold, strong, deep interior. The long persistence of lunar igneous activity also strongly suggests that the source region of the lunar basalts at least was strongly enriched in uranium. It must be at least high enough to counteract the effects of conduction through the outer shell in the first 10^9 years of lunar existence.

The observations presented in this paper suggest that the Moon accreted from high-temperature condensates, in particular, material that condensed out of the cooling solar nebula before Fe. This would lead to a Moon that is enriched in refractories and depleted in volatiles relative to the average composition of the inner solar system. This can be accomplished if the Moon accreted during condensation and was competing with a more massive or more favorably disposed body, such as the Earth. The accretion process is only vaguely understood at best, but it seems clear that the initial stages of accretion will take place most readily by the coalescence of hot particles orbiting in a dense, viscous cloud, i.e., during the early stages of condensation. This will certainly be true when the gravitational cross section of the protoplanet is small.

The Origin of the Moon

If the bulk of the Moon does represent a high-temperature condensate, the question

arises, why did the Moon not accrete substantial quantities of material that condensed at lower temperatures? There are several possibilities.

The temperature at which an element or compound condenses out of a cooling nebula depends on both the composition and the pressure of the gas. The temperature of the nebula (ref. 55) dies off rapidly away from the Sun and slowly with distance from the median plane. Pressure dies off with distance from the Sun and rapidly with height above the plane. At any given time the composition of the condensed material, prior to complete condensation, is a function of location in the nebula. If the uncondensed gas is removed at some stage, the planets and meteorites will differ in composition.

The difference in mass and composition of the Earth and the Moon can be explained if

1. The Earth were accreting in a dense part of the nebula, i.e., the median plane, and the Moon were accreting, on the average in a less dense part of the nebula. This could happen, even if the Moon were always at 1 AU, if it were in a highly inclined orbit—the orbit would eventually settle down to its present configuration by gas drag, collision, and tidal friction. The tendency of the Moon to grow more slowly than the Earth, and to get less of the later condensates, would be ever more pronounced by the lower temperatures required to condense material at the lower pressures encountered away from the ecliptic and the high encounter velocities due to the highly inclined orbit.
2. Even if the Moon were always in a low inclination orbit, the fact that it is orbiting the Earth makes its encounter velocity with solar orbiting gains higher than the Earth's and, therefore, its capture probability less (ref. 56).
3. If the Earth started accreting sooner than the Moon, or for some other reason got a head start, it would always have a larger capture cross section than the Moon. When it became large

enough to retain an atmosphere or, equivalently, to make a significant perturbation in the pressure of its surrounding gas envelope, it would retain infalling material more efficiently and material would condense in its vicinity at higher temperatures.

The observational fact that the Earth is bigger than the Moon and is enriched in iron and the volatiles compared with the Moon suggests that the Earth was more favorably disposed to collect the later condensates, and was possibly more favorably disposed throughout its accretional history. This is possibly related to its central position in the disc. If the Moon's orbit were initially highly inclined it would be accreting, on the average, in a less dense part of the nebula, even though it were accreting at the same distance from the Sun as the Earth. The Earth would be continuously sweeping up the material in the median plane while the proto-Moon only crossed it twice a year. An even more important effect is the pressure dependence of the condensation temperature. Condensation occurs first in a cooling nebula at the median plane, i.e., the high-pressure region. Condensation occurs at lower temperatures and later times away from the plane. This leads to a delayed start for the Moon, and gives the Earth a head start on sweeping up material near the central plane. The scenario leads naturally to a Moon that is smaller than the Earth and that is enriched in the early condensates and depleted in the later condensates.

Condensation temperatures depend on pressure as shown in figure 4. The mean pressure in the nebula is usually taken as 10^{-3} to 10^{-4} atmospheres, but the pressure varies with distance from the Sun and with height above the median plane. Note that the condensation intervals of the refractories, forsterite, and iron overlap at high pressures but diverge at low pressures. The vertical line labeled 1 AU is the temperature in the vicinity of the Earth's orbit during the high luminosity phase of the Sun (ref. 57). If the Earth were accreting in a dense, high-pressure part of the nebula, such as the

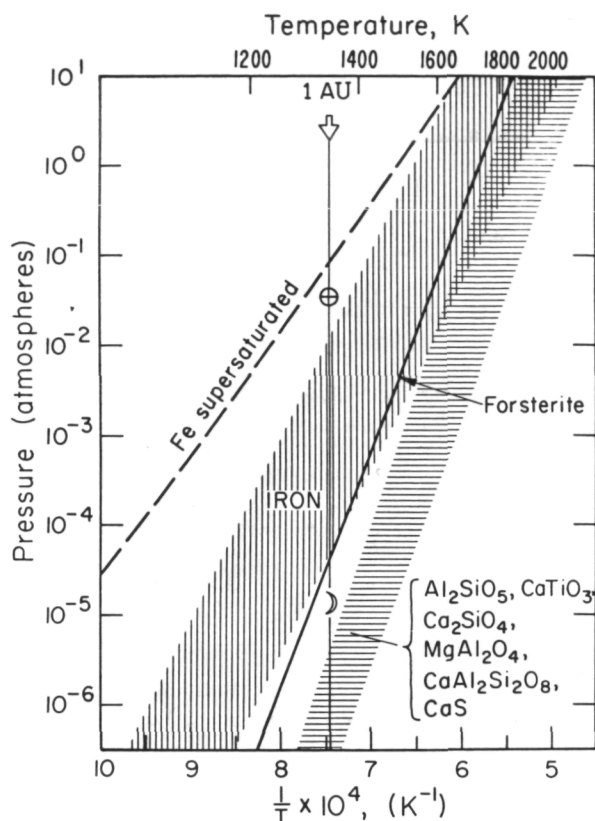


Figure 4.—Condensation temperature versus total pressure in the solar nebula. The temperature at 1 AU is from ref. 57. The Earth and the Moon are placed on this line in such a position as to explain their bulk compositions, assuming they accreted only from material that condensed at this and higher temperatures. The other terrestrial planets can be placed on this diagram in such a way as to explain their size and composition, and the presence or absence of satellites.

median plane, it would have iron and the magnesium silicates available for incorporation into its interior, as well as the early condensing refractories. As it grows, it perturbs the gas pressure in its vicinity, or, equivalently, develops a massive atmosphere, and the effective pressure in its vicinity will increase, which enhances condensation in its vicinity. The atmosphere will also make it a more efficient collector of the condensed material (ref. 58). Away from the median plane the temperature remains almost constant (ref. 55) but the gas pressure decreases rap-

idly. Condensation, therefore, occurs at lower temperatures, and in a cooling gas, at later times. As drawn in figure 4, the Earth will be more than 50 percent assembled before the Moon starts. If the cooling rate is constant, the Earth will have spent three times as much time accreting as the Moon. By the time the Moon nucleates, the Earth will have swept up most of the iron. Even after the Moon starts to form, the Earth will get most of the remaining iron and other later condensates, since it is spending all of its time in the median plane while the Moon only crosses it twice a year and does so with high encounter velocities and a relatively small capture cross section.

Summary

The enrichment of refractories in the Moon such as Ca, Al, Ti, Ba, Sr, REE, and U and the depletion of volatiles such as Fe, Rb, K, S, and H₂O relative to solar or carbonaceous chondritic abundances can be understood if the Moon represents a high-temperature (pre-iron) condensate. The pre-iron condensates represent about 6 percent of the total condensables (exclusive of H, S and C) and will therefore be enriched in the refractory trace elements (such as Ba, Sr, REE, U, and Th) by a factor of about 16, relative to carbonaceous chondrites. This is close to the average enrichment observed in the lunar surface material and in the Ca-Al-rich inclusions of Type II and Type III carbonaceous chondrites. The bulk surface chemistry of the Moon is consistent with the composition of the low-melting fraction of the early condensables. Trace elements plus seismic and heat flow data are consistent with "enrichment" of Ca, Al, and U at the surface and in the interior of the Moon. A Ca-Al-rich deep interior does not imply an unacceptably large mean density. Most of the Moon's complement of volatiles may be brought in by chondritic material in the terminal stages of accretion.

The differences between the Earth and the Moon and the terrestrial planets can be un-

derstood if accretion occurred during condensation.

Acknowledgment

This research was supported by National Aeronautics and Space Administration contract NASA NGL 05-002-069. The author wishes to acknowledge helpful conversations with H. Mizutani and a critical review of the manuscript by Arden Albee. Paul Gast kindly supplied the author with the results of some of his important studies, in advance of publication.

References

1. RINGWOOD, A. E., *Geochimica et Cosmochimica Acta*, Vol. 30, 1966, p. 41.
2. RINGWOOD, A. E., *Earth Planet. Sci. Letters*, Vol. 8, 1970, p. 131.
3. RINGWOOD, A. E., AND D. H. GREEN, *Proc. Third Lunar Science Conference*, 1972, p. 573.
4. GAST, P. W., *The Chemical Composition and Structure of the Moon*, In press.
5. PAPANASTASSIOU, D. A., AND G. V. WASSERBURG, *Earth Planet. Sci. Letters*, Vol. 11, 1971, p. 37.
6. ANDERSON, D. L., AND T. HANKS, *Science*, In press.
7. LEVINSON, A. A., AND S. R. TAYLOR, *Moon Rocks and Minerals*, Pergamon Press, 1971.
8. TOKSOZ, M. N., F. PRESS, K. ANDERSON, A. DAINITY, G. LATHAM, M. EWING, J. DORMAN, D. LAMMLEIN, G. SUTTON, F. DUENNEBIER, AND Y. NAKAMURA, *Science*, Vol. 176, 1972, p. 1012.
9. RINGWOOD, A. E., AND E. ESSENE, *Science*, Vol. 167, 1970, p. 607.
10. LANGSETH, M., S. P. CLARK, J. CHUTE, AND S. KEIHM, *Proc. Third Lunar Science Conference*, 1972, p. 422.
11. CLARK, S. P., K. K. TUNEKIAN, AND L. GROSSMAN, *The Nature of the Solid Earth*. E. C. Robertson, ed., McGraw-Hill Book Co., 1972, pp. 3-18.
12. ANDERSON, DON L., *Nature*. In press.
13. ANDERSON, DON L., *Comments on Earth Sciences. Geophysics*, Vol. 2, 1972, p. 93.
14. ANDERSON, DON L., AND T. HANKS, *Nature*.
15. GAST, P. W., AND R. K. MCCONNELL, *Proc. Third Lunar Science Conference*, 1972, p. 257.
16. WETHERILL, G. W., *Science*, Vol. 160, 1968, p. 1256.
17. MASON, B., AND W. MELSON, *The Lunar Rocks*. Wiley-Interscience, 1970.
18. GANAPATHY, R., R. KEAYS, J. LAUL, AND E. ANDERS, *Geochimica et Cosmochimica Acta*, Supplement 1, 1970, p. 1117.
19. LARIMER, J., *Geochimica et Cosmochimica Acta*, Vol. 31, 1967, p. 1215.
20. LORD, H. C., III, *Icarus*, Vol. 4, 1965, p. 279.
21. GROSSMAN, L., *Condensation, Chondrites and Planets*. Ph.D. Thesis, Yale Univ., 1972.
22. GREENLAND, L. P., *Geochimica et Cosmochimica Acta*, Vol. 35, 1971, p. 319.
23. RAZIN, L. V., V. P. KHVOSTOV, AND V. A. NOVIKOV, *Geochimistry International*, Vol. 2, 1965, p. 118.
24. CLARKE, R., E. JAROSEWICH, B. MASON, J. NELEN, M. GOMEZ, AND J. R. HYDE, *Smithsonian Contrib. Earth Sci.* No. 5, 1970.
25. MARVIN, V., J. WOOD, AND J. DICKEY, *Earth Planet. Sci. Letters*, Vol. 7, 1970, p. 346.
26. GAST, P., N. HUBBARD, AND H. WEISMANN, *Geochimica et Cosmochimica Acta*, Supplement 1, 1970, p. 1143.
27. COHEN, L. H., K. ITO, AND G. C. KENNEDY, *Am. J. Sci.*, Vol. 265, 1967, p. 475.
28. SZTROKAY, K., V. TOLNAY, AND M. FOLDVARI-VOGL, *Acta Geologica*, Vol. 7, 1961, p. 57.
29. FREDRIKSSON, K., AND A. REID, *Researches in Geochemistry*, P. Abelson, ed., Vol. II, Wiley, 1967, p. 143.
30. CHRISTOPHE, M., *Bull. Soc. Fr. Mineral. Cristallogr.*, Vol. 91, 1968, p. 212.
31. KURAT, G., *Earth Planet. Sci. Letters*, Vol. 9, 1970, p. 225.
32. CHRISTOPHE, M., *Meteorite Research*. P. Millman, ed., 1969, p. 492.
33. FUCHS, L. H., *Am. Mineralogist*, Vol. 54, 1969, p. 1645.
34. KEIL, K., AND L. FUCHS, *Earth Planet. Sci. Letters*, Vol. 12, 1971, p. 184.
35. WAKITA, H., AND R. SCHMITT, *Nature*, Vol. 227, 1970, p. 478.
36. HANKS, T., AND DON L. ANDERSON, *Phys. Earth Planet. Interiors*. In press.
37. WAKITA, H., AND R. SCHMITT, *Science*, Vol. 170, 1970, p. 969.
38. ITO, K., AND G. KENNEDY, *The Structure and Physical Properties of the Earth's Crust*. J. Heacock, ed., Am. Geophys. U., Geophys. Mono. Vol. 14, 1971, p. 303.
39. GREEN, T., *Phys. Earth Planet. Interiors*, Vol. 3, 1970, p. 441.
40. BOETTCHER, A., *The Structure and Physical Properties of the Earth's Crust*, J. Heacock, ed., Am. Geophys. U. Geophys. Mono. Vol. 14, 1971, p. 261.
41. SONETT, G., G. SHUBERT, B. SMITH, K. SCHWARTZ, AND D. COLBURN, *Proc. Apollo 12 Lunar Science Conf.* The MIT Press, 1971.
42. TURNER, F. J., AND J. VERHOOGEN, *Igneous and Metamorphic Petrology*. McGraw-Hill Book Co., 1951.

43. WOOD, J., J. DICKEY, U. MARVIN, AND B. POWELL, *Proc. Apollo 11 Lunar Sci. Conference*, Vol. 1, 1970, p. 965.
44. SMITH, J., A. ANDERSON, R. NEWTON, E. OLSEN, AND P. WYLLIE, *J. Geol.*, Vol. 78, 1970, p. 381.
45. KUSHIRO, I., *Yearbook 63*. Carnegie Institution of Washington, 1964, p. 84.
46. PRINCE, A., *Am. Ceramic Soc. J.*, Vol. 37, 1954, p. 402.
47. HUBBARD, N., C. MEYER, AND P. GAST, *Earth Planet. Sci. Letters*, Vol. 10, 1971, p. 341.
48. ANDERSON, DON L., AND R. KOVACH, *Phys. Earth Planet. Interiors*. In press.
49. RINGWOOD, A., *J. Geophys. Res.*, Vol. 75, 1970, p. 6453.
50. ÖPIK, E., *Astron. J.*, Vol. 66, 1961, p. 60.
51. MIZUTANI, H., *Moon*. In press.
52. BLANDER, M., AND J. KATZ, *Geochimica et Cosmochimica Acta*, Vol. 31, 1967, p. 1025.
53. O'HARA, M., G. BIGGAR, AND S. RICHARDSON, *Science*, Vol. 167, 1970, p. 605.
54. HAYS, J., *Yearbook 65*. Carnegie Institution of Washington, 1966, p. 234.
55. CAMERON, A. G. W., To be published, 1972.
56. GANAPATHY, R., R. KEAYS, J. C. LAUL, AND E. ANDERS, *Geochimica et Cosmochimica Acta*, Supplement 1, 1970, p. 1117.
57. HOYLE, F., AND N. WICKRAMASINGHE, *Nature*, Vol. 217, 1968, p. 415.
58. WASSON, J., *Earth Planet. Sci. Letters*, Vol. 11, 1971, p. 219.
59. LAUL, J., J. MORGAN, R. GANAPATHY, AND E. ANDERS, *Proc. Second Lunar Science Conf.*, Vol. 2, 1971, p. 1159.
60. HUBBARD, N., P. GAST, C. MEYER, L. NYQUIST, C. SHIH, AND H. WIESMANN, *Earth Planet. Sci. Letters*, Vol. 13, 1971, p. 71.
61. GAST, P. W., *The Moon*, 1972, pp. 5, 121.
62. HANKS, T. C., AND D. L. ANDERSON, *Phys. Earth Planet. Interiors*, Vol. 5, 1972, p. 409.
63. ANDERSON, D. L., AND T. C. HANKS, *Science*, Vol. 178, 1972, p. 1245.
64. ANDERSON, D. L., *Nature*, Vol. 239, 1972, p. 263.
65. ANDERSON, D. L., AND R. L. KOVACH, *Phys. Earth Planet. Interiors*, Vol. 6, 1972, p. 116.
66. ANDERSON, D. L., *Earth and Planet. Sci. Letters*, Vol. 18, 1973, p. 301.
67. ANDERSON, D. L., *The Moon*, Vol. 8, 1973, p. 33.

Page intentionally left blank

Page intentionally left blank

section 7

New Data on the Planets

Page intentionally left blank

Page intentionally left blank

The Interior Structure of Jupiter (Consequences of Pioneer 10 Data)¹

R. Smoluchowski
Princeton University
Princeton, N. J.

Models of the Jovian interiors are based on theoretical equations of state of hydrogen and helium supported by a few experimental points and on observed parameters such as oblateness, gravitational coefficients, heat emission, magnetic fields, etc. The models fall into three categories: (1) those that assume a uniform and rather low H_2/He ratio throughout the planet; (2) those in which this ratio is solar and thus higher; and (3) those that take into account the lack of complete miscibility of the two elements in the condensed state. Recent values of the observed parameters obtained by Pioneer 10 permit improvements of the first two models but also pose new questions. In the first category of models the new data indicate that the amount of hydrogen has to be increased, while in the "solar" models, which have a heavy core (made of SiO_2 , MgO , Fe , and Ni), the abundance of hydrogen has to be decreased. Both changes point in the direction of incomplete miscibility present in the third category of models. It appears now also that within the limits of error the planet is in a hydrostatic equilibrium. The large heat emission and the need for an efficient source of internal heat is confirmed, but the results do not indicate which one of the various possible mechanisms is favored, although new evolutionary models suggest that the primordial heat may be insufficient. A new red spot has been discovered. Finally, the presence of a highly eccentric and inclined magnetic field poses new problems related to the pattern of internal convection and to the possibility of a north-south asymmetry of the interior. Further analysis of the available data may throw additional light on these questions.

The chemistry and physics of our whole planetary system can be approximated by those of Jupiter and Saturn with an error of only 8 percent. While the knowledge of the interior of Saturn is still rather uncertain, there are good reasons to suspect that it is similar to Jupiter which is much better known. The purpose of this paper is to summarize briefly the recent developments in our knowledge of the Jovian interior and to show how it is affected by the results obtained by Pioneer 10 (ref. 1). In this sense, this paper is a sequel to the Hubbard and Smoluchowski paper (ref. 2) containing theoretical background and various numerical data.

¹ Paper also published in *Icarus*, Vol. 25, 1975, pp. 1-11.

The Hydrogen-Helium System

The low density of Jupiter requires that it is composed primarily of hydrogen and helium. Thus, the knowledge of the equations of state of the two elements and of their mixtures at high temperatures and pressures is essential. Equations for the pure elements have been proposed (ref. 2) by De Marcus, Peebles, Hubbard, Neece et al., Salpeter et al., Trubitsyn, and, more recently, by Caron (ref. 3), Graboske et al. (ref. 4), Slattery and Hubbard (ref. 5), Zharkov and Trubitsyn (ref. 6), and Podolak and Cameron (ref. 7). It is interesting to note that in the pressure region where hydrogen is metallic the

calculations obtained by the Wigner-Seitz, Thomas-Fermi-Dirac, and dielectric function methods do not differ from each other by more than about 10 percent. The theoretical situation is less satisfactory in the H_2 region, although new experimental results of Swenson (ref. 8) have confirmed the older data of Stewart (ref. 2), and shock-wave compression results up to nearly 1 Mb of van Thiel et al. (ref. 9) permit further refinements. Grigoriev et al. (ref. 2) observed that the molecular to metallic transition occurs near 2.8 Mb, which falls in the range of theoretical predictions. An intriguing question is the nature of the molecular to metallic phase transition in the liquid: if it is a first-order transition, it may require the existence of a second critical point (ref. 2). The problem of the nature of the hydrogen-helium system is in a much less satisfactory condition than that of the pure elements. The additive volume approximation is reasonable in the range of solid solubility, but there are theoretical indications suggested by Smoluchowski's (ref. 2) physico-chemical arguments and by Hubbard and Slattery's (ref. 2) Monte Carlo results that the solubility is limited in the metallic hydrogen range. Streett's (ref. 10) experimental data extrapolated on the basis of Rigby et al.'s (ref. 11) theory show that this is true also of the H_2 range (ref. 2). Unfortunately, the solubility limits and their dependence on temperature and pressure are difficult to estimate; figure 1 summarizes in a qualitative manner the situation (ref. 12). (Recent unpublished theoretical results obtained by D. Stevenson confirm the existence of the solubility gap in the He-H system up to 10^4 K.)

Melting Temperatures

A particularly difficult problem is the question of the Debye temperature of the solid hydrogen-helium system and of the thermal and quantum stability. The errors in the melting and Debye temperatures, related to the problem of screening of protons by electrons (ref. 2) in metallic hydrogen, may

reach 1500 to 2000K. Furthermore, the effect of helium, which at sufficiently high pressures is supposed to be at least partially soluble in metallic hydrogen, will lower the latter's melting point to a degree difficult to ascertain (ref. 12). Similar uncertainty concerns the interactions between H_2 molecules (ref. 5). The recent trend toward Jovian models with very high central temperatures suggests that there may be no solid mantle at all. Nevertheless, the problem cannot be considered as being definitely settled at the present time. The central pressures of Jupiter are probably too low to imply the presence of a quantum liquid (ref. 2).

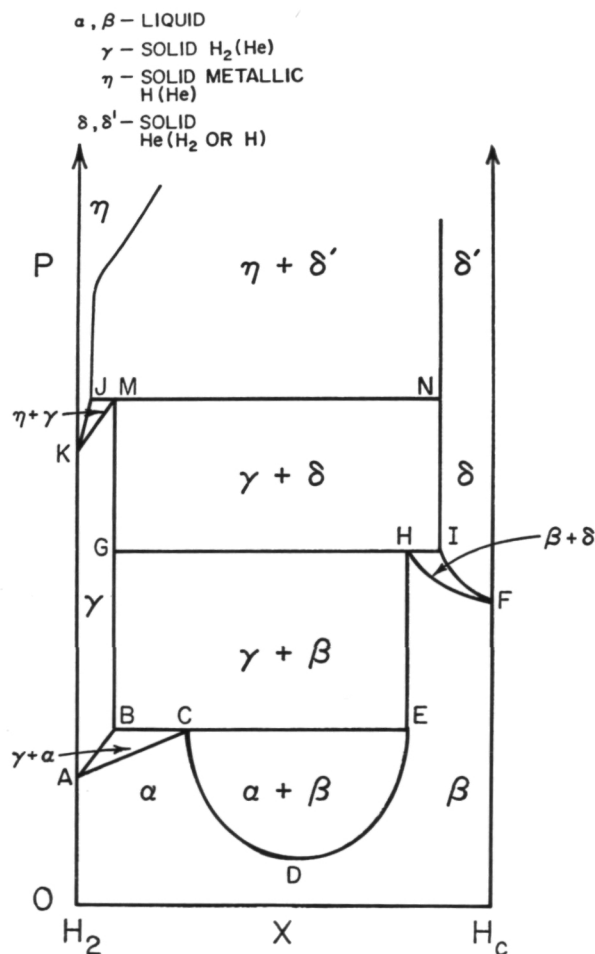


Figure 1.—Isothermal hydrogen-helium equilibrium diagram (ref. 12).

Table 1.—*Model of Jupiter*

Radius (10^4 km)	Fractional Mass	Pressure (M bars)	Density (g/cm^3)
6.9	.99	0.004	0.03
6.5	.97	0.24	0.4
6.0	.90	1.1	0.7
5.5 ⁽¹⁾	.80	2.5	1.1
5.0	.70	4.5	1.6
4.5	.60	7.6	1.9
4.0	.40	11	2.3
3.5	.30	15	2.6
3.0	.20	20	3.0
2.5	.10	24	3.4
2.0	.06	28	3.7
1.5	.03	32	3.9
1.0	.01	35	4.1
0.5	.001	36	4.2
0.0	0.0	37	4.2

NOTE: (1) H_2 metal phase change.

Models of the Interior

One can classify the models of the Jovian interior into three categories: (1) those of Peebles, Hubbard, and others (ref. 2) that assume a uniform hydrogen-helium ratio throughout the planet except perhaps for a small core; (2) those of Podolak and Cameron (ref. 7) that require that this ratio is close to the solar value of 3.4 to 3.6 by mass (or 13.6 to 14.4 by number); and (3) those that take into account the limited solubility of helium in hydrogen (ref. 12) in both forms. The first category leads to an agreement with the observed average density, gravitational coefficients, etc., if the hydrogen-to-helium ratio is about 1.6 by mass (or 6.5 by number). In this model the higher the temperature at the center of the planet, typically 10 000K and density over 4 g/cm^3 , the higher the abundance of helium has to be to give the correct planetary radius (table 1). Clearly, a problem arises concerning the mechanism of depletion of hydrogen from its initial abundance, which is presumably given by the composition of the original solar nebula. The capture of the solar wind by Jupiter would increase rather than lower the abun-

dance of hydrogen, while, according to Podolak and Cameron (ref. 7), the required gravitational escape time of hydrogen would be orders of magnitude longer than the age of the universe. One seems to be forced to assume that the planet is not homogenized convectively and that the hydrogen-to-helium ratio is a function of the radius. This will be discussed in greater detail below.

In the second category of models of the interior, the requirement of a solar hydrogen-to-helium ratio implies that there must be a dense central core to account for the total mass of the planet. This is reminiscent of the first Jovian model proposed by De Marcus (ref. 2). In particular, it is assumed that the core consists of "rock" that is SiO_2 , MgO , Fe , and Ni , which had to condense first out of the gradually cooling solar nebula. When the core was big enough and sufficiently cold, it became covered with a layer of ice that subsequently evaporated when the remaining gaseous constituents of the solar nebula were captured by the gravitational field of the growing planet. This led to a net enrichment of H_2O in the atmosphere above the solar value. The best fit to the gravitational coefficients and to a temperature of about

Table 2.—*Jupiter Model With 7.5 Enrichment of H_2O*

Radius (10^9 cm)	Temperature (K)	Pressure (Mb)	Density (g/cm ³)	Comments
0.05	19750	309	41.15	Core
0.20	19750	300	40.63	
0.50	19750	254	37.75	
1.00	19750	129	28.04	
1.29	19750	60.4	20.27	
1.29	19750	60.4	4.72	Metallic H
1.55	18810	48.4	4.24	
2.00	17485	36.3	3.66	
2.50	16256	27.1	3.17	
3.00	15133	20.2	2.74	
4.00	12933	10.3	2.00	
4.95	10663	4.27	1.36	
4.95	10663	4.27	1.21	Molecular H_2
5.51	8827	2.20	0.874	
6.01	7078	1.01	0.615	
6.50	5129	0.302	0.384	
7.00	1061	3.94×10^{-4}	0.010	
7.02	678	8.38×10^{-5}	3.6×10^{-3}	
7.04	192	1.01×10^{-6}	1.4×10^{-4}	

190K at 1 b pressure, as required by the usual model of the atmosphere (ref. 13), was obtained for an enrichment of water by a factor of 7.5 and a core that constitutes 12.5 percent of the total mass of the planet as shown in table 2. It is important to note that this model has a much higher central temperature and pressure and a twice as high ratio of the volumes of the molecular to the metallic hydrogen layers as in the first category of models. Pioneer 10 data indicate (ref. 1), however, that the value of the gravitational coefficient J_2 (obtained from the occultation of β -SCO) (ref. 2) on which these calculations were based is too low, and that the older higher value of Brouwer and Clemence is more correct. This leads to a dilemma, illustrated in figure 2, because the higher $J_2 = \frac{2}{3} J$ leads to a ratio of water to "rock" that exceeds the value of about 2 permitted by the solar composition (it also lowers the central temperature to about

16 000K). The way out is to assume that at least in the upper layers of the planet, which alone influence J_2 and other higher moments (ref. 16), the helium and water abundance is somewhat higher than solar. In particular, taking into account the lack of complete miscibility of helium and hydrogen may permit satisfaction of both the correct J_2 value and the permissible ratio of water to "rock."

The third category of models has not yet been evaluated quantitatively because of uncertainty about the actual limits of mutual solubility of hydrogen and helium as discussed above. An important feature of this model is the lack of a direct relation between the observable atmospheric hydrogen-helium ratio and the overall planetary composition. Figure 3 shows, in a qualitative manner, the expected sequence of layers in Jupiter in the absence of a "rock" core (ref. 12). If the central temperature were below

10 000K, there would be a solid mantle as indicated. In accord with Streett's (ref. 10) suggestion based on his experimental studies, the figure shows also that solid molecular hydrogen containing a small amount of dissolved helium can float at an appropriate level in liquid molecular hydrogen containing a higher than average amount of helium. This can be true even if the planet is so hot that there is no solid mantle, since the temperatures at that level will be sufficiently low. It appears, thus, that models based on a uniform composition and those based on solar composition encounter certain difficulties that may be resolved by taking into account the limited solubilities as suggested by the third category of models.

Atmospheric Structure and Composition

While the structure of the atmosphere of Jupiter is a huge topic by itself, it cannot be ignored here because, as is well known (ref. 17), it does have an important impact on the models of the interior. In particular, Anderson's interpretation of Pioneer 10 data (ref.

1) suggests that the gravitational coefficient J_4 is -0.00057 rather than the older value of -0.00067 (ref. 2). This throws new light on the nature of the outer envelope some 3000 km thick down to a pressure of about 800kb. According to Hubbard (private communication), the assumption of solar ratio and of the van Thiel (ref. 19) equation of the state of H_2 and its interaction potentials leads then to a very hot adiabatic atmosphere with a temperature of 250 to 300K at 1 b pressure. If helium is added, then the temperature is even higher, coming close to the values obtained by Kliore et al. from S-band occultation observation of Pioneer 10 (ref. 2). This is, however, in striking contrast with the spectroscopic data that seem to favor lower temperatures of the usual model mentioned earlier. It is important to note in this connection that a number of measurements (ref. 1) of the composition of the atmosphere made either by observing details of β -SCO occultation (Ververka et al.), by ultraviolet photometry (Judge and Carlson), from S-band absorption (Kliore et al.), or by airplane infrared data (Houck et al.) indicate that the hydrogen-to-helium ratio is 2.64 by mass (or 10.5 by number), with an

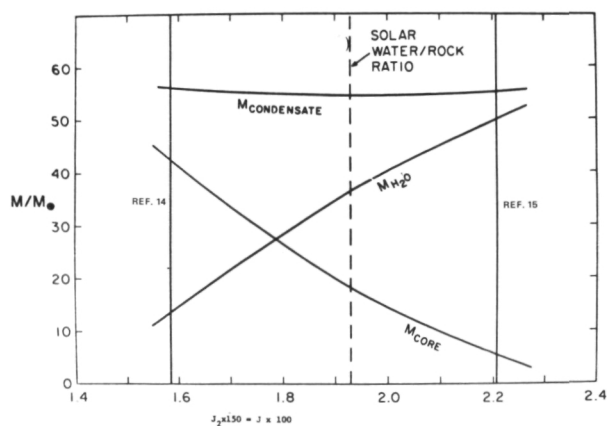
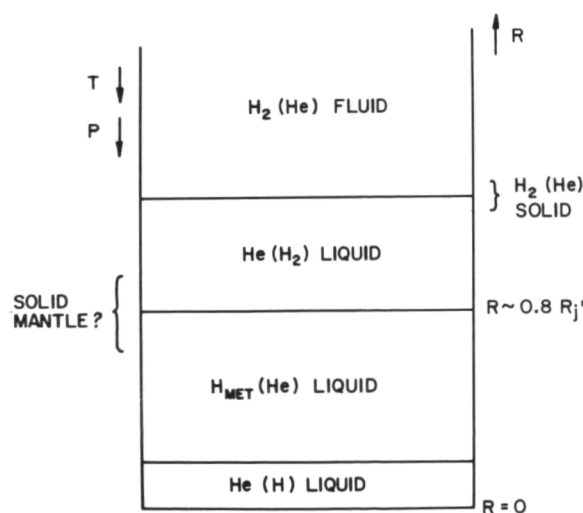


Figure 3.—Immiscible liquid layers on Jupiter (ref. 12).

Figure 2.—Mass of the Jovian rock core and of water as a function of $J = (3/2)J_2$ (ref. 7).



error of about 10 percent. This is lower than the solar abundance. If in the solar composition model of Podolak and Cameron the temperature at 1 b pressure were, say, 350K rather than 190K, then the dense core would be much smaller, and the enrichment in water still higher. This would make the water-to-"rock" ratio higher than permitted by the solar composition. Taking into account limited solubility of the two elements and an atmosphere independent of solar composition could bring this model into agreement with observations. As mentioned in the next section, the phase-change model of the gravitational contraction as the source of internal heat could imply an enrichment of helium in the atmosphere as observed.

It should be pointed out that while the Pioneer 10 values of the gravitational coefficients pose certain difficulties for some of the models of the Jovian interior they lead to a value of the dynamic oblateness that is within the limits of error equal to the oblateness observed directly by Pioneer 10. Thus the planet appears to be in hydrostatic equilibrium (Woiceshyn, ref. 1) in contrast to the earlier uncertainties (ref. 2).

Internal Heat Source

The fact that Jupiter (and probably also Saturn) emits much more heat than it receives from the Sun has been known for some time (ref. 2). Of the many proposed sources of this energy, three appear to lead to reasonable amounts: (1) gradual loss of primordial heat; (2) gradual increase of the radius of the metallic hydrogen layer at the expense of the molecular hydrogen layer (about 1 mm per year controlled by outward diffusion of helium), which would lead to the release of gravitational energy; and (3) self-controlled gravitational separation of the immiscible hydrogen-rich and helium-rich phases, as proposed first by Salpeter (ref. 18) for the metallic layer and extended to the H_2 layer by Smoluchowski (ref. 12). The self-regulation occurs because, as the planet slowly cools and the precipitation of the less buoyant helium-rich phase and the more

buoyant hydrogen-rich phase proceeds, the heating caused by the release of the gravitational energy slows down the rate of precipitation until a more or less steady state is reached. Nevertheless, the presence of an oscillatory variation of the heat flux is not excluded. Each of these sources easily yields enough heat during a period of several billions of years, provided that certain requirements are met: the first mechanism requires, naturally, a very high central temperature T_c as suggested by Trubitsyn (ref. 2), Hubbard (ref. 19), Podolak and Cameron (ref. 7) and others; the second and the third do not require a high T_c , but the limited solubilities in the hydrogen-helium system have to be taken into account. As discussed above, this assumption is not only theoretically plausible, but probably necessary in order to bring the models into agreement with the Pioneer 10 gravitational data. Preliminary conclusions obtained by G. Munch et al. from infrared measurements (ref. 1), and assuming an albedo of 0.45, suggest that the ratio of the emitted heat to that received from the Sun may be somewhat lower than 2.7 as proposed by Aumann et al. using their earlier observations (ref. 2). Lowering this ratio makes accounting for the excess energy easier than before and thus does not permit discrimination on this basis between the various mechanisms or models of the interior.

The Great Red Spot

An interpretation of the Great Red Spot (GRS) has to account not only for its existence, for its large azimuthal, negligible latitudinal, and small regular periodic motions, but also for variations in size and color (ref. 2). Kuiper looked at it as a purely atmospheric perturbation or storm analogous to those on Earth (ref. 2), but this model has not been evaluated in sufficient detail to account for the motions of the GRS. As pointed out by Golitsyn (ref. 20), a local perturbation in the Jovian atmosphere could exist for a very long time. Hide (ref. 2) suggested that the spot is the top of a Taylor column whose base is connected with the

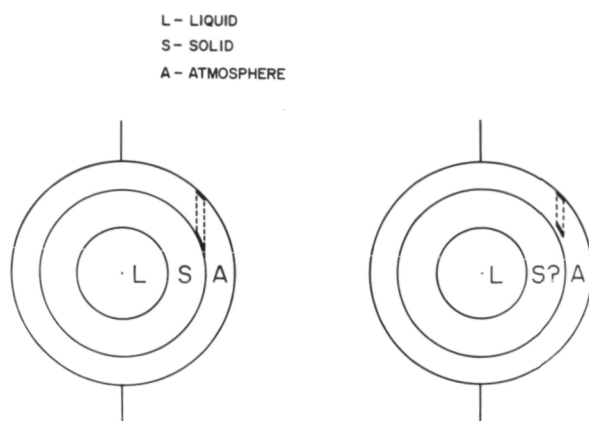


Figure 4.—The Great Red Spot as a top of a Taylor column based on solid mantle or on solid H_2 (He) floating in liquid $He(H_2)$ (ref. 2).

surface of a solid mantle; this has been further elaborated by Runcorn (ref. 2). Streett (ref. 10) pointed out that the column could be based on an island of solid H_2 floating in helium-rich liquid H_2 at the appropriate level of the supercritical atmosphere discussed above (fig. 4). This model is particularly attractive because in the absence of a solid mantle it accounts easily not only for the complicated large and small motions of the GRS but also for the periodic change of its size (ref. 2).

Pioneer 10 optical measurements as interpreted by Coffeen and by Dose (ref. 1) reveal a wealth of details within the GRS, anomalous polarization and contrast in scattering at large phase angles as compared with the surroundings. In particular, the presence of high clouds above the GRS is suggested. How closely these observations agree with the Taylor column or the tropical storm models remains to be shown. The most striking result is the confirmation of the existence of a Smaller Red Spot (SRS) between the north tropical zone and the north equatorial belt. This SRS is about one-third the size of the GRS, which is in the southern hemisphere, and it resembles it strongly in shape, color, and other features. Its azimuthal motion is slower than that of the GRS (Fountain, private communication), which further undermines the model of a Taylor column

based on a solid mantle. Its very presence suggests also that the GRS is not the result of an anomaly of a magnetic field of the planet as it has been variously suggested. It also casts further doubt on the frequently expressed point of view that the azimuthal motion of the GRS is coupled to the rotation of the magnetic field of the planet, the so-called System III of the decametric radiation (ref. 2).

Magnetic Field

The most likely source of the Jovian magnetic field is an internal convection-driven dynamo (ref. 2), although other mechanisms such as precessional motion or thermoelectric effects (ref. 21) cannot be ruled out. Either the high central temperature or the low melting point of hydrogen-helium alloys assures the presence of a liquid, highly conductive core (ref. 22). The most striking result deduced by E. J. Smith et al. (ref. 1) is that the field is about $4 R_J^{-3}$ Gs, which is much weaker than the initially deduced value based on decimetric radiation studies, and that it is not only inclined by as much as 15° to the rotational axis, but that the magnetic dipole is displaced by about $.2R_J$ away from the rotational axis and by about $0.1R_J$ northward from the equatorial plane as shown in figure 5. Thus, depending on latitude and longitude, the surface magnetic field varies from a 2.3 to 11.7 Gs. For comparison, the corresponding values for Earth are 12° , $0.07 R_e$, and $0.02 R_e$. The quantitative aspects of the theory of a hydromagnetic dynamo are not sufficiently developed to conclude whether the huge asymmetry of the Jovian field implies also an essential asymmetry of the liquid interior or of the mantle, if it exists. In this connection it should be mentioned that Anderson's preliminary results (ref. 1) obtained from an analysis of Pioneer 10 data suggest that the gravitational moment J_3 , which is a measure of north-south anomaly, is smaller than 10^{-4} . In any case, the magnetic poles of Jupiter do not seem to be associated with any particular surface

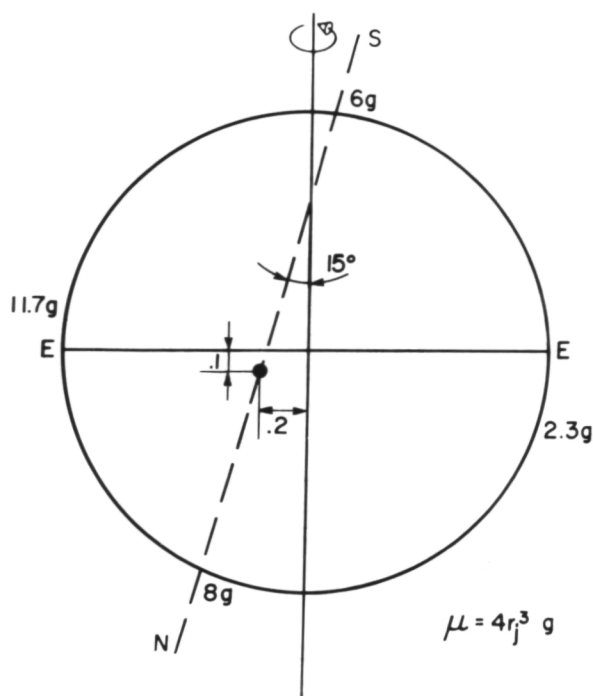


Figure 5.—Displacement and inclination of the Jovian magnetic dipole (the magnetic and the rotational axes are not actually co-planar) according to E. J. Smith *et al.* (ref. 1).

features, and the fact that the cloud zones and bands are perpendicular to the rotational axis and show essentially no strong azimuthal variation indicates that there is very little coupling between the magnetic field and the convective motions in the visible atmosphere.

It should be pointed out also that the Jovian magnetic field is reasonably dipolar up to about $10R_j$, but, as discussed by Wolfe and by Dessler *et al.* (ref. 1) and E. J. Smith, (*in press*), at larger distances it is elongated and concentrated along the equatorial plane. This effect appears to be due to centrifugal effects of corotation on the Jovian ionosphere which reaches, near the equatorial plane, temperatures corresponding to several keV. As a result of the inclination between the rotational and magnetic equatorial planes, the outer parts of the magnetic field are pulled toward the equatorial plane by about 5° (fig. 6). This situation complicates among others the quantitative interpretation of the intensity of the decimetric radiation and of the interaction of

the planetary field with the solar wind and its magnetic field.

Evolution of Jupiter

From the point of view of the cosmochemistry of the solar system and understanding of the present structure of Jupiter, a study of the history of the early evolution of that planet is of crucial importance. For this reason, Graboske *et al.* (ref. 23) made a study of the evolution of a star having an appropriate mass, i.e., 9.5×10^{-4} solar mass, and composed of a convective, adiabatic, and homogeneous fluid. Taking into account the sources of opacity and the deposition rate of solar energy, they discerned two phases: the first phase in which the fluid contraction is associated with a high luminosity and with central temperature reaching $4 \times 10^4 \text{K}$, and a second phase in which the cooling rate approaches that of a degenerate dwarf. The high luminosity phase has an important bearing upon the composition of the Jovian satellites. The model that gives best agreement with the present radius and luminosity of the planet has an age of 1.87×10^9 yr, which is much less than the expected age of 4.5×10^9 yr. At 4.5×10^9 yr the radius would be smaller by 2 percent and the luminosity 4.2 times smaller than the present value. It follows that if Jupiter is a homogeneous fluid it cannot be completely adiabatic as assumed in many models. The most likely explanation of the discrepancies is either that the fluid contraction stage is superadiabatic or that there is a slow post-fluid contraction stage. The latter would be related to the release of the latent heat of crystallization and of gravitational energy due to immiscibility and segregation as discussed by Smoluchowski (ref. 12) and Salpeter (ref. 18). These sources of energy could account for the present high luminosity of Jupiter and its present radius.

Recently Bodenheimer (ref. 1) has studied the very early stage of the gravitational collapse of a section of the primitive solar nebula having a density $1.5 \times 10^{-11} \text{g cm}^{-3}$, temperature 40K, radius $4.6 \times 10^3 R_j$, and assuming

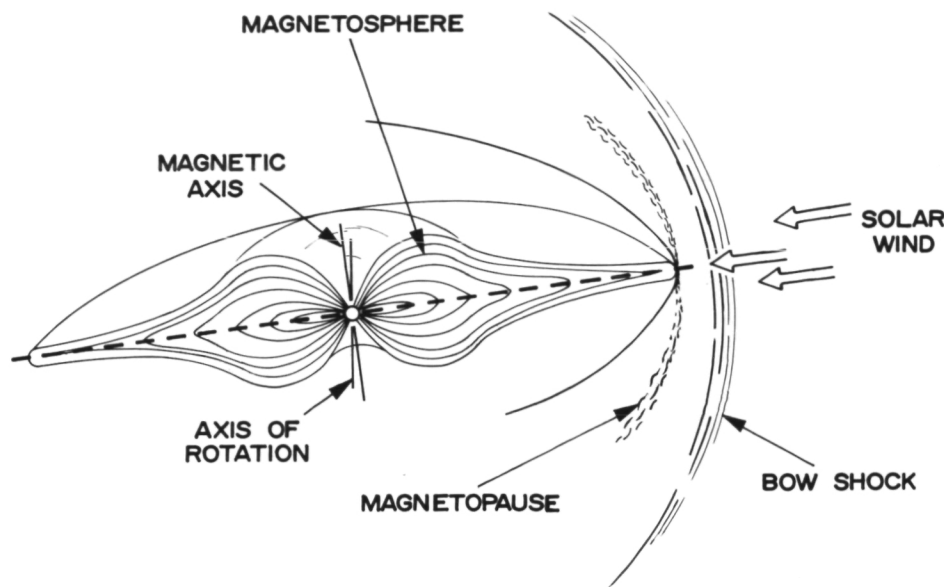


Figure 6.—Structure of the Jovian magnetic field according to Wolfe and to Dressler et al. (ref. 1).

65 percent of hydrogen by mass. After a decrease in size by about 10 percent, the object reaches hydrostatic equilibrium and contracts slowly for 7×10^4 yr. When the radius has decreased to 5 percent of its initial value, the central temperature reaches 2500K and the dissociation of H_2 begins with the resulting rapid hydrodynamic collapse. These results fit very nicely into the subsequent stage of evolution analyzed by Graboske et al., as described in the previous paragraph, and they are in reasonable agreement with the Hubbard and the Podolak and Cameron calculations (fig. 7).

Conclusions

Within the last year, important theoretical and observational progress has been made toward understanding the chemical and physical internal structure of Jupiter and its evolution. The results obtained by Pioneer 10 provide new parameters that require changes and improvements of the various models. For various reasons it seems that the assumption of a fully adiabatic and homogeneous interior is not tenable and that the

limited solubility in the hydrogen-helium system has to be taken into account. The planet appears to be in hydrostatic equilibrium, and there is no problem with accounting for the excess energy emitted by Jupiter nor for the presence of a magnetic field. The high eccentricity of the magnetic field is a notable new feature, as is its unusual external shape.

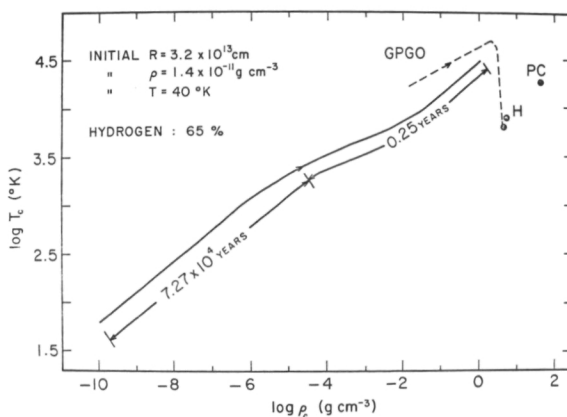


Figure 7.—Early evolution of Jupiter according to Bodenheimer (ref. 1). GPGO indicates the results of Graboske et al. (ref. 23), PC is the model of Podolak and Cameron (ref. 7), and H is that of Hubbard (ref. 2)

The nature of the Great Red Spot is perhaps now better understood, primarily because of the existence and behavior of the new Small Red Spot. There are still serious problems associated with the temperature profile and composition of the atmosphere.

Acknowledgment

The author wishes to express his appreciation to the quoted participants of the April meeting of the DPS-AAS and to Drs. Fountain, Grossman, Hubbard, Podolak, and Swenson for information concerning their most recent results.

References

1. Pioneer 10. *Science*, Vol. 183, 1974, pp. 301-324; and Abstracts of the April 1974 Meeting of the Div. of Planet. Science of the Am. Astr. Soc.
2. HUBBARD, W. B., AND R. SMOLUCHOWSKI, *Space Sci. Reviews*, Vol. 14, 1973, p. 599.
3. CARON, L. G., *Phys. Rev.*, to be published, 1974.
4. GRABOSKE, H. C., JR., R. J. OLNES, AND A. S. GROSSMAN, *Astrophys. J.*, in press, 1974.
5. SLATTERY, W. L., AND W. B. HUBBARD, *Astrophys. J.*, Vol. 181, 1973, p. 1031.
6. ZHARKOV, V. N., AND V. P. TRUBITSYN, *Icarus*, Vol. 21, 1974, p. 152.
7. PODOLAK, M., AND A. G. W. CAMERON, *Icarus*, in preparation, 1974.
8. SWENSON, C. A., AND M. S. ANDERSON, *Phys. Rev.*, in press, 1974.
9. VAN THIEL, M., M. ROSS, B. L. HORD, A. G. MITCHELL, W. H. GUST, M. J. D'ADDARIO, R. N. KELLER, AND K. BOUTWELL, *Phys. Rev. Letters*, Vol. 31, 1973, p. 982.
10. STREETT, W., *Astrophys. J.*, Vol. 186, 1973, p. 1107.
11. RIGBY, M., B. J. ALDER, D. M. SAPSE, AND C. E. HECHT, *J. Chem. Phys.*, Vol. 52, 1970, p. 3665.
12. SMOLUCHOWSKI, R., *Astrophys. J.*, Vol. 185, 1973, p. L95.
13. NEWBURN, R. L., JR., AND S. GULKIS, *Space Sci. Reviews*, Vol. 3, 1973, p. 179.
14. HUBBARD, W. E., AND T. C. VAN FLANDEREN, *Astron. J.*, Vol. 77, 1972, p. 65.
15. BROUWER, O., AND G. M. CLEMENCE, *Solar System*, G. Kuiper and B. Middlehurst, eds., Vol. 3, 1961.
16. HUBBARD, W. B., V. P. TRUBITSYN, AND V. N. ZHARKOV, *Icarus*, Vol. 21, 1974, p. 147.
17. GAUTIER, D., *IAU Symposium No. 65, Torun*. D. Reidel Publishing Co., Dordrecht, Holland, 1974.
18. SALPETER, E., *Astrophys. J.*, Vol. 181, 1973, p. L83.
19. HUBBARD, W. B., *Astrophys. J.*, Vol. 182, 1973, p. L35.
20. GOLITSYN, G. S., *Icarus*, Vol. 13, 1970, p. 1.
21. ELSASSER, W. M., *Phys. Rev.*, Vol. 55, 1939, p. 489.
22. HIDE, R., *Proc. Roy. Soc. London*, Vol. A336, 1974, p. 63.
23. GRABOSKE, H. C., JR., J. B. POLLACK, A. S. GROSSMAN, AND R. J. OLNES, *Astrophys. J.*, in press, 1974.

The Magnetic Field of Mars Estimated from the Data of Plasma Measurements by Soviet Artificial Satellites of Mars

K. I. Gringauz, V. V. Bezrukikh, T. K. Breus,
M. I. Verigin, and A. P. Remizov
*Moscow, U.S.S.R.
Institution for Space Research*

The dimensions of the obstacle forming the shock wave of Mars are estimated by use of electron trap data from Mars 2, 3, and 5. The mean altitude of the obstacle at the subsolar point can be convincingly explained if the obstacle is the magnetosphere of Mars. On the assumption that Mars has its own dipole magnetic field, the magnetic moment of Mars is estimated, $M^m \cong 2 \times 10^{22}$ gs x cm³.

The spacecraft Mars 2, Mars 3, and Mars 5 were injected into orbit around Mars on November 27 and December 2, 1971, and on February 12, 1974, respectively. The spacecraft used identical electron traps to measure the characteristics of the electron component of the solar wind plasma, while Mars 5 also used an ion trap to measure the ionic component (ref. 1). During each revolution of these satellites around Mars, a bow shock was recorded, the existence of which was first suggested after a single fly-by of Mars by the American Mariner 4 spacecraft (ref. 2).

Figures 1a and 1b show ion spectra and electron retardation curves, respectively, for the solar wind and the transition zone behind the front of the bow shock recorded by Mars 5. We can see that both ions and electrons behind the front of the bow shock are thermalized and their concentrations increase. The characteristic changes in the spectra also serve as the criterion for determining the front of the bow shock.

The position of the front of the bow shock depends on the dimensions and form of the obstacle which stops the solar wind. There-

fore, experimental determination of the position of the front of the bow shock near a planet allows us to estimate the dimensions of the obstacle and, consequently, to some extent to gain an idea of its nature.

Figure 2 shows sections of the orbits of the Mars 2, Mars 3, and Mars 5 spacecraft where they crossed the bow shock front. The characteristics of the plasma measured closest to the planet (fig. 2) are typical of the transition zone behind the bow shock (fig. 1b), while at the remotest points the measurements are characteristic of solar wind undisturbed by a planet (fig. 1a). The length of the orbital sections shown depends on the mode of operation of the instrument (2, 10, or 20 minutes) and the rate of movement of the satellite in orbit. Estimates of the dimensions of the obstacle were made by calculating the position of the front of the bow shock, on the assumption that the obstacle has the form of an extended body of rotation like that of the terrestrial magnetosphere (ref. 3). The solid line in figure 2 shows the shape and dimensions of the obstacle, and the dashed line shows the position of the front of the bow shock for Mach number $M_\infty = 8$

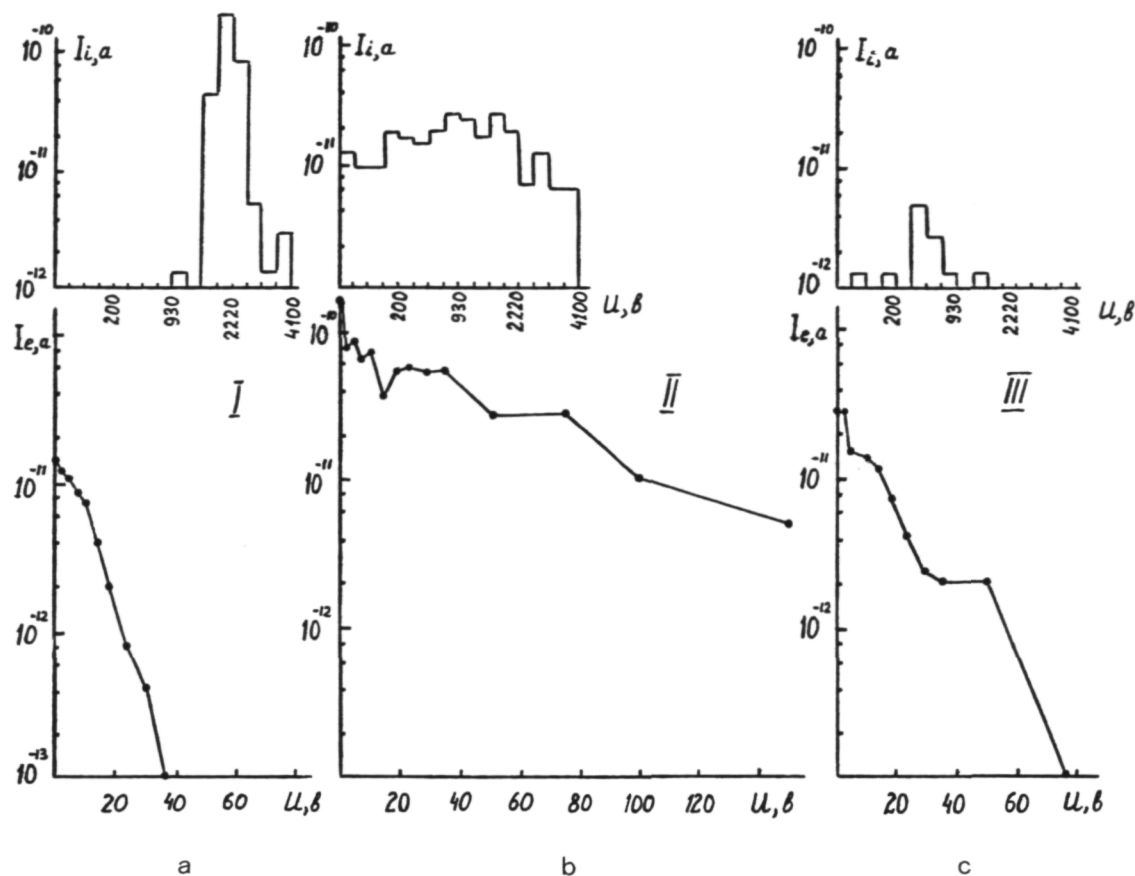


Figure 1.—Ion spectra and electron retardation curves are shown for Mars 5 data. Figure 1a is for the solar wind, 1b is for the transition zone, and 1c corresponds to entry of Mars 5 into the obstacle.

and $\gamma = 5/3$, calculated according to Spreiter and Alksne (ref. 3). The dimensions of the obstacle were selected such that the sum of squares of distances from both ends of the trajectory sectors shown in figure 2 to the front of the bow shock formed by the obstacle was minimal (ref. 4).

The areocentric distance to the subsolar point of the obstacle is $(4.6 \pm 0.8) \times 10^3$ km, and to the subsolar point of the shock wave $(5.7 \pm 1) \times 10^3$ km; or, respectively $(1.2 \pm 0.8) \times 10^3$ km and $(2.3 \pm 1) \times 10^3$ km from the surface of Mars. The relative dispersion in areocentric distances to the obstacle and shock wave front (about 17 percent) for Mars corresponds to the characteristic relative values of changes in geocentric distances to the subsolar point of the bow shock front and the magnetosphere of

the Earth (about 20 percent), for example, due to changes in the dynamic pressure of the solar wind (for example, see reference 5). The high relative dispersion of the height of the obstacle and front of the bow shock above the surface of Mars is related to the fact that on Mars the dimensions of the obstacle, expressed in planetary radii, are almost an order of magnitude less than on Earth.

With the use of Mars 2 and Mars 3 data, the minimum height of the obstacle was estimated from intersection of the bow shock front by the Mars 2 spacecraft on May 12, 1972 (see fig. 2) as about 600 km. From Mars 5 to the minimum estimate of height of the obstacle is apparently about 500 km, based on intersection of the front by the spacecraft in the February 20, 1974, session

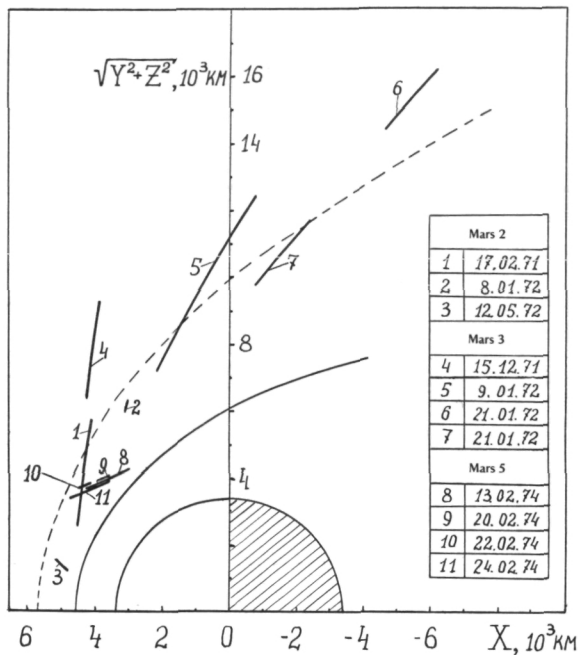


Figure 2.—Sections of the orbits of the Mars 2, 3, and Mars 5 spacecraft are shown where they crossed the bow shock front. The length of the orbital sections depends on the mode of operation of the instrument (2, 10, or 20 min.) and the rate of movement of the satellite in orbit. The solid line shows the shape and dimensions of the obstacle, and the dashed line shows the position of the front of the bow shock for Mach number $M_\infty = 8$ and $\gamma = 513$, calculated according to Spreiter and Alksne (ref. 3).

with 2-minute intervals between measurements. It should be noted that in the February 13, 1974, session, with 10-minute intervals between measurements, the estimate of the height of the obstacle based on the closest approach to the planet (fig. 2) yields lower values, while the estimate based on the farthest point in the trajectory sector yields higher values than in the February 20, 1974, session. However, since the dynamic pressure of the solar wind in this "10-minute" session (determined by the ion trap, with data produced before the bow shock front was intersected) was less than in the "2-minute" session of February 20, 1974, the front of the bow shock was apparently intersected on February 13, 1974, by the Mars 5 spacecraft no closer to the planet than on

February 20, 1974. One confirmation of the influence of changes in dynamic solar wind pressure on the position of the bow shock front is obtained by comparison of the measurement sessions of February 20 and 22, 1974. Between these sessions the solar wind pressure decreased and, correspondingly, the boundary of the obstacle rose to an altitude of about 900 km.

The size of the obstacle determined by our data, even with its minimum size of about 500 km, does not agree with the idea that solar wind is stopped by the ionosphere of Mars (ref. 6). As follows from radio occultation (refs. 7, 8, and 9) data on the altitude distribution of electron concentrations in the ionosphere of Mars, the maximum ionospheric ionization at Mars is at about 140-km altitude; and by about 300–350 km the pressure of the Martian ionosphere is some two orders of magnitude less than the dynamic pressure of the solar wind.

Weisberg and Bogdanov (ref. 10) consider that there is an "ion cushion" (on the day-side) and a "boundary layer" (on the night-side) between the ionosphere of Mars, bounded by the ionopause, and the transition zone behind the bow shock front; and that these layers form the obstacle creating the bow shock. This boundary layer, according to Weisberg and Bogdanov (ref. 10), is formed as a result of the viscous interaction of the incident flux (that is, obviously, the flux in the transition zone behind the front of the bow shock) with particles dissipating from the ionosphere of Mars. Obviously, the pressure of particles dissipating from the ionosphere is less than the pressure within the ionosphere or at the ionopause. Weisberg and Bogdanov do not present quantitative estimates explaining how the balance of pressures at the boundary of the obstacle is realized.

The results of observations, however, can explain if the obstacle is the magnetosphere of Mars. Assuming that the primary contribution to Mars' magnetic field is made by a dipole term, we can estimate the value of the magnetic moment of Mars using the following formula (ref. 3): $M_m = D^3$

$\sqrt{2\pi k\rho_\infty V_\infty}$, where $k = 0.88$, ρ_∞ and V_∞ are the density and velocity of the solar wind, and D is the areocentric distance to the sub-solar point of the magnetosphere. For $D = 4.6 \times 10^3$ km (dimensions of the obstacle estimated above), proton concentration $\rho_\infty \simeq 3 \text{ cm}^{-3}$ and $V_\infty \simeq 400 \text{ km/s}$, the value of the magnetic moment of Mars $M_m \sim 2 \times 10^{22}$ gauss cm^3 .

The magnetic measurements performed on the Mars 2 and Mars 3 satellites by Dolginov et al. (ref. 11) led the authors of these measurements to the conclusion that Mars might have its own magnetic field, and our estimates of the value of magnetic moment do not contradict the estimates of M_m made by Dolginov et al. (ref. 11) on the basis of the magnetic measurements.

One factor in favor of the existence of a Martian magnetosphere is the characteristic variations in the plasma and magnetic field as the spacecraft enter the obstacle. As the Mars 2 and Mars 3 spacecraft crossed the boundary of the obstacle, they observed an increase in the magnetic field modulus along with a drop in the electron flux. This behavior of the plasma and magnetic field is characteristic of the magnetosphere of Earth and non-characteristic of Venus which, apparently, has no magnetic field of its own (the plasma fluxes and magnetic field changed synchronously as Venera 4 approached the surface of Venus (ref. 12)).

Let us examine changes in the characteristics of the plasma as Mars 5 entered the obstacle. Figure 3 shows the trajectory sectors of Mars 5 near the planet in coordinates $X, \sqrt{Y^2 + Z^2}$ during two successive revolutions of the satellite around the planet (February 13 and 14, 1974). The roman numerals and various arbitrary symbols show the three characteristic zones intersected by the spacecraft, for which typical spectra are shown in figure 1. The first two zones correspond to the solar wind (fig. 1a) and the transition zone (fig. 1b). Zone III (fig. 1c) corresponds to entry of Mars 5 into the obstacle. For Zone III, a sharp drop in ion currents in comparison with Zones I and II and

a decrease in the fluxes of electrons and their temperatures in comparison with Zone II are characteristic. However, the electron currents and temperatures in Zone III are higher than in the unperturbed solar wind in Zone I.

Simultaneous magnetic measurements on Mars 5 (ref. 13) also showed the presence of three zones with mutually different characteristics, for which the boundaries of the zones according to our measurements and the magnetic measurements coincide. On the basis of magnetic data, there were no strong fluctuations of the magnetic field in Zone III, as characteristic of Zone II, and the predominate component of the magnetic field is directed along the Mars-Sun line.

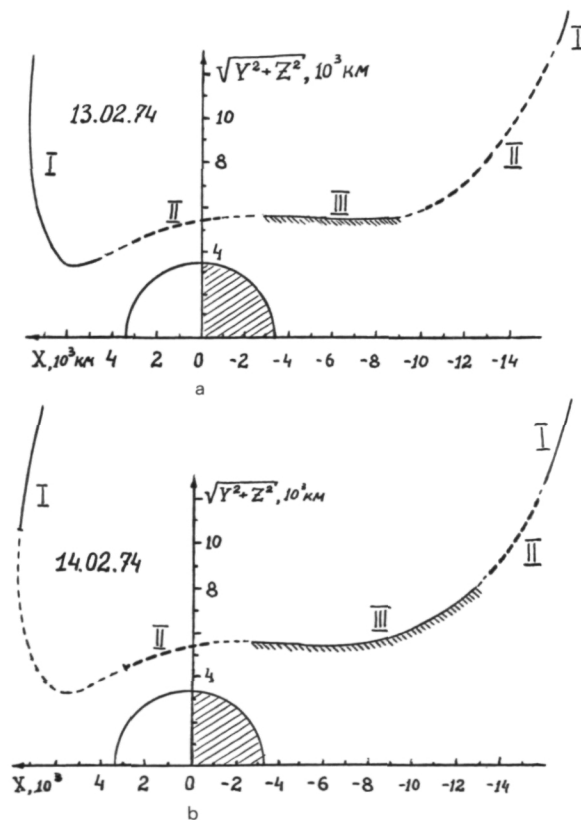


Figure 3.—The trajectory sectors of Mars 5 near the planet in coordinates $X, \sqrt{Y^2 + Z^2}$ for two successive revolutions of the satellite around the planet (13 and 14 February 1974). The roman numerals and various arbitrary symbols show the three characteristic zones intersected by the spacecraft, for which typical spectra are shown in figure 1.

Thus, variations in plasma and magnetic field recorded by Mars 5 also indicated that the obstacle at Mars is a magnetosphere, although Mars 5, due to its orbit, apparently recorded the tail of the Martian magnetosphere.

Plasma Zone III bounded by the transition zone behind the bow shock front, may be similar either to the boundary layer in the tail of the terrestrial magnetosphere (ref. 14) or its plasma layer. Comparison of the electron and ion spectra indicates that in this zone the ions are apparently highly isotropic. This allows us to consider Zone III to be more probably a plasma layer in the magnetosphere of Mars rather than its boundary layer. In the boundary layer, as we know from observations near Earth, the essential antisolar component of the directed velocity of the ions is retained. Of course, one should keep in mind the possibility that terrestrial analogues have, in general, little application to the physical phenomena observed on Mars in these experiments, due to essential difference in the relative role of internal and external sources in the Martian magnetic field.

References

1. GRINGAZ, K. I., AND V. V. BEZRUKIKH ET AL., *Kosmich. Issled.*, Vol. 12, 1974, p. 430.
2. DRYER, M., AND G. R. HECKMAN, *Solar Phys.*, Vol. 2, 1967, p. 112.
3. SPREITER, J. R., AND A. Y. ALKSNE, *Rev. of Geophys.*, Vol. 7, 1969, p. 11.
4. GRINGAUZ, K. I., AND V. V. BEZRUKIKH ET AL., *Kosmich. Issled.*, Vol. 12, No. 4., 1974. In press.
5. HESS, W. N., *The Radiation Belt and Magnetosphere*, 1972, p. 216.
6. SPREITER, J. R., AND A. W. RIZZI, *Planet. Sp. Sci.*, Vol. 20, 1972, p. 205.
7. KLIORÉ, A. J., AND D. L. CAIN ET AL., *Science*, Vol. 149, 1965, p. 1234.
8. KLIORÉ, A. J., AND G. FJELDBO ET AL., *Science* Vol. 175, 1972, p. 313.
9. KOLOSOV, M. A., AND N. A. SAVICH ET AL., *Radio-tekhn. i Electron.*, Vol. 18, 1973, p. 2009.
10. WEISBERG, O. L., AND A. V. BOGDANOV, *Kosmich. Issled.*, Vol. 12, 1974, p. 296.
11. DOLGINOV, SH. SH., YE. G. YEROSHENKO, AND L. N. ZHUZGOV, *DAN SSSR*, Vol. 207, 1972, p. 1296.
12. DOLGINOV, SH. SH., L. N. ZHUZGOV, AND YE. G. YEROSHENKO, *Kosmich. Issled.*, Vol. 6, 1968, p. 561.
13. DOLGINOV, SH. SH., YE. G. YEROSHENKO, L. N. ZHUZGOV, AND V. A. SHAROVA, *The Magnetic Field of Mars According to the Data of the Mars 5 Spacecraft*. This collection, paper 256.
14. ALASOFU, S. I., AND E. W. HONES, JR., ET AL., *J. Geophys. Res.*, Vol. 78, 1973, p. 7257.

Page intentionally left blank

Page intentionally left blank

Television Observations of Mercury by Mariner 10

Bruce C. Murray

*California Institute of Technology
Pasadena, California*

Michael J. S. Belton

*Kitt Peak National Observatory
Tucson, Arizona*

G. Edward Danielson

*Jet Propulsion Laboratory
Pasadena, California*

Merton E. Davies

*Rand Corporation
Santa Monica, California*

Donald E. Gault

*Ames Research Center
Moffett Field, California*

Bruce Hapke

*University of Pittsburgh
Pittsburgh, Pennsylvania*

Brian O'Leary

*Hampshire College
Amherst, Massachusetts*

Robert G. Strom

*University of Arizona
Tucson, Arizona*

Verner Suomi

*University of Wisconsin
Madison, Wisconsin*

Newell Trask

*U. S. Geological Survey
Reston, Virginia*

The morphology and optical properties of the surface of Mercury resemble those of the Moon in remarkable detail, recording a very similar sequence of events; chemical and mineralogical similarity of the outer layers is implied. Mercury is probably a differentiated planet with an iron-rich core. Differentiation is inferred to have occurred very early. No evidence of atmospheric modification of any landform is found. Large-scale scarps and ridges unlike lunar or Martian features may reflect a unique period of planetary compression near the end of heavy bombardment, perhaps related to contraction of the core.

Mariner 10 took over 2300 television pictures in the vicinity of Mercury in order to investigate the geologic history of the planet as manifested in the morphology and optical properties of the surface. A unique surface history was suggested by the planet's Earth-like density (5.5 g/cm^3) and small size (4870 km). Instead, an extraordinary similarity to the surface of the Moon has been found; the implications of this lunar-like exterior and probable Earth-like interior provide critical insight into processes of planetary formation at an earlier period of time than with any planet yet investigated.

We present experimental results and consequent interpretations from preliminary study of the pictures received in the March 1974 encounter, as well as quantitative analysis of about one-tenth the total. Table 1 summarizes the data set. High resolution photomosaics covering nearly all the lighted hemisphere of the planet were constructed from specially processed frames of the close encounter phase (fig. 1). In regions of favorable lighting and viewing geometry, the resolution is 1.5 to 2.0 km, comparable to good Earth-based photography of the Moon. There are about 200 additional individual

Table 1.—*Sequence Summary*

Phase	Range (km)	Resolution (km)	Frames
Incoming far encounter -6 days to -1 day	4 500 000-800 000	127-20	716
Incoming color mosaicking -1 day to -3 hours	800 000-100 000	20-4	212
Close-encounter -3 hours to +3 hours	100 000-10 000	4-0.15	548
Outgoing color mosaicking +3 hours to +1 day	100 000-800 000	4-20	220
Outgoing far encounter +1 day to +3 days	800 000-2 000 000	20-60	112
Satellite search +1 day to +3 days	1 000 000-3 500 000	—	555
		Total	2363

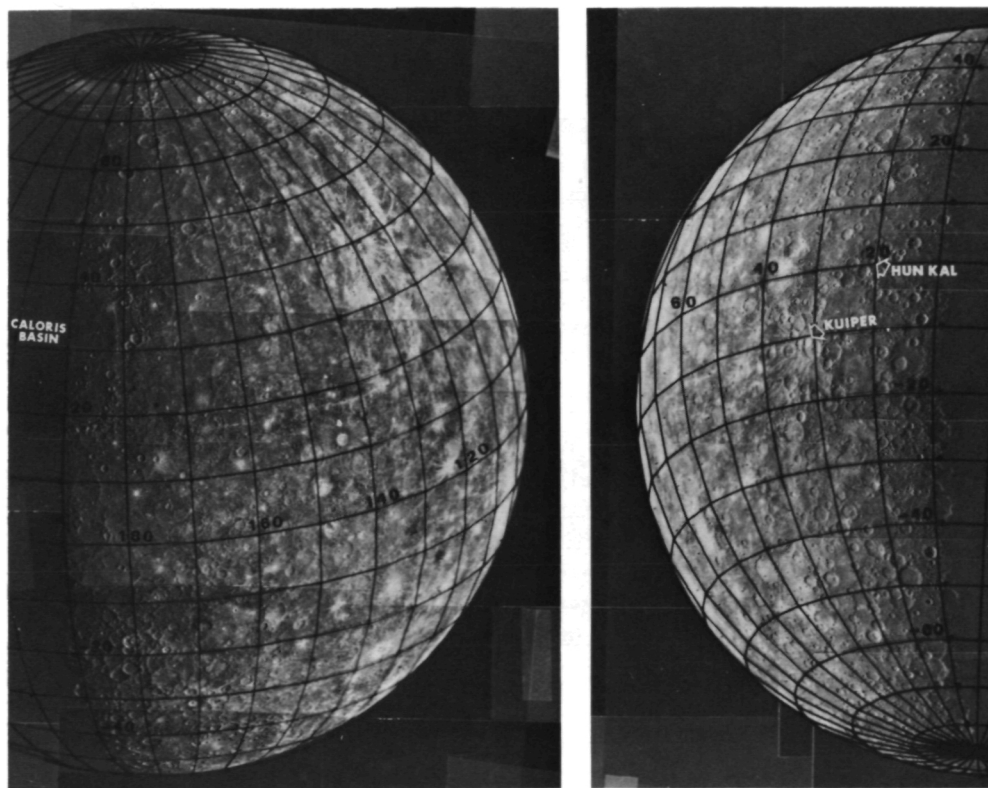


Figure 1.—Photomosaic of the incoming (right) and outgoing (left) view of Mercury with approximate coordinate system. The provisionally named features discussed in the text are indicated.

pictures of resolution ranging from 1.5 to 0.15 km. Figure 2 presents index maps showing the location and figure numbers of photographs discussed in this text.

Visual examination of the pictures from a satellite search phase of the imaging experiment reveals no Mercurian satellites, only stars (fig. 3). We place an upper limit of 5 km in the diameter of any hypothetical Mercurian satellite with an albedo similar to that of the planet. Spatial coverage is estimated to be at least 95-percent complete for equatorial satellites within 30 planetary radii. Further processing is expected to im-

prove the detection limit to about 2 km in diameter and to increase the completeness of spatial coverage.

The photographic coverage provided by Mariner 10 is so extensive that a Mercurian surface coordinate system and control net is necessary. Coordinates of features (control points) on Mercury are being computed photogrammetrically by methods similar to those developed for use with Mars (refs. 1, 2, and 3). As of May 1974, 635 measurements of 151 points on 45 pictures have been incorporated in the control system. A series of maps is planned as the cartographic base

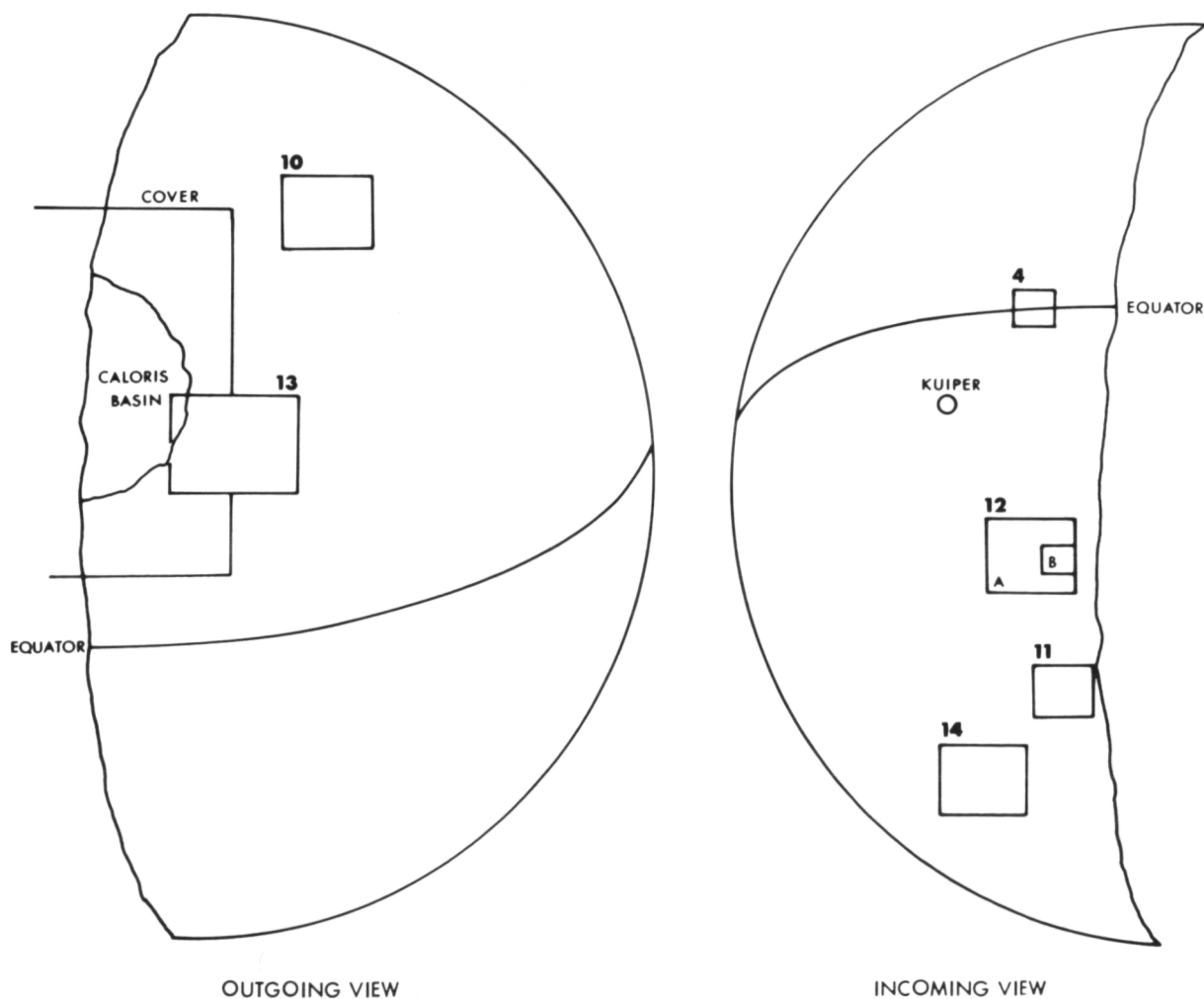


Figure 2.—Index maps showing the location and figure numbers of the photographs discussed in the text.

for future systematic geologic mapping.

In the Mariner 10 coordinate system the axis is assumed always to be normal to the orbital plane of Mercury (0° obliquity). The crater Hun Kal (fig. 4), about 1.5 km in diameter, has been chosen to define the system of longitudes; the 20° meridian passes through its center at latitude about 0.4° S. (fig. 3). Thus, the 20° meridian defines the longitude on Mercury in the same way that the 0° meridian (Greenwich) does on Earth.¹

Surface Optical Properties

Earth-based observations indicate that the integral optical properties of Mercury are closely similar to the global average of the Moon (refs. 4 through 10). The average microrelief and surface composition of the two objects, therefore, have been inferred to be similar. Mariner 10 provided an opportunity to determine whether this similarity extends to regional variations in optical properties such as the highland/maria dichotomy of the Moon. In addition to a comprehensive preflight photometric and geometric calibration, extensive photography of the Earth and Moon was carried out from Mariner 10 shortly after launch to permit direct comparison between Mercury and the Moon.

The relative brightness distribution in a selected image of Mercury, taken on the in-

coming leg of the trajectory, is virtually identical to similar plots of lunar data made from both Mariner 10 and earth-based observations at similar phase angle. Also, the ultraviolet plane polarization of Mercury in the phase angle range 80 to 100° is indistinguishable from that of the Moon down to a scale of about 50 km, at least. Evidently the Mercurian surface observed by Mariner 10 is everywhere covered with a fine-grained material analogous to the lunar regolith.

The normal albedos,² corrected to a wavelength of 0.55μ , were measured for 33 representative areas. Their locations are shown in figure 5, and the results of the measurements are summarized in table 2. Relative accuracy is estimated to be 10 to 15 percent; absolute errors may be somewhat larger. Crater Kuiper (number 1, fig. 4; also see figs. 1 and 2) is one of the brightest areas on the visible hemisphere of Mercury, with a normal albedo of 0.25. The interior of both the Caloris Basin and the smooth plains outside the basin rim have albedos of 0.12. Heavily cratered terrain has approximately the same average albedo as do the lunar highlands, and the smooth plains of Mercury are significantly darker. However, Mercury's appearance is more bland than that of the Moon. There is less contrast between adjacent units; albedo boundaries between light and dark regions are apparently less distinct on Mercury than on the Moon, as is illustrated in figure 6.

Regional scale color variations were investigated by forming ratios of pictures taken in the orange (OR) filter to those taken in the UV filter (see figure 7 for spectral responses of each filter). No pronounced regional color differences were apparent, the

¹In 1970, the International Astronomical Union (IAU) defined the origin of planetographic longitudes as the meridian containing the subsolar point at the first perihelion passage of 1950 (JD 2433292.63) and recommended the use of a rotational period of 58.6462 days. This definition is adequate for astronomical use; however, it does not tie the meridians directly to surface features, since intermediate steps of spacecraft trajectory, camera pointing angles, etc., must be known precisely. Thus, it was necessary to redefine the system of longitudes relative to a small, conspicuous crater (Hun Kal) so that the coordinate system is rigidly fixed to the surface features. A similar crater definition of longitudes was adopted for Mars in 1972, following the Mariner 9 mission. This Mariner 10 Mercury coordinate system can be related to the IAU system through the control net computations, which currently give a value of 359.92 for the longitude of the prime meridian of the IAU system.

²The normal albedo is defined as the ratio, at zero phase angle, of the brightness of an area to the brightness of a Lambert surface viewed from the normal. The minimum phase angle at which Mariner 10 observed Mercury was about 75° . The normal albedo of features on Mercury was estimated by interpolation using the lunar photometric phase function. The lunar observations made by Mariner 10 shortly after launch were used to confirm the prelaunch calibration. Normal albedos of several lunar regions were measured and compared with the Pohn-Wildey lunar albedo map (ref. 11) and with the measurements of Dollfus et al. (ref. 12), Bowell et al. (ref. 13), and Dollfus and Aueiere (ref. 5).

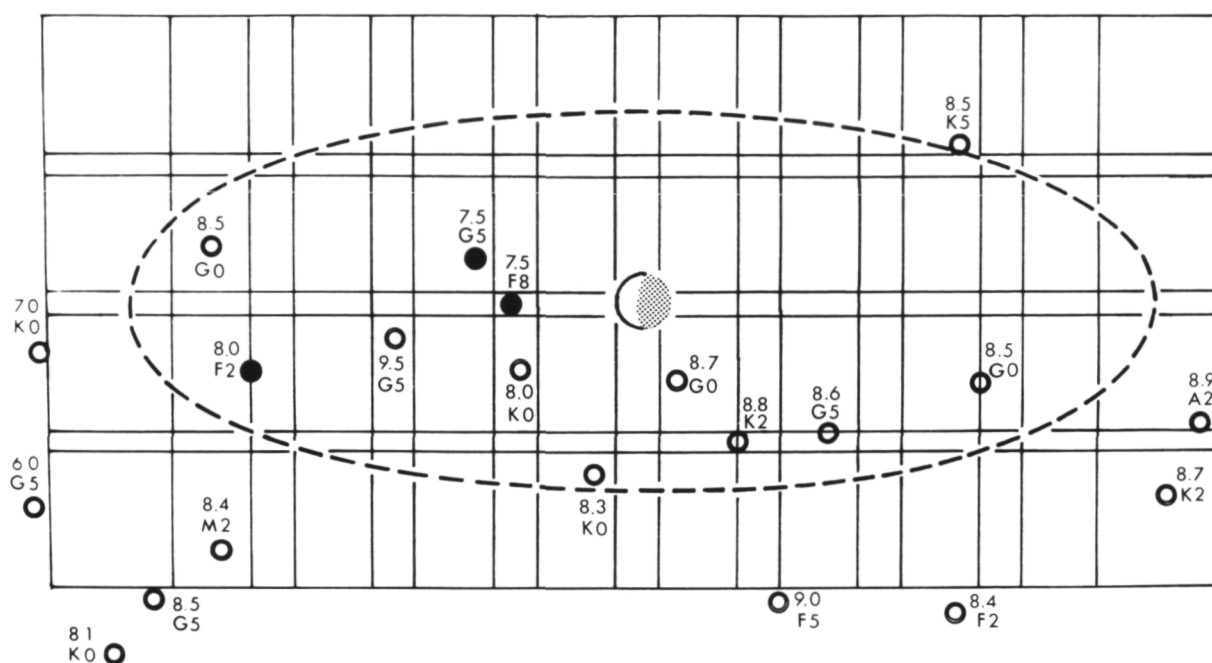


Figure 3.—A 36-picture satellite search sequence, taken 3.5 million km from Mercury, is shown with the background stars. The actual pointing for individual pictures is still slightly uncertain due to slight spacecraft angular motion. A satellite in a circular orbit at 30 Mercury radii would lie on the ellipse. The filled circles are three stars detected in preliminary processing of the TV pictures, while the open circles are undetected stars. The visual magnitude and spectral type of the star are indicated adjacent to each circle. The detectability of the stars sets an upper limit of about 5 km in diameter for a hypothetical satellite.

maximum dispersion in the OR/UV ratio being approximately ± 5 percent. In particular, no areas with nearly flat reflection spectra and high plane polarization which might indicate the presence of significant amounts of metallic Fe on the surface were noted. Like the Moon, brighter areas are generally redder than average, although many exceptions to this rule occur. For example, crater Kuiper (lat. -11° , long. 31°) is redder, but the bright crater near latitude 36° , longitude 127° , is bluer. The 440-km-diameter basin at latitude -15° , longitude 165° , has a light, reddish interior surrounded by a darker, bluish border. The interior plains of Caloris Basin are also redder than average. Such faint color differences very likely correspond to compositional differences in the surface materials on Mercury similar to those found on the Moon

within individual mare or associated with fresh craters. Thus, a surprising similarity to the Moon is exhibited in regional color variations as well as albedo variations. Mercury does indeed resemble the Moon on a regional basis as well as global. Regional differences in optical properties on the Moon generally reflect chemical and mineralogical variations within the overall iron silicate composition of surface material. Grossly similar variations are suggested for the surface of Mercury by the Mariner 10 picture data.

Craters and Circular Basins

Craters are the predominant landform on Mercury. The areal density differs from one part of the surface to another (fig. 8), simi-

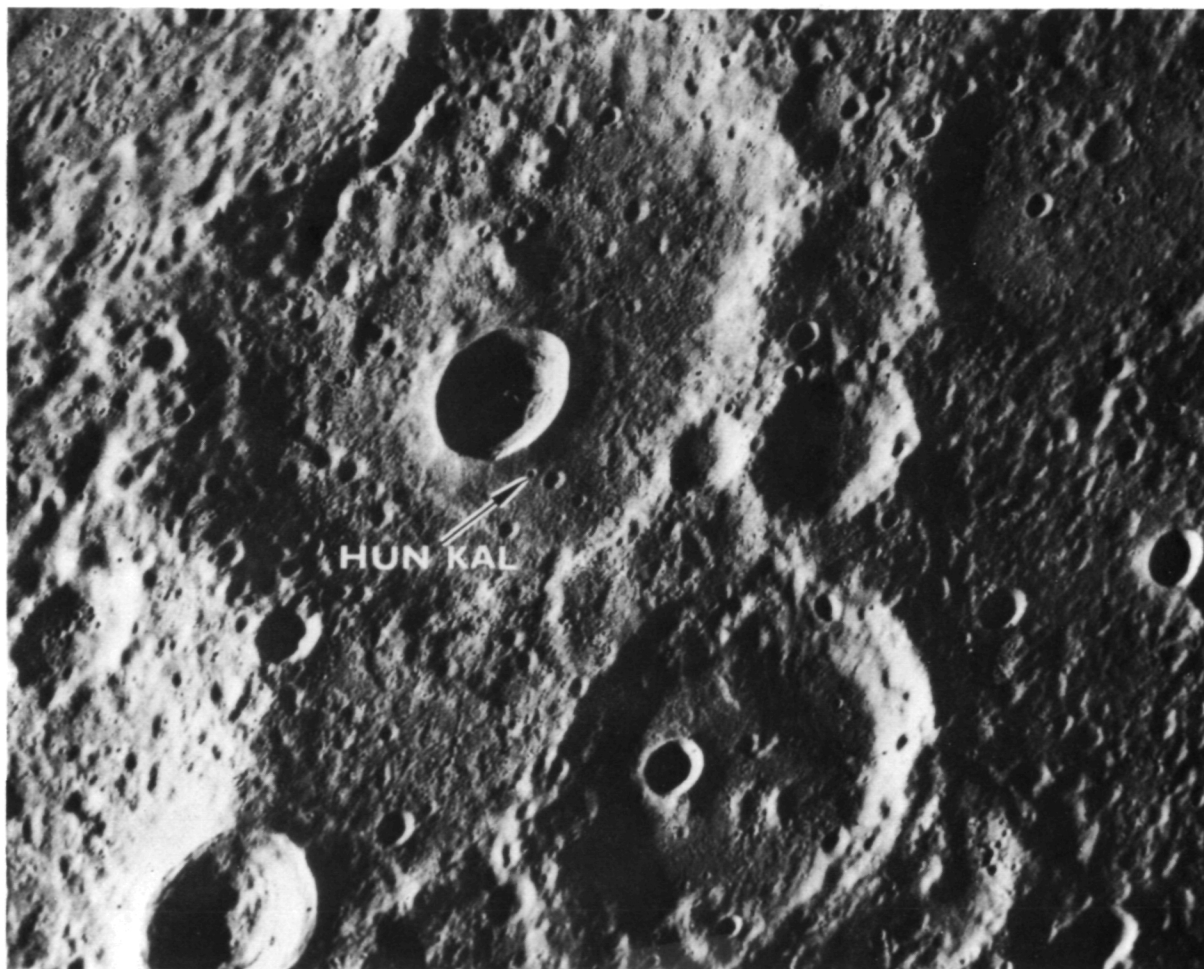


Figure 4.—The 20° meridian passes through the center of the small, 1-km crater, Hun Kal, in the Mariner 10 coordinate system. Hun Kal means the number 20 in the language of the Mayan Indians of Central America; the ancient Maya used a base 20 number system. Hun Kal lies less than a degree south of the equator and defines the Mariner 10 topocentric system of longitudes on Mercury. Numerous elongate craters of probable secondary impact origin are typical of many areas on the planet.

lar to the difference between the highlands and maria on the Moon. With increasing size, craters grade into basins—circular structures with an arbitrary lower limit, for purposes of this paper, 200 m in diameter. The craters are morphologically similar to lunar craters of the same size and evidence the same stages of degradation as their lunar counterparts. This indicates to us that similar formation and erosive processes have been active, especially meteoroid impact.

Craters smaller than ~ 10 km in diameter

grade from shallow, barely discernible depressions to bowl-shaped cavities exhibiting well-developed raised rims, ejecta deposits, secondary crater fields, and, around some craters, ray systems contrasting in albedo with the surrounding surface. Larger degraded craters, which have lost their ejecta deposits and secondary crater fields and have no prominent raised rims, are typically shallow, flat-floored, and sometimes filled with plains materials. Fresher and presumably younger features commonly exhibit essen-

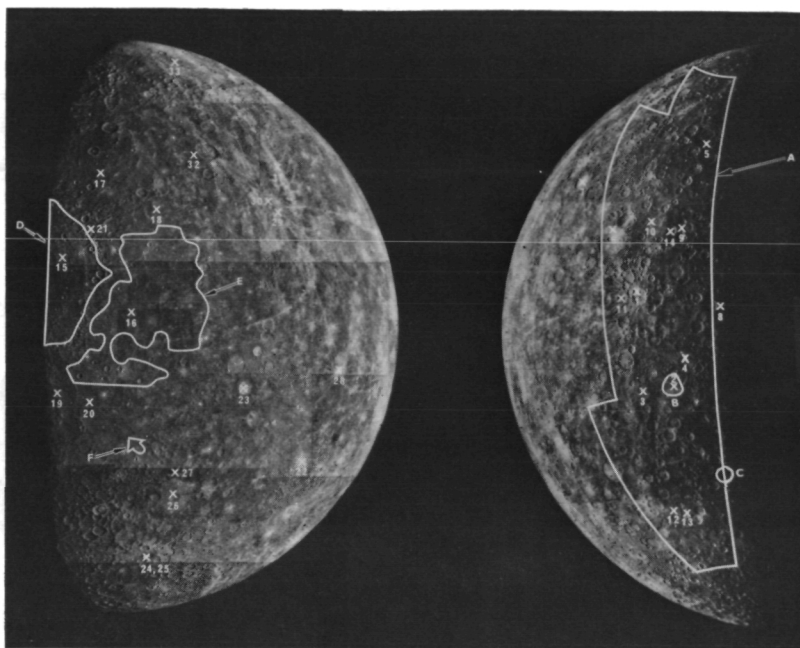


Figure 5.— The incoming (right) and outgoing (left) mosaics of Mercury depicting the points of albedo measurement referred to in table 2. The enclosed areas indicated by letters are those used in crater counting as listed in table 3 and shown in figure 9.

Table 2.—Normal Albedos

Lunar Features	Earth-Based	Mariner 10
Mare Crisium	0.085	0.10
Mare Serenitatis	0.09	0.10
Highlands Between Crisium and Serenitatis	0.16	0.17
Brightest Crater	0.23	
Integrated Disk	0.125	
Mercurian Features		
Bright Craters, Rays (1,6,7,11,14,22,23,28, 29,30,31)		0.19–0.25
Heavily Cratered Terrain and Textured Plains (4,9,10,12,13)		0.11–0.19
Flat-Floored Craters (3,2)		0.10–0.13
Smooth Plains (15,16,17,18,20,26, 27,33)		0.08–0.12
Integrated Disk	0.125	

tially flat floors and terracing on the interior walls; central peaks or ringed complexes are prevalent. The continuous ejecta deposits of the larger craters do not extend as far from the crater rim as for otherwise similar lunar craters. Similarly, the radial distance to the position of maximum areal density of secondary craters is closer to the rim of Mercurian craters, and preliminary depth-diameter measurements for 131 craters ranging from 3 to 200 km suggest that Mercurian craters are significantly shallower than similarly sized lunar craters. All three differences are consistent with Mercury's greater gravitational acceleration, which can reduce the ballistic range of ejecta.

Crater size-frequency distributions were obtained using the techniques and procedures described by Greeley and Gault (ref. 14) as a basis for determining the relative ages of major physiographic provinces and several selected surface units (table 3 and fig. 9). Areas in which the crater counts were made are indicated in figure 5. The heavily cratered terrain observed prior to encounter is

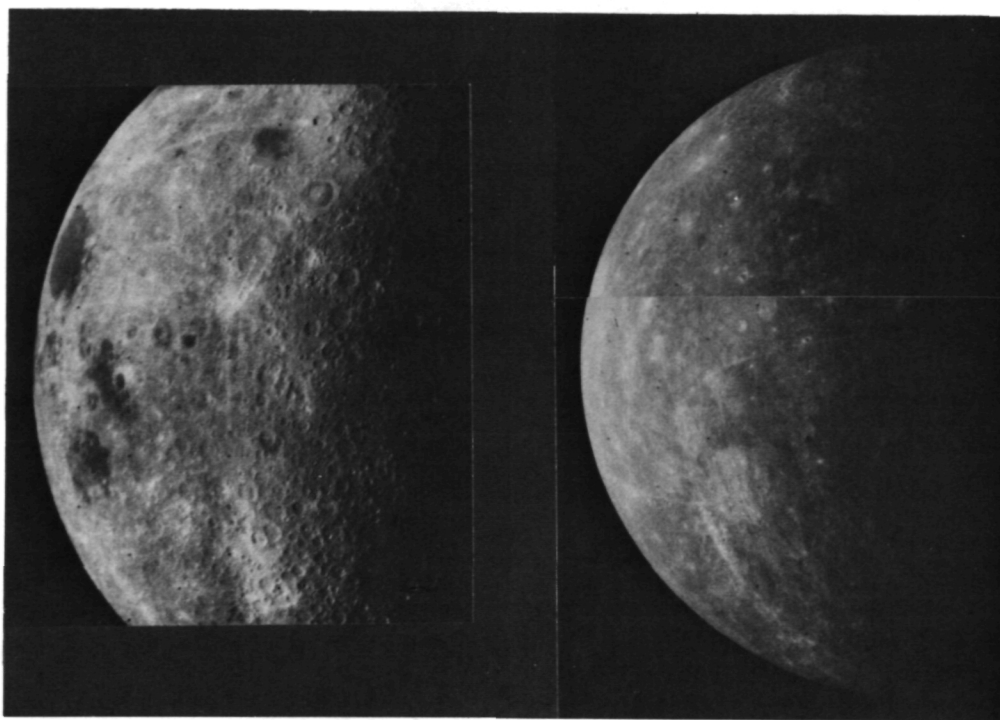


Figure 6.—Mariner 10 pictures of Mercury (left) and the Moon (right) processed to appear as they would with equal illumination. The relatively lower contrast of Mercury is apparent.

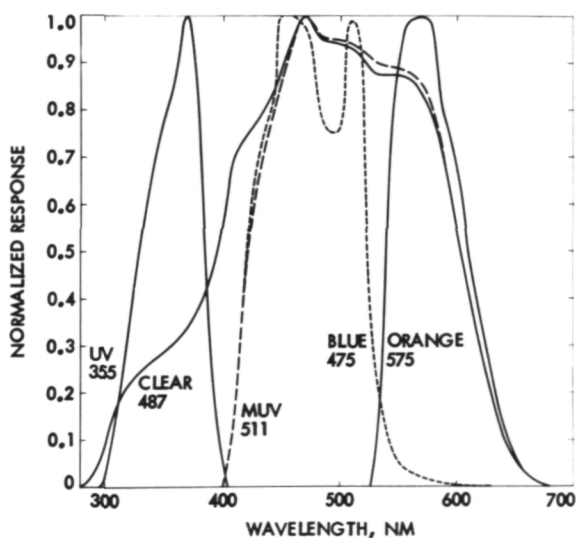


Figure 7.—The integrated optics, filter, and vidicon system response have been independently normalized for each spectral filter using the absolute Mercury spectrum and plotted as a function of wavelength. The effective wavelength in nanometers is shown by each filter name (UV = ultraviolet, MUV = minus ultraviolet).

not only grossly similar in general appearance to the lunar highlands but also has a crater frequency distribution (fig. 9) essentially identical to that of the southern highlands on the nearside of the Moon. Both surfaces have attained equilibrium or steady-state conditions (refs. 15 and 18), with craters as large as at least 100 km in diameter; landforms there have survived since the end of intense bombardment by small planetesimals.

Table 4 lists all basins larger than 200 km in diameter within the areas of favorable lighting outlined in figure 8. The basins show a variety of morphologies depending on their size, relative age, and degree of flooding by plains materials. The smaller basins tend to have two well-preserved rings, with the diameter of the outer ring close to twice that of the inner (fig. 10). Both rings are of relatively low relief. Radar measurements give a height of 1.5 km relative to the basin floor for the outer ring of basin 5 (ref. 19). In some basins, the inner ring is partially

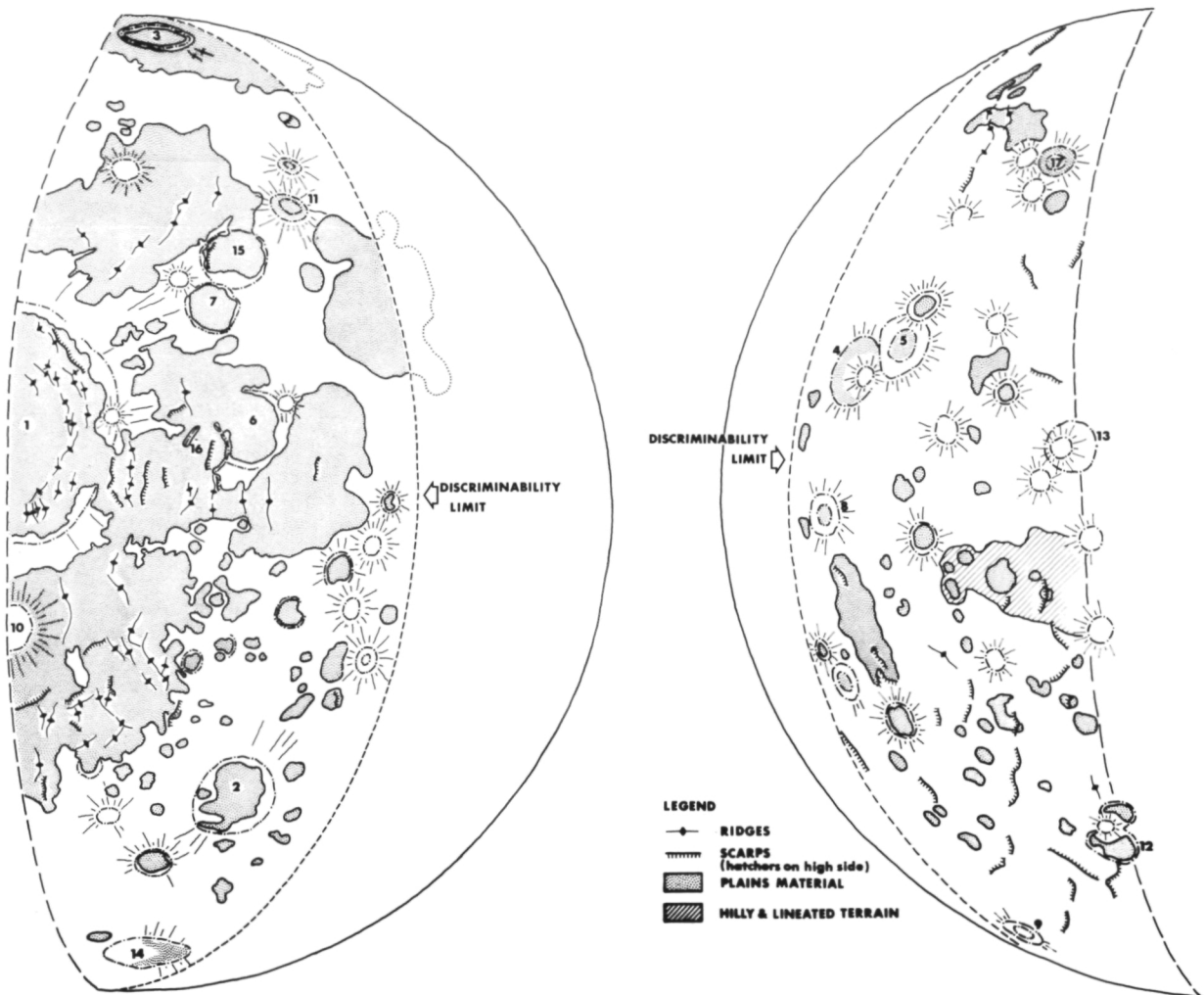


Figure 8.—Sketch map showing major physiographic provinces on Mercury within approximately 60° of the terminator on the two hemispheres viewed by Mariner 10 and shown in figures 1 and 5. The rim crests of basins, arbitrarily chosen as 200 km or larger, are shown by a dash-dot symbol and keyed by number to table 4. The more prominent craters larger than 100 km are also shown. Ejecta and secondary craters around craters and basins are indicated by radial lines.

covered with plains materials and the area between the two rings contains irregular hills. Exterior to the outer ring radial structures dominate, consisting of hills, valleys, gouges, and strings of craters. Secondary craters and gouges occur as close as 0.25-crater diameter to the outer ring and extend outward in a continuous field to 1-crater diameter in the freshest examples (fig. 10).

The Caloris Basin, the largest structural feature apparent in the Mariner 10 pictures, is similar in appearance and size to the lunar

Imbrium Basin, and undoubtedly originated by impact of a body at least tens of kilometers in diameter (fig. 11). The basin is bounded by a ring of mountains about 1300 km in diameter which forms an irregular scarp averaging around 2 km in height above the basin floor. Between about 23 and 30° N. latitude, the scarp is very subdued and appears to be mantled by plains material. In the northeastern part of the basin, a weak outer scarp occurs at a distance of about 150 km beyond the main scarp. Between

Table 3.—Crater Units

Surface Location (fig. 5)	Number of Craters Counted	Area (km ²)
1. Heavily Cratered (area A)	1538	4.28×10^6
2. Plains (area B)	107	2.33×10^4
3. Plains (area C)	56	1.14×10^4
4. Caloris Basin area D)	95 261	4.04×10^5 1.23×10^5
5. Plains East of Caloris Basin (area E)	416 2432	8.50×10^5 3.11×10^4
6. Plains (area F)	429	6.33×10^3

Table 4.—Circular Basins Observed in Mariner 10 Pictures (March 1974 Encounter)

Feature Number	Latitude	Longitude	Diameter
1. Caloris	+30	190	1300 km
2.	-15	165	440
3.	+85	30?	350
4.	-2	45	385
5.	0	37	330
6.	+31	159	410
7.	+43	158	240
8.	-18	52	220
9.	-77	100	200
10.	+10	190	220
11.	+52	133	200
12.	-64	20	250
13.	-16	13	240
14.	-45	178	430
15.	+48	150	310
16.	+27	163	240
17.	+21	19	230

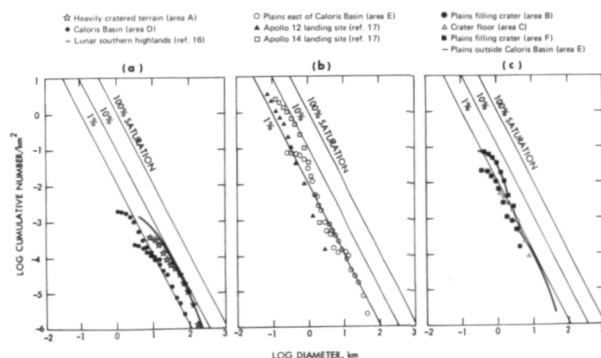


Figure 9.—Crater size-frequency distributions (for major physiographic provinces and selected areas shown in fig. 5) are expressed as the cumulative number of craters larger than a given diameter and compared with percentages of saturation as defined by Gault (ref. 15). Equilibrium conditions (i.e., rate of crater production equals rate of crater destruction) are attained for crater populations at 5- to 10 percent saturation.

these two scarps is a terrain characterized by relatively smooth hills or domes similar in appearance to the terrain basinward of the Rook Mountains in the lunar Orientale Basin. Surrounding the main scarp and extending outward for at least 1-basin diameter is a radial system of linear hills that is best developed northeast of the basin. The radial system is only weakly developed in the terrain between the two scarps; its main development begins beyond the outer scarp in this area. This radial system of hills is em-bayed by smooth plains material that com-

pletely surrounds at least the visible eastern portion of the basin.

Stuart-Alexander and Howard (ref. 20) counted 24 well-defined basins 300 km and larger on the Moon. In contrast, we have observed eight basins larger than 300 km over approximately one-third the surface of Mercury, suggesting about the same total of 24 for a body with a surface area twice that of the Moon. However, we observe no basins in the size range 500 to 1300 km; the total for the Moon in this size range is five (ref. 20). The relative deficiency of large basins

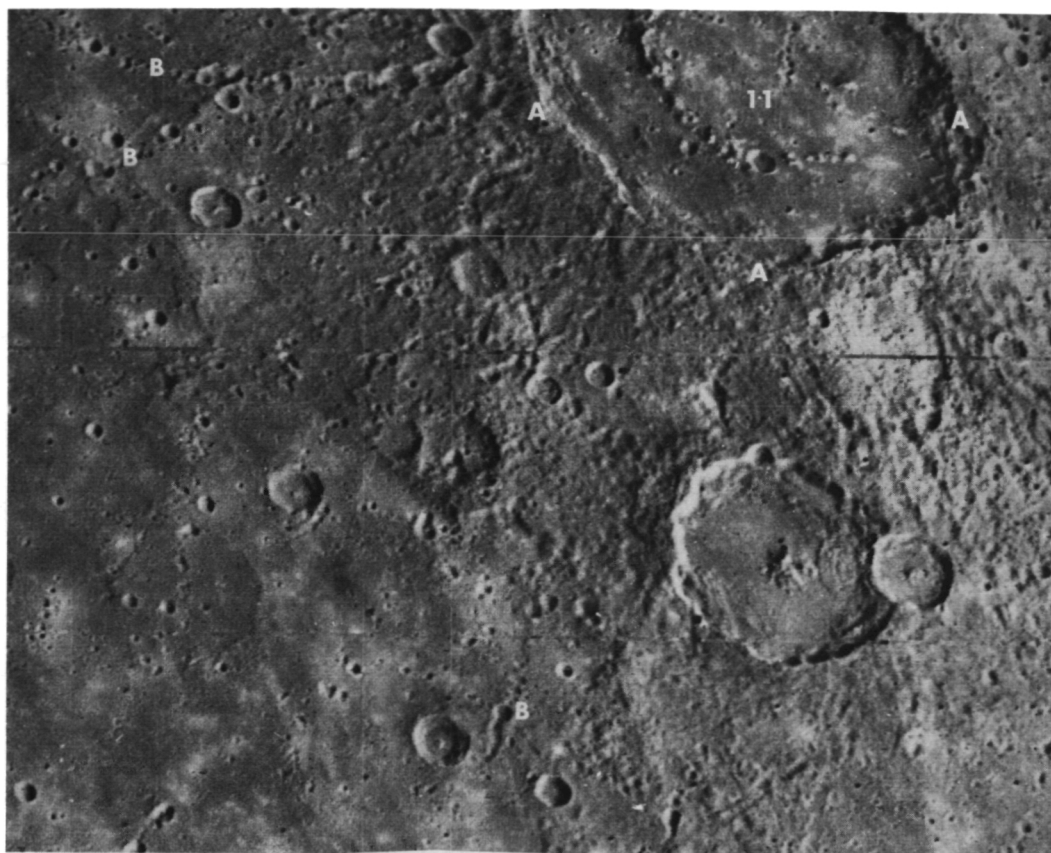


Figure 10.—Typical 200-km diameter, double-ring basin (number 11, table 4), showing a well-developed ejecta blanket (A) and a swarm of secondary craters (B). The basin is younger than the plains materials to the southwest because its secondary craters overlie the plains, in turn part of a concentric band around the Caloris Basin. This double-ringed basin is also flooded by plains material. North at top.

on the surface of Mercury so far viewed probably has affected the regional appearance of the planet when compared to the Moon. Ejecta blankets and secondary craters are observable around virtually all basins that are not flooded by plains materials exterior to the outer ring. Destruction of these features by subsequent basins larger than 500 km apparently has not occurred on the observed surface of Mercury to the same degree as on the Moon (ref. 21).

Plains

The floors of many basins and craters and the surfaces around several large basins are

level, except for scarps and ridges. These surfaces are relatively free of craters above 10 km in diameter and are referred to as plains; they are obviously younger than the surrounding heavily cratered terrain. The Mercurian plains seen in Mariner 10 pictures strongly resemble the lunar maria. It is important to establish whether a similar volcanic origin also can be inferred for at least some of the Mercurian plains. In the following we review the morphological evidence that bears on the origin of the plains.

The general distribution of plains materials seen by Mariner 10 is plotted in figure 8. Many craters in the diameter range 100 to 200 km are filled with plains materials, but others are not, including some that appear

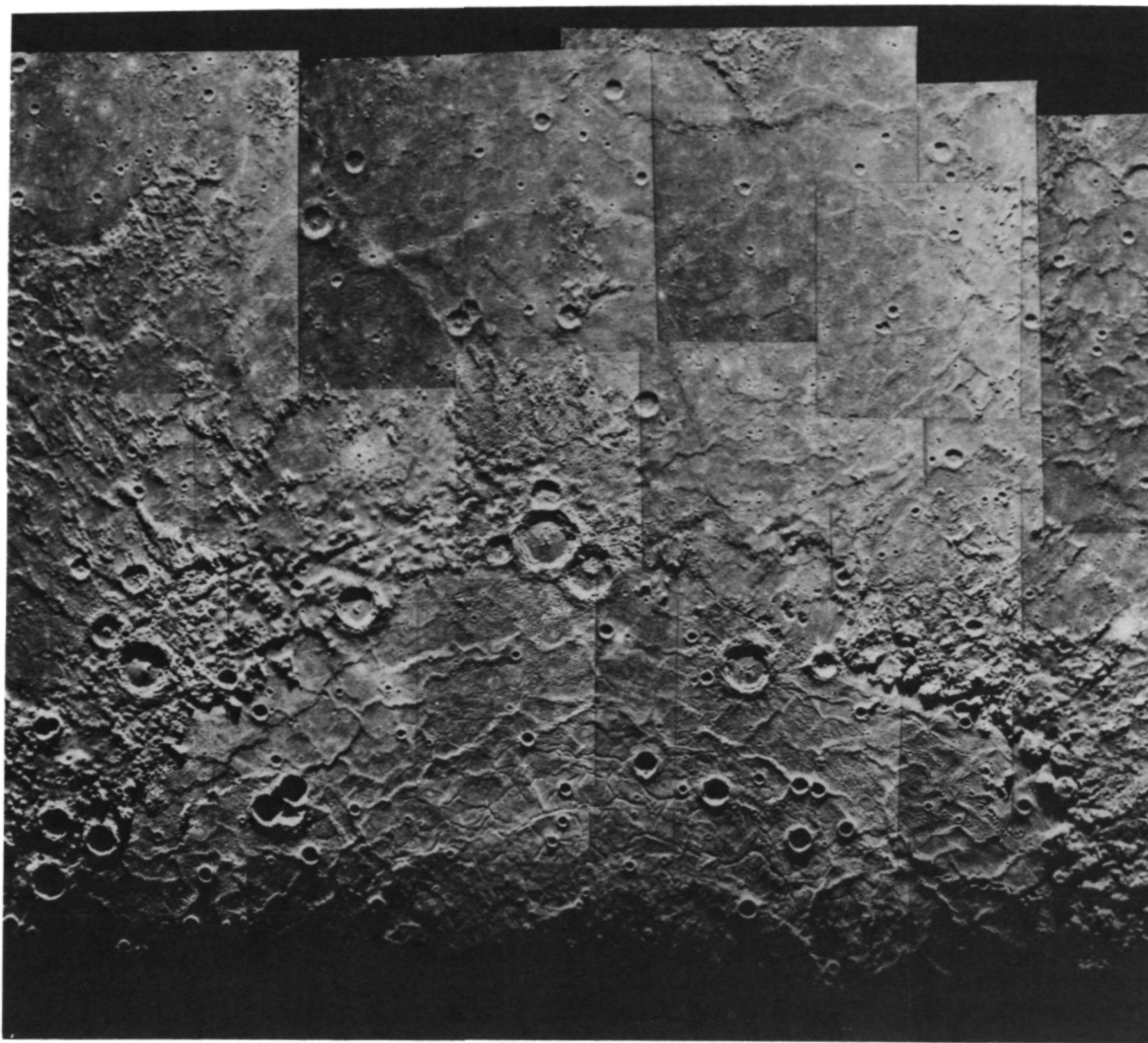


Figure 11.—The largest basin on Mercury seen by Mariner 10 and displayed in this specially processed photomosaic. It is centered at 190° W longitude and 30° N latitude (figure 1) and is provisionally named "Caloris" or "hot" basin for its position near one of the subsolar points when Mercury is at perihelion. The basin is bounded by a 1300-km-diameter ring of mountains up to 2 km in height, while the basin floor consists of intensely fractured and ridged plains.

to be as old as those that are filled. The plains materials on Mercury fill all of the basins on the planet, but to different degrees. Particularly important is the difference between the 350-km north polar basin (number 3, table 4), which is filled and surrounded by a broad belt of plains, and a basin of identical size at 45° S. (number 14, table 4), which contains only a restricted area of plains on its floor. These relations are more easily explained if the plains were formed in

episodes of volcanism following formation of most of the basins rather than as impact melts at the time of each cratering event.

Plains material containing the ridges and scarps surrounds the Caloris Basin in an arcuate band from 1000 to 1500 km wide (fig. 8). Radar studies (ref. 19) suggest that the band continues around at least the southwest rim of the basin some 1000 to 2000 km on the side not illuminated at the time of the Mariner 10 flyby. In places, hills of more

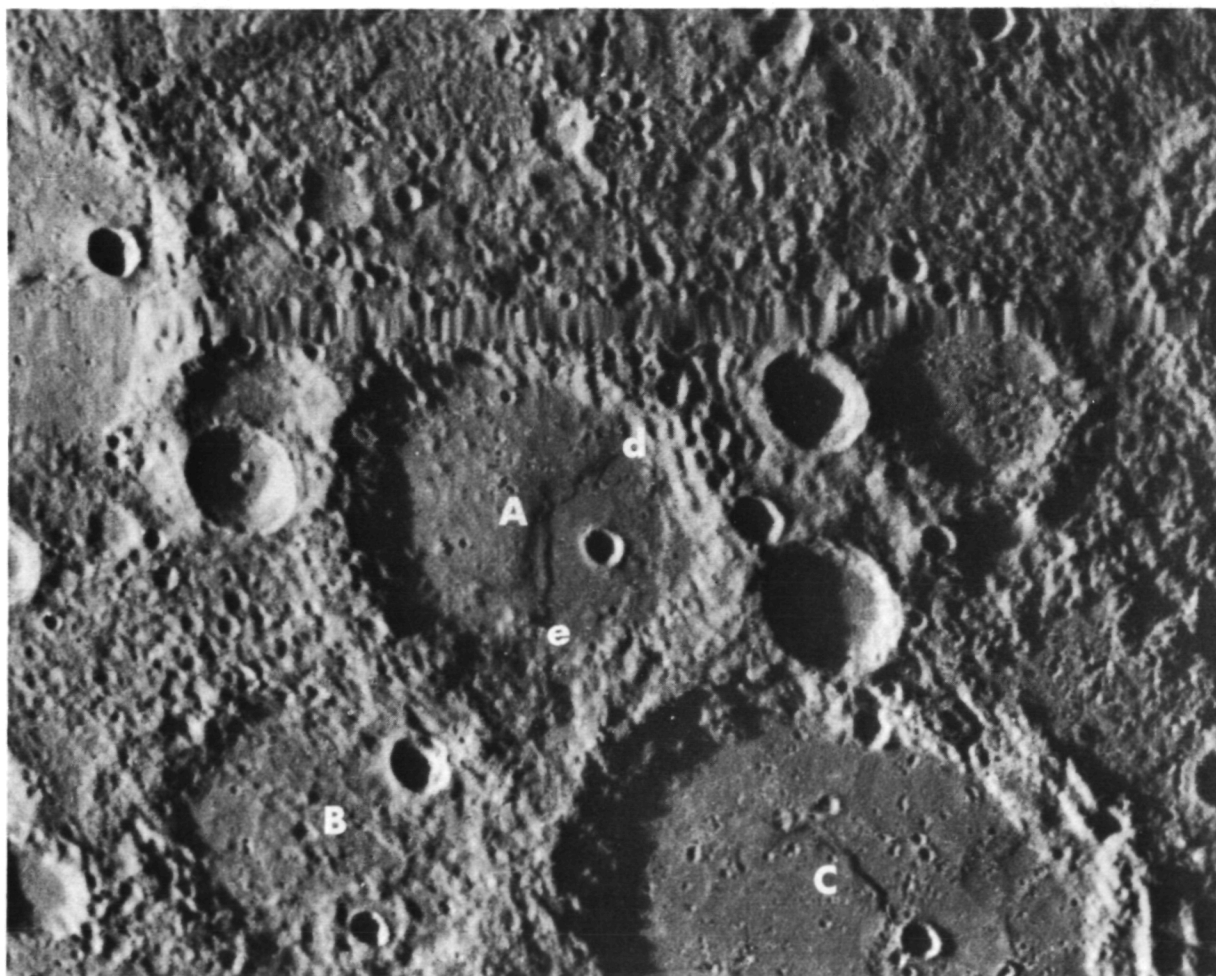


Figure 12.—Two patches of plains materials covering the floors of older craters (A and C) whose rims are much more heavily cratered. No external source for the plains materials is evident. Hypothetical impact melt from crater C should have filled both A and B, but only A is filled. A volcanic origin is indicated. The scarp (d,e) on the floor of crater A is about 400 meters high. Similar scarps have been recognized in numerous craters where they appear to be restricted to the crater floor. It is not yet clear whether they are of tectonic or volcanic origin. The blurred stripe about one-third the distance from the top of the picture is a processing defect. Crater A is 100 km across.

rugged material project through these plains suggesting that the material is relatively thin. The Caloris Basin itself is filled to within about 2 km of the highest peaks in the surrounding mountains.

The plains inside the Caloris Basin contain numerous ridges and are intensely fractured. The ridges range from 1.5 to 13 km in width, have heights of about 300 m and lengths in excess of 300 km, and are grossly similar to lunar mare ridges. The extent and complexity of ridges and associated fracturing on the plains inside the Caloris Basin are

greater than on lunar maria. Fractures are closely spaced, with some forming a polygonal pattern; others are almost sinuous, although unlike lunar sinuous rilles in detailed planimetric outline. They range in width from 6 km down to the resolution of the best photography of the basin floor (~ 700 meters). The widest fractures are flat-floored and graben-like. Fractures transect, are parallel to, and even occur along the tops of ridges. Directions of fractures tend to mimic the trend of the ridges, suggesting that the structures are related. The fracture pattern

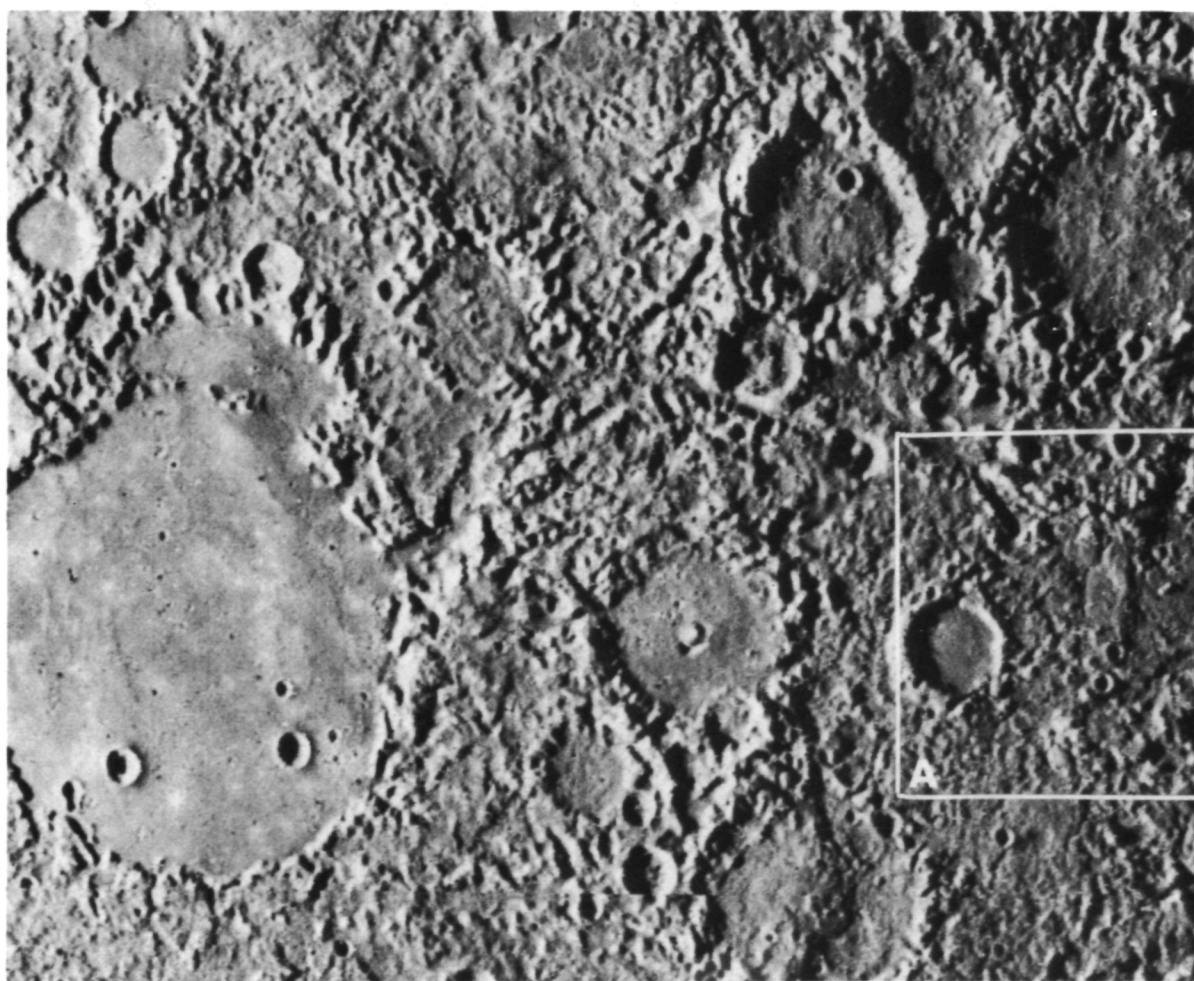


Figure 13a.—Hilly and lineated terrain whose distribution is shown in figure 8. The rims of flat-floored craters show varying degrees of structural disruption, suggesting that the terrain developed over a period of time. Plains materials on the crater floors are younger than the surrounding terrain; the plains in the largest crater (170 km in diameter) have a crater number density similar to that of the plains surrounding the Caloris Basin. Area A is shown in figure 12b.

seems consistent with gentle subsidence of the central part of the basin floor following emplacement of the plains.

A typical high resolution view of two areas of plains and their surroundings (fig. 12) shows that the rims of the enclosing craters have been battered by abundant craters not present on the younger, smooth floors. In another area (fig. 13), a series of filled craters shows progressively greater structural disruption of the crater rims, indicating a lapse of time between crater formation and filling by plains materials. These plains materials

are unaffected structurally and appear to be about the same age in each depression. Some plains materials fill craters and basins that are younger than the broad belt of plains around the Caloris Basin (fig. 9) and so are younger than parts of that belt.

Crater populations for plains within the Caloris Basin and the surrounding plains units east of Caloris (fig. 9) are indistinguishable, indicating that the emplacement ages of the two surfaces are similar.

The crater distribution for these Mercurian plains (fig. 9) is almost the same as



Figure 13b.—A high resolution (400 m) picture of the hilly and lineated terrain shown in figure 12. This terrain consists of numerous dissected hills (~ 0.1 to 1.8 km high) interspersed with smooth material. The southern rim (d) of the 31-km diameter crater (A) has been severely dissected, but the eastern rim (e) is largely intact. The crater rim of the smaller crater (B) is barely recognizable.

that obtained for the Apollo 14 landing site (ref. 17). The population of 1-km-diameter Mercurian craters is a factor of 10 greater than the Apollo 12 site which yielded rocks with the youngest crystallization ages from the Moon. However, any attempt to assess the age of the Mercurian plains by comparison of crater frequencies with the lunar maria must take into account differences in cratering mechanics between the two bodies, as well as possibly different fluxes of post-accretion impacting bodies.³ The Caloris Basin and other plains units exhibit production crater populations (ref. 15) in contrast to the heavily cratered terrain (fig. 9) that is in a state of crater saturation.

Patches of plains materials on the floors of craters and basins over the rest of Mercury are indistinguishable in age or morphology from the plains concentric to and inside Caloris. Some of these smaller tracts of plains materials could perhaps be impact melt from nearby craters or basins, although for many there is no well-defined source crater (fig. 12). Although we have observed no direct evidence of volcanism such as cones, domes, or flow fronts, we stress that such features are best observed under very low Sun illumination, and we see only a single narrow band on the planet with such lighting

The origin of the plains materials is of key importance because the occurrence of widespread volcanism in combination with its great bulk density would strongly imply that Mercury is differentiated. The volumes

and areal distribution of the plains materials are the main arguments in favor of a volcanic origin as opposed to an origin as solidified impact melt or debris flows. The plains materials filling the Caloris and north polar basins cannot be the direct result of the impact which formed these basins because their volume is very close to the volume of material that was excavated during the cratering event. Subsequent filling by fluid material is required.

The structure and morphology of the Caloris Basin, immediately after it formed, probably resembled those of the Orientale Basin on the Moon. The latter has numerous hummocky fissured areas on the floor and some smooth plains, both of which probably formed from impact melt, as well as relatively small dark plains (maria) believed to be of genuine volcanic origin. However, the volume of the Orientale melt material is insignificant compared to the volume of its impact cavity out to its outermost rim. Similarly, the plains materials concentrically surrounding the Caloris and north polar basins involve enormous volumes of melted material—more analogous to the mare flooding of Oceanis Procellarum adjacent to Mare Imbrium than to the light plains materials (sometimes called Cayley Formation) containing impact breccias which concentrically surround the Imbrium Basin in disconnected patches (ref. 22).

The plains-filled basins conceivably may be the site of gravity anomalies similar to the lunar mascons. O'Leary (ref. 23) speculated that a nonuniform distribution of regional gravity anomalies might provide the gravitational inhomogeneity required to keep Mercury in its 3/2 spin resonant period. The location of the large Caloris Basin near the Mercurian "hot" pole, i.e., near the equatorial region, preferentially pointed toward the Sun at perihelion, is suggestive in this regard. However, detailed measurements of the non-spherical portion of Mercury's gravity field (probably with an orbiting spacecraft) will be required to verify if Caloris and other circular basins on Mercury actually exhibit mascon-like gravity anomalies.

³ Mercury's gravitational acceleration is greater than that of the Moon by a factor of 2.2. This difference will tend to inhibit crater size. On the other hand, impact velocities at the surface of Mercury should be greater than for the Moon if the impacting bodies are from the same source, thus making larger craters for impacting objects of the same mass. Although these two factors are compensating, effects of velocity probably dominate. Mercurian craters produced by a given impacting mass could plausibly be two to three times larger than their lunar counterparts. This difference would be manifested as an increased number of craters of any given size for the same accumulated fluxes at both bodies. Thus, the similarity between the frequency distributions for the Caloris plains units and Apollo 14 site is only apparent, and the implied ages would be different even if the impact flux histories could be assumed equal.

Unique Surface Features

Large scarps of great linear extent that transect both craters and inter-crater areas appear to be unique features of Mercury. Several of the largest of these features are shown in figure 8. These features are best seen on the heavily cratered incoming side of Mercury. Preliminary shadow measurements indicate that several of the scarps may attain heights of 3 km or more. They generally have sinuous outlines with slightly lobate fronts, and commonly attain lengths well

over 500 km (fig. 14). The scarps face in various directions, although east-facing scarps appear to be more frequent in the incoming view. Often large craters interrupt their paths, suggesting that at least some of the scarps were formed during the final stages of intense bombardment of the surface. The lobate form of the scarps and their crater transection relation suggest that they may be thrust or reverse faults caused by compressive stresses. If this interpretation is correct, then Mercury is the first planet other than Earth to show evidence for global com-

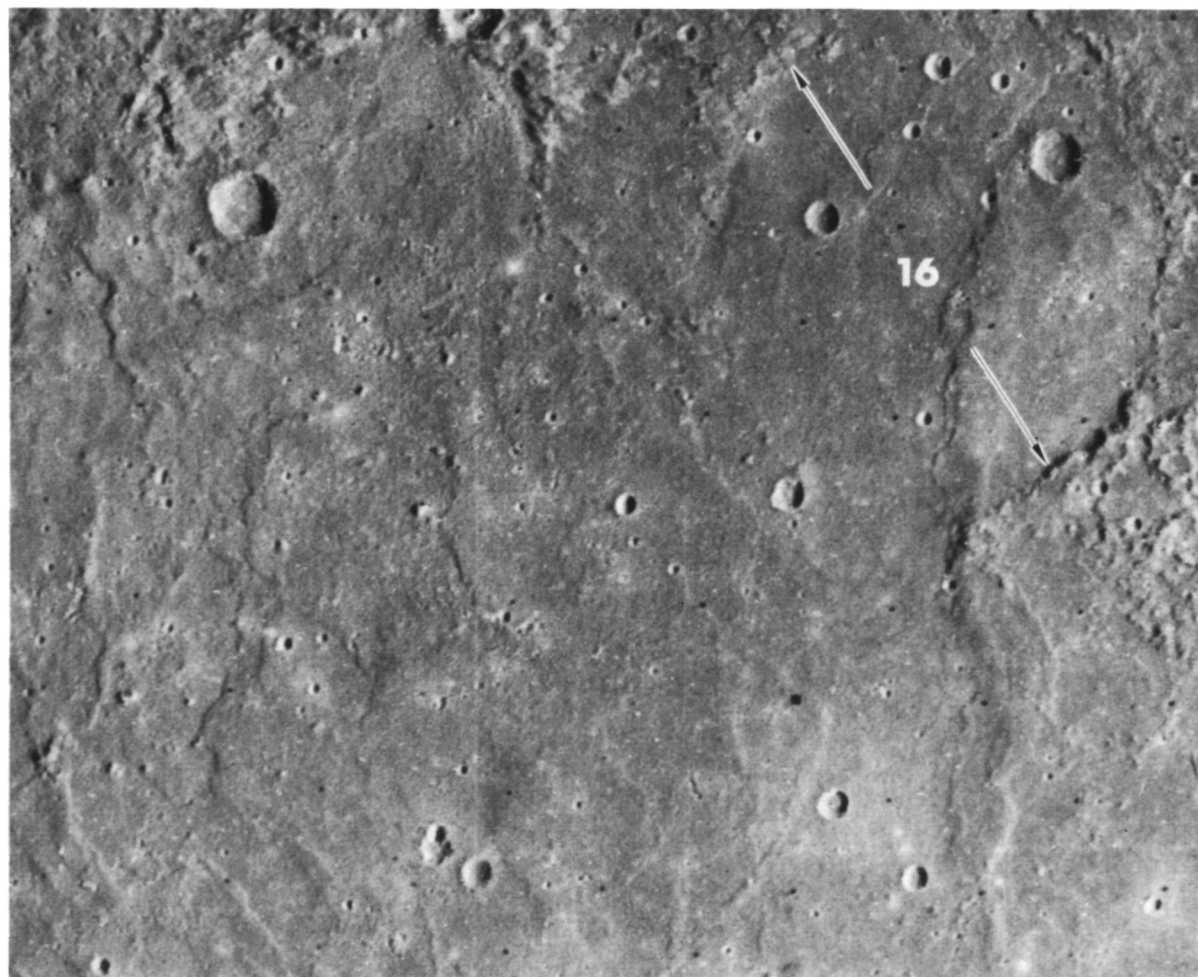


Figure 14.—A 240-km diameter basin (number 16, table 4) almost completely flooded by plains materials that are part of the concentric band around the Caloris Basin. The number 16 is centered in the basin, and arrows point to a ring of low unflooded hills which define the basin. The Caloris Basin lies 1300 km to the southwest. North at top.



Figure 15.—A sinuous, slightly lobate scarp (A, B) over 300 km long, which transects two craters. Preliminary shadow measurements indicate a maximum height on the order of 3 km. The form, dimensions, and crater transection relations suggest that this structure (and many others of similar nature) is a thrust or reverse fault due to compressive stresses. Craters cut by scarp are 55 and 35 km across.

pressive stresses on this scale. Such compressive deformation was evidently significant during the later phases of heavy bombardment, if not earlier.

A peculiar terrain of hills and lineations (fig. 15a, b), confined to a semielliptical area of at least 500 000 km², is centered at latitude 20° S. and longitude 20°, approximately antipodal to the Caloris Basin. Because the terrain extends into the terminator, the areal extent may be considerably greater. This terrain is grossly similar to the hilly and furrowed terrain northwest of the Lunar Mare Humorum (ref. 22). The hills

are generally wider than in the lunar example. Whether there are other significant differences is not clear without additional picture analysis. The hilly and lineated terrain on Mercury includes craters whose rims have been broken up into hills and depressions. Some craters are more strongly modified than others independent of size, suggesting that this type of terrain developed over an appreciable period of time rather than during a single catastrophic event. The extended duration yet limited geographic distribution point toward an internal origin.

The floors of many craters in the hilly and

lineated terrain are almost completely filled with plains material which embays dissected crater rims and is clearly younger than the hilly and lineated terrain. Hence, the formation of this terrain appears to fall between the end of heavy bombardment and the emplacement of the plains units filling the Caloris Basin and elsewhere.

Planetary History

The Mariner 10 picture data suggest to us that Mercury underwent a period of early heavy bombardment, including formation of huge basins, followed by the widespread volcanism represented by the plains materials. The inferred sequence of events is remarkably similar to that deduced for the Moon. We feel a strong chemical similarity to the Moon on the scale of these plains units is also indicated. However, Mercury is much denser than the Moon. Therefore, Mercury must be a chemically differentiated planet; silicate outer layers probably enclose an iron-rich core.

It has been indicated for many years by ground-based radio, radar, optical, and infrared measurements (ref. 24) that the materials of the uppermost centimeters to meters probably are iron-rich silicates at least grossly similar to those on the Moon (density range 3.0 to 3.3 g/cm³). Silicate composition for at least the outer few kilometers is now indicated directly by the Mariner 10 pictures because of the similarity in albedo and morphology of the Mercurian cratered terrains and plains to those of the lunar highlands and maria. Furthermore, it is likely that the resemblance to the Moon persists deeper; silicate material must extend to a considerable depth in order to have supplied the large amount of volcanic material that composes much of the extensive plains deposits. Indeed, Reynolds and Summers (ref. 25) estimate that the iron core of terrestrial composition for a differentiated Mercury would extend outward 75 to 80 percent of the radius of the planet; thus, the silicate outer layers would be approximately

500 to 600 km thick. Hence, the most straightforward interpretation of the strong resemblance to the Moon is that Mercury is indeed Moon-like for its outer 500 km or so.⁴

What additional planetary history is evidenced by Mercury's surface? A striking feature of Mercury (and of the Moon as well) is that an ancient heavily cratered terrain has been preserved in extensive regions without major modification by either internal processes like volcanism or surface processes such as atmospheric erosion. Some of the topographic features comprising such terrain are very probably of considerable antiquity, although the precise age of Mercurian heavily cratered terrain cannot be estimated with precision at this time. Analysis of samples from the heavily cratered lunar highlands has raised the possibility that the lunar heavy bombardment may have continued un-

⁴Three less likely alternative configurations of Mercury warrant brief mention. (1) Mercury has a thin skin of silicate material a few tens of kilometers thick, residing on a substratum of undifferentiated rock (density ~ 5.5 g/cm³); silicates that formed the plains have been drained laterally from over a large area. (2) The volcanic material of the plains has differentiated in situ into a lunar-like silicate phase and a much denser iron phase; the residual iron must then have moved downward tens if not hundreds of kilometers over a significant portion of the Mercurian surface to permit adequate silicate melt to collect near the surface. (3) The silicate melt that formed the plains was "sweated" out of a uniform, undifferentiated planetary mix maintained at the eutectic temperature throughout most of its mass; the iron component is postulated to have remained solid.

Besides internal difficulties with each of these ad hoc possibilities, all seem poorly suited to reproduce in such detail both the small-scale morphology and the broad three-dimensional form of the lunar maria. Production of extensive volcanic plains requires relatively uniform temperature and composition of source materials, as well as abundant (if intermittent) flow. Whereas the first alternative might provide uniform material, it seems implausible that the flow rates for entirely horizontal transport should match closely those of the lunar maria. Furthermore, there is no evidence of widespread subsurface withdrawal that should be present for large areas surrounding the plains units on Mercury. In-situ differentiation, the second alternative, hardly seems likely to produce a uniform melt over such large areas and extended times. A similar objection applies to the third alternative, especially because vertical transport through a porous mass over thousands of kilometers would be implied, making a mare-like flow rate of melt implausible.

til 4 b.y. ago (ref. 26), although some volcanic rocks returned from the highlands may be as old as 4.5 b.y. (ref 27). Further resolution of the history of the Moon, as well as detailed consideration of intrinsic differences in both accretion and flux of other solar system objects at Mercury as compared to the Moon, seems required before the terminal phases of heavy bombardment at Mercury can be assigned to a time period more precise than 4.0 to 4.5 b.y. ago.

Survival of ancient cratered terrain sets limits on when material now composing the planet became chemically differentiated. In particular, differentiation must have been complete by the time the oldest surviving landforms were created. The complete planetary heating required for in-situ differentiation of an originally homogeneous planet very likely would have significantly modified all surface topography through destructive volcanism, atmospheric effects, or even melting. Consequently, differentiation of Mercury must have occurred before the end of heavy bombardment. Since there is no evidence of any atmospheric modification to the ancient land surfaces, it seems that the planet has possessed a substantial atmosphere since the end of heavy bombardment. The most recent impact craters on Mars, for comparison, have lost their ray systems and secondary crater chains and demonstrate the capacity for even a very thin atmosphere to modify cratered surfaces. Differentiation can, perhaps, be expected to produce an atmosphere; hence, the absence of any atmospheric erosional effects suggests that differentiation substantially preceded the end of heavy bombardment.

The planetary scale scarps and ridges, suggestive of a major episode of compression, have been recognized only in the heavily cratered terrain and not in the plains units inside or outside the Caloris Basin. The lack of recognizably similar features on either the Moon or Mars suggests that these may record an episode peculiar to the internal constitution and evolution of Mercury. An obvious speculation is that an iron-rich interior underwent shrinkage resulting in compression of the outer layers, especially if a

core were as large as suggested by Reynolds and Summers. It is conceivable that the scarps and ridges may record such an episode that persisted at least into the end of heavy bombardment, but not throughout much of the rest of the history of the planet. Similarly, the hilly and lineated terrain may reflect localized internal processes. While we do not offer any particular suggestion as to the nature of these processes, it may be significant that they also appear to have occurred during the terminal phases of heavy bombardment, before emplacement of the plains units.

As on the Moon, the volcanic filling of the large basins, and probably the emplacement of much of the other plains material, took place after the end of heavy bombardment. Little subsequent internal or external activity is recorded in the observed portions of the planet. The sequence of events recorded on the surface of Mercury appears remarkably similar to that of the Moon. It is also possible that the incident impact flux versus time relationships may prove to be similar. If this proves to be the case, then absolute time scales would also be similar.

Of course, we have viewed only approximately 25 percent of the planet in useful viewing geometry. Previous exploration of the Moon and Mars provides ample reasons for caution in generalizing planetary history from only a limited surface sample. We cannot exclude the possibility that other kinds of volcanic processes and/or more recent internal activity are manifested on the presently unexplored parts of Mercury. Nevertheless, the constraints on differentiation and atmospheric history, and the general similarity to lunar history, remain quite valid conclusions even from the present limited surface sample.

What do these results about Mercury imply concerning the other terrestrial planets? The existence of large basins now has been recognized on the Moon, Mars, and Mercury; the three bodies also exhibit striking asymmetries in their major physiographic provinces. Although not well understood, these characteristics must be acknowledged to be a

rather common aspect of terrestrial planet formation. Additionally, early rather than late chemical differentiation seems supported by the Mercurian results. All of these circumstances may also pertain to the formation of the Earth, where direct information regarding these episodes is no longer available.

We have viewed a new world. Further study of the Mariner 10 pictures undoubtedly will contribute to a better understanding of the history of the terrestrial planets.

References

1. DAVIES, M. E., *Icarus*, Vol. 17, No. 1, 1972, p. 116.
2. DAVIES, M. E., *Photogrammetric Eng.*, Vol. 39, No. 12, 1973, p. 1297.
3. DAVIES, M. E., AND D. W. G. ARTHUR, *J. Geophys. Res.*, Vol. 78, No. 20, 1973, p. 4355.
4. DE VAUCOULEURS, G., *Icarus*, Vol. 3, 1964, p. 187.
5. DOLLFUS, A., AND M. AUEIERE, In press, 1974.
6. HEMEEN-ANTILLA, K., AND T. PIKKARAINEN, *The Moon*, Vol. 1, 1970, p. 440.
7. HARRIS, D., *Planets and Satellites*, G. Kuiper and B. Middlehurst, eds., University of Chicago Press, 1961, p. 272.
8. IRVINE, A. J., et al., *Astron. J.*, Vol. 73, 1968, p. 807.
9. LYOT, B., *Ann. Obsr. Paris*, Vol. 8, No. 1, 1929.
10. MCCORD, T., AND J. ADAMS, *Science*, Vol. 178, 1972, p. 745.
11. POHN, H., AND R. WILDEY, U.S.G.S. Prof. Paper 599-E, 1970.
12. DOLLFUS, A., J. E. GEAKE, AND C. TITULAER, *Proc. Second Lunar Science Conference*, Vol. 3, 1971, p. 2285.
13. BOWELL, E., A. DOLLFUS, AND J. E. GEAKE, *Proc. Third Lunar Science Conference*, Vol. 3, 1972, p. 3103.
14. GREELEY, R., AND D. E. GAULT, *The Moon*, Vol. 2, 1970, p. 10.
15. GAULT, D. E., *Radio Science*, Vol. 5, No. 2, 1970, p. 273.
16. HARTMANN, W. K., *Commun. Lunar and Planet. Lab.*, Vol. 4, No. 65, University of Arizona, 1966, p. 121.
17. GAULT, D. E., AND R. GREELEY, in preparation, 1974.
18. SHOEMAKER, E. M., M. H. HAIT, G. A. SWANN, D. L. SCHLEICKER, G. G. SCHOBBER, R. L. SUTTON, D. H. DAHLEN, E. N. GODDARD, AND A. C. WATERS, *Proc. Apollo 11 Lunar Science Conference*, Vol. 3, 1970, p. 2399.
19. GOLDSTEIN, R., AND S. ZOHAR, *Astro. Phys. J.*, Vol. 79, No. 1, 1974, p. 85.
20. STEWART-ALEXANDER, D. E., AND K. A. HOWARD, *Icarus*, Vol. 12, 1970, p. 440.
21. HOWARD, K. A., D. E. WILHELMS, AND D. H. SCOTT, *Rev. Geophys. and Space Phys.*, in press, 1974.
22. WILHELMS, D. E., AND J. F. MCCAULEY, U. S. Geol. Survey, Map I-703, 1971.
23. O'LEARY, B., *Nature*, Vol. 220, 1968, p. 1309.
24. KUIPER, G. P., *Commun. Lunar and Planet. Lab.*, Vol. 143, 1970, p. 165.
25. REYNOLDS, R. T., AND A. L. SUMMERS, *J. Geo. Res.*, Vol. 74, 1969, p. 2494.
26. TERA, F., D. A. PAPANASTASSIOU, AND G. J. WASSERBURG, *Earth Planet. Sci. Letters*, Vol. 22, 1974, p. 1.
27. ALBEE, A. L., A. A. CHODOS, R. F. DYMEK, A. J. GANCARZ, D. S. GOLDMAN, D. A. PAPANASTASSIOU, AND G. J. WASSERBURG, *Lunar Science*, Vol. V, *Abstracts to Fifth Lunar Science Conference*, 1974, pp. 3-5.

Page intentionally left blank

Page intentionally left blank

Studies of Chemical Abundances in the Outer Solar System

Tobias Owen

*State University of New York
Stony Brook, New York*

Ground-based observations and the Pioneer 10 mission have led to new discoveries and revisions of previous ideas about the outer solar system. Among these are the discovery of atmospheres on Io and Ganymede, emission from sodium and hydrogen in a cloud around Io, and the presence of acetylene, ethane, and phosphine in the atmosphere of Jupiter. Titan, the largest satellite of Saturn, continues to be an extremely interesting and baffling object, clearly very different in composition from the bodies we are familiar with in the inner solar system; this is also true of Ganymede and Callisto. New data on the abundances of methane and hydrogen in the atmospheres of Uranus and Neptune suggest that the values of C/H in these atmospheres may be much lower than had been previously thought. This result reinforces the apparent compositional differences between these two planets and Jupiter and Saturn, whose atmospheres exhibit a near-solar value for this ratio.

The exploration of the outer planets and their satellites by means of space probes has only just begun. Pioneer 10 flew past Jupiter on 3 December 1973, on its way to solar system escape. It will be followed by Pioneer 11 approximately 1 yr later, with the next outer planet mission planned by the U.S. to be launched in 1977. But we have been able to acquire a large amount of information about these distant bodies by means of ground-based observations, and such studies are becoming increasingly productive as ever more sophisticated instrumentation becomes available.

An excellent summary of current knowledge about the outer solar system, prior to Pioneer 10 has been published by Newburn and Gulkis (ref. 1). That survey has been updated with a special emphasis on applications to exobiology (ref. 2). A compendium of information about all the satellites has just appeared in print (ref. 3). The present review will therefore emphasize the most recent results and attempt to indicate prob-

lems on which substantial progress may be expected in the next few years.

The Satellites

It has been suspected for many years that the Galilean satellites of Jupiter show a systematic decrease in mean density with increasing distance from the planet. As our detailed knowledge about these objects has increased, this density gradient has proven to be less extreme than was thought, but still appears real. It is intriguingly similar to the density gradient observed in the solar system itself and leads to a mean density for the outermost member, Callisto, that requires this object to be radically different in composition from the rocky inner solar system bodies with which we are familiar. These general characteristics should be kept in mind when discussing the origin of the Earth-Moon system to provide some perspective for the interpretation of peculiarities observed in de-

Table 1.—*The Galilean Satellites of Jupiter*

Name	Radius (km)	Mass (10^{23} g)	Density (g/cm ³)
Io (J I)	1820 ± 10	900 ± 60	3.5
Europa (J II)	1550 ± 150	480 ± 10	3.1
Ganymede (J III)	2635 ± 25	1540 ± 2	2.0
Callisto (J IV)	2500 ± 150	910 ± 80	1.4

NOTE: Data from Morrison and Cruikshank (ref. 3), except Io mass revised by Anderson, et al. (ref. 4).

tail in that one case. A summary for the current bulk characteristics of the Galilean satellites is given in table 1.

Searches have repeatedly been made without definite success for evidence of atmospheres about these bodies. Just last year, Brown (ref. 5) reported the unexpected result that the spectrum of Io exhibits the D lines of sodium in emission. These observations have been confirmed and extended, and it now appears that the satellite is surrounded by a cloud of sodium atoms, whose exact shape, origin, and mode of excitation remain to be defined (refs. 6, 7, and 8). This promises to be an exciting subject for future research.

The occultation experiment on Pioneer 10 was successful in detecting the presence of a very tenuous atmosphere on this satellite (refs. 9 and 10). The mean surface pressure deduced was in the range 10^{-8} to 10^{-10} bars. Lyman alpha emission was observed in a torus around Jupiter and from Io itself, suggesting that hydrogen is at least a component of the satellite's atmosphere (ref. 11). Tentative proof for an atmosphere on Ganymede was adduced from a stellar occultation observation (refs. 9 and 10). The mean surface pressure served by Carlson et al. (ref. 12). The observations in this case were found to correspond to a surface pressure between 10^{-3} and 10^{-6} bars, but it would appear that additional observations are desirable to verify this finding. What is the composition of these atmospheres? How are they produced and maintained? What is their connection (if any)

with the post-eclipse brightening of J I and J II discovered by Binder and Cruikshank (ref. 13)? These and other questions remain to be answered.

Saturn's largest satellite, Titan, has been known for many years to have an atmosphere containing methane (ref. 14). More recently, hydrogen absorptions were detected in the spectrum by Trafton (ref. 15), and the thermal radiation emitted at 12μ was found to be anomalously high (ref. 16), confirming an earlier observation by Low (ref. 17). These new results spawned a series of interpretive papers attempting to understand the high temperature in terms of the relatively small amount of information about the satellite that was available. A comprehensive summary of the observations and their interpretations may be found in the proceedings of a conference on the atmosphere of Titan, edited by Hunten (ref. 18).

The latest observations of this puzzling object suggest that it is very dark at 5μ , that there is not a large amount of gaseous hydrogen in that part of the atmosphere that is probed at 20μ (e.g., not enough for a hydrogen greenhouse), that methane and probably ethane are in emission in a high-altitude inversion layer, and that the surface temperature is in the range 135 ± 45 K (refs. 19 through 22). A coherent picture has still not emerged from these observations, but it does appear that some extreme model atmospheres can be ruled out.

The material(s) responsible for the red coloration of Titan pose another interesting problem. The low albedo at 5μ limits the number of candidates, but the possibility of combining various substances to obtain the red color observed in the visible and the low albedo at 5μ makes the likelihood of an unequivocal determination very small. Another complication is posed by the need to decide how the materials responsible for the reflection characteristics of the satellite are distributed between the surface of the body and possible clouds or hazes in its atmosphere. Organic polymers are one of several interesting candidates (refs. 23 and 24). One thing that does seem certain is that the material(s)

causing the red color on Io are not identical with the chromophores on Titan (ref. 25).

Looking further outward in the solar system, we have examined the spectra of Pluto and Triton to see if they show evidence of the methane absorptions that are so prominent in Titan's spectrum (ref. 2). The results thus far have been negative, which may simply indicate that these bodies have always been too cold to permit substantial vapor pressures of infrared-active gases to exist.

The entire subject of satellites in the solar system will be reviewed at a forthcoming IAU Colloquium (No. 28) to be held at Cornell University; the interested reader is advised to obtain the *Proceedings* volume when it becomes available.

Planets

Until the Pioneer 10 mission, the atmosphere of Jupiter seemed reasonably well understood. However, the occultation experiment on that mission indicated that the upper atmosphere of Jupiter was very much warmer than had been expected, in serious contradiction to the results of ground-based optical spectroscopy and radio observations (refs. 9 and 10). At this writing, no one has been able to devise a model atmosphere that successfully explains both sets of data, and serious questions have consequently been raised about the possibilities of error in the occultation data or their interpretation (refs. 26 and 27). This is a significant confrontation because it affects the interpretation of ground-based data for the atmospheres of all the major planets, not just Jupiter. One may hope that the results to be obtained from the Pioneer 11 mission will prove to be helpful in resolving the present dilemma.

The mixing ratio of hydrogen to helium was also studied by experiments on the Pioneer 10 mission (see Smoluchowski, this conference). A new analysis of the infrared radiometer results by Hogan et al. (ref. 26) suggests that they imply a roughly solar value of $H/He = 10$ instead of the lower values obtained in the preliminary reports (ref. 28). Helium was directly detected for the first

time by the Pioneer 10 UV spectrophotometer (ref. 11).

Recent ground-based studies have resulted in the detection of several important trace constituents. The 4-0 P(1) line of HD was discovered by Trauger et al. (ref. 29) who derived a D/H ratio of $(2.1 \pm 0.4) \times 10^{-5}$ for the Jovian atmosphere. This is very similar to the corrected interstellar value of $(1.4 \pm 0.2) \times 10^{-5}$ derived by Rogerson and York (ref. 30) from observations of the Lyman absorption spectrum of interstellar atomic deuterium using the instrumentation on the Orbiting Astronomical Observatory (OAO-C). Taken together, these results imply that the material making up the planet has not undergone nuclear processing, and mass-dependent escape has not occurred from the upper atmosphere since the formation of the solar system.

Other processes have obviously been at work, however, as is evident from the presence of colored regions in the cloud belts (e.g., the Great Red Spot). Support for the hypothesis that these colors might be caused by the presence of complex organic polymers was provided by the recent discovery of small amounts of C_2H_2 and C_2H_6 in the planet's spectrum near 13μ (refs. 31 and 32). These products will not be present in detectable amounts under conditions of simple thermodynamic equilibrium (ref. 33), but they are expected to be formed as by-products of organic polymer synthesis through the action of ultraviolet light, lightning discharges, etc. Of course their existence does not *require* that these more complex substances be present. In fact, the discovery of a sodium cloud around the satellite Io invites a reinspection of the hypothesis of Wildt (ref. 34) that the colors might result in part from solutions of metallic sodium in ammonia. The discovery that PH_3 is also present in Jupiter's atmosphere (ref. 35) lends further weight to the idea that material contributed from outside the planet (e.g., through meteoritic infall) may play a significant role in the atmospheric chemistry.

The harvest of new results on the other outer planets has been less rich. Phosphine

Table 2.—*Abundances in the Outer Solar System*

Object	H ₂ (km atm)	NH ₃ (m atm)	CH ₄ (m atm)	H/ C
Jupiter	75 ± 15	12 ± 5	50 ± 15	3000 ± 300
Saturn	75 ± 20	2 ± 1	60 ± 12	2500 ± 400
Uranus	450 ± 100	< 2.5	> 10 × 10 ³	< 100
Neptune	450 ± 100	—	> 10 × 10 ³	< 100
Pluto	—	< 10	< 2?	—
Titan	5 ± 2.5	< 2.5	200 to 1600	6 to 50
Triton	—	—	< 2?	—
Sun				2700 ± 300

and ethane have been suspected in the atmosphere of Saturn, but available spectral resolution is not yet adequate for a definitive identification (ref. 36). Ammonia has been detected in the spectrum at 6450 Å, with an abundance of 2 ± 1 m atm (ref. 37). This result disagrees with an upper limit of < 2 cm atm derived at 1.55 μ m (ref. 38). This same discrepancy in abundances determined at these two wavelengths has been found on Jupiter and may represent a change in the opacity with wavelength in the atmospheres of these two planets. The relatively low ammonia abundance derived for Saturn implies a thick ammonia cloud and a model that carries with it a prediction that the ammonia abundance should vary with time, as appears to be the case (refs. 37, 39, and 40).

Recent work on the interpretation of spectra of Uranus and Neptune has indicated that the atmospheric methane abundances derived for these two planets may be seriously low. It has not been possible to observe some of the bands seen in the planetary spectra with laboratory pressure-path lengths as high as 10 km atm, implying vertical column abundances in the range 10 to 50 km atm (refs. 41 and 42). New values for the hydrogen abundances have also been reported, with mean values in the neighborhood of 450 km atm for the atmospheres of both planets (refs. 43 through 46).

A first attempt to identify the 4–0 P(1) line of HD in the spectrum of Uranus led to a crude upper limit of 20 mÅ on the equivalent

width of this line, corresponding to a limit of $D/H < 4 \times 10^{-4}$ (ref. 47). It would be useful to lower this limit, since these two planets have apparently experienced some early differentiation, being enriched in heavy elements in comparison with, say, Jupiter and Saturn. Hence, some enrichment of D relative to H may also have occurred. If the methane is enriched as much as the previous discussion implies, it will probably be necessary to consider the distribution of deuterium between methane and hydrogen in order to interpret this result properly. Thus, we are also planning to improve the present detection threshold for CH₃D absorption, which leads to a limit of $D/H < 3 \times 10^{-3}$ (ref. 48).

Summary

The current status of abundance studies for major constituents in the atmospheres of the bodies we have been discussing is given in table 2. This table should not be viewed as definitive, it is simply an attempt to summarize some current estimates for constituent abundances. All of these estimates were made from analyses of photographic and near-infrared planetary spectra. Simple reflecting models have been assumed throughout, so the figures should not be taken seriously as absolute abundances. The upper limits were established with the additional assumption that the absorption bands involved were not saturated. This implies that some other gas (e.g.,

neon) is present to provide the necessary pressure broadening.

The new discoveries of trace constituents (C_2H_2 , C_2H_6 , PH_3) are not included in the table since mixing ratios for these gases are still very uncertain. Ridgway's (ref. 31) original estimates of 4×10^{-3} and 8×10^{-5} for C_2H_6 and C_2H_2 seem rather high, since the mixing ratio for CH_4 is roughly 10^{-3} (see table 2). Combes et al. (ref. 32) suggest that these values should be reduced by a factor of 20. The difficulty lies in the fact that these gases are observed in the upper atmosphere where a thermal inversion occurs, and hence the interpretation of the observations is extremely model-dependent (refs. 27 and 49).

The relative abundances on a given planet shown in table 2 should have more significance; the final column giving values for C/H should therefore reflect real differences among the objects being surveyed. The new results for the methane abundances on Uranus and Neptune emphasize the difference between these planets and Jupiter and Saturn. The large depletion of light gases in the atmospheres of the outer two planets must be explained by any comprehensive theory for the origin and evolution of the solar system. In the case of Titan, we are really still in the beginning stages of a proper investigation, while even the gross characteristics of Pluto and Triton are presently only poorly known.

References

1. NEWBURN, R. L., AND S. GULKIS, *Space Sci. Rev.*, Vol. 14, 1973, p. 179.
2. OWEN, T., *Origins of Life*, Vol. 5, 1974, p. 41.
3. MORRISON, D., AND D. P. CRUIKSHANK, *Space Sci. Rev.*, Vol. 15, 1974, p. 641.
4. ANDERSON, J. D., G. W. NULL, AND S. K. WONG, *Science*, Vol. 183, 1974, p. 322.
5. BROWN, R. A., Paper presented at IAU Symposium No. 65, 1973, proceedings in press.
6. BROWN, R. A., AND F. H. CHAFFEE, JR., *Astrophys. J. Letters*, Vol. 187, 1974, p. L125.
7. McELROY, M. B., Y. L. YUNG, AND R. A. BROWN, *Astrophys. J. Letters*, Vol. 187, 1974, p. L127.
8. TRAFTON, L. M., T. PARKINSON, AND W. MACY, JR., *Astrophys. J. Letters*, Vol. 190, 1974, p. L85.
9. KLIORE, A., D. L. CAIN, G. FJELDBO, B. L. SEIDEL, AND S. I. RASOOL, *Science*, Vol. 183, 1974, p. 323.
10. KLIORE, A., D. L. CAIN, G. FJELDBO, B. L. SEIDEL, AND S. I. RASOOL, Paper presented at 17th Plenary Meeting of COSPAR, Sao Paulo, Brazil, 1974, proceedings in press.
11. JUDGE, D. L., AND R. W. CARLSON, *Science*, Vol. 183, 1974, p. 317.
12. CARLSON, R. W., J. C. BHATTACHARYYA, B. A. SMITH, T. V. JOHNSON, B. HIDAYAT, S. A. SMITH, G. E. TAYLOR, B. T. O'LEARY, AND R. T. BRINKMANN, *Science*, Vol. 182, 1973, p. 53.
13. BINDER, A. B., AND D. P. CRUIKSHANK, *Icarus*, Vol. 3, 1964, p. 299.
14. KUIPER, G. P., *Astrophys. J.*, Vol. 100, 1944, p. 378.
15. TRAFTON, L. M., *Astrophys. J.*, Vol. 175, 1972, p. 285.
16. ALLEN, D. A., AND T. L. MURDOCK, *Icarus*, Vol. 14, 1971, p. 1.
17. LOW, F. J., *Low. Obs. Bull.*, Vol. 6, 1965, p. 184.
18. HUNTEN, D. M., *The Atmosphere of Titan*, Proceedings of a conference held at the Ames Research Laboratory, July 25-27, 1973, NASA SP-340, 1973.
19. LOW, F. J., AND G. H. RIEKE, *Astrophys. J. Letters*, Vol. 190, 1974, p. L143.
20. KNACKE, R. F., T. OWEN, AND R. R. JOYCE, *Icarus*, in press, 1974.
21. GILLET, F. C., W. J. FORREST, AND K. M. MERRILL, *Astrophys. J. Letters*, Vol. 184, 1973, p. L93.
22. BRIGGS, F. H., *Icarus*, Vol. 22, 1974, p. 48.
23. SCATTERGOOD, T., P. LESSER, AND T. OWEN, *Nature*, Vol. 247, 1974, p. 100.
24. KHARE, B. N., AND C. SAGAN, *Icarus*, Vol. 20, 1973, p. 311.
25. JOYCE, R. R., R. F. KNACKE, AND T. OWEN, *Astrophys. J. Letters*, Vol. 183, 1973, p. L31.
26. HOGAN, J. S., R. D. CESS, TH. ENCRENAZ, AND D. GAUTIER, in press, 1974.
27. WALLACE, L., M. PRATHER, AND M. J. S. BELTON, *Astrophys. J.*, in press, 1974.
28. CHASE, S. C., R. D. RUIZ, G. MÜNCH, G. NEUGEBAUER, M. SCHROEDER, AND L. M. TRAFTON, *Science*, Vol. 183, 1974, p. 315.
29. TRAUGER, J. T., F. L. ROESLER, N. P. CARLETON, AND W. A. TRAUB, *Astrophys. J. Letters*, Vol. 184, 1973, p. L137.
30. ROGERSON, J. B., AND D. G. YORK, *Astrophys. J. Letters*, Vol. 186, 1973, p. L95.
31. RIDGWAY, S. T., *Astrophys. J. Letters*, Vol. 187, 1974, p. L41.
32. COMBES, M., TH. ENCRENAZ, L. VAPILLON, Y. ZEAU, AND C. LESQUEREN, *Astron. and Astrophys.*, in press, 1974.
33. LEWIS, J., *Icarus*, Vol. 10, 1969, p. 365.
34. WILDT, R., *Monthly Notices, Roy. Astron. Soc.*,

- Vol. 99, 1939, p. 616.
35. RIDGWAY, S. T., Paper presented at April 1974 meeting of Div. for Planet. Sci., Am. Astron. Soc., 1974.
 36. GILLET, F. C., AND W. J. FORREST, *Astrophys. J. Letters*, Vol. 187, 1974, p. L37.
 37. ENCRENAZ, TH., T. OWEN, AND J. H. WOODMAN, *Astron. and Astrophys.*, in press, 1974.
 38. MARTIN, T. Z., D. P. CRUIKSHANK, AND C. B. PILCHER, Paper presented at April 1974 meeting of Div. for Planet. Sci., Am. Astron. Soc., 1974.
 39. CESS, R. D., *Proc. Tenth Annual Meeting of the Society of Engineering Science*, in press, 1974.
 40. SPINRAD, H., AND L. M. TRAFTON, *Icarus*, Vol. 2, 1963, p. 19.
 41. OWEN, T., B. L. LUTZ, C. C. PORCO, AND J. H. WOODMAN, *Astrophys. J.*, Vol. 189, 1974, p. 379.
 42. ENCRENAZ, TH., J. HARDORP, T. OWEN, AND J. H. WOODMAN, Paper presented at IAU Symposium No. 65, 1973, proceedings in press.
 43. TRAFTON, L. M., Paper presented at March 1973 meeting of the Div. for Planet. Sci., Am. Astron. Soc., Tuscon, Arizona, 1973.
 44. TRAFTON, L. M., Paper presented at IAU Symposium No. 65, 1973, proceedings in press.
 45. LUTZ, B. L., *Astrophys. J.*, Vol. 182, 1973, p. 989.
 46. ENCRENAZ, TH., AND T. OWEN, *Astron. and Astrophys.*, Vol. 28, 1973, p. 119.
 47. LUTZ, B. L., AND T. OWEN, *Astrophys. J.*, Vol. 190, 1974, p. 731.
 48. OWEN, T., *On the Origin of the Solar System*, H. Reeves, ed., Paris, CNRS, 1972, p. 245.
 49. VARANASI, P., R. D. CESS, AND B. R. P. BANGARU, *J. Quant. Spec. and Radiat. Trans.*, in press, 1974.

Use of Ground-Based Telescopes in Determining the Composition of the Surfaces of Solar System Objects¹

Thomas B. McCord

*Planetary Astronomy Laboratory
Department of Earth and Planetary Sciences
Massachusetts Institute of Technology
Cambridge, Massachusetts*

John B. Adams

*West Indies Laboratory
Fairleigh Dickinson University
St. Croix, Virgin Islands*

The surfaces of solar system objects can be studied from Earth only by using electromagnetic radiation reflected and emitted from the surface materials. Of course one can leave the Earth's surface using spacecraft and study planetary surfaces more closely. Recent evidence suggests that the way that the surfaces of the solar system objects reflect solar radiation is controlled by the composition and mineralogy of the surface materials. The way sunlight is reflected from the surface as a function of wavelength, i.e., the spectral reflectance, is the most important property. This article reviews efforts by our laboratories to use ground-based optical telescope measurements to determine the composition of the surfaces of the solar system objects.

The spectral flux received at the Earth from a square kilometer of the lunar mare surface is plotted in figure 1. Here, flux in watts per square meter per micrometer is plotted against wavelength in micrometers. The radiation consists of two parts: (1) solar radiation passively reflected by the surface material, and (2) solar radiation which has been absorbed, converted to heat, and re-

emitted as thermal radiation. The shapes of these two components of the spectral flux curve are similar for the surfaces of other solar system objects.

We are interested here only in the reflected solar component of the spectral flux available to the planetary astronomer. The property of interest is the spectral reflectance. It is defined as the fraction of sunlight incident on the surface which is reflected back into space from the object toward the observer.

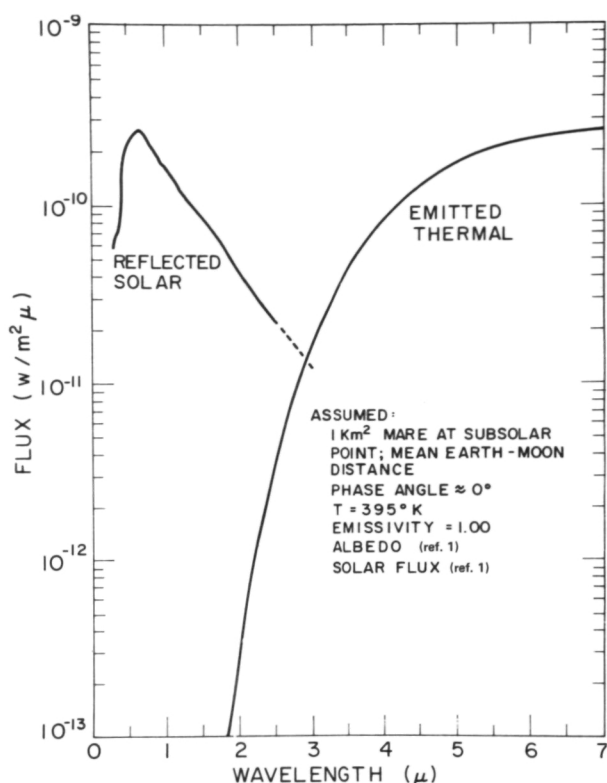
Spectral reflectance is measured by us at the telescope using several instruments: mainly a dual-beam 24-filter photoelectric photometer, a two-dimensional integrating television-like imaging system, and a Michelson interferometer spectrometer.

Measuring Spectral Reflectance

The function of interest in this discussion is the spectral reflectance $R(\lambda)$. It is defined as the fraction of incident radiation $F_{\odot}(\lambda)$ reflected back into space from the object $F_{obj}(\lambda)$ toward the observer.

$$R(\lambda) = F_{obj}(\lambda) / F_{\odot}(\lambda) \quad (1)$$

¹Massachusetts Institute of Technology, Planetary Astronomy Laboratory publication No. 102.



RADIATION FROM MOON [1 km² of mare] AT EARTH

Figure 1.—Radiation received from a 1-km square mare area, albedo 0.06 (ref. 1) at average Earth-Moon distance.

We have ignored angular dependence and polarization, for they are of second-order importance to most of this discussion. We care mostly only about the wavelength dependence of the spectral reflectance and not so much about the albedo or absolute amount of reflected radiation.

Spectral reflectance is measured by us at the telescope using several instruments, mainly a filter photometer (ref. 2), a vidicon imaging system (refs. 3 and 4), and a Michelson interferometer-spectrometer. The usual method of measurement is as follows:

1. The flux from the object of interest is measured.
2. At nearly the same time a nearby star is also observed.

3. The object/star flux ratio is formed, which should eliminate instrument response and atmospheric effects.
4. In previous studies the spectral flux of a series of these standard stars has been determined relative to a master standard star, α Lyrae, above the Earth's atmosphere (refs. 5 through 8).
5. Thus, the spectral flux received from the object is determined:

$$F_{obj} = \left(\frac{F_{obj}}{F_{ss}} \right) \left(\frac{F_{ss}}{F_{algr}} \right) F_{algr} \quad (2)$$

F_{ss} = flux for standard star

F_{algr} = flux for α Lyrae

6. Spectral reflectance is finally determined by using measurements and calculations of the spectral flux from the Sun above the Earth's atmosphere (ref. 9) (see equation (1)).

A more detailed discussion has been given by Chapman, McCord, and Johnson (ref. 10) and Elias (ref. 11).

Usually the spectral reflectance is displayed as a function scaled to unity at 0.56 μ m to eliminate albedo effects and concentrate on the spectral effects.

Theory

The spectral reflectance is of particular interest to us because there are several physical phenomena which cause selective absorption or sunlight. The theoretical basis for interpretation of visible and near-infrared spectra of minerals was established in a series of papers by Burns (refs. 12 and 13), White, and Keester (refs. 14 and 15) and Bancroft and Burns (ref. 16). These authors pioneered in the application of crystal-field theory to the interpretation of optical spectra of natural materials. White and Keester (ref. 14) and Adams and Filice (ref. 17) showed that diffuse reflectance spectra of powdered minerals retain the main spectral details that are observed in the transmission curves. Adams (ref. 18) presented evidence that absorption bands in the reflectance spec-

tra of planetary surfaces could be used to obtain information on remote mineralogy and petrology. Several authors have studied the reflectance properties of minerals and rocks from the point of view of interpreting remotely sensed spectra (refs. 19 through 27). Burns (ref. 13) provided a detailed discussion of the application of crystal-field theory to the study of minerals. Burns et al. (ref. 28), Bell et al. (ref. 29), and Gaffey and Burns (ref. 30) report on recent results in this rapidly expanding area of research where the spectra of single mineral grains are measured in polarized light.

Broad absorption bands appear at several wavelengths in the reflection spectrum. The best defined absorption bands are called electronic transition bands. They appear mostly at visible and near-infrared wavelengths. These are due to the photostimulated transition of d-shell electrons in transition element ions, principally iron. Less well defined, but often very strong, absorption features, appearing mostly at ultraviolet and visible wavelengths, are due to photostimulated transfers of electrons from one ion to another in the crystal lattice. These are called charge transfer bands.

Molecular vibrational bands also occur in the reflectance spectra of some minerals.

Variations in the wavelengths of the centers of the electronic absorption bands can be used to uniquely identify many mineral species. The energies of these absorptions are controlled by the kind of ions in the crystal lattice donating the electrons and by the electric field in which the ions are positioned. Therefore, the composition of the solid and the crystal structure of the solid control the wavelength position of the absorption bands.

The presence and wavelength position of the electronic absorption bands can be used to uniquely identify many mineral species. This is true regardless of whether one is studying silicates in the laboratory using an artificial light source or whether one is studying solar radiation reflected from the surface of the Moon using a ground-based optical telescope.

The Moon

It is appropriate to discuss the Moon first, for it is the object whose surface we know most about and for which we have the only ground-truth. A major portion of our effort in developing and applying the method or remote mineralogical analysis using reflection spectroscopy during the past 7 years has concerned the Moon. With the return of soil samples from eight lunar sites as a result of the U.S. and U.S.S.R. space programs, the opportunity for testing and expansion of the remote analysis is great. The experience gained in relating our ground-based telescope observations to the laboratory studies of lunar samples gives us confidence to proceed to the study of other solar system objects for which samples are not likely to be available in the near future.

Reflection spectra of small lunar regions with sufficient spectral resolution and intensity precision to define absorption features have only become available since 1968. The development of new instrumentation has allowed the determination of spectral reflectance curves for nearly 200 lunar regions of diameter 10 to 20 km, with photometric precision of about 1 percent (refs. 23 and 31).

A representative sample of these lunar spectral reflectance curves is shown in fig. 2, where reflectance as a function of wavelength is plotted. These curves represent the major morphologic units on the Moon: maria, uplands, and bright craters. Each curve is scaled to unity at $0.56\mu\text{m}$. All of the curves measured are basically similar in shape. The spectral reflectance for all lunar areas increases toward longer wavelengths, and a shallow absorption band near $0.95\mu\text{m}$ occurs in all curves, but with varying depth and wavelength position. Beyond the spectral region shown here, into the infrared region to $2.5\mu\text{m}$, the reflectivity continues to rise, and a very shallow, broad absorption band is evident near $2.0\mu\text{m}$ for many areas (ref. 32).

The absorption band in the lunar spectrum near $0.95\mu\text{m}$ is of direct mineralogical significance. There are small but important changes in its wavelength position from place

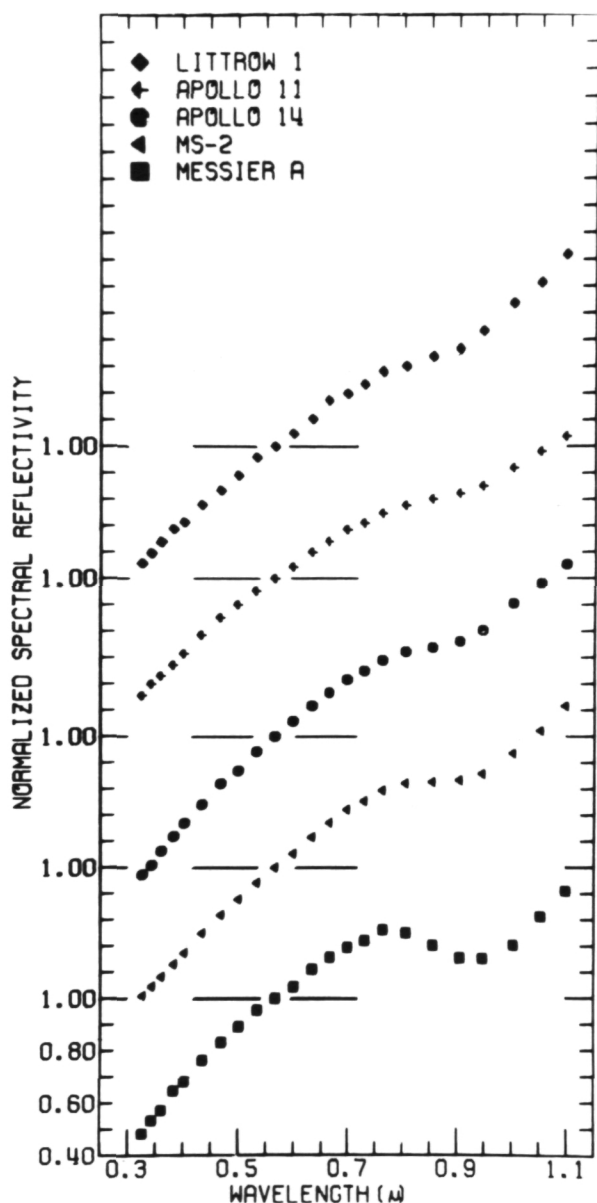


Figure 2.—Spectral reflectivity of several 10- to 20-km-diameter areas of the lunar surface measured using ground-based telescopes.

to place on the Moon, and the band depth varies greatly from strongest absorption at fresh bright crater sites to weakest absorption at "background" upland sites and at the very dark mare sites such as near the Apollo 17 site. From the laboratory studies of lunar and terrestrial metal-silicates and from theoretical analysis one would immedi-

ately interpret the absorption band in the lunar curves as indicating that pyroxene of pigeonite-augite composition is the major mafic mineral constituting the lunar mare surface material. This may not seem very profound after the return of samples from several U.S. and Soviet missions, but it was important when similar interpretations were made from less precise data before any lunar samples were available (refs. 2 and 18).

Changes in the position of the band near $0.95\mu\text{m}$ from place to place on the Moon are well documented (fig. 3). From the relationship between the wavelength position of this band and the composition of the pyroxenes causing it, it is clear that the average composition of the pyroxenes in the lunar soils varies from low calcium and iron at upland sites to high calcium and iron at mare sites. Deviations from this general rule do occur.

The slope of the spectral reflectance curve in the visible and near ultraviolet was a mystery until the first lunar samples were available. The slope is unlike that for normal pulverized silicates. The presence of glass rich in Fe^{2+} , Ti^{3+} , and Ti^{4+} ions and of the devitrified glasses rich in ilmenite and metallic iron are now known to be responsible for the unusual slope (refs. 33 through 37). An empirical relationship between the titanium content and curve slope of the reflection spectrum between 4000 and 5600 Å for mature (≥ 50 -percent glassy soil aggregates) mare soils has been established (ref. 38). Figure 4 shows a plot of TiO_2 content versus this curve slope. Recent study of lunar samples indicates that the presence of titanium in the glasses is principally responsible for this relationship. The relation of titanium content to curve slope has allowed us to make a successful prediction of the composition of the Apollo 17 soils before they were returned to Earth (ref. 39). Other relationships between the composition of the surface material and the spectral reflectance curves, such as those involving exposure age, plagioclase content, and upland rock type, are presently being developed.

The telescope curves for all lunar areas are generally similar in shape; however,

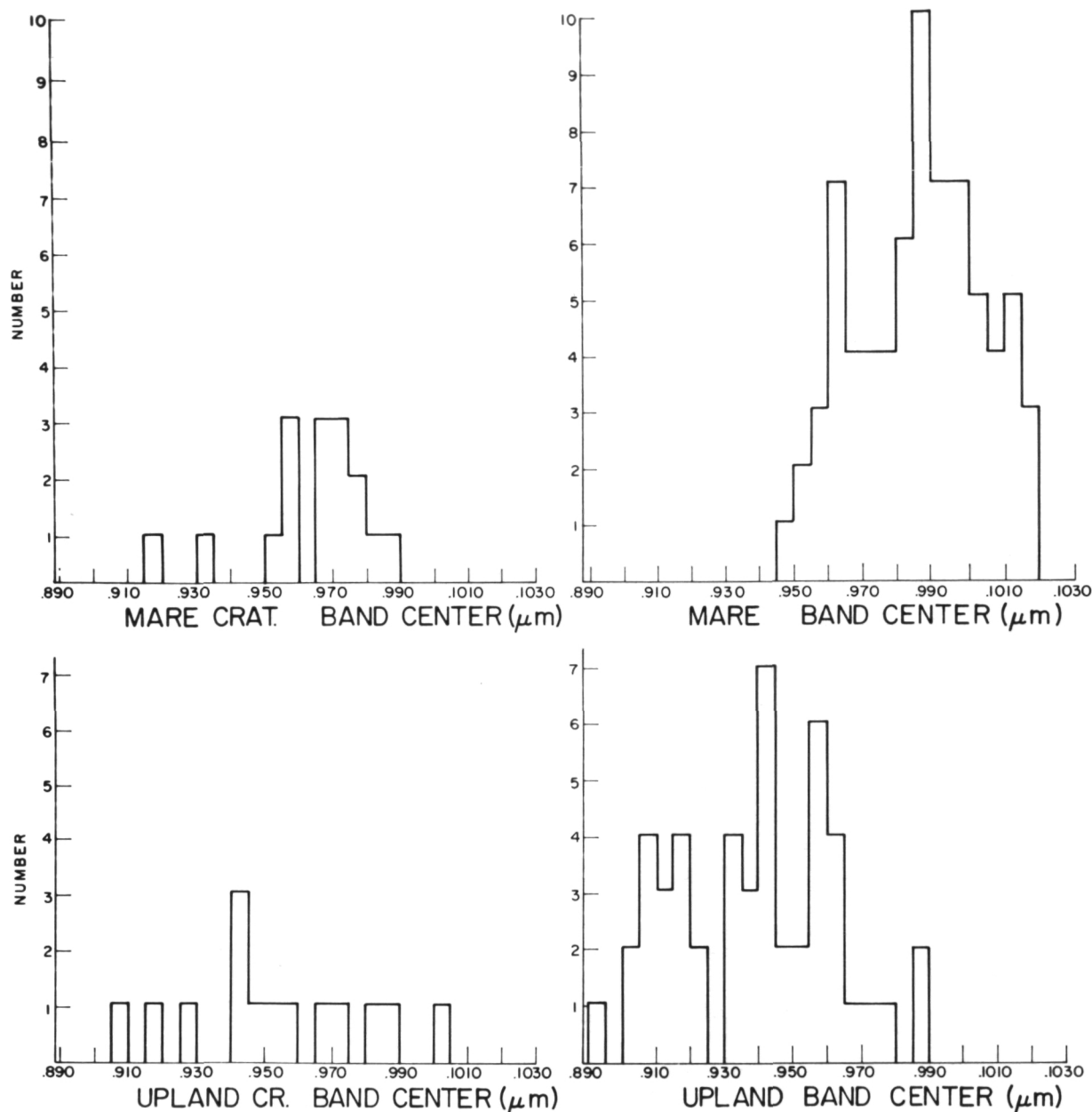


Figure 3.—A frequency distribution of absorption band positions for each of the four major lunar morphologies. Telescope data are used.

small but important differences exist that are best displayed by working with curve ratios. By dividing all spectral reflectance curves by the curve for a standard area on the Moon, one produces what we call relative reflectance curves, or curve ratios (ref. 3). We have

analyzed more than 150 relative spectral curves for different areas of the Moon, and it becomes apparent that all the curves obtained can be arranged into four sets according to their shape. These four sets, we call them spectral types, are directly correlated with

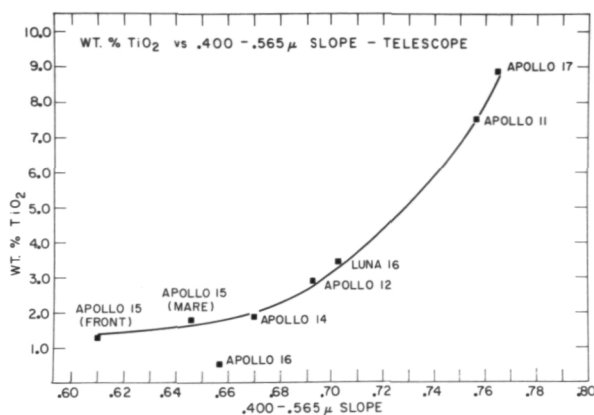


Figure 4.—Percentage TiO_2 versus 0.400- to 0.565- μ slope of telescope curve. TiO_2 contents of telescopic areas an average of sampled soils.

four morphologic units: mare, mare bright craters, uplands, and upland bright craters.

The relative curves, shown in figure 5a, illustrate the mare spectral type of curves. Notice the precision with which one can study the spectral properties of the lunar surface. The distance between each division on the plot axis is 2 percent in intensity. One can observe differences in these curves to well under 1 percent. Also note that there is not only one curve type, but a series of curves, indicating a series of mare materials. At the top of the series are the very dark "blue" maria such as are found in Mare Tranquillitatis. Near the middle of the series we have the brighter, "redder" mare such as Mare Serenitatis and the Apollo 12 site. At the bottom are the very "reddest" mare units such as Mare Frigoris. Some maria, especially imbrium, have patches of several types of material. Boundaries between different mare types seem to be accompanied by albedo boundaries, but all albedo boundaries are not color boundaries.

These relative plots are quite useful for quantitatively determining the compositional properties of the surface. For example, as shown in this figure, the mare relative curves exhibit a change in the slope of the curve in the blue and ultraviolet wavelengths. As stated before, this curve slope is related to titanium content in the mature soil. This

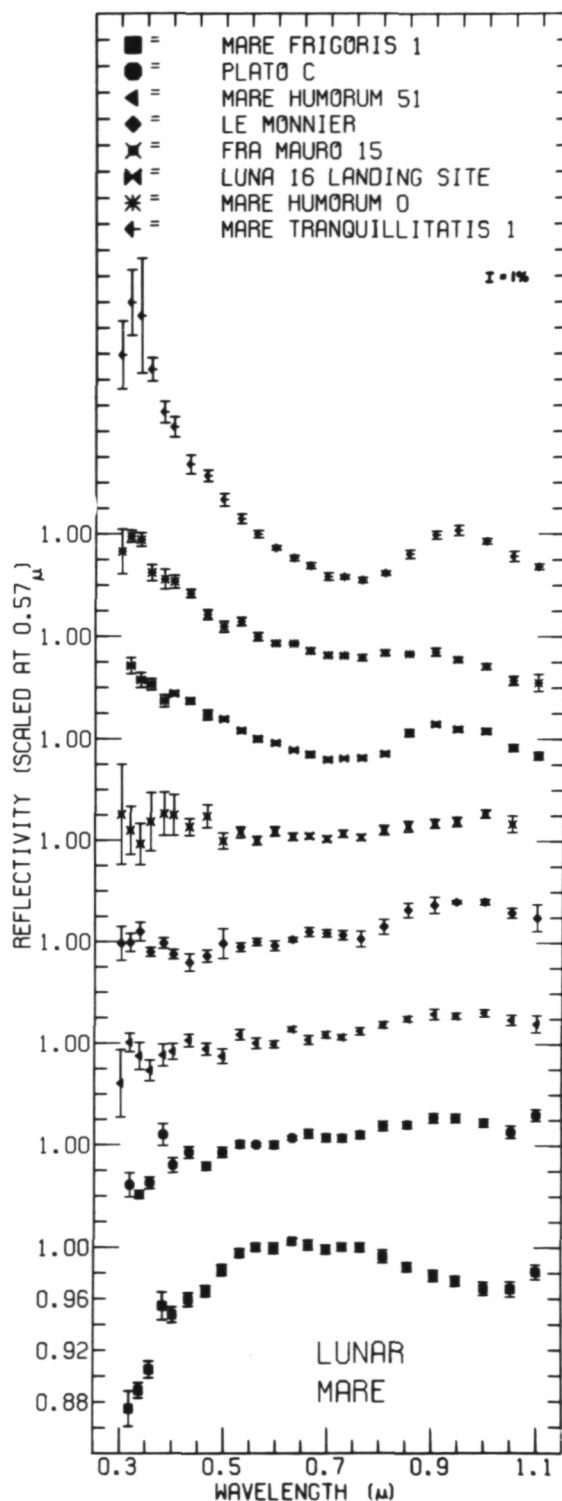


Figure 5a.—Relative spectral reflectance for a series of mare areas.

curve slope can be determined to better than 1 percent, and the titanium content can be determined to about 1 percent.

The next lunar spectral type is found in the uplands and is shown in figure 5b. In the uplands all curves are similar for the regions measured to date. The upland areas are defined here as almost any non-mare area other than bright craters. Notice as one progresses down the series of bright upland craters curves (fig. 5c) they become more

and more like the background upland curves. This aging process, whereby bright upland crater material is changed into background upland material, can be explained using the Apollo samples (refs. 36 and 40).

The fourth distinct lunar surface spectral type is illustrated in figure 5d. Here are shown relative spectral curves for a series of bright mare craters. Notice that the absorption band near 0.95μ is much deeper than for any other lunar area, including up-

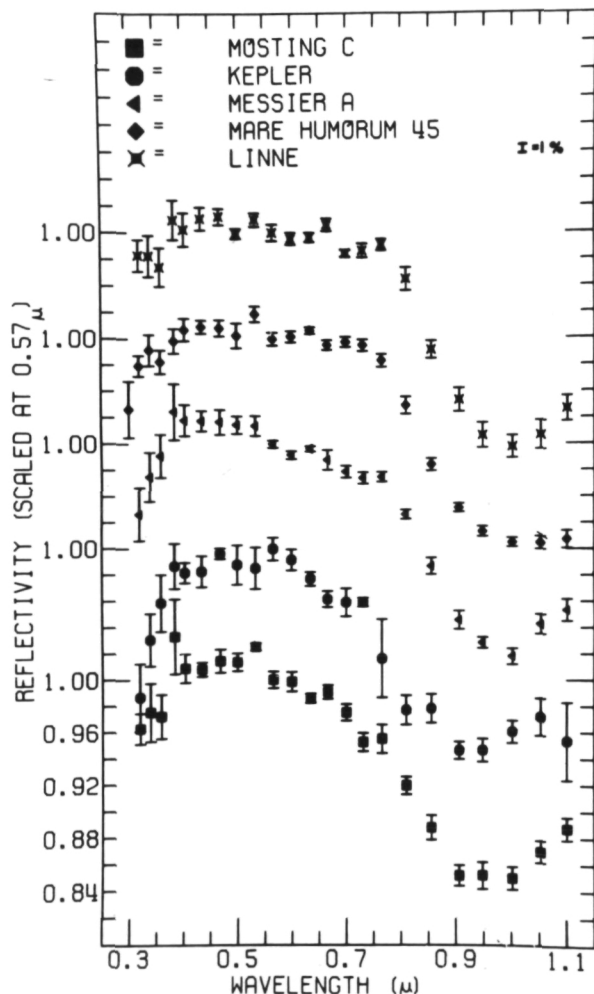
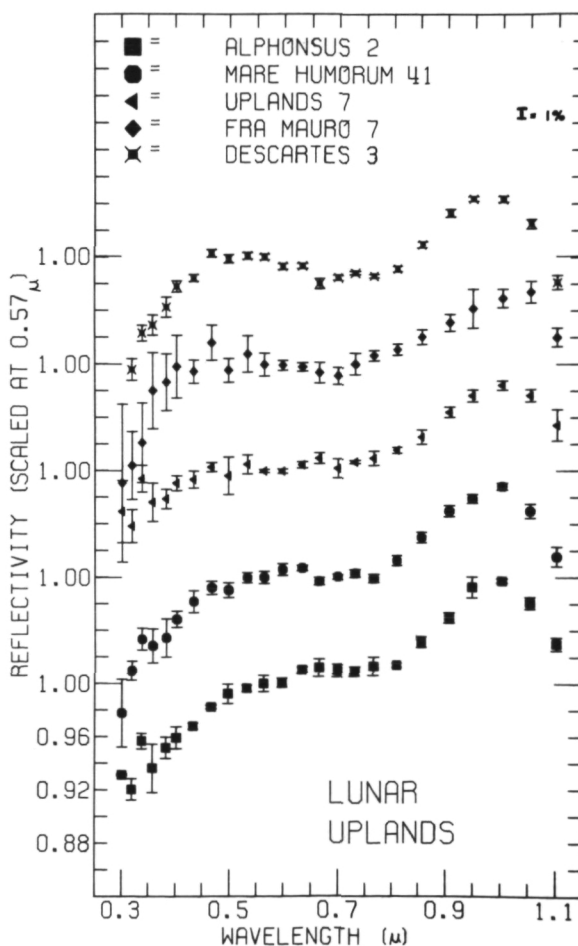


Figure 5c.—Relative spectral reflectance for a series of upland areas.

Figure 5b.—Relative spectral reflectance for a series of mare bright craters.



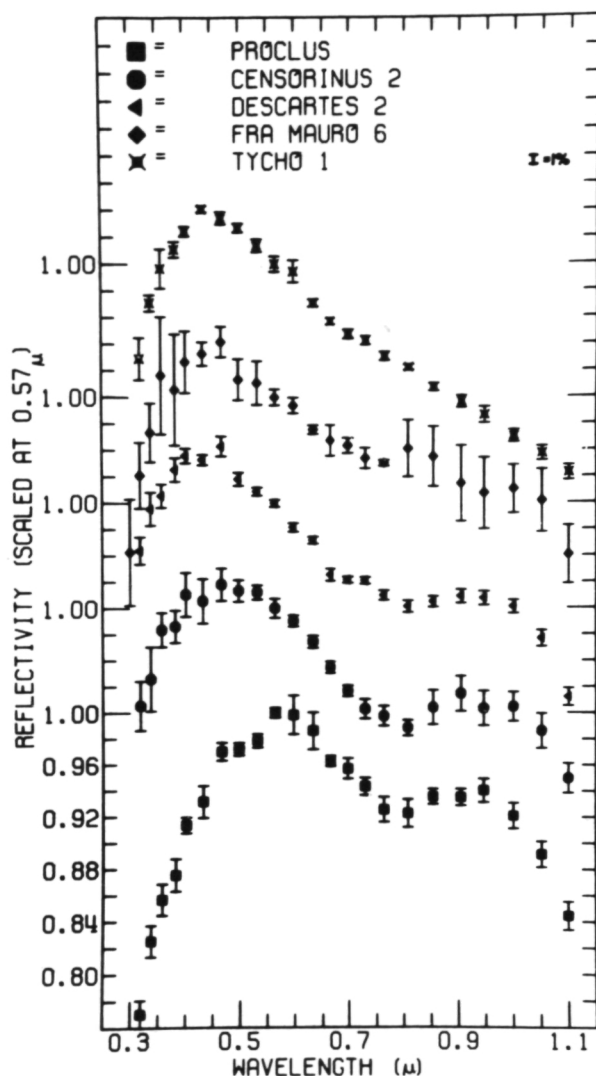


Figure 5d.—Relative spectral reflectance for a series of upland bright craters.

land bright craters. The mare bright craters also age, with their color as well as their brightness becoming nearer that of the background mare material.

It is of considerable interest that one can tell the difference between mare and upland materials even though the albedo may be the same, as say for bright craters. This technique has been used to show that Aristarchus is of the fresh upland crater type and Copernicus is of mature background upland material type, although they are formed in

mare regions. These craters expose upland material that was excavated from beneath the mare fill. This result also suggests that the concept of darkening of craters with time, which has been used to judge crater ages, must be used with caution.

One of the first applications of the measurements of the lunar sample optical properties was to determine the accuracy of the telescope data. The laboratory-measured spectral reflectance of Apollo 11 soil samples obtained at each of the Apollo sites was compared with the spectral reflectance measured by telescope of 18-km-diameter areas containing the landing sites. The agreement between laboratory and telescope measurements is within a few percent (ref. 33). This same sort of comparison has been carried out for the later Apollo missions (fig. 6). The conclusions drawn from this comparison are (1) the telescope data are accurate to about 1 percent, and one is measuring the actual physical properties of the lunar surface; (2) the telescope measurements refer mainly to the lunar soil rather than to rocks or breccia. We have also been able to reproduce in the laboratory the relative spectral reflectance curves using Apollo soil samples.

The reason spectral types exist is revealed by analysis of the lunar samples. It was found that the Apollo 12 soil has spectral properties very similar to those of the telescopic standard area in Mare Serenitatis. The Mare Serenitatis curve is used as the denominator in the ratio called relative reflectance. Thus, lunar sample relative curves, using the Apollo 12 soil as a standard, should be directly comparable to the telescope curves using the Mare Serenitatis standard area (ref. 41). Figure 7 shows the laboratory relative spectral reflectivity curve for Apollo 11 soil overlayed on the telescope curve for the landing site area. Notice the change in the vertical axis scale from figure 6. The Apollo 11 soil clearly has a mare spectral type (fig. 5).

By crushing a mare rock from Apollo 12, the mare bright crater spectral type is reproduced (fig. 7). The powdered rock curve has been reduced in scale by a factor of four

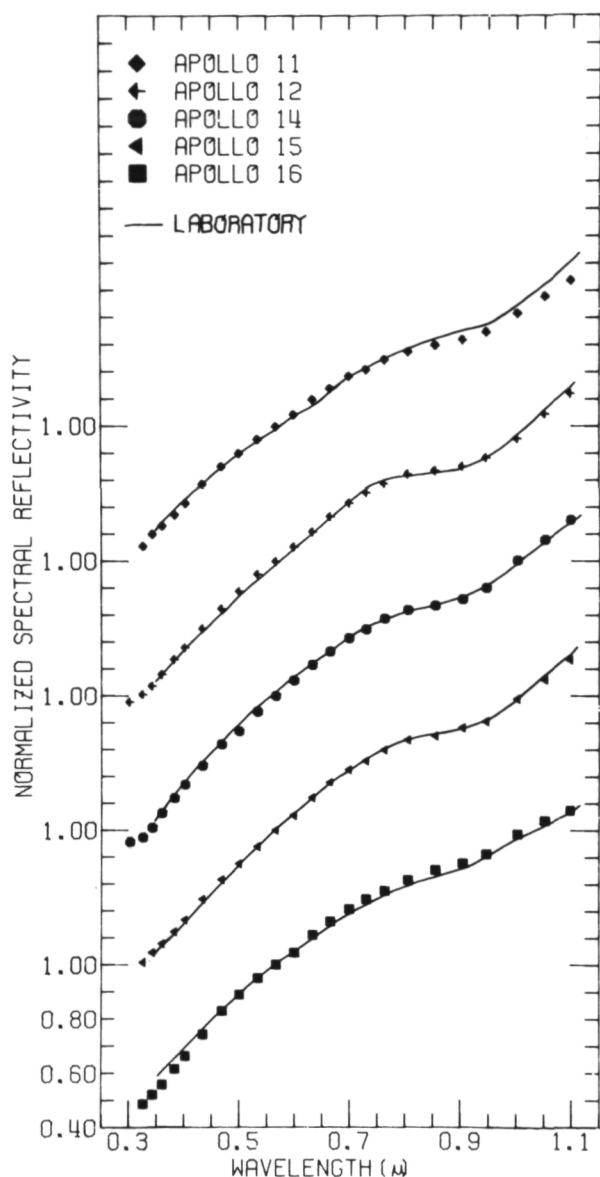


Figure 6.—Spectral reflectivity of areas containing Apollo landing sites compared to laboratory measurements of soil returned from these sites.

to better compare the shape of the two curves. The scale difference probably exists because the lunar soil even at a fresh mare crater is not entirely crystalline, but contains some glass.

The next comparison (fig. 7) is for Apollo 14 soil. Here the curve of the soil from the landing site matches the curve for the back-

ground upland spectral type. Finally, the upland bright crater curve is reproduced by a sample from Cone Crater, a bright fresh crater at the Apollo 14 site.

It is significant for remote analysis that the curves for lunar samples show the same subtle but important structures that also are seen in the telescope curves. Using the sample studies, the chemical and mineralogical properties that control the curve structure can be used to extend the compositional information gained at a few sites by direct sampling to the entire front surface of the Moon by ground-based remote observation.

Much of the work concerning the lunar telescope observations has been directed toward proving their accuracy and relevance to the properties of the surface material. Also, as discussed in other articles (e.g., ref. 42), considerable effort was expended to understand the optical properties of the lunar samples in order to better interpret the telescope curves.

We have also applied the telescope measurements to improve the understanding of the lunar surface. As discussed earlier in this article, telescopic curves were used to show that some mare bright craters had exposed upland material from beneath the mare, thereby defining a way of probing the depth of the maria and the composition of the subsurface material. Also, the titanium content and general rock type to be found at the Apollo 17 landing site was predicted correctly (ref. 39). The relationship of the regional geologic units at the Apollo 16 site (ref. 42) and the presence of Copernicus ray material in the Apollo 12 samples (ref. 40) were worked out partly by using telescopic data.

The current major effort to use the telescopic data is directed at mapping compositional units. Working with the spectral reflectance curves one learns to recognize several curve parameters, such as absorption band depth and curve slope in the blue, which are directly correlated with compositional information. It is obvious that one can map the spatial distribution of these curve parameters by imaging the Moon at certain

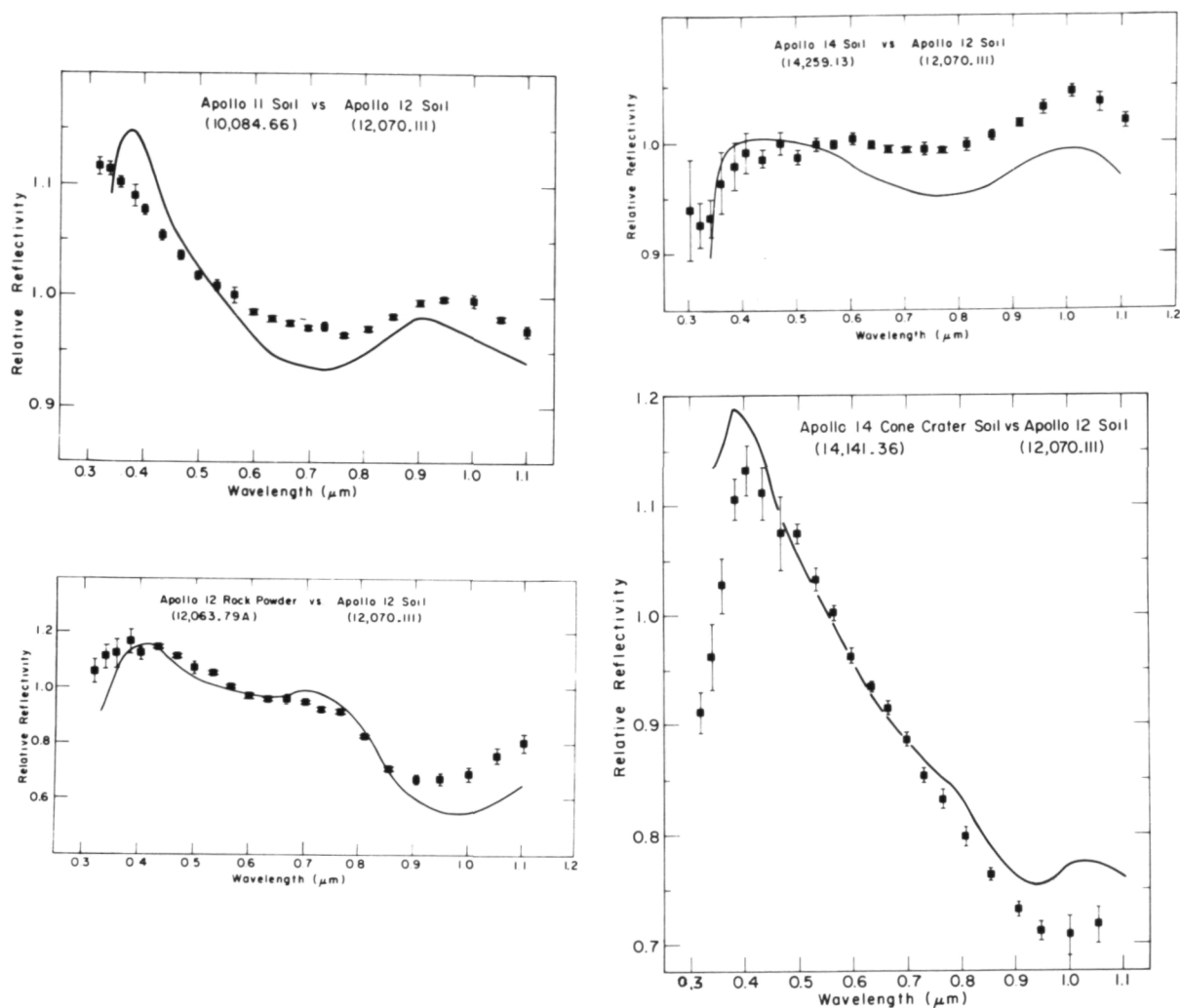


Figure 7.—Comparison of relative spectral reflectivity curves measured in the laboratory and at the telescope.

wavelengths and, thus, map the spatial distribution of the associated compositional properties. As an example, consider the relationship of curve slope between 0.40 and 0.56 μm , with titanium content in mature mare soils. This curve slope can be mapped by dividing images of a lunar area made at the two wavelengths and producing an image of the ratio. Because the change in spectral properties is small, i.e., on the order of 1 to 10 percent, it is necessary to map these spectral parameters with high photometric precision in order to obtain useful compositional maps. In order to do this, we have devel-

oped a special imaging system (refs. 3 and 4) that uses a silicon diode array vidicon tube. This television-like system integrates the optical image the telescope presents to it much as a photographic plate does. When sufficient signal has been integrated on the detector, the two-dimensional detector is read out in a single-frame mode to present to the observer a highly photometrically precise image of, say, an area of the Moon. The image is recorded in digital form in order to be computer processed.

Figure 8a is an example of the application of this technique for the southeast Mare

Serenitatis region of the Moon (ref. 39). This color difference image is essentially a map of titanium content in the mare region to a precision of about 1 percent TiO_2 . The Apollo 17 landing site is located in the Taurus-Littrow Valley shown in this figure. This map was produced by obtaining two images of this area of the Moon, using the vidicon imaging system. One image was made at 4000 Å and the other was made at 5600 Å. These digital images were calibrated in the computer, and then the calibrated images

were divided: the 4000 Å image divided by the 5600 Å image, point by point, to produce an array of numbers which is a measure of the ratio of these two images. This ratio array, or ratio image, was then converted to a photographic image using a cathode ray tube to write on photographic film.

The result is seen in the figure. Here brighter means higher in titanium content. The amplitude of the titanium content variations in the image is only a few percent. This ratio image has been contrast enhanced to

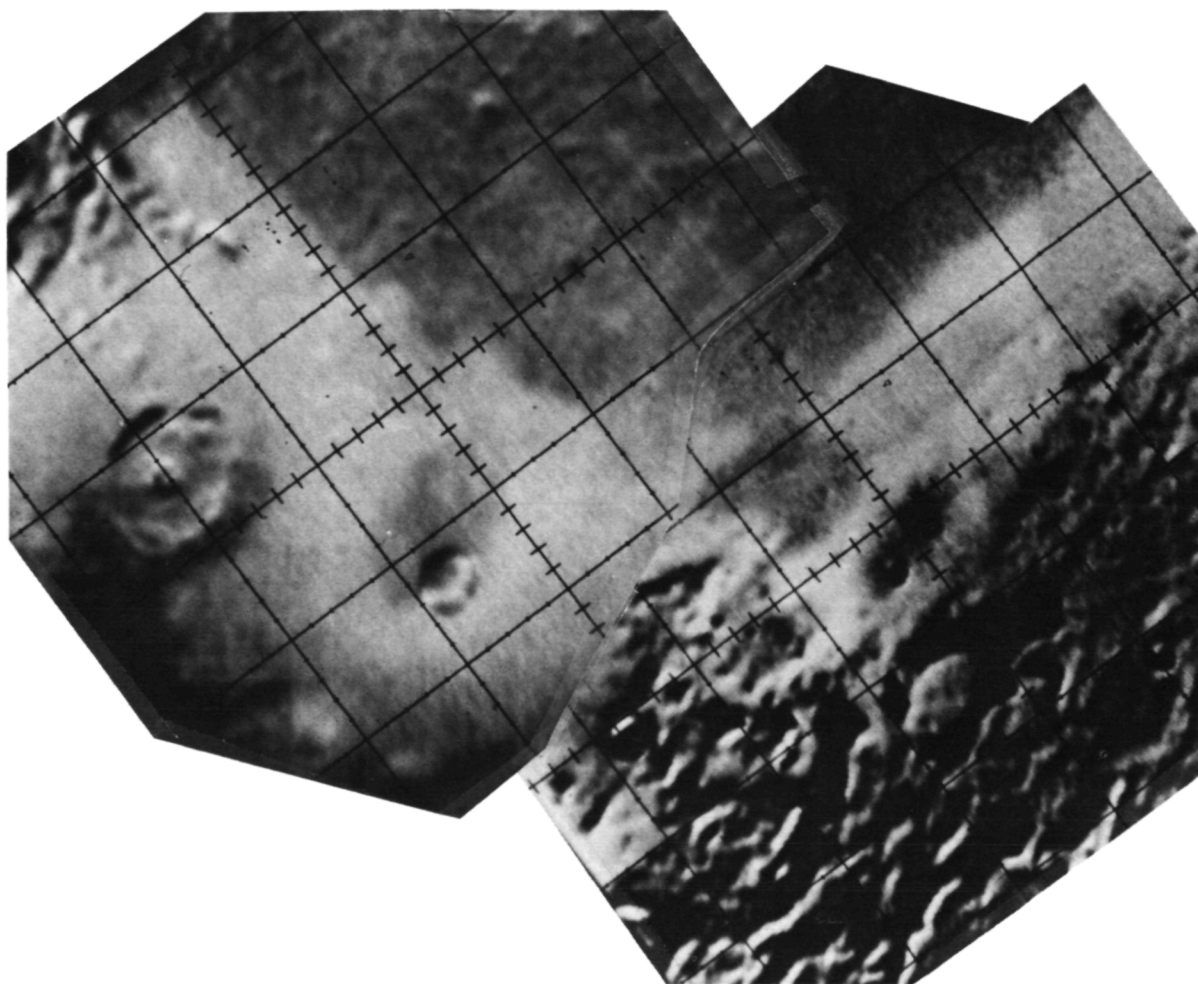


Figure 8a.—A photographic representation of the ratio of two digital images made through an interference filter centered at 0.35 and 0.56 μm . The MITPAL silicon vidicon imaging system was used at the 88-in telescope at Mauna Kea Observatory, Hawaii. The digital images are calibrated and then divided to produce a ratio image. Here bright indicates higher ultraviolet reflectances. The southeastern corner of Mare Serenitatis is shown to be about 2 km resolution. The ratio image is contrast-enhanced to show color differences of less than 1 percent.

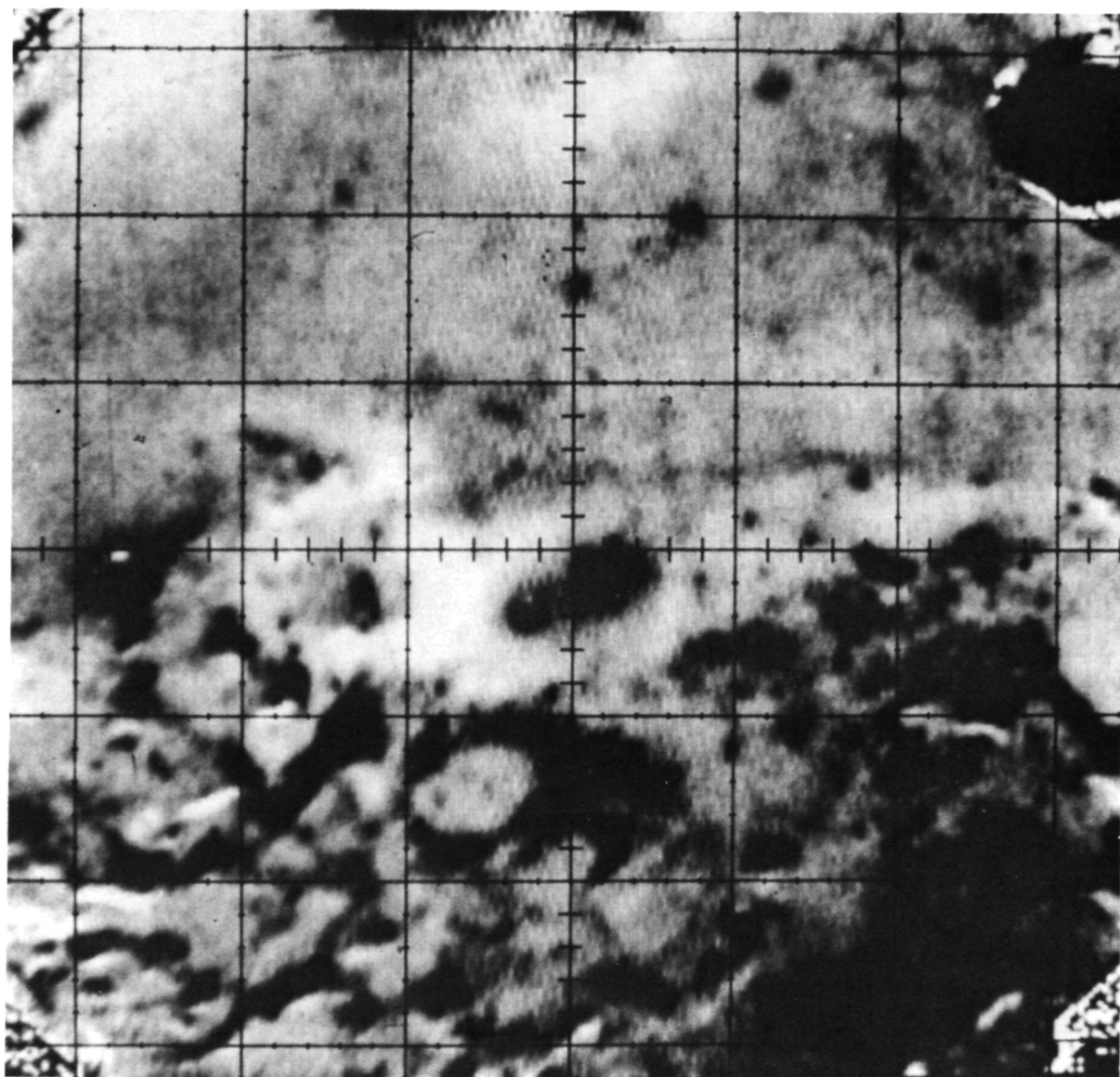


Figure 8b.—A similar ratio image made using images at $0.95\ \mu\text{m}$ and $0.56\ \mu\text{m}$. Only the northern half of the image in (a) is shown. Note how the different compositional units appear in different color ratio images.

bring out fine detail. It is of interest to note how the high titanium, dark mantling deposit near the Apollo 17 landing site stands out so prominently in this ratio image. Maps of other parameters, such as absorption band depth, can also be made. Figure 8b is the ratio image $0.95/0.56\ \mu\text{m}$ for a part of the same area as figure 8a. Notice that geologic units discernible in one ratio image may not

be in another. Measurements of the complete spectrum for areas within these images confirm the digital color difference images to about 1 percent.

These digital color difference maps display three different compositional units in the mare near the Apollo 17 landing site in the Taurus-Littrow Valley: Central Mare Serenitatis basalt with $\text{TiO}_2 \approx 2$ percent; Apollo

11-Mare Tranquillitatis-like basalt forming the dark ring around part of Mare Serenitatis with $\text{TiO}_2 \approx 8$ percent; and a dark mantling unit which covers a region outside the Taurus-Littrow Valley, with $\text{TiO}_2 \approx 12$ to 15 percent. This map has been used to show that the dark mantling unit does not extend into the Taurus-Littrow Valley at the Apollo 17 site with nearly the concentration that exists outside the valley. This explains why only remnants of the dark mantling material were found in the Apollo 17 samples (ref. 39).

Mercury

The experience gained working with telescopic and sample measurements of the Moon gives confidence to proceed to the study of other solar system objects using the same techniques. Observations of the optical albedo and polarization of the surface of Mercury have been interpreted in the past to indicate a lunar-like surface material, dark and backscattering (ref. 43). The spectral reflectance of Mercury (fig. 9) tells a similar, but more complete, story (refs. 44 and 45). The Mercury spectrum, when compared with the spectral reflectance for typical lunar mare and upland regions, indicates a lunar-like soil.

The lunar spectral reflectivity curves for mare and upland material have two major features: a uniform positive slope and a shallow absorption band near $0.95\mu\text{m}$. A study of lunar surface material has shown that the slope of the spectral reflectivity curve for the Moon is controlled by glass containing titanium and iron in the lunar soil, and that the absorption band at $0.95\mu\text{m}$ is mainly an expression of the mineral pyroxene in the soil.

The close similarity of the features in the reflection spectra of Mercury and the Moon strongly suggests a similarity in the mineralogy and composition of their soils. Titanium- and iron-bearing glasses created by impact should be common on Mercury. This is further supported by the fact that Mercury has a low albedo similar to that for the integral nearside of the Moon. The weak

$0.95\text{-}\mu\text{m}$ absorption band in the spectra of Mercury indicates that pyroxene is the major mafic mineral responsible for the band. The presence of dark glasses suggests that titanium-rich and iron-rich minerals such as ilmenite were there to be vitrified. The $0.95\text{-}\mu\text{m}$ band suggests that some crystalline pyroxenes still remain. All of this implies a heavily impacted, mafic silicate component to the surface material of Mercury. The recent Mariner 10 images of Mercury show surface features and albedos which support this conclusion reached several years before the Mariner 10 mission was flown.

Mars

A recent review of data on the Martian spectral reflectance was presented several

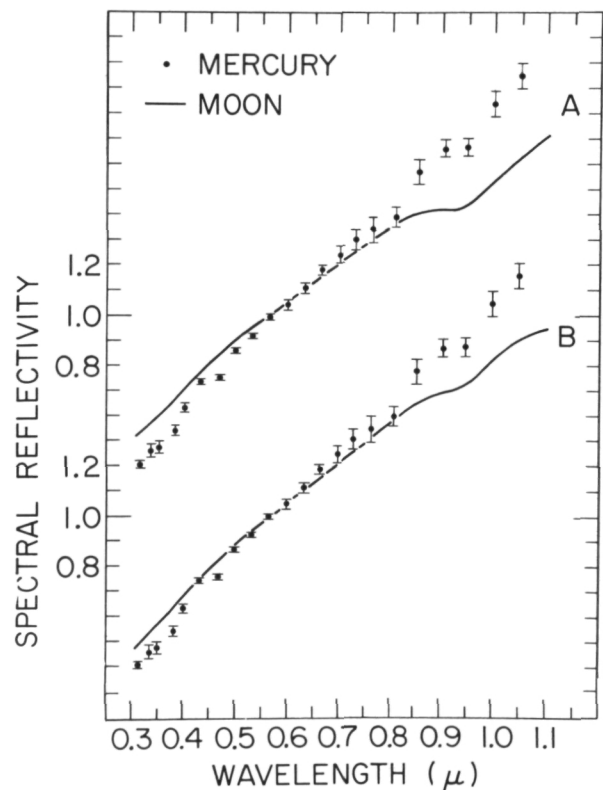


Figure 9.—The spectral reflectivity of Mercury scaled to unity at $0.564\mu\text{m}$ (filled circles) is compared with the reflection spectra for two different lunar terrains: (a) maria and (b) uplands.

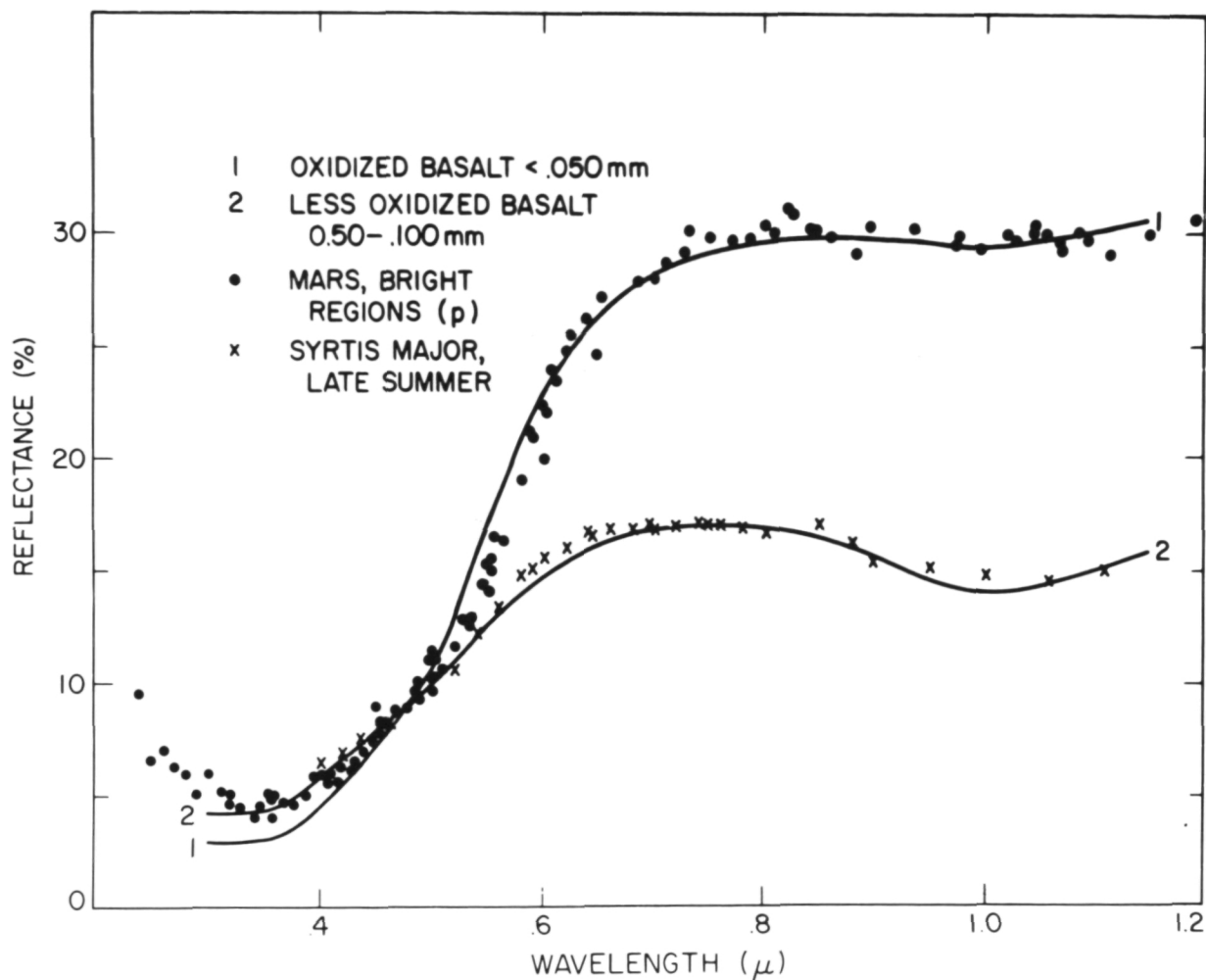


Figure 10.—Comparison of geometric albedo curves for bright and dark areas of Mars with laboratory reflectivity curves for oxidized basalt.

years ago (ref. 46). The spectral reflectance ($0.3\text{--}1.1\mu$) was developed for bright material (Arabia) and dark material (Syrtis Major) (fig. 10). The curves for the bright and the dark regions of Mars show two major absorption features. Strong absorption occurs in the blue and ultraviolet. A second absorption band centered at 1μ is stronger in the dark areas than in the bright areas. These were interpreted to indicate both regions are composed of a combination of ferric iron oxide and mafic silicate rock such as basalt (ref. 47). The line superimposed on the telescope points is the reflectance spectra of the modeling materials.

We have modeled the geometric albedo curves and the normal reflectivity curves for both the bright and dark Martian areas. It is well known from laboratory studies that the ferric oxides alone cannot match the bright-area curve. Adams (ref. 18) proposed that oxidized basaltic rock could account for the blue-UV and the 1μ absorption bands, as well as the overall curve of the bright areas. A fresh dense olivine basalt from Little Lake, California (described in ref. 17), was found to reproduce two of the essential features of the Mars curves: the 1μ band (which in this case is contributed by olivine) and a reasonable integral reflectance when

particulate. Aside from the $1\text{-}\mu$ band, the curve for this rock is essentially flat in the visible and near infrared.

To approximate the Martian curves, it was necessary to introduce the blue-UV Fe^{3+} band by adding ferric iron oxide and to adjust the integral reflectance by changing particle size. With the results of the laboratory study it was possible to achieve a close fit to the Martian curves for both the bright and dark areas (fig. 10). We were not able to approximate the Martian curves in the laboratory with any materials other than the oxidized basalt. In fact, of the eight basalts tried, only the olivine-bearing Little Lake basalt was satisfactory. Our experiments have shown that the Mars curves cannot be produced simply by various nonunique combinations of materials. If one is constrained to reproduce in the laboratory the several absorption bands and between-band structures that appear in the new Mars curves (rather than considering any single band), and, furthermore, if the modeling materials must be geochemically reasonable, then the possible solutions are severely limited.

We concluded that both the dark and the bright areas of Mars can be modeled by the same fundamental material (here the basalt), provided that the material modeling the bright regions is the more oxidized and has a smaller mean particle size ($< 50\mu$).

Spectral reflectance curves for seven Martian regions were obtained during the 1969 opposition (ref. 48). Geometric albedos were calculated for five areas between 0.3 and 1.1μ and for two additional areas between 0.3 and 2.5μ . These were compared with earlier measurements and were found consistent (ref. 49). During the 1973 opposition, approximately 25 additional Martian areas were measured between 0.3 and 1.1μ (ref. 50). Again the results are consistent with earlier data.

The spectra of three of the bright areas are presented in figure 11a. All display a strong blue-UV absorption feature, with a band center near 0.45μ , a band edge near 0.8μ , and slope changes at about 0.5μ and 0.6μ . The spectra display a weak absorp-

tion band near 0.95μ , with the reflectance at 1.1μ approximately equal to the reflectance at 0.8μ and equal to about twice the reflectance at 0.57μ . Three of the dark-area spectra are shown in figure 11b. Each of the dark-area spectra displays a blue-UV absorption feature centered near 0.45μ . The blue-UV band edge in the dark-area curves occurs near 0.7μ . There is a broad absorption envelope in the 0.9 - to $1.1\text{-}\mu$ region, with the reflectance at 1.1μ about 10 to 20 percent lower than the reflectance at 0.7μ and only about 1.3 to 1.4 times the reflectance at 0.57μ .

Mariner 9 IRIS spectra of the high albedo dust which was raised from the surface into a planetwide dust storm in 1971 (ref. 51) indicates an SiO_2 content of 60 ± 10 wt% (ref. 52) concluded from the shape and position of the $9\text{-}\mu$ Reststrahlen band that the principal constituent was montmorillonite. Both of these interpretations are consistent with one another and with the infrared spectroscopic evidence for widespread hydrate minerals on the surface (ref. 53).

The soils in the bright areas of Mars appear to be highly weathered according to both the Earth-based and spacecraft data. The reflectance spectra of 200-km-diameter spots in the dark areas indicate that the soils in these regions are not as weathered. The presence of clay minerals (kaolinite, montmorillonite) are consistent with our early analysis and a more recent analysis (ref. 54) of the new reflectance data, although more work is needed before a detailed interpretation can be given. It is clear that hydrated iron oxide is present.

One model which has been generally suggested to account for the presence of ferric oxides and widespread hydrate minerals is that these materials are metastably preserved from an early epoch when Mars had a wetter, more oxidizing Earth-like environment. An alternative model has been proposed by Huguenin (ref. 55), who suggests that the present-day Martian surface environment has a sufficiently high oxidation potential.

Based on a series of laboratory experi-

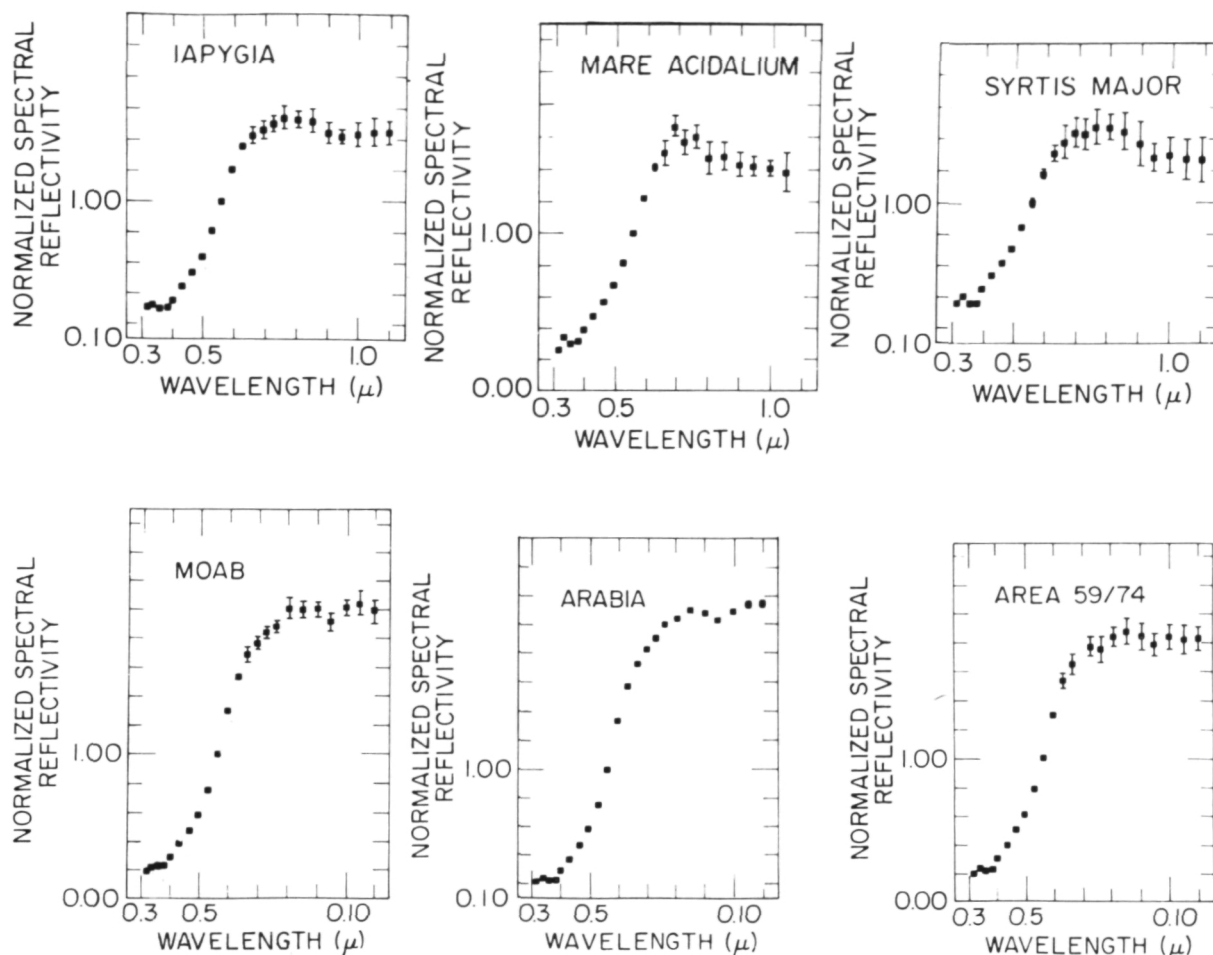


Figure 11.—Spectral reflectance for three bright regions (lower plots) and three dark regions (upper plots) about 200 km in diameter on the surface of Mars. See reference 49 for location.

ments, Huguenin (refs. 55, 56, and 57) predicts that reduced-state metal oxides (magnetite, ilmenite) and ferrosilicates alter to hydroxylated and hydrated oxides and clay minerals upon exposure to absorbed H_2O , solar UV-illumination, atmospheric O_2 , and eolian abrasion, through a process called "photostimulated oxidation weathering."

In an attempt to map the spectra features found to indicate composition on the Martian surface, the same vidicon digital imaging system used on the Moon was used to observe Mars during the fall of 1973. Although many images were obtained through interference filters centered at 25 wavelengths between 0.34 and 1.1μ , only a few have been analyzed at this writing. The series of images

shown in figure 12 indicates the quality of images possible with 1-percent photometer precision. The clouds and dust storms visible reveal an unexpected bonus from this type of two-dimensional photometry. These images are presently being used to determine characteristics of dust clouds and related surface material.

The Asteroids

It has long been realized that studies of the colors of asteroids provide useful clues to their composition (refs. 58 through 62). Until recently, attempts to determine asteroid composition by comparing color indices

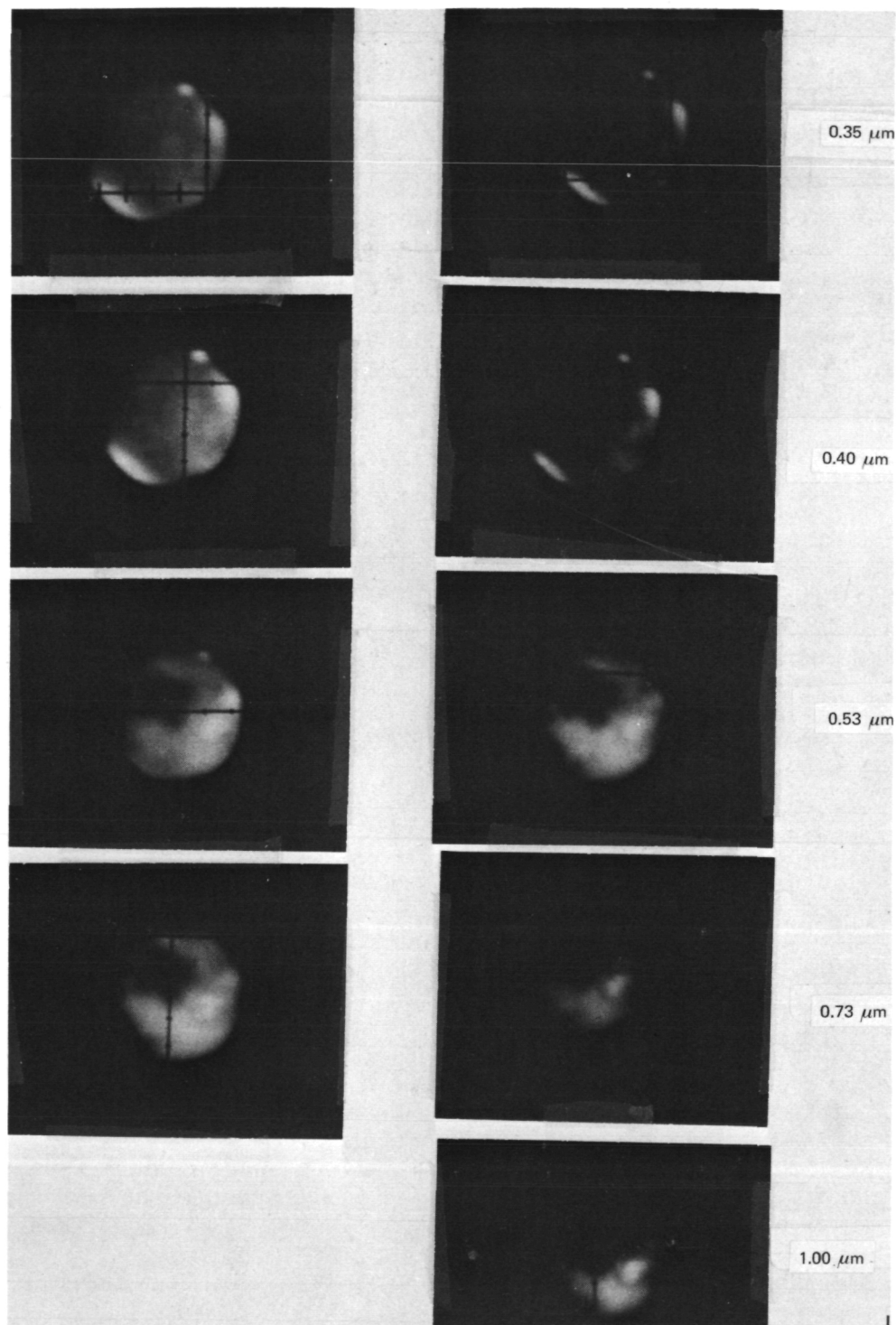


Figure 12.—Photographic representations of a series of digital images of Mars using the MITPAL silicon vidicon imaging system. Images were made through interference filters centered at 0.35, 0.40, 0.53, 0.73, and 1.00 μm using the 88-in telescope at Mauna Kea Observatory, Hawaii, during the 1973 opposition. Surface features and clouds are visible.

for asteroids with spectral reflectivities or color indices for meteorites and terrestrial rocks have not been fruitful (ref. 10). It has been noted that the mean color indices for asteroids fall within the range for rocks and meteorites. However, there are far too many minerals for a one-dimensional characterization of asteroid color (color index) to suggest even a compositional class, let alone a specific composition.

McCord, Adams, and Johnson (ref. 1) reported on the observation and analysis of the spectral reflectance of the asteroid Vesta between 0.32 and 1.1 μ m, with spectral resolu-

tion and photometer precision sufficient to show a number of important absorption features. A strong absorption band is centered near 0.9 μ m, and a weaker absorption feature appears between 0.5 and 0.6 μ m. The reflectance decreases strongly in the ultraviolet. The strong 0.9- μ band arises from electronic absorptions in ferrous iron on the M2 site of a magnesian pyroxene. Comparison with laboratory measurements on meteorites and Apollo samples indicates that the surface of Vesta has a composition very similar to that of certain basaltic achondrite meteorites (fig. 13).

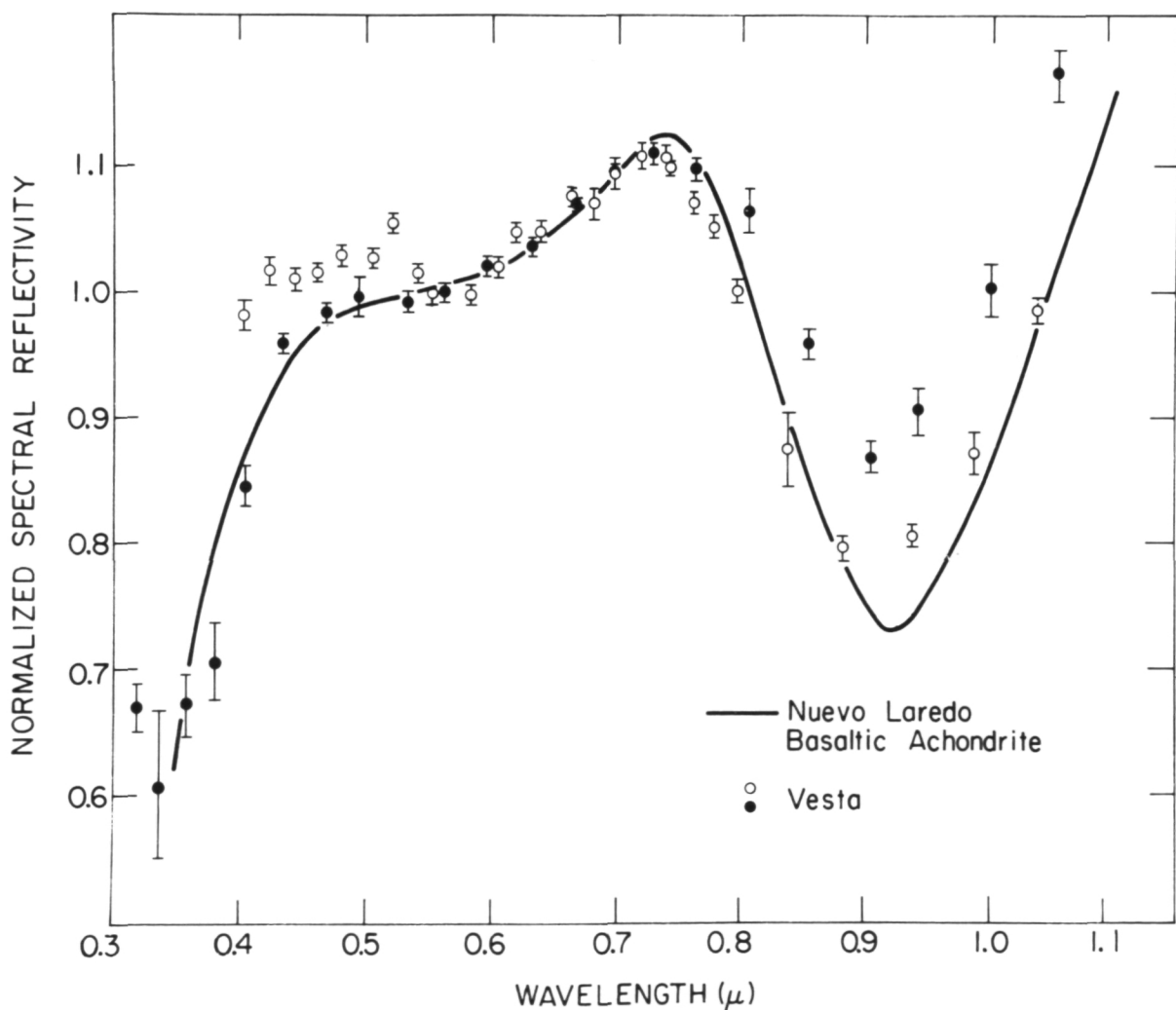


Figure 13.—Laboratory measurements of the spectral reflectivity of the Nuevo Laredo meteorite shown with the telescope data.

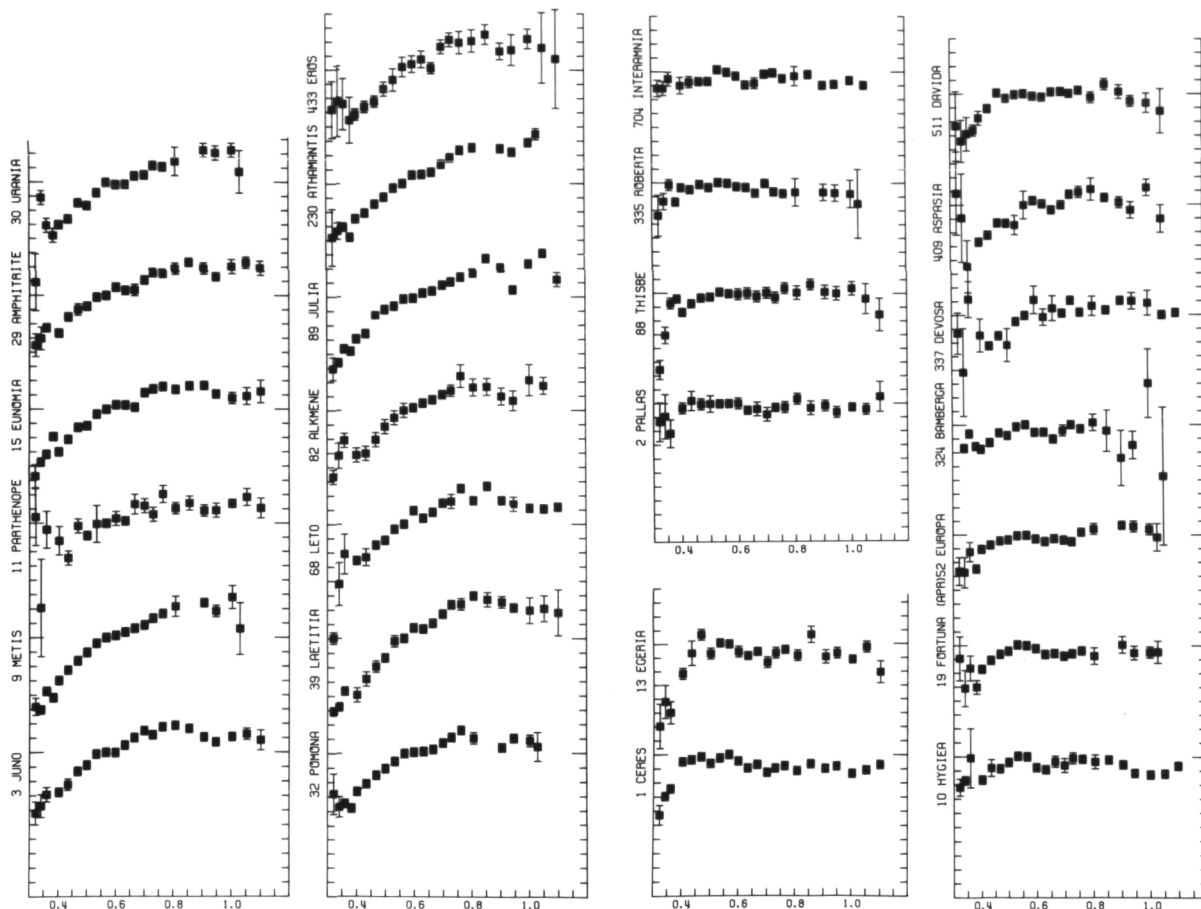


Figure 14a,b.—Spectral reflectance of several asteroids showing a variety of curve shapes.

An extensive program has been underway in our laboratories since this discovery to obtain reflection spectra for many asteroids using ground-based telescopes. So far, about 100 asteroids have been observed (refs. 10, 63, and 64). Various spectral reflectance curves for asteroids are shown in figure 14.

The early work with Vesta has suggested the direct relation between meteorites and asteroids. The mineral assemblages found in meteorites should, on cosmochemical arguments, represent a mineralogical and petrological series which shares many of the compositional characteristics of asteroidal material. Therefore, to expand the laboratory and theoretical basis for interpreting the reflectance spectra for asteroids, a study was made of the optical properties of 156

meteorite specimens from essentially all meteorite classes (refs. 26 and 27). The meteorite spectra are grouped in figure 15 according to class and therefore according to mineralogy. Note that the variation of the spectra within a class is less than the differences between classes. Metamorphic grading and changes in mineralogy through the classes are easily seen in the spectra.

The reflectance characteristics of meteorite curves are understandable in terms of the type, composition, abundance, and distribution of the component mineral phases. Four classes of minerals can be defined on the basis of their contribution to spectra of mixtures of phases: metals, opaques, and silicates with and without transition metal ions such as Fe^{2+} . The effect a mineral has on the

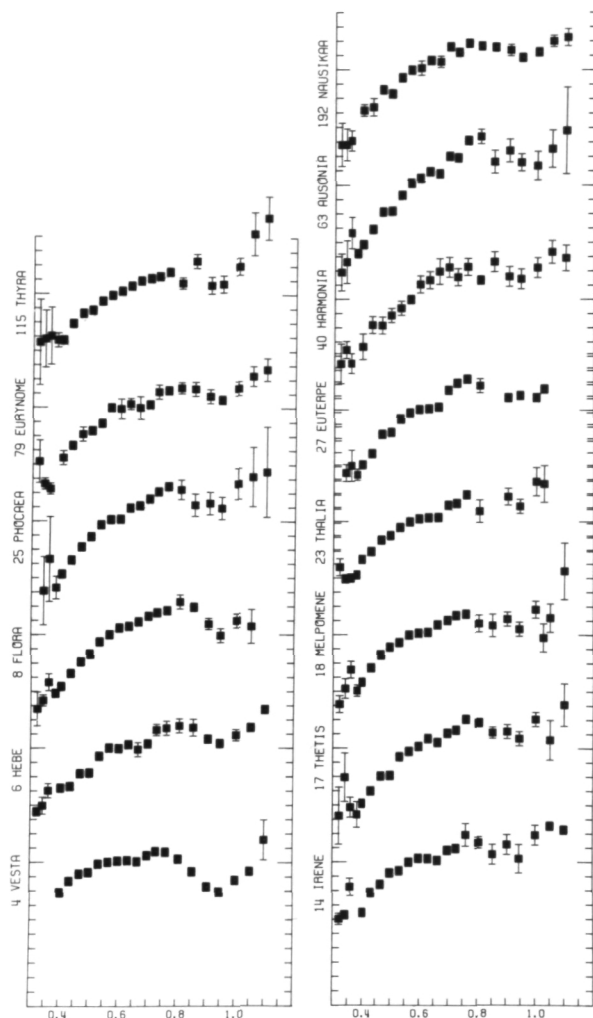


Figure 14c.—Spectral reflectance of several asteroids showing a variety of curve shapes.

spectrum is approximately proportional to its abundance and its optical density in the spectral region of interest. Opaques, most commonly represented by carbon and the carbon compounds, tend to dominate a spectrum even when present in small quantities (a few percent). Opaques produce low reflectances throughout the visible and infrared spectrum and have a relatively strong ultraviolet absorption. Silicates containing transition metal ions (pyroxene, olivine, feldspar) exhibit crystal field absorption features near 1μ . The wavelength position of the bands depends on the composition of the mineral.

These silicates are also characterized by increasingly more efficient charge transfer absorptions as one moves toward higher energies. Metals (Fe, Ni) become steadily more reflective toward longer wavelengths and exhibit a very nearly linear change in reflectance with energy.

Previous spectral reflectance work on meteoritic materials, primarily by Hunt and Salisbury (ref. 65), Chapman and Salisbury (ref. 66), and Johnson and Fanale (ref. 67), provides good agreement with this work in the areas where there is overlap.

The philosophy applied in our study (ref. 68) is to interpret absorption features in the asteroid curves in terms of the minerals producing or modifying each feature. A set of features reveals a suite of minerals, which defines a rock type in many cases. This rock type may or may not conform to the definition of an established meteorite class. This approach does not rely on the match of asteroid spectra with meteorite spectra. The meteorite sample material, which is used to study the optical properties of solids, is used as a source of mineral assemblages which are cosmochemically reasonable to occur in the asteroid belt. Blind curve matching without understanding the physical explanation for each spectral feature often leads to error.

The interpretation of two asteroid reflection spectra is treated here (fig. 16). The same procedure has been applied to other spectra (ref. 68).

1 Ceres: The uniform visible and infrared reflectance and the strong ultraviolet absorption indicates, and for meteoritic material is characteristic only of, the higher grade carbonaceous chondrites (right column, bottom). Ceres' surface is composed of a mineral assemblage rich in opaque material (probably carbon) and probably is a type of carbonaceous chondrite material.

3 Juno: This spectrum is characterized by a more or less linear increase in reflectance with wavelength, a relatively strong, broad, asymmetric absorption near 1.0μ m, and a weak absorption near 0.6μ m. The linear reddening indicates a large metal component, and the absorption features near 0.60, 0.95,

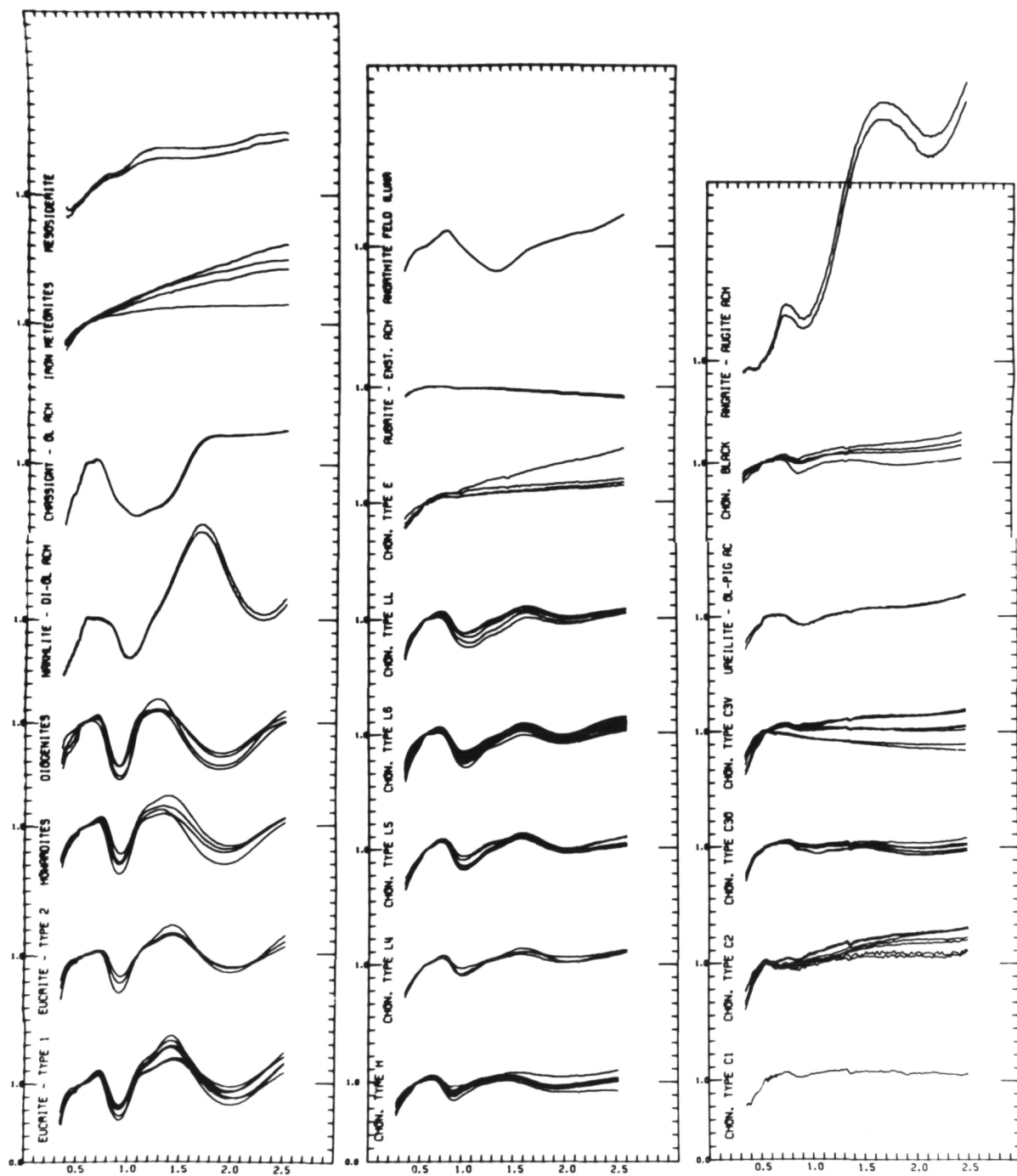


Figure 15.—Spectral reflectance of 156 meteorite specimens grouped according to mineralogy and meteorite class. All samples were carefully studied to eliminate weathered or otherwise damaged samples.

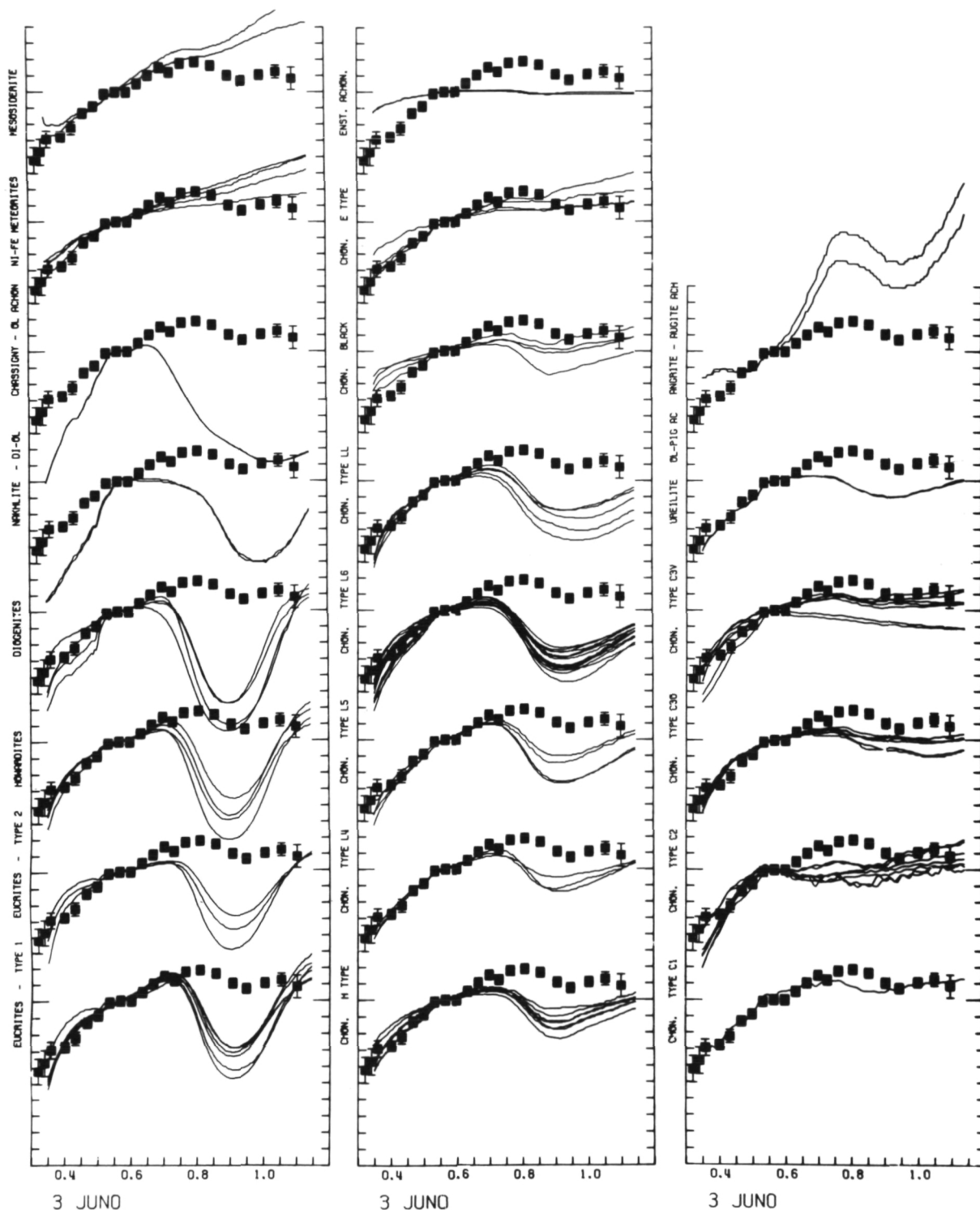


Figure 16b.—Spectral reflectance for 3 Juno superimposed on the spectra for 156 meteorites. The meteorite spectra are arranged according to class. Reflectance is plotted against wavelength in micrometers. Each division in reflectance is 0.1. All curves are sealed to unity at $0.56 \mu\text{m}$.

and 1.1μ indicates plagioclase, pyroxene, and olivine, respectively. The modification of the spectrum of an iron meteorite by the addition of the silicate absorption would produce the best agreement with meteorite material. This is an example where the direct matching technique is inappropriate and would produce spurious results.

The preliminary analysis that has been made indicates several conclusions about the asteroids. The mineral assemblages that appear to compose the asteroids are similar to those found in meteorites. However, it is clear that the population of meteorite classes is not the same as for asteroids. For example, in the asteroid belt there appear to be many objects with composition similar to carbonaceous chondrites, but very few objects simi-

lar to ordinary chondrite meteorites, unlike the distribution of compositions of meteorites. The one asteroid measured with a chondritic surface is Toro (ref. 63), an Apollo asteroid. This may be a hint of the origin of most meteorites.

It also appears that asteroids are mostly homogeneous over their surfaces; i.e., all sides seem to have similar composition. There is little difference in the spectral reflectance with rotational phase for the vast majority of asteroids measured. However, there are striking differences among asteroids. Inner-belt asteroids appear to be more commonly of high-grade iron-silicate composition, while outer-belt asteroids are more often of more primitive carbonaceous chondrite nature.

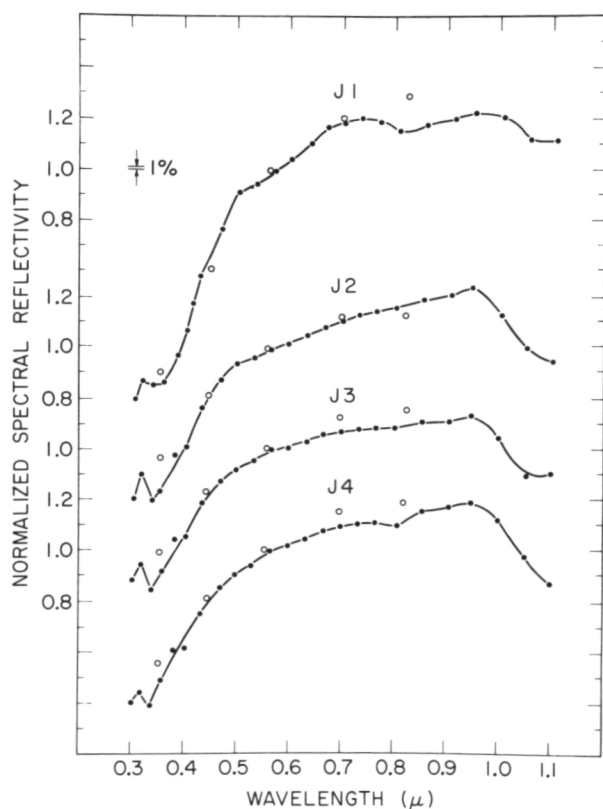
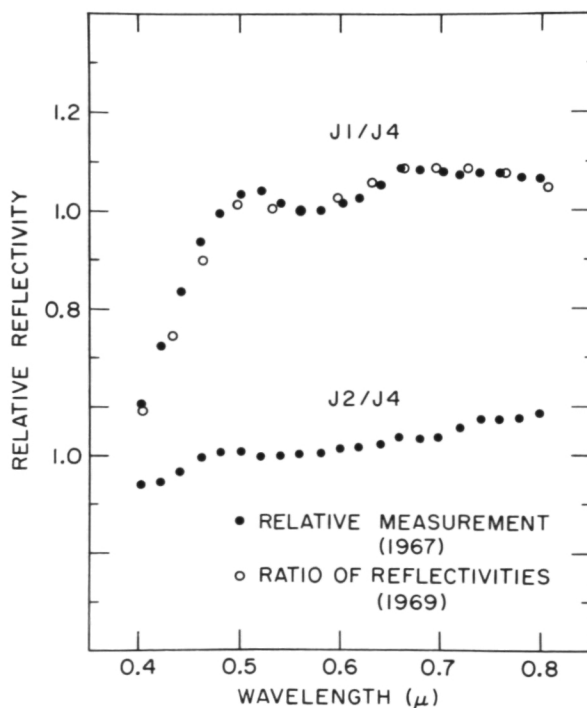


Figure 18.—Normalized relative reflectivities for J1 versus J4 and J2 versus J4. Filled circles are direct double-beam measurements, and the open circles are ratios of individual reflectivity curves.

Figure 17.—Normalized spectral reflectivity 0.3 to 1.1μ for the Galilean satellites.



Jupiter Satellites

In the outer solar system we see a different kind of material than is present in the inner solar system. For example, in figure 17 is shown the spectral reflectance for the Galilean satellites, the four largest satellites of Jupiter. They are the only ones bright enough to be easily studied. The spectral reflectance for the 0.3 to 1.1 μm spectral region (refs. 69 and 70) is unlike any spectrum seen so far in this discussion (fig. 17). The strong UV absorption is reminiscent of the

charge transfer feature found for iron silicates, but the match is really quite poor. The shallow absorption band seen (especially for Io) (fig. 18) between 0.5 and 0.6 μm was also a puzzle.

The reflection spectrum was measured more recently from 1.0 to 2.5 μm (refs. 71 and 72) (fig. 19). Water frost absorptions were detected in the infrared reflectivities of Jupiter's Galilean satellites JII (Europa) and JIII (Ganymede). The percentage of frost-covered surface area was determined to be 50 to 100 percent for JII, 20 to 65 percent

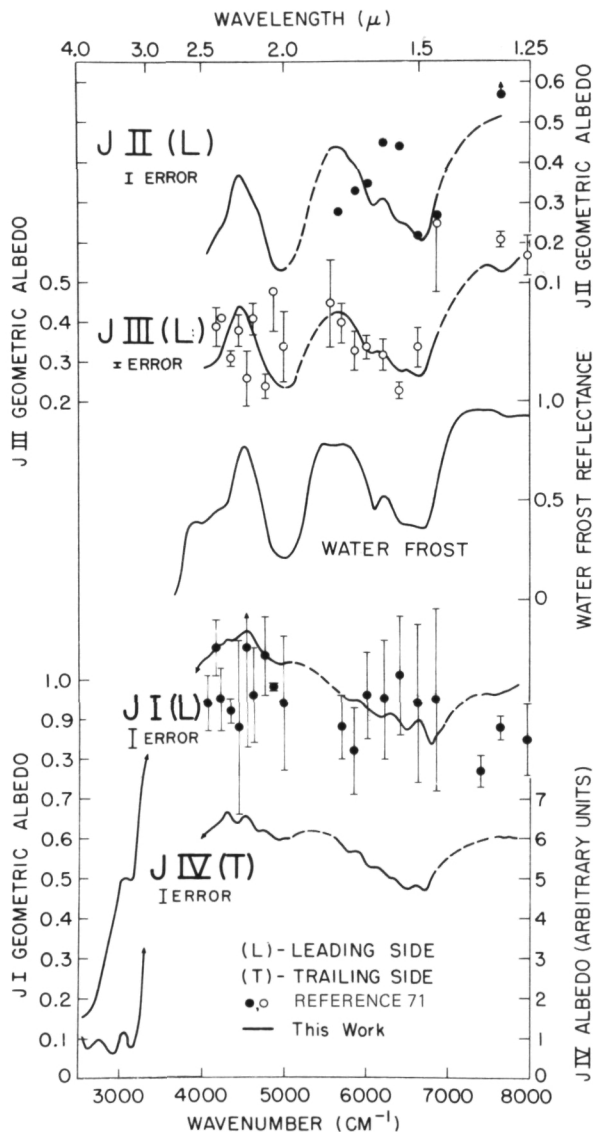


Figure 19a.—Reflectivities of the Galilean satellites and water frost. The reflectivities of JI, JII, and JIII have been scaled approximately to the geometric albedos of Johnson and McCord (ref. 71). Each error bar is the average of the standard deviations for all wavelengths. The intensities of the reflectivities of JI and JIV between 2500 and 3300 cm^{-1} are reduced to an MgO standard.

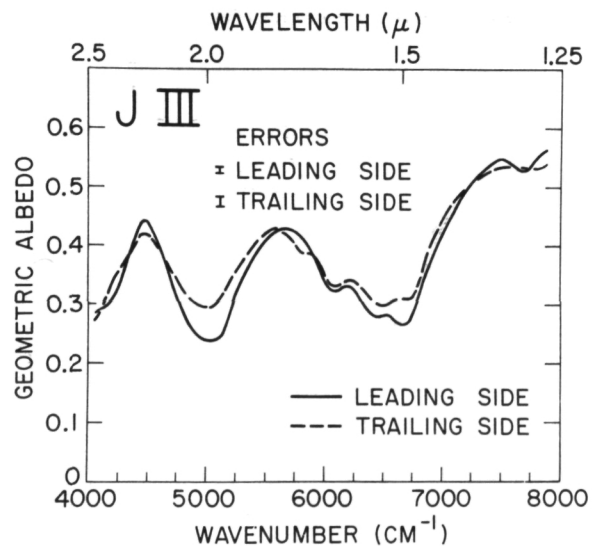


Figure 19b.—The reflectivities of the leading and trailing sides of JIII scaled to the same value at 5625 cm^{-1} . Both reflectivities are also scaled to the geometric albedos of Johnson and McCord (ref. 71). Each error bar is the average of the standard deviations for all wavelengths.

for JIII, and possibly 5 to 25 percent for JIV (Callisto). The leading side of JIII has 20 percent more frost cover than the trailing side, which explains the visible geometric albedo differences between the two sides. The reflectivity of the material underlying the frost on JII, JIII, and JIV resembles that of silicates. The surface of JI (Io) may be covered by frost particles much smaller than those on JII and JIII.

But the visible spectrum does not look anything like it should for water ice. Lebofsky (ref. 73), following suggestions from work

by Lewis (refs. 74 and 75) and considerably expanding on some early work by Sills at the University of Arizona, studied the optical properties of sulfur-contaminated ices. Lebofsky irradiated these compounds with solar-like ultraviolet flux and observed color properties similar to the satellites.

Saturn Rings

The rings show a reflection spectrum quite similar to those for the Galilean satellites of

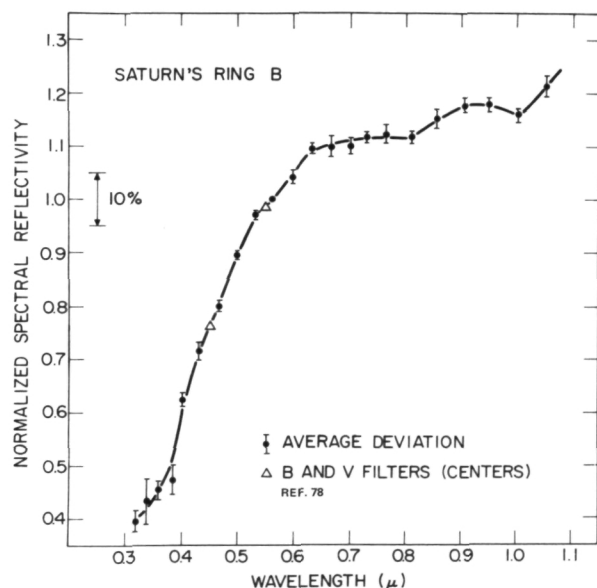
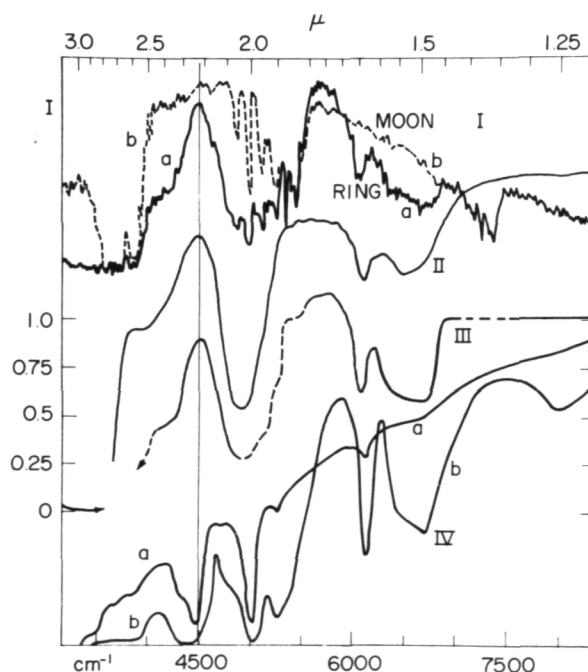


Figure 21.—Comparison of reflectance spectra for H_2O and NH_3 frosts and Saturn's rings. The major region of disagreement between the ring and NH_3 frost spectra is indicated by a vertical line at 2.22μ (4500 cm^{-1}). With the exception of curve III, the vertical axis is not calibrated, and sloping trends can be ignored for purposes of comparison. The vertical calibration for curve III is along the left side of the figure. Curve Ia—the Saturn ring spectrum. Curve Ib—lunar comparison spectrum. Curve II—fine-grained H_2O frost spectrum. $\Delta\lambda \approx 0.05 \mu$, $\lambda < 1.58 \mu$; $\Delta\lambda \approx 0.03 \mu$, $\lambda > 1.58 \mu$. Curve III—normalized Saturn ring spectrum (Ia divided by Ib): the dashed portions of the curve indicate regions affected telluric absorption. There is a gap in the curve near the saturated $2.7\text{-}\mu$ telluric band. Curve IV— NH_3 frost spectra: (IVa) fine-grained frost; (IVb) coarse-grained frost; same resolution as in curve II.

Figure 20.—The normalized reflectivity of Saturn's ring B as a function of wavelength is shown. Each point represents an average of measurements through one interference filter. The standard deviation of the average value is shown as an error bar. A smooth curve has been drawn through the data points (see ref. 78).



Jupiter. Between 0.3 and 1.1 μm (refs. 76 and 77) (fig. 20) there appears the strong UV absorption. The infrared reflection spectrum (ref. 79) contains strong water-ice bands (ref. 80) (fig. 21). Probably the same interpretation applies as for the Galilean satellites.

Saturn Satellites

The spectral reflectance for the satellites observed is flat and featureless (ref. 76) (fig. 22). Two possibilities exist based on our past experience. The spectra are consistent with uncontaminated solid water or ammonia and these are cosmochemically quite reasonable materials. The data for the spectral region available are also consistent with carbonaceous chondritic material, another reasonable material. Spectra for the ultraviolet spectral region should determine this uncertainty (see the section on asteroids). If the conclusion is ice for the composition of the surfaces of these objects, why are the ring particles contaminated and radiation damaged and the satellites not? Perhaps because of a Saturnian magnetic field.

General Comments

The data are not complete enough to discuss the remaining solar system objects that have visible solid surfaces (outer planet satellites and Pluto). Clearly these objects deserve more study considering what has been thus far possible. But measurements are difficult because of their faintness and, often, their close proximity to bright planets.

The composition of solar system objects is one of the more fundamental properties to aid in unraveling the origin and evolution of the solar system. It is our hope that this exciting task will be easier with the development of this new remote sensing technique.

References

1. McCORD, T. B., J. B. ADAMS, AND T. V. JOHNSON, Asteroid Vesta: Spectral Reflectivity and Com-

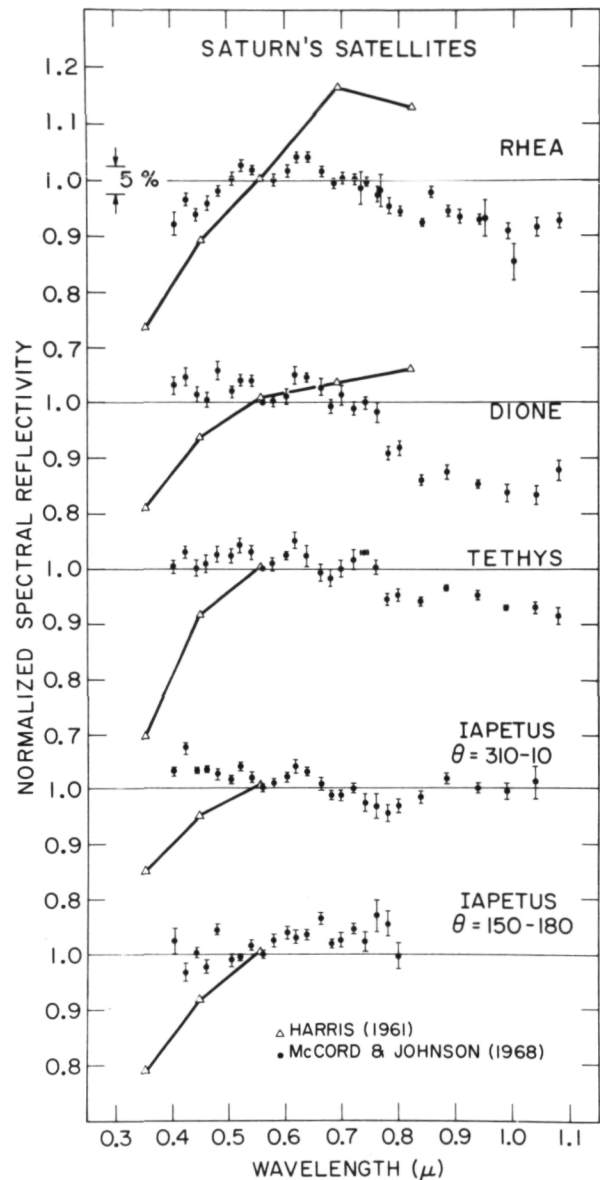


Figure 22.—Spectral reflectance of Saturn's satellites scaled to unity at 0.56 μm .

- positional Implications. *Science*, Vol. 168, 1970, p. 1445.
2. McCORD, T. B., *Color Differences of the Lunar Surface*. Ph.D. dissertation, Calif. Inst. of Technol., Pasadena, Calif., 1968.
3. McCORD, T. B., AND J. A. WESTPHAL, A Two-Dimensional Silicon Vidicon Astronomical Photometer. *Applied Optics*, Vol. 11, 1972, p. 522.
4. McCORD, T. B., AND J. BOSEL, Silicon Vidicon Astronomy at MIT. *Astronomical Observa-*

- tions With Television Type Sensors, J. W. Glaspey, and G. A. H. Walker, eds., Institute of Astronomy, Univ. of B.C., Vancouver, 1973, pp. 137-161.
5. OKE, J. B., Photoelectric Spectrophotometry of Stars Suitable for Standards. *Astrophys. J.*, Vol. 140, 1964, p. 689.
 6. SCHILD, R., D. M. PETERSON, AND J. B. OKE, Effective Temperatures of B- and A-Type Stars. *Astrophys. J.*, Vol. 166, 1971, p. 95.
 7. OKE, J. B., AND R. E. SCHILD, The Absolute Spectral Energy Distribution of Alpha Lyrae. *Astrophys. J.*, Vol. 161, 1970, p. 1015.
 8. HAYES, D. S., An Absolute Spectrophotometric Calibration of the Energy Distribution of Twelve Standard Stars. *Astrophys. J.*, Vol. 159, 1970, p. 165.
 9. ARVESEN, J. C., R. N. GRIFFIN, AND B. D. PEARSON, JR., Determination of Extraterrestrial Solar Spectral Irradiance From a Research Aircraft. *Applied Optics*, Vol. 8, 1969, p. 2215.
 10. CHAPMAN, C. R., T. B. MCCORD, AND T. V. JOHNSON, Asteroidal Spectral Reflectivities. *Astron. J.*, Vol. 78, 1973, p. 1.
 11. ELIAS, J., *Calibration of Standard Stars for Planetary Reflectivity Studies*. Masters dissertation, M.I.T., Cambridge, Mass., 1972.
 12. BURNS, R. G., *Electronic Spectra of Silicate Minerals: Application of Crystal-Field Theory to Aspects of Geochemistry*. Unpublished Ph.D. thesis, U. of Calif., Berkeley, Calif., 1965.
 13. BURNS, R. G., *Mineralogical Applications of Crystal-Field Theory*, Cambridge U. Press, Cambridge, England, 1970.
 14. WHITE, W. B., AND K. L. KEESTER, Optical Absorption Spectra of Iron in the Rock-Forming Silicates. *Am. Mineralogist*, Vol. 51, 1966, pp. 774-791.
 15. WHITE, W. B., AND K. L. KEESTER, Selection Rules and Assignments for the Spectra of Ferrous Iron in Pyroxenes. *Am. Mineralogist*, Vol. 52, 1967, pp. 1508-1514.
 16. BANCROFT, G. M., AND R. G. BURNS, Interpretation of the Electronic Spectra of Iron in Pyroxenes. *Am. Mineralogist*, Vol. 52, 1967, pp. 1278-1287.
 17. ADAMS, J. B., AND A. L. FILICE, Spectral Reflectance 0.4 to 2.0 Microns of Silicate Rock Powders. *J. Geophys. Res.*, Vol. 72, 1967, pp. 5705-5715.
 18. ADAMS, J. B., Lunar and Martian Surfaces: Petrologic Significance of Absorption Bands in the Near-Infrared. *Science*, Vol. 159, 1968, pp. 1453-1455.
 19. HUNT, G. R., AND J. W. SALISBURY, Visible and Near-Infrared Spectra of Minerals and Rocks: I. Silicate Minerals. *Modern Geol.*, Vol. 1, 1970, pp. 283-300.
 20. HUNT, G. R., AND J. W. SALISBURY, Visible and Near-Infrared Spectra of Minerals and Rocks: II. Carbonates. *Modern Geol.*, Vol. 2, 1971, pp. 23-30.
 21. HUNT, G. R., J. W. SALISBURY, AND C. J. LENHOFF, Visible and Near-Infrared Spectra of Minerals and Rocks: III. Oxides and Hydroxides. *Modern Geol.*, Vol. 2, 1971, pp. 195-205.
 22. HUNT, G. R., J. W. SALISBURY, AND C. J. LENHOFF, Visible and Near-Infrared Spectra of Minerals and Rocks: IV. Sulphides and Sulphates. *Modern Geol.*, Vol. 3, 1971, pp. 1-14.
 23. HUNT, G. R., J. W. SALISBURY, AND C. J. LENHOFF, Visible and Near-Infrared Spectra of Minerals and Rocks: V. Halides, Phosphates, Arsenates, Vanadates and Borates. *Modern Geol.*, Vol. 3, 1972, pp. 121-132.
 24. ADAMS, J. B., Uniqueness of Visible and Near-Infrared Diffuse Reflectance Spectra of Pyroxenes and Other Rock-Forming Minerals. In *Infrared and Raman Spectroscopy of Lunar and Terrestrial Minerals*, Kerr, ed., Academic Press, in press, 1974.
 25. ADAMS, J. B., Visible and Near-Infrared Diffuse Reflectance Spectra of Pyroxenes as Applied to Remote Sensing of Solid Objects in the Solar System. *J. Geophys. Res.*, in press, 1974.
 26. GAFFEY, M. J., *A Systematic Study of the Spectral Reflectivity Characteristics of the Meteorite Classes with Application to the Interpretation of Asteroid Spectra for Mineralogical and Petrological Information*, Ph.D. thesis, M.I.T., Cambridge, Mass., February 1974.
 27. GAFFEY, M. J., *Spectral Reflectance Characteristics of the Meteorite Classes*, in preparation, 1974.
 28. BURNS, R. G., AND D. J. VAUGHAN, Polarized Electronic Spectra. In *Infrared and Raman Spectroscopy of Lunar and Terrestrial Minerals*, Academic Press, in press, 1974.
 29. BELL, P. M., H. K. MAO, AND G. R. ROSSMAN, Absorption Spectroscopy of Ionic and Molecular Units in Crystals and Glasses. In *Infrared and Raman Spectroscopy of Lunar and Terrestrial Minerals*, Kerr, ed., Academic Press, in press, 1974.
 30. GAFFEY, M. J., AND R. G. BURNS, *The Angular Dependence of Photon-Electron Interaction in Transition Metal Silicates*, in preparation, 1974.
 31. MCCORD, T. B., Color Differences on the Lunar Surface. *J. Geophys. Res.*, Vol. 74, 1969, p. 12.
 32. MCCORD, T. B., AND T. V. JOHNSON, Spectral Lunar Reflectivity (0.30 to 2.50 Microns) and Implications for Remote Mineralogical Analysis. *Science*, Vol. 169, 1970, p. 855.
 33. ADAMS, J. B., AND T. B. MCCORD, Remote Sensing of Lunar Surface Mineralogy; Implications From Visible and Near-Infrared Reflectivity of Apollo 11 Samples. In *Proc. Apollo 11 Lunar*

- Science Conference*, Vol. 3, A. A. Levinson, ed., 1970.
34. CONEL, J. E., Coloring of Synthetic and Natural Lunar Glass by Titanium and Iron. *Jet Propulsion Laboratory Space Programs Summary*, Vol. 3, 1970, pp. 26-31.
 35. CONEL, J. E., AND D. B. NASH, Spectral Reflectance and Albedo of Apollo 11 Lunar Samples: Effects of Irradiation and Vitrification and Comparison with Telescopic Observations. *Proc. Apollo 11 Lunar Science Conference, Geochimica et Cosmochimica Acta*, Supplement 1, Vol. 3, 1970, pp. 2013-2023.
 36. ADAMS, J. B., AND T. B. MCCORD, Optical Properties of Mineral Separates, Glass and Anorthositic Fragments from Apollo Mare Samples. In *Proc. Second Lunar Science Conference*, Vol. 3, A. A. Levinson, ed., 1971.
 37. MAO, H. K., D. VIRGO, AND P. M. BELL, Sample 74220: Analysis of the Apollo 17 Orange Soil From Shorty Crater. *EOS, Trans. Am. Geophys. Union*, Vol. 54, 1973, pp. 598-599.
 38. CHARETTE, M. P., T. B. MCCORD, C. PIETERS, AND J. B. ADAMS, Application of Remote Spectral Reflectance Measurements to Lunar Geology Classification and Determination of Titanium Content of Lunar Soils. *J. Geophys. Res.*, Vol. 79, 1974, p. 1239.
 39. PIETERS, C., T. B. MCCORD, M. CHARETTE, AND J. B. ADAMS, Dark Mantling Material in the Apollo 17 Soil Samples. *Science*, Vol. 183, 1974, p. 1191.
 40. ADAMS, J. B. AND T. B. MCCORD, Alteration of Lunar Optical Properties: Age and Composition Effects. *Science*, Vol. 171, 1971, p. 567.
 41. ADAMS, J. B., AND T. B. MCCORD, Electronic Spectra of Pyroxene and Interpretation of Telescopic Reflectivity Curves of the Moon. In *Proc. Third Lunar Science Conference*, Vol. 3, D. R. Criswell, ed., 1972.
 42. ADAMS, J. B. AND T. B. MCCORD, Vitricification Darkening in the Lunar Highlands and Identification of Descartes Material at the Apollo 16 Site. *Proc. Fourth Lunar Conference*, Vol. 1, 1973, p. 163.
 43. DOLLFUS, A., Resultats Recents sur les Planetes Mercury, Venus et Mars Obtenus par les Observations Astronomiques au Sol. In *Moon and Planets*, Vol. II, A. Dollfus, ed., North-Holland Publishing Co., Amsterdam, 1967.
 44. MCCORD, T. B., AND J. B. ADAMS, Mercury: Surface Composition From the Reflection Spectrum. *Science*, Vol. 178, 1972, p. 745.
 45. MCCORD, T. B., AND J. B. ADAMS, Mercury: Interpretation of Optical Observations. *Icarus*, Vol. 17, 1972, p. 585.
 46. MCCORD, T. B., AND J. B. ADAMS, The Spectral Reflectivity of Mars. *Science*, Vol. 163, 1969, p. 1058.
 47. ADAMS, J. B., AND T. B. MCCORD, Mars: Interpretation of Spectral Reflectivity of Light and Dark Regions. *J. Geophys. Res.*, Vol. 74, 1969, pp. 4851-4856.
 48. MCCORD, T. B., AND J. A. WESTPHAL, Mars: Narrowband Photometry 0.3 to 3.5 Microns of Surface Regions During the 1969 Apparition. *Ap. J.*, Vol. 168, 1971, pp. 143-153.
 49. MCCORD, T. B., J. ELIAS, AND J. A. WESTPHAL, Mars: Spectral Albedo (0.3 to 2.5 Microns) of Small Bright and Dark Regions. *Icarus*, Vol. 14, 1971, pp. 245-251.
 50. MCCORD, T. B., C. PIETERS, AND R. L. HUGUENIN, in preparation.
 51. HANEL, R., B. CONRATH, W. HOVIS, V. KUNDE, P. LOWMAN, W. MAGUIRE, J. PEARL, J. PIRAGLIA, C. PRABHAKARA, B. SCHLACHMAN, G. LEVIN, P. STRAAT, AND T. BURKE, Investigation of the Martian Environment by Infrared Spectroscopy on Mariner 9. *Icarus*, Vol. 17, 1972, p. 423.
 52. HUNT, G. R., L. M. LOGAN, AND J. W. SALISBURY, Mars: Components of Infrared Spectra and the Composition of the Dust Cloud. *Icarus*, Vol. 18, 1973, p. 459.
 53. HOUCK, J. R., J. B. POLLACK, C. SAGAN, D. SCHAAK, AND J. A. DECKER, JR., High Altitude Infrared Spectroscopic Evidence for Bound Water on Mars. *Icarus*, Vol. 18, 1973, p. 470.
 54. HUGUENIN, R. L., T. B. MCCORD, AND J. B. ADAMS, in preparation.
 55. HUGUENIN, R. L., Photo-Stimulated Oxidation of the Martian Surfaces. *J. Geophys. Res.*, in press, 1974.
 56. HUGUENIN, R. L., Photo-Stimulated Oxidation of Magnetite: 1. Kinetics and Alteration Phase Identification. *J. Geophys. Res.*, Vol. 78, 1973, p. 8481.
 57. HUGUENIN, R. L., Photo-Stimulated Oxidation of Magnetite: 2. Mechanism. *J. Geophys. Res.*, Vol. 78, 1973, p. 8495.
 58. SANDAKOVA, E. V., Concerning Color Indices of Minor Planets. *Astron. Circ., Acad. Sci. U.S.S.R.*, 1955, p. 163.
 59. SANDAKOVA, E. V., Interpretation of Color Indices of Minor Planets. *Pub. Kiev Univ. Astron. Obs.*, Vol. 8, 1959.
 60. SANDAKOVA, E. V., Concerning the Color Indices of Minor Planets. *Pub. Kiev Univ. Astron. Obs.*, Vol. 10, 1962.
 61. WATSON, F. G., *Small Bodies and the Origin of the Solar System*. Ph.D. dissertation, Harvard University, Cambridge, Mass., 1938.
 62. KITAMURA, M., A Photoelectric Study of Colors of Asteroids and Meteorites. *Pub. Astron. Soc. Japan*, Vol. 11, 1959, pp. 79-89.
 63. CHAPMAN, C. R., T. B. MCCORD, AND C. PIETERS, Spectrophotometric Study of the Composition of (1685) Toro. *Astron. J.*, Vol. 78, 1973, p. 502.

64. MCCORD, T. B., AND C. R. CHAPMAN, Asteroid Spectral Reflectivities: II. To be submitted to *Astro. Phys. J.*, 1973.
65. HUNT, G. R., AND J. W. SALISBURY, Visible and Near-Infrared Spectra of Minerals and Rocks: VIII. Meteorites. In preparation, 1974.
66. CHAPMAN, C. R., AND J. W. SALISBURY, Comparison of Meteorite and Asteroid Spectral Reflectivities. *Icarus*, Vol. 19, 1973, p. 507.
67. JOHNSON, T. V., AND F. P. FANALE, Optical Properties of Carbonaceous Chondrites and Their Relationship to Asteroids. *J. Geophys. Res.*, Vol. 78, 1973, p. 8507.
68. MCCORD, T. B., AND M. J. GAFFEY, Asteroids: Surface Composition Using Reflection Spectroscopy. Submitted to *Science*, 1974.
69. JOHNSON, T. V., AND T. B. MCCORD, Galilean Satellites: The Spectral Reflectivity 0.30–1.10 Micron. *Icarus*, Vol. 13, 1970, pp. 37–42.
70. JOHNSON, T. V., Galilean Satellites: Narrowband Photometry 0.30 to 1.10 Microns. *Icarus*, Vol. 14, 1971, p. 94.
71. JOHNSON, T. V., AND T. B. MCCORD, Spectral Albedo of the Galilean Satellites—0.3–2.5 Microns. *Ap. J.*, Vol. 169, 1971, pp. 589–594.
72. PILCHER, C. B., S. T. RIDGEWAY, AND T. B. MCCORD, Galilean Satellites: Identification of Water Frost. *Science*, Vol. 178, 1972, p. 1087.
73. LEBOWSKY, L. A., *Chemical Composition of Saturn's Rings and Icy Satellites*. Ph.D. dissertation, M.I.T., Cambridge, Mass., 1973.
74. LEWIS, J. S., Low Temperature Condensation From the Solar Nebula. *Icarus*, Vol. 16, 1971, pp. 241–252.
75. LEWIS, J. S., Origin and Composition of the Terrestrial Planets and Satellites of the Outer Planets. In *Origin of the Solar System*, C.N.R.S., Paris, France, 1973.
76. MCCORD, T. B., T. V. JOHNSON, AND J. ELIAS, Saturn's Satellites: Narrowband Spectral Photometry (0.3 to 1.1 microns). *Ap. J.*, Vol. 165, 1971, pp. 413–424.
77. LEBOWSKY, L. S., T. V. JOHNSON, AND T. B. MCCORD, Saturn's Rings: Spectral Reflectivity and Compositional Implications. *Icarus*, Vol. 13, 1970, pp. 226–230.
78. FRANKLIN, F. A., AND A. F. COOK, Optical Properties of Saturn's Rings II: Two-Color Phase Curves of the Two Bright Rings. *Astron. J.*, Vol. 70, 1965, pp. 704–720.
79. CRUIKSHANK, D. P., Paper presented at International Astronomical Union, 40th Symposium, Marfa, Texas, October 1969.
80. PILCHER, C. B., C. R. CHAPMAN, L. A. LEBOWSKY, AND H. KIEFFER, Saturn's Rings: Identification of Water Frost. *Science*, Vol. 167, 1970, pp. 1372–1373.

Comets: Data, Problems, and Objectives

Fred L. Whipple
*Center for Astrophysics
Cambridge, Massachusetts*

A highly abridged review of new relevant results from the observations of Comet Kohoutek (1973f) is followed by an outline summary of our basic knowledge concerning comets, both subjects being confined to data related to the nature and origin of comets rather than the phenomena (for example, plasma phenomena are omitted).

The discussion then centers on two likely places of cometary origin in the developing solar system, the proto-Uranus-Neptune region versus the much more distant fragmented interstellar cloud region, now frequented by comets of the Öpik-Oort cloud. The Comet Kohoutek results add new insights, particularly with regard to the parent molecules and the nature of meteoric solids in comets, to restrict the range of the physical circumstances of comet formation.

A few fundamental and outstanding questions are asked, and a plea made for unmanned missions to comets and asteroids in order to provide definitive answers as to the nature and origin of comets, asteroids, and the solar system generally.

A Few of the Major Advances in Comet Knowledge From Observations of Comet Kohoutek (1973f)

The first radio observations of a comet leading to the discovery of the new parent molecules methyl cyanide (CH_3CN) and hydrogen cyanide (HCN) were made by Ulrich and Conklin (ref. 1) and Snyder et al. (ref. 2), respectively, both near 3-mm wavelengths. The latter investigators (ref. 3) find that HCN contributes approximately 1 percent and CH_3CN approximately 2 percent of the cometary molecular loss rate near perihelion, the total exceeding 100 T/s. They find evidence for radiation from ethyl alcohol ($\text{C}_2\text{H}_5\text{OH}$) at 86.247GHz and possibly SiO at 86.242GHz. Biraud et al. (ref. 4) and Turner (ref. 5) observed OH in absorption in two 18-cm lines, while Rydbeck et al. (ref. 6) and Black et al. (ref. 7) observed CH in emission at 9-cm wavelength. Hobbs et al. (ref. 8) observed continuum radiation at 3.7 and 2.8 cm, the first from a comet.

Lew and Heiber (ref. 9) and Herzberg and Lew (ref. 10) made a major step forward by identifying H_2O^+ bands which were measured by Benevenuti and Wurm (ref. 11) and by Wehinger et al. (ref. 12). Definitive studies of this vital ion should solidify our knowledge of the abundance and behavior of H_2O , apparently the most abundant and controlling material in comets.

From the Ames-NASA Convair 990, Blamont and Festou (ref. 13) established that the OH radical has a half-life of only 8.5 hours at 0.62 AU solar distance, an order of magnitude shorter than previously estimated. They thus find the radical being created within 15 000 km of the nucleus at a total rate of 10^{29} OH/s at 0.62 AU post-perihelion, January 15, 1974. This result, as a minimum rate loss for H_2O atoms, confirms beautifully the conclusion of Code and Savage (ref. 14) by L_α measurements from the Orbiting Astronomical Observatory (OAO) that Comet Bennett (1970II) was losing 10^{29} H_2O /Ster/s at a comparable solar distance, with an absolute magnitude about 2.5 magnitudes brighter than Kohoutek.

The prediction of an antitail by Sekanina (ref. 15) and its observation near perihelion first by Gibson from Skylab (ref. 16), then by Ney and Ney (ref. 17) in the infrared, followed by many observations in the post-perihelion period, establishes the expulsion of large particles (~ 1 mm) from the nucleus. Even though Kohoutek was not a "dusty" comet, based on its color (ref. 18) and the appearance of its visual spectrum, its red continuum (ref. 19) was very strong, and the comet was excessively bright in the infrared as measured by many observers. The observed microwave continuum probably represented thermal radiation from large particles, perhaps icy grains.

There is no time here to discuss the invaluable results from observations of $L\alpha$ and the far ultraviolet from Mariner 10, Skylab, and rockets, the numerous infrared measurements, and the extensive classical observations. Comet Kohoutek has been the most thoroughly observed comet in history. The completeness of the spectral record from He I at $\lambda 304 \text{ \AA}$ (negative result) to the cm-wave radio region will provide answers to a number of critical questions concerning comets. In particular these extensive data will give us the first precise measure of the mass ratio of volatile ices to meteoric solids, a ratio that is vital in determining the nature and place of origin. The extensive data, including a number of important negative results (NH_3 , CH_4 , He, and acetone), will certainly add other knowledge to restrict substantially the possibilities regarding the origin of comets.

Basic Facts and Deductions About the Nature of Comets

In discussing the role of comets in the evolution of the solar system we may confidently assume the following basic facts and deductions about their character:

1. *Comets are members of the solar system.* No evidence exists for orbits of interstellar origin (ref. 20).
2. *Comets have been stored for an unknown length of time in very large*

orbits in the Öpik-Oort cloud out to solar distances of tens of thousands of astronomical units (refs. 21 and 22). Perhaps 10^{11} comets with a total mass comparable to that of the Earth still remain, as Oort suggested.

3. *The basic cometary entity is a discrete nucleus (rarely, if ever, double) of kilometer dimensions consisting of ices and clathrates, including specifically H_2O , CH_3CN , HCN , CO_2 , and probably CO .* Other parent molecules of the abundant H, C, N, and O atoms mixed in an unknown fashion with a comparable amount of heavier elements as meteoric solids must occur in comets because of the observed radicals, molecules, and ions, C_2 , C_3 , CH , CN , NH , NH_2 , N_2^+ , CO^+ , and CH^+ (refs. 23 through 26).
4. *Cometary meteoroids are fragile and of low density (refs. 27, 28, and 29).*
5. *The comet nuclei as a whole must have never been heated much above a temperature of about 100 K for a long period of time, otherwise new comets could not show so much activity at large solar distances (Kohoutek (1973f), for example). Possible internal heating by radioactivity and temporary external heating, e.g., by supernovae, are not excluded.*
5. *Comets were formed in regions of low temperature, probably much below 100 K.*
6. *Comet nuclei are generally rotating, but in no apparent systematic fashion and with unknown periods in the range from about 3 hours to a few weeks, based on nongravitational motions and the delayed jet action of the icy nucleus.*
7. *The nuclei, at least of three tidally split comets, show evidence of a weak internal compressive strength the order of 10^4 to 10^6 dyn cm^{-2} (ref. 30) and evidence of little internal cohesive strength.*
8. *The surface material of active comets must be extremely friable and porous to permit the ejection by vapor pressure of solids and ices at great solar dis-*

tances. The evidence of clathrates by Delsemme and Swings (ref. 25), coupled with the probable ejection of ice grains at great solar distances (ref. 31), supports this deduction.

The following probable limits of cometary knowledge or negative conclusions appear valid:

1. *Roughly a solar abundance of elements may reasonably be assumed for the original material from which comets evolved.* Note Millman's (ref. 32) evidence regarding the relative abundances of Na, Mg, Ca, and Fe in cometary meteor spectra and the solar value of the $^{12}\text{C}/^{13}\text{C}$ ratio measured by Stawikowski and Greenstein (ref. 33) and Owen (ref. 34).
2. *The material in the region of comet formation (with roughly solar abundances of elements) could not have cooled slowly in quasi-equilibrium conditions from high temperatures.* The significant abundances of CO, CO₂, C₂, C₃, and now CH₃CN and HCN in comets, along with the low density and friability of the cometary meteoroids, indicate nonequilibrium cooling in which the carbon did not combine almost entirely into CH₄ and the meteoroids generally did not have time to aggregate into more coherent high-density solids before they agglomerated with ices.
3. *The existence of an original plane of formation of comets beyond some 3000 to 5000 AU appears to be unknowable.* The perturbations by passing stars would have so disturbed the orbits that the lack of evidence for a common plane in the motions of new comets tells nothing about the place or plane of origin (ref. 22). (Note exception in 4 below.)
4. *That the comets formed concurrently with the solar system some 4.6×10^9 yr ago is an assumption* based on the lack of a tenable theory for more recent or current formation. The lack of evi-

dence for a common plane of motion implies an origin remote in time or, if recent, no common plane of origin.

5. *The highly variable ratio of dust to gas observed from comet to comet proves a large variation in particle size distribution,* but has not yet been shown to measure a true variation in the dust/gas mass ratio. Periodic Comet Encke (P/Encke), for example, shows a low dust/gas ratio in its spectrum, but has contributed enormously to the interplanetary meteoroid population.

The Role of Comets in the Origin of the Solar System¹

The above evidence points conclusively to the origin of comets by the growth and agglomeration of small particles from gas (and dust?) at very low temperatures. But where? If concurrently with the origin of the solar system (and necessarily associated with it gravitationally), two locations in space are, a priori, possible: (1) in the other regions of the forming planetary system beyond proto-Saturn (refs. 24 and 35); or (2) in interstellar clouds gravitationally associated with the forming solar system but at proto-solar distances out to a moderate fraction of a parsec; that is to say, in orbits like those in the Öpik-Oort cloud of present-day comets (refs. 24, 44, and 52).

There can be little doubt that comets were the building blocks for the great outer planets Uranus and Neptune. The mean densities of these planets (ref. 53) are consistent with their origin largely from the accretion of comets, assumed to consist of the compounds possible (excluding H₂) in a solar mix of elements. This process of building Uranus

¹The reader is referred to reference 36 for a modern development of the Kant-LaPlace concept, including the important contributions by O. J. Schmidt and a general historical background of this general concept. For less general special treatments see references 35 and 37 through 44. For concepts of comet or solar system origin deviating from the "classical," see references 45 through 50 and especially Cameron and other contributors to the Symposium at Nice (ref. 51).

and Neptune is precisely analogous to building the terrestrial planets from planetesimals. Temperature was the controlling factor, being too high within the orbit of proto-Jupiter for water to freeze. For this reason Oort's (ref. 22) suggestion that the comets formed within the Jupiter region appears unlikely because asteroids clearly formed there. Similarly, Öpik's requirement for solid H_2 in the proto-Jupiter region appears untenable. Nevertheless, Oort's idea that comets were thrown out from the inner regions of the solar system by planetary perturbations is highly significant.

Thus, the possible origin of the presently observed comets in the Uranus-Neptune region rests solely on the premise that the major planets (or protoplanets) could indeed throw the comets into stable orbits with aphelia out to some 50 000 AU or more. The low efficiency of the process is only restrictive in the sense that too much angular momentum may be required of the outer planets to accomplish the feat successfully. Approximately a solar mass of comets in large orbits appears to be required as an end product, but a hundred solar masses may originally have been involved. Öpik (refs. 43 and 54) is doubtful about the process unless the comets formed near Jupiter; Everhart (ref. 55) finds it highly unlikely, while Levin (ref. 56) provides the angular momentum from proto-Uranus and proto-Neptune by forming these planets at very great solar distances (up to 200 AU) from a very large nebular mass and drawing them into their present orbits by the ejection of comets (mostly to infinity).

Everhart's doubts may possibly be removed if the space density of comets originally fell off rapidly with solar distance and if the supply at great distances (ref. 20) has been replenished by those in smaller orbits, more stable against stellar perturbations. Indeed, Öpik (ref. 21) showed that stellar perturbations will systematically increase perihelion distances to remove the comets from the region of perturbation by the outer planets. The number of comets thrown into the inner solar system during

the immediate post-nebula period could have been significant and may account for major crater formation on the Moon (ref. 57) and volatiles on the terrestrial planets (ref. 58).

Alternative 2—forming the comets directly in the orbits of the Öpik-Oort cloud—is highly attractive, except for the difficulty of agglomerating kilometer-sized bodies in the low-density fragmented interstellar clouds. Such a possibility must be demonstrated before one can accept the tempting solution to the problem. Öpik (ref. 43) finds the process quite impossible.

Let us now look to the comets themselves to see whether their structure can help us distinguish between the two possible regions of origin. Most conspicuous are the numerous carbon radicals, molecules, and ions not in low-temperature equilibrium with excess hydrogen. The gas, if once hot, could not have cooled slowly. Note too the friability and low density (0.5 to < 0.01 g/cm³) for meteoric "solids." Sekanina (private communication) finds evidence that for Comet Kohoutek the larger grains tend to shrink appreciably in a period of a few days. We must conclude that the ices, earthy material, and clathrates were all accumulated simultaneously at very low temperatures.

More specifically, the ices, clathrates, and "solids" collected together intimately in such a fashion that earthy molecules were somewhat bonded together in order to provide some degree of physical strength after the ices sublimated. Note that any sintering process to make the earthy grains coherent physically would remove the highly volatile substances necessary to provide the activity of Comet Kohoutek and other comets at great solar distances where the vapor pressure of H_2O is negligible. Thus, the process of grain growth must have involved the "whisker" type of growth commonly observed in laboratory crystals. *We can confidently visualize a comet as a complex lacy structure of "whiskers" and "snowflakes" that grew atom-by-atom and molecule-by-molecule while highly volatile molecules were trapped as clathrates.*

The temperature could have been sufficiently low for such cometary growth any-

where in space beyond perhaps 30 to 50 AU from the center of the proto-solar-system. Levin's (ref. 56) concept of comet growth up to 200 AU is entirely consistent with such growth, as is alternative 2, fragmented interstellar clouds at far greater distances. Safronov and Levin's requirement of excessive material (perhaps 30 to 100 times the present-day mass of Uranus and Neptune) to provide a reasonably rapid growth rate for Uranus and Neptune confirms Öpik's vehement denial that fragmented interstellar clouds may be capable of producing comets. Careful analysis of grain growth rates under imaginative sets of assumptions as to the nature and stability of such clouds is clearly needed. Note that a comet does not appear to be an aggregate of interstellar grains if, indeed, these grains are solids covered with icy mantles. Such grains would not cohere when exposed to solar radiation sublimating the ices.

At the present, then, we have no criterion to identify the unique region in space where comets formed, if indeed they all formed in the same general region. We need more precise knowledge concerning the identity and abundances of the more volatile parent molecules. Did CH_4 , CO, Ar, or Ne, for example, actually freeze out in comets? As Lewis (ref. 59) shows, the mass percentages of such volatiles can be used as thermometers. Even the dimensions of comet nuclei are uncertain, while we have no knowledge whatsoever of their detailed structure. Are they layered? Do they contain "pockets" of ices or "pockets" of dust? How fast do they rotate? What produces comet bursts in luminosity? What causes "new" comets to split?

Furthermore, we do not know whether comets generally or indeed any comets contain cores of asteroidal nature. It is tempting to identify many of the Apollo or Earth-orbit crossing asteroids as "burned-out" comets. Proof of a truly asteroidal core for an old comet would require a further knowledge of the chemistry and structure of the core to ascertain whether meteoric material collected first or whether radioactive heating drove out the volatiles. Such knowledge

would, of course, be invaluable in ascertaining the physical and chemical circumstances of the origin. No definitive answer is likely without such data.

It is clear that far more ground-based and space-based research on comets is necessary. Comet Kohoutek has shown that a massive attack on one comet can produce extraordinary results. There are too many comets to permit an overall observational attack on each one. Nevertheless, we need to accumulate data on all observable comets. A reasonable program is to institute massive observing programs from time to time for especially selected comets, while accumulating basic data for all comets.

Only space missions to comets can give us the "quantum jump" in knowledge necessary to solve the most fundamental problems of comets. Equally, we need to study a few asteroids at their surfaces to understand their nature and to identify the sources of meteorites. Because meteorites have given us extraordinary insight regarding early conditions in the developing solar system, we can expect asteroid space missions to answer some basic direct questions, while "calibrating" our laboratory data on meteorites. Furthermore, the extraordinary successes in exploring the Moon and Mars have given us limited data concerning the early phases of solar system formation because these bodies have been severely altered since they were originally agglomerated.

Space missions to comets and to asteroids are the essential next steps toward understanding how the solar system came into being. Such missions are entirely feasible in the present state of our space technology.

The following references are related to space missions to comets and asteroids:

- Report of the Comet and Asteroid Mission Study Panel*, NASA TM X-64677, 1972.
- Alfvén, H., and G. Arrhenius, Mission to an Asteroid. *Science*, Vol. 167, 1970, p. 139.
- Lüst, Reah, Cometary Probes. *Space Sci., Rev.*, Vol. 10, 1969, pp. 217-299.
- The 1973 Report and Recommendations of the NASA Science Advisory Committee on Comets and Asteroids*, NASA TM-X-71917, 1973.
- Physical Studies of Minor Planets*, T. Gehrels, ed., NASA SP-267, 1971.

- Proc. Cometary Science Working Group*, D. L. Roberts, ed., IIT Research Institute, 1971.
- Comets, Scientific Data and Missions*, E. Roemer and G. P. Kuiper, eds., Lunar and Planetary Laboratory, Univ. of Arizona, 1972.
- Nobel Symposium 21, From Plasma to Planet*, Aina Elvius, ed., Almquist and Wiksell, Stockholm, 1972.
- On the Origin of the Solar System*, Hubert Reeves, ed., Centre National de la Recherche Scientifique, Paris, 1972.
- Comets and Asteroids, Strategy for Exploration*, NASA TMX-64677, 1972.
- ## References
- ULRICH, B. L., AND E. K. CONKLIN, I.A.U. Circ. 2607, 1973.
 - SNYDER, L., V. BUHL, AND W. HUEBNER, *Icarus*, Vol. 23, 1974, p. 580.
 - SNYDER, L., V. BUHL, AND W. HUEBNER, A.A.S. DPS (abs.), April 1974.
 - BIRAUD, F., G. BOURGOIS, R. CROVISIER, R. FILIT, E. GÉRARD, AND I. KAZÉS, I.A.U. Circ. 2607, 1973.
 - TURNER, *Ap. J. Letters*, Vol. 189, L137, 1974.
 - RYDBECK, O. E. H., J. ELLDÉR, AND W. M. IRVINE, I.A.U. Circ. 2618, 1974.
 - BLACK, J. H., E. J. CHAISSON, J. A. BALL, H. PENFIELD, AND A. E. LILLEY, I.A.U. Circ. 2621, 1974.
 - HOBBS, R. W., S. P. MARAN, AND W. J. WEBSTER, JR., I.A.U. Circ. 2626, 1974.
 - LEW, H., AND I. HEIBER, *J. Chem. Phys.*, Vol. 58, 1973, p. 1246.
 - HERZBERG, G., AND H. LEW, I.A.U. Circ. 2618, 1974.
 - BENVENUTE, P., AND K. WURM, *Astron. and Astrophys.*, in press, 1974; I.A.U. Circ. 2628.
 - WEHINGER, P. A., S. WYCOFF, G. H. HERBIG, G. HERZBERG, AND H. LEW, *Ap. J. Letters*, in press, 1974.
 - BLAMONT, J., AND M. FESTOU, *Comptes Rend.*, in press, 1974.
 - CODE, A. D., AND B. D. SAVAGE, *Science*, Vol. 177, 1972, pp. 213-221.
 - SEKANINA, Z., I.A.U. Circular 2580, 1973.
 - Skylab, I.A.U. Circ. 2614, 1973.
 - NEY, E. P., AND W. F. NEY, I.A.U. Circ. 2616, 1974.
 - SHIPMAN, H. L., I.A.U. Circ. 2632, 1974.
 - ANDRILLAT, Y., I.A.U. Circ. 2610, 1973.
 - MARSDEN, B. G., AND Z. SEKANINA, *A. J.*, Vol. 78, 1973, pp. 1118-1124.
 - ÖPIK, E., *Proc. Amer. Acad. Arts and Sci.*, Vol. 67, 1932, pp. 169-183.
 - OORT, J. H., *Bull. Astr. Inst. Neth.*, Vol. 11, 1950, pp. 91-110.
 - WHIPPLE, F. L., *Ap. J.*, Vol. 111, 1950, p. 375.
 - WHIPPLE, F. L., *Ap. J.*, Vol. 113, 1951, pp. 464-474.
 - DELSEMMER, A. H., AND P. SWINGS, *Ann. d'Astrophys.*, Vol. 15, 1952, pp. 1-6.
 - SWINGS, P., *Quart. J. Roy. Ast. Soc.*, Vol. 6, 1965, pp. 28-69.
 - MCCROSKY, R. E., *A. J.*, Vol. 60, 1955, p. 170.
 - MCCROSKY, R. E., *A. J.*, Vol. 63, 1958, pp. 97-106.
 - JACCHIA, L. G., *Ap. J.*, Vol. 121, 1955, pp. 521-527.
 - ÖPIK, E. J., *Irish Ast. J.*, Vol. 7, 1966, pp. 141-161.
 - HEUBNER, W., AND A. WEIGERT, *Z. f. Astrophys.*, Vol. 64, 1966, pp. 185-201.
 - MILLMAN, P. M., *Nobel Symposium 21, From Plasma to Planet*, A. Elvius, ed., Almquist and Wiksell, Stockholm, 1972, pp. 156-166.
 - STAWIKOWSKI, A., AND J. L. GREENSTEIN, *Ap. J.*, Vol. 140, 1964, p. 1280.
 - OWEN, T., *Ap. J.*, Vol. 184, 1973, pp. 33-43.
 - KUIPER, G. P., *Astrophysics*, J. A. Hynek, ed., McGraw-Hill Book Co., N.Y., London, 1951, Ch. 8.
 - SAFRONOV, U. S., *Evolution of the Protoplanetary Cloud and Formation of the Earth and Planets*. Izdatel'stvo Nauka, Moscow, 1969; Translation published by NASA, 1972.
 - UREY, H. C., *The Planets, Their Origin and Development*, Yale Univ. Press, New Haven, 1952.
 - LEVIN, B., *L'Origine de la Terre et des Planets*, Moscow, 1958.
 - WHIPPLE, F. L., *Proc. National Acad. Sci.*, Vol. 52, 1964, p. 565.
 - ALFVÉN, H., AND G. ARRHENIUS, *Ap. & Sp. Sci.*, Vol. 8, 1970, pp. 338-421.
 - ALFVÉN, H., AND G. ARRHENIUS, *Ap. & Sp. Sci.*, Vol. 9, 1970, pp. 3-33.
 - Nobel Symposium 21, From Plasma to Planet*, A. Elvius, ed., Almquist and Wiksell, Stockholm, and Wiley & Sons, N.Y., London, Sydney, 1972.
 - ÖPIK, E. J., *Ap. & Sp. Sci.*, Vol. 21, 1973, pp. 307-398.
 - CAMERON, A. G. W., *Icarus*, Vol. 1, 1962, pp. 13-69.
 - SOUREK, J., *Mem. and Obs. of Czech. Ast. Soc.*, No. 7, Prague, 1946.
 - LYTTLETON, R. A., *Mon. Not. Roy. Ast. Soc.*, Vol. 108, 1948, p. 465.
 - WHIPPLE, F. L., *Sci. Amer.*, Vol. 178, 1948, pp. 34-45.
 - WHIPPLE, F. L., *Harv. Obs. Mon.*, No. 7, 1948, pp. 109-142.
 - TRULSEN, J., *Nobel Symposium 21, From Plasma to Planet*, A. Elvius, ed., Almquist and Wiksell, Stockholm, 1972, pp. 179-192.
 - O'DELL, C. R., *Icarus*, Vol. 19, 1973, pp. 137-146.
 - On the Origin of the Solar System*, Hubert Reeves, ed., Centre National de la Recherche

- Scientifique, Paris, 1972.
52. MCCREA, W. H., *Proc. Roy. Soc. (London)*, Vol. A256, 1960, pp. 245-266.
53. RAMSEY, W. H., *Planet. Space Sci.*, Vol. 15, 1967, pp. 1609-1633.
54. ÖPIK, E. J., *Mem. Soc. Roy. Sci. Liège*, Ser. 5, Vol. 12, 1965, pp. 523-574.
55. EVERHART, E., *A. J.*, Vol. 73, 1973, pp. 329-337.
56. LEVIN, B., *On the Origin of the Solar System*, Symposium at Nice, Centre National de la Recherche Scientifique, Paris, 1972.
57. HARTMANN, W. K., *Ap. & Sp. Sci.*, Vol. 17, 1972, pp. 48-64.
58. LEWIS, J. S., *Science*, Vol. 186, 1974, p. 440.
59. LEWIS, J. S., *Icarus*, Vol. 16, 1972, p. 241.
60. ÖPIK, E. J., *Advances in Astronomy and Astrophysics*, Z. Kopal, ed., Academic Press, Vol. 2, 1963, pp. 219-262.